

AD-A204 329

NUMERICAL SIMULATION OF ACTIVE CONTROL  
OF BOUNDARY LAYER TRANSITION

by

Linda D. Kral and Hermann F. Fasel

Prepared from work done under Grant

<sup>84-</sup>  
ONR-N00014-K-0515

DTIC  
ELECTE  
FEB 03 1989  
S D CS



DISTRIBUTION STATEMENT A  
Approved for public release  
Distribution Unlimited

Department of Aerospace and Mechanical Engineering

University of Arizona

Tucson, Arizona 85721

December 1988

89 1 03 053

NUMERICAL SIMULATION OF ACTIVE CONTROL  
OF BOUNDARY LAYER TRANSITION

by

Linda D. Kral and Hermann F. Fasel

Prepared from work done under Grant

ONR-N00014-K-0515



Accession For	
NTIS CRA&I	<input checked="checked" type="checkbox"/>
DTIC TAB	<input type="checkbox"/>
Unannounced	<input type="checkbox"/>
Justification	
By <i>per lti</i>	
Distribution	
Availability Codes	
Dist	Avail. and/or Special
<i>A-1</i>	

Department of Aerospace and Mechanical Engineering

University of Arizona

Tucson, Arizona 85721

December 1988

## ACKNOWLEDGMENTS

This work was carried out by the transition research group under the sponsorship of the Office of Naval Research (ONR Grant Number N00014-K-0515). Support was also provided by the NASA Graduate Student Researchers Program (NASA Grant Number NGT-03002809). The support by both the Office of Naval Research and NASA is gratefully acknowledged.

## TABLE OF CONTENTS

	Page
LIST OF ILLUSTRATIONS . . . . .	10
LIST OF TABLES . . . . .	22
ABSTRACT . . . . .	23
1. INTRODUCTION . . . . .	25
1.1 Boundary Layer Transition . . . . .	26
1.2 Passive Control . . . . .	31
1.3 Active Control . . . . .	35
2. PROBLEM STATEMENT . . . . .	43
3. GOVERNING EQUATIONS . . . . .	49
3.1 Equations of Motion in Primitive Variable Representation . . . . .	49
3.2 Nondimensionalization . . . . .	52
3.3 Equations of Motion in Vorticity-Velocity Representation . . . . .	55
3.4 Viscosity Variation with Temperature . . . . .	62
4. BOUNDARY AND INITIAL CONDITIONS . . . . .	64
4.1 Time Domain for Passive Control . . . . .	64
4.2 Time Domain for Active Control . . . . .	65
4.3 Coordinate System and Spatial Domain . . . . .	66
4.4 Boundary and Initial Conditions for the Undisturbed Flow . . . . .	66
4.4.1 Initial Conditions for the Undisturbed Flow . . . . .	68
4.4.2 Inflow Boundary Conditions for the Undisturbed Flow . . . . .	68
4.4.3 Outflow Boundary Conditions for the Undisturbed Flow . . . . .	69
4.4.4 Outer Boundary Conditions for the Undisturbed Flow . . . . .	69
4.4.5 Wall Boundary Conditions for the Undisturbed Flow . . . . .	70
4.5 Boundary and Initial Conditions for the Disturbed Flow . . . . .	72
4.5.1 Initial Conditions for the Disturbed Flow . . . . .	72



4.5.2	Lateral Boundary Conditions for the Disturbed Flow . . .	73
4.5.3	Inflow Boundary Conditions for the Disturbed Flow . . .	74
4.5.4	Outflow Boundary Conditions for the Disturbed Flow . . .	74
4.5.5	Outer Boundary Conditions for the Disturbed Flow . . .	77
4.5.6	Wall Boundary Conditions for the Disturbed Flow . . . .	78
5.	NUMERICAL METHOD . . . . .	82
5.1	Computational Domain . . . . .	83
5.2	Spanwise Spectral Approximation . . . . .	84
5.2.1	Boundary and Initial Conditions in Fourier Space for the Undisturbed Flow . . . . .	88
5.2.2	Boundary and Initial Conditions in Fourier Space for the Disturbed Flow . . . . .	89
5.3	Implicit Finite Difference Method . . . . .	97
5.3.1	Discretization of the Governing Equations in Fourier Space . . . . .	99
5.3.2	Discretization of the Undisturbed Flow Boundary and Initial Conditions . . . . .	104
5.3.3	Discretization of the Disturbed Flow Boundary and Initial Conditions . . . . .	109
5.3.4	Solution of the Tridiagonal Systems . . . . .	123
5.3.5	Evaluation of the Nonlinear Terms . . . . .	126
5.3.6	Viscosity Calculation . . . . .	127
5.4	Consistency, Stability, and Convergence . . . . .	129
6.	RESULTS . . . . .	132
6.1	Passive Control of Linear Disturbances . . . . .	132
6.1.1	Uncontrolled Linear Disturbances . . . . .	136
6.1.2	Uniform Passive Control Applied to Linear Disturbances . . . . .	141
6.1.3	Nonuniform Passive Control Applied to Linear Disturbances . . . . .	152
6.2	Active Control of Linear Disturbances . . . . .	160
6.2.1	Receptivity of a Surface Heater Strip . . . . .	161

6.2.2 Active Control Using a Surface Heater Strip . . . . .	166
6.3 Passive Control of Secondary Instability . . . . .	170
6.3.1 Passive Control of the Fundamental Breakdown Process . .	171
6.3.2 Passive Control of the Subharmonic Breakdown Process .	179
6.4 Active Control of Secondary Instability . . . . .	184
7. CONCLUSIONS . . . . .	195
FIGURES . . . . .	199
APPENDIX A: SIMILARITY SOLUTION OF THE FLAT PLATE BOUNDARY LAYER WITH UNIFORM WALL HEATING . . . . .	394
APPENDIX B: SOLUTION OF THE THREE-DIMENSIONAL ORR-SOMMERFELD EQUATION . . . . .	397
REFERENCES . . . . .	402

## LIST OF ILLUSTRATIONS

Figure		Page
1.1	Spatial stability diagram for a flat plate boundary layer (from Jordinson (1970)) . . . . .	199
4.1	Time history of input disturbance for passive control simulations .	200
4.2	Time history of input disturbances for active control simulations .	200
4.3	Spatial domain and coordinate system . . . . .	201
4.4	Boundary conditions for the undisturbed flow . . . . .	202
4.5	Boundary conditions for the disturbed flow . . . . .	203
5.1	Spatial computational domain . . . . .	205
5.2	Computational molecule . . . . .	205
6.1	Solution domain for linear Navier-Stokes calculations a) stability diagram from experiments of Strazisar, Reshotko, and Prahl (1977) b) stability diagram from linear stability theory of Lowell (1974) .	206
6.2	Viscosity variation with temperature . . . . .	207
6.3	First derivative of viscosity versus temperature . . . . .	207
6.4	Second derivative of viscosity versus temperature . . . . .	208
6.5	Undisturbed flow without control applied, $F = 1$ a) streamwise velocity, $u_{ST}$ , b) normal velocity, $v_{ST}$ , c) spanwise vorticity, $\omega_{zST}$ , d) temperature, $T_{ST}$ . . . . .	209
6.6	Growth of undisturbed boundary layer without control applied, $F = 1$ . . . . .	211
6.7	Comparison of skin friction without control applied, $F = 1$ . . . .	211
6.8	Velocity divergence of the undisturbed flow without control	

	applied, $F = 1$	
	a) with heater strip, b) without heater strip . . . . .	212
6.9	Uncontrolled disturbed flow after nine periods of oscillation, $F = 1$	
	a) 2D streamwise velocity, $U_0$ , b) 2D normal velocity, $V_0$ , c) 2D spanwise vorticity, $\Omega_{z_0}$ , d) 2D temperature, $\Theta_0$ e) 3D streamwise velocity, $U_1$ , f) 3D normal velocity, $V_1$ , g) 3D spanwise velocity, $W_1$ , h) 3D streamwise vorticity, $\Omega_{x_1}$ , i) 3D normal vorticity, $\Omega_{y_1}$ , j) 3D spanwise vorticity, $\Omega_{z_1}$ , k) 3D temperature, $\Theta_1$ . . . . .	213
6.10	Velocity divergence of the uncontrolled disturbed flow, $F = 1$	
	a) mode 0, b) mode 1 . . . . .	224
6.11	Vorticity divergence of the uncontrolled disturbed flow, $F = 1$ . . . . .	225
6.12	Amplitude and phase comparison with linear stability theory without control applied, $F = 1$	
	a) 2D streamwise velocity, $U_0$ , b) 2D normal velocity, $V_0$ , c) 2D spanwise vorticity, $\Omega_{z_0}$ , d) 3D streamwise velocity, $U_1$ , e) 3D normal velocity, $V_1$ , f) 3D spanwise velocity, $W_1$ , g) 3D streamwise vorticity, $\Omega_{x_1}$ , h) 3D normal vorticity, $\Omega_{y_1}$ , i) 3D spanwise vorticity, $\Omega_{z_1}$ . . . . .	226
6.13	Uncontrolled disturbed flow after eleven periods of oscillation, $F = 1.55$	
	a) 2D streamwise velocity, $U_0$ , b) 3D streamwise velocity, $U_1$ . . . . .	235
6.14	Amplitude and phase comparison with linear stability theory without control applied, $F = 1.55$	
	a) 2D streamwise velocity, $U_0$ , b) 3D streamwise velocity, $U_1$ . . . . .	237
6.15	Undisturbed flow with uniform passive heating applied, $\Delta \bar{T} = 8^\circ F$ , $F = 1$	
	a) streamwise velocity, $u_{ST}$ , b) normal velocity, $v_{ST}$ , c) spanwise vorticity, $\omega_{zST}$ , d) temperature, $T_{ST}$ . . . . .	239
6.16	Growth of undisturbed boundary layer with uniform passive heating applied, $F = 1$ . . . . .	241
6.17	Comparison of skin friction with uniform passive heating applied, $F = 1$ . . . . .	241

- 6.18 Disturbed flow after nine periods of oscillation with  $\Delta T = 8^\circ F$  passive control applied,  $F = 1$
- a) 2D streamwise velocity,  $U_0$ , b) 2D normal velocity,  $V_0$ ,
  - c) 2D spanwise vorticity,  $\Omega_{x_0}$ , d) 2D temperature,  $\Theta_0$
  - e) 3D streamwise velocity,  $U_1$ , f) 3D normal velocity,  $V_1$ ,
  - g) 3D spanwise velocity,  $W_1$ , h) 3D streamwise vorticity,  $\Omega_{x_1}$ ,
  - i) 3D normal vorticity,  $\Omega_{y_1}$ , j) 3D spanwise vorticity,  $\Omega_{z_1}$ ,
  - k) 3D temperature,  $\Theta_1$  . . . . . 242
- 6.19 Amplitude and phase comparison at  $Re_{\delta_1} = 800$  with uniform passive control applied,  $F = 1$
- a) 2D streamwise velocity,  $U_0$ , b) 2D normal velocity,  $V_0$ ,
  - c) 2D spanwise vorticity,  $\Omega_{x_0}$ , d) 2D temperature,  $\Theta_0$
  - e) 3D streamwise velocity,  $U_1$ , f) 3D normal velocity,  $V_1$ ,
  - g) 3D spanwise velocity,  $W_1$ , h) 3D streamwise vorticity,  $\Omega_{x_1}$ ,
  - i) 3D normal vorticity,  $\Omega_{y_1}$ , j) 3D spanwise vorticity,  $\Omega_{z_1}$ ,
  - k) 3D temperature,  $\Theta_1$  . . . . . 253
- 6.20 Influence of uniform passive control on the amplitude growth,  $F = 1$
- a) first maximum of the 2D streamwise velocity,  $U_0$ ,
  - b) first maximum of the 3D streamwise velocity,  $U_1$  . . . . . 264
- 6.21 Influence of uniform passive control on the growth rates  $\alpha_i$ ,  $F = 1$
- a) first maximum of the 2D streamwise velocity,  $U_0$ ,
  - b) maximum of the 2D normal velocity,  $V_0$ ,
  - c) first maximum of the 3D streamwise velocity,  $U_1$ ,
  - d) maximum of the 3D normal velocity,  $V_1$  . . . . . 265
- 6.22 Influence of uniform passive control on the wavenumbers  $\alpha_r$ ,  $F = 1$
- a) maximum of the 2D normal velocity,  $V_0$ ,
  - b) maximum of the 3D normal velocity,  $V_1$  . . . . . 267
- 6.23 Disturbed flow after eleven periods of oscillation with  $\Delta T = 8^\circ F$  passive control applied,  $F = 1.55$
- a) 2D streamwise velocity,  $U_0$ , b) 3D streamwise velocity,  $U_1$  . . . 268
- 6.24 Amplitude and phase comparison at  $Re_{\delta_1} = 800$  with uniform passive control applied,  $F = 1.55$
- a) 2D streamwise velocity,  $U_0$ , b) 3D streamwise velocity,  $U_1$  . . . 270

- 6.25 Influence of uniform passive control on the amplitude growth,  $F = 1.55$   
 a) first maximum of the 2D streamwise velocity,  $U_0$ ,  
 b) first maximum of the 3D streamwise velocity,  $U_1$  . . . . . 272
- 6.26 Influence of uniform passive control on the growth rates  $\alpha_i$ ,  $F = 1.55$   
 a) first maximum of the 2D streamwise velocity,  $U_0$ ,  
 b) maximum of the 2D normal velocity,  $V_0$ ,  
 c) first maximum of the 3D streamwise velocity,  $U_1$ ,  
 d) maximum of the 3D normal velocity,  $V_1$  . . . . . 273
- 6.27 Influence of uniform passive control on the wavenumbers  $\alpha_r$ ,  $F = 1.55$   
 a) maximum of the 2D normal velocity,  $V_0$ ,  
 b) maximum of the 3D normal velocity,  $V_1$  . . . . . 275
- 6.28 Comparison of amplification rates for uniform passive control with theory and experiment,  $F = 1$   
 a) first maximum of the 2D streamwise velocity,  $U_0$ ,  
 b) maximum of the 2D normal velocity,  $V_0$  . . . . . 276
- 6.29 Comparison of amplification rates for uniform passive control with theory and experiment,  $F = 1.55$   
 a) first maximum of the 2D streamwise velocity,  $U_0$ ,  
 b) maximum of the 2D normal velocity,  $V_0$  . . . . . 277
- 6.30 Comparison of amplification rates for the uncontrolled flow at the first maximum of the 2D streamwise velocity,  $U_0$   
 a) comparison of nonparallel theories and experiments,  $F = 1$   
 b) comparison of nonparallel theory and experiments,  $F = 1.55$  . . 278
- 6.31 Comparison of neutral points for uniform passive control with theory and experiment,  $F = 1$   
 a) first maximum of the 2D streamwise velocity,  $U_0$   
 b) maximum of the 2D normal velocity,  $V_0$  . . . . . 279
- 6.32 Power law temperature distributions for  $\Delta \bar{T} = A_0 x_n^p = 8^\circ F$  at  $Re_{\delta_1} = 800$   
 a)  $F = 1$ , b)  $F = 1.55$  . . . . . 280
- 6.33 Undisturbed temperature distributions with nonuniform passive heating applied,  $\Delta \bar{T} = A_0 x_n^p = 8^\circ F$  at  $Re_{\delta_1} = 800$ ,  $F = 1$

- a)  $p = -0.5$ , b)  $p = 1.0$  . . . . . 281
- 6.34 Growth of undisturbed boundary layer with nonuniform passive heating applied,  $\Delta\bar{T} = A_0 x_n^p$ ,  $F = 1$   
 a)  $p = -0.5$ , b)  $p = 1.0$  . . . . . 282
- 6.35 Comparison of skin friction with nonuniform passive heating applied,  $\Delta\bar{T} = A_0 x_n^p$ ,  $F = 1$   
 a)  $p = -0.5$ , b)  $p = 1.0$  . . . . . 283
- 6.36 Disturbed flow after nine periods of oscillation with nonuniform surface temperature distribution  
 $\Delta\bar{T} = A_0 x_n^{-0.5} = 8^\circ F$  at  $Re_{\delta_1} = 800$  passive control applied,  $F = 1$   
 a) 2D streamwise velocity,  $U_0$ , b) 3D streamwise velocity,  $U_1$  . . . 284
- 6.37 Disturbed flow after nine periods of oscillation with nonuniform surface temperature distribution  
 $\Delta\bar{T} = A_0 x_n^{1.0} = 8^\circ F$  at  $Re_{\delta_1} = 800$  passive control applied,  $F = 1$   
 a) 2D streamwise velocity,  $U_0$ , b) 3D streamwise velocity,  $U_1$  . . . 286
- 6.38 Amplitude and phase comparison at  $Re_{\delta_1} = 800$  with  $\Delta\bar{T} = A_0 x_n^{-0.5}$  nonuniform passive control applied,  $F = 1$   
 a) 2D streamwise velocity,  $U_0$ , b) 3D streamwise velocity,  $U_1$  . . . 288
- 6.39 Amplitude and phase comparison at  $Re_{\delta_1} = 800$  with  $\Delta\bar{T} = A_0 x_n^{1.0}$  nonuniform passive control applied,  $F = 1$   
 a) 2D streamwise velocity,  $U_0$ , b) 3D streamwise velocity,  $U_1$  . . . 290
- 6.40 Influence of nonuniform passive control on the amplitude growth for  $A_0 x_n^{-0.5}$ ,  $F = 1$   
 a) first maximum of the 2D streamwise velocity,  $U_0$ ,  
 b) first maximum of the 3D streamwise velocity,  $U_1$  . . . . . 292
- 6.41 Influence of nonuniform passive control on the amplitude growth for  $A_0 x_n^{1.0}$ ,  $F = 1$   
 a) first maximum of the 2D streamwise velocity,  $U_0$ ,  
 b) first maximum of the 3D streamwise velocity,  $U_1$  . . . . . 293
- 6.42 Influence of nonuniform heating on the growth rates  $\alpha_i$ ,  $F = 1$   
 a) first maximum of the 2D streamwise velocity,  $U_0$  ( $p = -0.5$ ),  
 b) maximum of the 2D normal velocity,  $V_0$  ( $p = -0.5$ ),  
 c) first maximum of the 3D streamwise velocity,  $U_1$  ( $p = -0.5$ ),  
 d) maximum of the 3D normal velocity,  $V_1$  ( $p = -0.5$ ) . . . . . 294

- 6.43 Influence of nonuniform heating on the growth rates  $\alpha_i$ ,  $F = 1$   
 a) first maximum of the 2D streamwise velocity,  $U_0$  ( $p = 1.0$ ),  
 b) maximum of the 2D normal velocity,  $V_0$  ( $p = 1.0$ ),  
 c) first maximum of the 3D streamwise velocity,  $U_1$  ( $p = 1.0$ ),  
 d) maximum of the 3D normal velocity,  $V_1$  ( $p = 1.0$ ) . . . . . 296
- 6.44 Influence of nonuniform heating on the wavenumbers  $\alpha_r$ ,  $F = 1$   
 a) maximum of the 2D normal velocity,  $V_0$   $p = -0.5$ ),  
 b) maximum of the 3D normal velocity,  $V_1$   $p = -0.5$ ) . . . . . 298
- 6.45 Influence of nonuniform heating on the wavenumbers  $\alpha_r$ ,  $F = 1$   
 a) maximum of the 2D normal velocity,  $V_0$  ( $p = 1.0$ ),  
 b) maximum of the 3D normal velocity,  $V_1$  ( $p = 1.0$ ) . . . . . 299
- 6.46 Disturbed flow after eleven periods of oscillation with nonuniform surface temperature distribution  $\Delta\bar{T} = A_0 x_n^{-0.5} = 8^\circ F$  at  $Re_{\delta_1} = 800$  passive control applied,  $F = 1.55$   
 a) 2D streamwise velocity,  $U_0$ , b) 3D streamwise velocity,  $U_1$  . . . 300
- 6.47 Disturbed flow after eleven periods of oscillation with nonuniform surface temperature distribution  $\Delta\bar{T} = A_0 x_n^{1.0} = 8^\circ F$  at  $Re_{\delta_1} = 800$  passive control applied,  $F = 1.55$   
 a) 2D streamwise velocity,  $U_0$ , b) 3D streamwise velocity,  $U_1$  . . . 302
- 6.48 Amplitude and phase comparison at  $Re_{\delta_1} = 800$  with  $\Delta\bar{T} = A_0 x_n^{-0.5}$  nonuniform passive control applied,  $F = 1.55$   
 a) 2D streamwise velocity,  $U_0$ , b) 3D streamwise velocity,  $U_1$  . . . 304
- 6.49 Amplitude and phase comparison at  $Re_{\delta_1} = 800$  with  $\Delta\bar{T} = A_0 x_n^{1.0}$  nonuniform passive control applied,  $F = 1.55$   
 a) 2D streamwise velocity,  $U_0$ , b) 3D streamwise velocity,  $U_1$  . . . 306
- 6.50 Influence of nonuniform passive control on the amplitude growth for  $A_0 x_n^{-0.5}$ ,  $F = 1.55$   
 a) first maximum of the 2D streamwise velocity,  $U_0$ ,  
 b) first maximum of the 3D streamwise velocity,  $U_1$  . . . . . 308
- 6.51 Influence of nonuniform passive control on the amplitude growth for  $A_0 x_n^{1.0}$ ,  $F = 1.55$   
 a) first maximum of the 2D streamwise velocity,  $U_0$ ,  
 b) first maximum of the 3D streamwise velocity,  $U_1$  . . . . . 309
- 6.52 Influence of nonuniform heating on the growth rates  $\alpha_i$ ,  $F = 1.55$



- a) first maximum of the 2D streamwise velocity,  $U_0$  ( $p = -0.5$ ),
  - b) maximum of the 2D normal velocity,  $V_0$  ( $p = -0.5$ ),
  - c) first maximum of the 3D streamwise velocity,  $U_1$  ( $p = -0.5$ ),
  - d) maximum of the 3D normal velocity,  $V_1$  ( $p = -0.5$ ) . . . . . 310
- 6.53 Influence of nonuniform heating on the growth rates  $\alpha_i$ ,  $F = 1.55$ 
  - a) first maximum of the 2D streamwise velocity,  $U_0$  ( $p = 1.0$ ),
  - b) maximum of the 2D normal velocity,  $V_0$  ( $p = 1.0$ ),
  - c) first maximum of the 3D streamwise velocity,  $U_1$  ( $p = 1.0$ ),
  - d) maximum of the 3D normal velocity,  $V_1$  ( $p = 1.0$ ) . . . . . 312
- 6.54 Influence of nonuniform heating on the wavenumbers  $\alpha_r$ ,  $F = 1.55$ 
  - a) maximum of the 2D normal velocity,  $V_0$  ( $p = -0.5$ ),
  - b) maximum of the 3D normal velocity,  $V_1$  ( $p = -0.5$ ) . . . . . 314
- 6.55 Influence of nonuniform heating on the wavenumbers  $\alpha_r$ ,  $F = 1.55$ 
  - a) maximum of the 2D normal velocity,  $V_0$  ( $p = 1.0$ ),
  - b) maximum of the 3D normal velocity,  $V_1$  ( $p = 1.0$ ) . . . . . 315
- 6.56 Comparison of wall heat input and level of control achieved,  
 $F = 1$ 
  - a) first maximum of the 2D streamwise velocity,  $U_0$ ,
  - b) first maximum of the 3D streamwise velocity,  $U_1$  . . . . . 316
- 6.57 Comparison of wall heat input and level of control achieved,  
 $F = 1.55$ 
  - a) first maximum of the 2D streamwise velocity,  $U_0$ ,
  - b) first maximum of the 3D streamwise velocity,  $U_1$  . . . . . 317
- 6.58 Comparison of amplification rates for nonuniform passive control  
( $p = -0.5$ ) with theory and experiment,  $F = 1$ 
  - a) first maximum of the 2D streamwise velocity,  $U_0$ ,
  - b) maximum of the 2D normal velocity,  $V_0$  . . . . . 318
- 6.59 Comparison of amplification rates for nonuniform passive control  
( $p = 1.0$ ) with theory and experiment,  $F = 1$ 
  - a) first maximum of the 2D streamwise velocity,  $U_0$ ,
  - b) maximum of the 2D normal velocity,  $V_0$  . . . . . 319
- 6.60 Comparison of amplification rates for nonuniform passive control  
( $p = -0.5$ ) with theory and experiment,  $F = 1.55$ 
  - a) first maximum of the 2D streamwise velocity,  $U_0$ ,
  - b) maximum of the 2D normal velocity,  $V_0$  . . . . . 320

- 6.61 Comparison of amplification rates for nonuniform passive control ( $p = 1.0$ ) with theory and experiment,  $F = 1.55$   
 a) first maximum of the 2D streamwise velocity,  $U_0$ ,  
 b) maximum of the 2D normal velocity,  $V_0$  . . . . . 321
- 6.62 Comparison of heat transferred to heater strip for four different widths of heater strips . . . . . 322
- 6.63 Comparison of spanwise wall vorticity amplitude  $\Omega_{z_0}$  for different amounts of heat input and heater strip width . . . . . 322
- 6.64 Comparison of receptivity at a suction surface hard wall junction from theoretical analysis of Heinrich, Choudari, and Kerschen (1988).  $F(d)$  is the receptivity coefficient defined as the ratio between the Tollmien-Schlichting amplitude and the input amplitude and  $d$  is the width of the suction blowing strip. The distance from the leading edge is defined by  $l$ , the location of the neutral stability point is defined by  $l_{nsp}$ , and the location of maximum growth is defined by  $l_{max \text{ growth rate}}$  . . . . . 323
- 6.65 Amplitude and phase comparison with linear stability theory over heater strip,  $Re_{\delta_1} = 576$ ,  $F = 1$   
 a) 2D streamwise velocity,  $U_0$ , b) 2D normal velocity,  $V_0$ ,  
 c) 2D spanwise vorticity,  $\Omega_{z_0}$ , d) 2D temperature,  $\Theta_0$  . . . . . 324
- 6.66 Amplitude and phase comparison with linear stability theory near heater strip,  $Re_{\delta_1} = 646$ ,  $F = 1$   
 a) 2D streamwise velocity,  $U_0$ , b) 2D normal velocity,  $V_0$ ,  
 c) 2D spanwise vorticity,  $\Omega_{z_0}$ , d) 2D temperature,  $\Theta_0$  . . . . . 328
- 6.67 Schematic of surface heater strip arrangement for active control simulations . . . . . 332
- 6.68 Undisturbed temperature distribution for active control simulations . . . . . 332
- 6.69 Disturbed flow with out of phase active control applied,  $F = 1$   
 a) 2D streamwise velocity,  $U_0$ , b) 3D streamwise velocity,  $U_1$  . . . 333
- 6.70 Disturbed flow with in phase active control applied,  $F = 1$   
 a) 2D streamwise velocity,  $U_0$ , b) 3D streamwise velocity,  $U_1$  . . . 335

- 6.71 Comparison of amplitude profiles with active control applied,  $F = 1$   
 a) 2D streamwise velocity,  $U_0$ , b) 3D streamwise velocity,  $U_1$  . . . 337
- 6.72 Influence of active control on the amplitude growth,  $F = 1$   
 a) 2D streamwise velocity,  $U_0$ , b) 3D streamwise velocity,  $U_1$  . . . 338
- 6.73 Uncontrolled disturbed flow for fundamental breakdown,  $F_{2D} = 0.588$ ,  $F_{3D} = 0.588$   
 a) 2D streamwise velocity,  $U_0$ , b) 3D streamwise velocity,  $U_1$  . . . 339
- 6.74 Disturbed flow for fundamental breakdown with  $\Delta\bar{T} = 15^\circ F$  control applied,  $F_{2D} = 0.588$ ,  $F_{3D} = 0.588$   
 a) 2D streamwise velocity,  $U_0$ , b) 3D streamwise velocity,  $U_1$ ,  
 c) 2D temperature,  $\Theta_0$ , d) 3D temperature,  $\Theta_1$  . . . 340
- 6.75 Amplitude and phase comparison at  $x = 10.65$  for fundamental breakdown with uniform passive control applied  
 a) 2D streamwise velocity,  $U_0$ ,  $F_{2D}$ ,  
 b) 2D streamwise velocity,  $U_0$ ,  $2 F_{2D}$ ,  
 c) 3D streamwise velocity,  $U_1$ ,  $F_{3D}$ ,  
 d) 3D streamwise velocity,  $U_1$ ,  $2 F_{3D}$ ,  
 e) 3D streamwise velocity,  $U_1$ , mean component . . . 342
- 6.76 Influence of uniform passive control on the amplitude growth for fundamental breakdown  
 a) 3D streamwise velocity,  $U_1$ , mean component,  
 b) 2D streamwise velocity,  $U_0$ ,  $F_{2D}$ ,  
 c) 3D streamwise velocity,  $U_1$ ,  $F_{3D}$  . . . 346
- 6.77 Comparison of the disturbed flow for fundamental breakdown without control applied and with uniform passive heating applied at the peak plane in the spanwise direction  
 a) streamwise velocity,  $u$ ,  $z = 0$  and  $\Delta\bar{T} = 0^\circ F$   
 b) streamwise velocity,  $u$ ,  $z = 0$  and  $\Delta\bar{T} = 15^\circ F$   
 c) normal velocity,  $v$ ,  $z = 0$  and  $\Delta\bar{T} = 0^\circ F$   
 d) normal velocity,  $v$ ,  $z = 0$  and  $\Delta\bar{T} = 15^\circ F$   
 e) spanwise velocity,  $w$ ,  $z = \lambda_z/4$  and  $\Delta\bar{T} = 0^\circ F$   
 f) spanwise velocity,  $w$ ,  $z = \lambda_z/4$  and  $\Delta\bar{T} = 15^\circ F$   
 g) streamwise vorticity,  $\omega_x$ ,  $z = \lambda_z/4$  and  $\Delta\bar{T} = 0^\circ F$   
 h) streamwise vorticity,  $\omega_x$ ,  $z = \lambda_z/4$  and  $\Delta\bar{T} = 15^\circ F$   
 i) normal vorticity,  $\omega_y$ ,  $z = \lambda_z/4$  and  $\Delta\bar{T} = 0^\circ F$   
 j) normal vorticity,  $\omega_y$ ,  $z = \lambda_z/4$  and  $\Delta\bar{T} = 15^\circ F$

- k) spanwise vorticity,  $\omega_z$ ,  $z = 0$  and  $\Delta\bar{T} = 0^\circ F$   
 l) spanwise vorticity,  $\omega_z$ ,  $z = 0$  and  $\Delta\bar{T} = 15^\circ F$   
 m) temperature,  $T$ ,  $z = 0$  and  $\Delta\bar{T} = 15^\circ F$  . . . . . 348
- 6.78 Comparison of the disturbed flow for fundamental breakdown without control applied and with uniform passive heating applied at  $y = 3.186$   
 a) streamwise vorticity,  $\omega_x$ ,  $\Delta\bar{T} = 0^\circ F$   
 b) streamwise vorticity,  $\omega_x$ ,  $\Delta\bar{T} = 15^\circ F$  . . . . . 355
- 6.79 Comparison of the disturbed flow for fundamental breakdown without control applied and with uniform passive heating applied at  $x = 11.0$   
 a) streamwise vorticity,  $\omega_x$ ,  $\Delta\bar{T} = 0^\circ F$   
 b) streamwise vorticity,  $\omega_x$ ,  $\Delta\bar{T} = 15^\circ F$   
 c) normal vorticity,  $\omega_y$ ,  $\Delta\bar{T} = 0^\circ F$   
 d) normal vorticity,  $\omega_y$ ,  $\Delta\bar{T} = 15^\circ F$   
 e) spanwise vorticity,  $\omega_z$ ,  $\Delta\bar{T} = 0^\circ F$   
 f) spanwise vorticity,  $\omega_z$ ,  $\Delta\bar{T} = 15^\circ F$  . . . . . 356
- 6.80 Uncontrolled disturbed flow for subharmonic breakdown,  $F_{2D} = 1.24$ ,  $F_{3D} = 0.62$   
 a) 2D streamwise velocity,  $U_0$ , b) 3D streamwise velocity,  $U_1$  . . . 359
- 6.81 Disturbed flow for subharmonic breakdown with  $\Delta\bar{T} = 15^\circ F$  control applied,  $F_{2D} = 1.24$ ,  $F_{3D} = 0.62$   
 a) 2D streamwise velocity,  $U_0$ , b) 3D streamwise velocity,  $U_1$ ,  
 c) 2D temperature,  $\Theta_0$ , d) 3D temperature,  $\Theta_1$  . . . . . 360
- 6.82 Amplitude and phase comparison at  $x = 3.0$  for subharmonic breakdown with uniform passive control applied  
 a) 2D streamwise velocity,  $U_0$ ,  $F_{2D}$ ,  
 b) 2D streamwise velocity,  $U_0$ ,  $2 F_{2D}$ ,  
 c) 3D streamwise velocity,  $U_1$ ,  $\frac{1}{2} F_{2D}$ ,  
 d) 3D streamwise velocity,  $U_1$ ,  $\frac{3}{2} F_{2D}$  . . . . . 362
- 6.83 Influence of uniform passive control on the amplitude growth for subharmonic breakdown  
 a) 2D streamwise velocity,  $U_0$ ,  $F_{2D}$ ,  
 b) 3D streamwise velocity,  $U_1$ ,  $F_{3D}$  . . . . . 366
- 6.84 Comparison of the disturbed flow for subharmonic breakdown without control applied and with uniform passive heating

- applied at the peak plane in the spanwise direction
- a) streamwise velocity,  $u$ ,  $z = 0$  and  $\Delta\bar{T} = 0^\circ F$
  - b) streamwise velocity,  $u$ ,  $z = 0$  and  $\Delta\bar{T} = 15^\circ F$
  - c) normal velocity,  $v$ ,  $z = 0$  and  $\Delta\bar{T} = 0^\circ F$
  - d) normal velocity,  $v$ ,  $z = 0$  and  $\Delta\bar{T} = 15^\circ F$
  - e) spanwise velocity,  $w$ ,  $z = \lambda_z/4$  and  $\Delta\bar{T} = 0^\circ F$
  - f) spanwise velocity,  $w$ ,  $z = \lambda_z/4$  and  $\Delta\bar{T} = 15^\circ F$
  - g) streamwise vorticity,  $\omega_x$ ,  $z = \lambda_z/4$  and  $\Delta\bar{T} = 0^\circ F$
  - h) streamwise vorticity,  $\omega_x$ ,  $z = \lambda_z/4$  and  $\Delta\bar{T} = 15^\circ F$
  - i) normal vorticity,  $\omega_y$ ,  $z = \lambda_z/4$  and  $\Delta\bar{T} = 0^\circ F$
  - j) normal vorticity,  $\omega_y$ ,  $z = \lambda_z/4$  and  $\Delta\bar{T} = 15^\circ F$
  - k) spanwise vorticity,  $\omega_z$ ,  $z = 0$  and  $\Delta\bar{T} = 0^\circ F$
  - l) spanwise vorticity,  $\omega_z$ ,  $z = 0$  and  $\Delta\bar{T} = 15^\circ F$
  - m) temperature,  $T$ ,  $z = 0$  and  $\Delta\bar{T} = 15^\circ F$  . . . . . 367
- 6.85 Disturbed flow for fundamental breakdown with two-dimensional active control applied,  $F_{2D} = 0.588$ ,  $F_{3D} = 0.588$
- a) 2D streamwise velocity,  $U_0$ , b) 3D streamwise velocity,  $U_1$ ,
  - c) 2D temperature,  $\Theta_0$ , d) 3D temperature,  $\Theta_1$  . . . . . 374
- 6.86 Disturbed flow for fundamental breakdown with three-dimensional active control applied,  $F_{2D} = 0.588$ ,  $F_{3D} = 0.588$
- a) 2D streamwise velocity,  $U_0$ , b) 3D streamwise velocity,  $U_1$ ,
  - c) 2D temperature,  $\Theta_0$ , d) 3D temperature,  $\Theta_1$  . . . . . 376
- 6.87 Amplitude comparison at  $x = 10.65$  for fundamental breakdown with active control applied
- a) 2D streamwise velocity,  $U_0$ ,  $F_{2D}$ ,
  - b) 2D streamwise velocity,  $U_0$ ,  $2 F_{2D}$ ,
  - c) 3D streamwise velocity,  $U_1$ ,  $F_{3D}$ ,
  - d) 3D streamwise velocity,  $U_1$ ,  $2 F_{3D}$ ,
  - e) 3D streamwise velocity,  $U_1$ , mean component . . . . . 378
- 6.88 Influence of active control on the amplitude growth for fundamental breakdown
- a) 2D streamwise velocity,  $U_0$ ,  $F_{2D}$ ,
  - b) 3D streamwise velocity,  $U_1$ ,  $F_{3D}$  . . . . . 381
- 6.89 Influence of the two-dimensional amplitude level on the three-dimensional growth rate for both passive and active control of fundamental breakdown (quantities based on the maximum of the  $U_0$  and  $U_1$  velocities) . . . . . 382

- 6.90 Comparison of heat transferred versus the three-dimensional growth rates for both passive and active control of fundamental breakdown . . . . . 382
- 6.91 Comparison of the disturbed flow for fundamental breakdown with two-dimensional or three-dimensional active control applied at the peak plane in the spanwise direction
- a) streamwise velocity,  $u$ ,  $z = 0$  and 2D active control
  - b) streamwise velocity,  $u$ ,  $z = 0$  and 3D active control
  - c) normal velocity,  $v$ ,  $z = 0$  and 2D active control
  - d) normal velocity,  $v$ ,  $z = 0$  and 3D active control
  - e) spanwise velocity,  $w$ ,  $z = \lambda_z/4$  and 2D active control
  - f) spanwise velocity,  $w$ ,  $z = \lambda_z/4$  and 3D active control
  - g) streamwise vorticity,  $\omega_x$ ,  $z = \lambda_z/4$  and 2D active control
  - h) streamwise vorticity,  $\omega_x$ ,  $z = \lambda_z/4$  and 3D active control
  - i) normal vorticity,  $\omega_y$ ,  $z = \lambda_z/4$  and 2D active control
  - j) normal vorticity,  $\omega_y$ ,  $z = \lambda_z/4$  and 3D active control
  - k) spanwise vorticity,  $\omega_z$ ,  $z = 0$  and 2D active control
  - l) spanwise vorticity,  $\omega_z$ ,  $z = 0$  and 3D active control
  - m) temperature,  $T$ ,  $z = 0$  and 2D active control
  - n) temperature,  $T$ ,  $z = 0$  and 3D active control . . . . . 383
- 6.92 Comparison of the disturbed flow for fundamental breakdown with two-dimensional or three-dimensional active control applied at  $y = 3.186$
- a) streamwise vorticity,  $\omega_x$ , 2D active control
  - b) streamwise vorticity,  $\omega_x$ , 3D active control . . . . . 390
- 6.93 Comparison of the disturbed flow for fundamental breakdown with two-dimensional or three-dimensional active control applied at  $z = 11.0$
- a) streamwise vorticity,  $\omega_x$ , 2D active control
  - b) streamwise vorticity,  $\omega_x$ , 3D active control
  - c) normal vorticity,  $\omega_y$ , 2D active control
  - d) normal vorticity,  $\omega_y$ , 3D active control
  - e) spanwise vorticity,  $\omega_z$ , 2D active control
  - f) spanwise vorticity,  $\omega_z$ , 3D active control . . . . . 391

## LIST OF TABLES

Table	Page
6.1 Parameters for Uniform Heating Cases for Linear Amplitudes . .	141
6.2 Parameters for Nonuniform Heating Cases for Linear Amplitudes . . . . .	152
6.3 Comparison of Displacement Thickness to Heater Strip Width . .	164
6.4 Parameters for Phase Control of Linear Disturbances . . . . .	168
6.5 Parameters for Uniform Passive Control Cases of Fundamental Breakdown . . . . .	174
6.6 Parameters for Uniform Passive Control Cases of Subharmonic Breakdown . . . . .	181
6.7 Parameters for Active Control Cases of Fundamental Breakdown . . . . .	186

## ABSTRACT

A numerical model has been developed for investigating boundary layer transition control for a three-dimensional flat plate boundary layer. Control of a periodically forced boundary layer in an incompressible fluid is studied using surface heating techniques. The spatially evolving boundary layer is simulated. The Navier-Stokes and energy equations are integrated using a fully implicit finite difference/spectral method. The Navier-Stokes equations are in vorticity-velocity form and are coupled with the energy equation through the viscosity dependence on temperature.

Both passive and active methods of control by surface heating are investigated. In passive methods of control, wall heating is employed to alter the stability characteristics of the mean flow. Both uniform and nonuniform surface temperature distributions are studied. In the active control investigations, temperature perturbations are introduced locally along finite heater strips to directly attenuate the instability waves in the flow. A feedback control loop is employed in which a downstream sensor is used to monitor wall shear stress fluctuations.

Passive control of small amplitude two-dimensional Tollmien-Schlichting waves and three-dimensional oblique waves are numerically simulated with both uniform and nonuniform passive heating applied. Strong reductions in both amplitude levels and amplification rates are achieved. Active control of small amplitude two-dimensional and three-dimensional disturbances is also numerically simulated. With proper phase control, in phase reinforcement and out of phase attenuation is demonstrated.

A receptivity study is performed to study how localized temperature perturbations are generated into Tollmien-Schlichting waves. It is shown that



narrow heater strips are more receptive in that they maximize the amplitude level of the disturbances in the flow. It is also found that the local temperature fluctuations cause mainly a strong normal gradient in spanwise vorticity.

Control of the early stages of the nonlinear breakdown process is also investigated. Uniform passive control is applied to both the fundamental and sub-harmonic routes to turbulence. A strong reduction in amplitude levels and growth rates results. In particular, the three-dimensional growth rates are significantly reduced below the uncontrolled levels. Active control of the fundamental breakdown process is also numerically simulated. Control is achieved using either a two-dimensional or three-dimensional control input.

## CHAPTER 1

### INTRODUCTION

Control of the laminar-turbulent transition process is of considerable interest in aerodynamics and hydrodynamics. Delay or prevention of transition significantly reduces the viscous drag, while acceleration of transition may be desired to delay separation, to enhance mixing for combustion and chemical reactions or to simulate higher Reynolds number flows in an experimental facility. A sizable decrease in the viscous drag forces has the potential to significantly reduce fuel consumption and allow greater range and speed. According to Bushnell (1983), drag caused by the formation of the viscous boundary layer accounts for approximately 50% of the drag on transport aircraft and surface ships and 70% of the drag of underwater bodies. Hefner (1988) recently pointed out that as much as 50% of the fuel burned by commercial and general aviation aircraft is required to overcome the friction or viscous drag, and fuel costs could be reduced by as much as 2 to 5% with even modest reductions in viscous drag. This slight reduction in the viscous drag could save the U.S. airlines \$200 to \$500 million a year.

There are basically two approaches to control the transition process. The first approach is based on the idea of changing the stability characteristics of the base flow. The critical Reynolds number at which the flow becomes unstable is increased or reduced depending on what is being done to the base flow. This approach is characterized as passive control. The second approach to influence the transition process is active control in which the disturbance flow resulting from the instability of the base flow is directly influenced using wave superposition techniques. Before discussing these different approaches to transition control, a short review of the boundary layer transition process is given.

### 1.1 Boundary Layer Transition

In low disturbance boundary layer flows, the first stage of the transition to turbulent motion begins with the development of the two-dimensional Tollmien-Schlichting waves. These waves become amplified beyond a critical Reynolds number for which the base flow becomes unstable to periodic disturbances. This stage of transition, known as primary instability, has been studied by a consideration of the stability of small amplitude disturbances of the form of a travelling wave:

$$\mathbf{u}'(\mathbf{x}, t) = \hat{\mathbf{u}}(y)e^{i(\alpha x - \beta t)} \quad (1.1)$$

where  $\alpha$  is the streamwise wavenumber,  $\beta$  is the frequency,  $\mathbf{u}$  is the two-dimensional velocity vector  $\mathbf{u} = [u, v]$ , and  $\mathbf{x}$  is the two-dimensional position vector  $\mathbf{x} = [x, y]$ . Both  $\alpha$  and  $\beta$  are in general complex. The perturbation velocity field of Equation (1.1) is substituted into the linearized equations of motion and a fourth-order eigenvalue problem results:

$$(U - c)[\hat{v}'' - \alpha^2 \hat{v}] - U'' \hat{v} = \frac{-i}{\alpha Re} [\hat{v}'''' - 2\alpha^2 \hat{v}'' + \alpha^4 \hat{v}] \quad (1.2)$$

where the prime denotes differentiation with respect to  $y$ ,  $c$  is the propagation speed  $\left(c = \frac{\beta}{\alpha}\right)$ ,  $Re$  is the Reynolds number, and  $U = U(y)$  is the mean velocity profile, assumed parallel. Equation (1.2) is the Orr-Sommerfeld equation derived independently by Orr (1906) and Sommerfeld (1908). Although, in general,  $\alpha$  and  $\beta$  are complex, two special cases result with either  $\alpha$  or  $\beta$  purely real. Given a  $Re$  and  $\alpha = \alpha_r$ , the eigenvalue  $\beta$  is complex and the Orr-Sommerfeld equation describes a temporally growing or decaying wave with a growth rate of  $\beta_i$ . In the second case, the frequency  $\beta = \beta_r$  is purely real and for a given  $Re$ , the eigenvalue  $\alpha$  is complex and represents a spatially growing or decaying wave with a growth rate of  $-\alpha_i$ . The eigensolutions of Equation (1.2) are usually represented by a neutral

stability curve as shown in Figure 1.1. This neutral curve represents the spatial stability diagram of a boundary layer on a flat plate. The neutral curve separates the parameter space into stable and unstable regions. The flow is unstable inside the neutral curve and the disturbances grow exponentially. Outside the neutral curve, the flow is stable and the disturbance waves decay exponentially. This behavior was first demonstrated by the classical experiments of Schubauer and Skramstad (1948). In these experiments the evolution of Tollmien-Schlichting waves was observed for both controlled and natural transition. In the case of controlled transition, the Tollmien-Schlichting waves were excited by a vibrating ribbon subjected to oscillations at a fixed frequency. For the case of natural transition, the Tollmien-Schlichting waves were excited by the natural background disturbances that are always present in a real flow environment.

The existence of the disturbances predicted by linear theory is well established. However, it is not yet clearly understood how the two-dimensional, low frequency waves lead to the complicated three-dimensional, high frequency phenomena of turbulence. As the amplitude of the instability waves exceeds a certain threshold value, nonlinear effects become appreciable and three-dimensional structures appear. The nonlinear effects are manifested in the much larger growth rates of some of the disturbances, which are invariably three-dimensional. Two-dimensional nonlinear effects alter the growth rates and the region of unstable parameter space only slightly and are unable to induce transition.

A more complete understanding of the transition process requires some account of the origin of three-dimensionality in the flow. Squire (1933) was able to relate the stability of three-dimensional disturbances in the form of oblique waves. Considering an oblique wave of the form

$$u'(x, t) = \hat{u}(y)e^{i(\alpha x + \gamma z - \beta t)} \quad (1.3)$$

where  $\gamma$  is the spanwise wavenumber,  $\mathbf{u}$  is the three-dimensional velocity vector  $\mathbf{u} = [u, v, w]$ , and  $\mathbf{x}$  is the three-dimensional position vector  $\mathbf{x} = [x, y, z]$ , leads to the three-dimensional Orr-Sommerfeld equation for a two-dimensional base flow:

$$(U - c)[\hat{v}'' - (\alpha^2 + \gamma^2)\hat{v}] - U''\hat{v} = \frac{-i}{\alpha Re}[\hat{v}'''' - 2(\alpha^2 + \gamma^2)\hat{v}'' + (\alpha^2 + \gamma^2)^2\hat{v}] \quad (1.4)$$

By making the following substitutions

$$\bar{\alpha}^2 = \alpha^2 + \gamma^2$$

$$\bar{\alpha} \bar{Re} = \alpha Re$$

Equation (1.4) becomes

$$(U - c)[\hat{v}'' - \bar{\alpha}^2\hat{v}] - U''\hat{v} = \frac{-i}{\bar{\alpha} \bar{Re}}[\hat{v}'''' - 2\bar{\alpha}^2\hat{v}'' + \bar{\alpha}^4\hat{v}] \quad (1.5)$$

which is the same equation for a two-dimensional disturbance with wavenumber  $\bar{\alpha}$  and Reynolds number  $\bar{Re}$ . Thus a three-dimensional disturbance is exactly similar to that of a two-dimensional disturbance with wavenumber  $\bar{\alpha}$  and Reynolds number  $\bar{Re}$ . The result of this analysis is that the minimum critical Reynolds number occurs for purely two-dimensional disturbances, i.e.  $\gamma = 0$ . It was at least partly due to this analysis that few investigations into the three-dimensional nature of boundary layer transition were conducted.

The occurrence of the three-dimensional phenomena was observed experimentally in detail by Klebanoff, Tidstrom, and Sargent (1962) and also by Kovasznay, Komoda, and Vasudeva (1962). The three-dimensional structure that evolves is characterized by spanwise alternating peaks and valleys, or regions of enhanced and reduced wave amplitude, and an associated system of streamwise vortices. The peak-valley structure is ordered in that peaks follow peaks and valleys follow valleys. The spanwise wavelength,  $\lambda_z$ , is generally somewhat smaller

than the streamwise wavelength,  $\lambda_x$ . The growth rates at the peak positions are much larger than those for the primary instability. As the three-dimensional structures evolve, high-shear layers and highly inflectional velocity distributions form at the peak positions. Small-scale velocity fluctuations, or "spikes", develop from the shear layer at a much higher frequency than the primary wave, which are the first signs of turbulence. This sequence of events leading to turbulence is called fundamental or K-type breakdown after Klebanoff and his coworkers (1962). Herbert (1985) has proposed a linear secondary instability theory that predicts an instability of this type. In Herbert's theory, the temporal concept is used in which the flow is assumed periodic in the streamwise direction. The linear stability with respect to small spanwise periodic three-dimensional disturbances is studied. The basic flow is comprised of the Blasius boundary layer and a Tollmien-Schlichting wave of finite amplitude. Herbert's theory was able to show the essential features of the early stages of the secondary instability process. In addition, numerical simulations based upon the temporal stability model have been made by Wray and Hussani (1984), Laurien and Kleiser (1985), and Spalart and Yang (1986) to simulate this K-type transition. In these simulations the disturbances grow in time as opposed to the spatial growth of the experiments, but the results are consistent with the basic flow characteristics of the experiments. Spatial simulations, which more closely model the three-dimensional experiments of Klebanoff et al. (1962), have been conducted by Fasel, Rist, and Konzelmann (1987) using the complete Navier-Stokes equations. Their results are in excellent agreement with the experimental measurements.

The ordered peak-valley system does not constitute the only one which has been encountered. Only recently a second route to transition in the boundary layer has been observed by Kachanov and Levchenko (1984), Saric, Kozlov, and

Levchenko (1984), and Saric and Thomas (1983). This route is characterized by subharmonic three-dimensional disturbances in which the peaks and valleys are staggered. The streamwise period of the three-dimensional structures is twice the period of the fundamental wave. The experiments indicate the subharmonic breakdown occurs for low and intermediate amplitudes of the two-dimensional wave, while the K-type occurs for higher amplitudes. Craik (1971) and Herbert (1984) have proposed theories that predict the subharmonic type of instability. Craik (1971) investigated the interaction of a resonant triad consisting of a low-amplitude two-dimensional wave and two oblique waves, while Herbert's linear secondary instability theory (1984) describes the flow patterns at intermediate amplitude levels. In Craik's theory (1971), a two-dimensional Tollmien-Schlichting wave is present with the form

$$u'_{2D}(x, t) = \hat{u}_{2D}(y) e^{i(\alpha x - \beta t + \phi_{2D})} \quad (1.6)$$

where  $\phi_{2D}$  is the reference phase. In addition, two three-dimensional waves of the form

$$u'_{3D\pm}(x, t) = \hat{u}_{3D\pm}(y) e^{i(\alpha x/2 \pm \gamma z - \beta t/2 + \phi_{3D\pm}/2)} \quad (1.7)$$

are superimposed on the two-dimensional wave, where  $\gamma$  is the spanwise wavenumber and  $\phi_{3D}$  is the three-dimensional phase. A quadratic nonlinearity of  $u'_{3D+}$  and  $u'_{3D-}$  will be resonant with the fundamental two-dimensional wave  $u'_{2D}$  if the initial phase is synchronized ( $\phi_{2D} = \phi_{3D+} = \phi_{3D-}$ ) and if  $u'_{3D\pm}$  are subharmonics of  $u'_{2D}$  and have the same phase speed. For this staggered peak-valley structure, Saric and Thomas (1984) observed that the spanwise wavelength,  $\lambda_z$ , is larger than the streamwise wavelength,  $\lambda_x$ , by about 50%. This subharmonic structure appears for low amplitude levels of the two-dimensional wave ( $\sim 0.3\%$

at Branch II of the neutral curve, according to Saric and Thomas (1984)), and is called a C-type structure after Craik's resonant triad theory (1971). At slightly higher amplitude levels (0.3% to 0.6%), a different subharmonic structure appears in which  $\lambda_x$  is larger than  $\lambda_z$  by about 50% (Saric and Thomas (1984)). This pattern was explained by the linear secondary instability theory of Herbert (1984) and is called an H-type structure. Laurien and Kleiser (1985) and Spalart and Yang (1986) have also shown the subharmonic route to transition with their temporal numerical models. In addition, the spatial simulations of Fasel, Rist, and Konzelmann (1987) have predicted the subharmonic breakdown and their results are in very good agreement with the experimental measurements of Kachanov and Levchenko (1984).

For small amplitude disturbances, the Tollmien-Schlichting regime covers the largest downstream distance of the entire transition region. For the technical application of transition control, this region is particularly amenable to manipulations of the transition process. In the early nonlinear stages of transition, the flow is still smooth and thus easier to study than later strongly nonlinear stages. Full transition is inevitable once the strongly nonlinear stage has been reached. Thus efforts to prevent or delay transition applied at the early stages should prove more successful.

### 1.2 Passive Control

In passive methods of control, the stability characteristics of the base flow are altered. Several techniques have proven to be effective for passive control and can be easily identified by examining the boundary layer momentum equation, including the viscosity variation with temperature,  $\mu = \mu(T)$ :

$$\rho \frac{\partial u}{\partial t} + \rho u \frac{\partial u}{\partial x} + \rho v \frac{\partial u}{\partial y} = -\frac{dp}{dx} + \frac{\partial}{\partial y} \left( \mu \frac{\partial u}{\partial y} \right). \quad (1.8)$$



Applying Equation (1.8) at the wall of the plate and rearranging yields

$$\frac{dp}{dx} - \left(\frac{d\mu}{dT}\right)_{y=0} \left(\frac{\partial T}{\partial y}\right)_{y=0} \left(\frac{\partial u}{\partial y}\right)_{y=0} + \rho v_{y=0} \left(\frac{\partial u}{\partial y}\right)_{y=0} = \mu_{y=0} \left(\frac{\partial^2 u}{\partial y^2}\right)_{y=0} \quad (1.9)$$

where the chain rule for the viscosity dependence on temperature has been invoked. As shown by Lord Rayleigh (1880), a velocity profile that lacks an inflection point throughout is inviscidly stable, i.e.

$$\frac{\partial^2 u}{\partial y^2} < 0; \quad 0 \leq y \leq \infty. \quad (1.10)$$

The Blasius boundary layer does not have a point of inflection and thus is inviscidly stable. More generally, the stability of a velocity profile improves as its second derivative near the wall becomes more negative. It is readily seen that a favorable pressure gradient  $\left(\frac{dp}{dx} < 0\right)$ , wall suction ( $v_{y=0} < 0$ ), heating in water  $\left(\frac{d\mu}{dT} < 0, \left(\frac{\partial T}{\partial y}\right)_{y=0} < 0\right)$ , and cooling in air  $\left(\frac{d\mu}{dT} > 0, \left(\frac{\partial T}{\partial y}\right)_{y=0} > 0\right)$  tend to make  $\left(\frac{\partial^2 u}{\partial y^2}\right)_{y=0}$  more negative providing a stabilizing effect to the flow.

The concept of using favorable pressure gradients and suction for stabilizing laminar boundary layers dates back to the 1930's. Research in the area of favorable pressure gradients led NACA to the development of the 6-series natural laminar flow airfoils. Extensive laminar flow control by suction was achieved in flight tests in the 1960's as described by Antonatos (1966), Whites, Sudderth, and Wheldon (1966), Pfenninger and Reed (1966), and Nenni and Gluyas (1966). These flight experiments showed that extensive laminar flow could be achieved in flight. More recent developments in passive laminar flow control for transport aircraft are given by Wagner and Fischer (1983). The current state of linear stability theory as applied to transition prediction and passive laminar flow control system design for aerodynamics has been reviewed by Bushnell and Malik (1985).

According to this review article, substantial progress has been made in pressure gradient laminar flow control for subsonic applications and is currently in use, but questions concerning maintenance and reliability for the case of suction control remain. One problem with the application of suction is that additional disturbances can be introduced into the boundary layer at the suction slots. An experimental investigation of the boundary layer with suction and blowing applied has been conducted by Saric and Reed (1983) in which the stabilizing effect of suction was evident. In addition to the use of pressure gradient and suction as transition modifiers, Reshotko (1979) has shown in a study that drag reductions are possible for a hydrogen fueled aircraft by using the fuel to cool selected aerodynamic surfaces on its way to the engines.

The effects of passive heating were investigated as early as 1946 by Liepmann and Fila (1946) in which they experimentally showed that heating in air hastens transition. Hauptmann (1968) used a perturbation procedure to predict appreciable stabilization in water and slight destabilization in air for small variations in viscosity. The first numerical results of heated and cooled water boundary layers were conducted by Wazzan, Okamura, and Smith (1968, 1970a, 1970b). They formulated the linear stability problem to include the effects of viscosity variation with temperature in the base flow and showed neutral stability curves for several levels of heating and cooling. Lowell (1974) reformulated the heated boundary layer linear stability problem by including all fluid property variations in the boundary layer along with the disturbance energy equation, thus predicting fluid property fluctuations as well as temperature fluctuations. Lowell (1974) found his results to be somewhat insensitive to the thermal disturbances and viscosity the dominant property. The stabilization of the water boundary layer has been shown experimentally by Strazisar, Reshotko, and Prah1 (1977),

Barker and Jennings (1977), Barker (1979), and Nosenchuck (1982). Barker and Jennings (1977) and Barker (1979) studied the boundary layer flow on the inside of a cylindrical tube and found a considerable increase in transition Reynolds number with heating. Nosenchuck (1982) found the same overall trends as Barker and Jennings (1977) and Barker (1979), but Nosenchuck's results (1982) were less stable, which was attributed to a slight favorable pressure gradient in the flow tube. The results of Strazisar, Reshotko, and Prah1 (1977) show that as wall heating is increased the minimum critical Reynolds number at which the flow becomes unstable increases, the disturbance growth rates decrease, and the region of unstable frequencies decreases. These trends are consistent with the numerical analysis of Wazzan, Okurmura, and Smith (1968, 1970a, 1970b) and Lowell (1974). Differences in the experimental and numerical results were attributed to nonparallel effects. El-Hady and Nayfeh (1979) have performed a nonparallel stability analysis using the method of multiple scales and show that, when nonparallel effects are taken into account, better agreement with the experimental results can be reached. Bestek, Dittrich, and Fasel (1987) have numerically studied passive control by surface heating. The two-dimensional Navier-Stokes and energy equations were solved for incompressible flow using the spatial model of stability. The numerical results were consistent with the experimental results.

In addition to uniformly heating the flat plate, Strazisar and Reshotko (1978), Barker and Jennings (1977), and Nosenchuck (1982) have experimentally examined nonuniform surface temperature distributions. More efficient heat utilization can be achieved using nonuniform wall heating since the flow upstream of the critical Reynolds number is stable and does not need heating. Gazley and Wazzan (1985) have also studied a nonuniform surface temperature distribution using the linear stability theory model of Wazzan, Okurmura, and Smith (1968,

1970a, 1970b), while Nayfeh and El-Hady (1980) and Asrar and Nayfeh (1985) performed nonparallel stability analyses showing that the stability is strongly dependent on the actual heat distribution, but that the boundary layer is more stable than without heating.

Asrar and Nayfeh (1985) have extended their nonparallel stability analysis to linear three-dimensional waves propagating in two-dimensional liquid boundary layers for both uniform and nonuniform surface temperature distributions. The results show that three-dimensional disturbances result in lower growth rates than the two-dimensional disturbances irrespective of the wall overheat for the oblique angles considered. Zang and Hussani (1985a, 1985b) have examined three-dimensional passive control of the secondary instability process using heating, suction, and pressure gradient. They solved the three-dimensional, incompressible Navier-Stokes and energy equations with all fluid properties varying. In their model, the flow evolves in time instead of the streamwise direction of the experiments. They examined K-type transition and found that passive control did not prevent secondary instability, but is substantially weaker than for the uncontrolled boundary layer. In addition, Zang and Hussani (1985a, 1985b) showed that the suction and pressure gradient methods of passive control were somewhat more effective than the application of passive heating. They found that although the heated mean flow provides a stabilizing influence, the temperature perturbations are destabilizing. Lowell (1974), in studying the linear stability problem, has also found that the temperature perturbations are slightly destabilizing.

### 1.3 Active Control

It has been clearly demonstrated in the literature that stability can be greatly enhanced and transition delayed using passive methods of control. However, the expenses required for additional equipment and energy can negate some

of the benefits of enhanced stability. The second approach to influence the transition process, active control, appears more promising in this context. Instead of changing the stability characteristics of the base flow, as in passive control, the disturbance flow resulting from the instability is directly attacked. Wave superposition techniques are used to delay the transition process in active methods of control. The principle is to interactively detect growing disturbances and to introduce a control wave of equal amplitude and antiphased so as to cancel, or at least reduce, existing instabilities in the flow. From the theoretical point of view, wave cancellation in the linear stage is clearly achievable. The linear nature of the Orr-Sommerfeld equation, which describes Tollmien-Schlichting type disturbances, suggests this possibility. If  $v'_1 = \hat{v}_1(y)e^{i(\alpha x + \gamma z - \beta t)}$  represents the first wave generated and  $v'_2 = \hat{v}_2(y)e^{i(\alpha x + \gamma z - \beta t + \phi)}$  represents a second wave generated in the flow, then from the principle of linear superposition,  $v'_3 = v'_1 + v'_2$  is a solution of the Orr-Sommerfeld equation. It is easily seen that  $v'_3 = 0$  occurs when the two disturbances have equal amplitude and are  $180^\circ$  out of phase, i.e.  $\phi = \pm\pi$ . Active control applied at the linear stages of transition appears promising, but at later nonlinear stages of transition, the success of active control is less obvious.

The basic idea of the active control approach was first shown experimentally by Wehrmann (1965) and Schilz (1965/1966). The experimental configurations of both investigations were similar. They first excited a Tollmien-Schlichting wave using a vibrating ribbon and then used a flexible wall built into the flat plate to reduce the growing Tollmien-Schlichting wave by forcing the flexible wall to move in phase opposition to the wave. In addition, Wehrmann (1965) reported reinforcement was also achievable.

More recently, active control in boundary layers has been investigated in experimental studies by Milling (1981), Liepmann, Brown, and Nosenchuck

(1982), Gedney (1983), Thomas (1983), Strykowski and Sreenivasan (1985), and Maestrello (1985). Milling (1981) performed a brief study in a water channel in which Tollmien-Schlichting waves were introduced into the flow using a vibrating wire. A second wire placed a short distance downstream was used to introduce control disturbances at the same frequency, but with the phase and amplitude adjusted to minimize the disturbance from the first wire. The disturbances were nearly cancelled using this technique.

In an investigation in a water tunnel, Liepmann, Brown, and Nosenchuck (1982) used heating strips to excite instability waves in the boundary layer. The thin metal strips were flush-mounted on the plate and could be subjected to various forms of time-dependent temperature loading. A second set of heating strips was located downstream in order to control the deliberately excited Tollmien-Schlichting waves from the first heating element by inputting appropriate amplitude and phase perturbations to the second heating element. The reduction in the disturbance amplitude level and delay in transition were clearly evident from these experiments. In an application of this study, Liepmann and Nosenchuck (1982) used one heater strip and a hot film probe downstream to actively control the naturally occurring Tollmien-Schlichting waves. The heater strip was used as the actuator and the hot film probe the sensor. The probe measured the wall shear stress fluctuations, and from these measurements a signal was synthesized to drive the heater. The disturbance waves driven by the heater strip were superimposed on the naturally occurring Tollmien-Schlichting waves and, depending on the phase shift, the disturbances were attenuated or reinforced. This system formed a feedback control loop of transition.

Thomas (1983) has studied the development of the flow field in the boundary layer downstream of the active control measures. Using two vibrating ribbons

for the generation and control of the instability waves, transition was delayed by superimposing equal amplitude and antiphased Tollmien-Schlichting disturbances. However, downstream of the control measure very weak three-dimensional background disturbances in the flow interacted with the primary two-dimensional waves, and the flow could not be completely restored to its undisturbed state. In the experimental studies, either the ordered peak-valley or the staggered peak-valley structures were observed in the downstream region of study. These structures were significantly delayed when the control measures were applied. Thomas (1983) also investigated wave interactions further by using a waveform consisting of two waves of different frequency for both ribbons. Adjusting the amplitude and phase to minimize the downstream disturbances, the amplitudes of the two frequency components were reduced. However, the amplitude of the difference frequency component was only partially reduced and interacted with the three-dimensional disturbances in the flow.

In the experimental work of Gedney (1983), a Tollmien-Schlichting wave was excited by sound and then nearly cancelled by vibrating the plate near the leading edge at the same frequency as the sound signal. The amplitude and phase of the plate vibration was continuously adjusted until the transition point moved downstream as far as possible. The velocity fluctuations were reduced to approximately 1/50th the level of either the excitation by sound or plate vibration alone.

Active control has also been shown possible in the work of Strykowski and Sreenivasan (1985). A wire is vibrated in a slot in the plate to produce a disturbance and a second wire in another slot downstream of the first is used to control the disturbance. This technique is similar to periodic suction and blowing at the wall. Strykowski and Sreenivasan (1985) also attempted to generate Tollmien-Schlichting waves in air using the heating element technique of Liepmann, Brown,

and Nosenchuck (1982), but were unable to observe any perturbations. However, Liepmann and Nosenchuck (1983) have successively triggered laminar instability waves in air using heater strips. Maestrello (1985) has also generated instability waves on an airfoil using surface heating strips in a region of favorable pressure gradient. In addition, Maestrello (1985) was able to reduce the perturbations using sound as the control input at near normal incidence.

In addition to the experimental studies, several numerical investigations of active control have been undertaken recently. Three-dimensional numerical simulations of active control in the plane channel have been conducted by Kleiser and Laurien (1984, 1985), Biringen (1984), and Biringen, Nutt, and Caruso (1985) using the temporal model so that the disturbances grow in time instead of in the streamwise direction. The flow is also spanwise periodic. Kleiser and Laurien (1984, 1985) have applied periodic wall suction and blowing, fluctuating mass forces, and direct manipulation of Fourier modes as control inputs. Both the fundamental and subharmonic routes to turbulence were considered. Two-dimensional control applied at the early two-dimensional stages of the transition process provided the necessary control to reduce both the two-dimensional and three-dimensional amplitude levels. Two-dimensional control applied at later stages where significant three-dimensionality in the flow had developed was not effective in delaying transition. Biringen (1984) and Biringen, Nutt, and Caruso (1985) have found similar results applying periodic suction and blowing. In addition, applying three-dimensional control after the flow has undergone secondary instability provided a significant reduction in the disturbance amplitude levels.

Laurien and Kleiser (1985) and Laurien (1985) have also numerically simulated active transition control for the three-dimensional boundary layer using a similar numerical model as for the plane channel. Again the flow develops in



time instead of in the streamwise direction. Two-dimensional periodic suction-blowing was used as the control input. Control at the early two-dimensional stages was effective, but failed in the later three-dimensional stages of transition. Zang and Hussani (1985a, 1985b) performed similar three-dimensional temporal simulations of the boundary layer and plane channel in which they artificially suppressed spanwise velocity and pressure modes leading to a delay in transition. For the boundary layer, this spanwise mode control was in addition to passive heating.

In a two-dimensional numerical investigation of the boundary layer, McMurray, Metcalfe, and Riley (1983) studied active control using periodic wall motion. Control was achieved for both single frequency Tollmien-Schlichting waves and wave packet disturbances consisting of several frequency components. In addition, a "smart wall" algorithm was developed which linked the phase and amplitude of the wall forcing to the actual phase and amplitude of the normal velocity component in the flow field away from the wall. In addition, Metcalfe, Rutland, Duncan, and Riley (1985) found that part of the stabilizing effect due to the wall motion could be attributed to wave superposition, but through an energy analysis it was found that energy from the perturbed flow was transmitted to the mean flow also providing a stabilizing effect.

In addition to the numerical investigations using the temporal model to study active control, Bayliss, Maestrello, Parikh, and Turkel (1985) have numerically studied active control of the spatially growing compressible boundary layer. The two-dimensional compressible Navier-Stokes and energy equations were solved and control was achieved using localized periodic surface heating and cooling. The maximum amplitude reductions were 6% for heating and 12% for

cooling. These reductions are not as promising as has been shown in the laboratory, where near total attenuation was achieved. However, it was noted that an optimal phase and amplitude input to the heater strip signals was not investigated. Dittrich (1985) has also numerically simulated two-dimensional active control in water with surface heater strips using the same numerical method as was employed in the passive control simulations. A disturbance was introduced at a surface heater strip through local temperature fluctuations that were out of phase with the disturbance waves in the flow. A much stronger attenuation in amplitude of the perturbations was seen in comparison with the results of Bayliss, Maestrello, Parikh, and Turkel (1985).

Bower, Kegelmann, Pal, and Meyer (1987) have numerically investigated two-dimensional active control of a single frequency wave in the plane channel using periodic wall blowing and suction. The computational model is based on the solution of the Orr-Sommerfeld equation and an analytical expression is derived to provide the amplitude and phase of the downstream surface velocity distribution which results in the suppression of the instability wave. Bower, Pal, Cain, and Meyer (1987) have extended this analysis to the suppression of wave packets through localized velocity perturbations. In addition, Pal, Bower, Cain, and Meyer (1988) have used a similar numerical technique to generate and suppress a multifrequency instability wave in the Blasius boundary layer using localized suction and blowing. Bower, Pal, and Meyer (1987) have also applied a similar computational method to actively control two-dimensional instability waves in the boundary layer through time-periodic surface heating. The computational model is based on the linearized equations with temperature dependent viscosity and thermal conductivity. A two-dimensional single frequency disturbance was generated and suppressed through the application of surface heating.

In both the passive and active control investigations, it has been shown that transition can be prevented or at least delayed. However, in a comparison of active control using surface heating strips with passive control by uniform surface heating, Nosenchuck (1982) found a considerable difference in the power required to achieve an equivalent increase in transition length. Employing the previously described feedback control loop to reduce the naturally occurring disturbances in the flow resulted in a 25% increase in transition length and required only ten watts of power for the heater strip. Under identical flow conditions, the same delay in transition was accomplished with passive control, but required 1900 watts of power. Thus over two orders of magnitude more power was needed using passive control to obtain the same result. Therefore, these experiments provide solid evidence of the considerable advantages of active control over passive control for delaying transition.

## CHAPTER 2

## PROBLEM STATEMENT

The contributions of stability theory, physical experiments, and numerical simulations discussed in Chapter 1 have helped to provide a better understanding of transition control as applied to boundary layer flows. In particular, numerical simulations have become an increasingly important method of research. In numerical computations, linearity or weakly nonlinear interactions do not have to be assumed as in stability theory models. In addition, in numerical simulations, individual spectral components or combinations of these components can be considered, whereas, in physical experiments broad band noise is always present at some level. The parameter space can also be more easily varied in numerical computations than in physical experiments.

Transition control using surface heating or cooling is a viable alternative to pressure gradient control or control by suction and blowing. The application of pressure gradient control requires a change in shape of a profile and may create additional structural requirements. Although suction control does not necessitate a change in shape, a mass source is needed and the suction slots have to be carefully designed so as not to introduce additional disturbances into the flow. Surface heating is a nonintrusive method of control and can be applied to any geometry.

With the increase in computing capability over the past several years, the simulation of three-dimensional transition has become feasible. In this work, a three-dimensional numerical investigation of transition control using surface heating techniques is conducted. Both passive and active methods of transition

control are studied in an effort to provide insight into the potential of each mode of control.

The numerical simulation models the three-dimensional hydrodynamic stability of an initially laminar, incompressible boundary layer on a flat plate with constant or time-periodic surface heating applied. The complete unsteady three-dimensional Navier-Stokes and energy equations are the basic governing equations used in the simulations. As mentioned in Chapter 1, there are two conceptual frameworks in which to consider the stability problem, spatial and temporal.

Important contributions have already been made in investigations of laminar flow control. However, in the previous numerical investigations of passive and active transition control, except for the two-dimensional studies of Bayliss, Maestrello, Parikh, and Turkel (1985) and Dittrich (1985), the temporal stability model was chosen primarily for its simplicity. In the temporal approach, the base flow does not vary in the streamwise direction because the flow phenomena are assumed spatially periodic in this direction. The growth of the flow is in time. The spatially periodic results are then often transformed into temporally periodic results with spatial growth in the downstream direction using a transformation by Gaster (1962). This transformation is valid only if the growth rates are small and the mean flow is parallel. However, for the large growth rates of the secondary instability process, this transformation is no longer valid. The temporal model cannot capture all the features observed in the physical experiments. Nonparallel effects and the proper wave dispersion can be incorporated only in spatial models.

In this work, the numerical model allows for investigations of spatially growing, three-dimensional disturbance waves in a growing boundary layer. The difference between the temporal and spatial approaches is of fundamental importance because the effects of a localized disturbance input can be simulated

realistically only if the characteristics of the underlying base flow are not altered and if the disturbances are allowed to develop and propagate in the downstream direction. Direct comparison with laboratory experiments is then possible. In addition to this advantage, the feedback control loop in the active control experiments of Liepmann, Brown, and Nosenchuck (1982) can be realized only with the spatial model with feedback control applied in the streamwise direction.

Realistic two-dimensional numerical simulations of spatially growing and propagating small amplitude Tollmien-Schlichting waves in a boundary layer have been made by Fasel (1976). In these simulations, a vorticity-velocity formulation of the governing equations and a fully implicit finite difference method was used. Detailed quantitative comparisons with linear stability theory, the nonparallel theory of Gaster (1974), and also the experimental measurements of Schubauer and Skramstad (1948) and Ross, Barnes, Burns, and Ross (1970) has shown the simulations yield results of high accuracy. Fasel, Bestek, and Schefenacker (1977) have also used the same numerical method with larger oscillations to predict nonlinear effects in the two-dimensional stages of boundary layer transition. A modified version of this simulation was developed by Fasel and Bestek (1980) to study nonlinear oscillations in plane Poiseuille flow.

Fasel, Rist, and Konzelmann (1987) have developed a three-dimensional numerical method to investigate spatial three-dimensional disturbances in a boundary layer. The algorithm is a combined finite difference/spectral method with periodicity assumed in the spanwise direction. The underlying base flow is two-dimensional. Comparison with linear stability theory for small three-dimensional oblique waves shows results of the same degree of high accuracy as for the two-dimensional case. In addition, as mentioned in Chapter 1, both the nonlinear subharmonic and fundamental routes to transition have been simulated by Fasel,

Rist, and Konzelmann (1987) with excellent comparison to the experimental results of Kachanov and Levchenko (1984) and Klebanoff, Tidstrom, and Sargent (1962).

These previous numerical models are adapted in this current work to the problem of three-dimensional boundary layer transition control. The numerical model is extended to include the energy equation and the temperature dependent viscosity. The spectral representation in the spanwise direction exploits the periodic spanwise structures observed in the three-dimensional experimental investigations. Standard finite difference approximations are used in the streamwise and wall normal directions. In the following chapters the governing equations and the numerical model are described in detail. Chapter 3 describes the system of governing equations for incompressible fluid flow in three dimensions and time. The boundary and initial conditions for the spatial stability problem are presented in Chapter 4. The numerical method used to approximate the governing equations and boundary conditions is described in Chapter 5. In Chapter 6, numerical results of both passive and active transition control in a boundary layer flow are presented and compared to other investigations where appropriate. Finally, conclusions are given in Chapter 7.

This work focuses on the control of the secondary instability process in the boundary layer. However, in order to gain an understanding of the control aspects of transition, linear, small amplitude disturbances are first considered. Control of both two-dimensional Tollmien-Schlichting waves and three-dimensional oblique waves is studied. Through the simulation of the oblique waves, the applicability of the numerical model for investigating three-dimensional transition can then be verified. Both passive and active control by surface heating are investigated in these linear flow simulations. In the passive control investigations,

uniform and nonuniform surface temperature distributions are considered. The results are compared with available experimental measurements and theory.

In the active control simulations, a similar surface heating strip arrangement and feedback control loop is employed as was demonstrated in the two-dimensional control experiments of Liepmann and Nosenchuck (1982). Although these experiments are two-dimensional, the extension to three-dimensional, linear disturbances is straightforward. Robey (1987) has successfully triggered three-dimensional waves in the boundary layer by subjecting the heating strips to three-dimensional time-dependent temperature loading (The experiment was carried out in the same water channel that Liepmann and Nosenchuck (1982) used.).

In the active control numerical simulations, the physical mechanisms of how localized heat disturbances are transmitted into Tollmien-Schlichting waves in a boundary layer are investigated. This question addresses the complex problem of receptivity as first put forth by Morkovin (1969). As later described by Reshotko (1976), receptivity denotes the means by which a particular forced disturbance (in this case the localized wall temperature disturbance) enters the boundary layer and the nature of its signature in the disturbance flow. Insight into the physical mechanisms can be obtained by examining again the boundary layer momentum equation at the wall of the plate (Equation 1.9) in the absence of a pressure gradient and without suction or blowing:

$$\left(\frac{\partial^2 u}{\partial y^2}\right)_{y=0} = -\frac{1}{\mu_{y=0}} \left(\frac{d\mu}{dT}\right)_{y=0} \left(\frac{\partial T}{\partial y}\right)_{y=0} \left(\frac{\partial u}{\partial y}\right)_{y=0}. \quad (2.1)$$

With the spanwise vorticity,  $\omega_z$ , defined by

$$\omega_z = \frac{\partial u}{\partial y} - \frac{\partial v}{\partial x}, \quad (2.2)$$



Equation (2.1) becomes

$$\left(\frac{\partial \omega_z}{\partial y}\right)_{y=0} = -\frac{1}{\mu_{y=0}} \left(\frac{d\mu}{dT}\right)_{y=0} \left(\frac{\partial T}{\partial y}\right)_{y=0} \omega_{zy=0}. \quad (2.3)$$

Thus it is expected that the heat disturbances (creating viscosity perturbations) mainly cause a spanwise vorticity gradient normal to the wall. Better understanding of this receptivity mechanism is helpful in possibly improving active control by using heating strips, and is addressed in these numerical simulations. Maestrello (1984) has carried out a theoretical analysis of active surface heating in an incompressible flow and shows that small amounts of localized surface heating can excite disturbances. The local periodic heating was related to normal velocity disturbances and pressure disturbances. In the numerical simulations considered here, the signature of the spanwise vorticity disturbance is examined. An optimal width of the heating strip is also explored.

Control of the nonlinear secondary instability process is investigated with either passive or active heating applied. Both the fundamental ordered peak-valley and the subharmonic staggered peak-valley processes are studied. To limit computational costs, only one mode in the spanwise direction is retained so that reasonably high grid resolution in the streamwise and normal directions could be maintained. Therefore, control of the early stage of the secondary instability process of boundary layer transition is studied. Uniform surface heating is employed in the passive control simulations. For the active control simulations, the effectiveness of a two-dimensional control input versus a three-dimensional control input is examined.

## CHAPTER 3

## GOVERNING EQUATIONS

The flow of a nonisothermal viscous fluid is governed by the Navier-Stokes and energy equations. These equations form a nonlinear, second-order system of partial differential equations and have various forms depending on the physical properties of the fluid, the coordinate system, and the specific parameters chosen to describe the flow. In this work, the flow of a three-dimensional incompressible fluid in a rectangular coordinate system is considered. The vorticity-velocity formulation of the Navier-Stokes equations is preferred to the primitive variable (velocity-pressure) representation. The governing equations and assumptions made are described in detail below. Also, the nondimensionalization of the governing equations in regards to the length, velocity, temperature, and time scales of the problem is presented.

### 3.1 Equations of Motion in Primitive Variable Representation

The Navier-Stokes and energy equations describe the conservation of mass, momentum, and energy of a viscous fluid. For the incompressible, three-dimensional flow of a Newtonian fluid, the conservation laws are (in vector form and indicial notation)

Continuity:

$$\frac{D\bar{\rho}}{Dt} + \bar{\rho} \bar{\nabla} \cdot \bar{\mathbf{U}} = 0 \quad (3.1)$$

Momentum:

$$\bar{\rho} \frac{D\bar{\mathbf{U}}}{Dt} = \bar{\rho} \bar{\mathbf{g}} - \bar{\nabla} \bar{p} + \bar{\nabla} \cdot \bar{\boldsymbol{\tau}}'_{ij} \quad (3.2)$$

Energy:

$$\bar{\rho} \bar{c} \frac{D\bar{T}}{Dt} = \bar{\nabla} \cdot (\bar{k} \bar{\nabla} \bar{T}) + \bar{\Phi} \quad (3.3)$$

where  $\bar{\Phi}$  is the dissipation function:

$$\bar{\Phi} = \tau'_{ij} \frac{\partial \bar{u}_i}{\partial \bar{x}_j} \quad (3.4)$$

and  $\tau'_{ij}$  is the shear stress tensor defined by

$$\tau'_{ij} = \bar{\mu} \left( \frac{\partial \bar{u}_i}{\partial \bar{x}_j} + \frac{\partial \bar{u}_j}{\partial \bar{x}_i} \right) . \quad (3.5)$$

The velocity  $\bar{\mathbf{U}}$  is a vector field:

$$\bar{\mathbf{U}} = [\bar{u}, \bar{v}, \bar{w}] \quad (3.6)$$

and  $\bar{\mathbf{g}}$  is the vector of gravitational acceleration:

$$\bar{\mathbf{g}} = [\bar{g}_{\bar{x}}, \bar{g}_{\bar{y}}, \bar{g}_{\bar{z}}] \quad (3.7)$$

whose components are functions of spatial location  $\bar{\mathbf{x}}$  and time  $\bar{t}$ :

$$\bar{\mathbf{U}} = \bar{\mathbf{U}}(\bar{\mathbf{x}}, \bar{t}) \quad (3.8)$$

$$\bar{\mathbf{g}} = \bar{\mathbf{g}}(\bar{\mathbf{x}}, \bar{t}) \quad (3.9)$$

$$\bar{\mathbf{x}} = [\bar{x}, \bar{y}, \bar{z}] . \quad (3.10)$$

The pressure  $\bar{p}$  and temperature  $\bar{T}$  are scalar fields:

$$\bar{p} = \bar{p}(\bar{\mathbf{x}}, \bar{t}) \quad (3.11)$$

$$\bar{T} = \bar{T}(\bar{\mathbf{x}}, \bar{t}) . \quad (3.12)$$

The fluid properties are the density  $\bar{\rho}$ , thermal conductivity  $\bar{k}$ , specific heat  $\bar{c}$ , and dynamic viscosity  $\bar{\mu}$  and are also scalar fields:

$$\bar{\rho} = \bar{\rho}(\bar{\mathbf{x}}, \bar{t}) \quad (3.13)$$

$$\bar{k} = \bar{k}(\bar{\mathbf{x}}, \bar{t}) \quad (3.14)$$

$$\bar{c} = \bar{c}(\bar{\mathbf{x}}, \bar{t}) \quad (3.15)$$

$$\bar{\mu} = \bar{\mu}(\bar{\mathbf{x}}, \bar{t}) . \quad (3.16)$$

The relationship for the internal energy,  $d\bar{e} = \bar{c} d\bar{T}$ , has been employed. The upper bars denote dimensional quantities.

The term ' $\bar{\rho}\bar{g}$ ' in Equation (3.2) represents a body force impressed on the fluid. In fluid motions where temperature differences create density gradients, it is sometimes necessary to include this term as a buoyancy force. Generally density is a function of pressure and temperature, but the dependence on pressure is small in flows affected by gravitation. Therefore, the density can be expanded in a Taylor series in temperature:

$$\bar{\rho}(\bar{T}) = \bar{\rho}_\infty + (\bar{T} - \bar{T}_\infty) \left( \frac{d\bar{\rho}}{d\bar{T}} \right)_{\bar{T}=\bar{T}_\infty} + \frac{(\bar{T} - \bar{T}_\infty)^2}{2} \left( \frac{d^2\bar{\rho}}{d\bar{T}^2} \right)_{\bar{T}=\bar{T}_\infty} + \dots \quad (3.17)$$

where ' $\infty$ ' denotes the freestream flow conditions. Introducing the coefficient of thermal expansion,

$$\bar{\beta}_\infty = -\frac{1}{\bar{\rho}_\infty} \left( \frac{\partial \bar{\rho}}{\partial \bar{T}} \right)_{\bar{p}=\bar{p}_\infty, \bar{T}=\bar{T}_\infty} \quad (3.18)$$

and considering moderate temperature differences, Equation (3.17) can be then be approximated by

$$\bar{\rho} = \bar{\rho}_\infty (1 - \bar{\beta}_\infty (\bar{T} - \bar{T}_\infty)) . \quad (3.19)$$

Substitution of Equation (3.19) into Equation (3.2) yields

$$\bar{\rho} \frac{D\bar{U}}{Dt} = \bar{\rho}_\infty \bar{g} - \nabla \bar{p} - \bar{\rho}_\infty \bar{\beta}_\infty (\bar{T} - \bar{T}_\infty) \bar{g} + \nabla \cdot \bar{\tau}'_{ij} . \quad (3.20)$$

The first two terms on the right hand side can be combined into a single gradient function,  $-\nabla (\bar{p} - \bar{\rho}_\infty \bar{g} \cdot \bar{x})$ , and a new pressure can then be defined:

$$\bar{P} = \bar{p} - \bar{\rho}_\infty \bar{g} \cdot \bar{x} - \bar{p}_\infty . \quad (3.21)$$

Introducing this *modified pressure* term into Equation (3.20) results in the following form of the momentum equation:

$$\bar{\rho} \frac{D\bar{U}}{Dt} = -\nabla \bar{P} - \bar{\rho}_\infty \bar{\beta}_\infty (\bar{T} - \bar{T}_\infty) \bar{g} + \nabla \cdot \bar{\tau}'_{ij} . \quad (3.22)$$

Simplifications of the governing equations, leading to the exclusion of specific effects on the flow (e.g., buoyancy, viscous dissipation, and variable fluid properties), is made after examining the relevant nondimensional coefficients.

### 3.2 Nondimensionalization

The equations of continuity (3.1), momentum (3.22), and energy (3.3) are in dimensional form. Nondimensionalization of the basic equations allows for a more efficient form and produces physical insight into the flow. The equations are made dimensionless by choosing characteristic scales that correspond with the physical scales of the problem considered. The flow variables are nondimensionalized with the following constants:

$$\begin{aligned}
 x &= \frac{\bar{x}}{\bar{L}} & y &= \frac{\bar{y}}{\bar{L}} \sqrt{Re} & z &= \frac{\bar{z}}{\bar{L}} \\
 u &= \frac{\bar{u}}{\bar{U}_\infty} & v &= \frac{\bar{v}}{\bar{U}_\infty} \sqrt{Re} & w &= \frac{\bar{w}}{\bar{U}_\infty} \\
 t &= \frac{\bar{t} \bar{U}_\infty}{\bar{L}} & T &= \frac{\bar{T} - \bar{T}_\infty}{\bar{T}_w - \bar{T}_\infty} & P &= \frac{\bar{P} - \bar{P}_\infty}{\bar{\rho}_\infty \bar{U}_\infty^2} \\
 \mu &= \frac{\bar{\mu}}{\bar{\mu}_\infty} & c &= \frac{\bar{c}}{\bar{c}_\infty} & k &= \frac{\bar{k}}{\bar{k}_\infty} \\
 \rho &= \frac{\bar{\rho}}{\bar{\rho}_\infty}
 \end{aligned} \tag{3.23}$$

where the subscript 'w' represents the wall value and  $\bar{L}$  is a characteristic length. The parameter  $Re$  is the Reynolds number defined below. The  $y$  coordinate and normal velocity component  $v$  are stretched by the factor  $\sqrt{Re}$  to insure that all coordinates and velocity components are of the same order of magnitude in the numerical computations.

Substitution of these new nondimensional variables into the dimensional equations results in the following nondimensional set of equations:

$$\frac{D\rho}{Dt} + \rho \nabla_1 \cdot \mathbf{U} = 0 \tag{3.24}$$

$$\rho \frac{DU}{Dt} = -\nabla_2 P - \frac{Gr_x}{Re^2} T + \frac{1}{Re} \nabla_2 \cdot \tau'_{ij} \quad (3.25)$$

$$\rho c \frac{DT}{Dt} = \frac{1}{Re Pr} \nabla_2 \cdot (k \nabla_2 T) + \frac{Ec}{Re} \Phi \quad (3.26)$$

where

$$\nabla_1 = \frac{\partial}{\partial x} \mathbf{i} + \frac{\partial}{\partial y} \mathbf{j} + \frac{\partial}{\partial z} \mathbf{k}, \quad (3.27)$$

$$\nabla_2 = \frac{\partial}{\partial x} \mathbf{i} + \sqrt{Re} \frac{\partial}{\partial y} \mathbf{j} + \frac{\partial}{\partial z} \mathbf{k}, \quad (3.28)$$

$$\begin{aligned} \Phi = \mu \left[ 2 \left( \frac{\partial u}{\partial x} \right)^2 + 2 \left( \frac{\partial v}{\partial y} \right)^2 + 2 \left( \frac{\partial w}{\partial z} \right)^2 + \frac{1}{Re} \left( \frac{\partial v}{\partial x} + Re \frac{\partial u}{\partial y} \right)^2 \right. \\ \left. + \frac{1}{Re} \left( Re \frac{\partial w}{\partial y} + \frac{\partial v}{\partial z} \right)^2 + \left( \frac{\partial u}{\partial z} + \frac{\partial w}{\partial x} \right)^2 \right] \end{aligned} \quad (3.29)$$

and

$$\tau'_{ij} = \mu \begin{pmatrix} 2 \frac{\partial u}{\partial x} & \sqrt{Re} \frac{\partial u}{\partial y} + \frac{1}{\sqrt{Re}} \frac{\partial v}{\partial x} & \frac{\partial u}{\partial z} + \frac{\partial w}{\partial x} \\ \sqrt{Re} \frac{\partial u}{\partial y} + \frac{1}{\sqrt{Re}} \frac{\partial v}{\partial x} & 2 \frac{\partial v}{\partial y} & \frac{1}{\sqrt{Re}} \frac{\partial v}{\partial z} + \sqrt{Re} \frac{\partial w}{\partial y} \\ \frac{\partial u}{\partial z} + \frac{\partial w}{\partial x} & \frac{1}{\sqrt{Re}} \frac{\partial v}{\partial z} + \sqrt{Re} \frac{\partial w}{\partial y} & 2 \frac{\partial w}{\partial z} \end{pmatrix}. \quad (3.30)$$

The solutions of the above governing equations depend on the following four nondimensional parameters:

$$\text{Reynolds number : } Re = \frac{\bar{\rho} \bar{U}_\infty \bar{L}}{\bar{\mu}_\infty} \quad (3.31)$$

$$\text{Grashof number : } Gr_x = \frac{\bar{g} \bar{\beta}_\infty \bar{\rho}_\infty^2 \bar{L}^3 (\bar{T}_w - \bar{T}_\infty)}{\bar{\mu}_\infty^2} \quad (3.32)$$

$$\text{Prandtl number : } Pr = \frac{\bar{\mu}_\infty \bar{c}_\infty}{k_\infty} \quad (3.33)$$

$$\text{Eckert number : } Ec = \frac{\bar{U}_\infty^2}{\bar{c}_\infty (\bar{T}_w - \bar{T}_\infty)} \quad (3.34)$$

At this juncture, an assessment of the influence of the various force, energy, and variable property effects on the flow is made. The following conclusions are reached:

- 1.) Buoyancy effects can be neglected if  $\frac{Gr_x}{Re^2} \ll 1$ . The Grashof number becomes important only at very small flow velocities. With even moderate velocities, the buoyancy forces in Equation (3.25) are small compared with the inertia and viscous forces. The flow speeds considered in this work are large enough that the buoyancy forces do not contribute to the solution of the flow.
- 2.) Viscous dissipation (frictional heat) is negligible if  $Pr Ec \ll 1$ . The largest Eckert numbers estimated for the flow conditions in this work are  $O(10^{-3})$ . Dissipation is not important for the moderate velocities considered here.
- 3.) Finally, a consideration of the importance of the dependence of the fluid properties on temperature and pressure is made. Water is chosen as the representative fluid in this work so that the results of this investigation are applicable to technical situations occurring in nature. In addition, comparison with the results of previous experimental and theoretical investigations can be made since water was considered in these studies. For water, the fluid properties are not affected by moderate pressures. The specific heat and density are relatively independent of temperature and the thermal conductivity also varies little with temperature in water. However, the viscosity of water decreases very markedly with increasing temperature. Considering the normal liquid range of water ( $0^\circ C$  to  $100^\circ C$ ), the specific heat varies by only approximately 0.28%, the density by 4.2%, and the thermal conductivity by 18%. However

the viscosity varies by about 146% over this temperature range. Even for more moderate temperature differences, the viscosity variation with temperature becomes important. Therefore, in the flow considered here, the viscosity variation with temperature is included. The other fluid properties are held constant.

With the above assumptions now introduced, the nondimensional governing equations become

$$\nabla_1 \cdot \mathbf{U} = 0 \quad (3.35)$$

$$\frac{D\mathbf{U}}{Dt} = -\nabla_2 P + \frac{1}{Re} \nabla_2 \cdot \tau'_{ij} \quad (3.36)$$

$$\frac{DT}{Dt} = \frac{1}{Re Pr} \nabla_1^2 T \quad (3.37)$$

where

$$\nabla_1^2 = \frac{\partial^2}{\partial x^2} + Re \frac{\partial^2}{\partial y^2} + \frac{\partial^2}{\partial z^2} \quad (3.38)$$

### 3.3 Equations of Motion in Vorticity-Velocity Representation

The primitive variable formulation of the governing equations was presented in order to provide ease in the analysis of the influence of specific effects on the flow. However, vorticity dynamics plays an important role in the behavior of boundary layer flows and so the vorticity transport form of the Navier-Stokes equations is more advantageous than the primitive variable formulation of the governing equations.

The vorticity transport equation is derived by taking the curl of the momentum equation:

$$\frac{D\bar{\omega}}{Dt} - (\bar{\omega} \cdot \bar{\nabla}) \bar{\mathbf{U}} = \bar{\nabla} \times (\bar{\nabla} \cdot \bar{\tau}'_{ij}) \quad (3.39)$$



where  $\bar{\omega}$  is the vorticity vector field:

$$\bar{\omega} = [\bar{\omega}_x, \bar{\omega}_y, \bar{\omega}_z] \quad (3.40)$$

defined by

$$\bar{\omega} = -\bar{\nabla} \times \bar{U}. \quad (3.41)$$

The bars again denote dimensional quantities. The second term on the left hand side of Equation (3.40) arises from the convective derivatives and is called the vortex stretching term. The term on the right hand side is the viscous diffusion term. The pressure  $\bar{P}$  has disappeared from Equation (3.39) since, for a scalar field  $s(x, t)$

$$\nabla \times \nabla s = 0 \quad (3.42)$$

The viscous diffusion term can be rewritten as

$$\bar{\nabla} \times (\bar{\nabla} \cdot \bar{\tau}'_{ij}) = \bar{\mu} \bar{\nabla}^2 \bar{\omega} - \bar{\nabla} \bar{\mu} \times (\bar{\nabla} \times \bar{\omega}) + \bar{\nabla} \times (\bar{\nabla} \bar{\mu} \cdot \bar{\tau}_{ij}) \quad (3.43)$$

where

$$\bar{\tau}_{ij} = \frac{\bar{\tau}'_{ij}}{\bar{\mu}}. \quad (3.44)$$

Equation (3.43) was derived using the following vector relationships:

$$\begin{aligned} \bar{A} &= \bar{\nabla} \cdot (\bar{\mu} \bar{\tau}_{ij}) \\ &= \bar{\mu} \bar{\nabla} \cdot \bar{\tau}_{ij} + \bar{\nabla} \bar{\mu} \cdot \bar{\tau}_{ij}, \end{aligned} \quad (3.45)$$

but

$$\bar{\nabla} \cdot \bar{\tau}_{ij} = \bar{\nabla}^2 \bar{U} \quad (3.46)$$

so

$$\bar{A} = \bar{\mu} \bar{\nabla}^2 \bar{U} + \bar{\nabla} \bar{\mu} \cdot \bar{\tau}_{ij}. \quad (3.47)$$

Before taking the curl of Equation (3.47), the following vector identities are introduced, with  $\bar{\mathbf{B}} = \nabla^2 \bar{\mathbf{U}}$ .

$$\begin{aligned}\nabla \times (\bar{\mu} \bar{\mathbf{B}}) &= \bar{\mu} \nabla \times \bar{\mathbf{B}} + \nabla \bar{\mu} \times \bar{\mathbf{B}} \\ &= \bar{\mu} \nabla \times \bar{\mathbf{B}} - \bar{\mathbf{B}} \times \nabla \bar{\mu}\end{aligned}\quad (3.48)$$

and

$$\begin{aligned}\nabla \times (\nabla \times \bar{\mathbf{U}}) &= \nabla (\nabla \cdot \bar{\mathbf{U}}) - \nabla^2 \bar{\mathbf{U}} \\ &= \nabla (\nabla \cdot \bar{\mathbf{U}}) - \bar{\mathbf{B}}.\end{aligned}\quad (3.49)$$

The first term on the right hand side of Equation (3.49) vanishes by consideration of the continuity equation (3.35), so

$$\nabla \times (\nabla \times \bar{\mathbf{U}}) = -\bar{\mathbf{B}} \quad (3.50)$$

or

$$\nabla \times \bar{\boldsymbol{\omega}} = \nabla^2 \bar{\mathbf{U}}. \quad (3.51)$$

Now taking the curl of Equation (3.47) yields

$$\nabla \times \bar{\mathbf{A}} = -\bar{\mu} \nabla \times (\nabla \times \bar{\boldsymbol{\omega}}) + (\nabla \times \bar{\boldsymbol{\omega}}) \times (\nabla \bar{\mu}) + \nabla \times (\nabla \bar{\mu} \cdot \bar{\tau}_{ij}). \quad (3.52)$$

The following vector relationship is considered:

$$\nabla \times (\nabla \times \bar{\boldsymbol{\omega}}) = \nabla (\nabla \cdot \bar{\boldsymbol{\omega}}) - \nabla^2 \bar{\boldsymbol{\omega}}, \quad (3.53)$$

but for any vector  $\bar{\mathbf{C}}$

$$\nabla \cdot (\nabla \times \bar{\mathbf{C}}) = 0 \quad (3.54)$$

or

$$\nabla \cdot \bar{\boldsymbol{\omega}} = 0. \quad (3.54a)$$

Equation (3.54a) implies that vorticity, like velocity, must be divergence free. Equation (3.50) then becomes

$$\bar{\nabla} \times (\bar{\nabla} \times \bar{\omega}) = -\bar{\nabla}^2 \bar{\omega} \quad (3.55)$$

and so finally

$$\bar{\nabla} \times \bar{A} = \bar{\mu} \bar{\nabla}^2 \bar{\omega} - \bar{\nabla} \bar{\mu} \times (\bar{\nabla} \times \bar{\omega}) + \bar{\nabla} \times (\bar{\nabla} \bar{\mu} \cdot \bar{\tau}_{ij}) . \quad (3.56)$$

Thus the vorticity transport equation, with temperature dependent viscosity, becomes

$$\frac{D\bar{\omega}}{Dt} - (\bar{\omega} \cdot \bar{\nabla}) \bar{U} = \bar{\mu} \bar{\nabla}^2 \bar{\omega} - \bar{\nabla} \bar{\mu} \times (\bar{\nabla} \times \bar{\omega}) + \bar{\nabla} \times (\bar{\nabla} \bar{\mu} \cdot \bar{\tau}_{ij}) . \quad (3.57)$$

The velocity and vorticity components are related through Poisson type equations as seen by Equation (3.51). In this work, three Poisson equations are derived by relating the three velocity components to the three components of vorticity. The three Poisson equations are

$$\bar{\nabla}_2^2 \bar{u} = -\frac{\partial \bar{\omega}_y}{\partial \bar{z}} - \frac{\partial^2 \bar{v}}{\partial \bar{x} \partial \bar{y}} \quad (3.58)$$

$$\bar{\nabla}_1^2 \bar{v} = \frac{\partial \bar{\omega}_x}{\partial \bar{z}} - \frac{\partial \bar{\omega}_z}{\partial \bar{x}} \quad (3.59)$$

$$\bar{\nabla}_2^2 \bar{w} = \frac{\partial \bar{\omega}_y}{\partial \bar{x}} - \frac{\partial^2 \bar{v}}{\partial \bar{y} \partial \bar{z}} \quad (3.60)$$

where

$$\bar{\nabla}_1^2 = \frac{\partial^2}{\partial \bar{x}^2} + \frac{\partial^2}{\partial \bar{y}^2} + \frac{\partial^2}{\partial \bar{z}^2} \quad (3.61)$$

$$\bar{\nabla}_2^2 = \frac{\partial^2}{\partial \bar{x}^2} + \frac{\partial^2}{\partial \bar{z}^2} . \quad (3.62)$$

The Poisson equation for the  $u$  velocity, Equation (3.58), is derived by the following algebraic manipulations:

$$u \text{ Poisson Equation} = \frac{\partial}{\partial \bar{x}} (\bar{\nabla} \cdot \bar{U}) + \frac{\partial}{\partial \bar{z}} (\bar{\omega}_y) \quad (3.63)$$

where

$$\bar{\omega}_y = \frac{\partial \bar{w}}{\partial \bar{x}} - \frac{\partial \bar{u}}{\partial \bar{z}}. \quad (3.64)$$

The Poisson equation for the  $v$  velocity, Equation (3.59) is taken from the  $v$ -component of Equation (3.51). Finally, the Poisson equation for the  $w$  velocity component, Equation (3.60), stems from the following addition:

$$w \text{ Poisson Equation} = \frac{\partial}{\partial \bar{z}} (\nabla \cdot \bar{\mathbf{U}}) + \frac{\partial}{\partial \bar{x}} (\bar{\omega}_y). \quad (3.65)$$

Although two of the three Poisson equations appear nonstandard, in that Equation (3.51) is not used, the justification for these equations will become apparent when the wall boundary conditions for the vorticity are considered.

The vorticity-velocity formulation of the governing equations is nondimensionalized with the scales given by Equation (3.23) and with the following additional nondimensional flow variables:

$$\omega_x = \frac{\bar{\omega}_x \bar{L}}{\bar{U}_\infty \sqrt{Re}} \quad \omega_y = \frac{\bar{\omega}_y \bar{L}}{\bar{U}_\infty} \quad \omega_z = \frac{\bar{\omega}_z \bar{L}}{\bar{U}_\infty \sqrt{Re}}. \quad (3.66)$$

The nondimensional vorticity components are then defined by

$$\omega_x = \frac{1}{Re} \frac{\partial v}{\partial z} - \frac{\partial w}{\partial y} \quad (3.67a)$$

$$\omega_y = \frac{\partial w}{\partial x} - \frac{\partial u}{\partial z} \quad (3.67b)$$

$$\omega_z = \frac{\partial u}{\partial y} - \frac{1}{Re} \frac{\partial v}{\partial x} \quad (3.67c)$$

The vorticity transport equation, in nondimensional form, is

$$\frac{D\omega}{Dt} - (\omega \cdot \nabla_1) \mathbf{U} = \mu \nabla_1^2 \omega + c \quad (3.68)$$

where the components of the vector  $\mathbf{c} = [c_x, c_y, c_z]$  are defined as follows:

$$\begin{aligned}
 c_x = & + \frac{1}{Re} \frac{\partial \mu}{\partial x} \left( \frac{\partial \omega_x}{\partial x} \right) - \frac{\partial \mu}{\partial y} \left( \frac{1}{Re} \frac{\partial \omega_y}{\partial x} - 2 \frac{\partial \omega_x}{\partial y} \right) \\
 & + \frac{1}{Re} \frac{\partial \mu}{\partial z} \left( 2 \frac{\partial \omega_x}{\partial z} - \frac{\partial \omega_z}{\partial x} \right) - \frac{1}{Re} \frac{\partial^2 \mu}{\partial x \partial y} \left( \frac{\partial u}{\partial z} + \frac{\partial w}{\partial x} \right) \\
 & - \frac{2}{Re} \frac{\partial^2 \mu}{\partial y \partial z} \left( \frac{\partial w}{\partial z} - \frac{\partial v}{\partial y} \right) + \frac{1}{Re} \frac{\partial^2 \mu}{\partial x \partial z} \left( \frac{\partial u}{\partial y} + \frac{1}{Re} \frac{\partial v}{\partial x} \right) \\
 & - \left( \frac{\partial^2 \mu}{\partial y^2} - \frac{1}{Re} \frac{\partial^2 \mu}{\partial z^2} \right) \left( \frac{1}{Re} \frac{\partial v}{\partial z} + \frac{\partial w}{\partial y} \right)
 \end{aligned} \tag{3.69a}$$

$$\begin{aligned}
 c_y = & + \frac{\partial \mu}{\partial x} \left( \frac{2}{Re} \frac{\partial \omega_y}{\partial x} - \frac{\partial \omega_x}{\partial y} \right) + \frac{\partial \mu}{\partial y} \left( \frac{\partial \omega_y}{\partial y} \right) \\
 & - \frac{\partial \mu}{\partial z} \left( \frac{\partial \omega_x}{\partial y} - \frac{2}{Re} \frac{\partial \omega_y}{\partial z} \right) + \frac{\partial^2 \mu}{\partial x \partial y} \left( \frac{1}{Re} \frac{\partial v}{\partial z} + \frac{\partial w}{\partial y} \right) \\
 & - \frac{\partial^2 \mu}{\partial y \partial z} \left( \frac{\partial u}{\partial y} + \frac{1}{Re} \frac{\partial v}{\partial x} \right) - \frac{2}{Re} \frac{\partial^2 \mu}{\partial x \partial z} \left( \frac{\partial u}{\partial x} - \frac{\partial w}{\partial z} \right) \\
 & - \left( \frac{1}{Re} \frac{\partial^2 \mu}{\partial z^2} - \frac{\partial^2 \mu}{\partial x^2} \right) \left( \frac{\partial u}{\partial z} + \frac{\partial w}{\partial x} \right)
 \end{aligned} \tag{3.69b}$$

$$\begin{aligned}
 c_z = & - \frac{1}{Re} \frac{\partial \mu}{\partial x} \left( \frac{\partial \omega_x}{\partial z} - \frac{\partial \omega_z}{\partial x} \right) + \frac{\partial \mu}{\partial y} \left( 2 \frac{\partial \omega_x}{\partial y} - \frac{1}{Re} \frac{\partial \omega_y}{\partial z} \right) \\
 & + \frac{1}{Re} \frac{\partial \mu}{\partial z} \left( \frac{\partial \omega_x}{\partial z} \right) - \frac{2}{Re} \frac{\partial^2 \mu}{\partial x \partial y} \left( \frac{\partial v}{\partial y} - \frac{\partial u}{\partial x} \right) \\
 & + \frac{1}{Re} \frac{\partial^2 \mu}{\partial y \partial z} \left( \frac{\partial u}{\partial z} - \frac{\partial w}{\partial x} \right) - \frac{1}{Re} \frac{\partial^2 \mu}{\partial x \partial z} \left( \frac{1}{Re} \frac{\partial v}{\partial z} + \frac{\partial w}{\partial y} \right) \\
 & - \left( \frac{1}{Re} \frac{\partial^2 \mu}{\partial x^2} - \frac{\partial^2 \mu}{\partial y^2} \right) \left( \frac{\partial u}{\partial y} + \frac{1}{Re} \frac{\partial v}{\partial x} \right)
 \end{aligned} \tag{3.69c}$$

Equation (3.541) in nondimensional form becomes

$$\nabla \cdot \boldsymbol{\omega} = 0 \tag{3.70}$$

The three Poisson equations in nondimensional form are

$$\nabla_2^2 u = - \frac{\partial \omega_y}{\partial z} - \frac{\partial^2 v}{\partial x \partial y} \tag{3.71}$$

$$\nabla_1^2 v = \frac{\partial \omega_x}{\partial z} - \frac{\partial \omega_z}{\partial x} \tag{3.72}$$

$$\nabla_2^2 w = \frac{\partial \omega_y}{\partial x} - \frac{\partial^2 v}{\partial y \partial z} \tag{3.73}$$

where

$$\nabla_2^2 = \frac{\partial^2}{\partial x^2} + \frac{\partial^2}{\partial z^2} \quad (3.74)$$

and  $\nabla_1^2$  is as defined by Equation (3.38).

The fundamental set of equations used in this work are represented by Equations (3.69) through (3.73), the energy equation (3.37), and the continuity equation (3.35). These equations comprise a system of nine equations for the eight components  $u$ ,  $v$ ,  $w$ ,  $\omega_x$ ,  $\omega_y$ ,  $\omega_z$ ,  $T$ , and  $\mu$ . A final empirical equation relating the viscosity to the temperature,  $\mu = \mu(T)$ , is presented in the next section. With the inclusion of this relationship between the viscosity and temperature, ten equations for the eight components result. Thus not all ten conditions are independent. However, the continuity equation, which states that the divergence of velocity is zero, must be enforced only on the boundaries. This can be shown by taking the divergence of Equation (3.50) and imposing the vector identity (3.54) which yields

$$\nabla^2 (\nabla \cdot \bar{U}) = 0 \quad (3.75)$$

The maximum principle for Laplace's equation guarantees that the divergence of velocity will be zero everywhere in the domain if it is zero on the boundary. A similar principle does not exist for the vorticity divergence. In this work, Equation (3.70) is not enforced explicitly, but rather provides for a check of the quality of the numerical solution.

It can be seen from the dimensionless set of governing equations that two dimensionless parameters exist which govern the fluid motion, the Reynolds number,  $Re$ , and the Prandtl number,  $Pr$ . In addition to these two dimensionless parameters, five additional dimensionless parameters arise through the boundary conditions: 1.) the temperature ratio between the wall and the free stream

temperatures,  $\frac{\bar{T}_w}{\bar{T}_\infty}$ ; 2.) the disturbance frequency  $F = \frac{\bar{\beta} \bar{\nu}_\infty 10^4}{\bar{U}_\infty^2}$  where  $\bar{\nu}_\infty$  is the freestream kinematic viscosity and  $\bar{\beta}$  is the circular disturbance frequency; 3.) the ratio between the streamwise and spanwise disturbance wavelengths  $\frac{\bar{\lambda}_x}{\bar{\lambda}_z}$ ; 4.) the relative two-dimensional disturbance amplitude  $\frac{|\bar{u}'_{2D}|}{\bar{U}_\infty}$ ; and 5.) the relative three-dimensional disturbance amplitude  $\frac{|\bar{u}'_{3D}|}{\bar{U}_\infty}$ . In summary, the spatial stability problem for the heated boundary layer is characterized by the following seven nondimensional parameters:

- 1.) Reynolds number,  $Re$
- 2.) Prandtl number,  $Pr$
- 3.) temperature ratio,  $\frac{\bar{T}_w}{\bar{T}_\infty}$
- 4.) frequency parameter,  $F = \frac{\bar{\beta} \bar{\nu}_\infty 10^4}{\bar{U}_\infty^2}$
- 5.) ratio of streamwise to spanwise wavelengths,  $\frac{\bar{\lambda}_x}{\bar{\lambda}_z}$
- 6.) two-dimensional disturbance amplitude,  $\frac{|\bar{u}'_{2D}|}{\bar{U}_\infty}$
- 7.) three-dimensional disturbance amplitude,  $\frac{|\bar{u}'_{3D}|}{\bar{U}_\infty}$

### 3.4 Viscosity Variation with Temperature

Before proceeding further, the viscosity dependence on temperature is presented. The property data can be obtained by interpolating tabulated experimental data or by using an empirical viscosity-temperature relationship that is based on a curve fit of the experimental data. Since the viscosity variation with temperature is important in establishing the stability characteristics in a heated boundary layer, inaccurate viscosity information can cause discrepancies between the results of the numerical solutions and experimental investigations. Lowell (1974) has shown that even slight differences in property-temperature variations

can produce a marked effect on the stability characteristics. Since an empirical relationship provides values within acceptable experimental error limits, this method of determining the viscosity is preferred to that of using an interpolating polynomial since an interpolating polynomial can introduce deviations from experimental data. The empirical viscosity-temperature relationship chosen for this study is from the National Bureau of Standards from measurements in viscometers calibrated with water at  $20^{\circ}\text{C}$  and one atmosphere. The empirical relationship is for  $0^{\circ}\text{C} \leq \bar{T} \leq 20^{\circ}\text{C}$  :

$$\log_{10} \bar{\mu}_{\bar{T}} = \frac{1301}{998.333 + 8.1855(\bar{T} - 20) + 0.00585(\bar{T} - 20)^2} - 1.30233 \quad (3.76a)$$

for  $20^{\circ}\text{C} \leq \bar{T} \leq 100^{\circ}\text{C}$  :

$$\log_{10} \frac{\bar{\mu}_{\bar{T}}}{\bar{\mu}_{20}} = \frac{1.3272(20 - \bar{T}) - 0.001053(\bar{T} - 20)^2}{\bar{T} + 105} \quad (3.76b)$$

where temperature is in degrees Celsius, viscosity is in centipoise, and  $\bar{\mu}_{20} = 1.002$  cp. Equation (3.76a) was derived by Hardy and Cottington (1949) and Equation (3.76b) was derived by Swindels (1983).

To complete the mathematical model, the integration domain and boundary and initial conditions must be specified. This is the subject of the next chapter.



## CHAPTER 4

## BOUNDARY AND INITIAL CONDITIONS

The mathematical statement of the problem posed in Chapters 2 and 3 is not complete without specifying the integration domain and the boundary conditions on that domain. The particular problem considered here is complicated by the choice of studying the spatial development of the flow. In flow through systems, physically realistic inflow and outflow boundary conditions are difficult to prescribe. For this work, the boundary and initial conditions are based on physical insight, analytical work (Appendix A), and linear stability theory (Appendix B).

4.1 Time Domain for Passive Control

The time domains for the passive control and active control simulations differ slightly. For the passive control spatial stability problem, the time integration can be broken down into two steps:

- 1.) Obtain the steady, laminar, two-dimensional solution of the governing equations for the heated, undisturbed flow whose stability is to be investigated.
- 2.) Begin periodic forcing and obtain a time-dependent, three-dimensional, disturbed flow solution to the governing equations for several periods of the oscillation.

The time domain of Figure 4.1 shows the above two steps. From an initial condition at time  $t_0$ , the governing equations are integrated forward in time until a steady state is reached. Then at time  $t_1$ , the periodic disturbance perturbation is introduced to initiate the forcing. To minimize transient effects, a ramp function  $r(t)$  is prescribed during the interval  $t_1 \leq t \leq t_2$ . The full disturbance amplitude

is reached at time  $t = t_2$  with integration continuing for  $t_2 \leq t$  as the disturbance propagates downstream. The boundary conditions for the undisturbed flow are used for  $t \leq t_1$  and then switched to the disturbance flow boundary conditions at  $t = t_1$ .

#### 4.2 Time Domain for Active Control

For the active control spatial stability simulations, the time integration involves two disturbance inputs. The first input creates the initial disturbance in the flow and the second acts to control the initial instability wave. The time integration is broken down into the following three steps:

- 1.) Obtain the steady, laminar, two-dimensional solution of the governing equations for the undisturbed flow.
- 2.) Begin periodic forcing and obtain a time-dependent, three-dimensional, disturbed flow solution to the governing equations for several periods of the oscillation.
- 3.) Initiate periodic forcing at a heater strip that serves as the actuator, downstream of the input disturbance and obtain the solution to the governing equations for the two concurrent disturbances for several periods of the oscillation.

The time domain of Figure 4.2 depicts the above three steps. For the first two time steps the procedure is the same as for the passive control simulations. Again a ramp function  $r(t)$  is used to reduce transient harmonics. At time  $t_3 > t_2$ , the periodic disturbance perturbation is introduced at the heater strip to begin the actuator forcing. The integration continues for  $t_3 \leq t$  as the disturbances interact and propagate downstream. Again the boundary conditions are switched from the undisturbed flow to the disturbed flow conditions at time  $t = t_1$ .

### 4.3 Coordinate System and Spatial Domain

The spatial domain for the investigations considered in this work is a rectangular box shown in Figure 4.3. Although the origins of the coordinate system are arbitrary, the spanwise origin is chosen to be zero. The streamwise, normal, and spanwise dimensions are specified by input parameters  $l_x$ ,  $l_y$ , and  $l_z$ . The parameter  $l_x$  specifies the streamwise length of the box in terms of the three-dimensional disturbance wavelength,  $\bar{\lambda}_{x3D}$ , where the streamwise wavenumber  $\bar{\alpha}_{x3D}$  is a specified parameter. The parameter  $l_y$  specifies the dimension of the box in the normal direction based on the number of boundary layer displacement thicknesses,  $\bar{\delta}_1$ , at the inflow boundary. Finally, the parameter  $l_z$  specifies the spanwise extent of the box in terms of the spanwise wavelength,  $\bar{\lambda}_z$ , where the spanwise wavenumber  $\bar{\gamma}$  is also an input parameter. To enforce spanwise periodicity,  $l_z$  is an integer. The spatial domain is specified by the following equations:

$$\bar{x}_0 \leq \bar{x} \leq \bar{x}_N = \bar{x}_0 + l_x \bar{\lambda}_{x3D} = \bar{x}_0 + l_x \left( \frac{2\pi}{\bar{\alpha}_{x3D}} \right) \quad (4.1a)$$

$$0 = \bar{y}_0 \leq \bar{y} \leq \bar{y}_M = l_y \bar{\delta}_1 \quad (4.1b)$$

$$0 = \bar{z}_0 \leq \bar{z} \leq \bar{z}_K = \bar{z}_0 + l_z \bar{\lambda}_z = \bar{z}_0 + l_z \left( \frac{2\pi}{\bar{\gamma}} \right). \quad (4.1c)$$

### 4.4 Boundary and Initial Conditions for the Undisturbed Flow

In the analysis of boundary layer flows along a flat plate, the typical velocity profile used in stability analyses is the similarity solution of the boundary layer equations. For the case of isothermal flow, the well known Blasius boundary layer profile (1908) is widely used. For a uniform wall temperature distribution or for a power law temperature distribution ( $\bar{T}_w(\bar{x}) - \bar{T}_\infty = \bar{A}\bar{x}^n$ ) in a fluid with constant properties, the flow is also found to be self-similar. However, for a fluid with variable properties, the flow is not self-similar if the wall temperature

is nonuniform.<sup>1</sup> The similarity solutions of the momentum and energy equations with variable viscosity and a uniform wall temperature distribution are used to specify the inflow boundary conditions. The velocity, vorticity, and temperature components for this similarity solution are denoted by  $\bar{u}_{SIM}(\bar{x}, \bar{y})$ ,  $\bar{v}_{SIM}(\bar{x}, \bar{y})$ ,  $\bar{\omega}_{SIM}(\bar{x}, \bar{y})$ , and  $\bar{T}_{SIM}(\bar{x}, \bar{y})$ . These components are obtained as described in Appendix A. For the active control simulations, the wall at the inflow boundary is not heated and the similarity solution becomes the Blasius similarity solution. For the passive control simulations with nonuniform surface heating, the wall temperature prescribed at the inflow boundary is used in determining the similarity solution.

The streamwise coordinate,  $\bar{x}_0$ , specifies the location of the inflow boundary. It is convenient, however, to specify the Reynolds number based on displacement thickness,  $Re_{\delta_1}$ , to fix  $\bar{x}_0$ . This Reynolds number is defined by

$$Re_{\delta_1} = \frac{\bar{U}_\infty \bar{\delta}_1(\bar{x}_0)}{\bar{\nu}_\infty} \quad (4.2)$$

and is related to the Reynolds number,  $Re$ , by

$$Re_{\delta_1} = Re \left( \frac{\bar{\delta}_1}{\bar{L}} \right). \quad (4.3)$$

The boundary layer displacement thickness is defined by

$$\bar{\delta}_1 = \int_0^\infty \left( 1 - \frac{\bar{u}}{\bar{U}_\infty} \right) d\bar{y}. \quad (4.4)$$

Thus the upstream coordinate,  $\bar{x}_0$ , can be determined by Equations (4.2) and (4.4) given  $Re_{\delta_1}$ ,  $\bar{U}_\infty$ ,  $\bar{\nu}_\infty$ , and  $\bar{u}_{SIM}(\bar{x}, \bar{y})$ .

<sup>1</sup> Nayfeh and El-Hady (1980) found that nonsimilar boundary layer profiles are necessary in a stability analysis of nonuniform wall temperature distributions to even qualitatively agree with experimental data. In this work, the undisturbed flow is as solution of the full Navier-Stokes and energy equations and is thus a nonsimilar solution.

The complete set of boundary and initial conditions for the undisturbed flow is formulated below. The conditions are presented in dimensionless form based on the nondimensionalization given in Chapter 3. Since the undisturbed flow is two-dimensional, the  $w$  velocity and  $\omega_x$  and  $\omega_y$  vorticity components are identically zero everywhere and are omitted here. In addition, the boundary conditions on the lateral faces of the domain (B-F-G-C) and (A-E-H-D) of Figure 4.3 are also omitted since the base flow is two-dimensional.

#### 4.4.1 Initial Conditions for the Undisturbed Flow

The steady state solution to the governing equations can be obtained for any initial velocity, vorticity, and temperature distribution. However, computational time is significantly reduced if the initial conditions are close to the steady state solution. Therefore, the similarity solution is used to initialize the flow field for the undisturbed flow:

$$u(x, y, z, 0) = u_{SIM}(x, y) \quad (4.5a)$$

$$v(x, y, z, 0) = v_{SIM}(x, y) \quad (4.5b)$$

$$\omega_z(x, y, z, 0) = \omega_{zSIM}(x, y) \quad (4.5c)$$

$$T(x, y, z, 0) = T_{SIM}(x, y). \quad (4.5d)$$

#### 4.4.2 Inflow Boundary Conditions for the Undisturbed Flow

The similarity solution for the flat plate boundary layer is imposed at the inlet plane (A-B-C-D) as already described. The inflow conditions then are the following:

$$u(x_0, y, z, t) = u_{SIM}(x_0, y) \quad (4.6a)$$

$$v(x_0, y, z, t) = v_{SIM}(x_0, y) \quad (4.6b)$$

$$\omega_z(x_0, y, z, t) = \omega_{zSIM}(x_0, y) \quad (4.6c)$$

$$T(x_0, y, z, t) = T_{SIM}(x_0, y). \quad (4.6d)$$

#### 4.4.3 Outflow Boundary Conditions for the Undisturbed Flow

At the outflow plane (E-F-G-H), boundary conditions are imposed so as to minimize the upstream influence on the flow. These conditions are

$$\frac{\partial u}{\partial x}(x_N, y, z, t) = -\frac{\partial v}{\partial y}(x_N, y, z, t) \quad (4.7a)$$

$$\frac{\partial^2 v}{\partial x^2}(x_N, y, z, t) = 0 \quad (4.7b)$$

$$\frac{\partial^2 \omega_z}{\partial x^2}(x_N, y, z, t) = 0 \quad (4.7c)$$

$$\frac{\partial^2 T}{\partial x^2}(x_N, y, z, t) = 0. \quad (4.7d)$$

Equations (4.7) are derived from a consideration of the boundary layer equations and the continuity equation. For large Reynolds numbers, the viscous term  $\frac{\partial^2}{\partial x^2}$  is negligible. When this term is neglected, the equations become parabolic everywhere. For the current investigation with the full Navier-Stokes equations, this term is neglected only at the outflow boundary for the  $v$  Poisson, vorticity, and energy equations. Boundary condition (4.7a) is used to enforce continuity at the outflow boundary.

#### 4.4.4 Outer Boundary Conditions for the Undisturbed Flow

The boundary conditions at the outer boundary (D-C-G-H) are

$$u(x, y_M, z, t) = 1 \quad (4.8a)$$

$$\frac{\partial v}{\partial y}(x, y_M, z, t) = 0 \quad (4.8b)$$

$$\omega_z(x, y_M, z, t) = 0 \quad (4.8c)$$

$$T(x, y_M, z, t) = 0. \quad (4.8d)$$

Equation (4.8a) denotes that there is no freestream pressure gradient imposed on the flow. Equation (4.8b) is derived from the continuity equation and taking Equation (4.8a) into account. Condition (4.8c) is based on the physical consideration that the vorticity is confined to the region of high shear at the wall. Condition (4.8d) is also based on physical considerations. The thermal boundary layer for water is much smaller than the fluid boundary layer and the temperature gradients are confined to the wall region as well.

#### 4.4.5 Wall Boundary Conditions for the Undisturbed Flow

At the wall (A-B-F-E), the conditions for the undisturbed flow are

$$u(x, 0, x, t) = 0 \quad (4.9a)$$

$$v(x, 0, x, t) = 0 \quad (4.9b)$$

$$\frac{\partial v}{\partial y}(x, 0, x, t) = 0 \quad (4.9c)$$

$$\frac{\partial \omega_z}{\partial x}(x, 0, x, t) = -\frac{\partial^2 v}{\partial y^2} \quad (4.9d)$$

$$T(x, 0, x, t) = A(x) x^p. \quad (4.9e)$$

Boundary condition (4.9a) is the no slip condition and (4.9b) denotes no normal flow through the wall. Boundary condition (4.9c) is derived from the continuity equation. The boundary condition for the wall vorticity, (4.9d), is derived by applying the  $v$  Poisson equation (3.72) at the wall. Previous stability investigations by Fasel (1976) have shown that this boundary condition for the two-dimensional vorticity yields results in excellent agreement with experimental investigations.

Finally, for the wall temperature, boundary condition (4.9e) is imposed. This condition depends on the mode of control under investigation. The coefficient  $A(x)$  denotes the level of heating and the exponent  $p$  denotes the type of wall

temperature distribution. For  $A = 0$ , the wall is unheated. For the passive control investigations,  $A(x)$  is a constant  $A_0$ . For  $A_0 \neq 0$  and  $p = 0$ , a uniform wall temperature distribution is imposed. For  $A_0 \neq 0$  and  $p \neq 0$ , a nonuniform wall temperature distribution is used. For investigations using surface heater strips as disturbance inputs,  $A(x)$  is a specified local temperature distribution in the streamwise direction. The exponent  $p$  is zero for a heater strip simulation. This mean flow component to the temperature input at the heater strip represents the amount of overhear due to the presence of the heater strip and is discussed in more detail in Chapter 6. So in summary, the wall boundary condition for the temperature has the following form, depending on the mode of control:

1.) Temperature distribution for uniform wall heating:

$$A(x) = A_0 = \text{constant} \quad (4.10a)$$

$$p = 0 \quad (4.10b)$$

$$T(x, 0, z, t) = A_0. \quad (4.10c)$$

2.) Temperature distribution for nonuniform wall heating:

$$A(x) = A_0 = \text{constant} \quad (4.11a)$$

$$p \neq 0 \quad (4.11b)$$

$$T(x, 0, z, t) = A_0 x^p. \quad (4.11c)$$

3.) Temperature distribution for surface heater strip:

$$p = 0 \quad (4.12a)$$

$$T(x, 0, z, t) = \begin{cases} A(x) & \text{if } x_{HB_i} \leq x \leq x_{HE_i}, i = 1, \text{NHS;} \\ 0 & \text{otherwise.} \end{cases} \quad (4.12b)$$



where 'NHS' denotes the number of heater strips activated, with each heater strip employed for  $x_{HB,} \leq x \leq x_{HE,}$ . The choice of the function  $A(x)$  for the surface heater strips is presented in Chapter 6.

The enforcement of conservation of mass on the boundaries is necessary as already discussed. At the inflow boundary, mass conservation is automatically satisfied since the similarity solutions satisfy the continuity equation. The gradient conditions (4.8b) and (4.9c) at the outer and wall boundaries enforce continuity. At the outflow boundary, the continuity equation is directly applied as seen by boundary condition (4.7a). The complete set of boundary conditions for the undisturbed flow is shown schematically in Figure 4.4.

#### 4.5 Boundary and Initial Conditions for the Disturbed Flow

The disturbed flow problem is fundamentally different than for the undisturbed flow problem and requires different boundary conditions than for the steady flow. The conditions described below are three-dimensional and input periodic disturbances into the flow. These conditions represent a 'total flow' formulation of the stability problem in which the disturbances are superimposed upon the undisturbed solution.

##### 4.5.1 Initial Conditions for the Disturbed Flow

The two-dimensional steady state solution provides the initial condition at time  $t = t_1$  of Figures 4.1 and 4.2 for the time integration of the disturbed flow. This initial condition can be written as

$$u(x, y, z, t_1) = u_{ST}(x, y) \quad (4.13a)$$

$$v(x, y, z, t_1) = v_{ST}(x, y) \quad (4.13b)$$

$$w(x, y, z, t_1) = 0 \quad (4.13c)$$

$$\omega_x(x, y, z, t_1) = 0 \quad (4.13d)$$

$$\omega_y(x, y, z, t_1) = 0 \quad (4.13e)$$

$$\omega_z(x, y, z, t_1) = \omega_{zST} \quad (4.13f)$$

$$T(x, y, z, t_1) = T_{ST}(x, y), \quad (4.13g)$$

where the subscript 'ST' denotes the steady state solution. For the active control simulations, the initial condition at time  $t = t_2$  of Figure 4.2 is given by

$$u(x, y, z, t_2) = u_{ST}(x, y) + u'(x, y, z, t_2) \quad (4.14a)$$

$$v(x, y, z, t_2) = v_{ST}(x, y) + v'(x, y, z, t_2) \quad (4.14b)$$

$$w(x, y, z, t_2) = w'(x, y, z, t_2) \quad (4.14c)$$

$$\omega_x(x, y, z, t_2) = \omega'_x(x, y, z, t_2) \quad (4.14d)$$

$$\omega_y(x, y, z, t_2) = \omega'_y(x, y, z, t_2) \quad (4.14e)$$

$$\omega_z(x, y, z, t_2) = \omega_{zST}(x, y) + \omega'_z(x, y, z, t_2) \quad (4.14f)$$

$$T(x, y, z, t_2) = T_{ST}(x, y) + T'(x, y, z, t_2), \quad (4.14g)$$

where the prime denotes the perturbation components.

#### 4.5.2 Lateral Boundary Conditions for the Disturbed Flow

The flow is assumed to be spanwise periodic and, as discussed in Chapter 2, this assumption agrees well with experimental observations. The choice of spanwise periodicity greatly facilitates the numerical method. The periodicity conditions on the lateral boundaries (A-D-H-E) and (B-C-G-F) are

$$u(x, y, 0, t) = u(x, y, z_k, t) \quad (4.15a)$$

$$v(x, y, 0, t) = v(x, y, z_k, t) \quad (4.15b)$$

$$w(x, y, 0, t) = w(x, y, z_k, t) \quad (4.15c)$$

$$\omega_z(x, y, 0, t) = \omega_z(x, y, z_k, t) \quad (4.15d)$$

$$\omega_y(x, y, 0, t) = \omega_y(x, y, z_k, t) \quad (4.15e)$$

$$\omega_x(x, y, 0, t) = \omega_x(x, y, z_k, t) \quad (4.15f)$$

$$T(x, y, 0, t) = T(x, y, z_k, t). \quad (4.15g)$$

#### 4.5.3 Inflow Boundary Conditions for the Disturbed Flow

At the inlet plane (A-B-C-D), all disturbances are assumed to be zero.

Therefore, the similarity solution is imposed:

$$u(x_0, y, z, t) = u_{SIM}(x_0, y) \quad (4.16a)$$

$$v(x_0, y, z, t) = v_{SIM}(x_0, y) \quad (4.16b)$$

$$w(x_0, y, z, t) = 0 \quad (4.16c)$$

$$\omega_z(x_0, y, z, t) = 0 \quad (4.16d)$$

$$\omega_y(x_0, y, z, t) = 0 \quad (4.16e)$$

$$\omega_x(x_0, y, z, t) = \omega_{xSIM}(x_0, y) \quad (4.16f)$$

$$T(x_0, y, z, t) = T_{SIM}(x_0, y). \quad (4.16g)$$

#### 4.5.4 Outflow Boundary Conditions for the Disturbed Flow

Outflow boundary conditions are inherently difficult boundary conditions to prescribe for the spatial stability problem. A radiation condition is desired which is transparent to all disturbance wavelengths. For two-dimensional, small amplitude, monochromatic waves, Fasel (1976) has applied the following boundary conditions to the spatial stability problem with large success:

$$\frac{\partial^2 u}{\partial x^2}(x_N, y, t) = -\alpha_{rN}^2 u(x_N, y, t) \quad (4.17a)$$

$$\frac{\partial^2 v}{\partial x^2}(x_N, y, t) = -\alpha_{rN}^2 v(x_N, y, t) \quad (4.17b)$$

$$\frac{\partial^2 \omega_z}{\partial x^2}(x_N, y, t) = -\alpha_{rN}^2 \omega_z(x_N, y, t), \quad (4.17c)$$

where  $\alpha_{rN}$  is the real part of the wavenumber from the resulting perturbation flow. The flow is thus tuned to pass the disturbance of wavelength  $\lambda_N = \frac{2\pi}{\alpha_{rN}}$ . The wavenumber can be determined iteratively if it is not known a priori (Fasel (1976)). Equations (4.17) are derived by considering the form of the two-dimensional disturbance from linear stability theory, Equation (1.1):

$$u'(x, y, t) = \hat{u}(y)e^{i(\alpha x - \beta t)}. \quad (1.1)$$

Differentiating Equation (1.1) twice with respect to  $x$  gives Equations (4.17). Only the real part of the wavenumber is retained, but for the boundary layer  $\alpha_i \ll \alpha_r$ , so the assumption is valid. With these boundary conditions, the disturbances at the right boundary are sinusoidal and neither damp nor amplify there.

For the three-dimensional flow, analogous radiation conditions can be derived from Equation (1.3):

$$u'(x, y, z, t) = \hat{u}(y)e^{i(\alpha x + \gamma z - \beta t)} \quad (1.3)$$

and the three-dimensional boundary conditions become

$$\frac{\partial^2 u}{\partial x^2}(x_N, y, z, t) = \frac{\partial^2 u_{ST}}{\partial x^2}(x_N, y, z, t) - \alpha_{rN}^2 u(x_N, y, z, t) \quad (4.18a)$$

$$\frac{\partial^2 v}{\partial x^2}(x_N, y, z, t) = -\alpha_{rN}^2 (v(x_N, y, z, t) - v_{ST}(x_N, y)) \quad (4.18b)$$

$$\frac{\partial^2 w}{\partial x^2}(x_N, y, z, t) = -\alpha_{rN}^2 w(x_N, y, z, t) \quad (4.18c)$$

$$\frac{\partial^2 \omega_x}{\partial x^2}(x_N, y, z, t) = -\alpha_{rN}^2 \omega_x(x_N, y, z, t) \quad (4.18d)$$

$$\frac{\partial^2 \omega_y}{\partial x^2}(x_N, y, z, t) = -\alpha_{rN}^2 \omega_y(x_N, y, z, t) \quad (4.18e)$$

$$\frac{\partial^2 \omega_z}{\partial x^2}(x_N, y, z, t) = -\alpha_{rN}^2 (\omega_z(x_N, y, z, t) - \omega_{zST}(x_N, y)) \quad (4.18f)$$

$$\frac{\partial^2 T}{\partial x^2}(x_N, y, z, t) = -\alpha_{rN}^2 (T(x_N, y, z, t) - T_{ST}(x_N, y)). \quad (4.18g)$$

However, when this condition was applied, the two-dimensional propagating disturbances appeared to pass the outflow boundary, but the three-dimensional disturbances were reflected. The reflections were present for both the small amplitudes and larger nonlinear amplitudes, although the reflections were more severe for the larger amplitudes.

Wave reflection is a problem in numerical simulations when finite computational domains are used. However, if the integration domain is large enough in the streamwise direction, the upstream influence of the boundary on the flow is relatively insignificant. A propagating wave exhibits a characteristic wave front that is essentially a wave packet disturbance. In front of this wave packet, the flow is undisturbed.

To resolve the problem of wave reflections, a long integration domain is used with an outflow boundary propagating ahead of the disturbances. The moving boundary is propagated sufficiently ahead of the disturbance waves to minimize any upstream influence. The choice of a moving boundary, instead of a large integration domain for the entire time integration, makes the method much more efficient computationally since fewer computations are required. The boundary is propagated downstream with the following equation:

$$x_0 < x_B = x_{B_i} + V_B(t - t_1) \leq x_N \quad \text{for } t \geq t_1, \quad (4.19)$$

where  $x_B$  is the position of the right boundary,  $x_{B_i}$  is the position at time  $t_1$ , and  $V_B$  is the propagation speed of the right boundary. If the outflow boundary position reaches its maximum,  $x_B = x_N$ , the boundary remains fixed thereafter. The boundary conditions (4.18) are used at the propagating outflow boundary (E-F-G-H). (Note: For the computation of the undisturbed flow, this outflow boundary is fixed at  $x_B = x_N$ .)

#### 4.5.5 Outer Boundary Conditions for the Disturbed Flow

At the freestream boundary (C-D-H-G), exponential decay for the  $v$  velocity component is assumed:

$$\frac{\partial v}{\partial y}(x, y_M, z, t) = -\frac{\alpha^*}{\sqrt{Re}}(v(x, y_M, z, t) - v_{ST}(x, y_M)) , \quad (4.20a)$$

where  $\alpha^*$  is a wavenumber. The boundary conditions for the vorticity and temperature are

$$\omega_x(x, y_M, z, t) = 0 \quad (4.20b)$$

$$\omega_y(x, y_M, z, t) = 0 \quad (4.20c)$$

$$\omega_z(x, y_M, z, t) = 0 \quad (4.20d)$$

$$T(x, y_M, z, t) = 0 . \quad (4.20e)$$

Boundary conditions (4.20b), (4.20c), (4.20d) and (4.20e) follow from the same considerations given the undisturbed flow. Vorticity and temperature gradients are concentrated in the region near the wall and the freestream boundary is far enough from the wall so that these quantities can be assumed to be zero. Note that only a boundary condition for the  $v$  velocity component is prescribed for the velocity field. This is due to the fact that the  $u$  Poisson and  $w$  Poisson equations contain no  $y$  derivatives for the  $u$  velocity and  $w$  velocity, but only for the  $v$  velocity.

The choice of  $\alpha^*$  will be discussed later in the context of the numerical method. For now, a look at the travelling wave ansatz for a three-dimensional disturbance, Equation (1.3), along with the  $v$  Poisson equation (3.72) in the outer region leads to the following:

$$\nabla_1^2 v(x, y_M, z, t) = 0 \quad (4.21a)$$

or

$$\frac{1}{Re} \frac{\partial^2 v}{\partial x^2}(x, y_M, z, t) + \frac{\partial^2 v}{\partial y^2}(x, y_M, z, t) + \frac{1}{Re} \frac{\partial^2 v}{\partial z^2}(x, y_M, z, t) = 0. \quad (4.21b)$$

Differentiating Equation (1.3) and inserting into Equation (4.21) leads to

$$\frac{\partial^2 \hat{v}}{\partial y^2}(y_M) - \frac{\alpha^2 + \gamma^2}{Re} \hat{v}(y_M) = 0. \quad (4.22)$$

The solution to the above equation is

$$\hat{v}(y_M) = c_1 e^{-\sqrt{\frac{\alpha^2 + \gamma^2}{Re}} y_M} + c_2 e^{+\sqrt{\frac{\alpha^2 + \gamma^2}{Re}} y_M}. \quad (4.23)$$

Since the disturbance is assumed to vanish at infinity, it follows that  $c_2 = 0$  because the velocity fluctuations damp exponentially. Thus the  $v$  velocity can be written as

$$v'(x, y_M, z, t) = c_1 e^{-\sqrt{\frac{\alpha^2 + \gamma^2}{Re}} y_M} e^{i(\alpha x + \gamma z - \beta t)}. \quad (4.24)$$

Differentiation of Equation (4.24) with respect to the normal direction leads to

$$\frac{\partial v'}{\partial y}(x, y_M, z, t) = -\sqrt{\frac{\alpha^2 + \gamma^2}{Re}} v'(x, y_M, z, t). \quad (4.25)$$

Thus, considering a three-dimensional linear wave,  $\alpha_{LST}^* = \sqrt{\alpha^2 + \gamma^2}$  where the subscript 'LST' denotes linear stability theory. Again, the choice of  $\alpha^*$  will be discussed in the next chapter, but appears similar to that derived by Equation (4.25).

#### 4.5.6 Wall Boundary Conditions for the Disturbed Flow

The disturbances are introduced into the integration domain at the wall (A-B-F-E) by superimposing on the steady flow a periodic perturbation. These perturbations are introduced into the domain using one of two different techniques, depending on the application. In the first technique, localized time-dependent

normal velocity fluctuations are introduced within a narrow strip. In the second technique, localized time-dependent heating on a finite length heating strip creates the perturbations. The following boundary conditions at the wall are then imposed:

$$u(x, 0, z, t) = 0 \quad (4.26a)$$

$$v(x, 0, z, t) = v_w(x, z, t) \quad (4.26b)$$

$$w(x, 0, z, t) = 0 \quad (4.26c)$$

$$\begin{aligned} \frac{\partial^2 \omega_x}{\partial x^2}(x, 0, z, t) + \frac{\partial^2 \omega_x}{\partial z^2}(x, 0, z, t) = & -\frac{\partial^2 \omega_y}{\partial x \partial y}(x, 0, z, t) \\ & + \frac{1}{Re} \frac{\partial}{\partial z} (\nabla_1^2 v(x, 0, z, t)) \end{aligned} \quad (4.26d)$$

$$\omega_y(x, 0, z, t) = 0 \quad (4.26e)$$

$$\begin{aligned} \frac{\partial \omega_z}{\partial x}(x, 0, z, t) = & \frac{\partial \omega_z}{\partial z}(x, 0, z, t) \\ & - \frac{1}{Re} \nabla_1^2 v(x, 0, z, t) \end{aligned} \quad (4.26f)$$

$$T(x, 0, z, t) = A(x)x^p + T_w(x, z, t) \quad (4.26g)$$

Equation (4.26a) and (4.26c) are the no slip conditions. The  $v$  velocity component at the wall is prescribed by Equation (4.26b). This condition allows for the introduction of localized streamwise, spanwise, and time-dependent velocity disturbances into the flow field and simulates a suction and blowing strip. Equations (4.26d), (4.26e), and (4.26f) provide the boundary conditions for the three vorticity components at the wall. Equation (4.26d) results from applying the definition of vorticity (3.67), the continuity equation (3.35), and conservation of vorticity (3.70). Equation (4.26e) results from applying the definition of  $\omega_y$  at the wall (3.67b) and Equation (4.26f) results from applying the  $v$  Poisson equation (3.72) at the wall. The boundary condition for the temperature (4.26g) is similar to the



boundary condition for the  $v$  velocity component. This condition allows for localized streamwise, spanwise, and time-dependent temperature perturbations to be introduced into the flow field. Several comments are in order regarding boundary condition (4.26b) and (4.26g). For both the passive and active control simulations, a perturbation input into the flow field is necessary to create a forced disturbance flow. Whether the initial disturbance input into the flow is created through a suction and blowing slot or by a surface heater strip is not important. For the active control simulations, however, the disturbance at the actuator is created by temperature perturbations (Equation 4.26g) on a finite heater strip with proper phase and amplitude control applied. The functions  $v_w(x, z, t)$  and  $T_w(x, z, t)$  for the suction and blowing input and for the temperature input have the following forms, depending on the mode of control:

1.) Passive control

a.) Disturbance input with periodic suction and blowing:

$$v_w(x, z, t) = \begin{cases} r(t) f_v(x, z, t) & \text{if } x_{SB_1} \leq x \leq x_{SE_1}; \\ 0 & \text{otherwise.} \end{cases} \quad (4.27a)$$

$$T_w(x, z, t) = 0 \quad (4.27b)$$

or

b.) Disturbance input with periodic heating:

$$v_w(x, z, t) = 0 \quad (4.28a)$$

$$T_w(x, z, t) = \begin{cases} r(t) f_T(x, z, t) & \text{if } x_{HB_1} \leq x \leq x_{HE_1}; \\ 0 & \text{otherwise.} \end{cases} \quad (4.28b)$$

2.) Active control

a.) Disturbance input with periodic suction and blowing and flow controlled with periodic heating:

$$v_w(x, z, t) = \begin{cases} r(t) f_v(x, z, t) & \text{if } x_{SB_1} \leq x \leq x_{SE_1}; \\ 0 & \text{otherwise.} \end{cases} \quad (4.29a)$$

$$T_w(x, z, t) = \begin{cases} f_T(x, z, t) & \text{if } x_{HB_i} \leq x \leq x_{HE_i}, i = 1, \text{NHS}; \\ 0 & \text{otherwise.} \end{cases} \quad (4.29b)$$

or

- b.) Disturbance input with periodic heating and flow controlled with periodic heating:

$$v_w(x, z, t) = 0 \quad (4.30a)$$

$$T_w(x, z, t) = \begin{cases} r(t) f_T(x, z, t) & \text{if } x_{HB_1} \leq x \leq x_{HE_1}; \\ 0 & \text{otherwise.} \end{cases} \quad (4.30b)$$

$$T_w(x, z, t) = \begin{cases} f_T(x, z, t) & \text{if } x_{HB_i} \leq x \leq x_{HE_i}, i = 2, \text{NHS}; \\ 0 & \text{otherwise.} \end{cases} \quad (4.30c)$$

Again 'NHS' denotes the number of heater strips employed for the active control simulations. The functional choices for  $f_v(x, z, t)$  and  $f_T(x, z, t)$  will be discussed in Chapters 5 and 6. The ramp function  $r(t)$ , used in this work has the following form:

$$r(t) = \begin{cases} 0 & \text{if } t_0 \leq t \leq t_1; \\ \exp \left[ \frac{R_A(t - t_1 - T_r)^2}{T_r^2} \right] & \text{if } t_1 \leq t \leq t_2; \\ 1 & \text{if } t \geq t_2. \end{cases} \quad (4.31)$$

The ramp time  $T_r = t_2 - t_1$  is an input parameter which is specified as a fraction of the disturbance period. The ramp amplitude parameter  $R_A$  controls the rate at which the ramp amplitude develops.

Finally, the disturbed flow boundary conditions described in this section are shown schematically in Figure 4.5.

## CHAPTER 5

## NUMERICAL METHOD

In this chapter, the numerical method for obtaining an approximate solution to the mathematical model presented in Chapters 3 and 4 is developed. The choice of the numerical algorithm was made after weighing several factors. Important considerations are accuracy, stability, and rate of convergence. In addition to the mathematical considerations are computational considerations that include computational speed, storage requirements, and the ability to vectorize. As already mentioned in previous chapters, Fasel, Rist, and Konzelmann (1987) have developed a numerical method for solving the three-dimensional spatial stability problem. This algorithm serves as a building block in this work and requires the addition of the energy equation and the viscosity variation with temperature. The numerical method is described in detail in the following sections, but first a brief summary is given.

In the numerical method, standard central finite difference approximations are used in the streamwise and normal directions and a spectral representation is used in the spanwise direction. The flow variables are assumed to exhibit periodicity in the spanwise direction and are approximated by a finite Fourier series. With the use of this spectral ansatz, the three-dimensional governing equation system reduces to  $3K$  vorticity transport equations,  $3K$  Poisson equations for the velocities,  $K$  energy equations, and  $K$  viscosity equations, where  $K$  is the number of Fourier modes retained in the spectral approximation. The resulting two-dimensional system of equations is solved in Fourier space. The vorticity transport and energy equations are advanced in time using one-sided backward

differences. At every time step, the vorticity transport and energy equations are elliptic in nature. The Poisson equations for the velocity modes are also elliptic. This set of elliptic equations is solved for using a Gauss-Seidel line relaxation procedure. The nonlinear terms are updated throughout the iterative procedure with the iteration loop continuing until convergence is achieved. The numerical method is second order accurate in time and in the streamwise and normal directions. Spectral accuracy is obtained in the spanwise direction.

The numerical algorithm is basically the same for computation of the undisturbed flow and the periodically forced disturbed flow except that the boundary and initial conditions differ as discussed in Chapter 4. These differences in the boundary conditions will be pointed out.

### 5.1 Computational Domain

The spatial domain described in Section 4.3 is discretized in the streamwise, normal, and spanwise directions into  $N$ ,  $M$ , and  $K$  intervals of lengths  $\Delta x$ ,  $\Delta y$ , and  $\Delta z$  respectively. The intervals  $N$ ,  $M$ , and  $K$  are input parameters and this spatial computational domain is shown in Figure 5.1. The grid point indices are denoted by  $n$ ,  $m$ , and  $k$  so that

$$\begin{aligned} x_n &= x_0 + n \Delta x & n &= (0, 1, 2, \dots, N) \\ y_m &= m \Delta y & m &= (0, 1, 2, \dots, M) \\ z_k &= z_0 + k \Delta z & k &= (0, 1, 2, \dots, K). \end{aligned} \quad (5.1)$$

Similarly, the time increment is  $\Delta t$  and  $l$  is the time index so that

$$t_l = t_0 + l \Delta t \quad l = (0, 1, 2, \dots, L_1, \dots, L_2, \dots, L_3, \dots, L) \quad (5.2)$$

where  $L$  is also an input parameter with  $L_1$ ,  $L_2$ , and  $L_3$  corresponding to times  $t_1$ ,  $t_2$ , and  $t_3$  respectively.

The following convention is adopted for relating the physical location to the discretized one:

$$\begin{aligned}
 U_{k,n,m}^l &= U(x_n, y_m, z_k, t_l) \\
 \omega_{k,n,m}^l &= \omega(x_n, y_m, z_k, t_l) \\
 T_{k,n,m}^l &= T(x_n, y_m, z_k, t_l) \\
 \mu_{k,n,m}^l &= \mu(x_n, y_m, z_k, t_l).
 \end{aligned}
 \tag{5.3}$$

Since the flow is spanwise periodic it follows that

$$\begin{aligned}
 U_{0,n,m}^l &= U_{qk,n,m}^l \\
 \omega_{0,n,m}^l &= \omega_{qk,n,m}^l \\
 T_{0,n,m}^l &= T_{qk,n,m}^l \\
 \mu_{0,n,m}^l &= \mu_{qk,n,m}^l
 \end{aligned}
 \tag{5.4}$$

for integral values of  $q$ .

## 5.2 Spanwise Spectral Approximation

In spectral methods, the solution to a problem is represented as a truncated series of known functions for the flow variables. A continuous real function  $\phi(z)$  which is periodic in the spanwise  $z$  direction with a period of  $2\pi$ ; i.e.,  $\phi(z) = \phi(z + \frac{2\pi}{\gamma})$ , can be approximated by

$$\phi(z) \simeq \sum_{k=-\frac{K}{2}}^{\frac{K}{2}} \Phi_k e^{ik\gamma z}
 \tag{5.5}$$

where the Fourier coefficients  $\Phi_k$  are complex conjugates

$$\Phi_{-k} = \Phi_k^*
 \tag{5.6}$$

and  $\gamma$  is the spanwise wavenumber. The velocity, vorticity, temperature, and viscosity are assumed continuous and periodic and so are expanded in a series of

the form of Equation (5.5) where

$$\phi = (u, v, w, \omega_x, \omega_y, \omega_z, T, \mu) \quad (5.7a)$$

and

$$\Phi = (U, V, W, \Omega_x, \Omega_y, \Omega_z, \Theta, \mathcal{M}) \quad (5.7b)$$

so that

$$u(x, y, z, t) \simeq \sum_{k=-\frac{K}{2}}^{\frac{K}{2}} U_k(x, y, t) e^{ik\gamma z} \quad (5.8a)$$

$$v(x, y, z, t) \simeq \sum_{k=-\frac{K}{2}}^{\frac{K}{2}} V_k(x, y, t) e^{ik\gamma z} \quad (5.8b)$$

$$w(x, y, z, t) \simeq \sum_{k=-\frac{K}{2}}^{\frac{K}{2}} W_k(x, y, t) e^{ik\gamma z} \quad (5.8c)$$

$$\omega_x(x, y, z, t) \simeq \sum_{k=-\frac{K}{2}}^{\frac{K}{2}} \Omega_{xk}(x, y, t) e^{ik\gamma z} \quad (5.8d)$$

$$\omega_y(x, y, z, t) \simeq \sum_{k=-\frac{K}{2}}^{\frac{K}{2}} \Omega_{yk}(x, y, t) e^{ik\gamma z} \quad (5.8e)$$

$$\omega_z(x, y, z, t) \simeq \sum_{k=-\frac{K}{2}}^{\frac{K}{2}} \Omega_{zk}(x, y, t) e^{ik\gamma z} \quad (5.8f)$$

$$T(x, y, z, t) \simeq \sum_{k=-\frac{K}{2}}^{\frac{K}{2}} \Theta_k(x, y, t) e^{ik\gamma z} \quad (5.8g)$$

$$\mu(x, y, z, t) \simeq \sum_{k=-\frac{K}{2}}^{\frac{K}{2}} \mathcal{M}_k(x, y, t) e^{ik\gamma z}. \quad (5.8h)$$

Before substituting the expressions (5.8) into the governing equations, the following nonlinear terms are defined:

$$\mathbf{a} = (\mathbf{U} \cdot \nabla_1) \boldsymbol{\omega} - (\boldsymbol{\omega} \cdot \nabla_1) \mathbf{U} \quad (5.9a)$$

$$\mathbf{b} = \mu \nabla_1^2 \omega \quad (5.9b)$$

$$d = (\mathbf{U} \cdot \nabla_1) T \quad (5.9c)$$

where  $\mathbf{a}$  is the vector  $\mathbf{a} = [a_x, a_y, a_z]$ ,  $\mathbf{b}$  is the vector  $\mathbf{b} = [b_x, b_y, b_z]$ , and the vector  $\mathbf{c}$  is as defined by Equation (3.69). The nonlinear term for the energy equation  $d$  is a scalar. The spectral representations for these nonlinear terms are

$$\mathbf{a}(x, y, z, t) \simeq \sum_{k=-\frac{K}{2}}^{\frac{K}{2}} \mathbf{A}_k(x, y, t) e^{ik\gamma z} \quad (5.10a)$$

$$\mathbf{b}(x, y, z, t) \simeq \sum_{k=-\frac{K}{2}}^{\frac{K}{2}} \mathbf{B}_k(x, y, t) e^{ik\gamma z} \quad (5.10b)$$

$$\mathbf{c}(x, y, z, t) \simeq \sum_{k=-\frac{K}{2}}^{\frac{K}{2}} \mathbf{C}_k(x, y, t) e^{ik\gamma z} \quad (5.10c)$$

$$d(x, y, z, t) \simeq \sum_{k=-\frac{K}{2}}^{\frac{K}{2}} D_k(x, y, t) e^{ik\gamma z} \quad (5.10d)$$

where  $\mathbf{A} = [A_x, A_y, A_z]$ ,  $\mathbf{B} = [B_x, B_y, B_z]$ , and  $\mathbf{C} = [C_x, C_y, C_z]$ . Substitution of the expressions (5.8) and (5.10) into the governing equations (3.35), (3.37), (3.68), (3.70), (3.71), (3.72), and (3.73) yields a new set of governing equations in terms of Fourier modes rather than physical variables. The resulting equation system is

$$\frac{\partial U_k}{\partial x} + \frac{\partial V_k}{\partial y} + i\gamma k W_k = 0 \quad (5.11a)$$

$$\frac{\partial \Omega_{xk}}{\partial x} + \frac{\partial \Omega_{yk}}{\partial y} + i\gamma k \Omega_{zk} = 0 \quad (5.11b)$$

$$\frac{\partial \Omega_{xk}}{\partial t} + A_{xk} = B_{xk} + C_{xk} \quad (5.11c)$$

$$\frac{\partial \Omega_{yk}}{\partial t} + A_{yk} = B_{yk} + C_{yk} \quad (5.11d)$$

$$\frac{\partial \Omega_{zk}}{\partial t} + A_{zk} = B_{zk} + C_{zk} \quad (5.11e)$$

$$\frac{\partial^2 U_k}{\partial x^2} - \gamma^2 k^2 U_k = -i\gamma k \Omega_{y_k} - \frac{\partial^2 V_k}{\partial x \partial y} \quad (5.11f)$$

$$\frac{1}{Re} \frac{\partial^2 V_k}{\partial x^2} + \frac{\partial^2 V_k}{\partial y^2} - \frac{\gamma^2 k^2}{Re} V_k = i\gamma k \Omega_{x_k} - \frac{\partial \Omega_{z_k}}{\partial x} \quad (5.11g)$$

$$\frac{\partial^2 W_k}{\partial x^2} - \gamma^2 k^2 W_k = \frac{\partial \Omega_{y_k}}{\partial x} - i\gamma k \frac{\partial V_k}{\partial y} \quad (5.11h)$$

$$\frac{\partial \Theta_k}{\partial t} + D_k = \frac{1}{Re} \frac{\partial^2 \Theta_k}{\partial x^2} + \frac{\partial^2 \Theta_k}{\partial y^2} - \frac{\gamma^2 k^2}{Re} \Theta_k \quad (5.11i)$$

for

$$k = \left( -\frac{K}{2}, \dots, -1, 0, 1, \dots, \frac{K}{2} \right).$$

The viscosity variation with temperature  $\mathcal{M}_k(\Theta_k)$  completes the set of governing equations. The manner in which this viscosity relationship is incorporated into the numerical method is explained in Section 5.3.6.

Several comments regarding Equations (5.11) are now made. In deriving the system of equations in Fourier space, the following relations for the first and second partial derivatives with respect to  $z$  are utilized:

$$\frac{\partial \phi}{\partial z} \simeq \sum_{k=-\frac{K}{2}}^{\frac{K}{2}} i\gamma k \Phi_k e^{ik\gamma z} \quad (5.12a)$$

$$\frac{\partial^2 \phi}{\partial z^2} \simeq \sum_{k=-\frac{K}{2}}^{\frac{K}{2}} -\gamma^2 k^2 \Phi_k e^{ik\gamma z}. \quad (5.12b)$$

These expressions apply for the velocity, vorticity, temperature, and viscosity, assuming that Equation (5.5) is twice differentiable. Since the physical variables are purely real, Equation (5.6) applies. Therefore, the mode equations need only be solved for nonnegative values of  $k$ ; i.e.,  $k = (0, 1, \dots, \frac{K}{2})$ . The conservation of mass equations (5.11a) need to be enforced only at the boundaries as is the case for the physical mass conservation equation (3.35).



### 5.2.1 Boundary and Initial Conditions in Fourier Space for the Undisturbed Flow

The boundary and initial conditions in physical space that are presented in Chapter 4 are converted to corresponding boundary and initial conditions in Fourier space using the relations (5.8).

Since the undisturbed flow is two-dimensional, the three-dimensional components are zero everywhere for  $t < t_1$ , or

$$W_0(x, y, t) = \Omega_{z_0}(x, y, t) = \Omega_{y_0}(x, y, t) = 0$$

and for  $k > 0$ :

$$U_k(x, y, t) = V_k(x, y, t) = W_k(x, y, t) = 0$$

$$\Omega_{x_k}(x, y, t) = \Omega_{y_k}(x, y, t) = \Omega_{z_k}(x, y, t) = \Theta_k(x, y, t) = 0. \quad (5.13)$$

The boundary conditions for the zeroth mode are purely real by consideration of Equation (5.6).

The initial conditions in Fourier space follow from Equations (4.5):

$$U_0(x, y, 0) = u_{SIM}(x, y) \quad (5.14a)$$

$$V_0(x, y, 0) = v_{SIM}(x, y) \quad (5.14b)$$

$$\Omega_{z_0}(x, y, 0) = \omega_{zSIM}(x, y) \quad (5.14c)$$

$$\Theta_0(x, y, 0) = T_{SIM}(x, y). \quad (5.14d)$$

At the inflow boundary, the boundary conditions follow from (4.6):

$$U_0(x_0, y, t) = u_{SIM}(x_0, y) \quad (5.15a)$$

$$V_0(x_0, y, t) = v_{SIM}(x_0, y) \quad (5.15b)$$

$$\Omega_{z_0}(x_0, y, t) = \omega_{zSIM}(x_0, y) \quad (5.15c)$$

$$\Theta_0(x_0, y, t) = T_{SIM}(x_0, y). \quad (5.15d)$$

Fourier space outflow boundary conditions (4.7) are

$$\frac{\partial U_0}{\partial x}(x_N, y, t) = -\frac{\partial V_0}{\partial y}(x_N, y, t) \quad (5.16a)$$

$$\frac{\partial^2 V_0}{\partial x^2}(x_N, y, t) = 0 \quad (5.16b)$$

$$\frac{\partial^2 \Omega_{z_0}}{\partial x^2}(x_N, y, t) = 0 \quad (5.16c)$$

$$\frac{\partial^2 \Theta_0}{\partial x^2}(x_N, y, t) = 0. \quad (5.16d)$$

Following (4.8), the outer boundary conditions become

$$U_0(x, y_M, t) = 1 \quad (5.17a)$$

$$\frac{\partial V_0}{\partial y}(x, y_M, t) = 0 \quad (5.17b)$$

$$\Omega_{z_0}(x, y_M, t) = 0 \quad (5.17c)$$

$$\Theta_0(x, y_M, t) = 0. \quad (5.17d)$$

Finally, at the wall the boundary conditions (4.9) in Fourier space are

$$U_0(x, 0, t) = 0 \quad (5.18a)$$

$$V_0(x, 0, t) = 0 \quad (5.18b)$$

$$\frac{\partial V_0}{\partial y}(x, 0, t) = 0 \quad (5.18c)$$

$$\frac{\partial \Omega_{z_0}}{\partial x}(x, 0, t) = -\frac{\partial^2 V_0}{\partial y^2}(x, 0, t) \quad (5.18d)$$

$$\Theta_0(x, 0, t) = A(x)x^p. \quad (5.18e)$$

### 5.2.2 Boundary and Initial Conditions in Fourier Space for the Disturbed Flow

Analogous to the physical space initial conditions (4.13), the initial conditions in Fourier space at time  $t = t_1$  for the disturbed flow are the two-dimensional

steady state solutions:

$$U_0(x, y, t_1) = u_{ST}(x, y) \quad (5.19a)$$

$$V_0(x, y, t_1) = v_{ST}(x, y) \quad (5.19b)$$

$$\Omega_{z_0}(x, y, t_1) = \omega_{zST}(x, y) \quad (5.19c)$$

$$\Theta_0(x, y, t_1) = T_{ST}(x, y). \quad (5.19d)$$

All other components are identically zero at time  $t = t_1$ . For the active control simulations, the heater strip is turned on at time  $t = t_2$  leading to the following initial conditions at the wall for the temperature:

for  $k = 0$ :

$$\Theta_0(x, y, t_2) = \Theta_{w_0}(x, t_2), \quad (5.20a)$$

for  $k = 1$ :

$$\Theta_1(x, y, t_2) = \Theta_{w_1}(x, t_2), \quad (5.20b)$$

and for  $k > 0$ :

$$\Theta_k(x, y, t_2) = 0. \quad (5.20c)$$

At the inflow boundary, the two-dimensional physical space conditions (4.16) transform to the following two-dimensional Fourier space inflow conditions:

$$U_0(x_0, y, t) = u_{SIM}(x_0, y) \quad (5.21a)$$

$$V_0(x_0, y, t) = v_{SIM}(x_0, y) \quad (5.21b)$$

$$\Omega_{z_0}(x_0, y, t) = \omega_{zSIM}(x_0, y) \quad (5.21c)$$

$$\Theta_0(x_0, y, t) = T_{SIM}(x_0, y). \quad (5.21d)$$

All other components are again identically zero.

From the physical space conditions (4.18), the Fourier space outflow conditions are

for  $k = 0$ :

$$\frac{\partial^2 U_0}{\partial x^2}(x_{N_B}, y, t) = \frac{\partial^2 u_{ST}}{\partial x^2}(x_{N_B}, y) - \alpha_{r_N}^2 U_0(x_{N_B}, y, t) \quad (5.22a)$$

$$\frac{\partial^2 V_0}{\partial x^2}(x_{N_B}, y, t) = -\alpha_{r_N}^2 (V_0(x_{N_B}, y, t) - v_{ST}(x_{N_B}, y)) \quad (5.22b)$$

$$W_0(x_{N_B}, y, t) = 0 \quad (5.22c)$$

$$\Omega_{x_0}(x_{N_B}, y, t) = 0 \quad (5.22d)$$

$$\Omega_{y_0}(x_{N_B}, y, t) = 0 \quad (5.22e)$$

$$\frac{\partial^2 \Omega_{x_0}}{\partial x^2}(x_{N_B}, y, t) = -\alpha_{r_N}^2 (\Omega_{x_0}(x_{N_B}, y, t) - \omega_{xST}(x_{N_B}, y)) \quad (5.22f)$$

$$\frac{\partial^2 \Theta_{x_0}}{\partial x^2}(x_{N_B}, y, t) = -\alpha_{r_N}^2 (\Theta_{x_0}(x_{N_B}, y, t) - T_{ST}(x_{N_B}, y)) \quad (5.22g)$$

and for  $k > 0$ :

$$\frac{\partial^2 U_k}{\partial x^2}(x_{N_B}, y, t) = -\alpha_{r_N}^2 U_k(x_{N_B}, y, t) \quad (5.22h)$$

$$\frac{\partial^2 V_k}{\partial x^2}(x_{N_B}, y, t) = -\alpha_{r_N}^2 V_k(x_{N_B}, y, t) \quad (5.22i)$$

$$\frac{\partial^2 W_k}{\partial x^2}(x_{N_B}, y, t) = -\alpha_{r_N}^2 W_k(x_{N_B}, y, t) \quad (5.22j)$$

$$\frac{\partial^2 \Omega_{x_k}}{\partial x^2}(x_{N_B}, y, t) = -\alpha_{r_N}^2 \Omega_{x_k}(x_{N_B}, y, t) \quad (5.22k)$$

$$\frac{\partial^2 \Omega_{y_k}}{\partial x^2}(x_{N_B}, y, t) = -\alpha_{r_N}^2 \Omega_{y_k}(x_{N_B}, y, t) \quad (5.22l)$$

$$\frac{\partial^2 \Omega_{z_k}}{\partial x^2}(x_{N_B}, y, t) = -\alpha_{r_N}^2 \Omega_{z_k}(x_{N_B}, y, t) \quad (5.22m)$$

$$\frac{\partial^2 \Theta_k}{\partial x^2}(x_{N_B}, y, t) = -\alpha_{r_N}^2 \Theta_k(x_{N_B}, y, t). \quad (5.22n)$$

Here the subscript ' $N_B$ ' denotes the location of the moving boundary.

At the outer boundary, the physical boundary conditions (4.20) become

for  $k = 0$ :

$$\frac{\partial V_0}{\partial y}(x, y_M, t) = -\frac{\alpha_0^2}{\sqrt{Re}} (V_0(x, y_M, t) - v_{ST}(x, y_M)) \quad (5.23a)$$

$$\Omega_{x_0}(x, y_M, t) = 0 \quad (5.23b)$$

$$\Omega_{y_0}(x, y_M, t) = 0 \quad (5.23c)$$

$$\Omega_{x_0}(x, y_M, t) = 0 \quad (5.23d)$$

$$\Theta_0(x, y_M, t) = 0, \quad (5.23e)$$

and for  $k > 0$ :

$$\frac{\partial V_k}{\partial y}(x, y_M, t) = -\frac{\alpha_k^*}{\sqrt{Re}} V_k(x, y_M, t) \quad (5.23f)$$

$$\Omega_{x_k}(x, y_M, t) = 0 \quad (5.23g)$$

$$\Omega_{y_k}(x, y_M, t) = 0 \quad (5.23h)$$

$$\Omega_{x_k}(x, y_M, t) = 0 \quad (5.23i)$$

$$\Theta_k(x, y_M, t) = 0. \quad (5.23j)$$

The appropriate choice of  $\alpha_k^*$  is now discussed. In Fourier space, the  $V_k$  Poisson equation at the outer boundary follows from (4.21a) and (5.11g), or

$$\frac{1}{Re} \frac{\partial^2 V_k}{\partial x^2}(x, y_M, t) + \frac{\partial^2 V_k}{\partial y^2}(x, y_M, t) - \frac{\gamma^2 k^2}{Re} V_k(x, y_M, t) = 0. \quad (5.24)$$

Equation (1.3) is modified to include several spanwise modes:

$$v'(x, y, z, t) = \sum_{k=-\frac{K}{2}}^{\frac{K}{2}} \hat{V}_k(y) e^{i(\alpha x - \beta t + k \gamma z)} \quad (5.25)$$

where

$$V_k = \hat{V}_k(y) e^{i(\alpha x - \beta t)}.$$

Differentiating Equation (5.25) with respect to  $x$  and inserting into Equation (5.24) leads to

$$\frac{\partial^2 \hat{V}_k}{\partial y^2}(y_M) - \frac{\alpha^2 + \gamma^2 k^2}{Re} \hat{V}_k(y_M) = 0. \quad (5.26)$$

As in Chapter 4, the exponentially growing solution is neglected, and the the  $v$  perturbation velocity becomes:

$$v'(x, y_M, z, t) = \sum_{k=-\frac{K}{2}}^{\frac{K}{2}} c_1 e^{-\sqrt{\frac{\alpha^2 + \gamma^2 k^2}{Re}} y_M} e^{i(\alpha z - \beta t)}. \quad (5.27)$$

After differentiating Equation (5.27) with respect to  $y$ , the appropriate choice of  $\alpha_k^*$  becomes  $\alpha_k^* = \sqrt{\alpha_r^2 + \gamma^2 k^2}$ . As discussed in Chapter 4, only the real part of the wavenumber is retained since  $\alpha_i \ll \alpha_r$  for boundary layer flows.

Finally, from the physical space conditions (4.26) for the wall boundary, the Fourier space boundary conditions become  
for  $k = 0$ :

$$U_0(x, 0, t) = 0 \quad (5.28a)$$

$$V_0(x, 0, t) = V_{w_0}(x, t) \quad (5.28b)$$

$$W_0(x, 0, t) = 0 \quad (5.28c)$$

$$\Omega_{x_0}(x, 0, t) = 0 \quad (5.28d)$$

$$\Omega_{y_0}(x, 0, t) = 0 \quad (5.28e)$$

$$\frac{\partial \Omega_{x_0}}{\partial x}(x, 0, t) = -\frac{1}{Re} \nabla_0^2 V_0(x, 0, t) \quad (5.28f)$$

$$\Theta_0(x, 0, t) = A(x)x^p + \Theta_{w_0}(x, t) \quad (5.28g)$$

where

$$\nabla_0^2 = \frac{\partial^2}{\partial x^2} + Re \frac{\partial^2}{\partial y^2},$$

and for  $k > 0$ :

$$U_k(x, 0, t) = 0 \quad (5.28g)$$

$$V_k(x, 0, t) = V_{w_k}(x, t) \quad (5.28h)$$

$$W_k(x, 0, t) = 0 \quad (5.28i)$$

$$\begin{aligned} \frac{\partial^2 \Omega_{xk}}{\partial x^2}(x, 0, t) - \gamma^2 k^2 \Omega_{xk}(x, 0, t) = & -\frac{\partial^2 \Omega_{yk}}{\partial x \partial y}(x, 0, t) \\ & + \frac{i \gamma k}{Re} \nabla_k^2 V_k(x, 0, t) \end{aligned} \quad (5.28j)$$

$$\Omega_{yk}(x, 0, t) = 0 \quad (5.28k)$$

$$\begin{aligned} \frac{\partial \Omega_{xk}}{\partial x}(x, 0, t) = & i \gamma k \Omega_{xk}(x, 0, t) \\ & - \frac{1}{Re} \nabla_k^2 V_k(x, 0, t) \end{aligned} \quad (5.28l)$$

$$\Theta_k(x, 0, t) = \Theta_{w0}(x, t) \quad (5.28m)$$

where

$$\nabla_k^2 = \frac{\partial^2}{\partial x^2} + Re \frac{\partial^2}{\partial y^2} - \frac{\gamma^2 k^2}{Re}.$$

The  $V$  velocity and temperature boundary conditions at the wall depend on the mode of control as discussed in Chapter 4. They become the following in Fourier space:

1.) Passive control

a.) Disturbance input with periodic suction and blowing:

for  $k = 0$ :

$$V_{w0}(x, z, t) = \begin{cases} r(t) \epsilon_{V0} \hat{f}_{V0}(x, t) & \text{if } x_{SB1} \leq x \leq x_{SE1}; \\ 0 & \text{otherwise.} \end{cases} \quad (5.29a)$$

for  $k = 1$ :

$$V_{w1}(x, z, t) = \begin{cases} r(t) \epsilon_{V1} \hat{f}_{V1}(x, t) & \text{if } x_{SB1} \leq x \leq x_{SE1}; \\ 0 & \text{otherwise.} \end{cases} \quad (5.29b)$$

and for  $k > 1$ :

$$V_{wk}(x, z, t) = 0 \quad (5.29c)$$

for all  $k$ :

$$T_{wk}(x, z, t) = 0 \quad (5.29d)$$

or

b.) Disturbance input with periodic heating:

for all  $k$ :

$$V_{w_k}(x, z, t) = 0 \quad (5.30a)$$

for  $k = 0$ :

$$\Theta_{w_0}(x, z, t) = \begin{cases} A(x)x^p + r(t)\epsilon_{\Theta_0}\hat{f}_{\Theta_0}(x, t) & \text{if } x_{HB_1} \leq x \leq x_{HE_1}; \\ 0 & \text{otherwise.} \end{cases} \quad (5.30b)$$

for  $k = 1$ :

$$\Theta_{w_1}(x, z, t) = \begin{cases} r(t)\epsilon_{\Theta_1}\hat{f}_{\Theta_1}(x, t) & \text{if } x_{HB_1} \leq x \leq x_{HE_1}; \\ 0 & \text{otherwise.} \end{cases} \quad (5.30c)$$

and for  $k > 1$ :

$$\Theta_{w_k}(x, z, t) = 0. \quad (5.30d)$$

2.) Active control

a.) Disturbance input with periodic suction and blowing and flow controlled with periodic heating:

for  $k = 0$ :

$$V_{w_0}(x, z, t) = \begin{cases} r(t)\epsilon_{V_0}\hat{f}_{V_0}(x, t) & \text{if } x_{SB_1} \leq x \leq x_{SE_1}; \\ 0 & \text{otherwise.} \end{cases} \quad (5.31a)$$

for  $k = 1$ :

$$V_{w_1}(x, z, t) = \begin{cases} r(t)\epsilon_{V_1}\hat{f}_{V_1}(x, t) & \text{if } x_{SB_1} \leq x \leq x_{SE_1}; \\ 0 & \text{otherwise.} \end{cases} \quad (5.31b)$$

and for  $k > 1$ :

$$V_{w_k}(x, z, t) = 0 \quad (5.31c)$$

for  $k = 0$ :

$$\Theta_{w_0}(x, z, t) = \begin{cases} \epsilon_{\Theta_0}\hat{f}_{\Theta_0}(x, t) & \text{if } x_{HB_i} \leq x \leq x_{HE_i}, i = 1, N, H, S; \\ 0 & \text{otherwise.} \end{cases} \quad (5.31d)$$

for  $k = 1$ :



$$\Theta_{w_1}(x, z, t) = \begin{cases} \epsilon_{\Theta_1} \hat{f}_{\Theta_1}(x, t) & \text{if } x_{HB_i} \leq x \leq x_{HE_i}, i = 1, \text{NHS;} \\ 0 & \text{otherwise.} \end{cases} \quad (5.31e)$$

and for  $k > 1$ :

$$\Theta_{w_k}(x, z, t) = 0 \quad (5.31f)$$

or

b.) Disturbance input with periodic heating and flow controlled with periodic heating:

for all  $k$ :

$$V_{w_0}(x, z, t) = 0 \quad (5.32a)$$

for  $k = 0$ :

$$\Theta_{w_0}(x, z, t) = \begin{cases} r(t) \epsilon_{\Theta_0} \hat{f}_{\Theta_0}(x, t) & \text{if } x_{HB_i} \leq x \leq x_{HE_i}; \\ 0 & \text{otherwise.} \end{cases} \quad (5.32b)$$

$$\Theta_{w_0}(x, z, t) = \begin{cases} \hat{f}_{\Theta_0}(x, t) & \text{if } x_{HB_i} \leq x \leq x_{HE_i}, i = 2, \text{NHS;} \\ 0 & \text{otherwise.} \end{cases} \quad (5.32c)$$

for  $k = 1$ :

$$\Theta_{w_1}(x, z, t) = \begin{cases} r(t) \epsilon_{\Theta_1} \hat{f}_{\Theta_1}(x, t) & \text{if } x_{HB_i} \leq x \leq x_{HE_i}; \\ 0 & \text{otherwise.} \end{cases} \quad (5.32d)$$

$$\Theta_{w_1}(x, z, t) = \begin{cases} \hat{f}_{\Theta_1}(x, t) & \text{if } x_{HB_i} \leq x \leq x_{HE_i}, i = 2, \text{NHS;} \\ 0 & \text{otherwise.} \end{cases} \quad (5.32e)$$

and for  $k > 1$ :

$$\Theta_{w_k}(x, z, t) = 0. \quad (5.32f)$$

A few remarks are in order regarding conditions (5.29) through (5.32). The functions  $f_v(x, z, t)$  and  $f_T(x, z, t)$  are chosen to be of the following form:

$$f_v(x, z, t) = \hat{f}_v(x, t) (\epsilon_{v_0} + \epsilon_{v_1} \cos \gamma z) \quad (5.33a)$$

$$f_T(x, z, t) = \hat{f}_T(x, t) (\epsilon_{T_0} + \epsilon_{T_1} \cos \gamma z). \quad (5.33b)$$

This particular form of the  $z$  dependence has several implications. The disturbances are introduced through the zeroth and first modes only. The higher modes emerge in the computations through nonlinear interactions only. The parameters  $\epsilon_{v_0}$ ,  $\epsilon_{v_1}$ ,  $\epsilon_{T_0}$ , and  $\epsilon_{T_1}$  determine the two-dimensional and three-dimensional input amplitudes. By choosing these parameters to be purely real constants, the disturbance waves evolving in the flow field are such that  $u$ ,  $v$ ,  $\omega_x$ ,  $T$ , and  $\mu$  are symmetric with respect to the plane  $z = 0$ , while  $w$ ,  $\omega_z$ , and  $\omega_y$  are antisymmetric with respect to  $z = 0$ . Therefore, although Equations (5.11) are in general complex, only the real parts of  $U_k$ ,  $V_k$ ,  $\Omega_{xk}$ ,  $\Theta_k$ , and  $\mathcal{M}_k$  and the imaginary parts of  $W_k$ ,  $\Omega_{zk}$ , and  $\Omega_{yk}$  are calculated and stored.

### 5.3 Implicit Finite Difference Method

The choice of the numerical method to solve the two-dimensional equation system (5.11) is based on several factors as already mentioned in the introduction to this chapter. The numerical method is first presented and a discussion of these different considerations follows.

The numerical technique used in these simulations is a fully implicit finite difference method. The method is fully implicit in that all the nonlinear terms are evaluated at the most recent time level. A three-level difference scheme is used to obtain second order accuracy for the time derivatives. The spatial derivatives in the streamwise  $x$  and normal  $y$  directions are approximated in the interior of the domain using standard second order central differences. The time and spatial discretizations are as follows:

$$\frac{\partial \Phi_k}{\partial t}(x, y, t) = \frac{3\Phi_k(x, y, t) - 4\Phi_k(x, y, t - \Delta t) + \Phi_k(x, y, t - 2\Delta t)}{2\Delta t} + O(\Delta t^2) \quad (5.34a)$$

$$\frac{\partial \Phi_k}{\partial x}(x, y, t) = \frac{\Phi_k(x + \Delta x, y, t) - \Phi_k(x - \Delta x, y, t)}{2\Delta x} + O(\Delta x^2) \quad (5.34b)$$

$$\frac{\partial \Phi_k}{\partial y}(x, y, t) = \frac{\Phi_k(x, y + \Delta y, t) - \Phi_k(x, y - \Delta y, t)}{2 \Delta y} + O(\Delta y^2) \quad (5.34c)$$

$$\begin{aligned} \frac{\partial^2 \Phi_k}{\partial x^2}(x, y, t) &= \frac{\Phi_k(x + \Delta x, y, t) - 2 \Phi_k(x, y, t) + \Phi_k(x - \Delta x, y, t)}{\Delta x^2} \\ &+ O(\Delta x^2) \end{aligned} \quad (5.34d)$$

$$\begin{aligned} \frac{\partial^2 \Phi_k}{\partial y^2}(x, y, t) &= \frac{\Phi_k(x, y + \Delta y, t) - 2 \Phi_k(x, y, t) + \Phi_k(x, y - \Delta y, t)}{\Delta y^2} \\ &+ O(\Delta y^2) \end{aligned} \quad (5.34e)$$

$$\begin{aligned} \frac{\partial^2 \Phi_k}{\partial x \partial y}(x, y, t) &= \frac{\Phi_k(x + \Delta x, y + \Delta y, t) - \Phi_k(x - \Delta x, y + \Delta y, t)}{4 \Delta x \Delta y} \\ &+ \frac{-\Phi_k(x + \Delta x, y - \Delta y, t) + \Phi_k(x - \Delta x, y - \Delta y, t)}{4 \Delta x \Delta y} \\ &+ O(\Delta x^2, \Delta y^2) \end{aligned} \quad (5.34f)$$

or in index notation:

$$\left. \frac{\partial \Phi}{\partial t} \right|_{k,n,m}^l = \frac{3 \Phi_{k,n,m}^l - 4 \Phi_{k,n,m}^{l-1} + \Phi_{k,n,m}^{l-2}}{2 \Delta t} + O(\Delta t^2) \quad (5.35a)$$

$$\left. \frac{\partial \Phi}{\partial x} \right|_{k,n,m}^l = \frac{\Phi_{k,n+1,m}^l - \Phi_{k,n-1,m}^l}{2 \Delta x} + O(\Delta x^2) \quad (5.35b)$$

$$\left. \frac{\partial \Phi}{\partial y} \right|_{k,n,m}^l = \frac{\Phi_{k,n,m+1}^l - \Phi_{k,n,m-1}^l}{2 \Delta y} + O(\Delta y^2) \quad (5.35c)$$

$$\left. \frac{\partial^2 \Phi}{\partial x^2} \right|_{k,n,m}^l = \frac{\Phi_{k,n+1,m}^l - 2 \Phi_{k,n,m}^l + \Phi_{k,n-1,m}^l}{\Delta x^2} + O(\Delta x^2) \quad (5.35d)$$

$$\left. \frac{\partial^2 \Phi}{\partial y^2} \right|_{k,n,m}^l = \frac{\Phi_{k,n,m+1}^l - 2 \Phi_{k,n,m}^l + \Phi_{k,n,m-1}^l}{\Delta y^2} + O(\Delta y^2) \quad (5.35e)$$

$$\begin{aligned} \left. \frac{\partial^2 \Phi}{\partial x \partial y} \right|_{k,n,m}^l &= \frac{\Phi_{k,n+1,m+1}^l - \Phi_{k,n-1,m+1}^l - \Phi_{k,n+1,m-1}^l + \Phi_{k,n-1,m-1}^l}{4 \Delta x \Delta y} \\ &+ O(\Delta x^2, \Delta y^2). \end{aligned} \quad (5.35f)$$

The computational molecule for this second-order approximation is shown in Figure 5.2.

Application of the above difference approximations to Equations (5.11c) through (5.11i) leads to a system of  $7K$  nonlinear equations for calculation of the

flow variables at the discretization points (Equations (5.11a) and (5.11b) serve only as a check on the quality of the solution.). The addition of  $K$  equations for computation of the viscosity at the grid points completes the equation system. This difference equation system is solved using a line iteration method with simultaneous iteration of all  $7K$  equations. The line iteration proceeds in the  $x$  direction for Equations (5.11c), (5.11d), (5.11e), (5.11g), and (5.11i) for the calculation of  $\Omega_{xk}$ ,  $\Omega_{yk}$ ,  $\Omega_{zk}$ ,  $V_k$ , and  $\Theta_k$ . The unknown variables are obtained on grid lines parallel to the  $y$  axis using a direct method for tridiagonal systems of equations. However, the discretized systems that result from Equations (5.11f) and (5.11h) for the evaluation of the  $U_k$  velocities and the  $W_k$  velocities are solved with the iteration sweep proceeding in the  $y$  direction since the  $y$  derivatives for  $U_k$  and  $W_k$  do not appear in these equations. The same method for tridiagonal systems is used with the unknown variables obtained on grid lines parallel to the  $x$  axis. The  $U_k$  velocities and  $W_k$  velocities are updated after each iterative sweep in the  $x$  direction. A detailed description of the numerical procedure is now given.

### 5.3.1 Discretization of the Governing Equations in Fourier Space

After applying the time and spatial finite difference relations defined above to the Equations (5.11c) through (5.11i), the following discretized equations result:

$$\frac{1}{2\Delta t} \left( 3\Omega_{x,n,m}^l - 4\Omega_{x,n,m}^{l-1} + \Omega_{x,n,m}^{l-2} \right) + A_{x,n,m}^l = B_{x,n,m}^l + C_{x,n,m}^l \quad (5.36a)$$

$$\frac{1}{2\Delta t} \left( 3\Omega_{y,n,m}^l - 4\Omega_{y,n,m}^{l-1} + \Omega_{y,n,m}^{l-2} \right) + A_{y,n,m}^l = B_{y,n,m}^l + C_{y,n,m}^l \quad (5.36b)$$

$$\frac{1}{2\Delta t} \left( 3\Omega_{z,n,m}^l - 4\Omega_{z,n,m}^{l-1} + \Omega_{z,n,m}^{l-2} \right) + A_{z,n,m}^l = B_{z,n,m}^l + C_{z,n,m}^l \quad (5.36c)$$

$$\frac{1}{\Delta x^2} (U_{k,n+1,m}^l - 2U_{k,n,m}^l + U_{k,n-1,m}^l) - \gamma^2 k^2 U_{k,n,m}^l = \gamma k \Omega_{y,n,m}^l$$

$$-\frac{1}{4\Delta x\Delta y}(V_{k,n+1,m+1}^l - V_{k,n-1,m+1}^l - V_{k,n+1,m-1}^l + V_{k,n-1,m-1}^l) \quad (5.36d)$$

$$\begin{aligned} & \frac{1}{Re\Delta x^2}(V_{k,n+1,m}^l - 2V_{k,n,m}^l + V_{k,n-1,m}^l) \\ & + \frac{1}{\Delta y^2}(V_{k,n,m+1}^l - 2V_{k,n,m}^l + V_{k,n,m-1}^l) - \frac{\gamma^2 k^2}{Re}V_{k,n,m}^l = \\ & -\gamma k\Omega_{xk,n,m}^l - \frac{1}{2\Delta x}(\Omega_{xk,n+1,m}^l - \Omega_{xk,n-1,m}^l) \end{aligned} \quad (5.36e)$$

$$\begin{aligned} & \frac{1}{\Delta x^2}(W_{k,n+1,m}^l - 2W_{k,n,m}^l + W_{k,n-1,m}^l) - \gamma^2 k^2 W_{k,n,m}^l = \\ & \frac{1}{2\Delta x}(\Omega_{yk,n+1,m}^l - \Omega_{yk,n-1,m}^l) - \frac{\gamma k}{2\Delta y}(V_{k,n,m+1}^l - V_{k,n,m-1}^l) \end{aligned} \quad (5.36f)$$

$$\begin{aligned} & \frac{1}{2\Delta t}(3\Theta_{k,n,m}^l - 4\Theta_{k,n,m}^{l-1} + \Theta_{k,n,m}^{l-2}) + D_{k,n,m}^l = \\ & \frac{1}{RePr\Delta x^2}(\Theta_{k,n+1,m}^l - 2\Theta_{k,n,m}^l + \Theta_{k,n-1,m}^l) \\ & + \frac{1}{Pr\Delta x^2}(\Theta_{k,n,m+1}^l - 2\Theta_{k,n,m}^l + \Theta_{k,n,m-1}^l) - \frac{\gamma^2 k^2}{RePr}\Theta_{k,n,m}^l \end{aligned} \quad (5.36g)$$

for

$$\begin{aligned} k &= \left(0, 1, \dots, \frac{K}{2}\right), \quad n = (1, 2, \dots, N-1), \\ m &= (1, 2, \dots, M-1), \quad \text{and } l = (2, 3, \dots). \end{aligned}$$

In the above equations, the imaginary unit 'i' has been eliminated by taking into account Equations (5.33). Since the Fourier variables are either purely real or purely imaginary, this imaginary unit is replaced by a + sign or a - sign, depending on the terms in the equation.

The iteration loop for the above difference equation system is now introduced. The iteration index is denoted using the superscript 'i'. The nonlinear terms are calculated at the previous iteration level, but several terms are added at the current iteration step and subtracted at the previous iteration step. These additional terms are necessary to insure diagonal dominance of the tridiagonal

system and to improve the rate of convergence. These terms are also chosen so that the coefficients in the tridiagonal matrix are constants. Therefore the entire tridiagonal reduction does not have to be made for each new iteration or time level. Part of the reduction is done before the calculation begins. This is an important aspect to the numerical method because tridiagonal solvers inhibit vectorization because of their recursive nature. This reduction scheme is discussed later. First the terms to be added to the nonlinear terms  $A_{k,n,m}^l$ ,  $B_{k,n,m}^l$ ,  $C_{k,n,m}^l$ , and  $D_{k,n,m}^l$  are as follows:

$$A_{k,n,m}^l = A_{k,n,m}^{l,i-1} + \frac{1}{2\Delta x} u_{STN,m} \left( 2\Omega_{x_{k,n,m}}^{l,i} - 2\Omega_{x_{k,n,m}}^{l,i-1} \right) \quad (5.37a)$$

$$\begin{aligned} B_{k,n,m}^l &= B_{k,n,m}^{l,i-1} \\ &\quad - \left( \frac{2}{Re\Delta x^2} + \frac{2}{\Delta y^2} + \frac{\gamma^2 k^2}{Re} \right) \left( \Omega_{x_{k,n,m}}^{l,i} - \Omega_{x_{k,n,m}}^{l,i-1} \right) \\ &\quad + \frac{1}{\Delta y^2} \left( \Omega_{x_{k,n,m+1}}^{l,i} + \Omega_{x_{k,n,m-1}}^{l,i} - \Omega_{x_{k,n,m+1}}^{l,i-1} - \Omega_{x_{k,n,m-1}}^{l,i-1} \right) \end{aligned} \quad (5.37b)$$

$$C_{k,n,m}^l = C_{k,n,m}^{l,i-1} \quad (5.37c)$$

$$D_{k,n,m}^l = D_{k,n,m}^{l,i-1} + \frac{1}{2\Delta x} u_{STN,m} \left( 2\Theta_{k,n,m}^{l,i} - 2\Theta_{k,n,m}^{l,i-1} \right) \quad (5.37d)$$

for

$$\begin{aligned} k &= \left( 0, 1, \dots, \frac{K}{2} \right), \quad n = (1, 2, \dots, N-1), \\ m &= (1, 2, \dots, M-1), \quad \text{and } l = (2, 3, \dots). \end{aligned}$$

When the iteration loop has converged, the above additions to the nonlinear terms cancel. The terms added to Equations (5.37a) and (5.37d) do not have anything to do with the difference approximations, but are added to improve the convergence characteristics of the iteration loop. These terms stem from the  $u \frac{\partial \omega_x}{\partial x}$  convective term. The choice of  $u_{STN,m}$  is made since this term is used only for diagonal dominance and so the tridiagonal system does not have to be completely reduced

at each iteration step as would be required if  $U_{0,n,m}^{l,i-1}$  would have been used. For the undisturbed flow computation, the similarity solution is used for  $u_{STN,m}$ , i.e.,  $u_{STN,m} = u_{SIMN,m}$ , so that the coefficient matrix remains constant. The terms added to Equations (5.37b) result from the diffusion term  $\mu \nabla_1^2 \omega$ . This term is a quadratic nonlinearity and this nonlinearity would have caused the tridiagonal systems to have nonconstant coefficients. Therefore additional terms were chosen without the variation in viscosity. The convergence properties are not greatly affected by adding a viscous term with uniform viscosity and the coefficient matrix remains constant. The first additional term is from the center grid point of the term  $\frac{\partial^2 \Omega_{xh}}{\partial x^2}$ , the second and fourth terms are from  $\frac{\partial^2 \Omega_{xh}}{\partial y^2}$ , and the third term is from  $\frac{\partial^2 \Omega_{xh}}{\partial z^2}$ . No additional terms are added to Equations (5.37c) which contain derivatives of the viscosity.

Introducing the additional terms from Equations (5.37) into the discretized Equations (5.36) and rearranging leads to the following set of discrete equations:

$$\begin{aligned}
 & -\Omega_{xh,n,m+1}^{l,i} \\
 & + \left( \frac{3\Delta y^2}{2\Delta t} + \frac{2\Delta y^2}{Re\Delta x^2} + 2 + \frac{\gamma^2 k^2 \Delta y^2}{Re} + \frac{\Delta y^2}{\Delta x} u_{STN,m} \right) \Omega_{xh,n,m}^{l,i} \\
 & - \Omega_{xh,n,m-1}^{l,i} = \\
 & \frac{\Delta y^2}{2\Delta t} \left( 4\Omega_{xh,n,m}^{l,i-1} - \Omega_{xh,n,m}^{l,i-2} \right) + \Delta y^2 \left( B_{xh,n,m}^{l,i-1} + C_{xh,n,m}^{l,i-1} - A_{xh,n,m}^{l,i-1} \right) \\
 & + \frac{\Delta y^2}{\Delta x} u_{STN,m} \Omega_{xh,n,m}^{l,i-1} - \left( \Omega_{xh,n,m+1}^{l,i-1} + \Omega_{xh,n,m-1}^{l,i-1} \right) \quad (5.38a) \\
 & -\Omega_{yh,n,m+1}^{l,i} \\
 & + \left( \frac{3\Delta y^2}{2\Delta t} + \frac{2\Delta y^2}{Re\Delta x^2} + 2 + \frac{\gamma^2 k^2 \Delta y^2}{Re} + \frac{\Delta y^2}{\Delta x} u_{STN,m} \right) \Omega_{yh,n,m}^{l,i} \\
 & - \Omega_{yh,n,m-1}^{l,i} = \\
 & \frac{\Delta y^2}{2\Delta t} \left( 4\Omega_{yh,n,m}^{l,i-1} - \Omega_{yh,n,m}^{l,i-2} \right) + \Delta y^2 \left( B_{yh,n,m}^{l,i-1} + C_{yh,n,m}^{l,i-1} - A_{yh,n,m}^{l,i-1} \right)
 \end{aligned}$$

$$+ \frac{\Delta y^2}{\Delta x} u_{STN,m} \Omega_{y_{k,n,m}}^{l,i-1} - \left( \Omega_{y_{k,n,m+1}}^{l,i-1} + \Omega_{y_{k,n,m-1}}^{l,i-1} \right) \quad (5.38b)$$

$$\begin{aligned} & - \Omega_{z_{k,n,m+1}}^{l,i} \\ & + \left( \frac{3\Delta y^2}{2\Delta t} + \frac{2\Delta y^2}{Re\Delta x^2} + 2 + \frac{\gamma^2 k^2 \Delta y^2}{Re} + \frac{\Delta y^2}{\Delta x} u_{STN,m} \right) \Omega_{z_{k,n,m}}^{l,i} \\ & - \Omega_{z_{k,n,m-1}}^{l,i} = \\ & \frac{\Delta y^2}{2\Delta t} \left( 4\Omega_{z_{k,n,m}}^{l-1} - \Omega_{z_{k,n,m}}^{l-2} \right) + \Delta y^2 \left( B_{z_{k,n,m}}^{l,i-1} + C_{z_{k,n,m}}^{l,i-1} - A_{z_{k,n,m}}^{l,i-1} \right) \\ & + \frac{\Delta y^2}{\Delta x} u_{STN,m} \Omega_{z_{k,n,m}}^{l,i-1} - \left( \Omega_{z_{k,n,m+1}}^{l,i-1} + \Omega_{z_{k,n,m-1}}^{l,i-1} \right) \end{aligned} \quad (5.38c)$$

$$\begin{aligned} & - U_{k,n+1,m}^{l,i} + (2 + \gamma^2 k^2 \Delta x^2) U_{k,n,m}^{l,i} - U_{k,n-1,m}^{l,i} = -\gamma k \Delta x^2 \Omega_{y_{k,n,m}}^{l,i} \\ & + \frac{\Delta x}{4\Delta y} \left( V_{k,n+1,m+1}^{l,i} - V_{k,n-1,m+1}^{l,i} - V_{k,n+1,m-1}^{l,i} + V_{k,n-1,m-1}^{l,i} \right) \end{aligned} \quad (5.38d)$$

$$\begin{aligned} & - V_{k,n,m+1}^{l,i} + \left( 2 + \frac{2\Delta y^2}{Re\Delta x^2} + \frac{\gamma^2 k^2 \Delta y^2}{Re} \right) V_{k,n,m}^{l,i} - V_{k,n,m}^{l,i} = \\ & \gamma k \Delta y^2 \Omega_{z_{k,n,m}}^{l,i} + \frac{\Delta y^2}{2\Delta x} \left( \Omega_{z_{k,n+1,m}}^{l,i-1} + 2\Omega_{z_{k,n,m}}^{l,i} - 2\Omega_{z_{k,n,m}}^{l,i-1} - \Omega_{z_{k,n-1,m}}^{l,i} \right) \\ & + \frac{\Delta y^2}{Re\Delta x^2} \left( V_{k,n+1,m}^{l,i-1} + V_{k,n-1,m}^{l,i} \right) \end{aligned} \quad (5.38e)$$

$$\begin{aligned} & - W_{k,n+1,m}^{l,i} + (2 + \gamma^2 k^2 \Delta x^2) W_{k,n,m}^{l,i} - W_{k,n-1,m}^{l,i} = \\ & - \frac{\Delta x}{2} \left( \Omega_{y_{k,n+1,m}}^{l,i} - \Omega_{y_{k,n-1,m}}^{l,i} \right) + \frac{\gamma k \Delta x^2}{2\Delta y} \left( V_{k,n,m+1}^{l,i} - V_{k,n,m-1}^{l,i} \right) \end{aligned} \quad (5.38f)$$

$$\begin{aligned} & - \Theta_{k,n,m+1}^{l,i} \\ & + Pr \left( \frac{3\Delta y^2}{2\Delta t} + \frac{2\Delta y^2}{RePr\Delta x^2} + \frac{2}{Pr} + \frac{\gamma^2 k^2 \Delta y^2}{RePr} + \frac{\Delta y^2}{\Delta x} u_{STN,m} \right) \Theta_{k,n,m}^{l,i} \\ & - \Theta_{k,n,m-1}^{l,i} = \\ & \frac{Pr\Delta y^2}{2\Delta t} \left( 4\Theta_{k,n,m}^{l-1} - \Theta_{k,n,m}^{l-2} \right) - Pr\Delta y^2 D_{k,n,m}^{l,i-1} \\ & + \frac{Pr\Delta y^2}{\Delta x} u_{STN,m} \Theta_{k,n,m}^{l,i-1} \end{aligned} \quad (5.38g)$$

for

$$\begin{aligned} k &= \left( 0, 1, \dots, \frac{K}{2} \right), \quad n = (1, 2, \dots, N-1), \\ m &= (1, 2, \dots, M-1), \quad \text{and } l = (2, 3, \dots). \end{aligned}$$



The  $V_k$  Poisson equation contains the additional term  $\frac{\Delta y^2}{2 \Delta x} (2 \Omega_{z,n,m}^{l,i} - 2 \Omega_{z,n,m}^{l,i-1})$  which is again added to speed convergence.

### 5.3.2 Discretization of the Undisturbed Flow Boundary and Initial Conditions

The boundary and initial conditions for the undisturbed flow that were presented in Fourier space in Section 5.2.1 are now shown in discretized notation. Again, the three-dimensional components are zero everywhere for  $l < L_1$ . Thus Equation (5.13) in discrete form is

$$W_{0,n,m}^l = \Omega_{z0,n,m}^l = \Omega_{y0,n,m}^l$$

and for  $k > 0$ :

$$\begin{aligned} U_{k,n,m}^l &= V_{k,n,m}^l = W_{k,n,m}^l = 0 \\ \Omega_{z,n,m}^l &= \Omega_{y,n,m}^l = \Omega_{x,n,m}^l = 0. \end{aligned} \quad (5.39)$$

Initial Conditions:  $l = 0$  and  $l = 1$ ,  $0 \leq n \leq N$ ,  $0 \leq m \leq M$ ,  $k = 0$

In order to start the calculation, information is needed at the first two time levels. These first two time levels are set to the similarity solution. The discrete form of the initial conditions then follows from Equations (5.14):

$$U_{0,n,m}^0 = U_{0,n,m}^1 = u_{SIM,n,m} \quad (5.40a)$$

$$V_{0,n,m}^0 = V_{0,n,m}^1 = v_{SIM,n,m} \quad (5.40b)$$

$$\Omega_{z0,n,m}^0 = \Omega_{z0,n,m}^1 = \omega_{zSIM,n,m} \quad (5.40c)$$

$$\Theta_{0,n,m}^0 = \Theta_{0,n,m}^1 = T_{SIM,n,m} \quad (5.40d)$$

Inflow Boundary Conditions:  $n = 0$ ,  $0 \leq m \leq M$ ,  $2 < l \leq L_1$ ,  $k = 0$

The inflow boundary conditions follow simply from Equations (5.15):

$$U_{0,0,m}^l = u_{SIM0,m} \quad (5.41a)$$

$$V_{0,0,m}^l = v_{SIM0,m} \quad (5.41b)$$

$$\Omega_{z0,0,m}^l = \omega_{zSIM0,m} \quad (5.41c)$$

$$\Theta_{0,0,m}^l = T_{SIM0,m} \quad (5.41d)$$

Outflow Boundary Conditions:  $n = N, 1 \leq m \leq M-1, 2 < l \leq L_1, k = 0$

At the outflow boundary, the discrete form of Equations (5.16b), (5.16c), and (5.16d) is:

$$V_{0,N+1,m}^l - 2V_{0,N,m}^l + V_{0,N-1,m}^l = 0 \quad (5.42a)$$

$$\Omega_{z0,N+1,m}^l - 2\Omega_{z0,N,m}^l + \Omega_{z0,N-1,m}^l = 0 \quad (5.42b)$$

$$\Theta_{0,N+1,m}^l - 2\Theta_{0,N,m}^l + \Theta_{0,N-1,m}^l = 0 \quad (5.42c)$$

The discrete form of the boundary condition for the  $U$  velocity is found by using boundary condition (5.16a) and the  $U$  Poisson equation applied at the boundary:

$$\left. \frac{\partial U}{\partial x} \right|_{0,N,m}^l = - \left. \frac{\partial V}{\partial y} \right|_{0,N,m}^l \quad (5.43a)$$

$$\left. \frac{\partial^2 U}{\partial x^2} \right|_{0,N,m}^l = - \left. \frac{\partial^2 V}{\partial x \partial y} \right|_{0,N,m}^l \quad (5.43b)$$

The derivative  $\left. \frac{\partial^2 U}{\partial x^2} \right|_{0,N,m}^l$  is discretized as follows:

$$\begin{aligned} \left. \frac{\partial^2 U}{\partial x^2} \right|_{0,N,m}^l &= -\frac{6}{\Delta x^2} (U_{0,N,m}^l - U_{0,N-1,m}^l) \\ &\quad + \frac{2}{\Delta x} \left( 2 \left. \frac{\partial U}{\partial x} \right|_{0,N,m}^l + \left. \frac{\partial U}{\partial x} \right|_{0,N-1,m}^l \right) + O(\Delta x^2). \end{aligned} \quad (5.44)$$

Introducing Equation (5.43a) into (5.44) leads to:

$$\begin{aligned} \left. \frac{\partial^2 U}{\partial x^2} \right|_{0,N,m}^l &= -\frac{6}{\Delta x^2} (U_{0,N,m}^l - U_{0,N-1,m}^l) \\ &\quad - \frac{2}{\Delta x} \left( 2 \left. \frac{\partial V}{\partial y} \right|_{0,N,m}^l + \left. \frac{\partial V}{\partial y} \right|_{0,N-1,m}^l \right). \end{aligned} \quad (5.45)$$

The derivative  $\frac{\partial^2 V}{\partial x \partial y} \Big|_{0,N,m}^l$  from Equation (5.43b) is approximated by

$$\frac{\partial^2 V}{\partial x \partial y} \Big|_{0,N,m}^l = \frac{1}{2 \Delta x \Delta y} \left( V_{0,N,m+1}^l - V_{0,N-1,m+1}^l - V_{0,N-1,m+1}^l + V_{0,N-1,m-1}^l \right) + O(\Delta x^2, \Delta y^2) \quad (5.46)$$

where the boundary condition (5.42a) is introduced. Standard central difference approximations are used for the term  $\frac{\partial V}{\partial y} \Big|_{0,N,M}^l$ . The boundary condition for the  $U$  velocity thus becomes

$$U_{0,N,m}^{l,i} = U_{0,N-1,m}^{l,i} - \frac{\Delta x}{4 \Delta y} \left( V_{0,N,m+1}^{l,i} - V_{0,N,m-1}^{l,i} + V_{0,N-1,m+1}^{l,i} - V_{0,N-1,m-1}^{l,i} \right) \quad (5.47)$$

The additional grid points at ' $N + 1$ ' are eliminated for the flow components of Equations (5.42) using the following procedure. For the outflow boundary condition for the  $V$  velocity, Equation (5.42b) and the  $V$  Poisson equation (5.38e) are applied at the right boundary along with Equation (5.42a). This leads to the following boundary condition for the  $V$  velocity:

$$-V_{0,N,m+1}^{l,i} + 2V_{0,N,m}^{l,i} - V_{0,N,m-1}^{l,i} = \frac{\Delta y^2}{\Delta x} \left( \Omega_{z_0,N,m}^{l,i} - \Omega_{z_0,N-1,m}^{l,i} \right). \quad (5.48)$$

For the spanwise vorticity at the outflow boundary, conditions (5.42) and (5.47) are used along with the application of the spanwise vorticity transport equation (5.38c) at the right boundary. This leads to the following boundary condition:

$$\begin{aligned} & -\Omega_{z_0,N,m+1}^{l,i} + \left( \frac{3 \Delta y^2}{2 \Delta t} + 2 + \frac{\Delta y^2}{\Delta x} u_{SIM,N,m} \right) \Omega_{z_0,N,m}^{l,i} - \Omega_{z_0,N,m-1}^{l,i} = \\ & \frac{\Delta y^2}{2 \Delta t} \left( 4 \Omega_{z_0,N,m}^{l-1} - \Omega_{z_0,N,m}^{l-2} \right) + \Delta y^2 \left( B_{z_0,N,m}^{l,i-1} + C_{z_0,N,m}^{l,i-1} - A_{z_0,N,m}^{l,i-1} \right) \\ & + \frac{\Delta y^2}{\Delta x} u_{SIM,N,m} \Omega_{z_0,N,m}^{l,i-1} - \left( \Omega_{z_0,N,m+1}^{l,i-1} + \Omega_{z_0,N,m-1}^{l,i-1} \right). \end{aligned} \quad (5.49)$$

Finally, the outflow boundary condition for the temperature is found using the conditions (5.42) and (5.47) and applying the energy equation (5.38g) at the right boundary. This leads to the following form of the boundary condition for the temperature:

$$\begin{aligned}
 & -\Theta_{0,N,m+1}^{l,i} + Pr \left( \frac{3\Delta y^2}{2\Delta t} + \frac{2}{Pr} + \frac{\Delta y^2}{\Delta x} u_{SIMN,m} \right) \Theta_{0,N,m}^{l,i} - \Theta_{0,N,m-1}^{l,i} = \\
 & \frac{Pr\Delta y^2}{2\Delta t} \left( 4\Theta_{0,N,m}^{l-1} - \Theta_{0,N,m}^{l-2} \right) - Pr\Delta y^2 D_{0,N,m}^{l,i-1} \\
 & + \frac{Pr\Delta y^2}{\Delta x} u_{SIMN,m} \Theta_{0,N,m}^{l,i-1}.
 \end{aligned} \tag{5.50}$$

The nonlinear terms in Equations (5.49) and (5.50) also require special consideration at the outflow boundary. For the spatial derivatives in these terms, standard second order central differences are used and the additional point at ' $N + 1$ ' is eliminated by applying boundary conditions (5.42).

Outer Boundary Conditions:  $m = M, 1 \leq n \leq N - 1, 2 < l \leq L_1, k = 0$

For the outer boundary, conditions (5.17) in discrete form are

$$U_{0,n,M}^l = 1 \tag{5.51a}$$

$$V_{0,n,M+1}^l - V_{0,n,M-1}^l = 0 + O(\Delta y^2) \tag{5.51b}$$

$$\Omega_{x0,n,M}^l = 0 \tag{5.51c}$$

$$\Theta_{0,n,M}^l = 0. \tag{5.51d}$$

The  $V$  velocity at the grid point ' $M + 1$ ' of Equation (5.51b) is removed by again applying the discrete  $V$  Poisson equation (5.38e) at the upper boundary. This leads to the following form of the outer boundary condition for the  $V$  velocity:

$$\left( 1 + \frac{\Delta y^2}{Re\Delta x^2} \right) V_{0,n,M}^{l,i} - V_{0,n,M-1}^{l,i} = \frac{\Delta y^2}{2Re\Delta x^2} \left( V_{0,n+1,M}^{l,i-1} + V_{0,n-1,M}^{l,i} \right). \tag{5.52}$$

Wall Boundary Conditions:  $m = 0, 1 \leq n \leq N, 2 \leq l \leq L_1, k = 0$

At the wall, the boundary conditions of Equations (5.18) yield:

$$U_{0,n,0}^l = 0 \quad (5.53a)$$

$$V_{0,n,0}^l = 0 \quad (5.53b)$$

$$\left. \frac{\partial V}{\partial y} \right|_{0,n,0}^l = 0 \quad (5.53c)$$

$$\left. \frac{\partial \Omega_z}{\partial x} \right|_{0,n,0}^l = - \left. \frac{\partial^2 V}{\partial y^2} \right|_{0,n,0}^l \quad (5.53d)$$

$$\Theta_{0,n,0}^l = A(x_n) x_n^p. \quad (5.53e)$$

The spanwise wall vorticity boundary condition (5.53d) is discretized as follows for  $2 \leq n \leq N$ :

$$\left. \frac{\partial \Omega_z}{\partial x} \right|_{0,n,0}^l = \frac{1}{2 \Delta x} \left( 3 \Omega_{z_{0,n,0}}^l - 4 \Omega_{z_{0,n-1,0}}^l + \Omega_{z_{0,n-2,0}}^l \right) + O(\Delta x^2) \quad (5.54a)$$

and for  $n = 1$ :

$$\left. \frac{\partial \Omega_z}{\partial x} \right|_{0,1,0}^l = \frac{1}{\Delta x} \left( \Omega_{z_{0,1,0}}^l - \Omega_{z_{0,0,0}}^l \right) + O(\Delta x). \quad (5.54b)$$

For the difference approximation of  $\left. \frac{\partial^2 V}{\partial y^2} \right|_{0,n,0}^l$ , an interpolating polynomial that is second order accurate is used. The boundary condition (5.53c) is introduced into this polynomial approximation so that a one-sided difference approximation with three nodal points results:

$$\left. \frac{\partial^2 V}{\partial y^2} \right|_{0,n,0}^l = \frac{1}{2 \Delta y^2} \left( -7 V_{0,n,0}^l + 8 V_{0,n,1}^l - V_{0,n,2}^l \right) + O(\Delta y^2). \quad (5.55)$$

However,  $V_{0,n,0}^l = 0$ , so the difference approximation for the wall vorticity follows from Equations (5.54) and (5.55)

for  $n = 1$ :

$$\Omega_{z_{0,1,0}}^{l,i} = \Omega_{z_{0,0,0}}^l - \frac{\Delta x}{2 \Delta y^2} \left( +8 V_{0,1,1}^{l,i} - V_{0,1,2}^{l,i} \right) \quad (5.56a)$$

and for  $n \geq 2$ :

$$\Omega_{z_0,n,0}^{l,i} = \frac{4}{3}\Omega_{z_0,n-1,0}^{l,i} - \frac{1}{3}\Omega_{z_0,n-2,0}^{l,i} - \frac{\Delta x}{3\Delta y^2} (+8V_{0,n,1}^{l,i} - V_{0,n,2}^{l,i}) . \quad (5.56b)$$

Corner Point Boundary Conditions:  $n = N, m = M, 2 < l \leq L_1, k = 0$

The upper right hand corner point of the integration domain requires special consideration for the  $V$  velocity. At this nodal point, the outflow boundary condition (5.16b) and the outer boundary condition (5.17b) are applied along with the  $V$  Poisson equation (5.38e). For this corner point the boundary conditions are then

$$U_{0,N,M}^l = 1 \quad (5.57a)$$

$$V_{0,N,M}^{l,i} - V_{0,N,M-1}^{l,i} = 0 \quad (5.57b)$$

$$\Omega_{z_0,N,M}^l = 0 \quad (5.57c)$$

$$\Theta_{0,N,M}^l = 0 . \quad (5.57d)$$

### 5.3.3 Discretization of the Disturbed Flow Boundary and Initial Conditions

The boundary and initial conditions for the disturbed flow that were presented in Fourier space in Section 5.2.2 are now shown in discretized form.

Initial Conditions:  $l = L_1$  and  $l = L_1 - 1, 0 \leq n \leq N, 0 \leq m \leq M$

Again, it is necessary to prescribe two time levels to start the calculation. The discrete form of the initial conditions at time  $l = L_1$  and  $l = L_1 - 1$  follow from Equations (5.19):

$$U_{0,n,m}^{L_1} = U_{0,n,m}^{L_1-1} = u_{ST_{n,m}} \quad (5.58a)$$

$$V_{0,n,m}^{L_1} = V_{0,n,m}^{L_1-1} = v_{ST_{n,m}} \quad (5.58b)$$

$$\Omega_{z_0,n,m}^{L_1} = \Omega_{z_0,n,m}^{L_1-1} = \omega_{zST_{n,m}} \quad (5.58c)$$

$$\Theta_{0,n,m}^{L_1} = \Theta_{0,n,m}^{L_1-1} = T_{ST_{n,m}} . \quad (5.58d)$$

All other discrete components are identically zero at time  $l = L_1$  and  $l = L_1 - 1$ .

Initial Conditions:  $l = L_2$  and  $l = L_2 - 1$ ,  $0 \leq n \leq N$ ,  $0 \leq m \leq M$

For the active control simulations, the initial conditions at time  $l = L_2$  and  $l = L_2 - 1$  for the wall temperatures follow from Equations (5.20) for  $l = L_2$ :

$$\Theta_{k,n,0}^{L_2} = \Theta_{w_h}(x_n, t_2) \quad (5.59a)$$

and for  $l = L_2 - 1$ :

$$\Theta_{k,n,m}^{L_2-1} = \Theta_{w_h}(x_n, t_2 - \Delta t). \quad (5.59b)$$

Inflow Boundary Conditions:  $n = 0$ ,  $0 \leq m \leq M$ ,  $l > L_1$

At the inflow boundary, the discrete boundary conditions follow from Equations (5.21):

$$U_{0,0,m}^l = u_{SIM_{0,m}} \quad (5.60a)$$

$$V_{0,0,m}^l = v_{SIM_{0,m}} \quad (5.60b)$$

$$\Omega_{x0,0,m}^l = \omega_{zSIM_{0,m}} \quad (5.60c)$$

$$\Theta_{0,0,m}^l = T_{SIM_{0,m}}. \quad (5.60d)$$

All other discrete Fourier components are again identically zero.

Outflow Boundary Conditions:  $n = N_B$ ,  $1 \leq m \leq M - 1$ ,  $l > L_1$

The outflow boundary conditions follow from Equations (5.22) and in discretized notation are

for  $k = 0$ :

$$\begin{aligned} & \frac{1}{\Delta x^2} (U_{0,N_B+1,m}^l - 2U_{0,N_B,m}^l + U_{0,N_B-1,m}^l) = \\ & - \frac{6}{\Delta x^2} (u_{ST_{N_B,m}} - u_{ST_{N_B-1,m}}) \end{aligned}$$

$$\begin{aligned}
& - \frac{1}{\Delta x \Delta y} \left( 2v_{ST_{N_B, m+1}} - 2v_{ST_{N_B, m-1}} + v_{ST_{N_B-1, m+1}} - v_{ST_{N_B-1, m-1}} \right) \\
& - \alpha_{r_N}^2 U_{0, N_B, m}^l
\end{aligned} \tag{5.61a}$$

$$\frac{1}{\Delta x^2} (V_{0, N_B+1, m}^l - 2V_{0, N_B, m}^l + V_{0, N_B-1, m}^l) = -\alpha_{r_N}^2 V_{0, N_B, m}^l \tag{5.61b}$$

$$W_{0, N_B, m}^l = 0 \tag{5.61c}$$

$$\Omega_{z0, N_B, m}^l = 0 \tag{5.61d}$$

$$\Omega_{y0, N_B, m}^l = 0 \tag{5.61e}$$

$$\frac{1}{\Delta x^2} (\Omega_{z0, N_B+1, m}^l - 2\Omega_{z0, N_B, m}^l + \Omega_{z0, N_B-1, m}^l) = -\alpha_{r_N}^2 \Omega_{z0, N_B, m}^l \tag{5.61f}$$

$$\frac{1}{\Delta x^2} (\Theta_{0, N_B+1, m}^l - 2\Theta_{0, N_B, m}^l + \Theta_{0, N_B-1, m}^l) = -\alpha_{r_N}^2 \Theta_{0, N_B, m}^l \tag{5.61g}$$

and for  $k > 0$ :

$$\frac{1}{\Delta x^2} (U_{k, N_B+1, m}^l - 2U_{k, N_B, m}^l + U_{k, N_B-1, m}^l) = -\alpha_{r_N}^2 U_{k, N_B, m}^l \tag{5.61h}$$

$$\frac{1}{\Delta x^2} (V_{k, N_B+1, m}^l - 2V_{k, N_B, m}^l + V_{k, N_B-1, m}^l) = -\alpha_{r_N}^2 V_{k, N_B, m}^l \tag{5.61i}$$

$$\frac{1}{\Delta x^2} (W_{k, N_B+1, m}^l - 2W_{k, N_B, m}^l + W_{k, N_B-1, m}^l) = -\alpha_{r_N}^2 W_{k, N_B, m}^l \tag{5.61j}$$

$$\frac{1}{\Delta x^2} (\Omega_{zk, N_B+1, m}^l - 2\Omega_{zk, N_B, m}^l + \Omega_{zk, N_B-1, m}^l) = -\alpha_{r_N}^2 \Omega_{zk, N_B, m}^l \tag{5.61k}$$

$$\frac{1}{\Delta x^2} (\Omega_{yk, N_B+1, m}^l - 2\Omega_{yk, N_B, m}^l + \Omega_{yk, N_B-1, m}^l) = -\alpha_{r_N}^2 \Omega_{yk, N_B, m}^l \tag{5.61l}$$

$$\frac{1}{\Delta x^2} (\Omega_{zk, N_B+1, m}^l - 2\Omega_{zk, N_B, m}^l + \Omega_{zk, N_B-1, m}^l) = -\alpha_{r_N}^2 \Omega_{zk, N_B, m}^l \tag{5.61m}$$

$$\frac{1}{\Delta x^2} (\Theta_{k, N_B+1, m}^l - 2\Theta_{k, N_B, m}^l + \Theta_{k, N_B-1, m}^l) = -\alpha_{r_N}^2 \Theta_{k, N_B, m}^l \tag{5.61n}$$

The index for the location of the moving boundary is represented here as ' $N_B$ '.

The additional grid points at ' $M+1$ ' are eliminated from the above difference approximations by applying the discrete set of Equations (5.38) at the outflow boundary. Using the boundary conditions (5.61) and the discrete  $U$  Poisson equation (5.38d), the following form of the discrete outflow condition for the  $U$  velocity is found:



for  $k = 0$ :

$$\begin{aligned}
 U_{0,N_B,m}^{l,i} &= u_{ST_{N_B,m}} \\
 &+ \frac{1}{2\alpha_{r_N}^2 \Delta x \Delta y} \left[ \left( 1 - \frac{\alpha_{r_N}^2 \Delta x^2}{2} \right) (V_{0,N_B,m+1}^{l,i} - V_{0,N_B,m-1}^{l,i}) \right. \\
 &\quad \left. - V_{0,N_B-1,m+1}^{l,i} + V_{0,N_B-1,m-1}^{l,i} \right] + \frac{\Delta x}{4\Delta y} (v_{ST_{N_B,m+1}} - v_{ST_{N_B,m-1}}) \\
 &\frac{1}{\alpha_{r_N}^2} \left[ -\frac{6}{\Delta x^2} (u_{ST_{N_B,m}} - u_{ST_{N_B-1,m}}) - \frac{1}{\Delta x \Delta y} (2v_{ST_{N_B,m+1}} - 2v_{ST_{N_B,m-1}} \right. \\
 &\quad \left. + v_{ST_{N_B-1,m+1}} + v_{ST_{N_B-1,m-1}}) \right] \quad (5.62a)
 \end{aligned}$$

and for  $k > 0$ :

$$\begin{aligned}
 U_{k,N_B,m}^{l,i} &= + \frac{1}{\alpha_{r_N}^2 + \gamma^2 k^2} \left\{ \left[ \frac{1}{2\Delta x \Delta y} \left( 1 - \frac{\alpha_{r_N}^2 \Delta x^2}{2} \right) (V_{k,N_B,m+1}^{l,i} - V_{k,N_B,m-1}^{l,i}) \right. \right. \\
 &\quad \left. \left. - V_{k,N_B-1,m+1}^{l,i} + V_{k,N_B-1,m-1}^{l,i} \right] - \gamma k \Omega_{y_{k,N_B,m}}^{l,i} \right\}, \quad (5.62b)
 \end{aligned}$$

For the  $V$  velocity, boundary conditions (5.61) and the discrete  $V$  Poisson equation (5.38e) applied at the outflow boundary lead to the following form of the discrete boundary condition for the  $V$  velocity

for  $k = 0$ :

$$\begin{aligned}
 &- V_{0,N_B,m+1}^{l,i} + \left( 2 + \frac{\alpha_{r_N}^2 \Delta y^2}{Re} \right) V_{0,N_B,m}^{l,i} - V_{0,N_B,m-1}^{l,i} \\
 &= \frac{\Delta y^2}{\Delta x} \left[ \left( 1 - \frac{\alpha_{r_N}^2 \Delta x^2}{2} \right) \Omega_{x_{0,N_B,m}}^{l,i} - \Omega_{x_{0,N-1,m}}^{l,i} + \frac{\alpha_{r_N}^2 \Delta x^2}{2} \Omega_{x_{ST_{N_B,m}}} \right] \\
 &+ \frac{\alpha_{r_N}^2 \Delta y^2}{Re} v_{ST_{N_B,m}} \quad (5.63a)
 \end{aligned}$$

and for  $k > 0$ :

$$\begin{aligned}
 &- V_{k,N_B,m+1}^{l,i} + \left[ 2 + \frac{(\alpha_{r_N}^2 + \gamma^2 k^2) \Delta y^2}{Re} \right] V_{k,N_B,m}^{l,i} - V_{k,N_B,m-1}^{l,i} \\
 &= \gamma k \Delta y^2 \Omega_{x_{k,N_B,m}} + \frac{\Delta y^2}{\Delta x} \left[ \left( 1 - \frac{\alpha_{r_N}^2 \Delta x^2}{2} \right) \Omega_{x_{k,N_B,m}}^{l,i} - \Omega_{x_{k,N-1,m}}^{l,i} \right]. \quad (5.63b)
 \end{aligned}$$

For the  $W$  velocity, conditions (5.61) and the discrete  $W$  Poisson equation (5.38f) are used resulting in the following outflow boundary condition

for  $k = 0$ :

$$W_{0,N_B,m}^l = 0 \quad (5.64a)$$

and for  $k > 0$ :

$$W_{k,N_B,m}^{l,i} = -\frac{1}{\alpha_{r_N}^2 + \gamma^2 k^2} \left[ \frac{1}{\Delta x} \left( 1 - \frac{\alpha_{r_N}^2 \Delta x^2}{2} \right) (\Omega_{y_{k,N_B,m}}^{l,i} - \Omega_{y_{k,N_B-1,m}}^{l,i}) - \frac{\gamma k}{2 \Delta y} (V_{k,N_B,m+1}^{l,i} - V_{k,N_B,m-1}^{l,i}) \right]. \quad (5.64b)$$

Before proceeding with the outflow boundary conditions for the vorticity and temperature, an addendum is first made to the additional quantities added to the nonlinear terms. These changes are made at the outflow boundary and are

$$A_{k,N_B,m}^l = A_{k,N_B,m}^{l,i-1} + \frac{1}{\Delta x} \left( 1 - \frac{\alpha_{r_N}^2 \Delta x^2}{2} \right) u_{ST_{N,m}} (\Omega_{x_{k,N_B,m}}^{l,i} - \Omega_{x_{k,N_B,m}}^{l,i-1}) \quad (5.65a)$$

$$B_{k,N_B,m}^l = B_{k,N_B,m}^{l,i-1} - \left( \frac{\alpha_{r_N}^2}{Re} + \frac{2}{\Delta y^2} + \frac{\gamma^2 k^2}{Re} \right) (\Omega_{x_{k,N_B,m}}^{l,i} - \Omega_{x_{k,N_B,m}}^{l,i-1}) + \frac{1}{\Delta y^2} (\Omega_{x_{k,N_B,m+1}}^{l,i} + \Omega_{x_{k,N_B,m-1}}^{l,i} - \Omega_{x_{k,N_B,m+1}}^{l,i-1} - \Omega_{x_{k,N_B,m-1}}^{l,i-1}) \quad (5.65b)$$

$$C_{k,N_B,m}^l = C_{k,N_B,m}^{l,i-1} \quad (5.65c)$$

$$D_{k,N_B,m}^l = D_{k,N_B,m}^{l,i-1} + \frac{1}{\Delta x} \left( 1 - \frac{\alpha_{r_N}^2 \Delta x^2}{2} \right) u_{ST_{N,m}} (\Theta_{k,N_B,m}^{l,i} - \Theta_{k,N_B,m}^{l,i-1}) \quad (5.65d)$$

for

$$k = \left( 0, 1, \dots, \frac{K}{2} \right), \quad n = N_B, \\ m = (1, 2, \dots, M-1), \quad \text{and } l = (L_1, \dots).$$

Introducing the above addendums into the discretized equations (5.36) and applying the boundary conditions (5.61) yields the following discrete boundary conditions for the vorticity and temperature components

for  $k = 0$ :

$$\Omega_{z_0, N_B, m}^l = \Omega_{y_0, N_B, m}^l = 0 \quad (5.66a)$$

$$\begin{aligned} & -\Omega_{z_0, N_B, m-1}^{l,i} \\ & + \left[ \frac{3\Delta y^2}{2\Delta t} + \frac{\alpha_{rN}^2 \Delta y^2}{Re} + 2 + \frac{\Delta y^2}{\Delta x} \left( 1 - \frac{\alpha_{rN}^2 \Delta x^2}{2} \right) u_{STN, m} \right] \Omega_{z_0, N_B, m-1}^{l,i} \\ & - \Omega_{z_0, N_B, m-1}^{l,i} \\ & = \frac{\Delta y^2}{2\Delta t} \left( 4\Omega_{z_0, N_B, m}^{l-1} - \Omega_{z_0, N_B, m}^{l-2} \right) \\ & + \Delta y^2 \left( B_{z_0, N_B, m}^{l,i-1} + C_{z_0, N_B, m}^{l,i-1} - A_{z_0, N_B, m}^{l,i-1} \right) \\ & + \frac{\Delta y^2}{\Delta x} \left( 1 - \frac{\alpha_{rN}^2 \Delta x^2}{2} \right) u_{STN, m} \Omega_{z_0, N_B, m}^{l,i-1} \\ & - \left( \Omega_{z_0, N_B, m+1}^{l,i-1} + \Omega_{z_0, N_B, m-1}^{l,i-1} \right) + \frac{\alpha_{rN}^2 \Delta y^2}{Re} \Omega_{STN, m} \end{aligned} \quad (5.66b)$$

$$\begin{aligned} & -\Theta_{0, N_B, m+1}^{l,i} \\ & + Pr \left( \frac{3\Delta y^2}{2\Delta t} + \frac{2}{Pr} + \frac{\alpha_{rN}^2 \Delta y^2}{Re Pr} + \frac{\Delta y^2}{\Delta x} \left( 1 - \frac{\alpha_{rN}^2 \Delta x^2}{2} \right) u_{STN, m} \right) \Theta_{0, N_B, m}^{l,i} \\ & - \Theta_{0, N_B, m-1}^{l,i} = \\ & \frac{Pr \Delta y^2}{2\Delta t} \left( 4\Theta_{0, N_B, m}^{l-1} - \Theta_{0, N_B, m}^{l-2} \right) - Pr \Delta y^2 D_{0, N_B, m}^{l,i-1} \\ & + \frac{Pr \Delta y^2}{\Delta x} \left( 1 - \frac{\alpha_{rN}^2 \Delta x^2}{2} \right) u_{STN, m} \Theta_{0, N_B, m}^{l,i-1} + \frac{\alpha_{rN}^2 \Delta y^2}{Re} T_{STN, m} \end{aligned} \quad (5.66c)$$

and for  $k > 0$ :

$$\begin{aligned} & -\Omega_{z_k, N_B, m-1}^{l,i} \\ & + \left[ \frac{3\Delta y^2}{2\Delta t} + \frac{\alpha_{rN}^2 \Delta y^2}{Re} + 2 + \frac{\gamma^2 k^2 \Delta y^2}{Re} + \frac{\Delta y^2}{\Delta x} \left( 1 - \frac{\alpha_{rN}^2 \Delta x^2}{2} \right) u_{STN, m} \right] \Omega_{z_k, N_B, m-1}^{l,i} \\ & - \Omega_{z_k, N_B, m-1}^{l,i} \\ & = \frac{\Delta y^2}{2\Delta t} \left( 4\Omega_{z_k, N_B, m}^{l-1} - \Omega_{z_k, N_B, m}^{l-2} \right) \\ & + \Delta y^2 \left( B_{z_k, N_B, m}^{l,i-1} + C_{z_k, N_B, m}^{l,i-1} - A_{z_k, N_B, m}^{l,i-1} \right) \\ & + \frac{\Delta y^2}{\Delta x} \left( 1 - \frac{\alpha_{rN}^2 \Delta x^2}{2} \right) u_{STN, m} \Omega_{z_k, N_B, m}^{l,i-1} - \left( \Omega_{z_k, N_B, m+1}^{l,i-1} + \Omega_{z_k, N_B, m-1}^{l,i-1} \right) \end{aligned} \quad (5.66d)$$

$$\begin{aligned}
& -\Omega_{y_h, N_B, m-1}^{l,i} \\
& + \left[ \frac{3\Delta y^2}{2\Delta t} + \frac{\alpha_{r_N}^2 \Delta y^2}{Re} + 2 + \frac{\gamma^2 k^2 \Delta y^2}{Re} + \frac{\Delta y^2}{\Delta x} \left( 1 - \frac{\alpha_{r_N}^2 \Delta x^2}{2} \right) u_{ST_{N,m}} \right] \Omega_{y_h, N_B, m-1}^{l,i} \\
& - \Omega_{y_h, N_B, m-1}^{l,i} \\
& = \frac{\Delta y^2}{2\Delta t} \left( 4\Omega_{y_h, N_B, m}^{l-1} - \Omega_{y_h, N_B, m}^{l-2} \right) \\
& + \Delta y^2 \left( B_{y_h, N_B, m}^{l,i-1} + C_{y_h, N_B, m}^{l,i-1} - A_{y_h, N_B, m}^{l,i-1} \right) \\
& + \frac{\Delta y^2}{\Delta x} \left( 1 - \frac{\alpha_{r_N}^2 \Delta x^2}{2} \right) u_{ST_{N,m}} \Omega_{y_h, N_B, m}^{l,i-1} - \left( \Omega_{y_h, N_B, m+1}^{l,i-1} + \Omega_{y_h, N_B, m-1}^{l,i-1} \right) \quad (5.66e)
\end{aligned}$$

$$\begin{aligned}
& -\Omega_{z_h, N_B, m-1}^{l,i} \\
& + \left[ \frac{3\Delta y^2}{2\Delta t} + \frac{\alpha_{r_N}^2 \Delta y^2}{Re} + 2 + \frac{\gamma^2 k^2 \Delta y^2}{Re} + \frac{\Delta y^2}{\Delta x} \left( 1 - \frac{\alpha_{r_N}^2 \Delta x^2}{2} \right) u_{ST_{N,m}} \right] \Omega_{z_h, N_B, m-1}^{l,i} \\
& - \Omega_{z_h, N_B, m-1}^{l,i} \\
& = \frac{\Delta y^2}{2\Delta t} \left( 4\Omega_{z_h, N_B, m}^{l-1} - \Omega_{z_h, N_B, m}^{l-2} \right) \\
& + \Delta y^2 \left( B_{z_h, N_B, m}^{l,i-1} + C_{z_h, N_B, m}^{l,i-1} - A_{z_h, N_B, m}^{l,i-1} \right) \\
& + \frac{\Delta y^2}{\Delta x} \left( 1 - \frac{\alpha_{r_N}^2 \Delta x^2}{2} \right) u_{ST_{N,m}} \Omega_{z_h, N_B, m}^{l,i-1} - \left( \Omega_{z_h, N_B, m+1}^{l,i-1} + \Omega_{z_h, N_B, m-1}^{l,i-1} \right) \quad (5.66f)
\end{aligned}$$

$$\begin{aligned}
& -\Theta_{k, N_B, m+1}^{l,i} \\
& + Pr \left( \frac{3\Delta y^2}{2\Delta t} + \frac{2}{Pr} + \frac{\alpha_{r_N}^2 \Delta y^2}{Re Pr} + \frac{\gamma^2 k^2}{Re} + \frac{\Delta y^2}{\Delta x} \left( 1 - \frac{\alpha_{r_N}^2 \Delta x^2}{2} \right) u_{ST_{N,m}} \right) \Theta_{k, N_B, m}^{l,i} \\
& - \Theta_{k, N_B, m-1}^{l,i} = \\
& \frac{Pr \Delta y^2}{2\Delta t} \left( 4\Theta_{k, N_B, m}^{l-1} - \Theta_{k, N_B, m}^{l-2} \right) - Pr \Delta y^2 D_{k, N_B, m}^{l,i-1} \\
& + \frac{Pr \Delta y^2}{\Delta x} \left( 1 - \frac{\alpha_{r_N}^2 \Delta x^2}{2} \right) u_{ST_{N,m}} \Theta_{k, N_B, m}^{l,i-1} \quad (5.66g)
\end{aligned}$$

As for the undisturbed flow outflow boundary conditions, the nonlinear terms in Equations (5.66) are discretized using second order central differences. The additional point at ' $N + 1$ ' is eliminated through the application of boundary conditions (5.61).

Outer Boundary Conditions:  $m = M, 1 \leq n \leq N-1, L_1 < l$

The discrete boundary conditions for the outer boundary are derived from Equations (5.23)

for  $k = 0$ :

$$\frac{1}{2\Delta y} (V_{0,n,M+1}^l - V_{0,n,M-1}^l) = -\frac{\alpha_{rM}^2}{\sqrt{Re}} (V_{0,n,M}^l - v_{ST_{n,M}}) \quad (5.67a)$$

$$\Omega_{x_{0,n,M}}^l = 0 \quad (5.67b)$$

$$\Omega_{y_{0,n,M}}^l = 0 \quad (5.67c)$$

$$\Omega_{z_{0,n,M}}^l = 0 \quad (5.67d)$$

$$\Theta_{0,n,M}^l = 0, \quad (5.67e)$$

and for  $k > 0$ :

$$\frac{1}{2\Delta y} (V_{k,n,M+1}^l - V_{k,n,M-1}^l) = -\sqrt{\frac{\alpha_{rM}^2 + k^2\gamma^2}{Re}} V_{k,n,M}^l \quad (5.67f)$$

$$\Omega_{x_{k,n,M}}^l = 0 \quad (5.67g)$$

$$\Omega_{y_{k,n,M}}^l = 0 \quad (5.67h)$$

$$\Omega_{z_{k,n,M}}^l = 0 \quad (5.67i)$$

$$\Theta_{k,n,M}^l = 0. \quad (5.67j)$$

The grid point at ' $M+1$ ' in Equation (5.67a) and (5.67f) is eliminated by applying the discrete Equations (5.38d), (5.38e), and (5.38f) for the three velocities. The following three equations result for the velocities

for  $k = 0$ :

$$\begin{aligned} & -U_{0,n+1,M}^{l,i} + 2U_{0,n,M}^{l,i} - U_{0,n-1,M}^{l,i} = \\ & -\frac{\Delta x}{2} \frac{\alpha_{rM}^2}{\sqrt{Re}} (V_{0,n+1,M}^{l,i-1} - V_{0,n-1,M}^{l,i} - v_{ST_{n+1,M}} + v_{ST_{n-1,M}}) \end{aligned} \quad (5.68a)$$

$$\begin{aligned} & \left(1 + \frac{\Delta y^2}{Re \Delta x^2} + \frac{\Delta y \alpha_{rM}}{\sqrt{Re}}\right) V_{0,n,M}^{l,i} - V_{0,n,M-1}^{l,i} = \\ & \frac{\Delta y^2}{2 Re \Delta x^2} (V_{0,n+1,M}^{l,i-1} + V_{0,n-1,M}^{l,i}) + \frac{\Delta y \alpha_{rM}}{\sqrt{Re}} v_{ST_{n,M}} \end{aligned} \quad (5.68b)$$

$$W_{0,n,M}^l = 0, \quad (5.68c)$$

and for  $k > 0$ :

$$\begin{aligned} & -U_{k,n+1,M}^{l,i} + (2 + \gamma^2 k^2 \Delta x^2) U_{k,n,M}^{l,i} - U_{k,n-1,M}^{l,i} = \\ & -\frac{\Delta x}{2} \sqrt{\frac{\alpha_{rM}^2 + \gamma^2 k^2}{Re}} (V_{k,n+1,M}^{l,i-1} - V_{k,n-1,M}^{l,i}) \end{aligned} \quad (5.68d)$$

$$\begin{aligned} & \left( 1 + \frac{\gamma^2 k^2 \Delta y^2}{2 Re} + \frac{\Delta y^2}{Re \Delta x^2} + \Delta y \sqrt{\frac{\alpha_{rM}^2 + \gamma^2 k^2}{Re}} \right) V_{k,n,M}^{l,i} - V_{k,n,M-1}^{l,i} = \\ & \frac{\Delta y^2}{2 Re \Delta x^2} (V_{k,n+1,M}^{l,i-1} + V_{k,n-1,M}^{l,i}) \end{aligned} \quad (5.68e)$$

$$\begin{aligned} & -W_{k,n+1,M}^{l,i} + (2 + \gamma^2 k^2 \Delta x^2) W_{k,n,M}^{l,i} - W_{k,n-1,M}^{l,i} = \\ & -\gamma k \Delta x^2 \sqrt{\frac{\alpha_{rM}^2 + \gamma^2 k^2}{Re}} V_{k,n,M}^{l,i} \end{aligned} \quad (5.68f)$$

Wall Boundary Conditions:  $m = 0, 1 \leq n \leq N, l > L_1$

At the wall, the discrete boundary conditions for the disturbed flow follow from Equations (5.28)

for  $k = 0$ :

$$U_{0,n,0}^l = 0 \quad (5.69a)$$

$$V_{0,n,0}^l = V_{w0}(x_n, t_l) \quad (5.69b)$$

$$W_{0,n,0}^l = 0 \quad (5.69c)$$

$$\Omega_{x0,n,0}^l = 0 \quad (5.69d)$$

$$\Omega_{y0,n,0}^l = 0 \quad (5.69e)$$

$$\frac{\partial \Omega_z}{\partial x} \Big|_{0,n,0}^l = -\frac{1}{Re} \nabla_0^2 V \Big|_{0,n,0}^l \quad (5.69f)$$

$$\Theta_{0,n,0}^l = A(x_n) x_n^2 + \Theta_{w0}(x_n, t_l), \quad (5.69g)$$

and for  $k > 0$ :

$$U_{k,n,0}^l = 0 \quad (5.69h)$$

$$V_{k,n,0}^l = V_{w_k}(x_n, t_l) \quad (5.69i)$$

$$W_{k,n,0}^l = 0 \quad (5.69j)$$

$$\left. \frac{\partial^2 \Omega_x}{\partial x^2} \right|_{k,n,0}^l - \gamma^2 k^2 \Omega_{x_{k,n,0}}^l = - \left. \frac{\partial^2 \Omega_y}{\partial x \partial y} \right|_{k,n,0}^l \frac{\gamma k}{Re} \nabla_k^2 V|_{k,n,0}^l \quad (5.69k)$$

$$\Omega_{y_{k,n,0}}^l = 0 \quad (5.69l)$$

$$\left. \frac{\partial \Omega_x}{\partial x} \right|_{k,n,0}^l = -\gamma k \Omega_{x_{k,n,0}}^l - \frac{1}{Re} \nabla_k^2 V|_{k,n,0}^l \quad (5.69m)$$

$$\Theta_{k,n,0}^l = \Theta_{w_k}(x_n, t_l) \quad (5.69n)$$

The boundary conditions (5.69f), (5.69k), and (5.69m) for the streamwise and spanwise wall vorticity are discretized as follows

for  $1 < n < N$ :

$$\left. \frac{\partial^2 \Omega_x}{\partial x^2} \right|_{k,n,0}^l = \frac{1}{\Delta x^2} \left( \Omega_{x_{k,n+1,0}}^l - 2 \Omega_{x_{k,n,0}}^l + \Omega_{x_{k,n-1,0}}^l \right) + O(\Delta x^2) \quad (5.70a)$$

$$\left. \frac{\partial^2 \Omega_y}{\partial x \partial y} \right|_{k,n,0}^l = \frac{1}{2 \Delta x} \left( \left. \frac{\partial \Omega_y}{\partial y} \right|_{k,n+1,0}^l - \left. \frac{\partial \Omega_y}{\partial y} \right|_{k,n-1,0}^l \right) + O(\Delta x^2). \quad (5.70b)$$

At the grid point ' $n = N_B$ ', the outflow boundary conditions (5.61d) and (5.61k) are introduced:

$$\left. \frac{\partial^2 \Omega_x}{\partial x^2} \right|_{k,N_B,0}^l = -\alpha_{r_N}^2 \Omega_{x_{k,N_B,0}}^l \quad (5.71a)$$

$$\left. \frac{\partial^2 \Omega_y}{\partial x \partial y} \right|_{k,N_B,0}^l = \frac{1}{\Delta x} \left( 1 - \frac{\alpha_{r_N}^2 \Delta x^2}{2} \right) \left( \left. \frac{\partial \Omega_y}{\partial y} \right|_{k,N_B,1}^l - \left. \frac{\partial \Omega_y}{\partial y} \right|_{k,N_B-1,1}^l \right) + O(\Delta x^2). \quad (5.71b)$$

The derivative  $\left. \frac{\partial \Omega_y}{\partial y} \right|_{k,n,0}^l$  is discretized using a one-sided forward difference:

$$\left. \frac{\partial \Omega_y}{\partial y} \right|_{k,n,0}^l = \frac{1}{2 \Delta y} \left( -3 \Omega_{y_{k,n,0}}^l + 4 \Omega_{y_{k,n,1}}^l - \Omega_{y_{k,n,2}}^l \right) + O(\Delta y^2). \quad (5.72)$$

For the discrete form of  $\nabla_k^2 V_{k,n,0}^l$ , the following difference formula is used for  $k = 0$  and  $k = 1$ :

$$\begin{aligned} \nabla_k^2 V_{k,n,0}^l &= \frac{\partial^2}{\partial x^2} (V_{w_k}(x_n, t_l)) \\ &+ \frac{1}{2\Delta y^2} (-7 V_{k,n,0}^l + 8 V_{k,n,1}^l - V_{k,n,2}^l) - \frac{\gamma^2 k^2}{Re} V_{k,n,0}^l \end{aligned} \quad (5.73a)$$

and for  $k > 1$ :

$$\nabla_k^2 V_{k,n,0}^l = \frac{1}{2\Delta y^2} (-7 V_{k,n,0}^l + 8 V_{k,n,1}^l - V_{k,n,2}^l) \quad (5.73b)$$

In the above two equations, the same one-sided difference formula for  $\left. \frac{\partial^2 V}{\partial y^2} \right|_{k,n,0}^l$  that was used for the undisturbed flow (Equation (6.55)) is employed here. For  $k > 1$ , the wall  $V_k$  velocity is zero, i.e.,

$$V_{k,n,0}^l = 0 \quad \text{for } k > 1.$$

The analytical derivative of the function  $\hat{f}_{V_k}$  is used in the above equation for the  $x$  derivative  $\left. \frac{\partial^2 V}{\partial x^2} \right|_{k,n,0}^l$ . The term  $\left. \frac{\partial \Omega_z}{\partial x} \right|_{k,n,0}^l$  is discretized as in Equation (5.54) for the undisturbed flow. Therefore, with the help of Equations (5.68) through (5.73), the wall boundary conditions for the spanwise and streamwise vorticities are

for  $k = 0$ :

$$\Omega_{x_0,n,0}^l = 0 \quad (5.74a)$$

for  $n = 1$ :

$$\begin{aligned} \Omega_{x_0,1,0}^{l,i} &= \Omega_{x_0,0,0}^l - \Delta x \left[ \frac{1}{Re} \frac{\partial^2}{\partial x^2} (V_{w_0}(x_1, t_l)) \right. \\ &\quad \left. + \frac{1}{2\Delta y^2} (-7 V_{0,1,0}^{l,i} + 8 V_{0,1,1}^{l,i} - V_{0,1,2}^{l,i}) \right] \end{aligned} \quad (5.74b)$$

and for  $2 \leq n \leq N$ :



$$\Omega_{x_0,n,0}^{l,i} = \frac{4}{3}\Omega_{x_0,n-1,0}^{l,i} - \frac{1}{3}\Omega_{x_0,n-2,0}^{l,i} - \frac{2\Delta x}{3} \left[ \frac{1}{Re} \frac{\partial^2}{\partial x^2} (V_{w_0}(x_n, t_l)) + \frac{1}{2\Delta y^2} (+8V_{0,n,1}^{l,i} - V_{0,n,2}^{l,i}) \right], \quad (5.74c)$$

for  $k = 1$ :

for  $1 \leq n \leq N-1$ :

$$\begin{aligned} & -\Omega_{x_1,n+1,0}^{l,i} + (2 + \gamma^2 \Delta x^2) \Omega_{x_1,n,0}^{l,i} - \Omega_{x_1,n-1,0}^{l,i} = \\ & -\frac{\Delta x}{4\Delta y} (4\Omega_{y_1,n+1,1}^{l,i} - \Omega_{y_1,n+1,2}^{l,i} - 4\Omega_{y_1,n-1,1}^{l,i} + \Omega_{y_1,n-1,2}^{l,i}) \\ & -\gamma \Delta x^2 \left[ \frac{1}{Re} \frac{\partial^2}{\partial x^2} (V_{w_1}(x_n, t_l)) + \frac{1}{2\Delta y^2} (7V_{1,n,0}^{l,i} - 8V_{1,n,1}^{l,i} + V_{1,n,2}^{l,i}) - \frac{\gamma^2}{Re} V_{1,n,0}^{l,i} \right], \end{aligned} \quad (5.74d)$$

and for  $n = N$ :

$$\begin{aligned} \Omega_{x_1,N,0}^{l,i} = & -\frac{1}{\alpha_{rN}^2 + \gamma^2} \left[ \frac{1}{Re} \frac{\partial^2}{\partial x^2} (V_{w_1}(x_{NB}, t_l)) + \frac{\gamma}{2\Delta y^2} (-7V_{1,NB,0}^{l,i} - 8V_{1,NB,1}^{l,i} + V_{1,NB,2}^{l,i}) + \frac{\gamma^2}{Re} V_{1,NB,0}^{l,i} \right] \\ & + \frac{1}{\Delta x} \left[ \left( 1 - \frac{\alpha_{rN}^2 \Delta x^2}{2} \right) (4\Omega_{y_1,NB,1}^{l,i} - \Omega_{y_1,NB,2}^{l,i} - 4\Omega_{y_1,NB-1,1}^{l,i} + \Omega_{y_1,NB-1,2}^{l,i}) \right], \end{aligned} \quad (5.74e)$$

for  $n = 1$ :

$$\begin{aligned} \Omega_{x_1,1,0}^{l,i} = & \Omega_{x_1,0,0}^{l,i} - \Delta x \left[ \frac{1}{Re} \frac{\partial^2}{\partial x^2} (V_{w_1}(x_1, t_l)) + \frac{1}{2\Delta y^2} (-7V_{1,1,0}^{l,i} + 8V_{1,1,1}^{l,i} - V_{1,1,2}^{l,i}) - \frac{\gamma^2}{Re} V_{1,1,0}^{l,i} + \gamma \Omega_{x_1,1,0}^{l,i} \right] \end{aligned} \quad (5.74f)$$

and for  $2 \leq n \leq N$ :

$$\begin{aligned}\Omega_{z_{1,n},0}^{l,i} = & \frac{4}{3}\Omega_{z_{1,n-1},0}^{l,i} - \frac{1}{3}\Omega_{z_{1,n-2},0}^{l,i} - \frac{2\Delta x}{3}\left[\frac{1}{Re}\frac{\partial^2}{\partial x^2}(V_{w_1}(x_n, t_l))\right. \\ & + \frac{1}{2\Delta y^2}\left(+8V_{1,n,1}^{l,i} - V_{1,n,2}^{l,i}\right) \\ & \left. - \frac{\gamma^2}{Re}V_{1,N_B,0}^i + \gamma\Omega_{z_{1,N_B},0}^{l,i}\right],\end{aligned}\quad (5.74g)$$

for  $k > 1$ :

for  $1 \leq n \leq N-1$ :

$$\begin{aligned}-\Omega_{z_{k,n+1},0}^{l,i} + (2 + \gamma^2 k^2 \Delta x^2)\Omega_{z_{k,n},0}^{l,i} - \Omega_{z_{k,n-1},0}^{l,i} = \\ -\frac{\Delta x}{4\Delta y}\left(4\Omega_{y_{k,n+1},0}^{l,i} - \Omega_{y_{k,n+1},2}^{l,i} - 4\Omega_{y_{k,n-1},1}^{l,i} + \Omega_{y_{k,n-1},2}^{l,i}\right) \\ - \gamma k \Delta x^2\left[\frac{1}{2\Delta y^2}\left(7V_{k,n,0}^i - 8V_{k,n,1}^{l,i} + V_{k,n,2}^{l,i}\right) - \frac{\gamma^2 k^2}{Re}V_{k,n,0}^i\right],\end{aligned}\quad (5.74h)$$

and for  $n = N$ :

$$\begin{aligned}\Omega_{z_{k,N},0}^{l,i} = & -\frac{1}{\alpha_{r_N}^2 + \gamma^2 k^2}\left[\frac{\gamma k}{2\Delta y^2}\left(-8V_{k,N_B,1}^{l,i} + V_{k,N_B,2}^{l,i}\right)\right] \\ & + \frac{1}{\Delta x}\left[\left(1 - \frac{\alpha_{r_N}^2 \Delta x^2}{2}\right)\left(4\Omega_{y_{k,N_B},1}^{l,i} - \Omega_{y_{k,N_B},2}^{l,i}\right.\right. \\ & \left.\left. - 4\Omega_{y_{k,N_B-1},1}^{l,i} + \Omega_{y_{k,N_B-1},2}^{l,i}\right)\right],\end{aligned}\quad (5.74i)$$

for  $n = 1$ :

$$\begin{aligned}\Omega_{z_{k,1},0}^{l,i} = & \Omega_{z_{k,0},0}^i - \Delta x\left[\frac{1}{2\Delta y^2}\left(-7V_{k,1,0}^{l,i} + 8V_{k,1,1}^{l,i} - V_{k,1,2}^{l,i}\right)i\right. \\ & \left. - \frac{\gamma^2 k^2}{Re}V_{k,1,0}^i + \gamma k \Omega_{z_{k,1},0}^{l,i}\right],\end{aligned}\quad (5.74j)$$

and for  $2 \leq n \leq N$ :

$$\begin{aligned}\Omega_{z_{k,n},0}^{l,i} = & \frac{4}{3}\Omega_{z_{k,n-1},0}^{l,i} - \frac{1}{3}\Omega_{z_{k,n-2},0}^{l,i} - \frac{2\Delta x}{3}\left[-\frac{1}{2\Delta y^2}\left(+8V_{k,n,1}^{l,i} - V_{k,n,2}^{l,i}\right)\right. \\ & \left. - \frac{\gamma^2 k^2}{Re}V_{k,N_B,0}^i + \gamma k \Omega_{z_{k,N_B},0}^{l,i}\right].\end{aligned}\quad (5.74k)$$

Corner Point Boundary Conditions:  $n = N, m = M, l > L_1$

The upper right hand corner point of the integration domain requires special treatment for the three velocity components. At this grid point, the outflow boundary conditions (5.61) together with the  $U$ ,  $V$ , and  $W$  Poisson equations (5.38d, 5.38e, and 5.38f) are applied. The boundary conditions are then for  $k = 0$ :

$$U_{0,N_B,M}^{l,i} = u_{ST_{N_B,M}} - \frac{1}{\Delta x \alpha_{r_N}^2} \frac{\alpha_{r_M}}{\sqrt{Re}} \left[ \left( 1 - \frac{\alpha_{r_N}^2 \Delta x^2}{2} \right) \left( V_{0,N_B,M}^{l,i} - v_{ST_{N_B,M}} \right) - \left( V_{0,N_B-1,M}^{l,i} - v_{ST_{N_B-1,M}} \right) \right] \quad (5.75a)$$

$$\left( 1 + \frac{\alpha_{r_N}^2 \Delta y^2}{2 Re} + \Delta y \frac{\alpha_{r_M}}{\sqrt{Re}} \right) V_{0,N_B,M}^{l,i} - V_{0,N_B,M-1}^{l,i} = \left( \Delta y \frac{\alpha_{r_M}}{\sqrt{Re}} + \frac{\alpha_{r_N}^2 \Delta y^2}{2 Re} \right) v_{ST_{N_B,M}} \quad (5.75b)$$

$$W_{0,N_B,M}^l = 0 \quad (5.75c)$$

$$\Omega_{x0,N_B,M}^l = 0 \quad (5.75d)$$

$$\Omega_{y0,N_B,M}^l = 0 \quad (5.75e)$$

$$\Omega_{x0,N_B,M}^l = 0 \quad (5.75f)$$

$$\Theta_{0,N_B,M}^l = 0 \quad (5.75g)$$

and for  $k > 0$ :

$$U_{k,N_B,M}^{l,i} = - \frac{1}{\Delta x (\alpha_{r_N}^2 + \gamma^2 k^2)} \sqrt{\frac{\alpha_{r_M}^2 + \gamma^2 k^2}{Re}} \left[ \left( 1 - \frac{\alpha_{r_N}^2 \Delta x^2}{2} \right) V_{k,N_B,M}^{l,i} - V_{k,N_B-1,M}^{l,i} \right] \quad (5.75h)$$

$$\left( 1 + \frac{\alpha_{r_N}^2 \Delta y^2 + \gamma^2 k^2}{2 Re} + \Delta y \sqrt{\frac{\alpha_{r_M}^2 + \gamma^2 k^2}{Re}} \right) V_{k,N_B,M}^{l,i} = V_{k,N_B,M-1}^{l,i} \quad (5.75i)$$

$$W_{k,N_B,M}^{l,i} = -\frac{\gamma k}{\alpha_{r_N}^2 + \gamma^2 k^2} \sqrt{\frac{\alpha_{r_M}^2 + \gamma^2 k^2}{Re}} V_{k,N_B,M}^{l,i} \quad (5.75j)$$

$$\Omega_{x_h,N_B,M}^l = 0 \quad (5.75k)$$

$$\Omega_{y_h,N_B,M}^l = 0 \quad (5.75l)$$

$$\Omega_{z_h,N_B,M}^l = 0 \quad (5.75m)$$

$$\Theta_{h,N_B,M}^l = 0 \quad (5.75n)$$

This completes the discretization of the governing equations and boundary conditions in Fourier space. In the next section, a description of the solution procedure for these equations is given.

#### 5.3.4 Solution of the Tridiagonal Systems

In presenting the discretized equations and boundary conditions, the iteration index 'i' was introduced. This iteration index is dependent on the solution procedure, i.e., the line iteration first sweeps in the  $x$  direction and then in the  $y$  direction. In addition, the order in which each equation system is solved also determines whether the terms are computed at the current iteration level or the previous iteration level.

The tridiagonal reduction scheme is an adaptation of Gaussian elimination and is commonly known as the Thomas algorithm (1949). This Thomas algorithm is modified so that the tridiagonal system for the  $\Omega_{x_h}$  and  $V_h$  equations are coupled together through the  $\Omega_{x_h}$  wall boundary condition. The coupling of these two equations speeds the overall convergence of the method. The specifics of this tridiagonal reduction scheme can be found in Fasel (1974).

The first step in the numerical procedure is the calculation of the undisturbed flow field using the boundary conditions presented in Section 5.3.2. After the steady state solution is found, the boundary conditions are changed to those

described in Section 5.3.3 and the disturbed flow is then calculated. The iteration begins first with the calculation of the 0th mode equations and then proceeds to the 1st mode equations. The procedure continues for all  $\frac{K}{2} + 1$  modes. For the 0th mode, only four equations need to be solved since the 0th mode is two-dimensional ( $W_0 = \Omega_{x_0} = \Omega_{y_0} = 0$ ). For the other Fourier mode equations, seven equations must be solved. In addition, the viscosity for each mode must be calculated.

The line iteration in the  $x$  direction begins with the solution of the streamwise and normal vorticity. The streamwise vorticity at the wall requires special consideration. The boundary condition (5.74) for  $\Omega_{x_{k,n},0}^{l,i}$  forms a tridiagonal system in  $x$  instead of the  $y$  direction that is necessary for the  $x$  sweep. Therefore, the streamwise wall vorticity is calculated during the  $y$  sweep and the values of the streamwise vorticity at the wall needed in the  $x$  line iteration are taken at the previous iteration level. After the  $\Omega_{x_k}$  and  $\Omega_{y_k}$  equations have been reduced, the  $V_k$  velocity and spanwise vorticity equations are solved. As already mentioned, these two equations are coupled through the wall boundary condition for the spanwise vorticity and are solved for using a modified tridiagonal solver. Finally, during the line iteration in the  $x$  direction, the temperature field is calculated. The  $U_k$  velocity and  $W_k$  velocity equations are solved next with the line iteration now proceeding in the  $y$  direction. Finally, the wall streamwise vorticity is reduced.

Once all mode equations have been solved, the solution is checked for convergence. The following convergence criteria is used:

$$\left| \Omega_{x_{k,n},0}^{l,i} - \Omega_{x_{k,n},0}^{l,i-1} \right| < \epsilon \quad (5.76)$$

for

$$k = \left( 0, 1, \dots, \frac{K}{2} \right), \quad n = (0, 1, 2, \dots, N)$$

where  $\epsilon$  is an input parameter. The difference of the spanwise vorticity between successive iterations was chosen after a convergence study of the other flow variables was made. The absolute difference between successive iterations was checked over the entire domain for each variable. It was found that the spanwise vorticity at the wall had the slowest rate of convergence. In view of the storage requirements and calculation costs, only the wall spanwise vorticity is monitored. Convergence criterion are generally based on the residual of the difference equations. However, due to the implicit nature of the numerical procedure, the residual is not easily available and requires several calculations to obtain. The residual was monitored in a two-dimensional simulation, and found to possess the same convergence behavior as the absolute error. In addition, the residual of the spanwise vorticity at the wall converged slowest.

The convergence rate of the method is increased through the following two additions to the algorithm. First, it was found that underrelaxing the wall spanwise vorticity significantly increases the convergence rate. Thus, after  $\Omega_{z_{h,n},0}^{l,i}$  is calculated from the coupled tridiagonal reduction scheme, it is underrelaxed with the following formula:

$$\Omega_{z_{h,n},0}^{l,i} = \omega_r \Omega_{z_{h,n},0}^{*,l,i} + (1 - \omega_r) \Omega_{z_{h,n},0}^{l,i-1} \quad (5.77)$$

where  $\omega_r$  is the relaxation parameter. A value of  $\omega_r = 0.9$  was found to give the largest improvement in convergence for the numerical simulations in this work.

In addition to underrelaxing the wall spanwise vorticity, Richardson extrapolation is used at each new time level to produce a better estimate of the first iteration. The following formula is used:

$$\Phi_{h,n,m}^{l,0} = 3 \Phi_{h,n,m}^{l-1} - 3 \Phi_{h,n,m}^{l-2} + \Phi_{h,n,m}^{l-3} + O(\Delta t^3) \quad (5.78)$$

for

$$k = \left(0, 1, \dots, \frac{K}{2}\right), \quad n = (0, 1, 2, \dots, N), \\ m = (0, 1, 2, \dots, M), \quad \text{and } l = (2, 3, \dots).$$

where  $\Phi$  represents all of the flow variables in Fourier space. The use of this extrapolation also significantly improved the overall convergence rate.

### 5.3.5 Evaluation of the Nonlinear Terms

The nonlinear terms A, B, C, and D in the difference equations must be evaluated at every iteration step, since these terms are treated implicitly. The evaluation of these terms requires several computer operations due to the spectral expansions. For example, the nonlinear term  $u \frac{\partial \omega_z}{\partial x}$  in the  $x$  vorticity transport equation is a quadratic product of two spectral expansions, that is:

$$\left( \sum_{k=-\frac{K}{2}}^{\frac{K}{2}} U_{k,n,m}^{l,i-1} e^{ik\gamma z} \right) \left( \sum_{k=-\frac{K}{2}}^{\frac{K}{2}} \frac{\partial \Omega_x}{\partial x} \Big|_{k,n,m}^{l,i-1} e^{ik\gamma z} \right).$$

Although the above expansion is straightforward to compute, the computational cost is considerable even for relatively small values of  $K$ .

An alternative to the direct computation of each nonlinear term in Fourier space is the pseudospectral method or collocation method developed by Gottlieb and Orszag (1977). The idea is to apply fast Fourier transforms to transform between Fourier space and physical space in an efficient manner. Thus the flow variables are transformed from Fourier space to physical space and then the nonlinear terms are computed in physical space. These nonlinear terms are then transformed back to Fourier space. Although the pseudospectral method appears to involve more work, it is considerably more efficient when  $K$  is moderately large, about  $K = 8$  or greater.

For the numerical simulations reported in this work, however, a value of  $K = 2$  is used. Therefore, the numerical method is presently a purely spectral method without collocation. The maximum number of modes in the nonlinear terms that can be presently evaluated is  $K = 4$ . This choice was made because it was decided that computational limitations would prohibit numerical simulations with more modes.

### 5.3.6 Viscosity Calculation

The viscosity variation with temperature that is used in this work was introduced in Chapter 3 by Equations (3.76). This empirical relationship allows for the calculation of the viscosity for a given temperature. The variable viscosity terms are present in the nonlinear terms B and C. In the nonlinear C terms, the first and second derivatives of viscosity with respect to the spatial dimensions are required. One could use the chain rule of differentiation which leads to the following equations:

$$\frac{\partial \mu}{\partial x} = \frac{\partial \mu}{\partial T} \frac{\partial T}{\partial x} \quad (5.79a)$$

$$\frac{\partial \mu}{\partial y} = \frac{\partial \mu}{\partial T} \frac{\partial T}{\partial y} \quad (5.79b)$$

$$\frac{\partial \mu}{\partial z} = \frac{\partial \mu}{\partial T} \frac{\partial T}{\partial z} \quad (5.79c)$$

$$\frac{\partial^2 \mu}{\partial x^2} = \frac{\partial^2 \mu}{\partial T^2} \left( \frac{\partial T}{\partial x} \right)^2 + \frac{\partial \mu}{\partial T} \frac{\partial^2 T}{\partial x^2} \quad (5.79d)$$

$$\frac{\partial^2 \mu}{\partial y^2} = \frac{\partial^2 \mu}{\partial T^2} \left( \frac{\partial T}{\partial y} \right)^2 + \frac{\partial \mu}{\partial T} \frac{\partial^2 T}{\partial y^2} \quad (5.79e)$$

$$\frac{\partial^2 \mu}{\partial z^2} = \frac{\partial^2 \mu}{\partial T^2} \left( \frac{\partial T}{\partial z} \right)^2 + \frac{\partial \mu}{\partial T} \frac{\partial^2 T}{\partial z^2} \quad (5.79f)$$

$$\frac{\partial^2 \mu}{\partial x \partial y} = \frac{\partial^2 \mu}{\partial T^2} \frac{\partial T}{\partial x} \frac{\partial T}{\partial y} + \frac{\partial \mu}{\partial T} \frac{\partial^2 T}{\partial x \partial y} \quad (5.79g)$$

$$\frac{\partial^2 \mu}{\partial x \partial z} = \frac{\partial^2 \mu}{\partial T^2} \frac{\partial T}{\partial x} \frac{\partial T}{\partial z} + \frac{\partial \mu}{\partial T} \frac{\partial^2 T}{\partial x \partial z} \quad (5.79h)$$



$$\frac{\partial^2 \mu}{\partial y \partial z} = \frac{\partial^2 \mu}{\partial T^2} \frac{\partial T}{\partial y} \frac{\partial T}{\partial z} + \frac{\partial \mu}{\partial T} \frac{\partial^2 T}{\partial y \partial z}. \quad (5.79i)$$

Therefore, only the spatial derivatives of the temperature are needed and the first and second derivatives  $\frac{\partial \mu}{\partial T}$  and  $\frac{\partial^2 \mu}{\partial T^2}$  could be easily calculated by differentiating Equations (3.76) with respect to temperature. However, this procedure would create some cubic nonlinearities and would be more computationally involved. On this basis, it was decided to differentiate the viscosity directly without the above chain rule employed. This choice does not necessitate the storage of another large array. Only three grid lines ( $N - 1$ ,  $N$ , and  $N + 1$ ) are necessary to hold the viscosity information. This is due to the line iteration procedure.

The empirical relationship (5.76) combined with the spanwise spectral ansatz presents a problem for the direct calculation of the viscosity in Fourier space. This is due to the nonlinear nature of Equations (5.76). To calculate the viscosity modes, the following procedure was developed to avoid this difficulty. First the temperature is transformed from Fourier space to physical space where the viscosity can be easily computed. After the viscosity is computed in physical space, it is transformed back to Fourier space. The following three steps are required:

$$\text{Step 1.)} \quad \Theta_{k,n,m}^{l,i} \xrightarrow{\text{inverse transform}} T(x, y, z_k, t) \quad (5.80a)$$

$$\text{Step 2.)} \quad T(x, y, z_k, t) \xrightarrow{\text{Equations (3.76)}} \mu(x, y, z_k, t) \quad (5.80b)$$

$$\text{Step 3.)} \quad \mu_{k,n,m}^{l,i} \xrightarrow{\text{forward transform}} \mathcal{M}_{k,n,m}^{l,i} \quad (5.80c)$$

In this procedure, collocation points are required and the method is analogous to the collocation procedure of Gottlieb and Orszag (1977). A fast Fourier transform could be used in Equations (5.80a) and (5.80c), but since the method is programmed for  $K = 4$  only, this calculation is programmed directly. The calculation of  $\mathcal{M}_{k,n,m}^{l,i}$  is programmed for a maximum number of 4 modes.

One further note on the calculation of the spatial derivatives of the viscosity is made. In the interior of the domain, standard second order central difference approximations are used. At the outflow boundary, the same boundary conditions applied to the temperature are used for the viscosity, i.e., for the undisturbed flow:

$$\frac{\partial^2 \mathcal{M}_0}{\partial x^2}(x_N, y, t) = 0 \quad (5.81a)$$

and for the disturbed flow

$$\frac{\partial^2 \mathcal{M}_k}{\partial x^2}(x_{N_B}, y, t) = -\alpha_{r_N}^2 \mathcal{M}_k(x_{N_B}, y, t). \quad (5.81b)$$

#### 5.4 Consistency, Stability, and Convergence

The conditions that must be satisfied for a solution of the finite difference equations to be a reasonably accurate approximation to the governing equations is discussed here. One concern is the convergence of the approximating difference equations to the exact mathematical solution as the spatial and temporal mesh is refined. A second concern is unbounded growth of any errors associated with the solution of the finite difference equations.

Lax's equivalence theorem (Smith (1978)) states that if a linear finite difference equation is consistent with a well posed linear initial value problem, stability is a necessary and sufficient condition for convergence. Mathematical proofs of stability and convergence for nonlinear problems such as the one posed here have not been accomplished. Although Lax's equivalence theorem does not apply directly to the nonlinear problem under investigation, this theorem often provides a good indication of the convergence of the numerical method.

The difference equations are consistent with the partial differential equations if the local truncation error approaches zero as the spatial and temporal step

sizes approach zero. The time discretization employed is second order accurate. Within the spatial computational domain, central difference approximations have been used that have second order spatial accuracy for all equations. Also, at the boundaries care has been taken to preserve second order spatial accuracy. However, the wall boundary condition for the spanwise vorticity at ' $n = 1$ ' (or the inflow boundary) is only first order accurate in  $z$ . The gradients in the  $z$  direction at this location are small and the first order discretization at this one grid point should not reduce the overall second order accuracy of the method. Thus it follows that

$$(5.11c - 5.11i) = (5.36a - 5.36g) + O(\Delta x^2, \Delta y^2, \Delta z^2). \quad (5.82)$$

By consideration of Equations (5.5), the finite Fourier series (5.11c-5.11i) converges to the governing equations presented in Chapter 3 as  $K \rightarrow \infty$  (or  $\Delta z \rightarrow 0$ ). Therefore, the numerical method presented in this chapter is consistent to second order in time and in the streamwise and normal directions with spectral accuracy in the spanwise direction.

A complete analysis of the stability of the finite difference system presented in Section 5.3 is an enormous task. The usual von Neumann method expresses the error terms in a Fourier series and then considers the growth of these terms. Nonlinear difference equations must first be linearized and the stability analysis is then applied. This leads to a necessary condition for stability. In the matrix method of stability analysis, boundary conditions are taken into account and a sufficient condition is generally found. However, the matrix method applied to nonlinear equations is inconsistent due to the necessary linearization procedure which then leads to a necessary condition only. Thus the von Neumann method of stability analysis should be applied to nonlinear partial differential equations.

However, the boundary conditions, including the time varying wall boundary conditions, would not be included in this analysis. Due to the enormous complexity of such a stability analysis for the discretized equations in this work, a complete analysis of stability is not feasible. Fortunately, implicit methods are generally much more stable than explicit methods, and for the simulation runs presented in this work, numerical stability was not a problem.

## CHAPTER 6

## RESULTS

The large number of flow parameters and the magnitude of the numerical computation of the Navier-Stokes and energy equations prohibits an exhaustive search of the parameter space. The parameters used in the numerical simulations are chosen so that comparison can be made with existing experimental or analytical results, when available. The numerical method presented in Chapter 5 is first tested extensively with calculations of two- and three-dimensional waves with very small amplitudes. The control of these linear amplitude waves is examined with either passive or active heating applied. Detailed comparison with theory and experiments is made to provide a thorough check of the numerical method. After the control of linear amplitudes is discussed, the influence of heating on the nonlinear secondary instability process is presented. Numerical simulations of active or passive control applied to the early nonlinear stages are shown. These simulations model the laboratory experiments of Klebanoff, Tidstrom, and Sargent (1962) for the fundamental breakdown and the laboratory experiments of Kachanov and Levchenko (1984) for the subharmonic breakdown. The effect of control on these two breakdown processes is investigated.

6.1 Passive Control of Linear Disturbances

The parameters chosen for the simulation of passive control of linear disturbances closely model the experiments of Strazisar, Reshotko, and Prah1 (1977) and Strazisar and Reshotko (1978). Although only control of two-dimensional waves was considered in these experiments, the control of three-dimensional oblique

waves in addition to the two-dimensional Tollmien-Schlichting wave is also investigated.

In the physical experiments, the fluid is water and this fluid is used for all the control investigations reported here. The freestream temperature  $\bar{T}_\infty$  in the experimental investigations is  $75^\circ F$  (or  $23.89^\circ C$ ). For water at this temperature, the dynamic viscosity  $\bar{\mu}_\infty$  is  $9.135 \times 10^{-4} \text{ kg/m}\cdot\text{s}$  and the Prandtl number  $Pr$  is 6.3. A Reynolds number  $Re$  of  $1 \times 10^5$  is used with a freestream velocity  $\bar{U}_\infty$  of  $3 \text{ m/s}$  and a reference length  $\bar{L}$  of  $0.0353 \text{ m}$ . In the experimental investigations, a wide range of forcing frequencies was considered, but it would be too computationally intensive to perform simulations with many frequencies and different levels of passive control. Therefore, in this work, control at two different frequencies ( $F = 1$  and  $F = 1.55$ ) is investigated. The frequency  $F = 1.55$  is chosen so that the influence of nonparallel effects can be examined. Strazisar, Reshotko, and Pahl (1977) found that nonparallel effects had a significant effect on the heated boundary layer. For each of these frequencies, the following parameters are used for  $F = 1$  ( $\beta = 10$ ):

$$Re_{\delta_i}(\text{at } x_0) = 500$$

$$\alpha_{r_M} = 28.8$$

$$\alpha_{r_N} = 27.8$$

$$\gamma = 20$$

$$K = 2$$

$$\Delta x = 7.4800 \times 10^{-3}$$

$$\Delta y = 3.1623 \times 10^{-1}$$

$$\Delta t = 1.0472 \times 10^{-2}$$

and for  $F = 1.55$  ( $\beta = 15.5$ ):

$$Re_{\delta_1}(\text{at } x_0) = 475$$

$$\alpha_{r_M} = 41.3$$

$$\alpha_{r_N} = 40.3$$

$$\gamma = 20$$

$$K = 2$$

$$\Delta x = 5.1083 \times 10^{-3}$$

$$\Delta y = 3.0042 \times 10^{-1}$$

$$\Delta t = 6.7561 \times 10^{-3}.$$

The same spanwise wavenumber  $\gamma$  is chosen for both frequencies. For  $F = 1$ , the oblique waves are about  $35^\circ$  with respect to the  $x$  axis and for  $F = 1.55$ , the oblique angle is approximately  $26^\circ$  with respect to the  $x$  axis. The step size in the streamwise direction  $\Delta x$  is chosen so that there are approximately 30 grid points per disturbance wavelength. The normal step size  $\Delta y$  is determined so that the  $y$  direction spans ten boundary layer displacement thicknesses at the inflow boundary and approximately five boundary layer displacement thicknesses at the outflow boundary. The grid has 51 nodal points in the normal direction and 481 points in the streamwise direction. Therefore, the solution domain contains approximately 16 disturbance wavelengths. The outflow boundary is initially positioned about six wavelengths downstream ( $x_{B_1} = 180$ ) of the inflow boundary and is propagated at a speed  $V_B = 0.6$ . The time increment  $\Delta t$  is chosen so that there are 60 time steps per period. The computations proceed for nine disturbance periods for the frequency  $F = 1$  and 11 disturbance periods for  $F = 1.55$ . The convergence criteria used for all investigations is  $\epsilon = 1 \times 10^{-6}$ . The extent of the

computational domain in relation to linear stability theory is shown in Figure 6.1 for both frequencies. The stability diagram in Figure 6.1a is from the experimental work of Strazisar, Reshotko, and Prahl (1977) and the stability diagram of Figure 6.1b is from the linear stability theory of Lowell (1974). The stabilizing influence of uniform passive heating can be observed in both stability diagrams where different levels of wall heating have been imposed. However, differences do exist between the two diagrams and these differences are discussed in conjunction with the numerical simulations of uniform passive control presented in this work.

For the passive control simulations of linear disturbances, the perturbations are input with periodic heating at the wall. The wall boundary conditions follow from Equations (5.30) and (5.69):

for the undisturbed flow:

$$\Theta_{0,n,0}^i = A_0 x_n^p + \sin^2(\xi_n) \quad (6.1a)$$

and for the disturbed flow:

$$\Theta_{0,n,0}^i = A_0 x_n^p + \sin^2(\xi_n) [1 + r(t)\epsilon_{\Theta_0} \sin(\beta t_i)] \quad (6.1b)$$

$$\Theta_{1,n,0}^i = r(t)\epsilon_{\Theta_1} \sin^2(\xi_n) \sin(\beta t_i) \quad (6.1c)$$

where

$$\xi_n = \frac{x_n - x_{HB_1}}{x_{HE_1} - x_{HB_1}} \pi$$

and

$$x_{HB_1} \leq x_n \leq x_{HE_1}.$$

The heater strip is located one disturbance wavelength downstream of the left boundary ( $x_{HB_1} = 30$  and  $x_{HE_1} = 45$ ) and covers about one half of a Tollmien-Schlichting wavelength. The location of the heater strip is shown in Figure 6.1a. The details of the width and streamwise shape function chosen are discussed in



Section 6.2.1. For the ramp function  $r(t)$ , the ramp parameters  $R_A = 0.1$  and  $T_r = 1/2$  disturbance period are used. These ramp parameters remain the same throughout all control investigations. The disturbance amplitudes  $\epsilon_{\theta_0}$  and  $\epsilon_{\theta_1}$  are chosen so that the temperature perturbations create linear disturbance velocities of approximately 0.05% of the maximum of the  $U$  disturbance velocity for both  $U_0$  and  $U_1$ . Also they are chosen so that the temperature input from the heater strip represents heating only and no cooling. This is seen by the addition of the steady state component  $\sin^2(\xi_n)$  to the oscillating component  $r(t)\epsilon_{\theta_0} \sin^2(\xi_n) \sin(\beta t_l)$  in Equation (6.1b). The temperature perturbation amplitudes are  $\epsilon_{\theta_0} = 2/3$  and  $\epsilon_{\theta_1} = 2/3$ . This amplitude input represents a temperature input of  $2^\circ C$  above the freestream temperature for the oscillatory component with the temperature nondimensionalized by  $3^\circ C$ . The steady state component over the heater strip thus has a  $3^\circ C$  increase above the freestream temperature.

The empirical relationship used for the viscosity variation with temperature was given in Chapter 3 by Equation (3.76). The viscosity as a function of temperature is plotted in Figure 6.2 and shows the decrease in the viscosity of water with increasing temperature. In Figures 6.3 and 6.4, the first and second derivatives of the empirical function are shown. The first derivative is negative and the second derivative is positive.

#### 6.1.1 Uncontrolled Linear Disturbances

Before presenting the results of the passive control simulations, the calculation of linear disturbance waves without control applied is shown first. The uncontrolled flow simulations form a basis for comparison with the controlled flow simulations. In addition, comparison with linear stability theory and divergence checks on the numerical solution are made, providing verification of the code.

First, the results for the simulations with the nondimensional frequency  $F = 1$  are presented. The converged undisturbed flow field for this frequency is shown in Figure 6.5. As previously mentioned, a steady state heating component has been added over the heater strip and this steady state component is seen in the temperature field of Figure 6.5d. The temperature gradients are localized around the heat source and die out quickly downstream and away from the wall where the temperature returns to the freestream temperature. The localized effect of the heater strip can also be observed in Figures 6.5b and 6.5c for the normal velocity and spanwise vorticity, but the effect of the heater strip is not observable in Figure 6.5a for the streamwise velocity. The influence of this nonfluctuating heat input is very small even one half a wavelength downstream of the heater strip.

The base flow solution is very close to the Blasius similarity solution although the full Navier-Stokes equations are used. In Figure 6.6, the growth of the boundary layer displacement thickness predicted by the Navier-Stokes and Blasius solutions is compared and the two are almost indistinguishable. In Figure 6.7, a comparison between the Navier-Stokes and Blasius solutions for the skin friction coefficient is made. The skin friction coefficient is defined by

$$c_f = \frac{2}{\bar{\rho}_\infty \bar{U}_\infty^2} \bar{\tau}_{\bar{y}=0} = \frac{2}{\bar{\rho}_\infty U_\infty^2} \bar{\mu}_{\bar{y}=0} \left( \frac{\partial \bar{u}_{ST}}{\partial \bar{y}} \right)_{\bar{y}=0} \quad (6.2)$$

where  $\bar{\tau}_{\bar{y}=0}$  represents the wall shear stress. Again the two computed solutions are in complete agreement, except at the location of the heater strip which has caused local changes in the streamwise velocity gradient at the wall. This is expected, since the steady state vorticity shows an increase over the heater strip (Figure 6.5c).

The computation conserves mass approximately. Figure 6.8a displays the velocity divergence of the base flow. The largest value of the divergence occurs

over the heater strip at the wall. This is due to the large gradients in the flow that are present in this region. However, when the heater strip is not included in the steady state computation, the velocity divergence is as shown in Figure 6.8b. The largest divergence now occurs at the inflow boundary and is on the order of  $10^{-4}$ . The differences between the Blasius similarity solution that is used at the inflow boundary and the Navier-Stokes solution cause the small divergence at the left boundary. The boundary conditions are effective in conserving mass at the outer boundary and the outflow boundary. The maximum principle (3.75) is satisfied since the largest divergence occurs at the boundaries.

The Fourier modes resulting from the time periodic disturbance input over the heater strip are shown in Figure 6.9 for all flow quantities. Both surface and contour representations of each Fourier mode are shown after nine periods have been computed (time step  $L = 540$ ). The two-dimensional modes ( $k = 0$ ) comprise the two-dimensional Tollmien-Schlichting wave and are shown in Figures 6.9a through 6.9d. The three-dimensional modes ( $k = 1$ ) comprise the three-dimensional oblique waves and are shown in Figures 6.9e through 6.9k. The local influence of the heater strip on the different flow components can be seen, but a detailed discussion of the effect of the heater strip is again delayed until Section 6.2.1. In Figures 6.9d and 6.9k, the two- and three-dimensional temperature fluctuations are shown. The temperature serves only as a perturbation input and the effect remains local to the heater strip. The disturbance waves show a decay at first and then begin to amplify downstream. This behavior is in agreement with the linear stability diagram of Figure 6.1 in which the calculation begins in a damped region and then crosses the neutral curve into a region of amplification. Although the stability diagram is for two-dimensional disturbances, the three-dimensional growth is similar to the two-dimensional growth for this particular oblique angle.

The conservation of mass for the disturbed flow is shown in Figure 6.10 for both Fourier modes 1 and 2 at time step  $L = 540$ . The velocity divergence is largest at the wall and over the heater strip. This is again due to the large gradients present at the wall. The maximum divergence occurs at the boundaries, satisfying the maximum principle. The vorticity divergence is also monitored in Fourier space as a check on the quality of the solution. Figure 6.11 shows mode 1 vorticity divergence at time step  $L = 540$ . Mode 0 vorticity divergence is satisfied trivially. There is again a noticeable spike at the wall over the heater strip due to the large gradients present there. Unlike the velocity equations, the vorticity equations do not satisfy a vorticity divergence maximum principle. The maximum divergence is in the region of maximum shear at the wall.

A verification of the code is that the disturbed flow computations for linear perturbations reproduce closely the Orr-Sommerfeld solution. Amplitude and phase profiles are obtained by a Fourier time series analysis over one period of oscillation from time steps 480 to 540. The Orr-Sommerfeld equation is solved as described in Appendix B for both two-dimensional Tollmien-Schlichting waves and three-dimensional oblique waves. The linear stability theory solution is compared with the Navier-Stokes solution at a displacement thickness Reynolds number  $Re_{\delta_1} = 800$  ( $n = 175$ ). Since the Orr-Sommerfeld solution is an eigenvalue problem, the amplitude is not part of the solution. In order to compare the amplitudes from the Navier-Stokes computation with the linear stability theory solution, a multiplication constant  $c_{LST}$  is found. This constant is determined by normalizing the Navier-Stokes solution with the linear stability theory calculation at the maximum of the  $U_k$  disturbance velocity, or

$$c_{LST} = \frac{U_k}{u_{LST}}. \quad (6.3)$$

All amplitudes are then multiplied by this coefficient. Figure 6.12 displays the exceptional agreement in amplitudes and phases for both mode 0 and mode 1 for each flow component. The temperature modes are not compared since the temperature perturbations have decayed rapidly shortly downstream of the heater strip and the flow field downstream is unheated. Comparison of growth rates and wavenumbers with theory and experiments is made in Section 6.1.2 in conjunction with a comparison for uniform passive control.

The results of the uncontrolled linear disturbances for the frequency  $F = 1.55$  are now presented. For brevity, however, not all flow quantities that were shown for the frequency  $F = 1$  are shown again for this frequency. Instead, only the quantities are shown that illustrate differences between the two frequencies. The Fourier modes are shown in Figure 6.13 for the  $U_k$  velocities. Each Fourier mode is shown after 11 periods have been computed (time step  $L = 660$ ) in both surface and contour representations. The two-dimensional mode ( $k = 0$ ) is shown in Figure 6.13a and the three-dimensional mode ( $k = 1$ ) is shown in Figure 6.13b. Both modes show a slight decay and then growth as the first branch of the neutral curve is crossed. For mode 1, the second branch of the neutral curve is also crossed towards the end of the periodic solution domain which can be seen by the reduction in growth in this region. Again, the two-dimensional growth is as expected from the linear stability theory diagram of Figure 6.1.

Amplitude and phase profiles for frequency  $F = 1.55$  are obtained by a Fourier time series analysis over one disturbance period from time steps 600 to 660. Comparison with the linear stability solution for the  $U_k$  velocities is shown in Figure 6.14 at a displacement thickness Reynolds number  $Re_{\delta_1} = 800$  ( $n = 272$ ). Again the Navier-Stokes solution is normalized by the coefficient  $c_{LST}$  given by Equation (6.3). The agreement is very good for both mode 0 and mode

1. Comparison of the growth rates and wavenumbers with theory is again delayed until the next section.

### 6.1.2 Uniform Passive Control Applied to Linear Disturbances

In the preceding section, the generation of uncontrolled linear two- and three-dimensional disturbances was shown. In this section, this same flow is controlled using a uniform surface temperature distribution. Four cases are shown for each frequency, three with uniform passive heating and one with uniform passive cooling applied at the wall. The three heating cases are chosen so that comparison with experimental and theoretical work can be made. The numerical simulation of a cooled wall is chosen to demonstrate the opposite effect cooling has on the stability characteristics of the flow. The parameter  $p$  in Equation (6.1) is 0 since the surface temperature distribution is constant at the wall. The final parameter in Equation 6.1 to be defined is  $A_0$ . The following four cases are considered:

Table 6.1 Parameters for Uniform Heating Cases for Linear Amplitudes				
$F$	$p$	$\bar{T}_w - \bar{T}_\infty$ ( $^{\circ}F$ )	$\bar{T}_w - \bar{T}_\infty$ ( $^{\circ}C$ )	$A_0$
1.00	0.0	3.0	1.667	1.667/3
1.00	0.0	5.0	2.778	2.778/3
1.00	0.0	8.0	4.444	4.444/3
1.00	0.0	-5.0	-2.778	-2.778/3
1.55	0.0	3.0	1.667	1.667/3
1.55	0.0	5.0	2.778	2.778/3
1.55	0.0	8.0	4.444	4.444/3
1.55	0.0	-5.0	-2.778	-2.778/3

The parameter  $A_0$  has the value of 3 in the denominator due to the nondimensionalization.

The results for  $\Delta\bar{T} = 8^{\circ}F$  are presented in detail for the frequency  $F =$

1 and then compared with the other cases. First the heated undisturbed flow solution is shown in Figure 6.15. The  $u_{ST}$ ,  $v_{ST}$ , and  $\omega_{zST}$  components appear very similar to the unheated base flow. The undisturbed temperature  $T_{ST}$  is shown in Figure 6.15d. The temperature at the wall is constant except over the heater strip location, where the steady state contribution to the heater strip input is seen.

The growth of the boundary layer for each case is shown in Figure 6.16 in which comparison is made with the unheated profile to discern the differences with the heated undisturbed flow. The boundary layer growth is about the same for each case, but the heated profiles show a slightly smaller boundary layer displacement thickness, while the cooled profile shows a slightly larger boundary layer displacement thickness. The skin friction coefficient for the heated and cooled wall is compared with the unheated base flow in Figure 6.17. The skin friction, hence the slope of  $u_{ST}$  at the wall (or  $\frac{\partial u_{ST}}{\partial y}$ ) is larger for the heated wall and smaller for the cooled wall. The heated flow thus has a fuller velocity profile at the wall.

The Fourier modes for the uniformly controlled disturbed flow for  $\Delta \bar{T} = 8^\circ F$  are shown in Figure 6.18 for all flow quantities. Both surface and contour representations of each Fourier mode are shown at time step  $L = 540$ . The same contour levels are chosen as in the uncontrolled flow simulations so that easy comparison can be made. For both the two- and three-dimensional components, the influence of the uniform passive control on the disturbed flow is clearly exhibited. The flow components show a strong damping downstream of the disturbance input. In Figures 6.18d and 6.18k, the two- and three-dimensional temperature fluctuations are also visible downstream of the disturbance input. The temperature perturbations are propagated due to the passive wall heating. The behavior

of the two-dimensional waves is in qualitative agreement with the linear stability diagram of Figure 6.1b for  $\Delta\bar{T} = 8^\circ F$  in which decay is expected for the computational domain investigated.

To illustrate the effects of heating for all four cases, amplitude and phase profiles are shown in Figure 6.19 for all cases as well as the uncontrolled solution. The comparison is made at a displacement thickness Reynolds number  $Re_{\delta_1} = 800$ . With each incremental increase in heating, the amplitude levels are reduced, while the cooled wall case shows an increase in the amplitudes. However, the temperature perturbations show a different picture. In Figures 6.19d and 6.19k, the amplitudes of the temperature perturbations increase with increasing wall heat input and the highest level reached is for the cooled temperature input (which is actually a negative heat input). For the unheated wall, the very low level temperature residual that is created at the heater strip can be seen. The influence of this low amplitude temperature on the flow is negligible. The temperature perturbations increase with increasing heat input due to the increasing temperature gradients at the wall. For all flow variables, the shape of the amplitudes does not significantly change. The phase profiles also do not show significant changes with uniform passive control applied. The location of the phase jumps remains in approximately the same location. The phases for the temperature perturbations do not show a similar trend. The temperature perturbation for the unheated wall is on the same order as the numerical resolution making a smooth phase difficult to compute. In addition, the cooled wall shows a shift of  $\pi$  with the heated wall case due to the opposite sign of the temperature.

For passive control, the amplitudes are reduced. In addition, the growth rates are also affected. The growth of the amplitude downstream is shown in Figure 6.20 for all cases. The amplitudes at the maximum of the  $U_0$  and  $U_1$



velocities are plotted versus the streamwise direction  $x$ . The reduction in growth rate with uniform wall heating can be seen for both the two-dimensional and three-dimensional components. In contrast, the influence of cooling is to increase the growth rates.

The influence of uniform passive control on the growth rates and wavenumbers is shown in Figures 6.21 and 6.22. The growth rate  $\alpha_i$  is calculated from the Navier-Stokes solution by

$$\alpha_{i2D} = -\frac{1}{A_0} \frac{dA_0}{dx} \quad (6.4a)$$

$$\alpha_{i3D} = -\frac{1}{A_1} \frac{dA_1}{dx} \quad (6.4b)$$

where  $A_0$  and  $A_1$  represent the two- and three-dimensional amplitudes, respectively, of the flow variable chosen for analysis. The wavenumber is calculated by

$$\alpha_{r2D} = \frac{d\phi_0}{dx} \quad (6.5a)$$

$$\alpha_{r3D} = \frac{d\phi_1}{dx} \quad (6.5b)$$

where  $\phi_0$  and  $\phi_1$  represent the two- and three-dimensional phases, respectively, for a particular flow variable. Both the amplification rates and wavenumbers are computed at the maximum of the  $U_k$  and the maximum of the  $V_k$  velocities. The growth rates versus the displacement thickness Reynolds number are shown in Figure 6.21 for the four passive control cases as well as the unheated wall. In addition, the growth rates predicted by linear stability theory for an unheated wall are also shown. The two-dimensional growth rates are shown in Figures 6.21a and 6.21b for the  $U_0$  and  $V_0$  velocities. The strong region of amplification near  $Re_{\delta_1} = 600$  occurs just downstream of the heater strip as the temperature perturbations

create the disturbance waves. At the downstream side, the amplification shows a slight jump where the flow is not yet periodic. However, comparison is possible in the central domain. For the unheated wall, the growth rates computed at the maximum of the  $V_0$  velocity agree very well with linear theory. The differences in the growth rates computed from the first maximum of the  $U_0$  velocity are attributed to nonparallel effects. The influence of nonparallel effects is discussed in more detail after comparison with experiments and theory for the heated flow is made. The effect of uniform passive heating is to reduce the growth rates, while uniform wall cooling causes an increase in the growth rates. In Figures 6.21c and 6.21d, the three-dimensional growth rates are shown. Again, the  $V_1$  velocity compares better with linear stability theory for the unheated wall than the  $U_1$  velocity. The three-dimensional growth rates are also reduced with increasing wall heating and are larger when wall cooling is applied.

The wavenumbers are shown in Figure 6.22 based on the maximum  $V_k$  velocity for both the two- and three-dimensional modes. Again, the wavenumbers predicted by linear stability theory for the unheated wall at a frequency  $F = 1$  are shown for comparison. The influence of heating on the wavenumbers is not large. However, with uniform wall heating, the wavenumber is increased for both the two- and three-dimensional components. This slight increase represents a slight decrease in the phase speeds with uniform passive heating applied. The opposite effect is observed for the cooled wall, i.e., the wavenumbers decrease with wall cooling.

Results of uniform passive control at the frequency  $F = 1.55$  are now shown. Again for brevity, only flow quantities are presented that illustrate differences between the two frequencies. The Fourier modes for the uniformly controlled disturbed flow for  $\Delta\bar{T} = 8^\circ F$  are shown in Figure 6.23 for the  $U_k$  velocities. Both

surface and contour plots are shown at time step  $L = 660$ . Again, both the two-dimensional and three-dimensional flow components exhibit a strong damping downstream of the disturbance input. The two-dimensional growth is in qualitative agreement with the linear stability diagram of Figure 6.1b for  $\Delta\bar{T} = 8^\circ F$  in which the flow is in a stable region.

To compare the effects of the different heating levels for  $F = 1.55$ , amplitude and phase profiles are shown in Figure 6.24 for the  $U_k$  velocities. The comparison is made at  $Re_{\delta_1} = 800$  and the uncontrolled solution is shown as well. As seen for the frequency  $F = 1$ , with each increase in heat input, the amplitude levels are reduced, while the cooled case shows an increase in amplitude level. Again, the shape of the amplitude does not significantly change and the location of the phase jumps remains in approximately the same location.

The growth of the amplitude downstream for all cases is shown in Figure 6.25 at  $F = 1.55$ . Again, the amplitudes at the maximum of the  $U_k$  velocities are plotted versus the streamwise direction  $x$ . The reduction in growth is clearly observable with the uniform passive heating applied and the increase in growth with uniform cooling can also be seen.

The influence of uniform heating and cooling on the growth rates and wavenumbers at the frequency  $F = 1.55$  is shown in Figures 6.26 and 6.27. The growth rates are shown in Figure 6.26 for the maximum of the  $U_0$  and  $U_1$  velocities and the maximum of the  $V_0$  and  $V_1$  velocities versus the displacement thickness Reynolds number. The growth rates from linear stability theory for an unheated wall at  $F = 1.55$  are also shown in Figure 6.26. As was seen for the frequency  $F = 1$ , the growth rates for the unheated flow agree better with linear stability theory for the  $V_k$  velocities. The differences with linear stability are attributed again to nonparallel effects. The influence of uniform passive heating is again to

uniformly reduce the growth rates, while cooling increases the growth rates. For this frequency, the influence of heating is to completely stabilize the flow (except for a small region calculated by the  $V_0$  velocity).

The influence of passive heating on the wavenumbers for  $F = 1.55$  is shown in Figure 6.27, where the wavenumbers are computed at the maximum of the  $V_0$  and  $V_1$  velocities. The same trends are seen for this frequency as for  $F = 1$ . The effect of heating is not large, but the wavenumbers increase with heating, while the effect of cooling is to slightly decrease the wavenumbers.

Comparison with theory and experiments is now made for both frequencies with uniform heating applied. Only the linear two-dimensional amplification rates are compared since the experimental and theoretical work was for two-dimensional Tollmien-Schlichting waves. Figure 6.28 shows a comparison for different heating levels at  $Re_{\delta_1} = 800$  for  $F = 1$  and Figure 6.29 shows a comparison at  $Re_{\delta_1} = 800$  for  $F = 1.55$ . In Figures 6.28a and 6.29a, the amplification rates from the numerical simulations are calculated at the first maximum of the  $U_0$  velocity and, in Figures 6.28b and 6.29b, the amplification rates from the numerical simulations are calculated at the maximum of the  $V_0$  velocity. Shown for comparison are the linear stability theory results of Lowell (1974) and El-Hady and Nayfeh (1979) for a parallel uniformly heated boundary layer. Also, the nonparallel analysis of El-Hady and Nayfeh (1979) and the experimental work of Strazisar, Reshotko, and Prah1 (1977) is shown in Figures 6.28a and 6.29a. In the nonparallel analysis and the experiments, the growth rates were calculated at the first maximum of the  $U_0$  velocity. Therefore, comparison with the full Navier-Stokes solution is made only for the  $U_0$  velocity for the nonparallel theory and experimental results. In addition, the experimental Reynolds number was near  $Re_{\delta_1} = 800$ , but not exactly at this Reynolds number.

First, it can be seen that the linear stability theory of Lowell (1974) and El-Hady and Nayfeh (1979) agree for the cases shown. Lowell (1974) does predict a damped growth for  $\Delta\bar{T} = 8^\circ F$  and  $F = 1$ , but an exact value could not be discerned. At  $F = 1.55$ , Lowell's results (1974) show a completely stabilized boundary layer for  $\Delta\bar{T} = 5^\circ F$  and  $\Delta\bar{T} = 8^\circ F$ , but again exact values were not available. The growth rates obtained from the Navier-Stokes calculations differ somewhat from linear stability theory for the  $U_0$  velocity, but the agreement is quite good for the  $V_0$  velocity. Differences are attributed to nonparallel effects and are discussed shortly. In the linear stability theory calculations, all fluid property variations with temperature were considered, while in the numerical investigations of this work, viscosity is the only fluid property that varies with temperature. However, Lowell's results (1974) showed no appreciable differences for even larger levels of heating with the linear stability investigations of Wazzan, Okamura, and Smith (1968, 1970a, and 1970b) in which only the viscosity variation with temperature for the base flow was considered.

Since there is a slight deviation between the Navier-Stokes solutions with linear stability theory and the nonparallel theory, a convergence study was performed. It was found that, with the step size in  $y$  halved, the growth rates agree even more closely with linear theory. In fact, the agreement is within 2% for the  $V_0$  velocity with this step size halved. The simulations reported in this work were not run with this finer step size to save on computational time. However, the trends are the same with both step sizes.

The nonparallel analysis of El-Hady and Nayfeh (1979) does not show good agreement with the Navier-Stokes solution. However, if the nonparallel theory of Gaster (1974) is compared for the unheated wall with the nonparallel theory of El-Hady and Nayfeh (1979), large discrepancies exist between the two

nonparallel theories. Gaster's nonparallel results (1974 and 1986) for  $F = 1$  are shown in Figure 6.30a for  $\Delta\bar{T} = 0^\circ F$ . Comparison is made with the Navier-Stokes solution and linear theory, as well as the nonparallel theory of El-Hady and Nayfeh (1979). Agreement with the Navier-Stokes calculations is better for Gaster's nonparallel theory (1974). The experimentally determined amplification rate is at  $Re_{\delta_1} = 770$  for  $\Delta\bar{T} = 0^\circ F$ . For comparison at this Reynolds number, the Navier-Stokes solution differs with the experimental results for the unheated boundary layer by less than 1%. With the step size in  $y$  halved, the agreement between the Navier-Stokes solution and the nonparallel theory of Gaster (1974) is excellent (less than 5% difference).

For  $F = 1.55$ , results for several Reynolds numbers from Gaster's nonparallel theory (1974) are not available, but comparison is made in Figure 6.30b for  $\Delta\bar{T} = 0^\circ F$  for both the nonparallel theory of El-Hady and Nayfeh (1979) and the experiments of Strazisar, Reshotko, and Prah1 (1977). The experimentally determined growth rate is again at  $Re_{\delta_1} = 770$ . The experimental results compare better with the numerical simulations than with the nonparallel theory for the unheated flow.

In addition, the experimental work for the heated boundary layer compares better with the Navier-Stokes calculations at  $F = 1$  than with the nonparallel theory. The experimentally determined amplification rates for  $F = 1$  are all positive with uniform heating near  $Re_{\delta_1} = 800$ , indicating a damped flow. The exact values are not discernible from the experimental figure. However, the amplification rates computed from the numerical solution of the uniformly heated boundary layer are also positive, showing better agreement than the nonparallel theory.

For the frequency  $F = 1.55$ , the experimental comparison is not as good. The amplification rates obtained from the experiments of Strazisar, Reshotko, and Pahl (1977) are near  $Re_{\delta_1} = 800$ , but not exactly at this Reynolds number. However, the slight differences in the experimental Reynolds numbers do not account for the discrepancies between the numerical simulations and the experimental results. In the experiments, the amplification rates decrease with increasing heating for  $\Delta T = 3^\circ F$  and  $\Delta T = 5^\circ F$  at  $F = 1.55$ , but the amplification rates show a slight increase for  $\Delta T = 8^\circ F$ . This same trend is not predicted by the nonparallel theory of El-Hady and Nayfeh (1979) or the full numerical simulations. The nonparallel effects alluded to in the experimental investigations are not seen in this work. In the numerical computations, the neutral curves do not cross for the two frequencies investigated, but the neutral curves did cross in the experimental investigations for  $F = 1.55$  (refer to Figure 6.1a). One comment on the experimental values presented here is in order. The experimental growth rates shown in Figures 6.28 through 6.30 were based on the curve fits of the experimental data. These curve fits were made by Strazisar, Reshotko, and Pahl (1977). However, the actual experimental data points show the same trends.

The growth rates predicted by the nonparallel theory of El-Hady and Nayfeh (1979), that are shown in Figure 6.28a and 6.29a, do not include the distortion of the eigenfunction with streamwise position in the definition of the growth rates. However, it appears from their analysis that agreement with the Navier-Stokes calculations is better when this distortion is included. However, comparison was not available for this Reynolds number and the temperature differences considered.

Comparison of the Reynolds number at the lower branch of the neutral curve is made with the linear stability theory of Lowell (1974) and the experimentally determined neutral curves of Strazisar, Reshotko, and Pahl (1977) for

frequency  $F = 1$ . Figure 6.31 shows the Reynolds number for  $\alpha_i = 0$  (lower branch) versus the different levels of heating. In Figure 6.31a, the neutral points are based on the first maximum of the  $U_0$  velocity and for Figure 6.31b, the neutral points are based on the maximum of the  $V_0$  velocity. The Reynolds numbers at which the flow becomes unstable increase with each incremental level of heating. Once again, the comparison with parallel linear stability theory is better for the  $V_0$  velocity than for the  $U_0$  velocity. The experimental comparison agrees well for  $\Delta\bar{T} = 0^\circ F$ ,  $\Delta\bar{T} = 5^\circ F$ , and  $\Delta\bar{T} = 8^\circ F$ . Comparison was not available with experiments at  $\Delta\bar{T} = 3^\circ F$ . In addition, the convergence study with the normal step size halved shows even closer agreement with linear stability theory for the neutral points.

For the frequency  $F = 1.55$ , only the  $\Delta\bar{T} = 0^\circ F$  and  $\Delta\bar{T} = 3^\circ F$  heating levels show a region of amplification based on the  $V_0$  velocity, while only the unheated wall becomes unstable for amplification rates based on the  $U_0$  velocity. The cooled wall becomes unstable based on either velocity. The values of the Reynolds numbers at the neutral points are difficult to predict since the neutral curves are close to the heater strip and the region of strong amplification is near the neutral curves. However, the parallel linear stability theory of Lowell (1974) shows a region of amplification for only the  $\Delta\bar{T} = 0^\circ F$  and  $\Delta\bar{T} = 3^\circ F$  heating cases, just as the numerical simulations showed for the amplification rates based on the  $V_0$  velocity. In contrast, the experimental work of Strazisar, Reshotko, and Prahl (1977) shows an unstable region for  $F = 1.55$  for all levels of heating. The behavior of the heated boundary layer at the higher frequencies that was predicted by the experiments is not predicted by the parallel theory, the nonparallel theory, or Navier-Stokes calculations.



### 6.1.3 Nonuniform Passive Control Applied to Linear Disturbances

The enhancement in stability was shown with uniform passive wall heating. However, a nonuniform wall temperature distribution can lead to even larger stabilization of the flow and requires less heat input than for uniform passive heating. Two different nonuniform temperature distributions of the power law form  $A_0 x_n^p$  are considered for both frequencies  $F = 1$  and  $F = 1.55$ . The two exponents considered are  $p = -0.5$  and  $p = 1.0$ . The following cases of nonuniform passive heating are considered, where the 3 in the denominator of  $A_0$  is again due to the nondimensionalization:

Table 6.2 Parameters for Nonuniform Heating Cases for Linear Amplitudes				
$F$	$p$	$\bar{T}_w - \bar{T}_\infty$ ( $^{\circ}F$ )	$\bar{T}_w - \bar{T}_\infty$ ( $^{\circ}C$ )	$A_0$
1.00	-0.5	3.0	1.667	2.499/3
1.00	-0.5	5.0	2.778	4.218/3
1.00	-0.5	8.0	4.444	6.879/3
1.00	1.0	3.0	1.667	0.764/3
1.00	1.0	5.0	2.778	1.265/3
1.00	1.0	8.0	4.444	2.004/3
1.55	-0.5	3.0	1.667	2.501/3
1.55	-0.5	5.0	2.778	4.226/3
1.55	-0.5	8.0	4.444	6.897/3
1.55	1.0	3.0	1.667	0.764/3
1.55	1.0	5.0	2.778	1.267/3
1.55	1.0	8.0	4.444	2.010/3

The parameters are chosen to simulate the experimental work of Strazisar and Reshotko (1978). Comparison of these two nonuniform surface heating distributions is made with the experiments of Strazisar and Reshotko (1978) and the nonparallel theory of Nayfeh and El-Hady (1980), as well as the uniform heating case  $p = 0.0$ . In the experiments, the wall temperature is held fixed at a ref-

erence location  $x_r$  corresponding to a Reynolds number  $Re_{\delta_1}(x_r) = 800$  for the unheated case. The temperature is held constant in the numerical simulations at this Reynolds number. This causes a slight shift in the physical reference location when heating is applied, but is small so that comparison with experiments can still be made. The power law temperature distributions are shown in Figure 6.32 for the case of  $\Delta\bar{T} = 8^\circ F$  at  $Re_{\delta_1} = 800$  for each frequency. For  $p = -0.5$ , the temperature difference is larger than for the uniform heating case at all locations upstream of  $Re_{\delta_1} = 800$ , while the temperature difference is below the uniformly heated case for  $p = 1.0$ . Downstream of  $Re_{\delta_1} = 800$ , the temperature difference decreases below the uniformly heated level for  $p = -0.5$ , but increases for  $p = 1.0$ . For an increased temperature difference, the velocity profile  $\frac{\partial u_{ST}}{\partial y}$  is fuller, thus enhancing stability. Therefore, the nonuniform wall heating case of  $A_0 x_n^{-0.5}$  should provide a more stabilizing influence than  $A_0 x_n^{1.0}$  and  $A_0 x_n^{0.0}$  upstream of  $Re_{\delta_1} = 800$ , while  $A_0 x_n^{1.0}$  is more stabilizing downstream of the reference location. This is an important point in comparing different nonparallel surface temperature distributions and has been discussed by Asrar and Nayfeh (1985).

For the nonuniform surface temperature distributions used in this work, the reference point is located towards the end of the periodic solution domain for the disturbed flow. Therefore, it is expected that the exponent  $p = -0.5$  is more stabilizing than  $p = 1.0$  for the numerical simulations performed in this work.

Results of nonuniform surface heating for the frequency  $F = 1$  are shown first followed by the results for the frequency  $F = 1.55$ . Once again, only a few flow quantities are shown that illustrate the differences between uniform and nonuniform passive control. First, Figure 6.33 shows the undisturbed temperature  $T_{ST}$  for  $p = -0.5$  and  $p = 1.0$  for  $\Delta\bar{T} = 8^\circ F$  at  $Re_{\delta_1} = 800$ . The decrease in

the steady state temperature with increasing streamwise location  $x$  is visible in Figure 6.33a for a temperature distribution of  $A_0 x_n^{-0.5}$ , while the increase in the steady state temperature in the streamwise direction is seen in Figure 6.33b for a temperature distribution of  $A_0 x_n^{1.0}$ .

To distinguish the effects of the three different heating levels and the two different surface temperature distributions on the undisturbed flow, the boundary layer growth is shown in Figure 6.34 for  $p = -0.5$  and  $p = 1.0$ . The influence of the negative value of  $p$  is similar to the uniform surface temperature distribution, as was seen in Figure 6.16. However, for  $p = 1.0$ , the boundary layer growth is nearly the same as for the unheated flow at the beginning of the solution domain. The skin friction coefficients are shown in Figure 6.35 for both nonuniform surface temperature distributions. The skin friction is larger for  $p = -0.5$  than for  $p = 1.0$  at the beginning of the streamwise domain, while the opposite occurs near the end of the domain. The larger skin friction denotes a fuller base flow velocity profile and enhanced stability.

To illustrate the effect of each nonuniform heat distribution, the Fourier modes for the case of  $\Delta \bar{T} = 8^\circ F$  at  $Re_{\delta_1} = 800$  are shown in Figures 6.36 and 6.37 for the  $U_0$  and  $U_1$  velocities. The two- and three-dimensional modes are shown at time step  $L = 540$  in both surface and contour representations. In Figures 6.36a and 6.36b, the results for  $p = -0.5$  are shown, while the  $U_0$  and  $U_1$  velocities for  $p = 1.0$  are shown in Figures 6.37a and 6.37b. The differences in the level of control achieved are apparent. Comparison with the uniformly controlled flow of Figures 6.18a and 6.18e show that the nonuniform temperature distributions for the exponent  $p = -0.5$  has created at least the same level of control, while the disturbance levels are not as strongly attenuated for  $p = 1.0$ . Comparison of the different cases is shown later based on the actual heat input at the wall.

The different levels of control for each nonuniform surface temperature distribution are compared in Figures 6.38 and 6.39. Amplitude and phase profiles are shown for the  $U_0$  and  $U_1$  velocities at  $Re_{\delta_1} = 800$ . As for the uniformly heated wall, the amplitude levels are reduced for each incremental increase in heating. In addition, the location of the phase jumps remains in approximately the same location. However, the differences between the two nonuniform surface temperature distributions are apparent in the amplitude levels. For  $p = -0.5$ , Figure 6.38 shows a slightly larger decrease in magnitude when compared with the uniformly controlled case shown in Figures 6.19a and 6.19e. The opposite effect is found for  $p = 1.0$ , as seen in Figure 6.39, where the amplitude levels are higher than for the uniformly heated wall.

The amplitude levels at one streamwise  $x$  location can be deceiving for the nonuniformly heated flow due to the location of the reference point. Therefore, the growth of the amplitude downstream is shown in Figures 6.40 and 6.41 at the maximum of the  $U_0$  and  $U_1$  velocities for both  $p = -0.5$  and  $p = 1.0$ . Again, the same observations can be made. The effect of heating is to decrease the amplitude levels and reduce the growth rates, but the stabilizing influence is more pronounced for  $p = -0.5$ . The periodic solution domain ends just downstream of the reference location. Thus the  $p = -0.5$  exponent should have a more stabilizing influence than  $p = 1.0$  and  $p = 0.0$ .

The change of the growth rates with  $Re_{\delta_1}$  for the nonuniform control simulations are shown in Figures 6.42 and 6.43. The growth rates for  $p = -0.5$  nonuniform control are shown in Figures 6.42a and 6.42b based on the  $U_0$  and  $V_0$  velocities and the growth rates for  $p = -0.5$  nonuniform control are shown in Figures 6.42c and 6.42d based on the  $U_1$  and  $V_1$  velocities. Figure 6.43 shows the analogous growth rates for  $p = 1.0$  nonuniform control. Several observations can

be made from these plots. The growth rates in all cases decrease with increasing wall heating. In comparison with Figure 6.21 for the uniform passive control simulations, the nonuniform distribution  $p = -0.5$  is more stabilizing, while  $p = 1.0$  has a smaller increase in stability. However, for both the two- and three-dimensional components, the amplification rates for  $p = 1.0$  are becoming more positive at a higher rate for increasing downstream distances. This is due to the increasing temperature difference between the wall and the freestream.

The wavenumbers based on the  $V_0$  and  $V_1$  velocities for both nonuniform surface temperature distributions are shown in Figures 6.44 and 6.45. For  $p = -0.5$ , the wavenumbers increase for both the two- and three-dimensional components with increasing wall heating, as was the case for uniform heating. The level of increase in the wavenumbers is larger for the uniform heating. However, for  $p = 1.0$ , the wavenumbers decrease with increasing heat input for both the two- and three-dimensional components. This decrease in  $\alpha_r$  for  $p = 1.0$  represents an increase in the phase speeds.

Results of nonuniform surface heating for the frequency  $F = 1.55$  are now presented. Again, only plots that illustrate differences between the two frequencies and the uniform heating cases are discussed. The Fourier modes for  $\Delta\bar{T} = 8^\circ F$  at  $Re_{\delta_1} = 800$  are shown in Figures 6.46 and 6.47 for the  $U_0$  and  $U_1$  velocities. Both surface and contour plots are displayed at time step  $L = 660$ . Figure 6.46 shows the downstream development of the disturbance waves for  $p = -0.5$ , while Figure 6.47 shows the downstream development for  $p = 1.0$ . The disturbance wave is attenuated for both nonuniform control distributions, but the  $p = -0.5$  case is more strongly attenuated.

To compare the different levels of control for each nonuniform surface temperature distribution, amplitude and phase profiles are shown in Figures 6.48

and 6.49 for the  $U_0$  and  $U_1$  velocities at  $Re_{\delta_1} = 800$  for  $F = 1.55$ . For each incremental increase in heating, the amplitude levels are reduced. The differences between the two nonuniform surface temperature distributions are again apparent. The nonuniform case of  $p = -0.5$  has a larger effect on the flow when compared with the  $p = 1.0$  wall heating case as well as the uniformly controlled case shown in Figure 6.24.

As was discussed for the frequency  $F = 1$ , the amplitude levels at one streamwise  $x$  location can be misleading when a nonuniform temperature distribution is used. Figures 6.50 and 6.51 show the growth of the amplitude downstream at the maximum of the  $U_0$  and  $U_1$  velocities for both  $p = -0.5$  and  $p = 1.0$ . Although the flow is more stabilized for  $A_0 x_n^{-0.5}$ , the  $A_0 x_n^{1.0}$  temperature distribution shows a stronger decrease in amplitude towards the end of the periodic solution domain.

The growth rates for frequency  $F = 1.55$  and nonuniform control are shown in Figures 6.52 and 6.53. Again the growth rate based on the  $U_k$  and  $V_k$  velocities are shown for both the two- and three-dimensional components. Similar observations are made as for  $F = 1$ . The growth rates decrease with increasing wall heating. The nonuniform distribution  $p = -0.5$  is more stabilizing than for uniform passive heating, as seen in Figure 6.26. In contrast, a smaller decrease in the growth rates occurs for  $p = 1.0$ . Once again, the amplification rates for  $p = 1.0$  become increasingly positive downstream for both the two- and three-dimensional components. This is attributed again to the increasing temperature difference for  $p = 1.0$  downstream.

The influence of nonuniform surface heating on the wavenumbers for  $F = 1.55$  is shown in Figures 6.54 and 6.55. The wavenumbers based on the maximum of the  $V_0$  and  $V_1$  velocities are shown. The results are similar to the

frequency  $F = 1$ . The wavenumbers increase with increasing wall heating for  $p = -0.5$  and decrease with increasing heat input for  $p = 1.0$ .

In order to accurately compare the nonuniform temperature distributions with the uniform heating cases, the actual heat input to the wall should be compared. Figures 6.56 and 6.57 show such a comparison for  $F = 1$  and  $F = 1.55$ . Figure 6.56 shows the amplitude at the maximum of the  $U_k$  velocity at  $Re_{\delta_1} = 800$  for  $F = 1$  versus the heat input for each passive heating case considered. Both the two-dimensional and three-dimensional modes are shown. Figure 6.57 shows a similar comparison for  $F = 1.55$ . The heat input shown in the figures is the integrated heat transferred at the wall for the periodic solution domain only. Thus

$$\bar{Q} = \int_{\bar{x}_0}^{\bar{x}_{N_p}} \bar{q} d\bar{x} \quad (6.6)$$

where  $q$  is the heat transfer rate per unit area and is given by Fourier's law of heat conduction, or

$$\bar{q} = -\bar{k} \left( \frac{\partial \bar{T}}{\partial \bar{y}} \right)_{\bar{y}=0} \quad (6.7)$$

For  $F = 1$ , the periodic solution domain ends at  $x_{N_p} = 2.8$  and for  $F = 1.55$ ,  $x_{N_p} = 2.6$ . Considering Figure 6.33, the periodic solution domain is just past the reference location where the  $A_0 x_n^{1.0}$  temperature distribution should be more stabilizing. For the largest extent of the solution domain, however, the temperature distribution  $A_0 x_n^{-0.5}$  should be more stabilizing. Figures 6.54 and 6.55 show that the actual heat input required for the same reduction in amplitude is smaller for  $p = -0.5$  than for  $p = 0.0$  and  $p = 1.0$ . This makes the temperature distribution  $A_0 x_n^{-0.5}$  the most energy efficient to apply.

Finally, comparison with theory and experiments for nonuniform surface heating is made for both frequencies. Again, only the linear two-dimensional amplification rates are compared since the experimental and theoretical work was for

two-dimensional waves. Figures 6.58 and 6.59 show a comparison of the amplification rates at  $Re_{\delta_1} = 800$  for different levels of heating and  $F = 1$ . In Figures 6.58a and 6.59a, the amplification rates from the numerical simulations are based on the first maximum of the  $U_0$  velocity and in Figures 6.58b and 6.59b, the amplification rates are calculated from the numerical simulations based on the maximum of the  $V_0$  velocity. In Figure 6.58, the temperature distribution applied at the wall is  $A_0 x_n^{-0.5}$  and in Figure 6.59 the temperature distribution is  $A_0 x_n^{1.0}$ . Figures 6.60 and 6.61 show a similar comparison for frequency  $F = 1.55$ . The linear stability theory results of Nayfeh and El-Hady (1980) for both a parallel nonuniformly heated boundary layer and a nonparallel nonuniformly heated boundary layer are also shown. In addition, the amplification rates from the experimental work of Strazisar and Reshotko (1978) are compared. As for the uniform passive heating cases, the growth rates were calculated at the first maximum of the  $U_0$  velocity in the nonparallel analysis and the experiments. Comparison of the experimental work and the nonparallel theory with the numerical computations is made for only the  $U_0$  velocity.

As was the case for uniform heating, comparison of parallel linear theory is better for the  $V_0$  velocity than the  $U_0$  velocity. The differences are again attributed to nonparallel effects. The nonparallel theory of Nayfeh and El-Hady (1980) shows the same trends in amplification rates as the Navier-Stokes calculations, but are more unstable. This trend is the same found in comparing the uniform passive heating results of El-Hady and Nayfeh (1979). It was shown then that Gaster's nonparallel theory (1974) agrees better with both the Navier-Stokes calculations and experiments for the unheated flow.

The amplification rates from the experiments of Strazisar and Reshotko (1978) show a different picture. For  $F = 1$  and  $p = -0.5$ , the exact experimental



growth rates are not discernible, but show a positive value with nonuniform heating applied. The amplification rates for the numerical simulations are also positive for  $p = -0.5$  and  $F = 1$ . However, the nonparallel analysis shows amplification, not damping. For  $F = 1$  and  $p = 1.0$ , the same situation occurs. The experimental points indicate a stabilized boundary layer in agreement with the Navier-Stokes calculations. However, only  $\alpha_i$  for the temperature difference  $\Delta\bar{T} = A_0 x_n^{1.0} = 3^\circ F$  at  $Re_{\delta_1} = 800$  is discernible. The higher heating levels, though, show increased damping.

The comparison with experiments for  $F = 1.55$  is not as good for both nonuniform heating distributions. For  $p = -0.5$ , the experimental amplification rates lie between the nonparallel theory and the Navier-Stokes calculations, but the trend towards stabilization for higher levels of heat input is found. However, for  $p = 1.0$ , the growth rate increases for  $A_0 x_n^{1.0} = 3^\circ F$  and then decreases for  $A_0 x_n^{1.0} = 5^\circ F$ . The growth rate for  $A_0 x_n^{1.0} = 8^\circ F$  is not discernible from the experimental work, but shows a damped value. The increase and decrease in growth rates was also seen in the experiments of Strazisar, Reshotko, and Prah1 (1977) for uniform passive heating at  $F = 1.55$ . This trend is again not seen in either the full Navier-Stokes simulations or the nonparallel analysis.

## 6.2 Active Control of Linear Disturbances

In the preceding section, small amplitude disturbances were controlled through the application of passive surface heating. The amplitude levels and growth rates were reduced significantly below the uncontrolled flow case. As promising as passive control appears, active methods of control can be just as effective in reducing amplitude levels and require a much smaller heat input than passive heating. Results of numerical simulations of active control using localized

temperature perturbations for control inputs are shown in Section 6.2.2. Before proceeding directly to the active control simulations, boundary layer receptivity mechanisms for the surface heater strip are discussed in Section 6.2.1.

### 6.2.1 Receptivity of a Surface Heater Strip

In Chapter 2, a brief discussion of receptivity was given. Receptivity refers to the process by which a particular forced disturbance enters the boundary layer and the signature of this disturbance wave on the flow field. In this work, the receptivity of the localized temperature perturbation is examined. By understanding the receptivity mechanisms of a discrete surface heater, more efficient heater strips can be designed to maximize (or minimize, depending on the application) a disturbance input. In addition, by attempting to understand the mechanisms by which a localized temperature perturbation creates disturbance waves in the flow, active control can be improved upon.

First a consideration of the width of the heater strip is given. As shown by Equation (6.1), the streamwise temperature distribution for the heater strip is of the form  $\sin^2(\xi_n)$ . This shape function was chosen to approximately simulate a physical heater strip. Although different shape functions would lead to differing amounts of receptivity, only the heater strip width is varied in this receptivity analysis. Four different discrete widths are studied in fractions of a two-dimensional Tollmien-Schlichting wavelength, i.e.,  $\frac{d_{HS}}{\lambda_{TS}} = \frac{1}{4}, \frac{1}{2}, \frac{3}{4},$  and 1. Only a receptivity analysis of the two-dimensional heater strip is considered, but the same analysis could be done for three-dimensional oblique waves. However, the trends should be similar for both two-dimensional and three-dimensional linear disturbance waves. For this application, the maximum receptivity is desired, or the maximum disturbance amplitude created for the smallest heat input to the heater strip. A constant

amount of heat input, as an input parameter, is not easily maintainable. Therefore, the parameter  $\epsilon_{\theta_0}$  of Equation (6.1b) is varied. Four different temperature disturbance amplitudes are considered:  $\epsilon_{\theta_0} = \frac{1}{3}, \frac{1.5}{3}, \frac{2}{3},$  and  $\frac{2.5}{3}$ . The value of 3 in the denominator is again due to the nondimensionalization. Thus, for each ratio of  $\frac{d_{HS}}{\lambda_{TS}}$ , four different levels of heating are considered. The same parameters used for the uncontrolled flow of Section 6.1.1 for the frequency  $F = 1$  are again used for this receptivity study. The heater strips all start at  $x_{HB_1} = 30$ . Figure 6.62 shows a comparison between the heat transferred over the heater strip and the level of heating (or  $\epsilon_{\theta_0}$ ) for the four different ratios of  $\frac{d_{HS}}{\lambda_{TS}}$ . The heat transferred over the heater strip is calculated by:

$$\bar{Q} = \int_{\bar{x}_{HB_1}}^{\bar{x}_{HB_2}} \bar{q} d\bar{x}. \quad (6.8)$$

The heat transferred increases with each incremental increase in heating. The wider heater strips also have larger heat inputs due to the larger surface area. To determine the most efficient width of heater strip, the amplitude of the two-dimensional wall vorticity is monitored at a downstream location of about seven Tollmien-Schlichting wavelengths. The amplitude level created by the time dependent temperature perturbation input versus the amount of heat input for each disturbance wavelength is shown in Figure 6.63. It can be seen from this figure that the smaller heater strips are able to produce larger disturbances for an equivalent heat input. The smaller heater strips are more receptive in terms of maximizing the disturbance levels in the flow field.

In an analytical study of boundary layer receptivity, Heinrich, Choudari, and Kerschen (1988) have found qualitatively similar results for a discrete suction strip. Figure 6.64 shows the results of the analysis of Heinrich, Choudari, and Kerschen (1988). A receptivity coefficient is plotted as a function of the strip width.

This receptivity coefficient  $F(d)$  is the ratio between the Tollmien-Schlichting amplitude created in the flow field and the input amplitude at the suction strip. The four different curves represent different streamwise locations of the suction strips where  $l$  is the distance from the leading edge and  $l_{nsp}$  denotes the location of the neutral stability point. For comparison, the discrete heater strip is located near the neutral stability point. From Figure 6.64, the maximum receptivity occurs for the very narrow suction strips of less than one Tollmien-Schlichting wavelength and receptivity is minimized for  $\frac{d_{HS}}{\lambda_{TS}} = 1$ . In the analysis, the mass flux at the wall is held constant.

Although the location of the heater strip was not varied in this receptivity analysis, Heinrich, Choudari, and Kerschen (1988) show that the receptivity is affected by the location of the heater strip in relation to the distance from the leading edge of the plate (or consequently the displacement thickness). In the experimental work of Nosenchuck (1982) and the analytical work of Maestrello (1984), an optimal ratio of width of the heater strip to the displacement thickness is found. For Nosenchuck (1982), the experimental criterion found is

$$2 \leq \frac{d_{HS}}{\delta_1} \leq 10$$

and for Maestrello (1984), the analytical criterion found is

$$6 \leq \frac{d_{HS}}{\delta_1} \leq 10.$$

Nosenchuck (1982) suggested that the heater strip width  $d_{HS}$  must be larger than the displacement thickness  $\delta_1$  so that the perturbations created at the wall would rapidly perturb the flow in the critical layer. The critical layer is near  $\delta_1$  where the most unstable waves begin to amplify. It was also suggested by Nosenchuck (1982) that  $d_{HS}$  should not be so large so as to make phase control difficult. For

the different widths of heater strips examined here, the following table shows the ratio of width to displacement thickness:

Table 6.3 Comparison of Displacement Thickness to Heater Strip Width	
$\frac{d_{HS}}{\lambda_{TS}}$	$\frac{d_{HS}}{\delta_1}$
0.25	9.8
0.50	19.4
0.75	28.8
1.00	38.0

Thus the 0.25 wavelength heater strip, which was found to be the most receptive, also falls within the criteria of both Nosenchuck (1982) and Maestrello (1984).

Although the heater strip of width  $\frac{d_{HS}}{\lambda_{TS}} = 0.25$  has the highest slope (or highest ratio of amplitude to heat input), a large temperature input  $\epsilon_{\theta_0}$  is needed to achieve the same amplitude levels as the wider heater strips. A disturbance amplitude of approximately 0.05% of the first maximum of the  $U_0$  velocity is desired in the numerical simulations and the heater strip of width  $d_{HS} = 0.5 \lambda_{TS}$  and  $\epsilon_{\theta_0} = 2/3$  creates waves of this amplitude level. Therefore, this heater strip is chosen for both the passive and active control simulations. The disturbance field on and near this heater strip is now more fully examined.

The perturbations created over the discrete heater strip propagate downstream and develop into Tollmien-Schlichting waves shortly downstream of the heater strip. Over the heater strip, the disturbances are not in agreement with the eigenfunctions of the Orr-Sommerfeld equation. The amplitudes and phases at the center of the heater strip are shown in Figure 6.65 for the  $U_0$  and  $V_0$  velocities, the  $\Omega_{x_0}$  vorticity, and the  $\Theta_0$  temperature. Also shown for comparison is the

solution from linear stability theory for  $U_0$ ,  $V_0$ , and  $\Omega_{z_0}$  for this Reynolds number of  $Re_{\delta_1} = 576$ . As before, the Navier-Stokes solution is normalized with the linear stability theory calculation at the first maximum of the  $U_0$  disturbance velocity. Each flow quantity shows a large difference in comparison with the amplitude and phase calculations from linear stability theory. The first maximum of the  $U_0$  velocity has moved very close to the wall and the phase does not show the jump of  $\pi$ . The  $V_0$  velocity is much smaller than the linear stability theory solution and the phase is changing rapidly near the wall. The spanwise vorticity  $\Omega_{z_0}$  shows the most dramatic effect of the surface heater strip. The gradient is very steep at the wall and the amplitude is almost six times as large as the linear stability theory amplitude due to the time dependent temperature perturbations. Although the gradients are steep, the step size used in  $y$  is sufficient to resolve the physics. A numerical simulation with  $\frac{1}{2}\Delta y$  was run to provide a check on the solution. The same strong gradients resulted. Finally, the amplitude of the temperature decays very rapidly close to the wall.

The disturbances over the heater strip are very different in shape than the linear stability solution, but the development into a Tollmien-Schlichting wave occurs shortly downstream of the heater strip. The amplitude and phase profiles located one disturbance wavelength downstream from the end of the discrete heater strip are shown in Figure 6.66 for the two-dimensional flow components. Comparison with linear stability theory is made at the Reynolds number  $Re_{\delta_1} = 646$ . The temperature perturbations have created instability waves in the flow in just a small distance. The amplitude of the temperature perturbations is now two orders of magnitude smaller than over the heater strip. The temperature perturbations decay very rapidly downstream of the heater strip.

It has been shown by both Nosenchuck (1982) and Maestrello (1984) that the local periodic surface heating can be related to normal velocity disturbances at the wall. However, as seen in Figure 6.65b, the normal velocity  $V_0$  over the heater strip is not strongly influenced by the temperature perturbations. Rather the spanwise vorticity  $\Omega_{z0}$  is the most strongly influenced quantity. A relationship between the spanwise vorticity and temperature at the wall was derived in Equation (2.3). This equation is repeated here for convenience:

$$\left(\frac{\partial \omega_z}{\partial y}\right)_{y=0} = -\frac{1}{\mu_{y=0}} \left(\frac{\partial \mu}{\partial T}\right)_{y=0} \left(\frac{\partial T}{\partial y}\right)_{y=0} \omega_{z_{y=0}}. \quad (2.3)$$

The localized heat disturbances are creating changes in viscosity. These changes in viscosity in turn are creating the strong gradients in the spanwise vorticity. The steep gradients remain local to the heater strip and the spanwise vorticity quickly reduces in amplitude level to linear values. Due to the close relationship between the temperature and spanwise vorticity, the spanwise vorticity is chosen as the flow quantity monitored for phase adjustments in the active control simulations.

### 6.2.2 Active Control Using a Surface Heater Strip

In the active control simulations, a surface heater strip is used to introduce the disturbances into the flow. The same parameters used in the numerical simulations of the uncontrolled linear disturbances of Section 6.1.1 are used here at the frequency  $F = 1$ . In addition to the first heater strip, a second heater strip is located downstream to serve as the actuator. A schematic of the heater strip arrangement for the active control simulations is shown in Figure 6.67. The location of the downstream sensor is also shown in Figure 6.67. This sensor monitors the spanwise wall vorticity (hence the wall shear stress). An appropriate phase relationship is then found between the sensor and actuator for controlling

the instability waves. This process is described below, but first the wall boundary conditions for the second heater strip are shown for the undisturbed flow:

$$\Theta_{0,n,0}^I = A_0 x_n^2 + \sin^2(\xi_n) \quad (6.9a)$$

and for the disturbed flow:

$$\Theta_{0,n,0}^I = A_0 x_n^2 + \sin^2(\xi_n)[1 + \epsilon_{\Theta_0} \sin(\beta t_l + j\pi - \Delta\phi_0)] \quad (6.9b)$$

$$\Theta_{1,n,0}^I = \epsilon_{\Theta_1} \sin^2(\xi_n) \sin(\beta t_l + j\pi - \Delta\phi_1) \quad (6.9c)$$

where

$$\xi_n = \frac{x_n - x_{HB_2}}{x_{HE_2} - x_{HB_2}} \pi$$

and

$$x_{HB_2} \leq x_n \leq x_{HE_2}.$$

This second heater strip is located between  $x_{HB_2} = 120$  and  $x_{HE_2} = 135$  and is also approximately one half a Tollmien-Schlichting wavelength wide. Several observations are made concerning the signal for the actuator. First, the amplitude input to the second heater strip is the same as that input to the initial heater strip (see Equation 6.1). Therefore, the amplification or damping that takes place between the two surface heater strips is not compensated for in these simulations. However, the neutral curve lies between the two heater strips and so strong decay or growth is not present in this region. Secondly, the phase is adjusted by the parameter  $j\pi - \Delta\phi_k$ , where  $j = 1$  for attenuation and  $j = 2$  for reinforcement. The phase adjustments  $\Delta\phi_k$  are determined at the downstream sensor. The phase change is calculated by

$$\Delta\phi_0 = \alpha_{r_{2D}} \Delta x \quad (6.10a)$$

$$\Delta\phi_1 = \alpha_{r_{3D}} \Delta x \quad (6.10b)$$



where  $\alpha_r$  is the wavenumber based on the spanwise wall vorticity  $\Omega_{x_0}$  and  $\Omega_{x_1}$ . The length  $\Delta x$  is the distance between the sensor and the actuator. For these active control simulations, the sensor is located at  $x_{HS} = 240$ , or about four Tollmien-Schlichting wavelengths downstream of the actuator. The phase inputs are calculated from the results of the uncontrolled flow of Section 6.1.1 and are summarized in the following table:

Table 6.4 Parameters for Phase Control of Linear Disturbances			
dimension	$\alpha_r$	$\Delta\phi$ (radians)	$\Delta\phi$ (degrees)
$2D$	28.094	0.096	$4.8^\circ$
$3D$	26.694	4.871	$292.8^\circ$

Two numerical simulation of active control of linear three-dimensional disturbances are run. The first case is with  $j = 1$  so that the actuator is  $180^\circ$  out of phase with the disturbances in the flow. The second case is with  $j = 2$  so that the temperature perturbations are in phase with the disturbances in the flow field. Results of both cases are now shown.

The undisturbed flow solution for the temperature is shown in Figure 6.68. The steady state contribution to each heater strip is readily seen and the influence of the steady state temperature remains in the vicinity of the heater strip.

The Fourier modes for the  $U_0$  and  $U_1$  velocities that result from the application of the second heater strip are shown in Figures 6.69 and 6.70. Figure 6.69 shows the results for the out of phase control (or  $j = 1$ ), while Figure 6.70 shows the velocity perturbations with the in phase control (or  $j = 2$ ) applied. Both contour and surface representations of the  $U_0$  and  $U_1$  velocities are shown. The contour levels are the same as for the uncontrolled flow of Section 6.1.1 so

that comparison can be made with Figure 6.9. Both the two-dimensional and three-dimensional modes show a strong reduction downstream of the actuator for the out of phase input, while the actuator that creates temperature perturbations in phase reinforces the existing instability waves in the flow.

In order to compare the active control simulations with the uncontrolled flow, the amplitude profiles for the  $U_0$  and  $U_1$  velocities are shown in Figure 6.71. The profiles are shown at the downstream sensor location of  $n = 240$  (or  $Re_{\delta_1} = 885$ ). The amplitudes are strongly reduced for the out of phase perturbations and significantly increased for the in phase temperature perturbations. It is also noted that, unlike the passive control results, the shape of the amplitude remains the same. This is because the base flow does not change, except locally over the heater strip. It should also be noted that cancellation is not achieved for the in phase heater strip case. If an adjustment in the amplitude levels had been made, an even larger reduction would have been seen. However, the reduction in amplitude level is already quite significant.

It was shown in the passive control simulations that the growth rates are strongly influenced with passive heating. However, the growth rates are not affected in active methods of control. Figure 6.72 shows the amplitude growth downstream for the  $U_0$  and  $U_1$  amplitudes for both active control cases, as well as the uncontrolled case. The strong reduction (or increase) in the amplitudes is seen downstream of the actuator input, but the growth rates are not altered.

Finally, a comparison between the passive and active control simulations is made. Similar reductions in amplitude levels occurred for the uniform passive heating case of  $\Delta\bar{T} = 8^\circ F$  as for the attenuation case here, while the cooling case of  $\Delta\bar{T} = -5^\circ F$  resulted in approximately the same increase in amplitude level as the in phase reinforcement case. The cooled wall requires five times more heat

input than the heat input to the actuator, while the passively heated wall requires seven times more heat input. This considerable savings in power makes active control an attractive approach.

### 6.3 Passive Control of Secondary Instability

To this point, only the control of linear amplitude disturbance waves has been demonstrated. Results of control applied at the early stages of the nonlinear three-dimensional secondary instability process are now presented. Uniform passive heating is applied to both the fundamental ordered peak-valley and the subharmonic staggered peak-valley breakdown processes. The parameters chosen for the simulation of secondary instability closely model the experiments of Klebanoff, Tidstrom, and Sargent (1962) for the fundamental breakdown and Kachanov and Levchenko (1984) for the subharmonic breakdown. Boundary layer control is not applied in these experimental investigations. However, neither theoretical nor experimental investigations exist in which passive control of the spatial secondary instability process is attempted. Therefore, the above experiments provide the reference cases for comparison of the influence of passive heating on the secondary instability processes.

The physical experiments are performed in wind tunnels, but water is the fluid that is again used in the numerical studies. Comparison can then be made with the linear amplitude control investigations. Several parameters remain the same as for the previous simulations including  $\bar{T}_\infty$ ,  $\bar{\mu}_\infty$ ,  $Pr$ ,  $Re$ ,  $\bar{U}_\infty$ ,  $\bar{L}$ ,  $\epsilon$ ,  $R_A$ , and  $T_r$ . These parameters were presented in Section 6.1. The remaining parameters differ for the two experimental studies of the secondary instability process. First, the results for the fundamental breakdown are shown, followed by the results for the subharmonic breakdown process.

### 6.3.1 Passive Control of the Fundamental Breakdown Process

The parameters used in the study of passive control of the ordered peak-valley breakdown process are listed below.

$$F_{2D} = 0.588 \quad (\beta_{2D} = 5.88)$$

$$F_{3D} = 0.588 \quad (\beta_{3D} = 5.88)$$

$$\alpha_{rM} = 16.0$$

$$\alpha_{rN} = 16.2$$

$$\gamma = 24.3$$

$$K = 2$$

$$\Delta x = 6.5043 \times 10^{-3}$$

$$\Delta y = 5.3100 \times 10^{-1}$$

$$\Delta t = 1.0686 \times 10^{-2}$$

$$\epsilon_{V_0} = 1.2 \times 10^{-3}$$

$$\epsilon_{V_1} = 2.4 \times 10^{-4}$$

The frequencies for both the two- and three-dimensional disturbances are the same. The parameters are chosen to match as closely as possible the conditions of the experiments of Klebanoff, Tidstrom, and Sargent (1962). The step size in the streamwise direction  $\Delta x$  is chosen so that there are approximately 60 grid points per disturbance wavelength. The normal step size  $\Delta y$  is determined so that the  $y$  direction spans 6.5 boundary layer displacement thicknesses at the inflow boundary and approximately five boundary layer displacement thicknesses at the outflow boundary. The grid has 61 points in the normal direction and 901 points in the streamwise direction. Thus, the streamwise domain contains

15 disturbance wavelengths. The position of the outflow boundary is initially five wavelengths downstream ( $x_{B_i} = 301$ ) of the inflow boundary and moves at a speed  $V_B = 0.8$ . The time discretization  $\Delta t$  is chosen so that there are 100 time steps per disturbance period. The computation proceeds for eight disturbance periods. The periodic solution domain extends to  $x_n = 480$ . In this region, tests have shown that the parameter  $K = 2$  is sufficient to resolve the spanwise flow.

For all passive control simulations of secondary instability, the disturbances are introduced through a discrete suction and blowing strip at the wall. The wall boundary conditions follow from Equations (5.29) and (5.69) for the undisturbed flow:

$$\Theta_{0,n,0}^l = A_0 \quad (6.11a)$$

and for the disturbed flow:

$$V_{0,n,0}^l = r(t)\epsilon_{V_0}\bar{V}_w(\xi_n)\sin(\beta_{2D}t_l) \quad (6.11b)$$

$$V_{1,n,0}^l = r(t)\epsilon_{V_1}\bar{V}_w(\xi_n)\sin(\beta_{3D}t_l) \quad (6.11c)$$

where

$$\bar{V}_w(\xi_n) = \xi_n^3 [20.25 + \xi_n (15.1875\xi_n - 35.4375)]$$

for

$$x_{SB_1} \leq x_n \leq \frac{x_{SE_1}}{2}$$

and

$$\bar{V}_w(\xi_n) = -\xi_n^3 [20.25 + \xi_n (15.1875\xi_n - 35.4375)]$$

for

$$\frac{x_{SE_1}}{2} < x_n \leq x_{SE_1}$$

with

$$\xi_n = \frac{x_n - x_{SB_1}}{x_{SE_1} - x_{SB_1}} 2$$

The suction and blowing strip is represented by a fifth order polynomial. The strip is located one disturbance wavelength downstream of the left boundary ( $x_{SB_1} = 60$  and  $x_{SE_1} = 120$ ) and covers one wavelength. The disturbance amplitudes  $\epsilon_{V_0}$  and  $\epsilon_{V_1}$  are chosen so that the velocity perturbations create disturbance waves of the same amplitude as observed in the experiments. A suction and blowing strip is used to introduce the disturbances in the flow for the simulations of secondary instability instead of a heater strip that was used in the passive control simulations of linear amplitude disturbances. A suction and blowing strip is used because there are some difficulties in creating nonlinear amplitudes with a heater strip. This difficulty is discussed in Section 6.4 in conjunction with active control of secondary instability.

Although care has been taken to simulate the experimental conditions, at least one deviation exists. Fasel, Rist, and Konzelmann (1987) have shown quite good agreement with the experiments of Klebanoff, Tidstrom, and Sargent (1962) through their numerical simulations, but a small pressure gradient appears to have existed in the experiments. The amplification rates with zero pressure gradient are smaller in the numerical simulations than in the experiments. With a small adverse pressure gradient of  $\frac{\partial p}{\partial x} \simeq 0.004$  applied in the numerical simulations, the numerical growth rates show very good agreement with the experimental growth rates. Although a slight pressure gradient may have been present in the experiments, this aspect of the flow is not simulated here since the objective is to

study the influence of control by surface heating for a flat plate boundary layer. As discussed in the introduction, pressure gradients have a similar influence on the stability of the flow as wall heating. Therefore, combining together these two passive control mechanisms is not desirable for this study since the influence of heating is the focal point.

As shown by Equation (6.1a), the wall has a uniform temperature distribution ( $p = 0$ ) applied to it. The following three cases are considered for the passive control of the fundamental breakdown process:

Table 6.5 Parameters for Uniform Passive Control Cases of Fundamental Breakdown			
$Re_{\delta_1}$ (at $x_0$ )	$\bar{T}_w - \bar{T}_\infty$ ( $^{\circ}F$ )	$\bar{T}_w - \bar{T}_\infty$ ( $^{\circ}C$ )	$A_0$
1550	0.0	0.000	0.0
1501	8.0	4.444	4.444/4.444
1460	15.0	8.332	8.332/8.332

The base flow changes for the passive control simulations and hence the Reynolds number  $Re_{\delta_1}$ . The Reynolds number  $Re_{\delta_1}$  is varied at the inflow boundary depending on the level of heating so that the physical location at the left boundary remains the same. The parameter  $A_0$  is now nondimensionalized with the temperature difference between the wall and the freestream, since a surface heater strip is not present. The influence of passive heating on the base flow characteristics was shown in detail in Section 6.1 and is not repeated here.

The Fourier modes for the uncontrolled flow are shown in Figure 6.73 for the  $U_0$  and  $U_1$  velocities. Surface representations are shown at time step  $L = 800$ . The  $U_0$  velocity appears similar in shape to the results of Section 6.1.1 for the uncontrolled linear disturbances, but is at a nonlinear amplitude. However,

the  $U_1$  velocity clearly exhibits different characteristics. A time invariant, three-dimensional disturbance is now present and is spanwise periodic. This perturbation represents a stationary modulation of the base flow and was first observed in the experiments of Klebanoff, Tidstrom, and Sargent (1962). This nonperiodic term is present in all flow components and represents a longitudinal vortex system in the  $V_1$  and  $W_1$  mean velocities. The three-dimensional mean component creates the peak-valley structure and the effect of passive heating on this component is discussed further. The influence of uniform passive control on the Fourier modes for  $\Delta\bar{T} = 15^\circ F$  is shown in Figure 6.74 for the  $U_0$  and  $U_1$  velocities. The influence of uniform heating is evident. Both the two-dimensional and three-dimensional components are reduced in amplitude downstream. The Fourier modes for the  $\Theta_0$  and  $\Theta_1$  temperatures are also shown in Figure 6.74. Since the disturbances are created at a suction and blowing strip, the strong temperature perturbations that existed over the heater strip are not seen here. The temperature fluctuations follow the same growth characteristics downstream as the  $U_k$  velocity perturbations.

To more closely examine the influence of uniform passive heating on the fundamental breakdown process, amplitude and phase profiles are shown in Figure 6.75 for each case of Table 6.5. The comparison is made at  $x = 10.65$  ( $n \simeq 389$ ). The amplitude and phase distributions are shown for both the fundamental frequency  $F_1 = 0.588$  and for the first harmonic  $F_2 = 2F_1$  for both the two-dimensional and three-dimensional wave components. The reduction in amplitude is clearly evident for both frequencies. The  $U_0$  velocity with fundamental frequency  $F_1$  shows similar trends as seen in the linear passive control results. The shapes of the amplitude profiles are not strongly affected and the phase jumps remain in approximately the same location. However, the case of  $\Delta\bar{T} = 15^\circ F$  does



not appear to have as strong an influence as might be expected for this high temperature when compared with the  $\Delta\bar{T} = 8^\circ F$  case. For the first harmonic  $F_2$  of the  $U_0$  velocity shown in Figure 6.75b, the amplitude level shows an even stronger reduction since the nonlinear amplitude of the fundamental has been reduced. In addition, the amplitude profiles show a slight change in shape, as a second maximum appears. The phases also show changes, but it is mentioned that the phases become increasingly difficult to compute for lower amplitude waves. In Figure 6.75c, the influence of uniform heating on the  $U_1$  velocity for the fundamental frequency  $F_1$  is shown. Here the influence of uniform heating is more significant. The amplitudes are more strongly reduced than for the two-dimensional component. The amplitude and phase profiles for the first harmonic of the  $U_1$  velocity are shown in Figure 6.75d and the reduction in amplitude is again evident. The location of the maximum is also shifted for  $\Delta\bar{T} = 15^\circ F$ . Finally, Figure 6.75e shows the three-dimensional mean component that has already been discussed. This component is on the same order of magnitude as the three-dimensional component with the fundamental frequency for the uncontrolled case. The shape is slightly different. However, the most dramatic impact is that the time invariant component is not significantly reduced with passive heating when compared with Figure 6.75c.

To explore the behavior of the spanwise periodic mean flow component further, the  $U_1$  mean component is plotted versus the streamwise direction  $x$  in Figure 6.76a. The amplitudes are at the maximum of the  $U_1$  mean velocity. This mean component develops rapidly downstream and shows a significant increase in growth rate towards the end of the periodic computational domain for the uncontrolled flow. However, for the heated boundary layer, this mean component begins to decrease near the end of the solution domain. Thus the passive heating is also

reducing the strength of the longitudinal vortex system. Figure 6.76b and 6.76c show the streamwise amplitude growth for the  $U_0$  and  $U_1$  velocities, respectively, for the fundamental frequency. The two-dimensional amplitude shows a growth downstream for the uncontrolled case, but is clearly damped with passive heating applied. The three-dimensional amplitude without passive control applied shows a reduction in growth downstream and then a very sharp increase in the growth rate as secondary instability strongly sets in. A three-dimensional solution of the Orr-Sommerfeld equation shows that a linear amplitude wave should decay over the Reynolds number region considered here. The strong three-dimensional growth rate at the end of the solution domain is thus attributed to nonlinear effects. With passive heating applied, the three-dimensional amplitude levels and growth rates are reduced. Although the growth rates increase towards the end of the solution domain, they are at a much smaller level than without control applied.

One of the most important questions, in observing the influence of passive heating on the secondary instability process, is whether the three-dimensional growth rates are influenced more directly through the heated base flow or directly through the reduction in the two-dimensional nonlinear amplitudes. Both factors obviously have some influence. It was demonstrated in the linear passive control investigations that surface heating dramatically alters both the two-dimensional and the three-dimensional growth rates. Herbert (1984) has shown that the three-dimensional growth rate is strongly influenced by the two-dimensional amplitude level in his secondary instability theory, i.e., as the two-dimensional amplitude level increases, the three-dimensional growth rate increases. Below a certain threshold amplitude, secondary instability does not set in. Since it is difficult to separate the two factors in the passive control investigations, this question is delayed until the active control results are presented. In active control, the base

flow does not change, except locally over the heater strip, so a comparison will be made between the passive and active control results.

To complete the discussion of the effects of passive control on the early stages of fundamental breakdown, contours of several flow components are shown in different planes in the three-dimensional flow field. First, contours are shown in Figure 6.77 for the disturbed flow in the  $x$ - $y$  plane at the peak position in the spanwise direction and at time step  $L = 800$ . The uncontrolled flow is compared with the flow field resulting with  $\Delta\bar{T} = 15^\circ F$  surface heating applied. The contour levels are the same for both cases so that easy comparison can be made. For the components  $u$ ,  $v$ ,  $\omega_x$ , and  $T$ , the peak plane is at  $z = 0$ , while the peak plane is at  $z = \lambda_z/4$  for the three components  $w$ ,  $\omega_y$ ,  $\omega_z$ . The negative contours are denoted by the dashed lines, while the positive contours are solid. For the uncontrolled flow, the growth in the streamwise direction  $x$  is evident in each flow component. For the purely three-dimensional components  $w$ ,  $\omega_x$ , and  $\omega_y$ , a reduction in growth near  $n = 300$  (or  $x \simeq 10.1$ ) is observable. This is in agreement with Figure 6.76c for the  $U_1$  velocity. The passively controlled flow shows a reduction in all flow components downstream. In particular, the increase in the perturbations away from the wall does not occur with the uniformly heated wall.

The spanwise structure is of course periodic. The flow field looking down at the plate in the  $x$ - $z$  plane is shown in Figure 6.78 for the  $\omega_x$  vorticity. Both the uncontrolled flow and the  $\Delta\bar{T} = 15^\circ F$  passively heated flow are shown at  $m = 6$  (or  $y = 3.186$ ) at time step  $L = 800$ , which is at the maximum of the  $\omega_x$  vorticity in the normal direction. Two spanwise wavelengths are shown. The periodic nature of the flow in both directions is noted. In addition, the decay and then strong amplification for the uncontrolled flow is seen. For the passively controlled flow, the reduction in the amplitude growth downstream is observable.

The final plane to consider is the  $y$ - $z$  plane for a single  $x$  location. The three disturbance vorticity components are shown in Figure 6.79 at  $n = 447$  (or  $x = 11.0$ ). This location is near a maximum in the streamwise direction at time step  $L = 800$ . Both the  $\Delta\bar{T} = 15^\circ F$  uniformly heated case and the uncontrolled case are shown. Again, two spanwise wavelengths are displayed. The structures are significantly reduced with passive control applied. Thus, passive heating applied at the early stages of the fundamental breakdown process shows a significant stabilizing influence.

### 6.3.2 Passive Control of the Subharmonic Breakdown Process

Passive control of the staggered peak-valley breakdown process is now shown and compared with passive control of the fundamental breakdown process. The parameters used in the numerical calculations of subharmonic breakdown are as follows:

$$F_{2D} = 1.24 \quad (\beta_{2D} = 12.4)$$

$$F_{3D} = 0.62 \quad (\beta_{3D} = 6.2)$$

$$\alpha_{rM} = 17.0$$

$$\alpha_{rN} = 17.0$$

$$\gamma = 32.47$$

$$K = 2$$

$$\Delta x = 6.1600 \times 10^{-3}$$

$$\Delta y = 3.3151 \times 10^{-1}$$

$$\Delta t = 5.0671 \times 10^{-3}$$

$$\epsilon_{V_0} = 1.45 \times 10^{-3}$$

$$\epsilon_{V_1} = 6.00 \times 10^{-6}$$

The parameters are chosen to simulate the laboratory experiments of Kachanov and Levchenko (1984) as closely as possible. The two-dimensional fundamental frequency is twice the three-dimensional fundamental frequency. The step size in the streamwise direction  $\Delta x$  is chosen so that there are approximately 30 points per two-dimensional streamwise wavelength and 60 grid points per three-dimensional streamwise disturbance wavelength. The normal step size  $\Delta y$  is determined so that the normal direction spans ten boundary layer displacement thicknesses at the inflow boundary and approximately 4.5 boundary layer displacement thicknesses at the outflow boundary. There are 61 grid points in the normal direction and 901 points in the streamwise direction. The streamwise domain contains approximately 30 two-dimensional disturbance wavelengths and 15 three-dimensional disturbance wavelengths. The right boundary is initially positioned at  $x_{B_i} = 301$  and moves at a speed  $V_B = 0.8$ . The time discretization  $\Delta t$  is chosen so that there are 60 time steps per two-dimensional disturbance period and 120 time steps per three-dimensional disturbance period. Five disturbance periods of the subharmonic wave component (until  $L = 600$ ) are computed. As for the fundamental breakdown case, tests have shown that the parameter  $K = 2$  is sufficient to resolve the spanwise flow in the periodic computational region.

As in the previous section, the disturbances are introduced through a discrete suction and blowing strip at the wall. The same wall boundary conditions are used to create the disturbance waves as for fundamental breakdown and are given by Equation 6.11. The suction and blowing strip is located between  $x_{SB_1} = 50$  and  $x_{SE_1} = 110$  and covers one three-dimensional wavelength. The disturbance amplitudes  $\epsilon v_0$  and  $\epsilon v_1$  are chosen to match the velocity perturbations observed in the experiments.

For the passive control of subharmonic breakdown, the following three cases are considered:

Table 6.6 Parameters for Uniform Passive Control Cases of Subharmonic Breakdown			
$Re_{\delta_1}$ (at $x_0$ )	$\bar{T}_w - \bar{T}_\infty$ ( $^{\circ}F$ )	$\bar{T}_w - \bar{T}_\infty$ ( $^{\circ}C$ )	$A$
650	0.0	0.000	0.0
629	8.0	4.444	4.444/4.444
612	15.0	8.332	8.332/8.332

Again the Reynolds number  $Re_{\delta_1}$  at the inflow boundary is varied so that the physical location at the left boundary remains constant. The same three analogous cases that were simulated in the passive control of fundamental breakdown are simulated here.

Surface representations of the Fourier modes for the uncontrolled flow are shown in Figure 6.80 for the  $U_0$  and  $U_1$  velocities. The  $U_0$  velocity for the subharmonic breakdown appears similar to the  $U_0$  velocity for fundamental breakdown. The  $U_1$  velocity has different characteristics for the subharmonic breakdown. The increased growth towards the end of the domain is similar when compared with Figure 6.73. However, the stationary modulation of the base flow that was present in the fundamental breakdown simulation is not present here. Subharmonic modes do not have a nonperiodic component and hence no longitudinal vortex system. The three-dimensional streamwise wavelength is also seen to be approximately twice the two-dimensional streamwise wavelength ( $\lambda_{x_{3D}} = 2\lambda_{x_{2D}}$ ). The influence of uniform passive heating on the Fourier modes for the  $U_0$  and  $U_1$  velocities for  $\Delta\bar{T} = 15^{\circ}F$  is shown in Figure 6.81. The effect of uniform passive control on the flow is clearly seen. Both the two-dimensional and three-dimensional components show a reduction in amplitude and are decaying downstream. The Fourier

modes for the  $\Theta_0$  and  $\Theta_1$  temperature components are also shown in Figure 6.81. These temperature fluctuations have similar growth characteristics as the velocity perturbations.

The influence of uniform passive heating on the amplitude and phase profiles for the subharmonic breakdown process is shown in Figure 6.82 for each case of Table 6.6. Comparison is made at  $x = 3.0$  ( $n \simeq 255$ ). The amplitude and phase profiles for the fundamental frequency and the first harmonic are shown for both the two-dimensional and three-dimensional wave components. The  $U_0$  velocity with fundamental frequency  $F_1 = F_{2D} = 1.24$  is shown in Figure 6.82a and shows similar trends as seen in the control of fundamental breakdown. However, the passive heating reduces the amplitude levels by a slightly higher level. The subharmonic breakdown is at a different frequency and in a different Reynolds number range than the fundamental breakdown simulations so the stability characteristics of the flow are different. The first harmonic  $F_2 = 2F_1$  of the  $U_0$  velocity is shown in Figure 6.82b. As for the fundamental breakdown cases, the amplitude level shows an even stronger reduction than the fundamental frequency. The change in shape with heating is again noted. The influence of uniform passive heating on the  $U_1$  velocity for the three-dimensional fundamental frequency  $F_{1/2} = F_{3D} = \frac{1}{2}F_1$  is shown in Figure 6.82c. As seen in the control of fundamental breakdown, the three-dimensional amplitudes are reduced by a larger percentage than the two-dimensional components. The shift of the maximum and the appearance of a second maximum is observed. The phase profiles also have slight changes, but again the phase is difficult to compute for low amplitude waves. Finally, the first harmonic of the  $U_1$  velocity is shown in Figure 6.82d for the frequency  $F_{3/2} = 3F_{3D} = \frac{3}{2}F_1$ . The first harmonic of the three-dimensional  $U_1$  velocity has nearly died out.

The amplitude growth downstream for the subharmonic breakdown is shown in Figure 6.83 for both the  $U_0$  and  $U_1$  velocities for the fundamental two-dimensional frequency and the fundamental three-dimensional frequency. The amplitude is plotted at the maximum value in the normal direction. The two-dimensional growth is again similar to that observed in the fundamental breakdown simulations. With uniform heating applied, the disturbances are damped downstream. The three-dimensional growth rates are also similar to the fundamental breakdown process. Without control applied, the amplitudes decay slightly and then a strong increase in growth rate appears. As for the fundamental breakdown case, the three-dimensional Orr-Sommerfeld equation shows that linear three-dimensional disturbances are stable for the Reynolds numbers considered. Therefore, the increased three-dimensional growth is attributed to the occurrence of secondary instability. With passive heating employed, the three-dimensional amplitude levels and growth rates are significantly reduced. The fact that passive control of subharmonic breakdown appears slightly more effective when compared with fundamental breakdown is most likely due to the lower amplitude levels present in these early stages of subharmonic breakdown.

Thus, as was seen for fundamental breakdown, passive heating appears effective in reducing the high three-dimensional growth rates associated with transition. The question again arises as to whether the three-dimensional growth rates are more strongly influenced by the heated base flow or the reduction in two-dimensional amplitudes. This question is once again delayed until the next section on active control of secondary instability.

The physical flow field is now shown in a similar fashion as in the previous section. The disturbed flow in the  $x$ - $y$  plane at the peak position in the spanwise direction is shown at time step  $L = 600$  in Figure 6.83. Contours are shown with



negative contours denoted by dashed lines and positive contours by solid lines. The location of the peak plane for each flow component is the same as in Section 6.3.1. Comparison is shown between the uncontrolled flow field  $\Delta\bar{T} = 0^\circ F$  and the uniformly heated flow  $\Delta\bar{T} = 15^\circ F$ . The contour levels are held constant for each component so that comparison can be made. The strong growth of the flow field downstream is apparent in all flow components. The reduction in growth before the sharp increase is observable in the purely three-dimensional flow components. Comparison between the uncontrolled and passively controlled flow reveals a significant reduction downstream for the heated flow. In fact, the three-dimensional components are dying out. Also observable in these contour plots is the different streamwise wavelengths for the purely three-dimensional flow components. The three-dimensional components of  $u$ ,  $v$ ,  $\omega_z$  and  $T$  are overshadowed by the large two-dimensional amplitude levels. For the  $x$ - $z$  and  $y$ - $z$  planes, the influence of passive heating on the flow field for this early stage of subharmonic breakdown appears very similar to the fundamental breakdown plots and are not shown here for the sake of brevity.

#### 6.4 Active Control of Secondary Instability

The effectiveness of passive heating to control the early stages of the secondary instability process appears very promising. The amplitude levels and growth rates are strongly reduced. As in the control of linear amplitude disturbances, active heating can also be an effective and more efficient means of reducing the amplitude levels of the flow. Active control of the early stages of the secondary instability process is demonstrated in this section. Control of only the fundamental breakdown process is simulated since the influence of passive heating was shown to be very similar for both the fundamental and subharmonic secondary instability

processes. The fundamental breakdown process poses the more difficult case due to the higher amplitudes that are present in the flow.

The same parameters presented in Section 6.3.1 for the passive control simulations are used for the active control simulations, except where noted below. The disturbances are again introduced into the flow using the suction and blowing strip. In addition to this suction and blowing strip, a surface heater strip is located downstream. The arrangement is similar to that shown in Figure 6.67, but the first heater strip depicted in this figure is now a suction and blowing slot. A downstream sensor again monitors the spanwise wall vorticity (or wall shear stress). The phase relationship between the actuator and sensor for controlling the secondary instability process is found using a transfer parameter. The wall boundary conditions for the heater strip are as follows for the undisturbed flow:

$$\Theta_{0,n,0}^i = \sin(\xi_n) \quad (6.12a)$$

and for the disturbed flow:

$$\Theta_{0,n,0}^i = \sin(\xi_n)[1 + \epsilon_{\Theta_0} \sin(\beta_2 D t_l + \Delta\phi_0)] \quad (6.12b)$$

$$\Theta_{1,n,0}^i = \epsilon_{\Theta_1} \sin(\xi_n) \sin(\beta_3 D t_l + \Delta\phi_1) \quad (6.12c)$$

where

$$\xi_n = \frac{x_n - x_{HB_1}}{x_{HE_1} - x_{HB_1}} \pi$$

and

$$x_{HB_1} \leq x_n \leq x_{HE_1}.$$

The functional relationship over the heater strip is now  $\sin(\xi_n)$  instead of  $\sin^2(\xi_n)$ . As previously alluded to, some additional difficulties are encountered in attempting active control of secondary instability. For active control to be effective, the

amplitude levels created at the heater strip must be much larger than for the linear control simulations. These higher amplitude levels are difficult to create with a single heater strip, so the  $\sin(\xi_n)$  distribution is used to allow for more heat input than the  $\sin^2(\xi_n)$  distribution.

Two active control cases are considered. In the first case, control of only the two-dimensional wave is attempted. In the second case, active control of only the three-dimensional wave component is considered. A comparison is then made of the effectiveness of a two-dimensional control input versus a three-dimensional control input. The following table summarizes the control parameters for the two cases:

Table 6.7 Parameters for Active Control of of Fundamental Breakdown								
$\epsilon_{\theta_0}$	$\epsilon_{\theta_1}$	$x_{HB_1}$	$x_{HE_1}$	$\Delta\phi_{2D}$ (rad)	$\Delta\phi_{3D}$ (rad)	$\Delta\phi_{2D}$ (deg)	$\Delta\phi_{3D}$ (deg)	$x_S$
30/31	0	164	192	3.5563	—	203.8°	—	220
0	10/11	150	182	—	6.1781	—	354.0°	219

The first row represents the two-dimensional control case and the second row represents the three-dimensional control case. For the two-dimensional case, the two-dimensional amplitude input  $\epsilon_{\theta_0}$  represents a temperature input of 30°C heating above the freestream with a steady state heating of 31°C. The heater strip covers about one half of the two-dimensional streamwise wavelength. For the three-dimensional control case, the three-dimensional amplitude input  $\epsilon_{\theta_1}$  represents a 10°C heating above the freestream temperature with a steady state overheat of 11°C. The three-dimensional heater strip covers one-half of the three-dimensional streamwise wavelength. The width of the heater strip is chosen based on the receptivity study of Section 6.2.1. Several tests were made to determine an

appropriate heating level. The level of heating appears high, but the heater strip is not in a region of strong amplification or a lower heat input would have been sufficient. The three-dimensional amplitude level that is generated from the heater strip closely matches the amplitude level of the uncontrolled three-dimensional flow for fundamental breakdown. The two-dimensional heat input is not sufficient to create the nonlinear amplitude level existing in the flow. The amplitude generated from the two-dimensional heater strip is about one half as large as the uncontrolled amplitude level. Also, it was found in test calculations that increased heat input did not result in the same increase in disturbance amplitudes. At higher temperatures, the viscosity variation with temperature is not as strong, as seen from Figure 6.2. The higher levels of heating become less effective. However, additional heater strips could be used to bring down the two-dimensional amplitude levels even further.

In Equation (6.13), the phase adjustment is different in form when compared with Equation (6.9) for the linear active control investigations. For these nonlinear simulations, a transfer parameter is used that is based on a method to determine transfer functions that Dittrich (1988) has successfully applied to active control of two-dimensional wave packet disturbances. Although the same method described in Section 6.2.2 could be applied here, the phase is undergoing rapid adjustments downstream, making the previous method less reliable. The transfer parameter is for a single frequency wave and is now described. First, a numerical simulation run is made with the heater strip only and without the suction and blowing strip. The transfer parameter is determined from this run and is defined as follows:

$$\widehat{TP} = \frac{\widehat{\Omega}_{x_h}^1(x_S, y = 0)}{\widehat{T}_h^1(x_{HSC}, y = 0)} \quad (6.14)$$

where  $\hat{\Omega}_{x_k}^1(x_S, y = 0)$  is the complex amplitude of the spanwise wall vorticity at the location of the sensor and  $\hat{T}_k^1(x_{HSC}, y = 0)$  is the complex amplitude of the wall temperature at the center of the heater strip. This transfer parameter is linear and represents the downstream response of the spanwise wall vorticity to the local temperature perturbations. To determine the appropriate phase adjustments that should be made for active control, the spanwise vorticity at the sensor is monitored with just the disturbances emanating from the suction and blowing strip. The complex amplitude for this quantity  $\hat{\Omega}_{x_k}^0(x_S, y = 0)$  is then used to formulate the correct temperature input for the heater strip:

$$\hat{T}_k^2(x_{HSC}, y = 0) = -\frac{\hat{\Omega}_{x_k}^0(x_S, y = 0)}{\overline{TP}}. \quad (6.15)$$

The minus sign denotes a 180° phase adjustment necessary for cancellation. From this complex temperature, amplitude and phase adjustments to the heater strip can then be determined. The amplitude levels, however, are not adjusted in the active control simulations because unreasonably high temperature inputs would be required. The phases shown in Table 6.7 are determined from Equation 6.15. The phase is calculated from

$$\Delta\Phi_k = \tan^{-1} \left( \frac{\Im(\hat{T}_k^2)}{\Re(\hat{T}_k^2)} \right). \quad (6.16)$$

The procedure for determining the transfer parameter is carried out for both the two-dimensional and three-dimensional heater strips. Results of both simulations are now shown.

First, the Fourier modes resulting from the two-dimensional active control investigations of the fundamental breakdown process are shown in Figure 6.85. Both the  $U_0$  and  $U_1$  velocities and  $\Theta_0$  and  $\Theta_1$  temperature fluctuations are shown in surface representations at time step  $L = 800$ . Figure 6.86 shows the same

flow quantities for the three-dimensional active control numerical simulations. In comparing the results with the uncontrolled flow shown in Figure 6.73 and the passively controlled flow of Figure 6.74, several observations can be made. First, the two-dimensional control input causes a reduction downstream in amplitudes of the two-dimensional  $U_0$  velocity. The three-dimensional control input appears not to have a significant impact on the  $U_0$  velocity. Secondly, in comparison with the uncontrolled  $U_1$  velocity, both the two-dimensional and three-dimensional heat inputs result in a reduction in the  $U_1$  velocities. The presence of the spanwise periodic stationary modulation is again seen. In Figure 6.85, the large temperature fluctuations over the heater strip for  $\Theta_0$  is seen for the two-dimensional active control case. The temperature distribution for  $\Theta_1$  is similar to that observed in the passive control simulations. These three-dimensional temperature perturbations have been created through nonlinear interactions, but are one order of magnitude smaller than those observed in the passive control simulations. Figure 6.86 shows a similar picture for the three-dimensional heat input. The three-dimensional temperature  $\Theta_1$  is very large over the heater strip. The  $\Theta_0$  disturbance temperature again appears similar to the  $\Theta_0$  temperature of the passive control investigations, but is one order of magnitude smaller.

To more closely examine the effect of active control on the fundamental breakdown process, amplitude profiles are shown in Figure 6.87 for both active control cases, as well as the uncontrolled case presented in Section 6.3.1. Comparison is made at  $x = 10.65$  ( $n \simeq 389$ ). Both the amplitude at the fundamental frequency  $F_1 = 0.588$  and the first harmonic  $F_2 = 2 F_1$ , are shown for both the two-dimensional and three-dimensional wave components. The first observation is that the  $U_0$  velocity with both fundamental frequency  $F_1$  and the first harmonic are reduced even for the three-dimensional active control investigation. Although

only a three-dimensional temperature perturbation has been input at the heater strip for the three-dimensional active control case, a steady state component has also been introduced. This steady state component remained very local to the heater strip in the linear active control investigations due to the lower heating levels required. The steady state overheat in the nonlinear investigations is larger and convects further downstream. An analysis of the mean  $u$  velocity has revealed fuller velocity profiles over the heater strip and downstream of the heater strip. This fuller profile is more stable. Therefore, the two-dimensional amplitude is also slightly controlled with three-dimensional active control applied. This provides an additional enhancement in stability. Also, it is noted that the two-dimensional active heating has caused a significant reduction in amplitude level of both the fundamental frequency and the first harmonic. The important aspect to consider is the influence of active control on the three-dimensional components. Considering Figure 6.87c and 6.87d, the three-dimensional amplitude levels for both the fundamental frequency and the first harmonic are significantly reduced with active control applied. The purely three-dimensional control input shows a slightly stronger reduction than two-dimensional control. The three-dimensional mean component for the  $U_1$  velocity is shown in Figure 6.87e and shows an almost identical reduction for both control cases.

A better picture of the influence of active control on the fundamental breakdown process can be obtained by looking at the amplitude versus the stream-wise direction  $x$ . This amplitude growth for the  $U_k$  velocities at the maximum value in the normal direction are shown in Figure 6.88 for the fundamental frequency  $F_1$  for both active control cases. A significant reduction in amplitude and a nearly neutral growth rate downstream of the heater strip are seen. For the

three-dimensional control cases, the  $U_0$  velocity shows the slight reduction in amplitude downstream, but a positive growth rate still prevails. In contrast, passive control results in decaying amplitudes downstream as shown in Figure 6.76. The three-dimensional downstream growth for the fundamental frequency shows the best overall picture of the influence of the two active control cases. First, the three-dimensional active control input results in an immediate suppression of the  $U_1$  velocity. In the linear active control results, the immediate attenuation of the waves was also observed. The three-dimensional amplitude level is significantly reduced enough to delay the strong growth of the secondary instability process. For the two-dimensional control case, the  $U_1$  velocity is not significantly reduced until about  $x = 10.2$ . The two-dimensional amplitude level has been reduced enough to delay the large growth of the uncontrolled case. However, at the end of the integration domain, the  $U_1$  velocity is beginning to show a higher growth rate for the two-dimensional active control case than is seen for the three-dimensional active control case or in the passive control simulations.

Now an attempt is made to answer the question posed in the previous section, i.e., are the three-dimensional growth rates more strongly influenced by the heated mean flow in passive control or directly through the reduction in the two-dimensional amplitude level. To heuristically answer this question, the three-dimensional amplification rate is shown in Figure 6.89 versus the two-dimensional amplitude at  $x = 10.65$ . The amplitude and amplification rate are calculated at the maximum of the  $U_k$  velocities. The uncontrolled case, as well as the two passive control cases are shown for the fundamental breakdown simulations. A curve fit has been drawn through these three points. In addition, the two-dimensional and three-dimensional active control cases are shown. With a subsequent reduction in two-dimensional amplitude level for each level of passive heating employed,



the three-dimensional growth rates are reduced. However, there appears to be a diminishing return for the higher heating case of  $\Delta\bar{T} = 15^\circ F$ . Comparison is now made to the two-dimensional active control case with the dashed curve fit. For the two-dimensional active control simulation, the reduction in two-dimensional amplitude is due to wave superposition, although a slight reduction is caused through the steady state heating over the heater strip. The reduction in the three-dimensional growth rate is almost as large as for passive heating, but not quite the same level of reduction is achieved. The difference between the amplification rate of the two-dimensional active control case and the curve fit for the passive control cases is attributed to the more stable mean flow base profile. Thus the overriding cause for the reduction in three-dimensional growth rates with passive heating applied to the nonlinear secondary instability process is the reduction in the two-dimensional amplitude and a smaller additional enhancement in stability is derived directly from the stabilizing influence of the heated mean flow.

It is also noted in Figure 6.89 that the three-dimensional active control case results in a similar reduction in growth rate as for the  $\Delta\bar{T} = 8^\circ F$  passive heating case. To make an accurate comparison between passive and active heating, the heat transferred at the wall must be considered. The heat transfer is calculated in the same manner as previously shown for the linear control calculations. The same three-dimensional amplification rates are shown in Figure 6.90 versus the heat input at the wall  $Q$  as were shown in Figure 6.89. For the uncontrolled case, no power input is required. Although the  $\Delta\bar{T} = 15^\circ F$  passive heating case results in the smallest three-dimensional amplification rate, it requires almost four times as much power as the  $\Delta\bar{T} = 8^\circ F$  passive heating case. The power required for the three-dimensional active control is slightly smaller than for the two-dimensional active control case considered here. The  $\Delta\bar{T} = 8^\circ F$  passive

heating requirement is nearly the same as the two-dimensional active control heat input. However, if additional heater strips are used to further bring down the two-dimensional amplitude level, a larger power requirement would be necessary. Overall, the three-dimensional active control case appears the most promising in terms of reduction in the three-dimensional amplification rate and the small amount of power required to achieve this reduction.

Finally, contours of the flow component in different planes in the physical three-dimensional flow field are shown for the two active control cases. The same contour levels and physical locations are chosen as was shown in the passive control results for fundamental breakdown so that final comparison between the two control techniques can be made. First, Figure 6.91 shows the disturbed flow in the  $x$ - $y$  plane at the peak position in the spanwise direction at time step  $L = 800$ . Both the two-dimensional and three-dimensional active control cases are shown. In comparing with Figure 6.77, the reduction in the perturbations downstream for the components with large two-dimensional amplitude levels ( $u$ ,  $v$ ,  $\omega_z$ , and  $T$ ) is observable for the two-dimensional active control case. These same components appear only slightly influenced for the three-dimensional active control case. The purely three-dimensional components  $w$ ,  $\omega_x$ , and  $\omega_y$  exhibit a significant reduction in amplitude level and growth rate for both active control cases. However, the three-dimensional active control case exhibits a smaller growth rate at the end of the periodic solution domain. The large gradients in temperature over the heater strips are also observable.

The spanwise structure in the  $x$ - $z$  plane is shown in Figure 6.92 for the  $\omega_x$  vorticity. Again the two-dimensional and three-dimensional active control cases are shown at  $y = 3.186$  and time step  $L = 800$ . Two spanwise wavelengths are shown. In comparing the resultant flow with Figure 6.78 for the uncontrolled case,

the influence of active control is again obvious. It should be noted here that the influence of the heater strip has reached to  $n \simeq 455$  only and the flow downstream of this location is not yet periodic. In comparing with the uncontrolled flow, the reduction in amplitude level and growth is apparent.

The last plane to consider is the  $y$ - $z$  plane at  $n = 447$ . The three disturbance vorticity components are shown in Figure 6.93 at  $L = 800$ . Both the two-dimensional and three-dimensional active control cases show a significant reduction in strength when compared with the uncontrolled flow shown in Figure 6.79. Once again, the stronger reduction in the purely three-dimensional components  $\omega_x$  and  $\omega_y$  is seen with three-dimensional active control applied, while the stronger reduction in the two-dimensional flow is seen for  $\omega_z$  with two-dimensional active control applied.

## CHAPTER 7

## CONCLUSIONS

A numerical method has been developed for studying the influence of control in the three-dimensional boundary layer. Passive and active methods of control using surface heating techniques have been numerically investigated. Control of linear amplitude two-dimensional Tollmien-Schlichting waves and three-dimensional oblique waves is achieved with uniform passive heating applied. The amplitude levels and growth rates are reduced. Nonuniform surface heating has been shown to be an even more efficient means of controlling linear amplitude disturbance waves. The amplitude levels are reduced more with nonuniform surface heating than with uniform wall heating. However, the effectiveness of a particular nonuniform temperature distribution was shown to be dependent on the location of the reference point.

Comparison of the passive control investigations was made with linear theory, nonparallel theory, and experiments. The agreement with the linear theory of Lowell (1974) was good. The results agreed qualitatively with the nonparallel theory of Nayfeh and El-Hady (1980) and Asrar and Nayfeh (1985), but the growth rates of the nonparallel theory were consistently higher than the growth rates from the numerical simulations. However, differences were shown to exist between the unheated nonparallel theory of Nayfeh and El-Hady (1980) with the unheated nonparallel theory of Gaster (1974). The nonparallel theory of Gaster (1974) showed very good agreement with the unheated Navier-Stokes simulations. Agreement with the experiments of Strazisar, Reshotko, and Prah1 (1977) and Strazisar and Reshotko (1978) was quite good at a moderate frequency, but the

experimental trends at a higher frequency were not predicted by the numerical simulations. However, neither the linear theory nor the nonparallel theory predicted the experimental trends well at the higher frequency. The calculations presented here are not considered conclusive enough to disqualify various theories. More extensive calculations are necessary to provide a thorough comparison with the theories.

Numerical simulations of active control of linear amplitude two-dimensional Tollmien-Schlichting waves and three-dimensional oblique waves was also shown to be an effective method of control. Localized periodic wall temperature perturbations antiphased with the disturbances present in the flow resulted in a significant reduction in the amplitude levels in the flow. The heat input required for active control was three times less than that required for passive control with the same resultant decrease in amplitude level.

A receptivity study of a surface heater strip shows that smaller heater strips are more receptive in that they maximized the disturbance levels generated in the flow field. It was also shown that the heater strip generates disturbance waves in less than one wavelength. It was also demonstrated that the localized temperature perturbation create steep localized gradients in the spanwise wall vorticity.

Control of the secondary instability process also proved to be effective. Uniform passive heating of both the fundamental and subharmonic breakdown processes resulted in reductions in the amplitude levels and growth rates for both the two-dimensional and three-dimensional components. The level of control achieved was similar for both breakdown processes. The three-dimensional growth rates were significantly reduced and it was heuristically demonstrated that the main influence of passive heating on the secondary instability process is to reduce the

two-dimensional nonlinear amplitudes, which in turn causes a reduction in the three-dimensional growth rates. The heated mean flow provides a stabilizing influence on the three-dimensional growth rates as well, but is smaller than the influence of the two-dimensional amplitudes levels.

Finally, numerical simulations of active control of the fundamental breakdown process showed active control to be a viable technique for control at the early stages of nonlinear secondary instability. Both two-dimensional and three-dimensional localized temperature perturbations were used with the three-dimensional control input providing a more stabilizing influence with a smaller amount of heat input required. Due to the high level of heating required to bring down the two-dimensional nonlinear amplitudes, two-dimensional active control is less efficient in terms of power input required. Three-dimensional active control was also more efficient when compared with passive control of the secondary instability process.

It is felt that future work should focus on several points. First, computational speed could be improved by using an explicit method so that the nonlinear terms do not need to be updated at every iteration step. In addition, the line iteration process, which requires the reduction of the tridiagonal system of equations could be vectorized. Also, the method should be programmed pseudospectrally for efficiency when more spanwise modes are used. Radiation conditions at the downstream boundary should also be explored that inhibit reflections so that a smaller computational domain can be employed.

Future work should also focus on simulations of transition control of three-dimensional wave packet disturbances with surface heating instead of the monochromatic forcing studied here. The frequency spectrum in natural transition

is broad band and control of wave packets is more realistic of the control required in natural flow environments.

The work should also be extended to control the three-dimensional breakdown process further downstream. This would require more spanwise modes and necessitate the change to a pseudospectral method.

Finally, numerical simulations of control by suction and blowing or pressure gradients should be considered. The current numerical algorithm could be used to investigate these control processes. These other modes of control could prove more effective when compared with passive and active control by surface heating. A combination of these different control methods could also lead to the most efficient design.

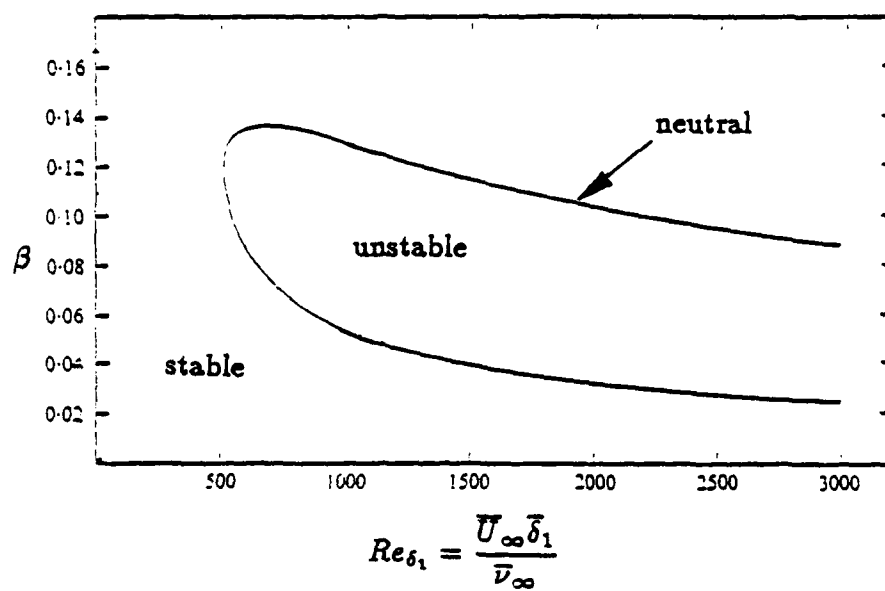


Figure 1.1 Spatial stability diagram for a flat plate boundary layer (from Jordinson (1970))



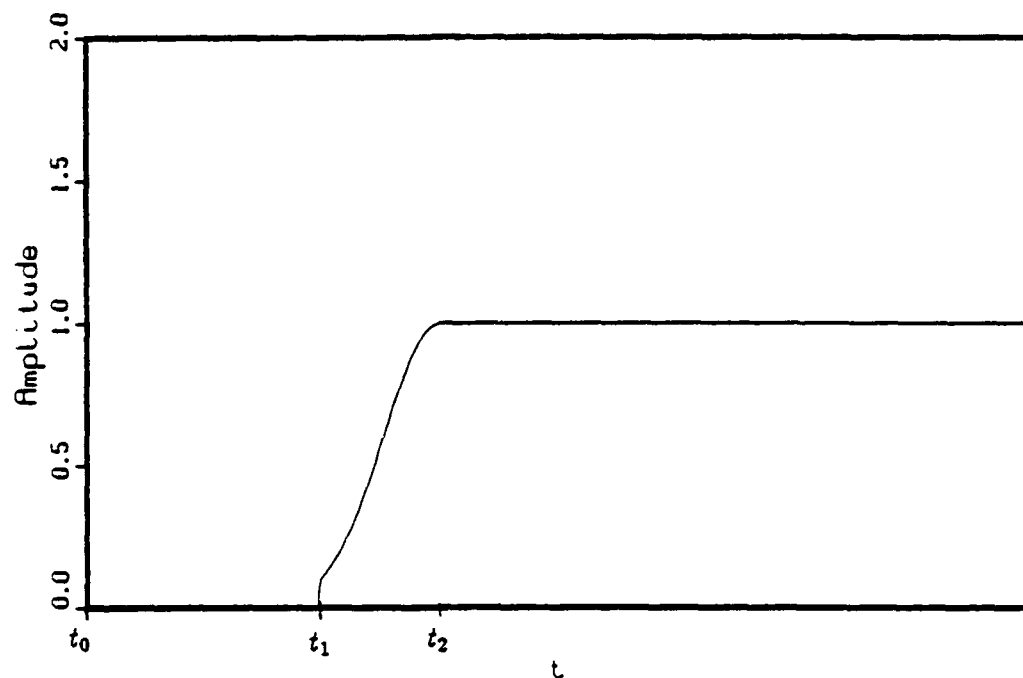


Figure 4.1 Time history of input disturbance for passive control simulations

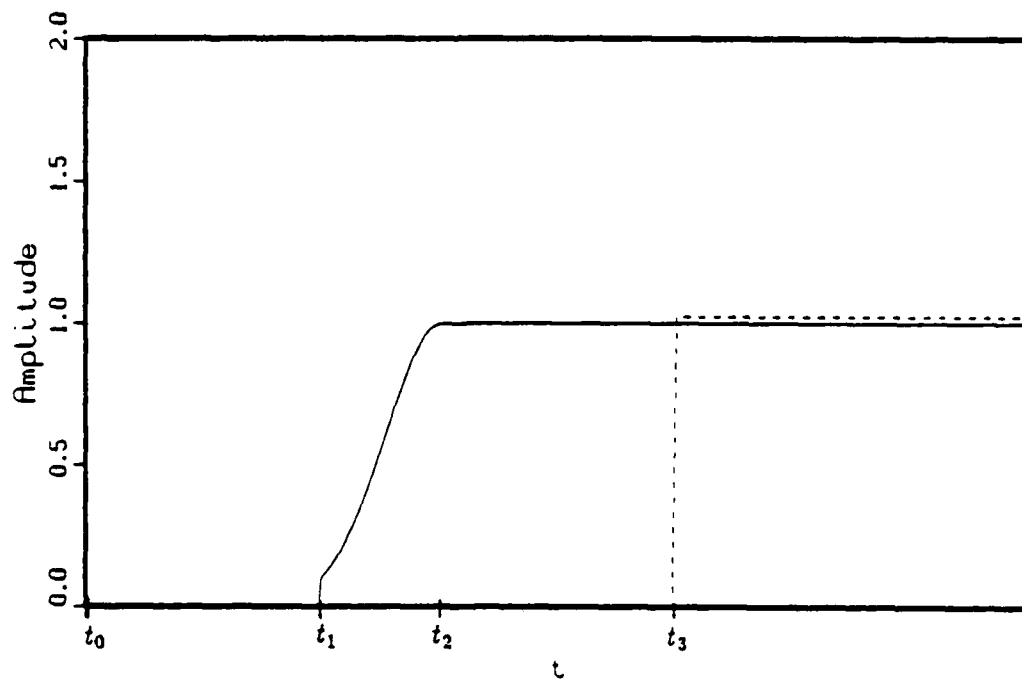


Figure 4.2 Time history of input disturbances for active control simulations

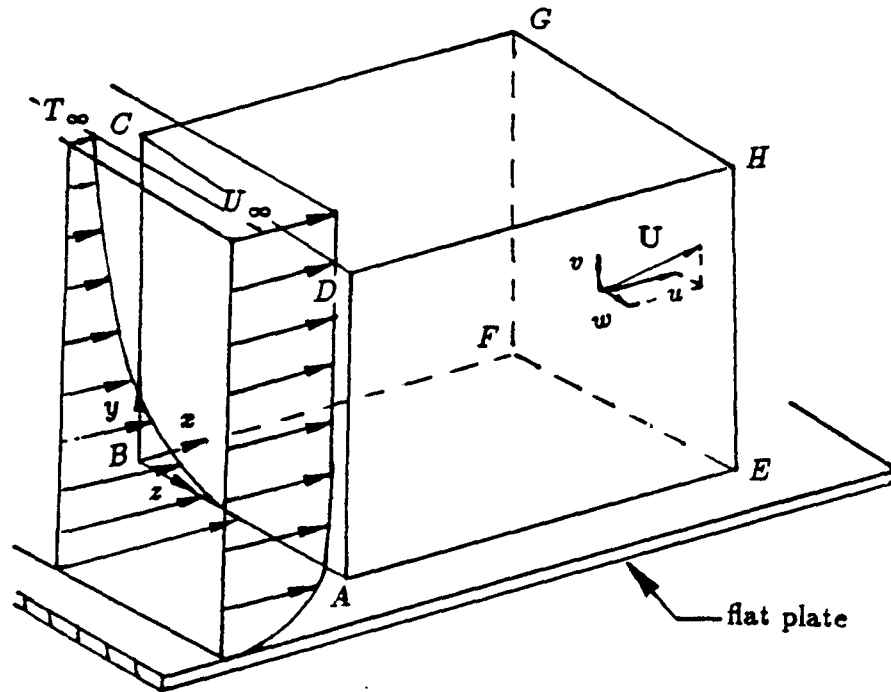


Figure 4.3 Spatial domain and coordinate system

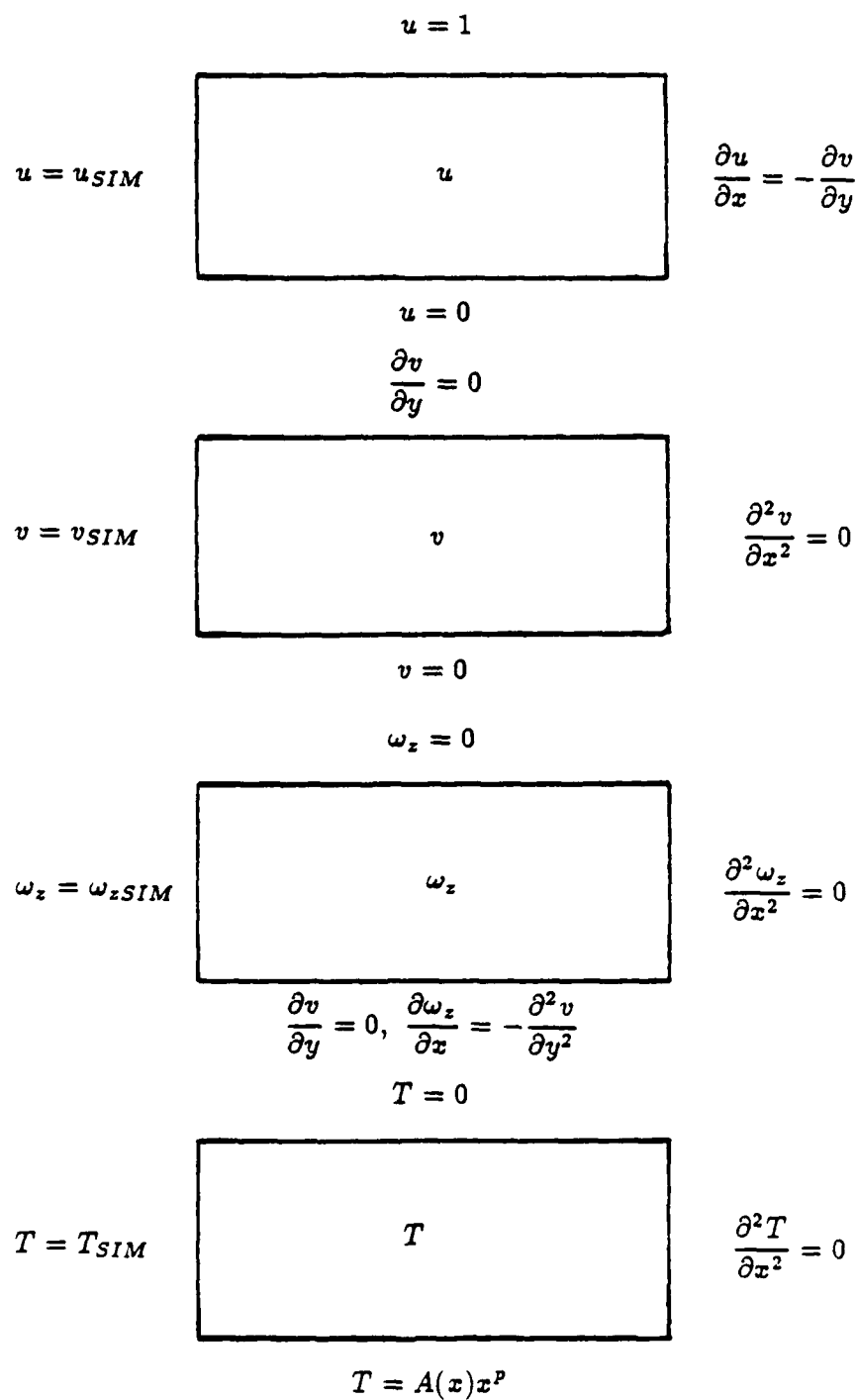
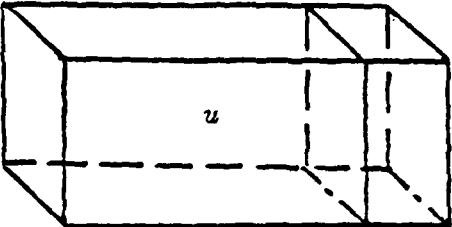


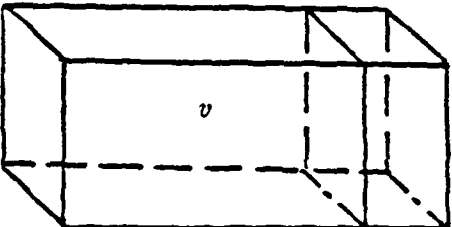
Figure 4.4 Boundary conditions for the undisturbed flow

$$\frac{\partial v}{\partial y} = -\frac{\alpha^*}{\sqrt{Re}}(v - v_{ST})$$

$u = u_{SIM}$ 

 $\frac{\partial^2 u}{\partial x^2} = \frac{\partial^2 u_{ST}}{\partial x^2} - \alpha_{rN}^2 u$

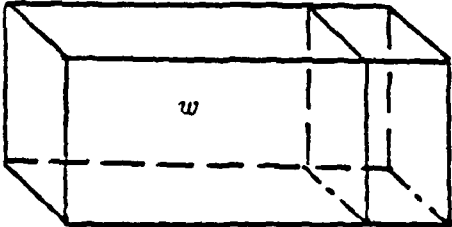
$u = 0$

$$\frac{\partial v}{\partial y} = -\frac{\alpha^*}{\sqrt{Re}}(v - v_{ST})$$

$v = v_{SIM}$ 

 $\frac{\partial^2 v}{\partial x^2} = -\alpha_{rN}^2 v$

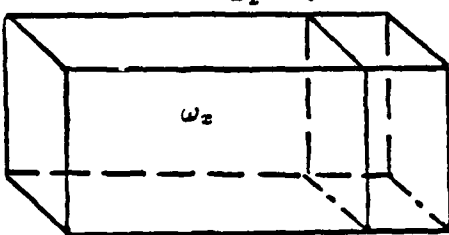
$v = v_w$

$$\frac{\partial v}{\partial y} = -\frac{\alpha^*}{\sqrt{Re}}(v - v_{ST})$$

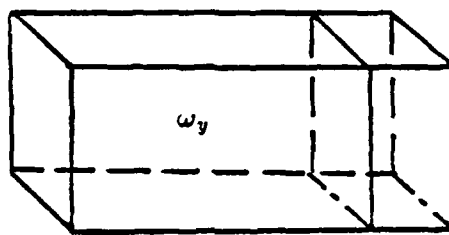
$w = 0$ 

 $\frac{\partial^2 w}{\partial x^2} = -\alpha_{rN}^2 w$

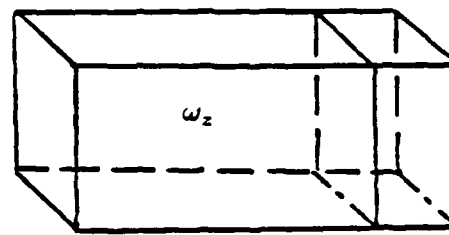
$w = 0$

Figure 4.5 Boundary conditions for the disturbed flow

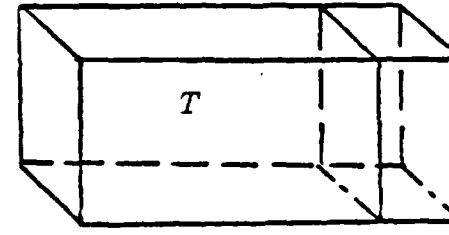
$\omega_x = 0$ 

 $\frac{\partial^2 \omega_x}{\partial x^2} = -\alpha_{rN}^2 \omega_x$ 

$$\frac{\partial^2 \omega_x}{\partial x^2} + \frac{\partial^2 \omega_x}{\partial z^2} = -\frac{\partial^2 \omega_y}{\partial x \partial y} + \frac{1}{Re} \frac{\partial}{\partial z} (\nabla_1^2 v)$$

$\omega_y = 0$ 

 $\frac{\partial^2 \omega_y}{\partial x^2} = -\alpha_{rN}^2 \omega_y$

$\omega_z = \omega_{zSIM}$ 

 $\frac{\partial^2 \omega_z}{\partial x^2} = -\alpha_{rN}^2 \omega_z$ 

$$\frac{\partial v}{\partial y} = 0, \quad \frac{\partial \omega_z}{\partial x} = \frac{\partial \omega_x}{\partial z} - \frac{1}{Re} \nabla_1^2 v$$

$T = T_{SIM}$ 

 $\frac{\partial^2 T}{\partial x^2} = -\alpha_{rN}^2 T$ 

$$T = A(x)x^p + T_w$$

Figure 4.5 continued

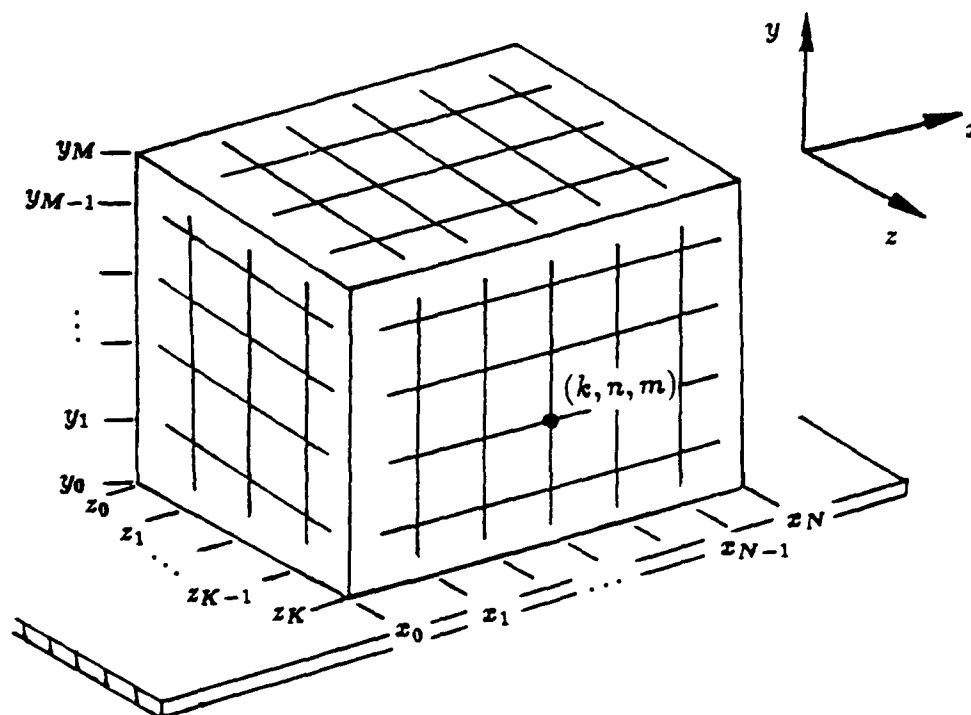


Figure 5.1 Spatial computational domain

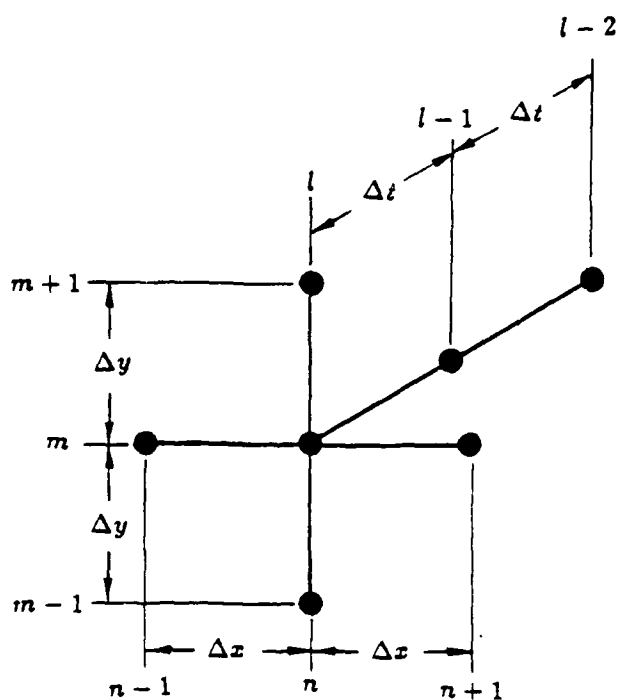
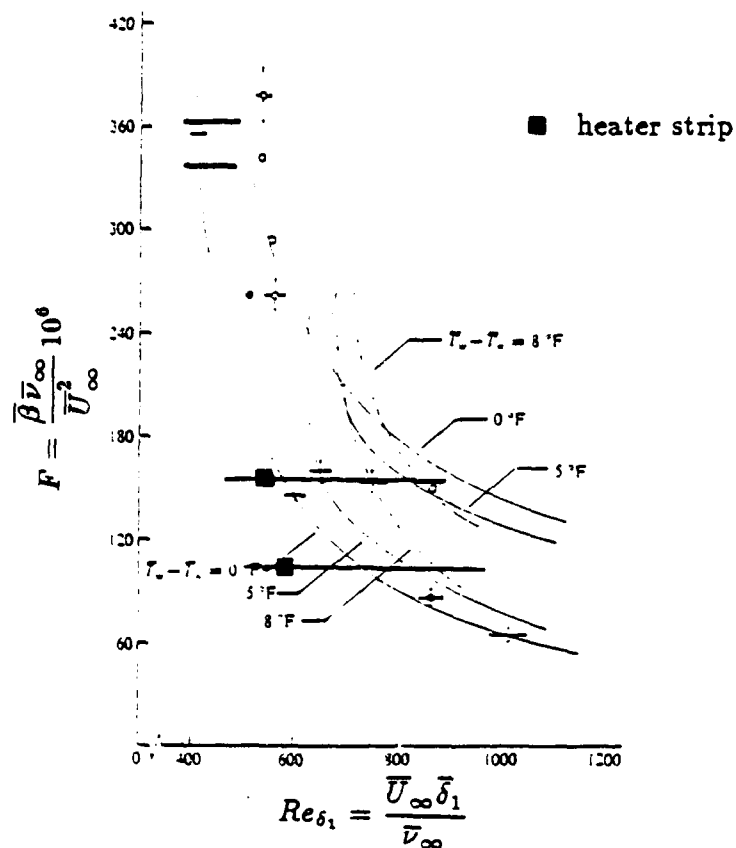
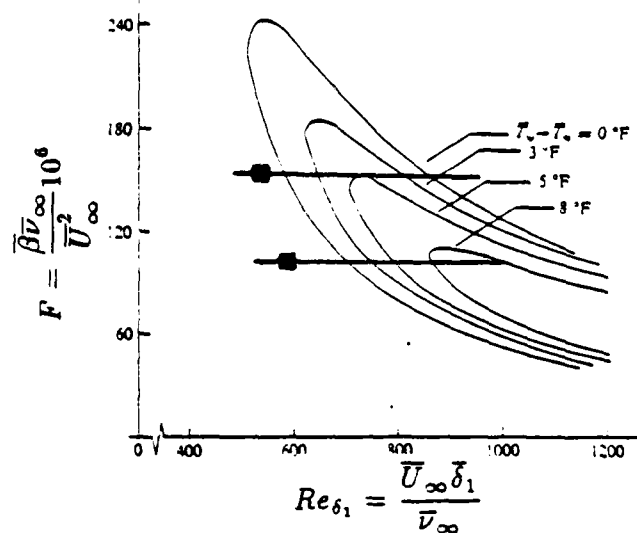


Figure 5.2 Computational molecule



a) stability diagram from experiments of Strazisar, Reshotko, and Prahl (1977)



b) stability diagram from linear stability theory of Lowell (1974)

Figure 6.1 Solution domain for linear Navier-Stokes calculations

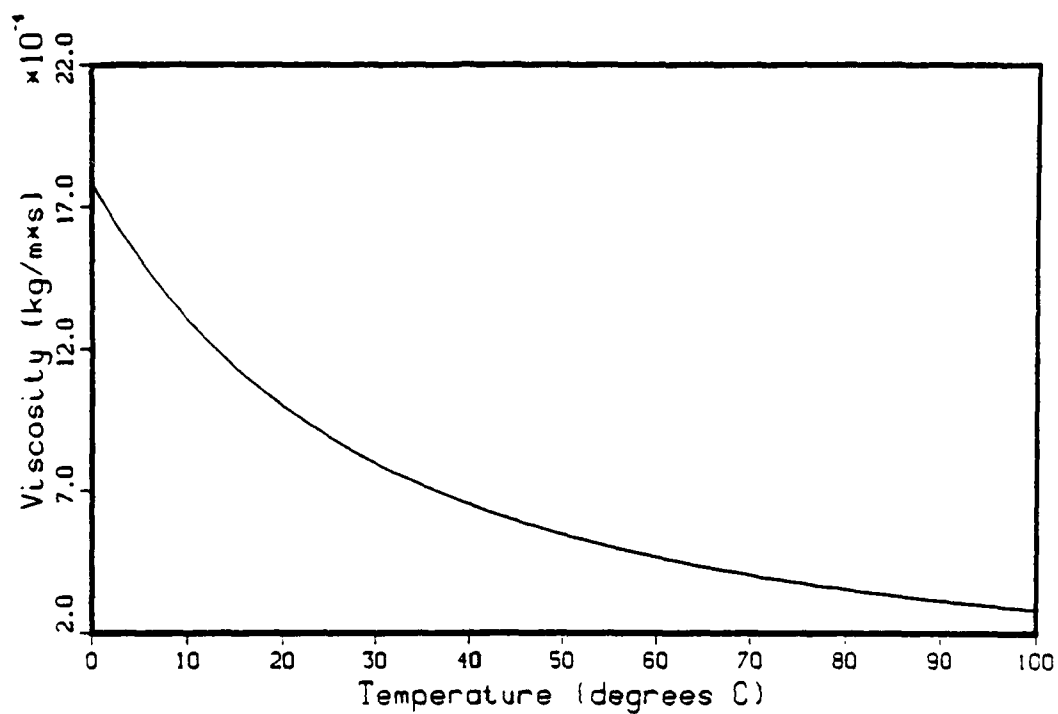


Figure 6.2 Viscosity variation with temperature

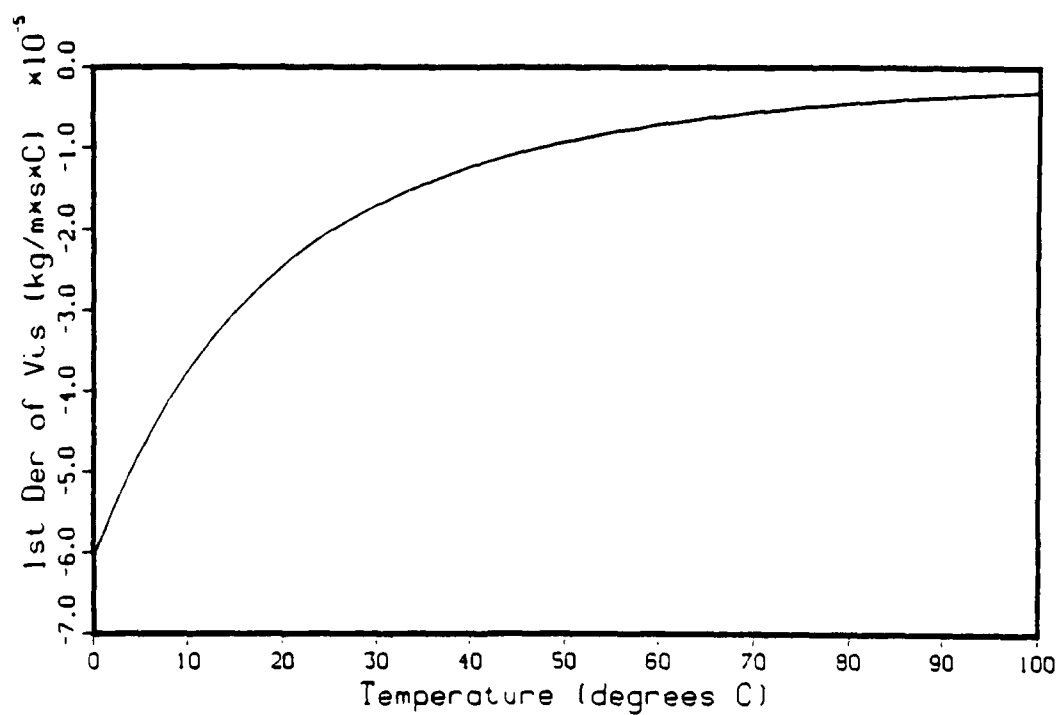


Figure 6.3 First derivative of viscosity versus temperature



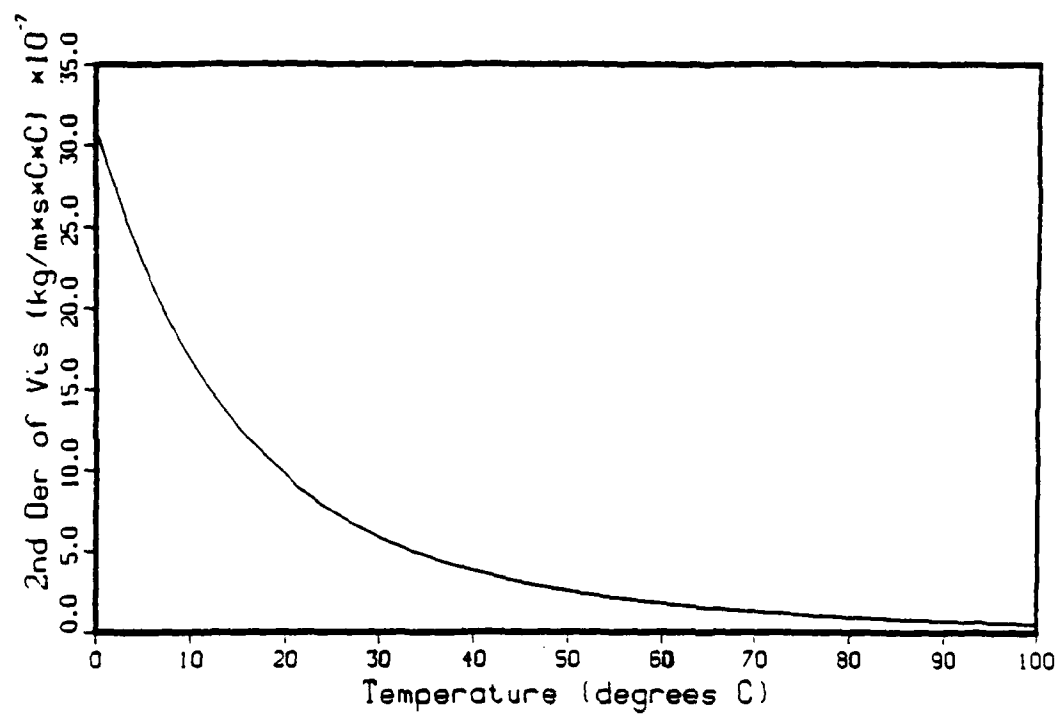
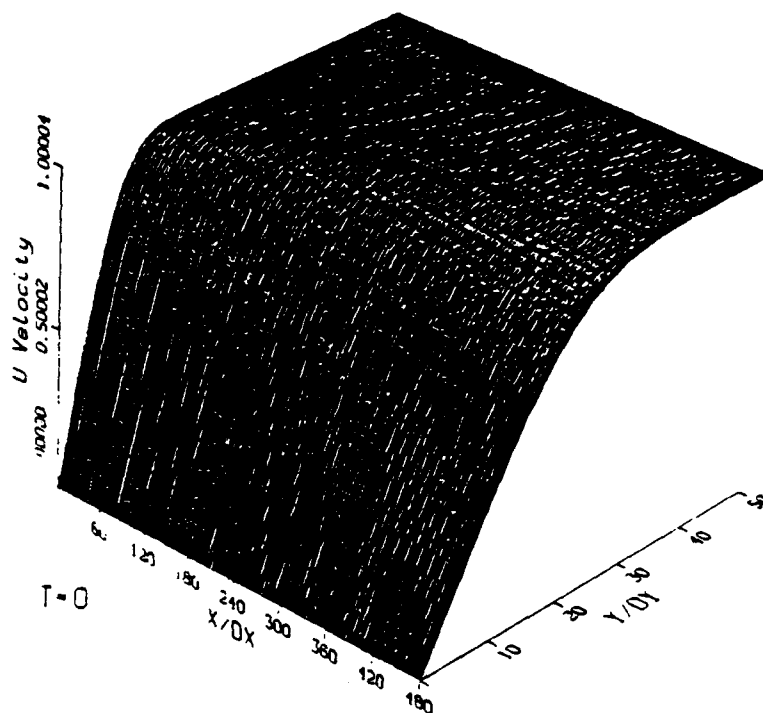
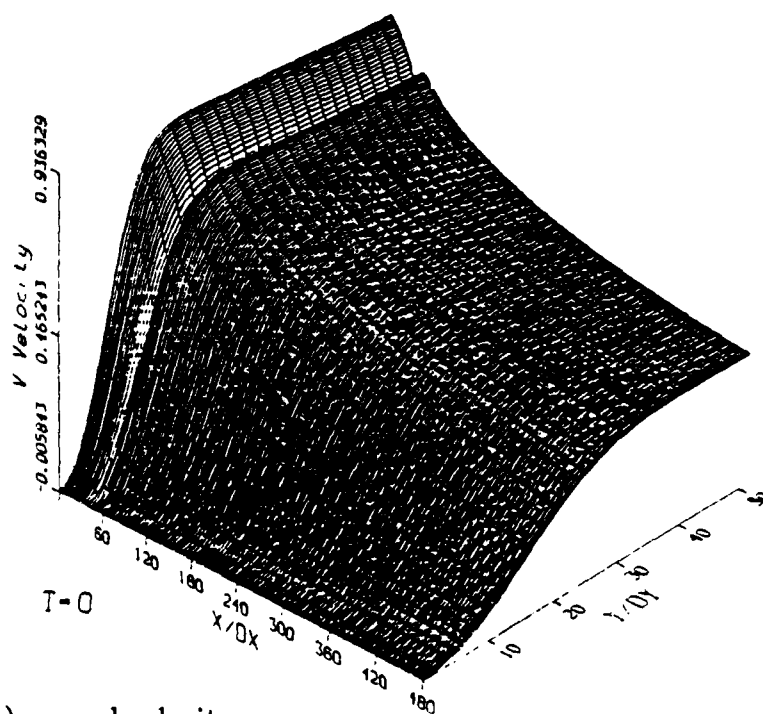
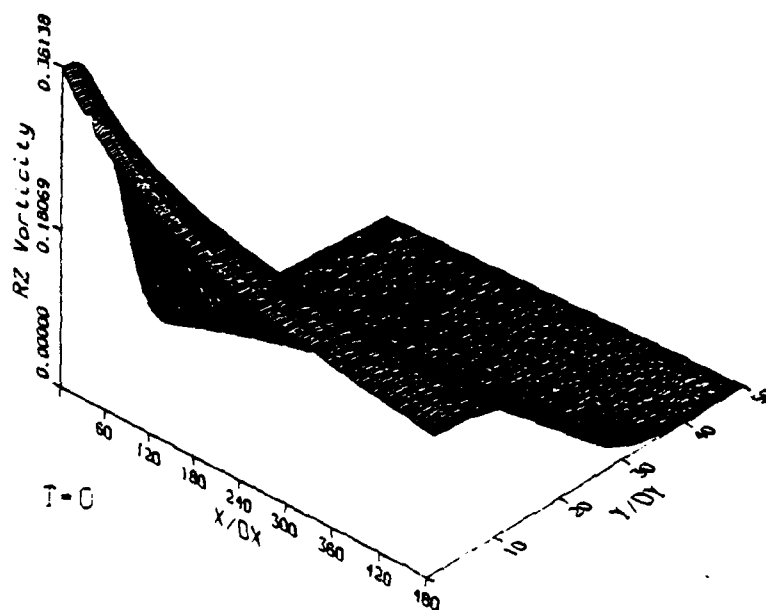


Figure 6.4 Second derivative of viscosity versus temperature

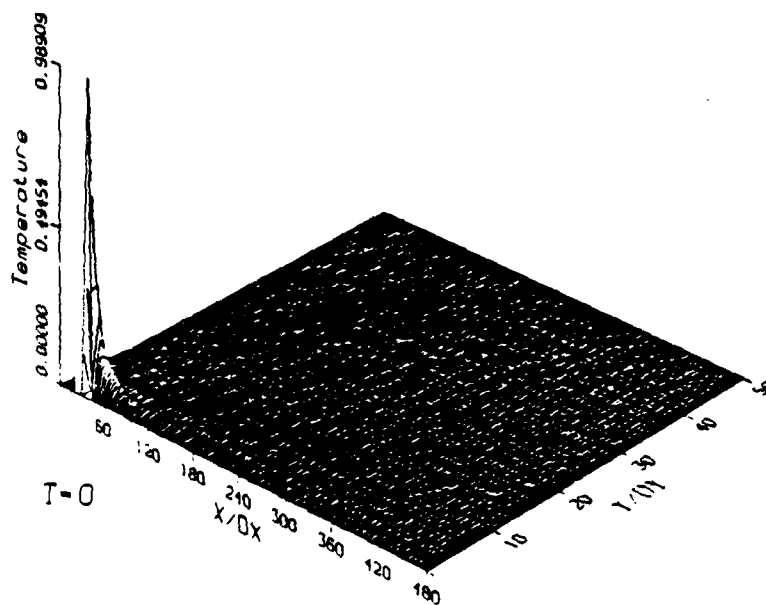


a) streamwise velocity

b) normal velocity,  $v_{ST}$ Figure 6.5 Undisturbed flow without control applied,  $F = 1$



c) spanwise vorticity,  $\omega_{zST}$



d) temperature,  $T_{ST}$

Figure 6.5 continued

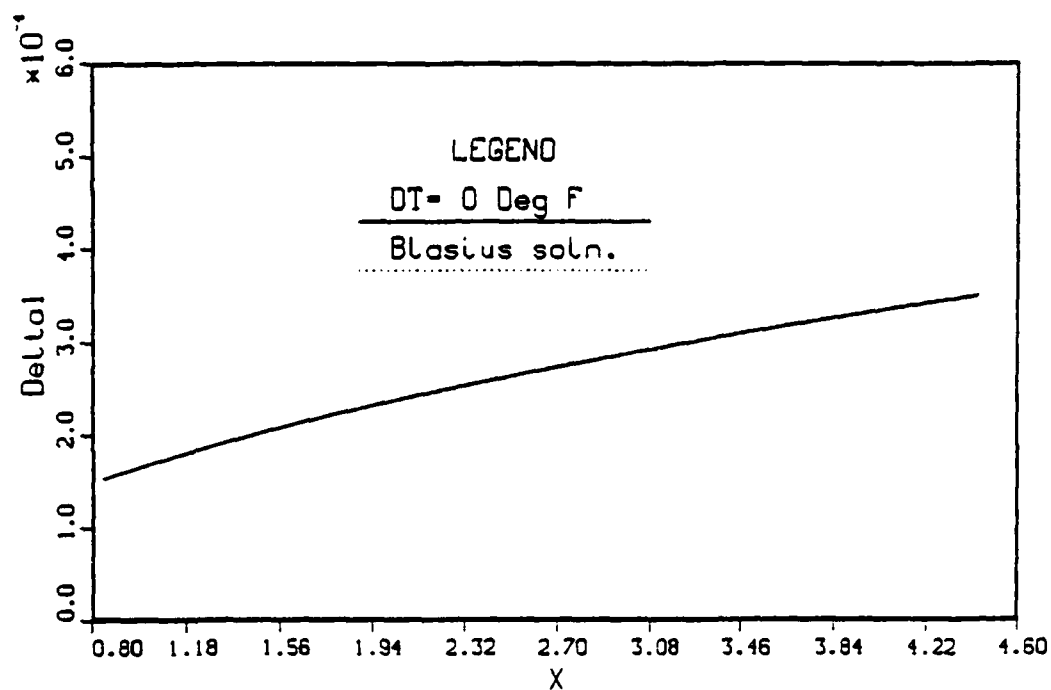


Figure 6.6 Growth of undisturbed boundary layer without control applied,  $F = 1$

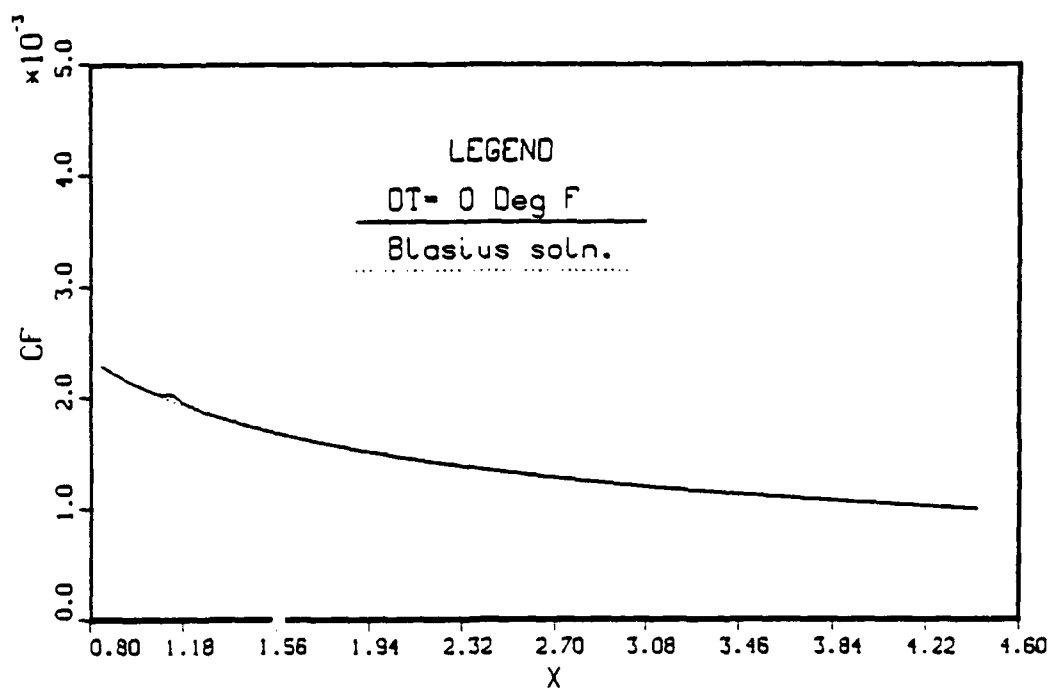
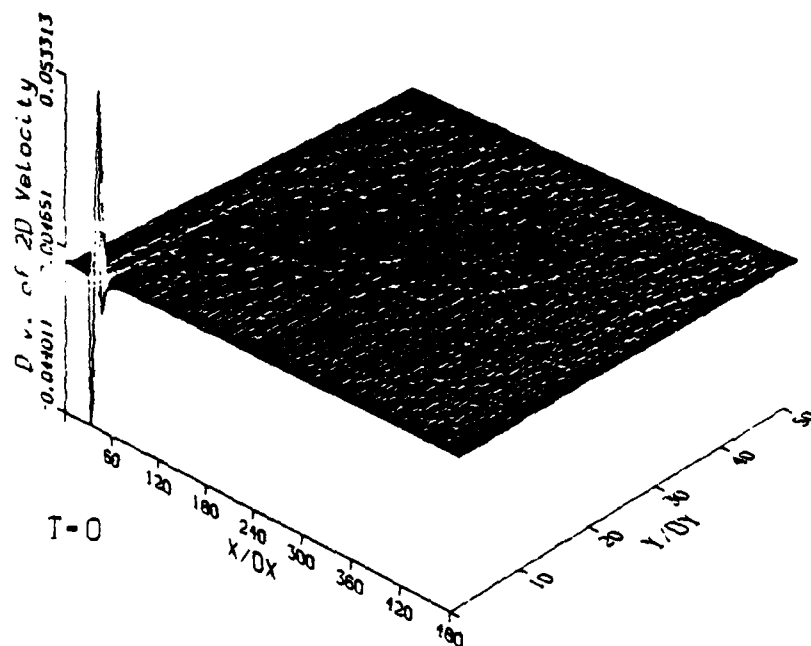
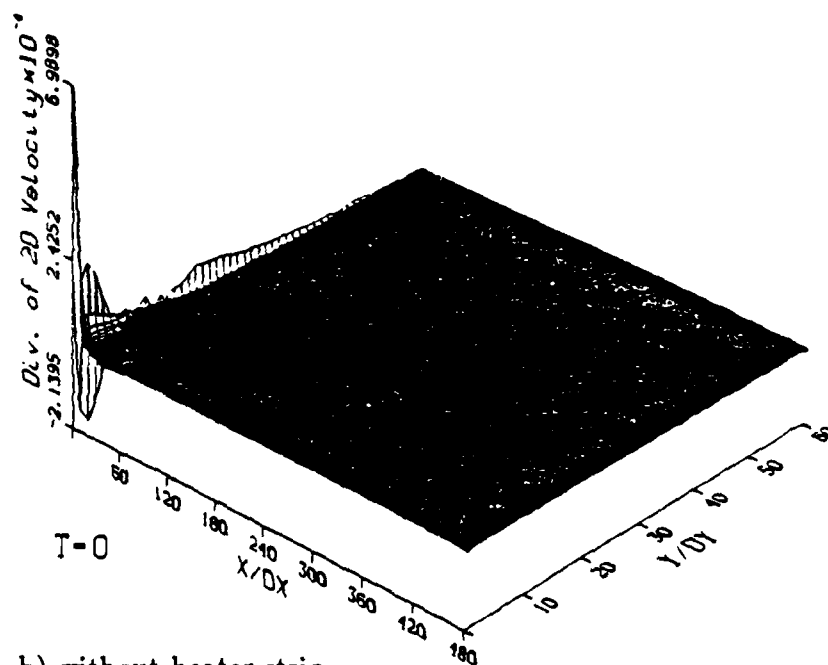


Figure 6.7 Comparison of skin friction without control applied,  $F = 1$

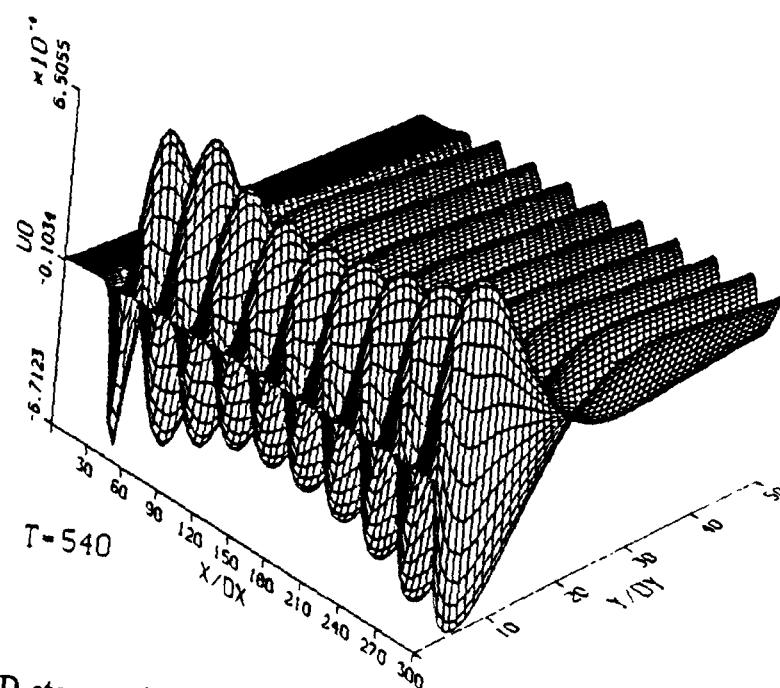
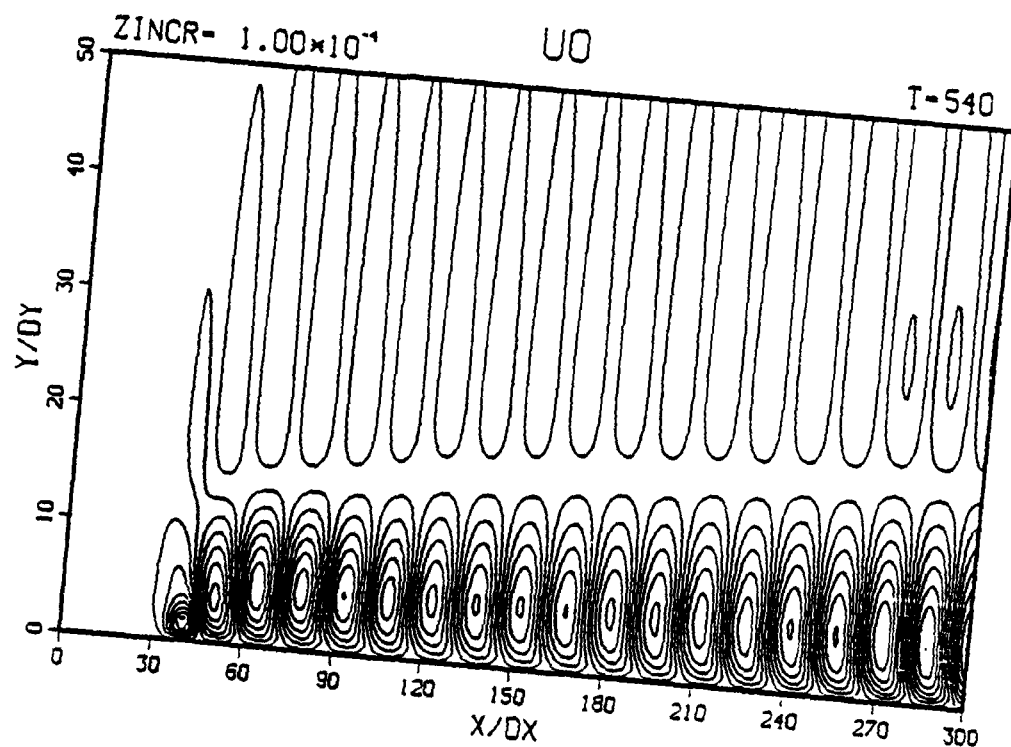


a) with heater strip



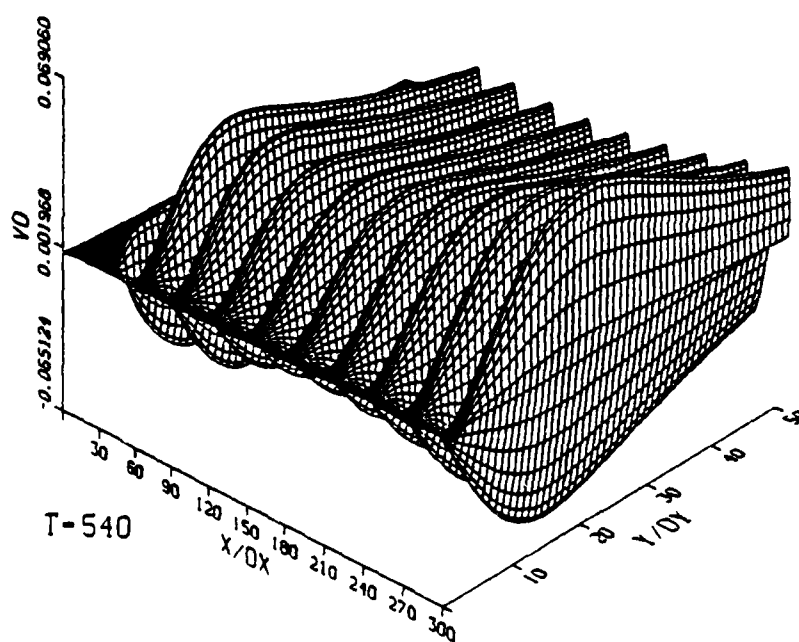
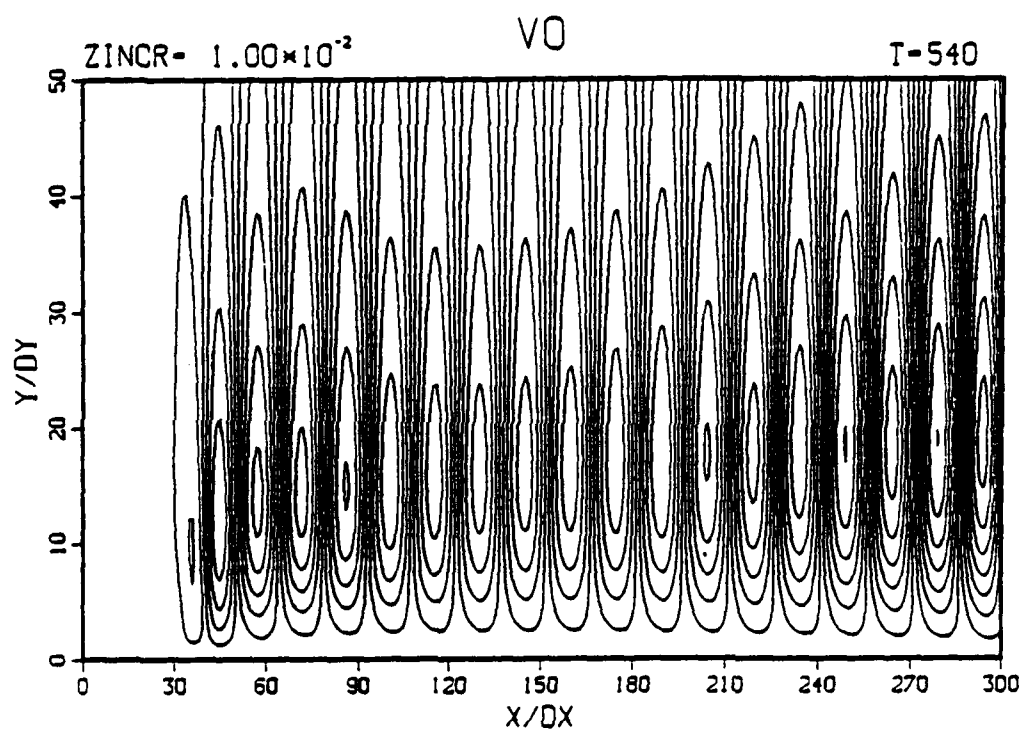
b) without heater strip

Figure 6.8 Velocity divergence of the undisturbed flow without control applied,  
 $F = 1$



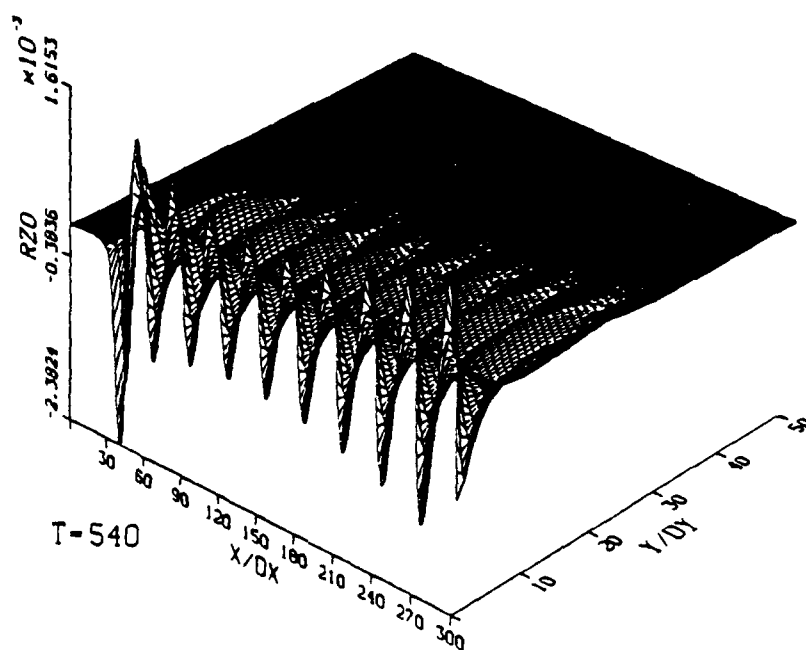
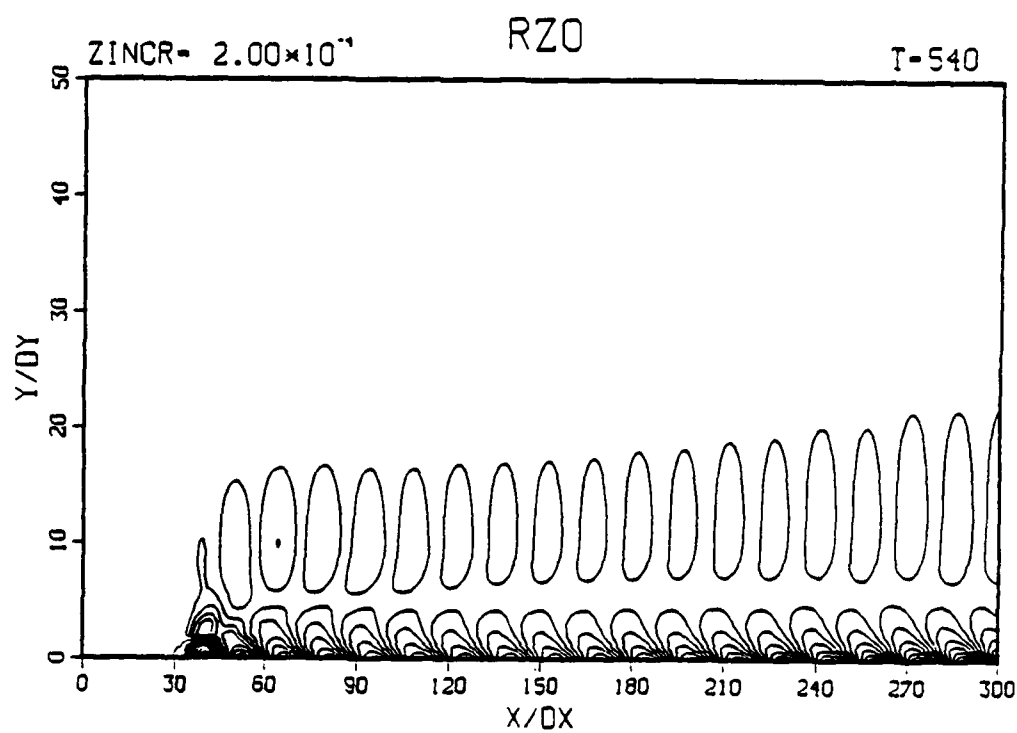
a) 2D streamwise velocity,  $U_0$

Figure 6.9 Uncontrolled disturbed flow after nine periods of oscillation,  $F = 1$



b) 2D normal velocity,  $V_0$

Figure 6.9 continued



c) 2D spanwise vorticity,  $\Omega_{z0}$

Figure 6.9 continued



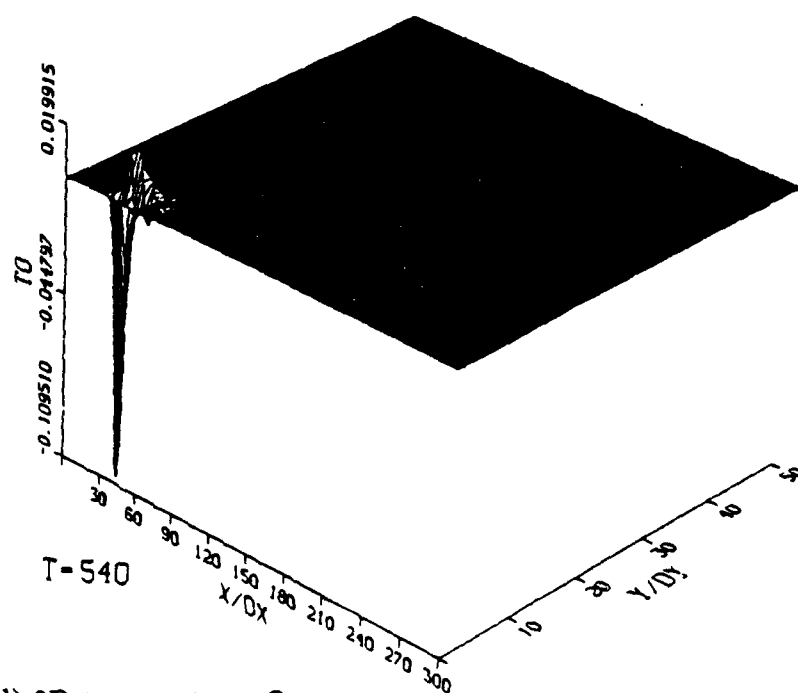
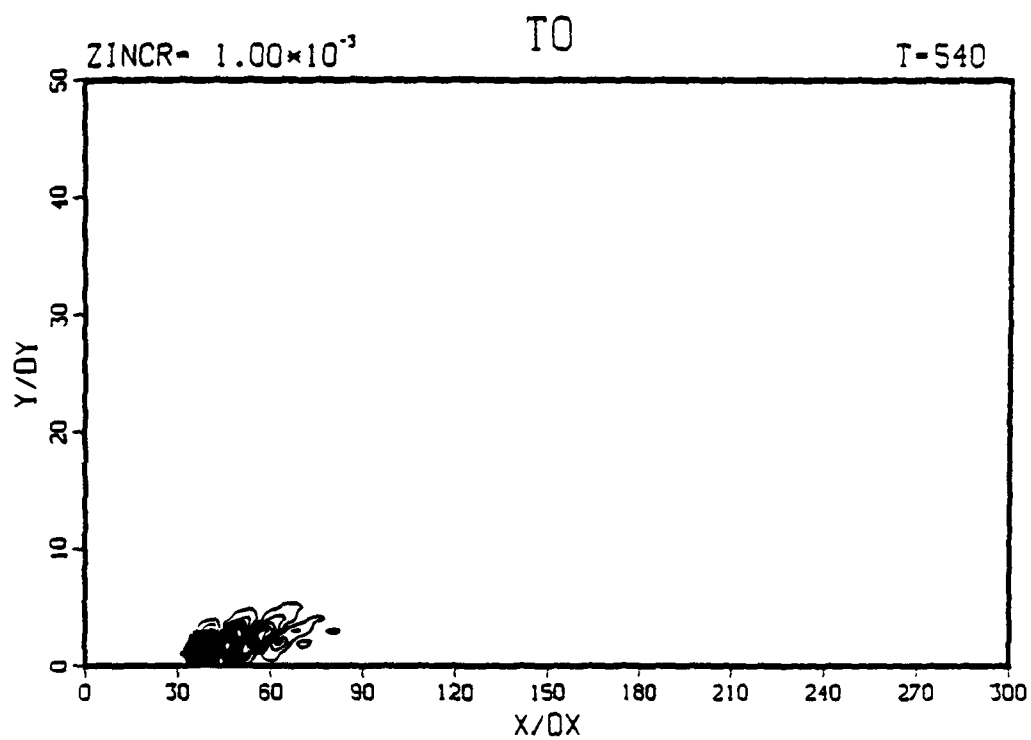
d) 2D temperature,  $\Theta_0$ 

Figure 6.9 continued

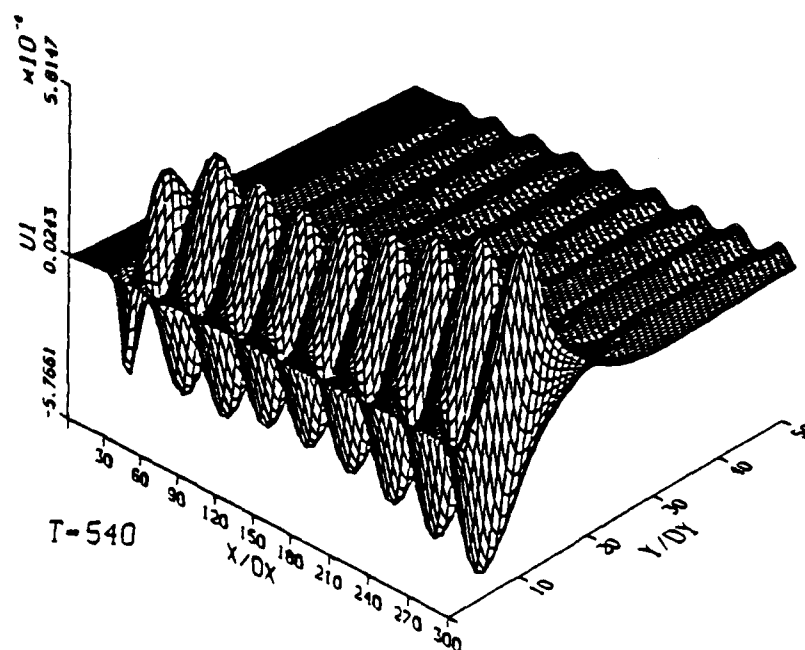
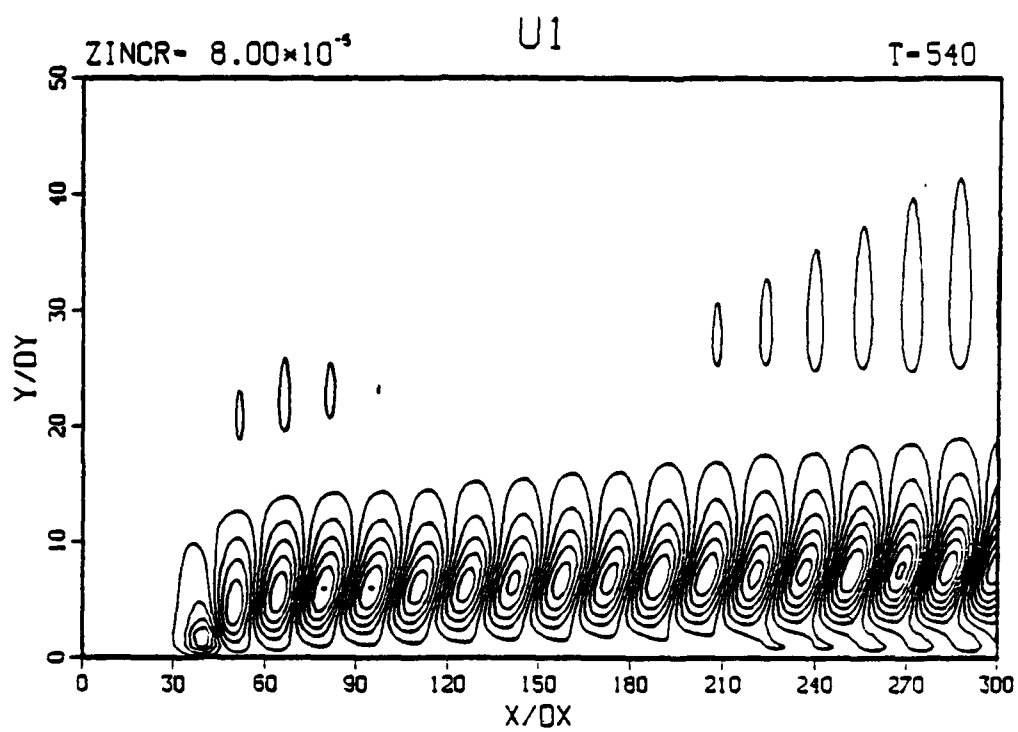
e) 3D streamwise velocity,  $U_1$ 

Figure 6.9 continued

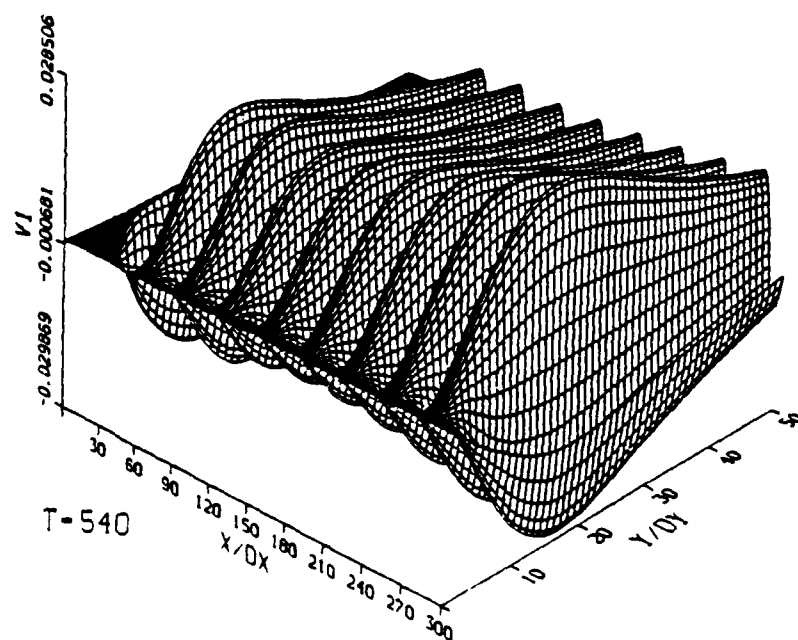
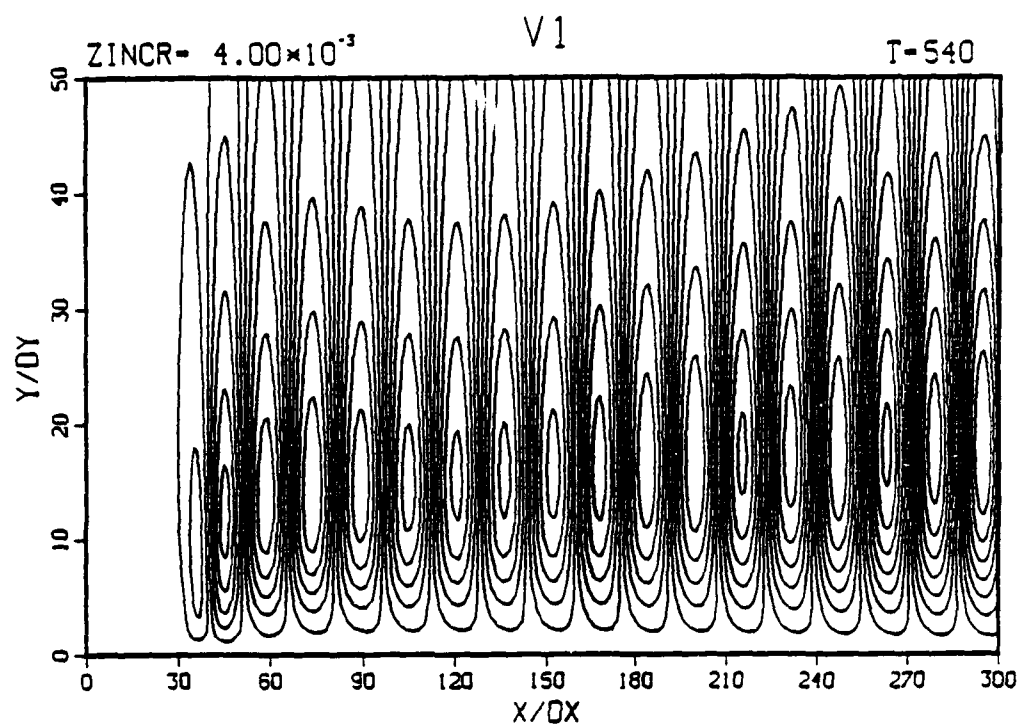
f) 3D normal velocity,  $V_1$ 

Figure 6.9 continued

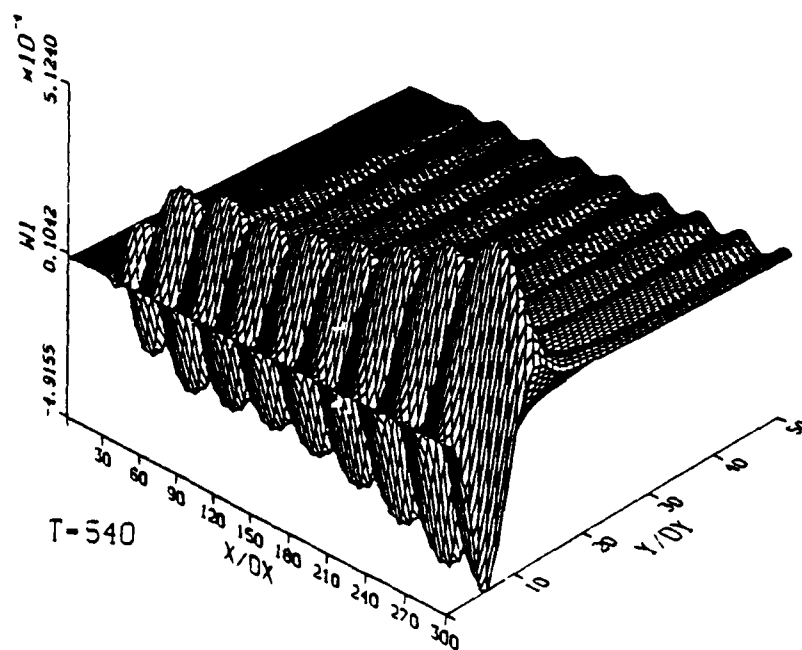
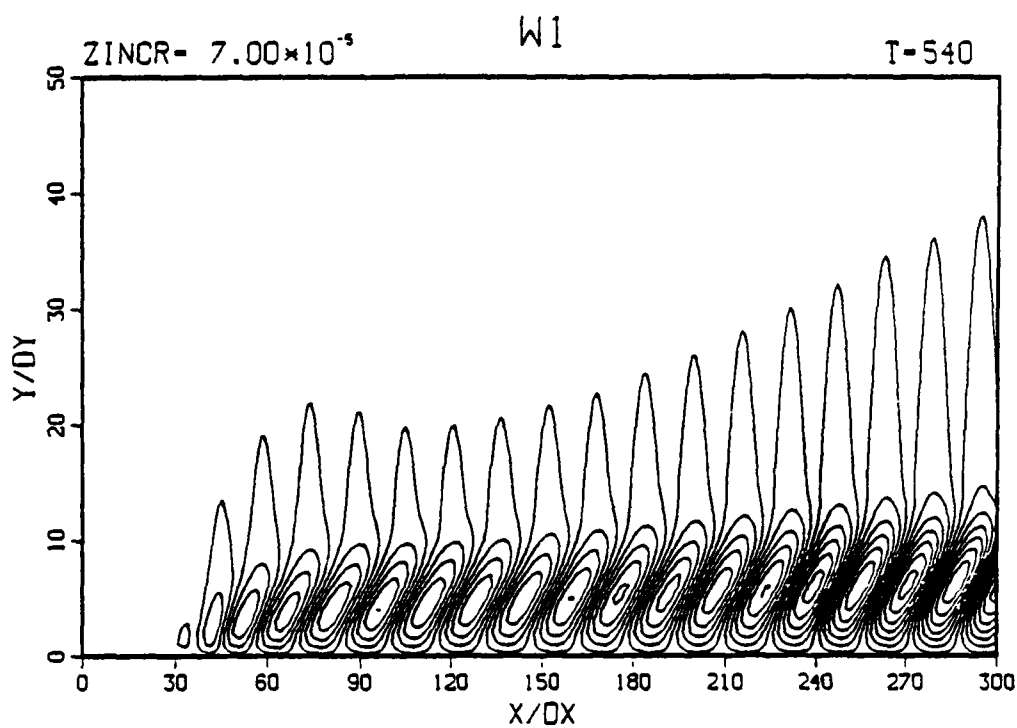
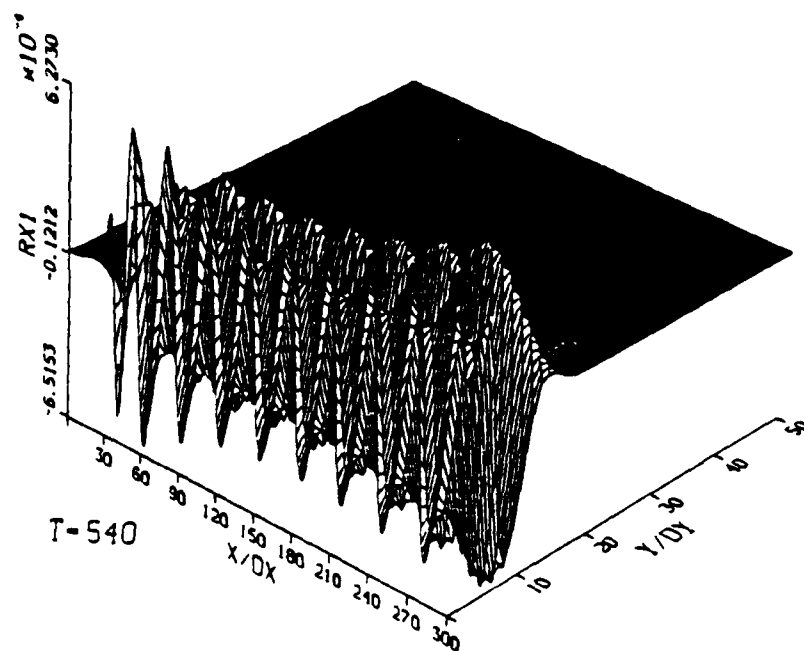
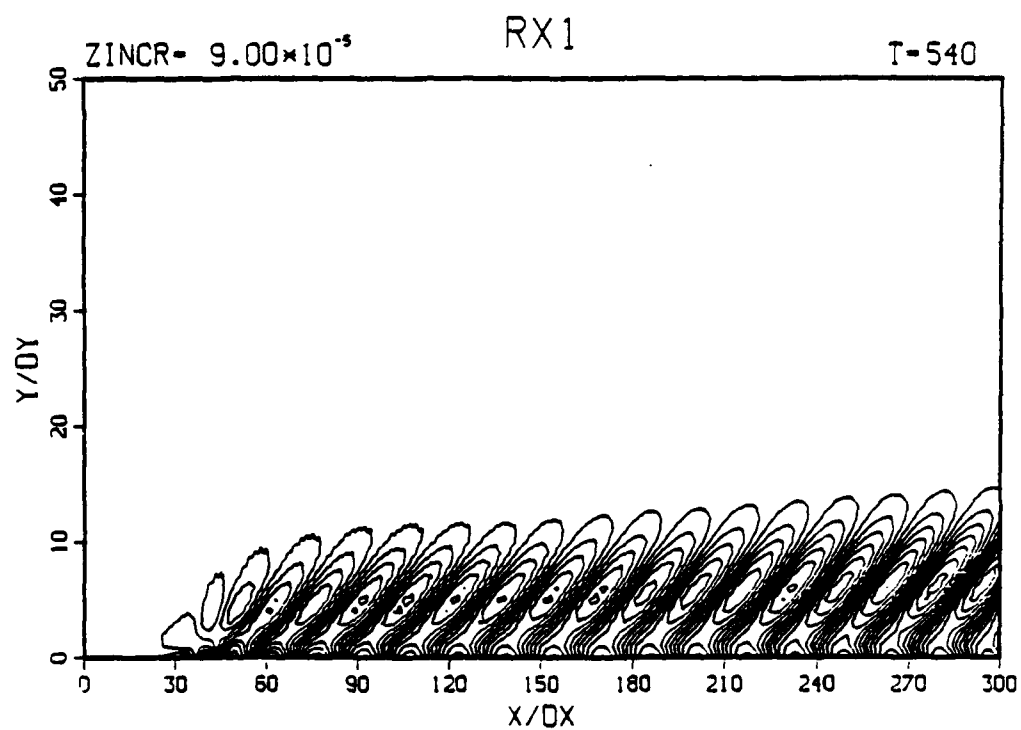
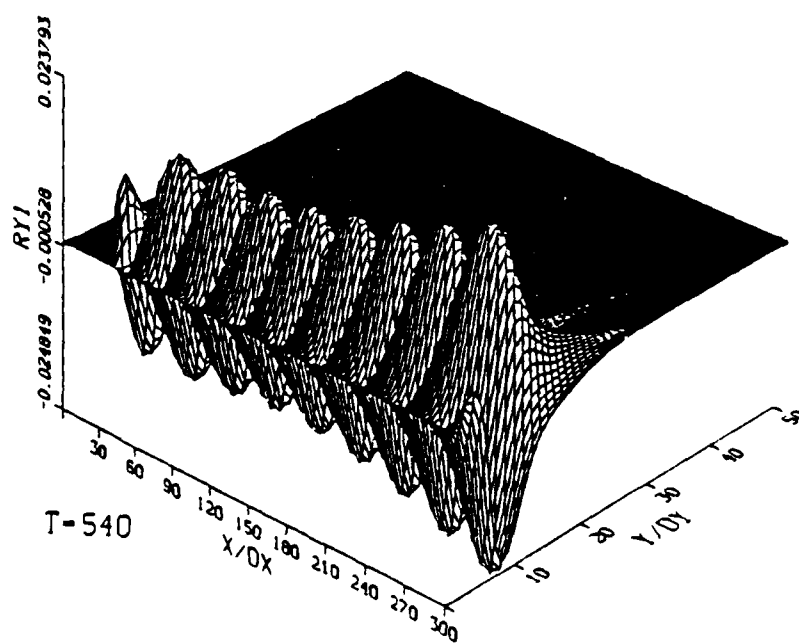
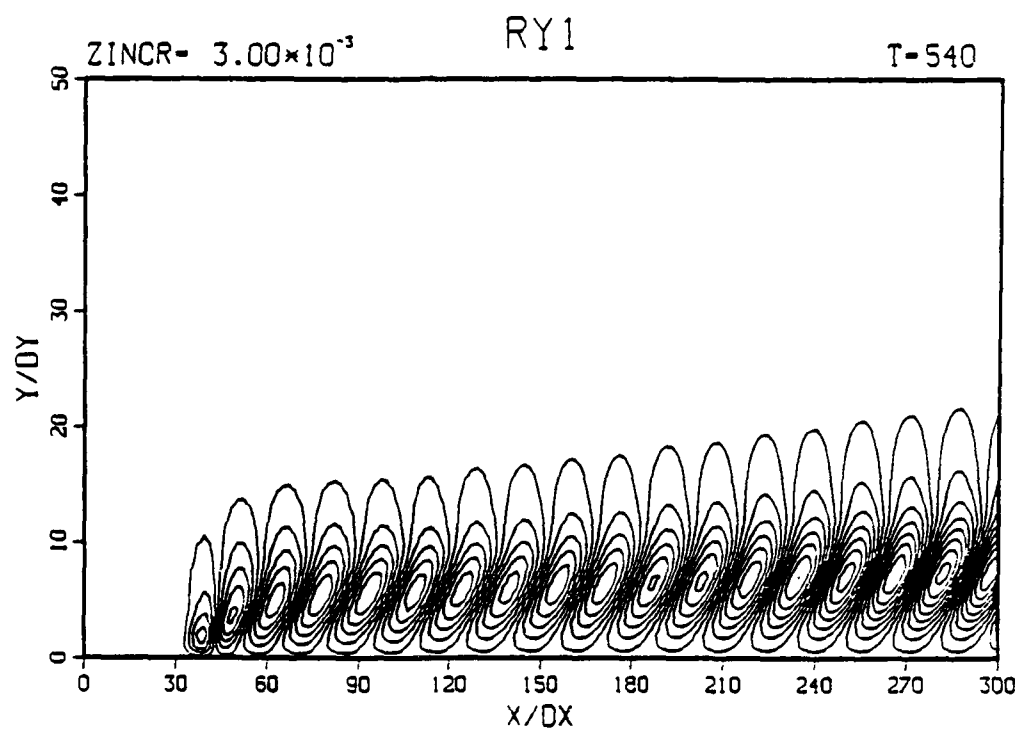
g) 3D spanwise velocity,  $W_1$ 

Figure 6.9 continued



b) 3D streamwise vorticity,  $\Omega_{x1}$

Figure 6.9 continued



i) 3D normal vorticity,  $\Omega_{y1}$

Figure 6.9 continued

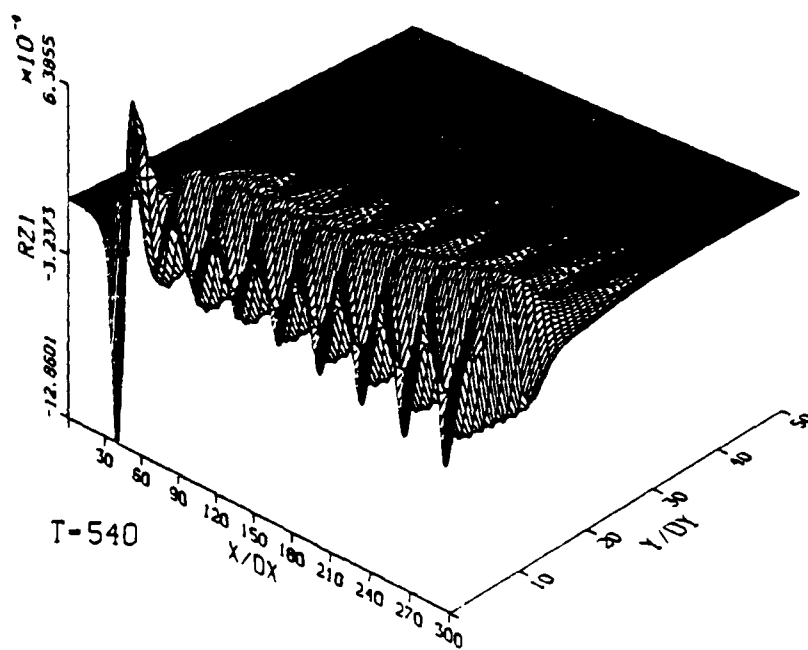
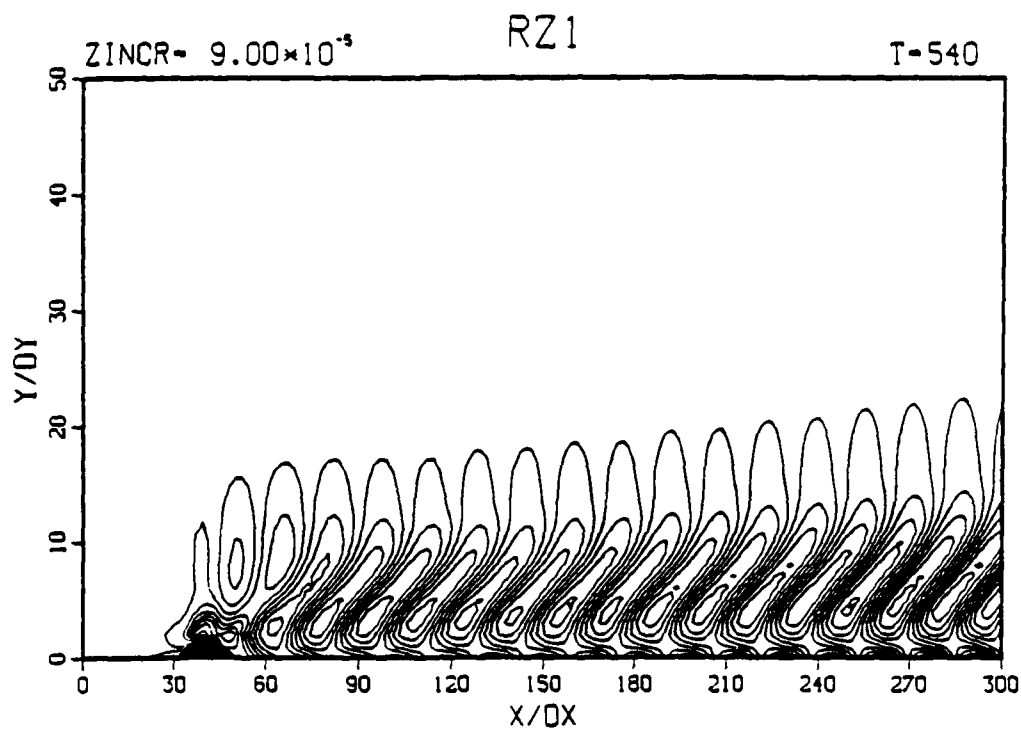
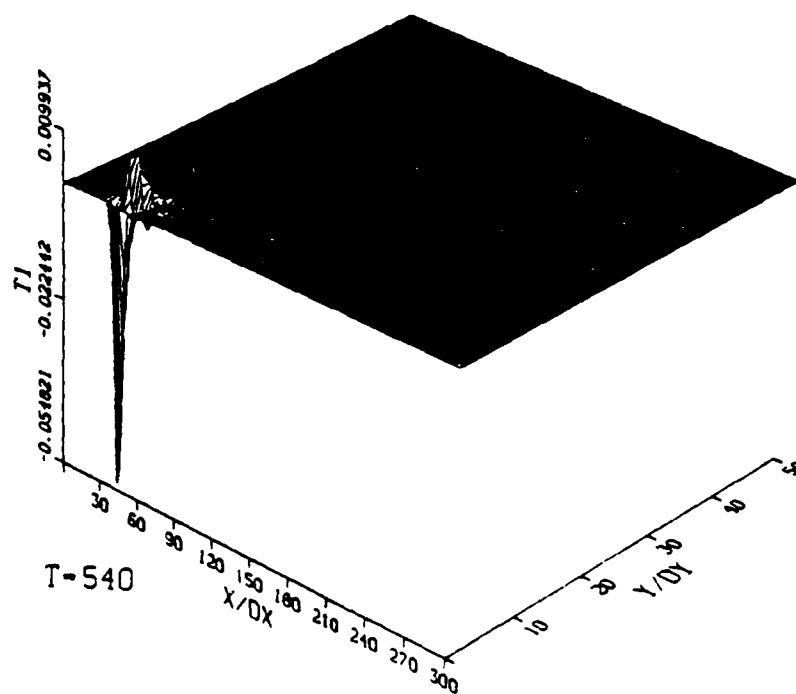
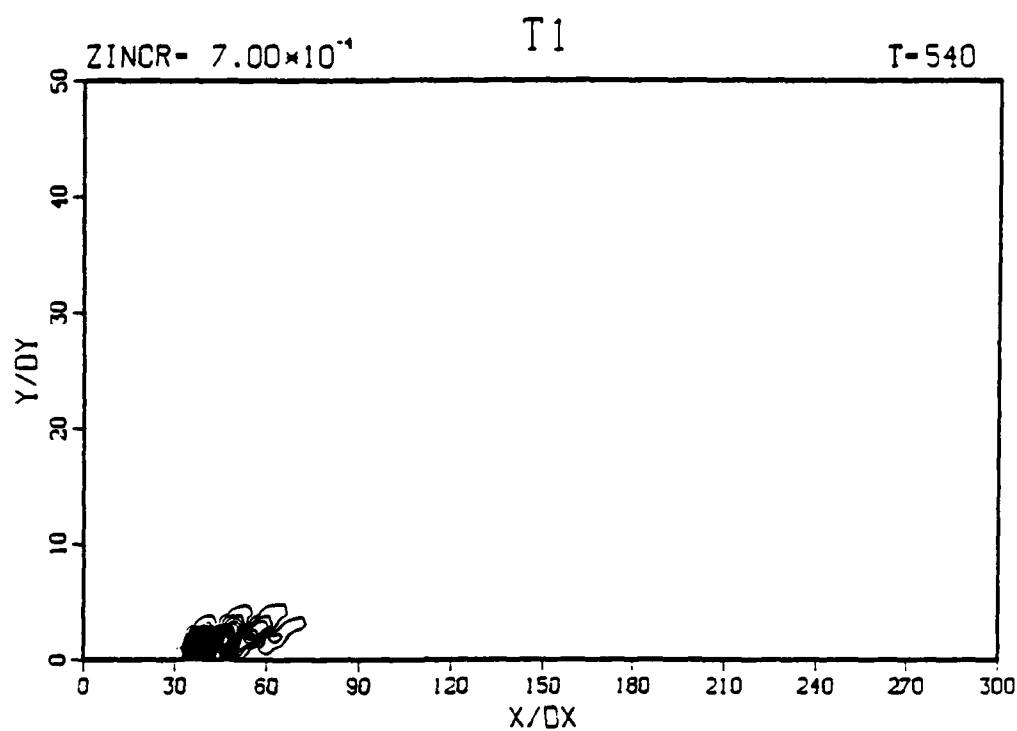
j) 3D spanwise vorticity,  $\Omega_{z1}$ 

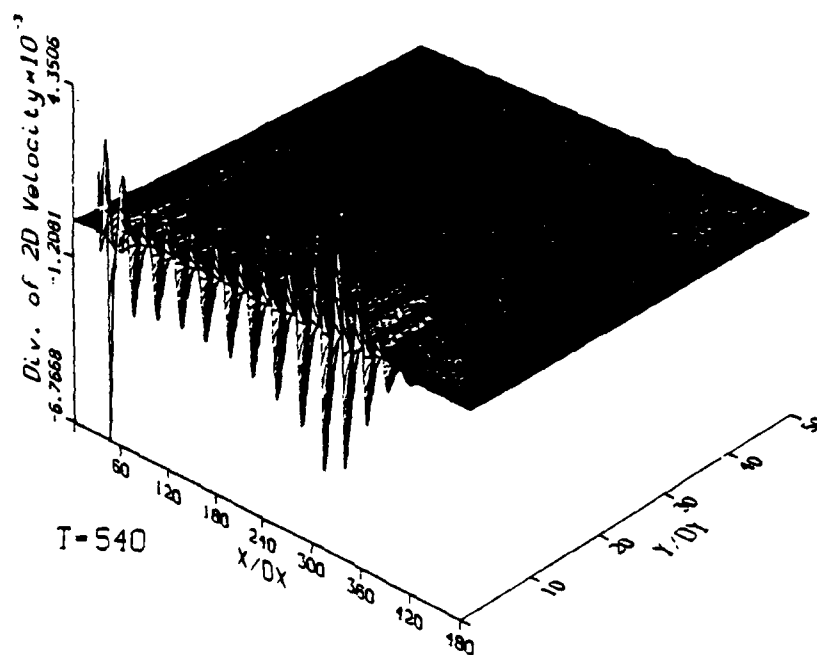
Figure 6.9 continued



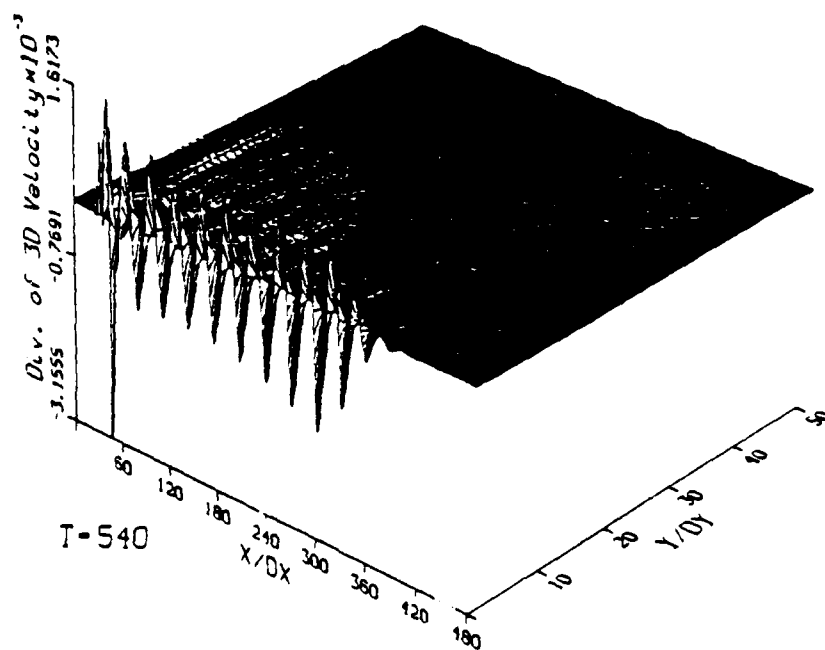
k) 3D temperature,  $\Theta_1$

Figure 6.9 continued





a) mode 0



b) mode 1

Figure 6.10 Velocity divergence of the uncontrolled disturbed flow,  $F = 1$

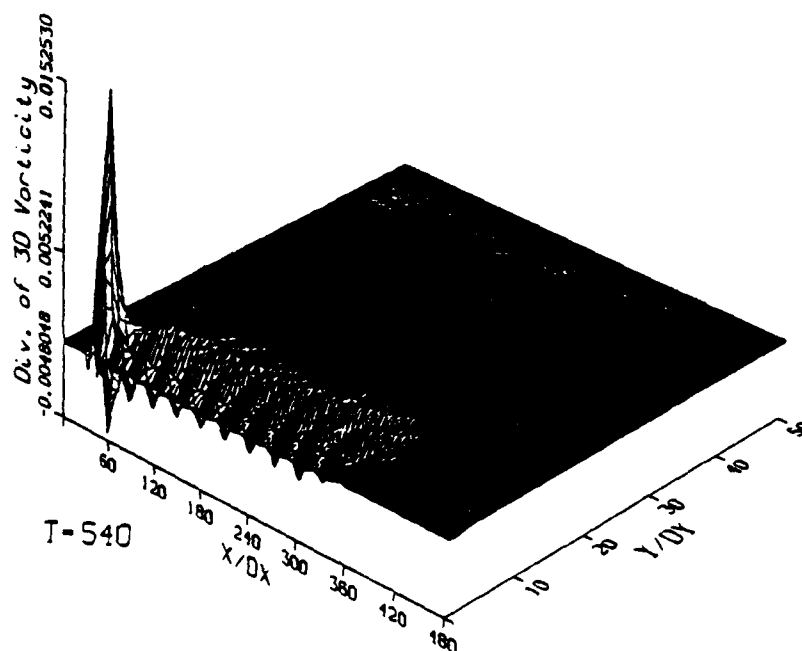
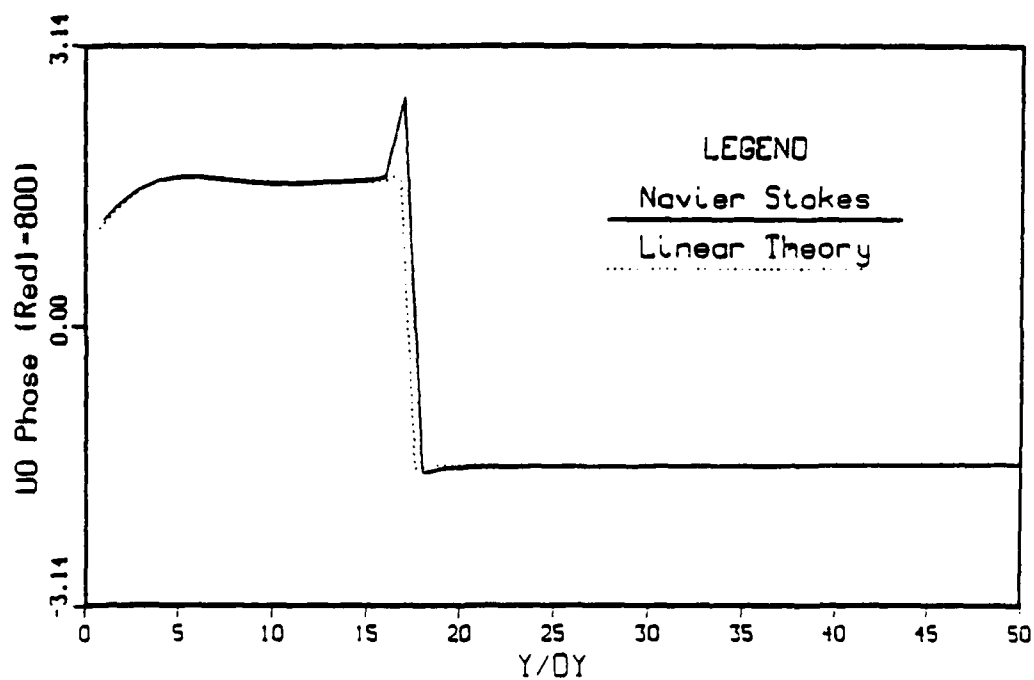
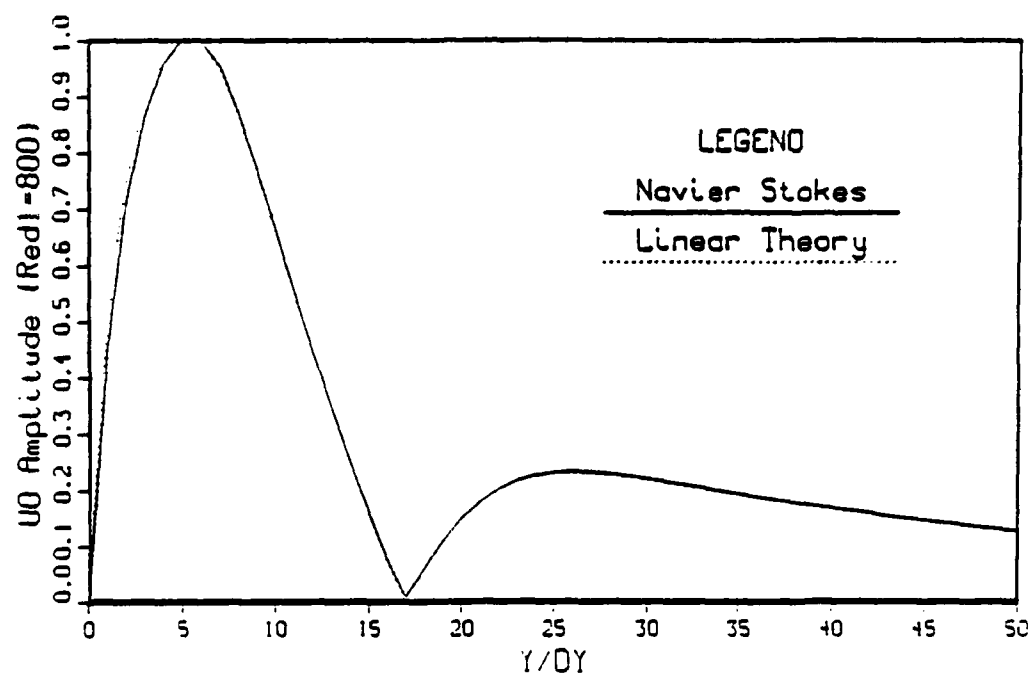
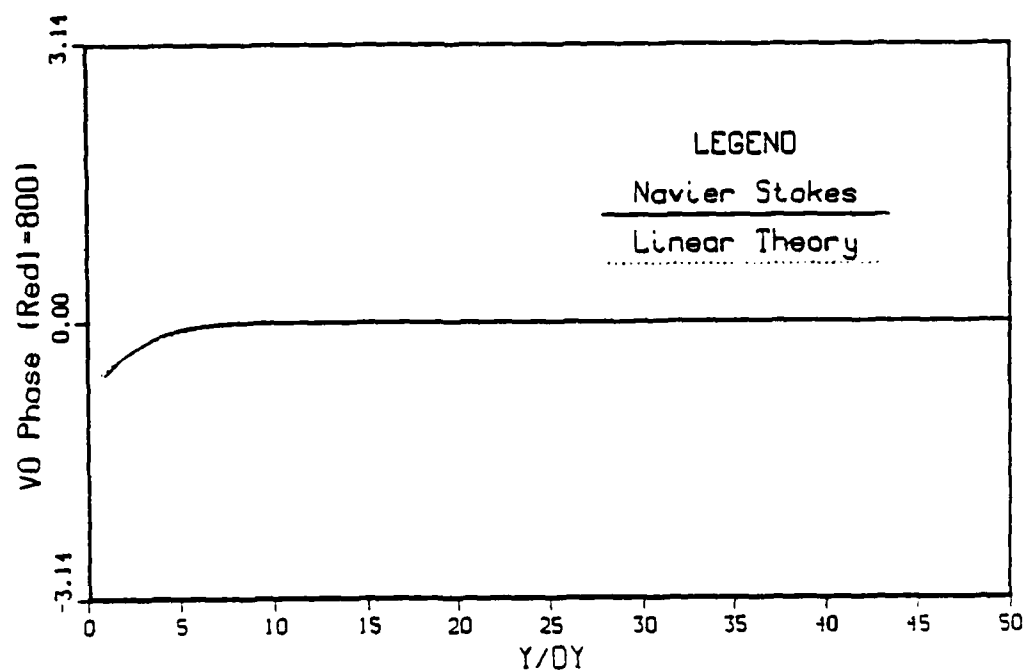
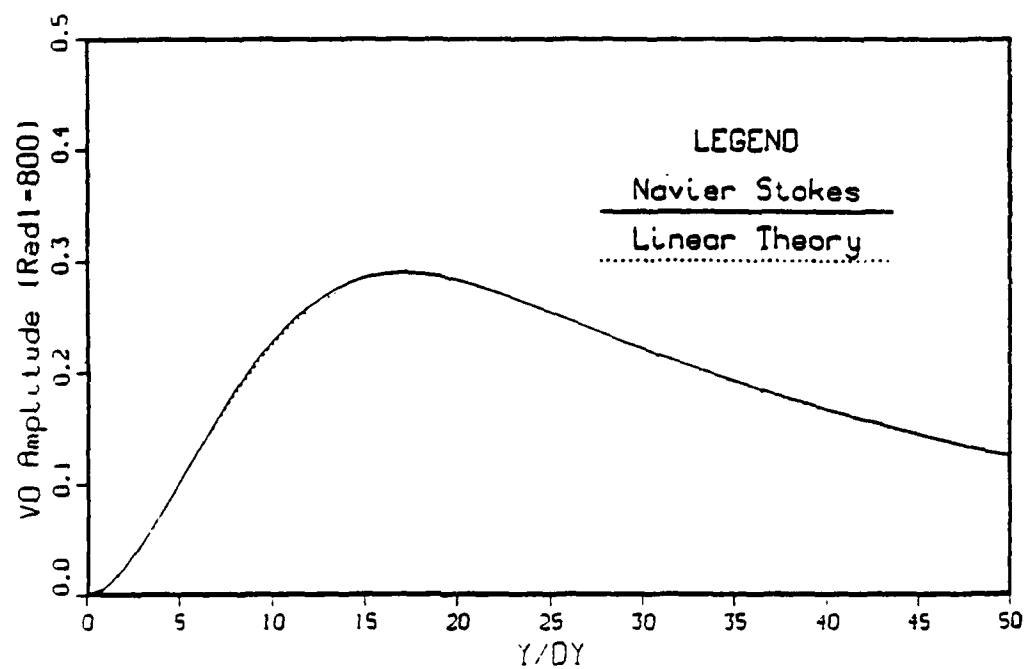


Figure 6.11 Vorticity divergence of the uncontrolled disturbed flow,  $F = 1$



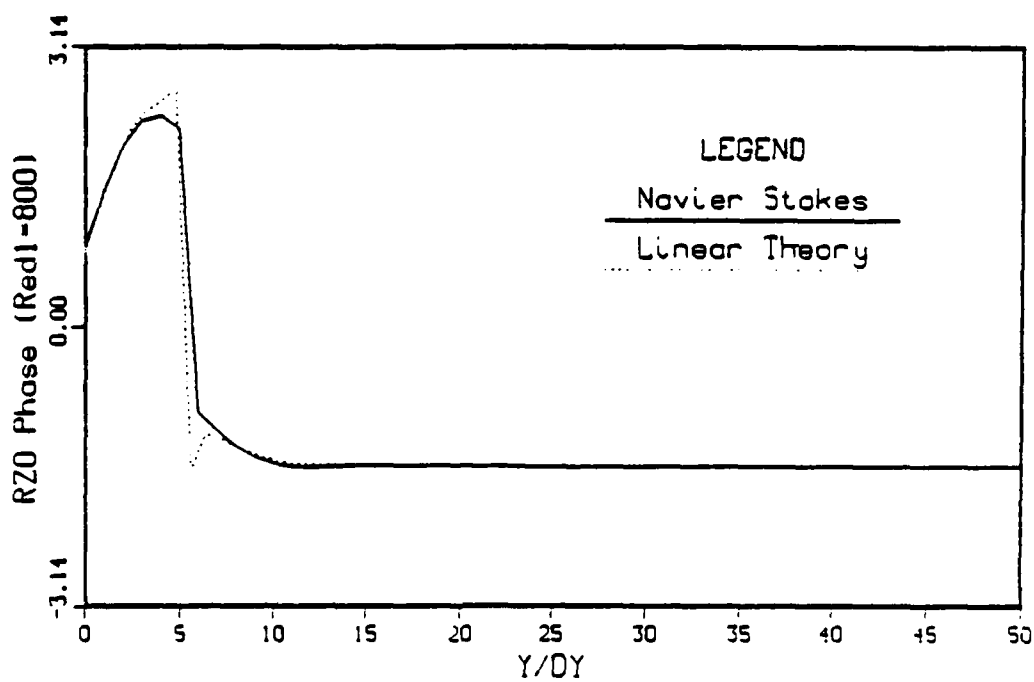
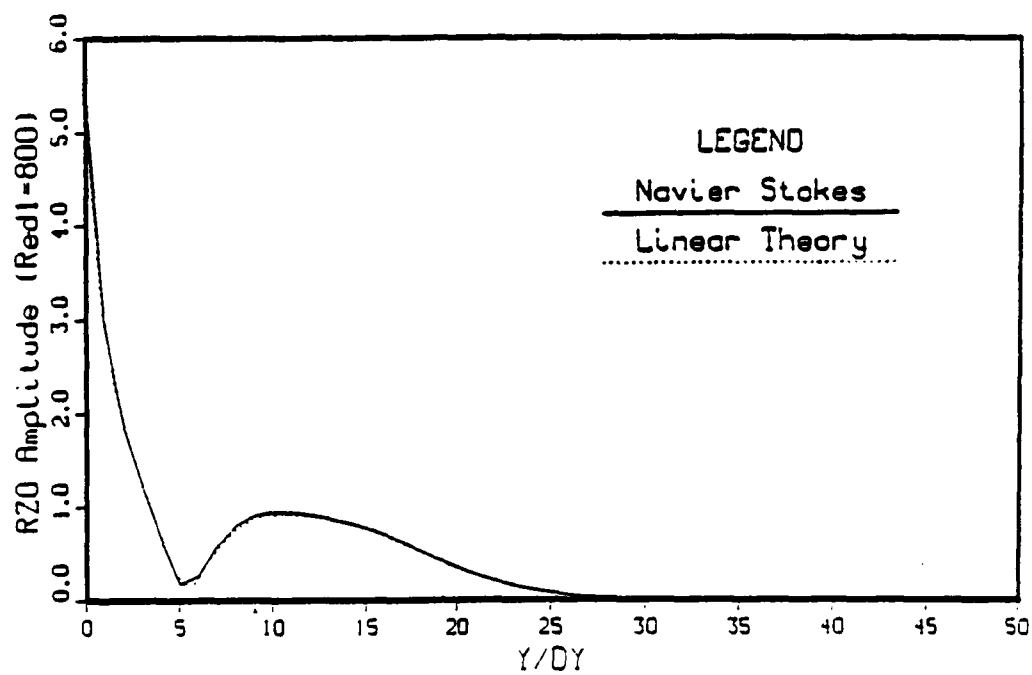
a) 2D streamwise velocity,  $U_0$

Figure 6.12 Amplitude and phase comparison with linear stability theory without control applied,  $F = 1$



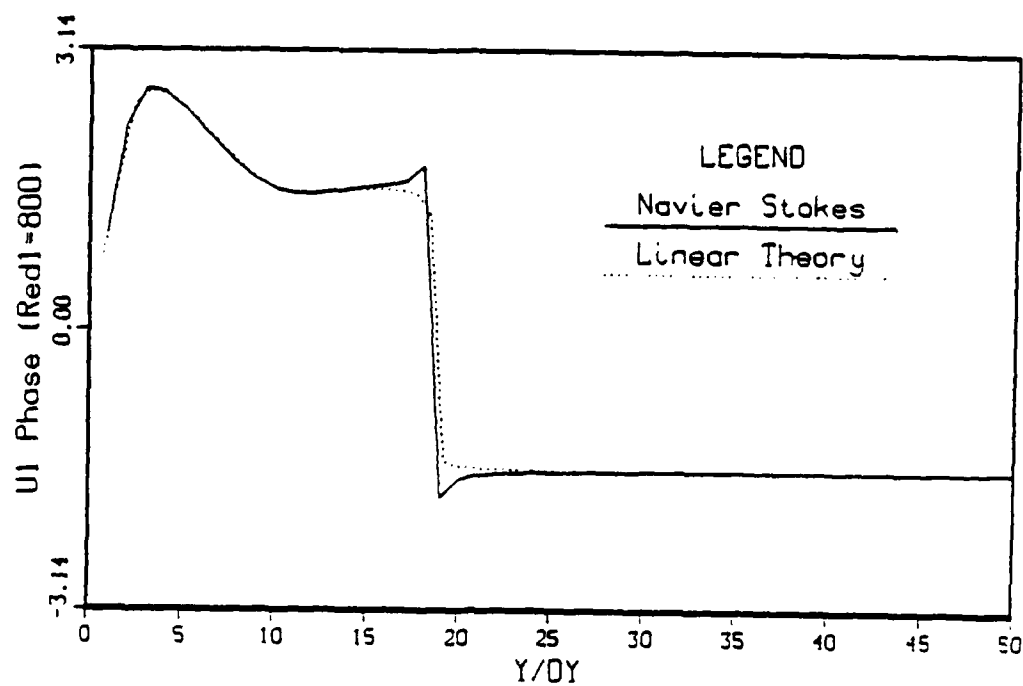
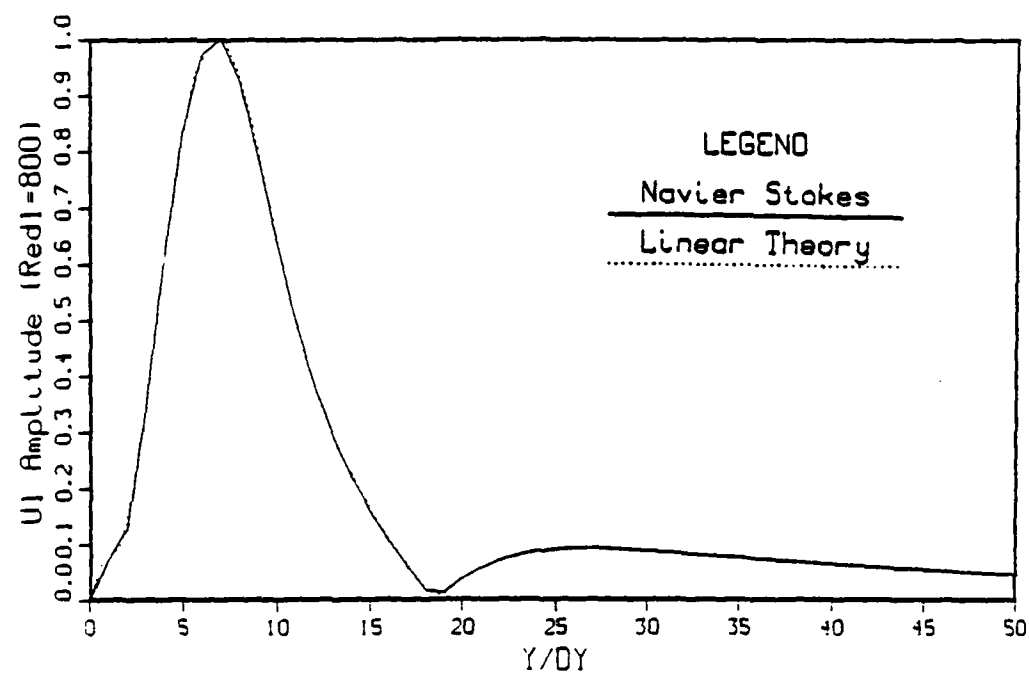
b) 2D normal velocity,  $V_0$

Figure 6.12 continued



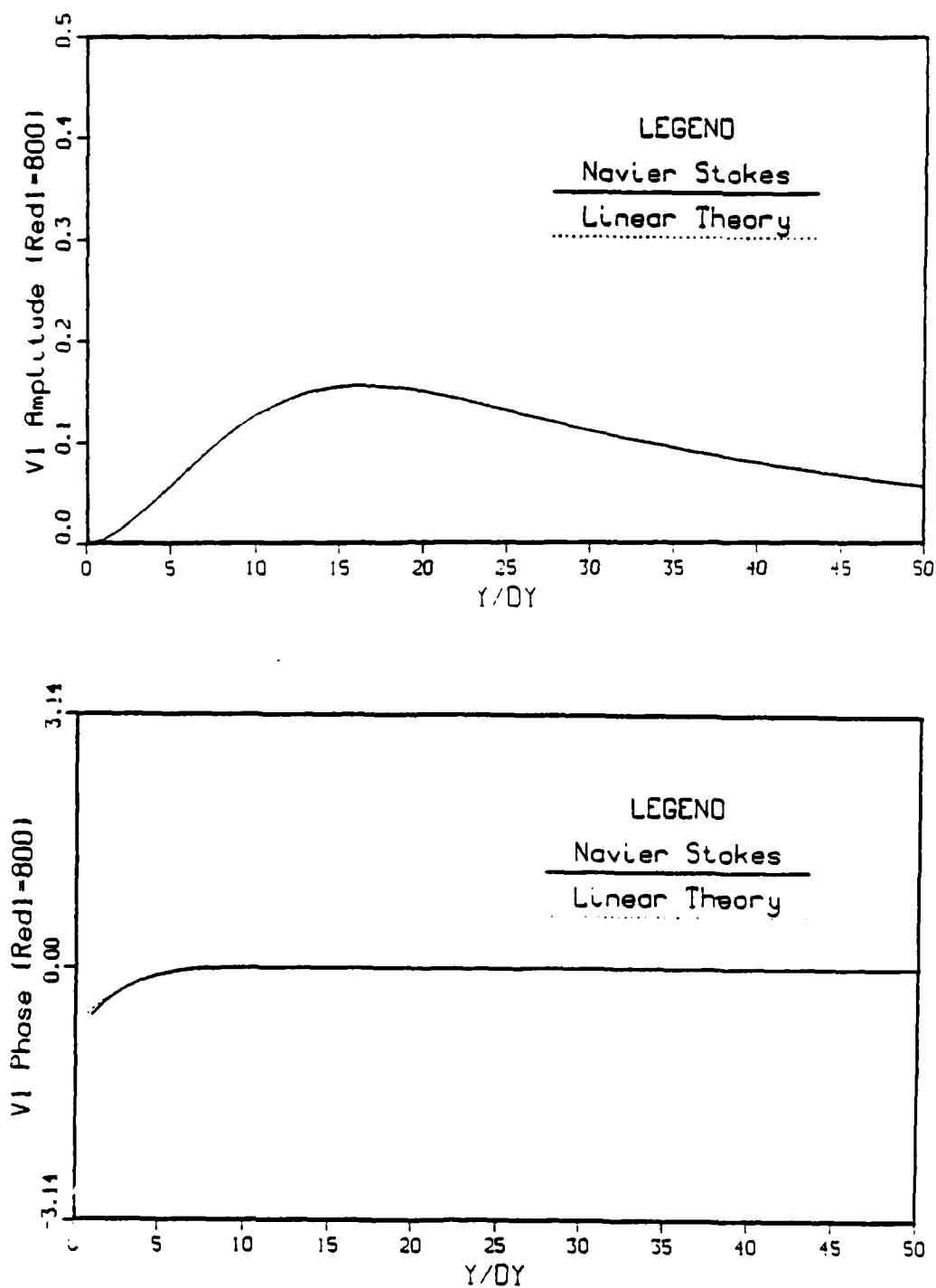
c) 2D spanwise vorticity,  $\Omega_{z0}$

Figure 6.12 continued



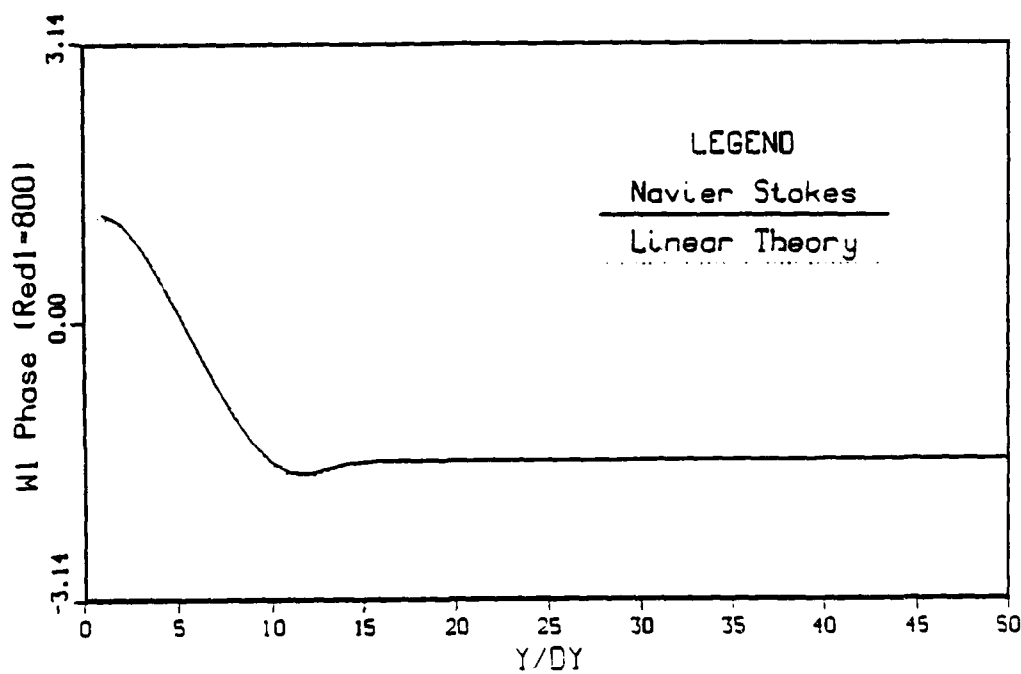
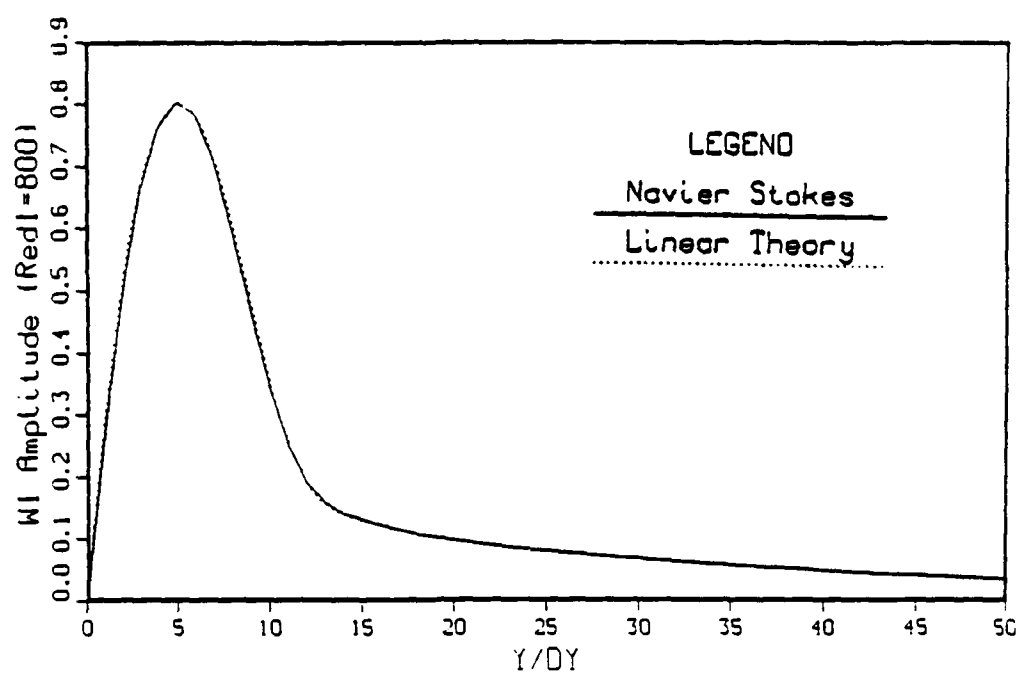
d) 3D streamwise velocity,  $U_1$

Figure 6.12 continued



e) 3D normal velocity,  $V_1$

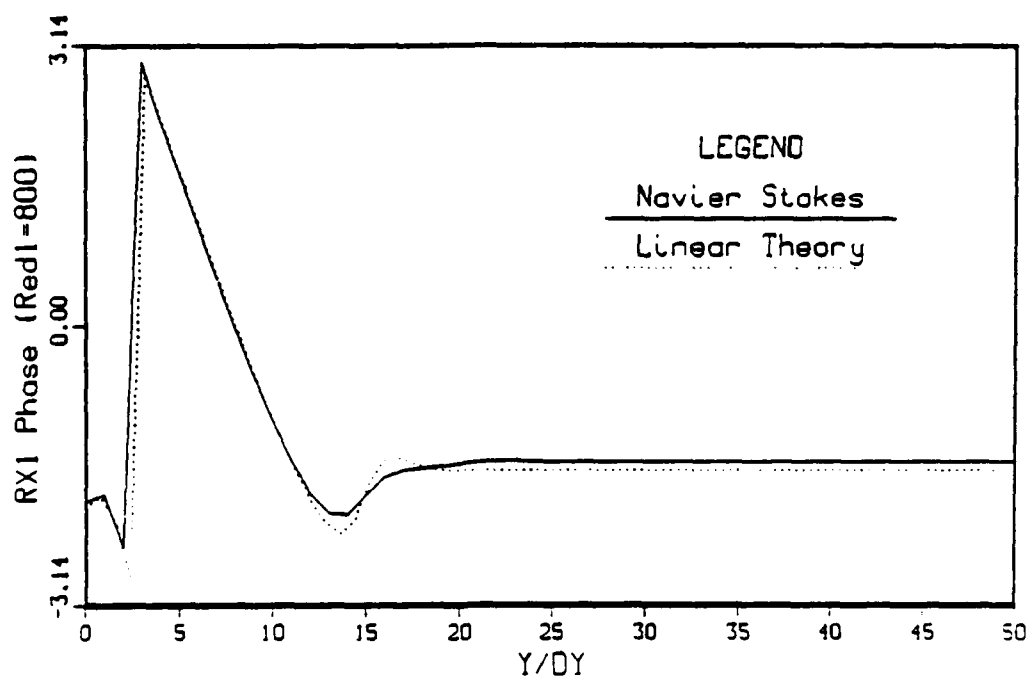
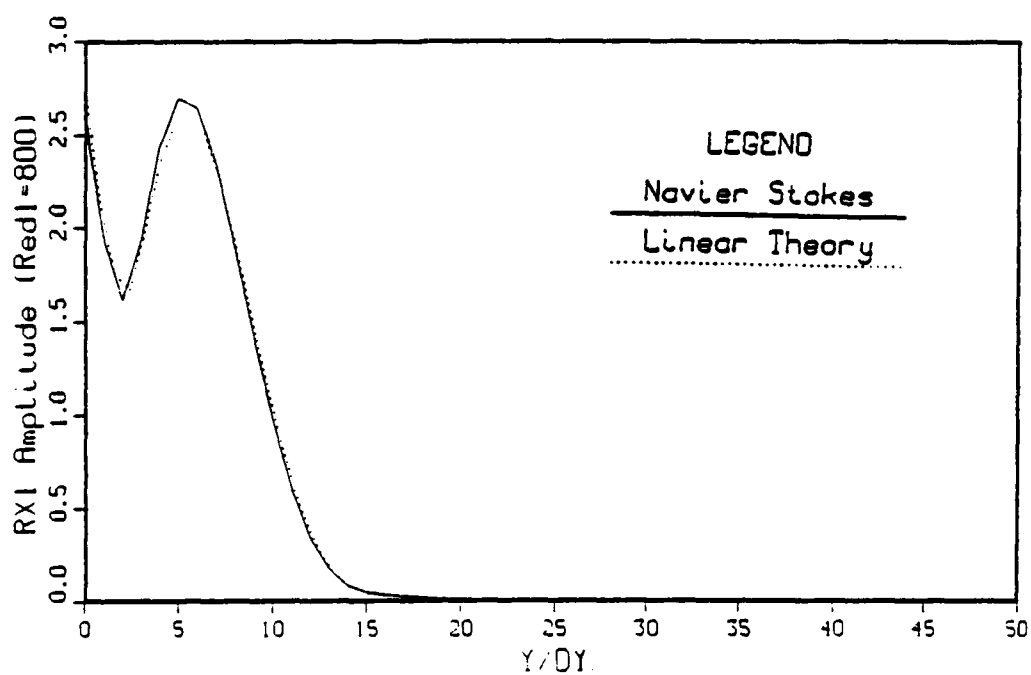
Figure 6.12 continued



f) 3D spanwise velocity,  $W_1$

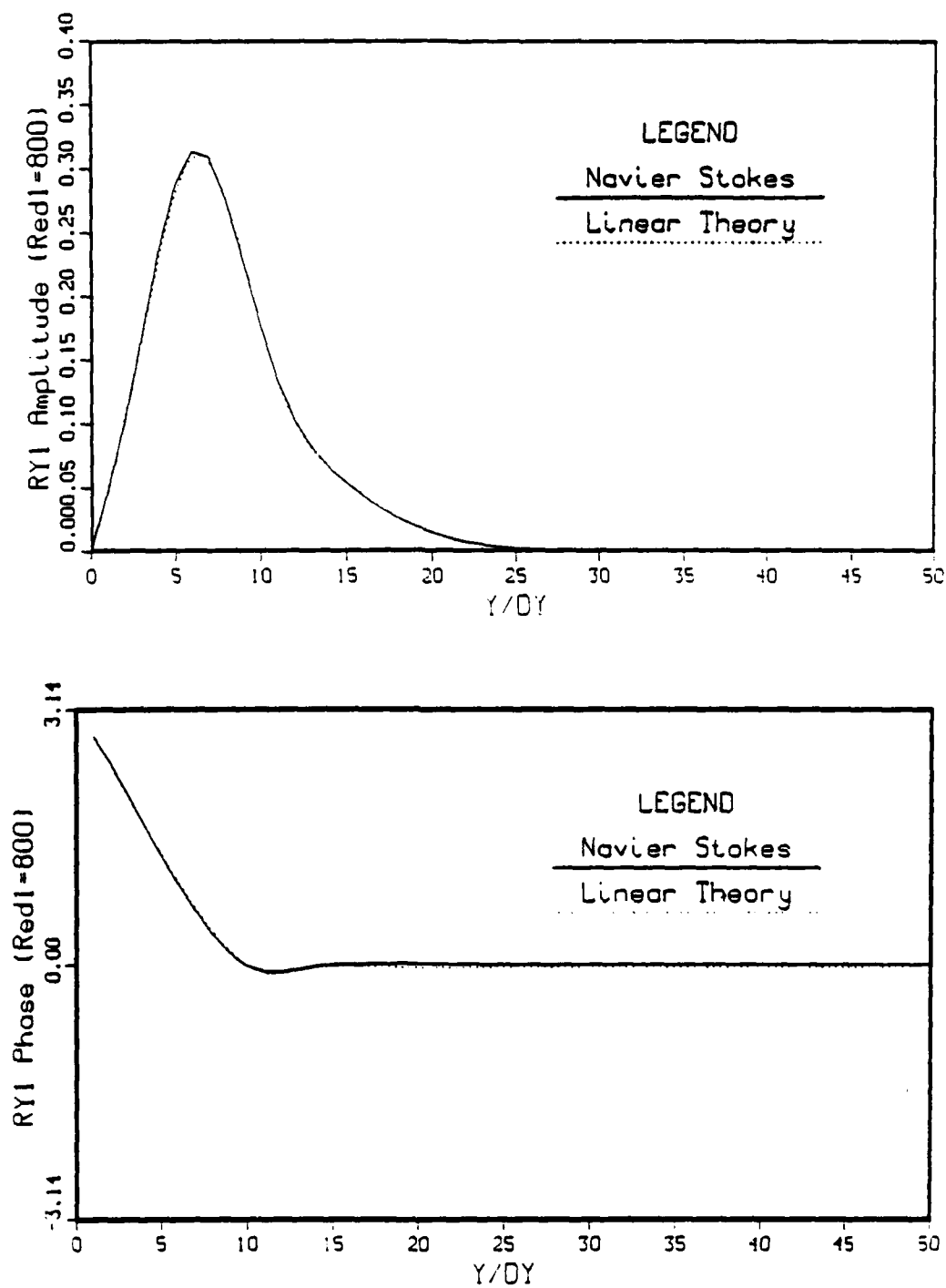
Figure 6.12 continued





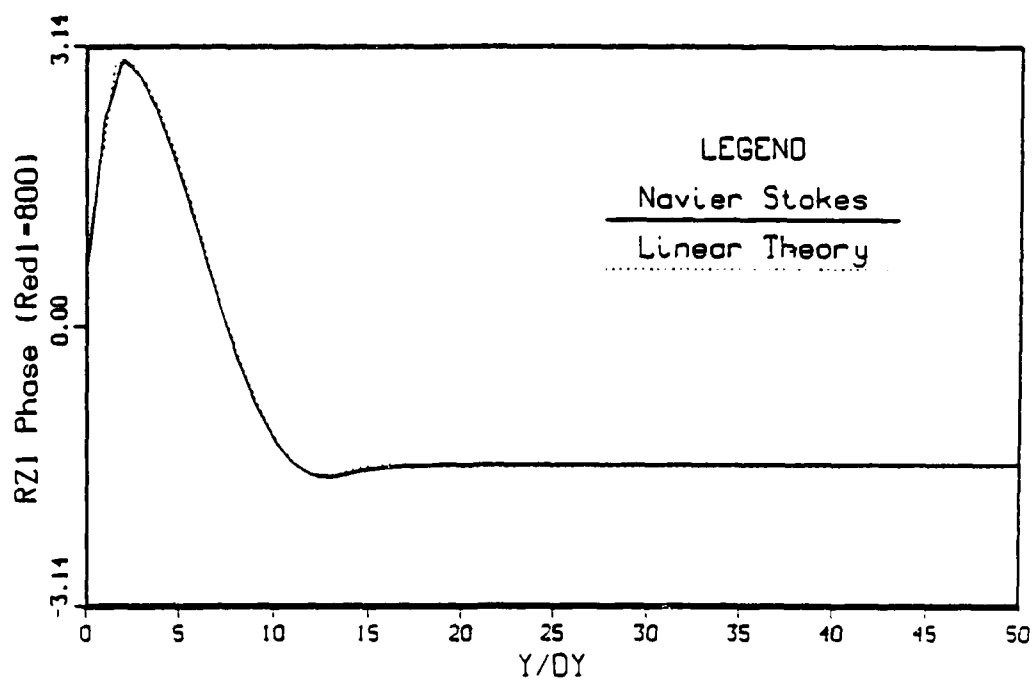
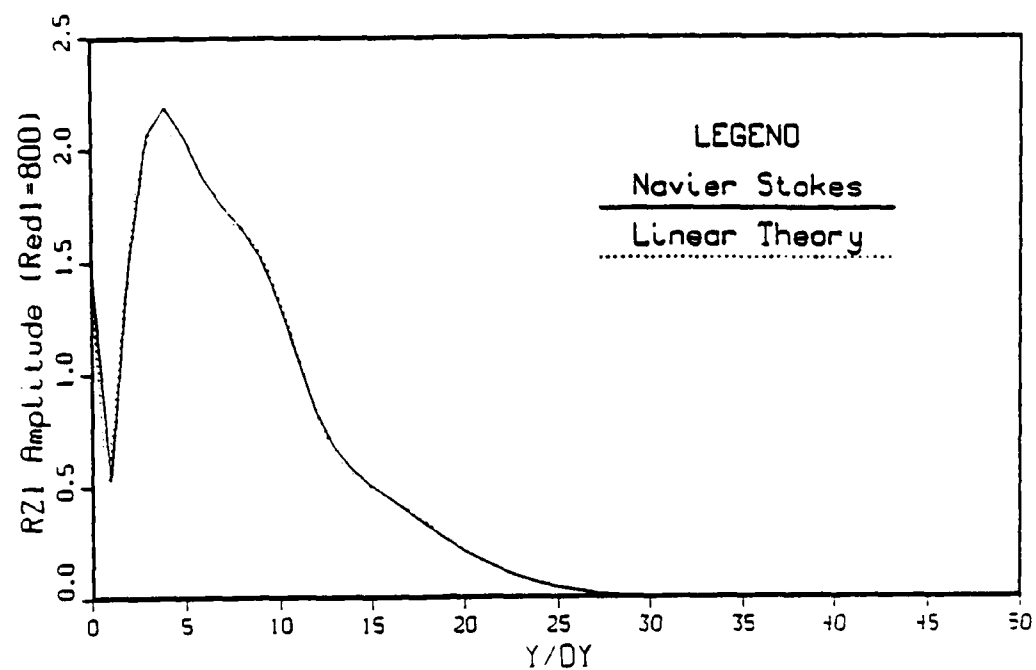
g) 3D streamwise vorticity,  $\Omega_{x1}$

Figure 6.12 continued



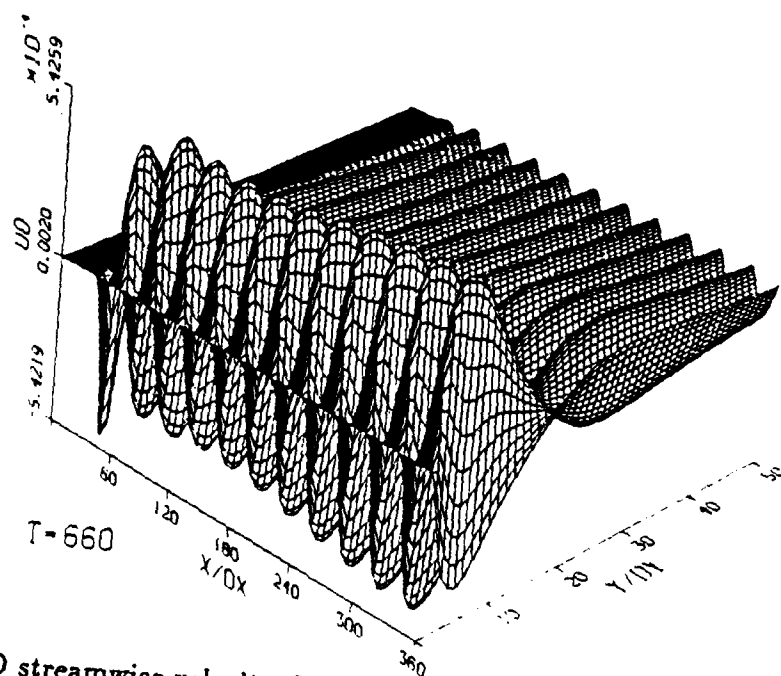
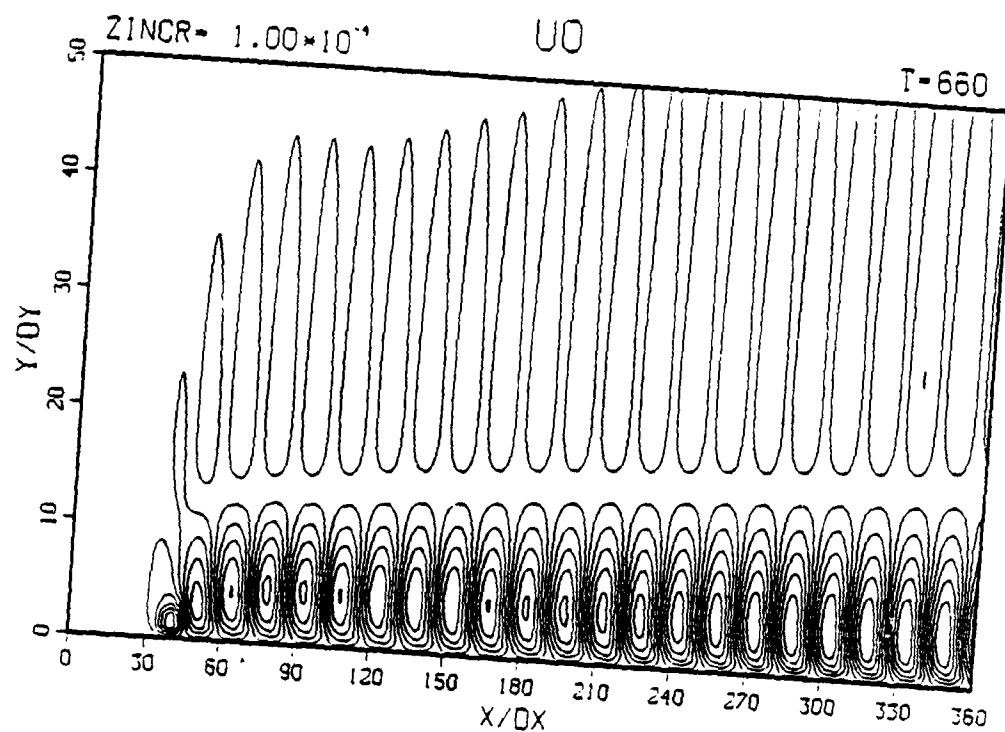
h) 3D normal vorticity,  $\Omega_{y_1}$

Figure 6.12 continued

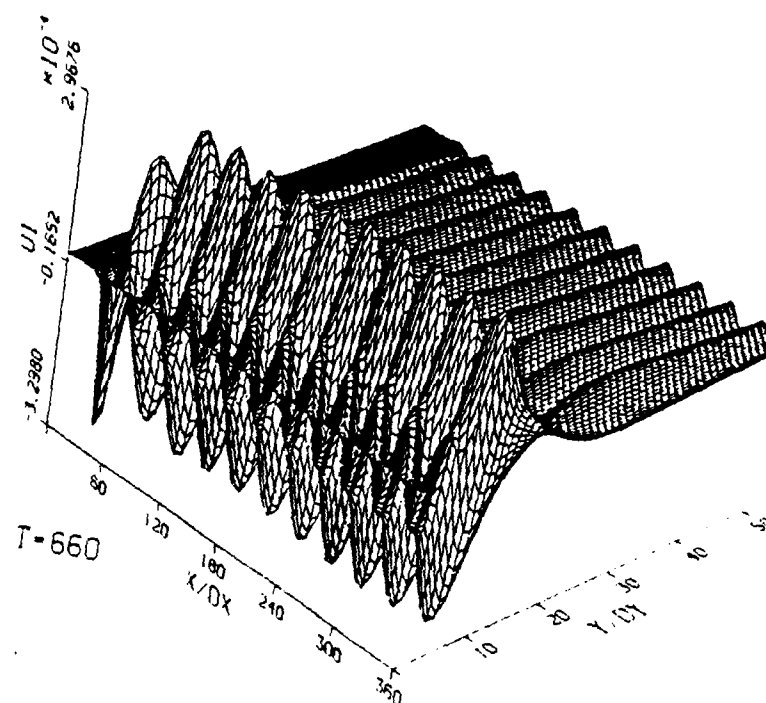
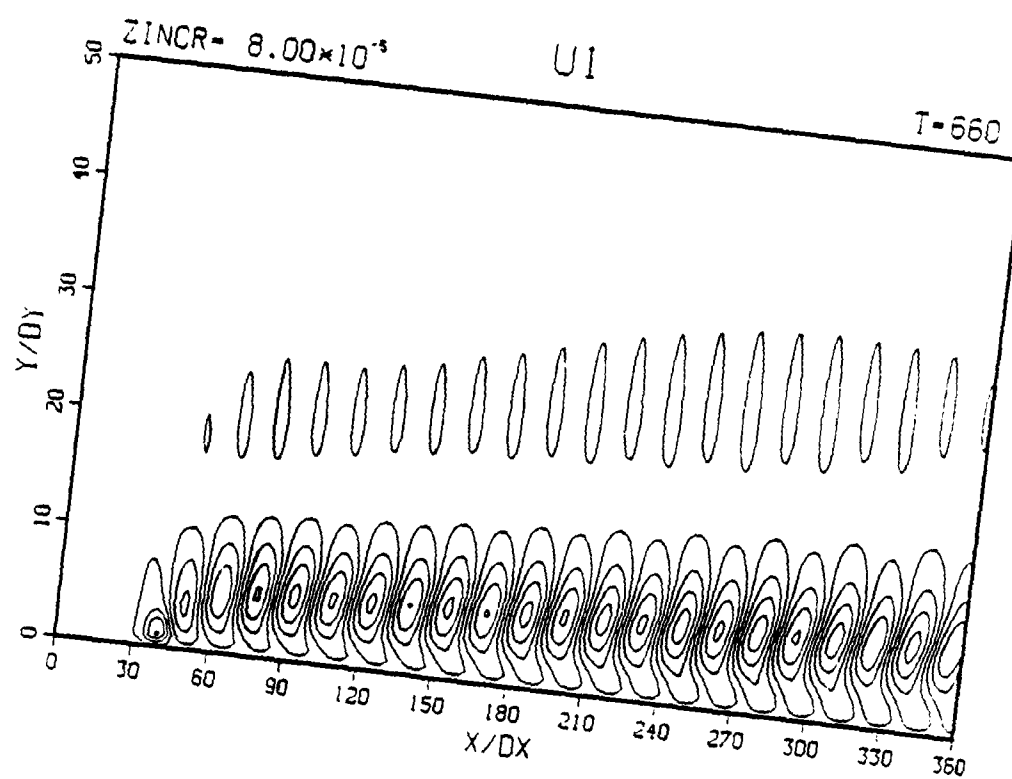


i) 3D spanwise vorticity,  $\Omega_{z1}$

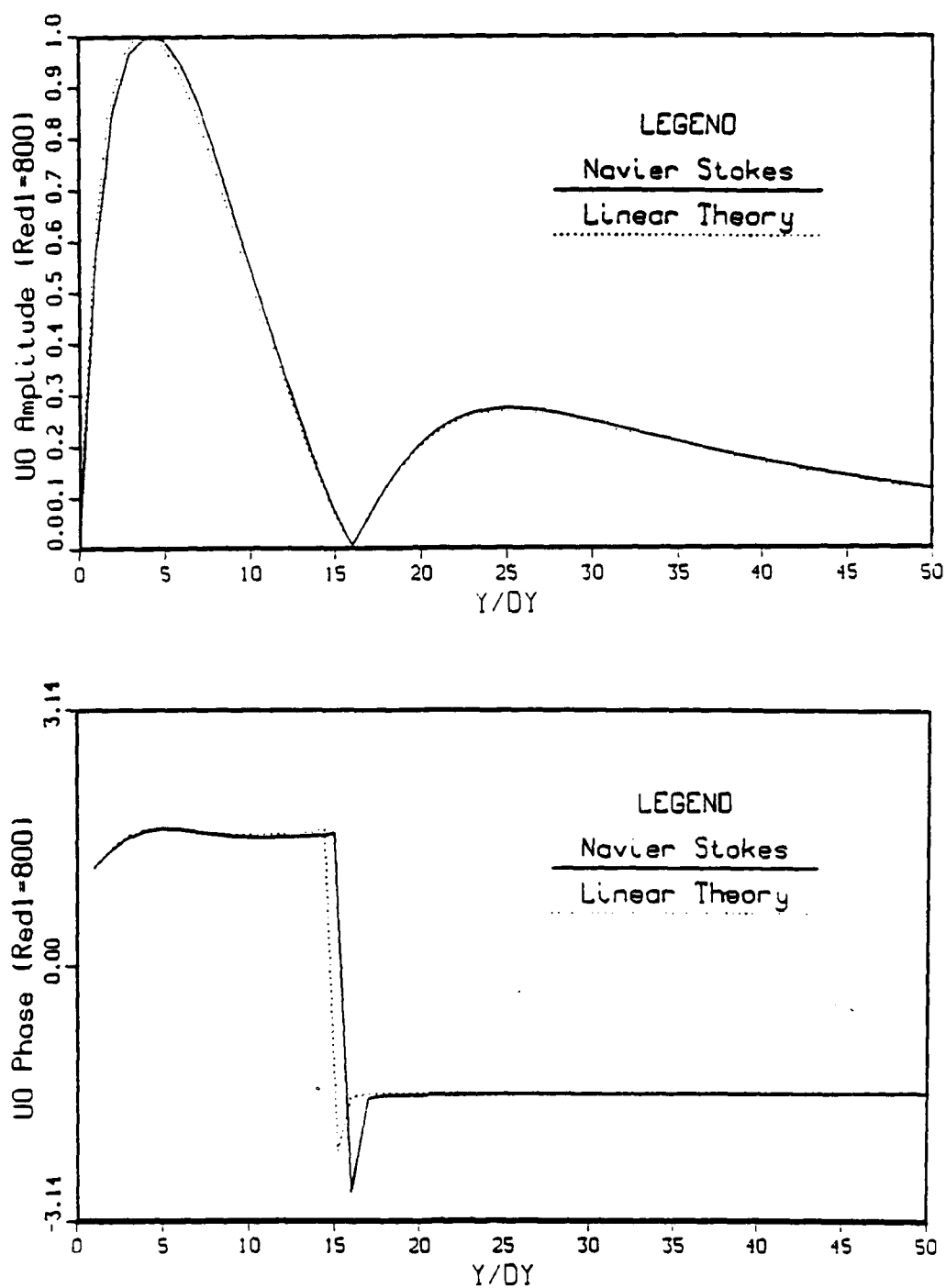
Figure 6.12 continued



a) 2D streamwise velocity,  $U_0$   
 Figure 6.13 Uncontrolled disturbed flow after eleven periods of oscillation,  $F = 1.55$

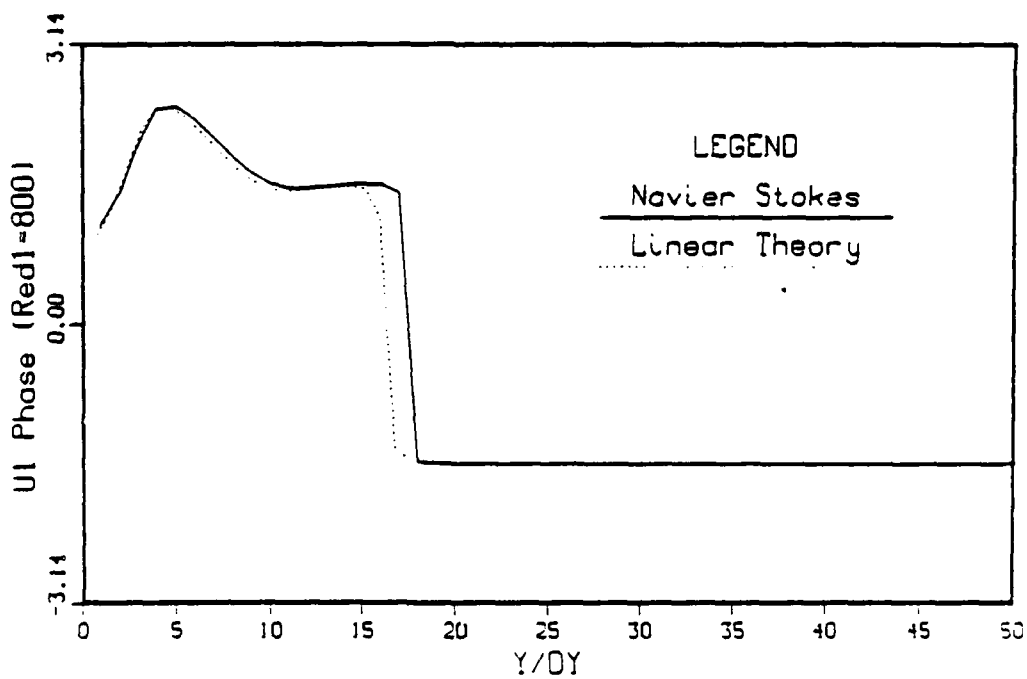
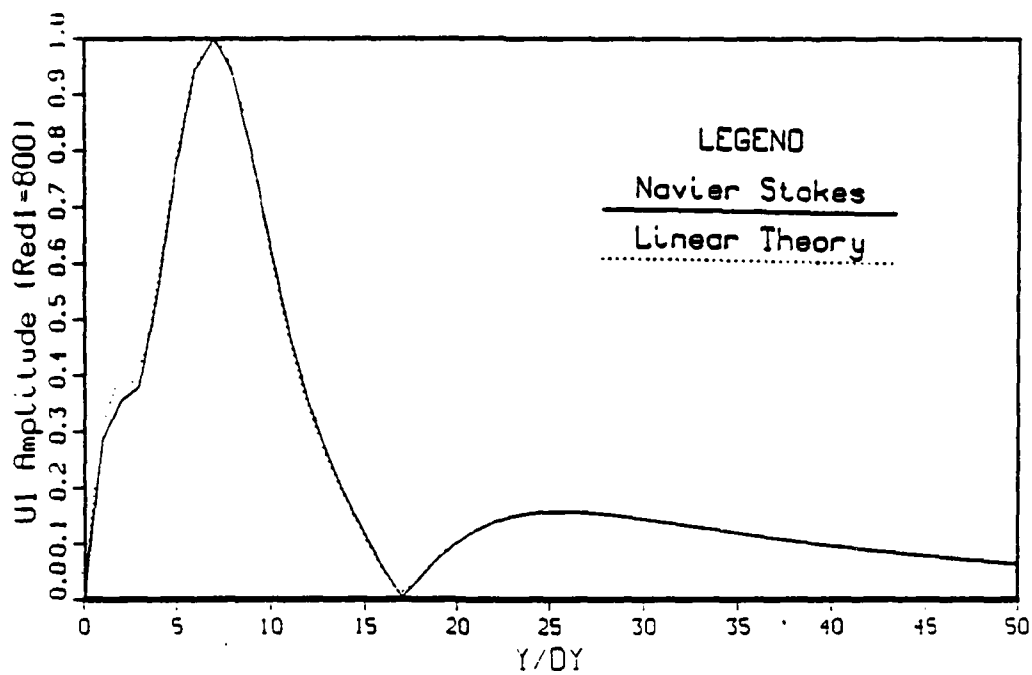


b) 3D streamwise velocity,  $U_1$   
 Figure 6.13 continued

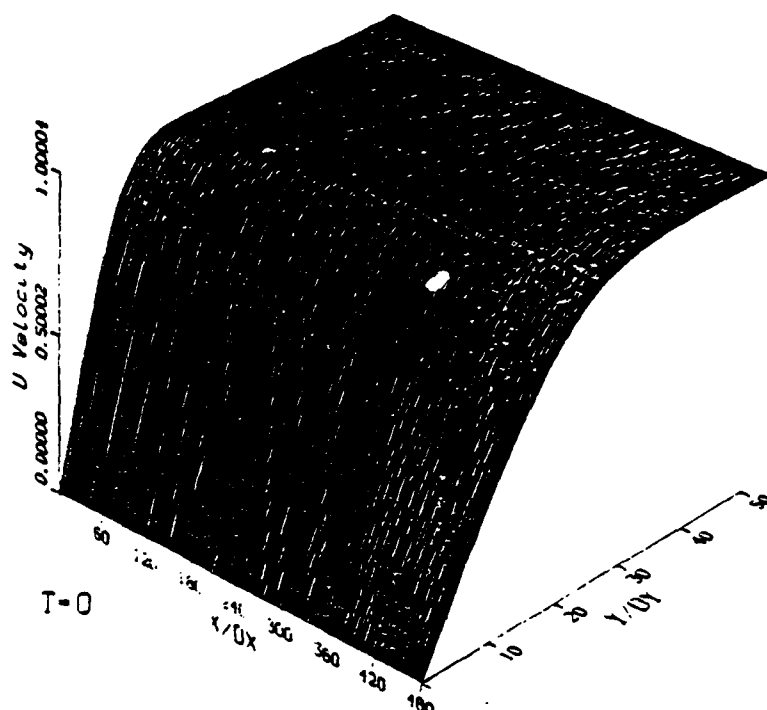
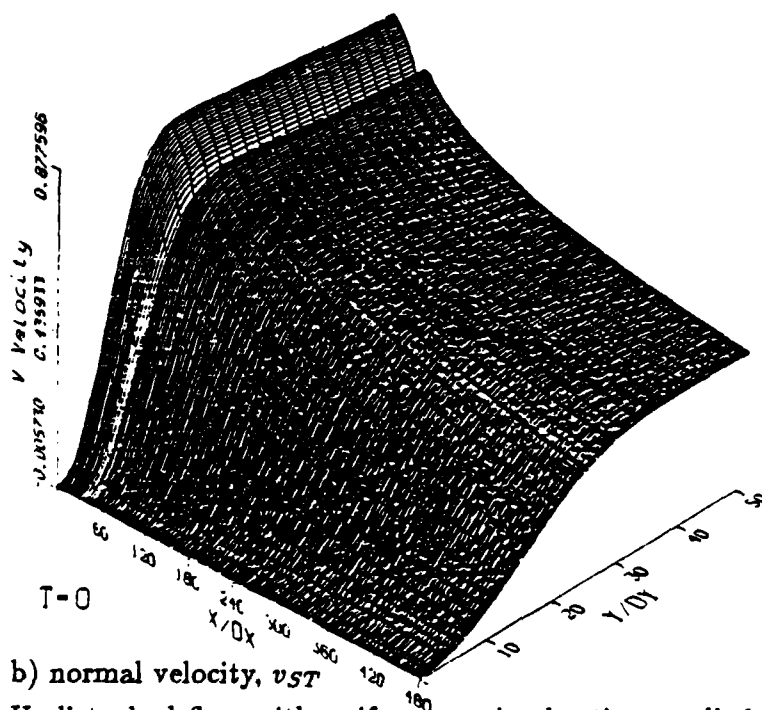


a) 2D streamwise velocity,  $U_0$

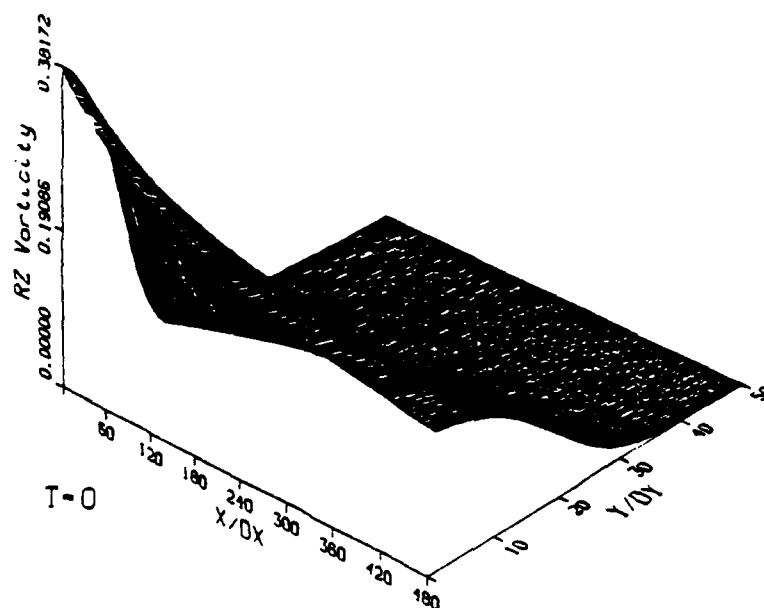
Figure 6.14 Amplitude and phase comparison with linear stability theory without control applied,  $F = 1.55$



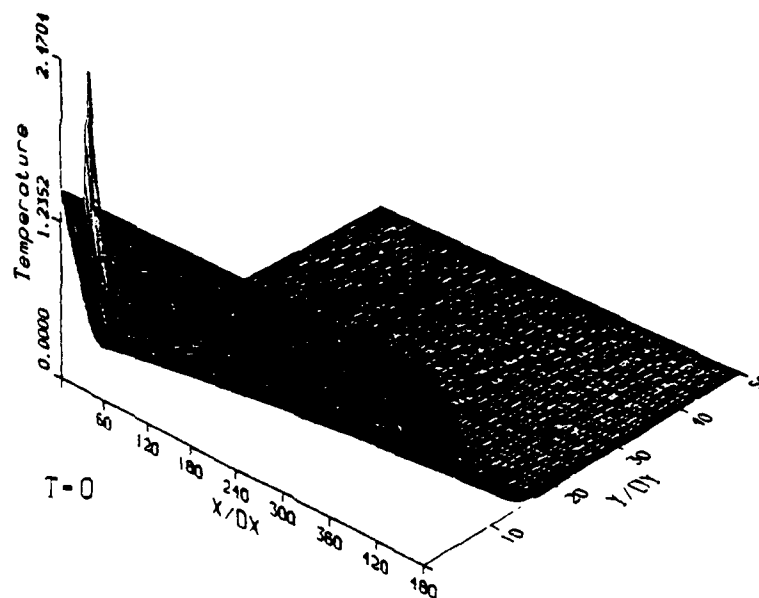
b) 3D streamwise velocity,  $U_1$   
Figure 6.14 continued

a) streamwise velocity,  $u_{ST}$ b) normal velocity,  $v_{ST}$ Figure 6.15 Undisturbed flow with uniform passive heating applied,  $\Delta \bar{T} = 8^\circ F$ ,  $F = 1$





c) spanwise vorticity,  $\omega_{zST}$



d) temperature,  $T_{ST}$

Figure 6.15 continued

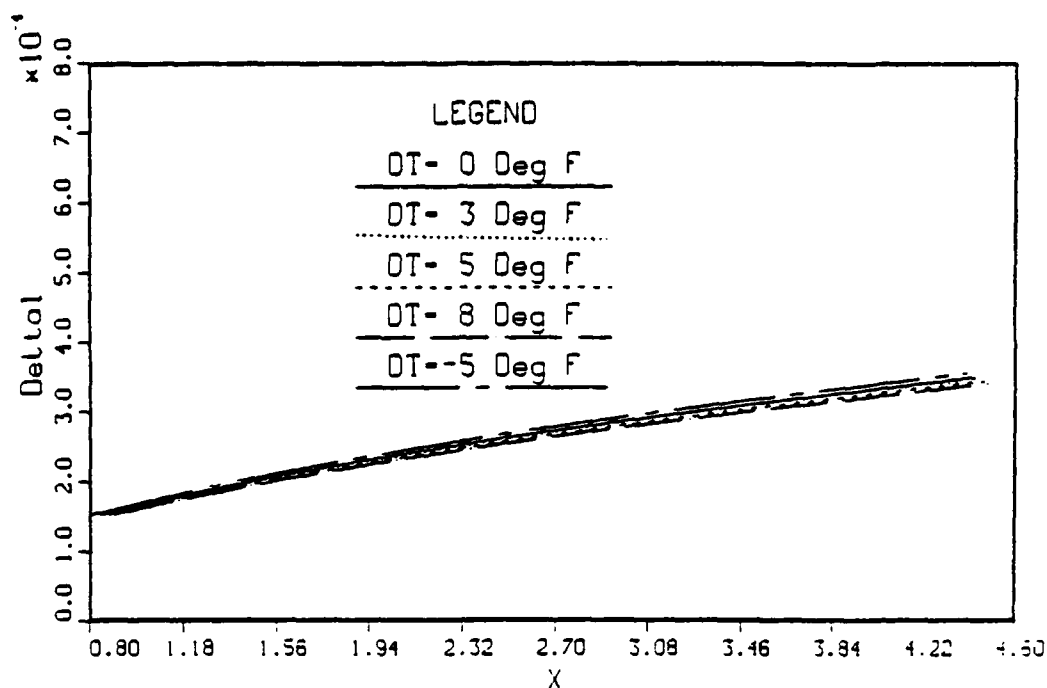


Figure 6.16 Growth of undisturbed boundary layer with uniform passive heating applied,  $F = 1$

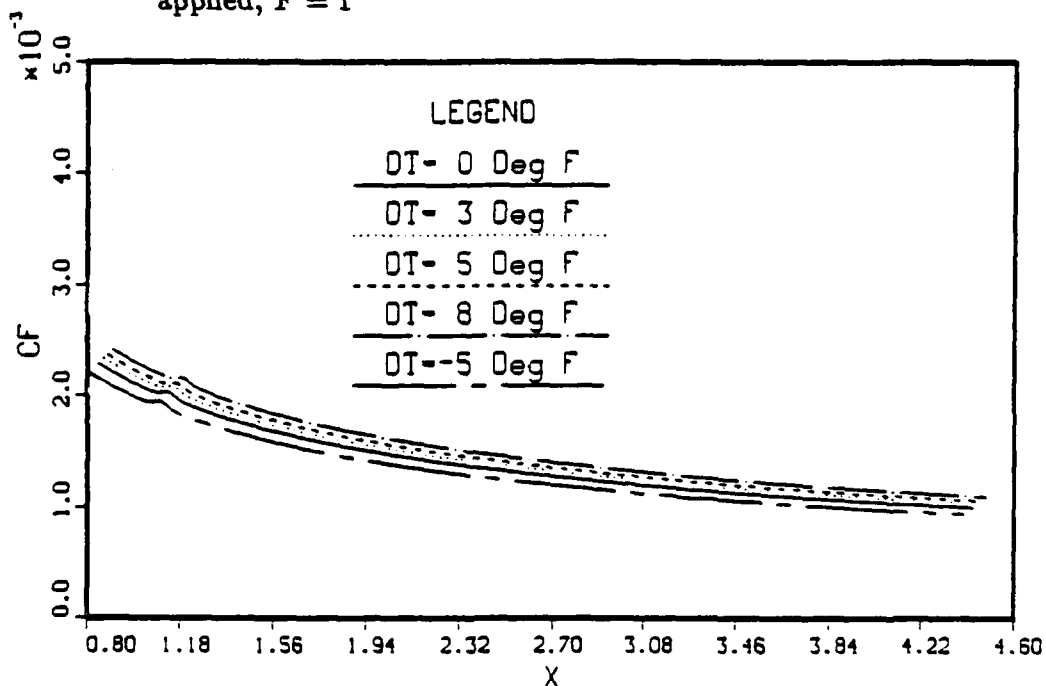
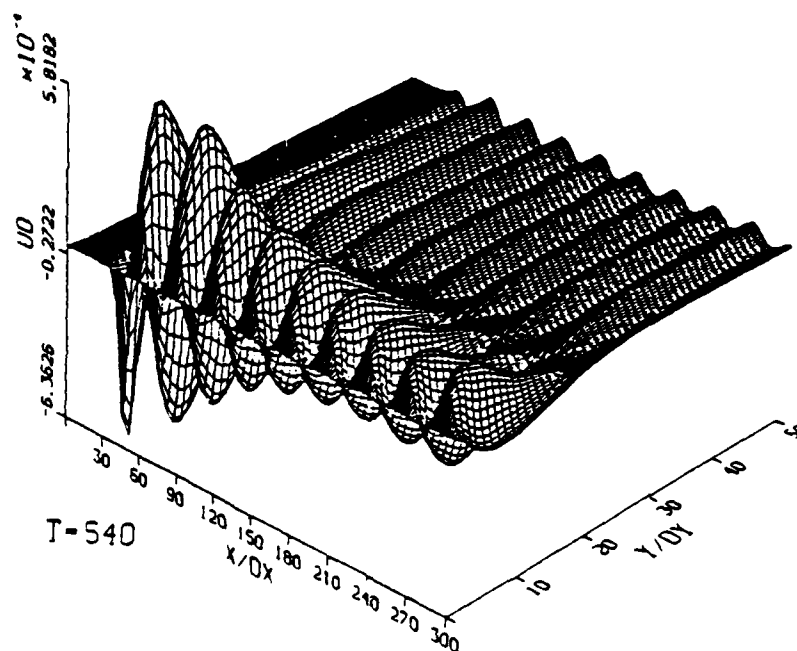
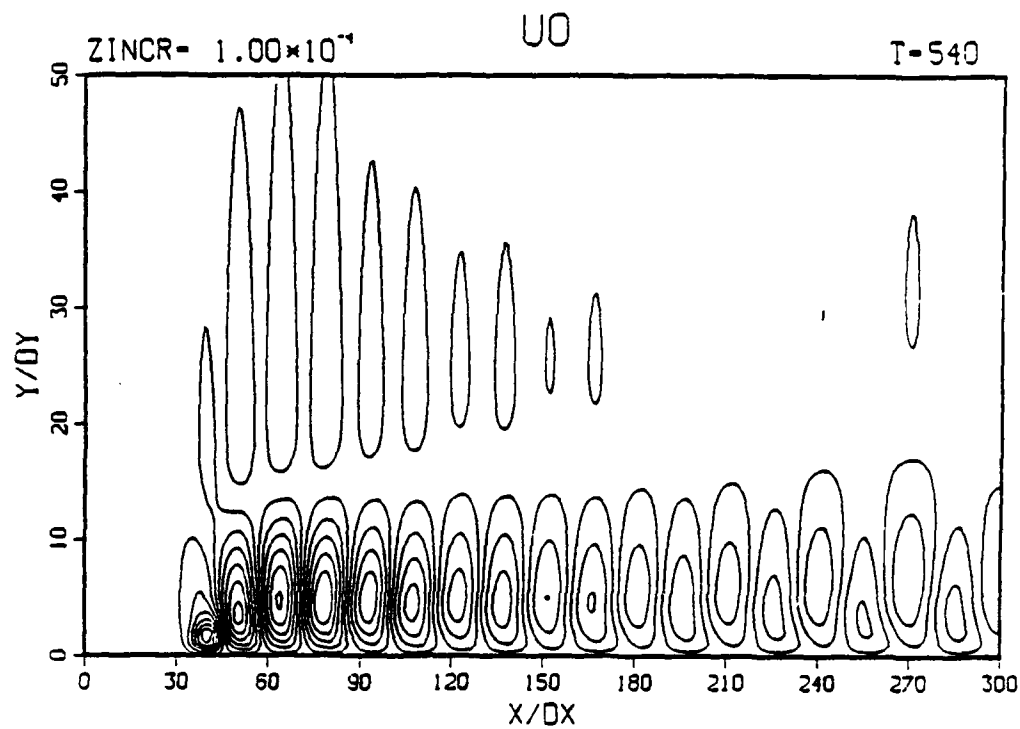
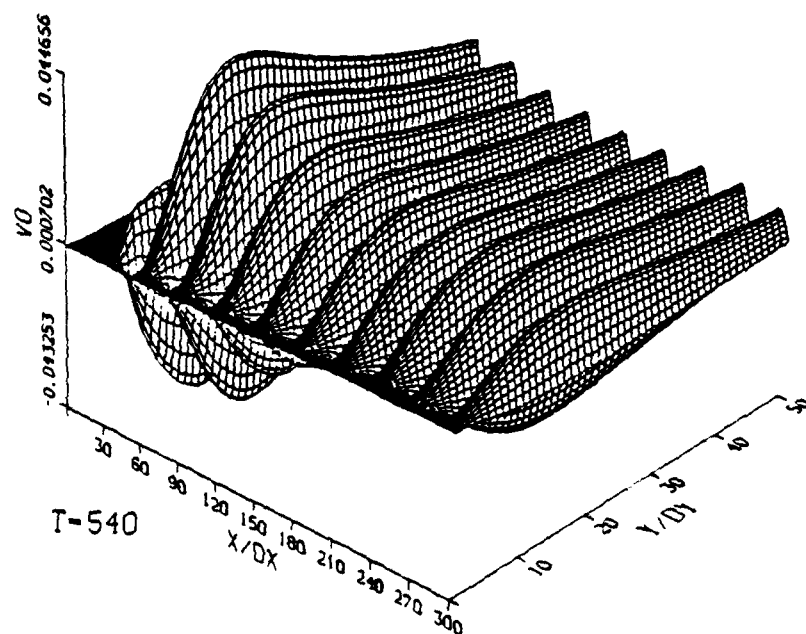
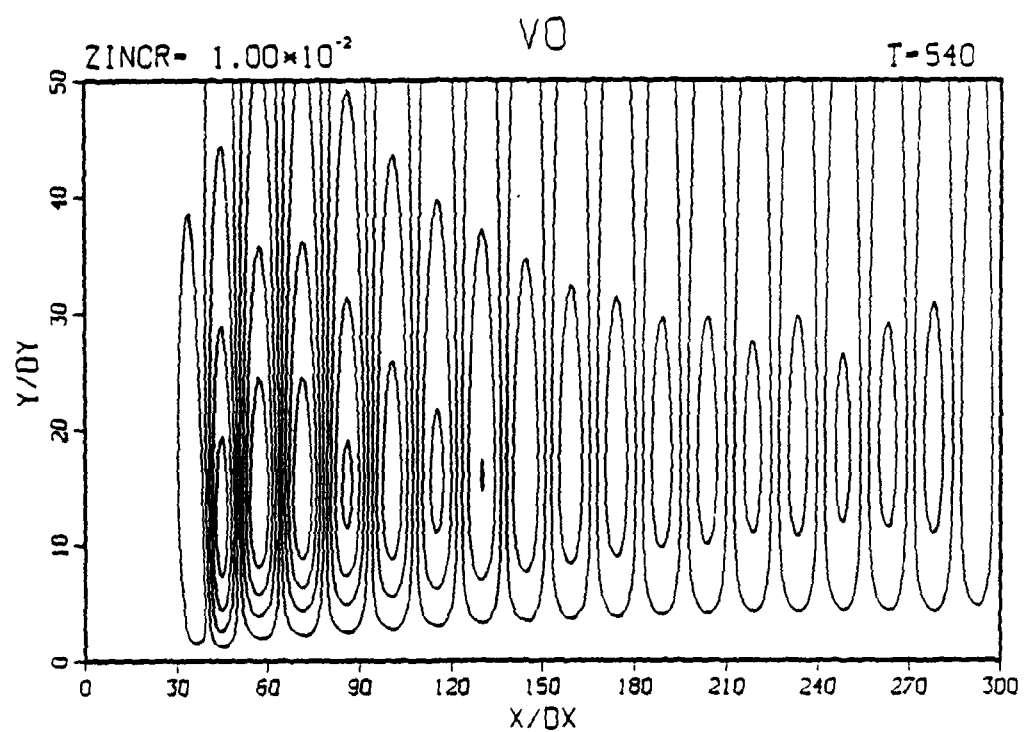


Figure 6.17 Comparison of skin friction with uniform passive heating applied,  $F = 1$



a) 2D streamwise velocity,  $U_0$

Figure 6.18 Disturbed flow after nine periods of oscillation with  $\Delta \bar{T} = 8^\circ F$  passive control applied,  $F = 1$



b) 2D normal velocity,  $V_0$

Figure 6.18 continued

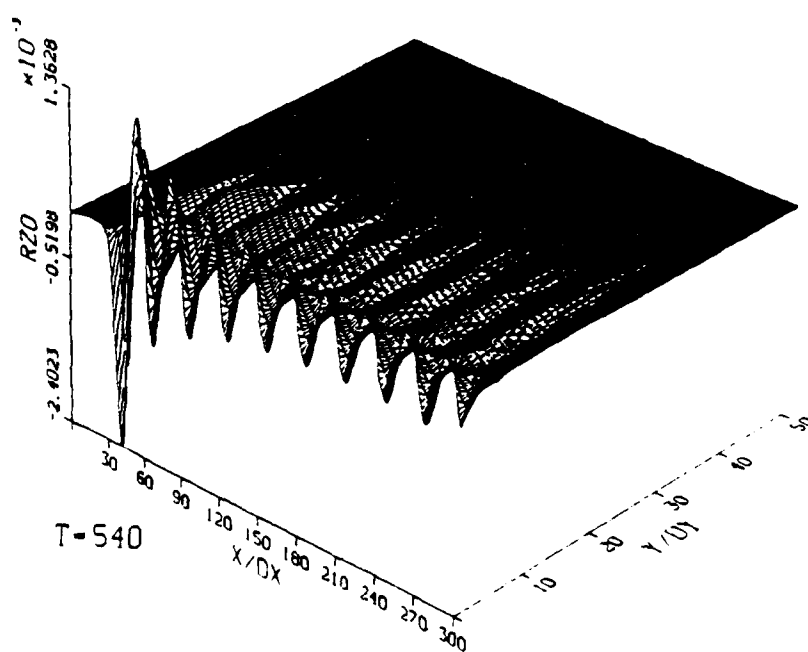
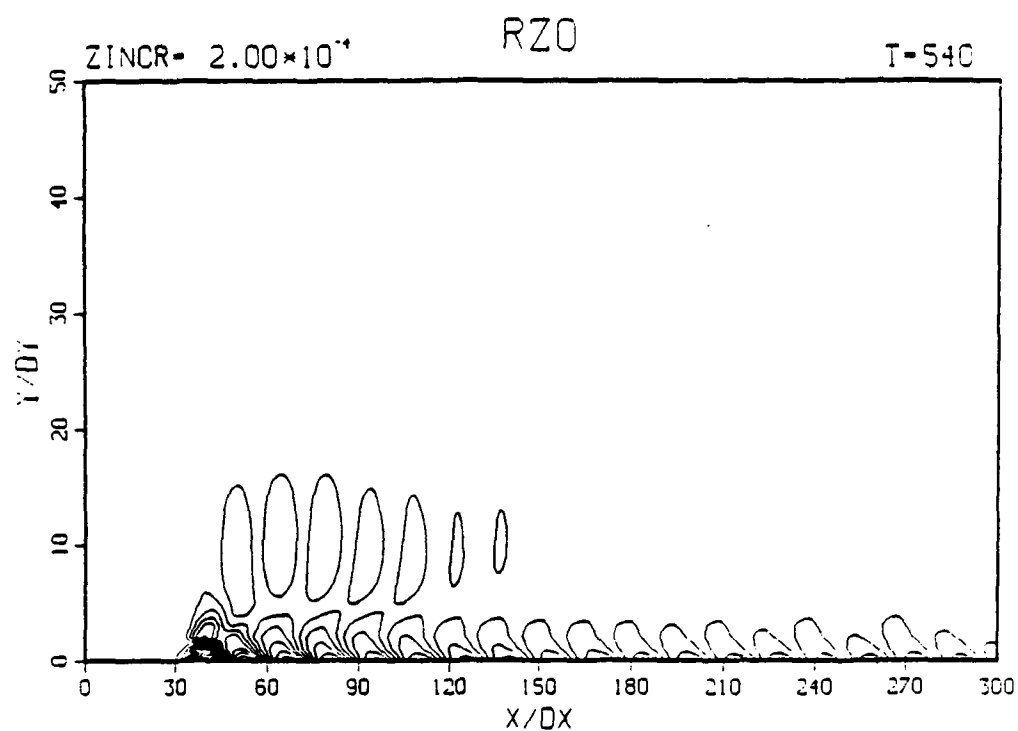
c) 2D spanwise vorticity,  $\Omega_{z0}$ 

Figure 6.18 continued

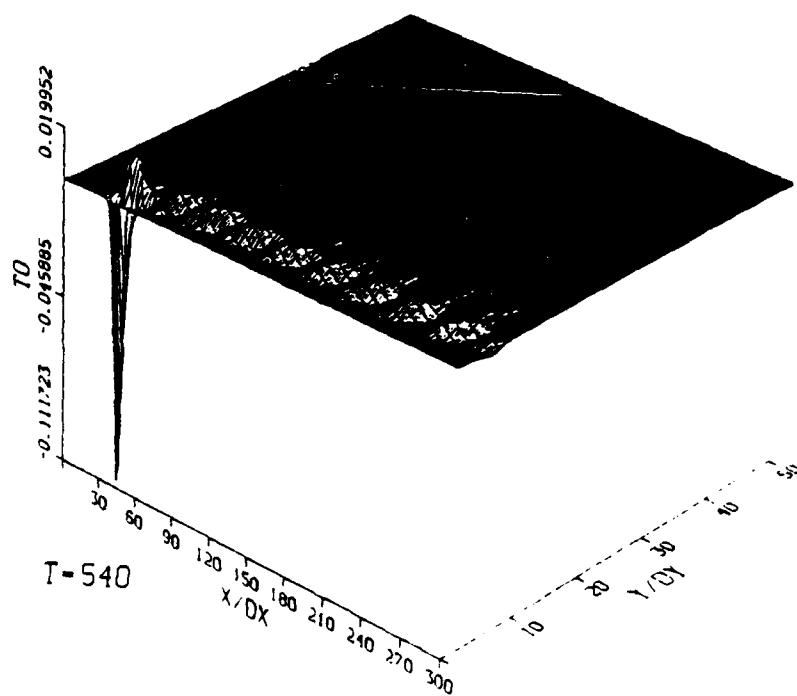
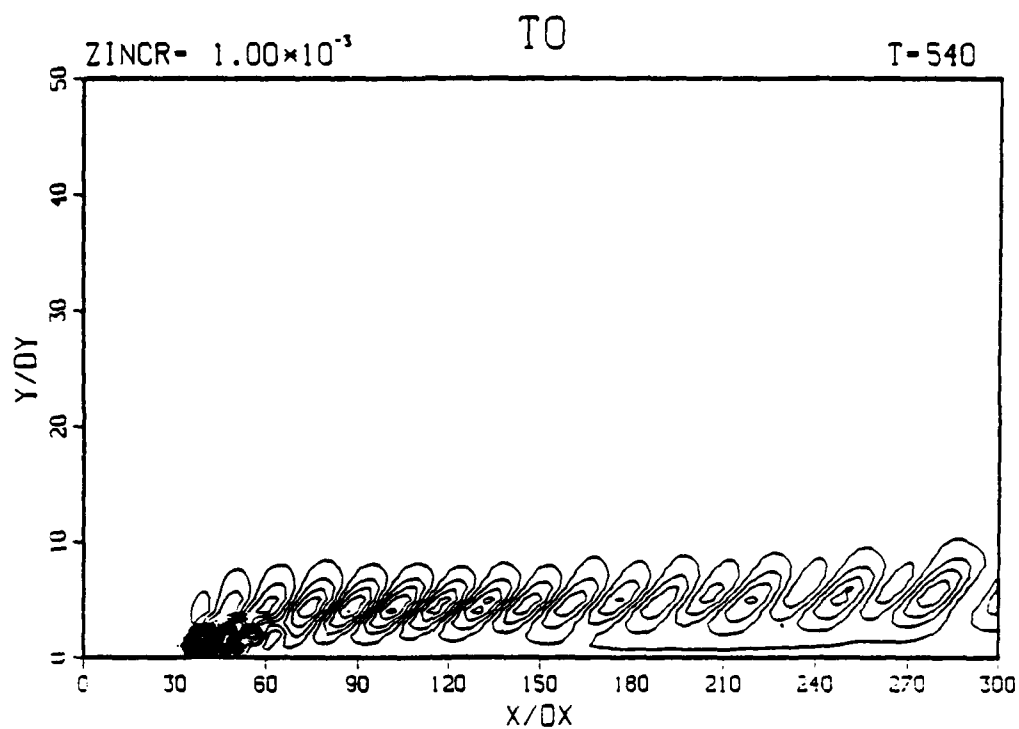
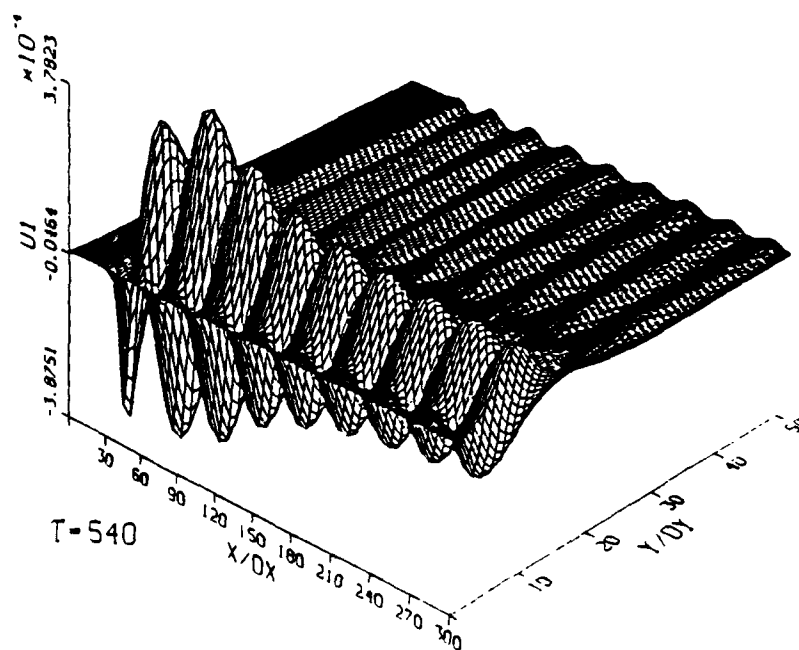
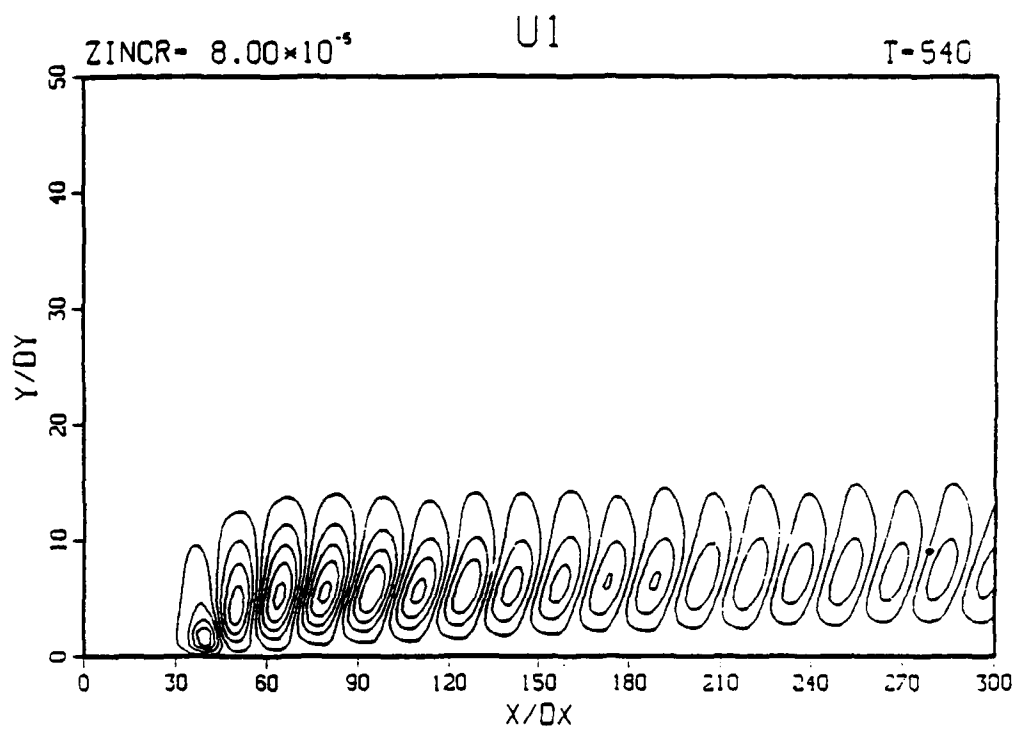
d) 2D temperature,  $\Theta_0$ 

Figure 6.18 continued



e) 3D streamwise velocity,  $U_1$

Figure 6.18 continued

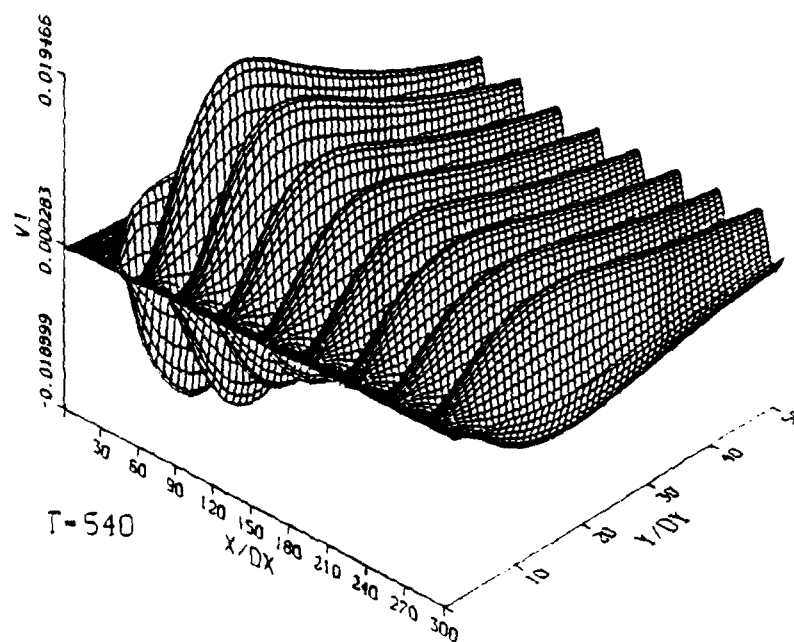
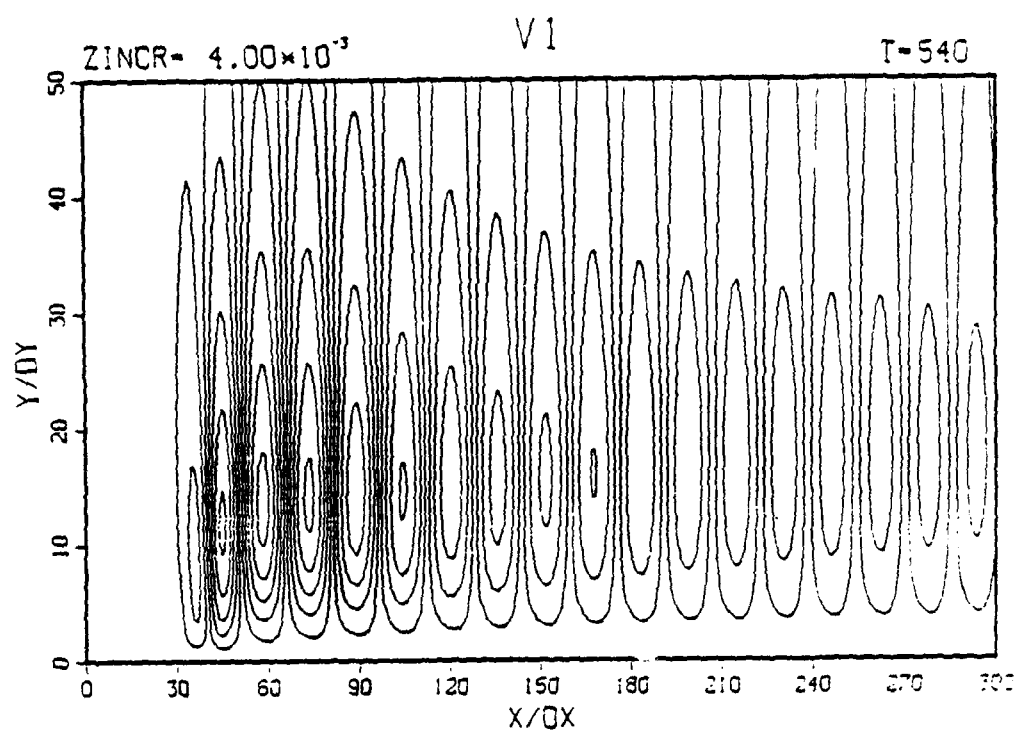
f) 3D normal velocity,  $V_1$ 

Figure 6.18 continued



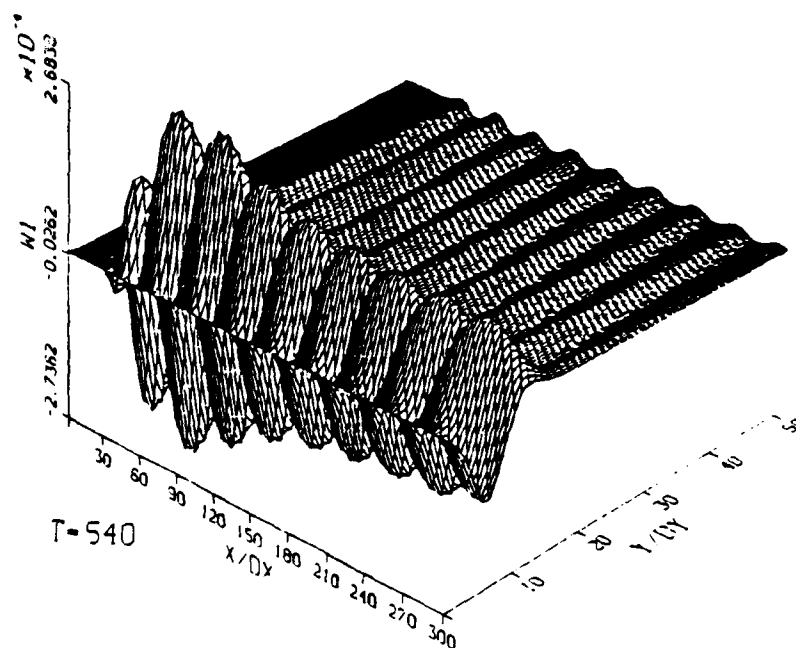
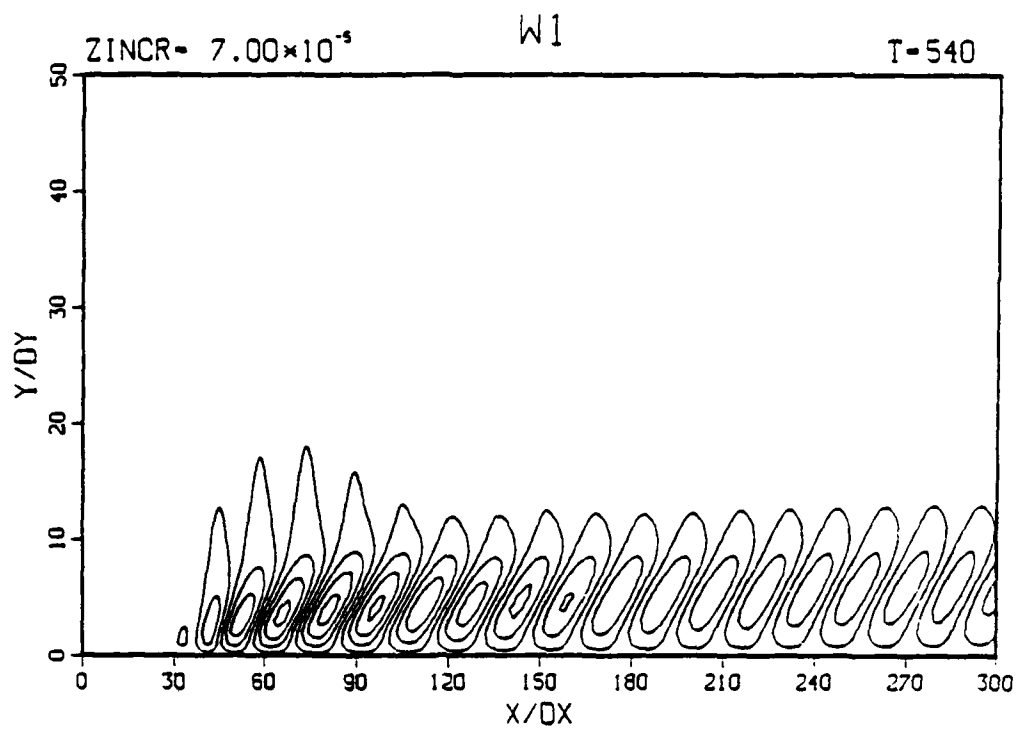
g) 3D spanwise velocity,  $W_1$ 

Figure 6.18 continued

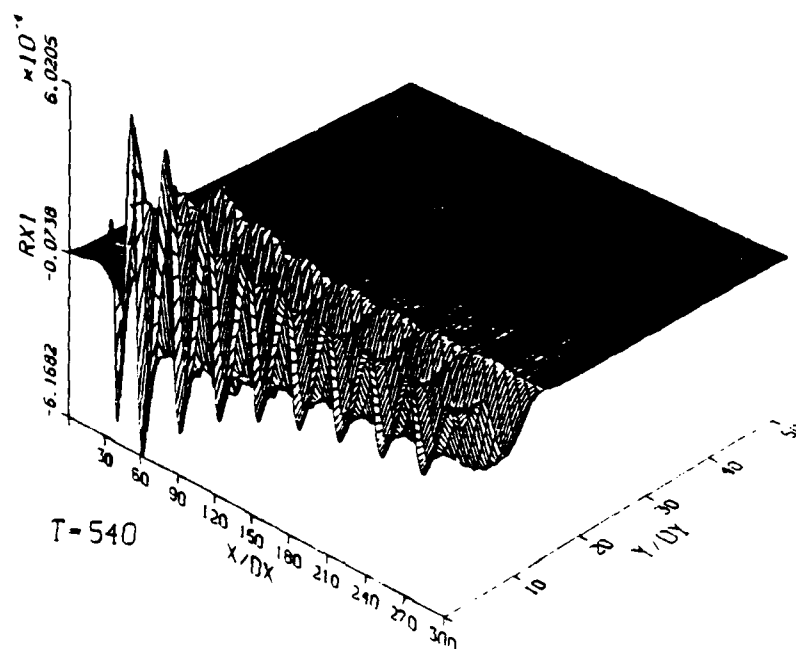
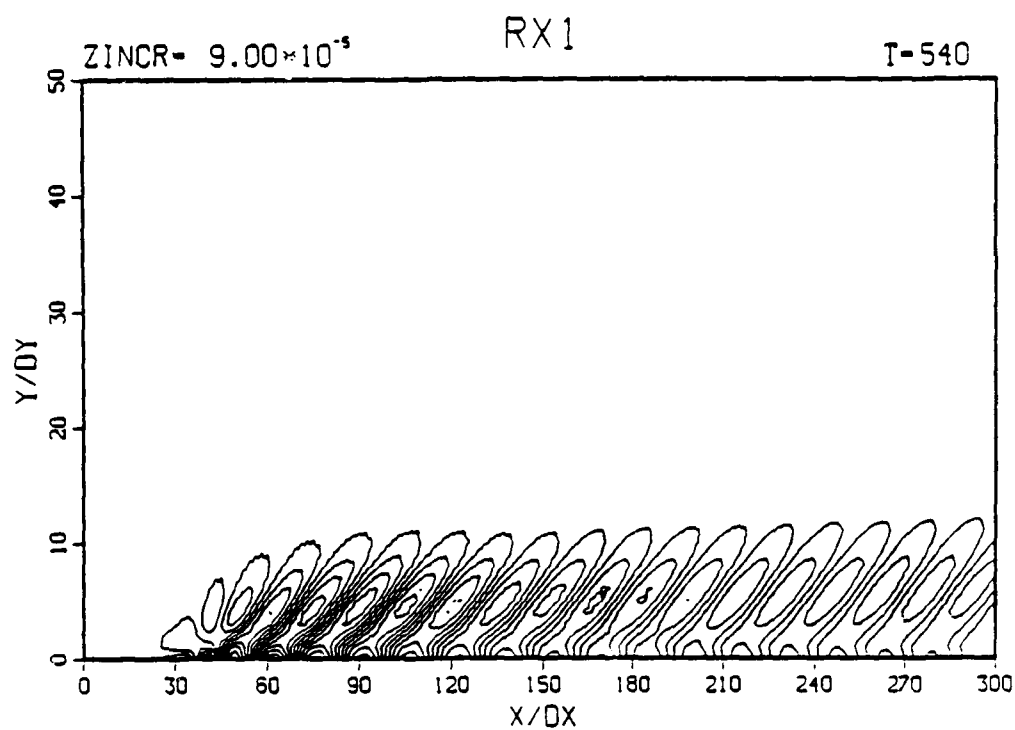
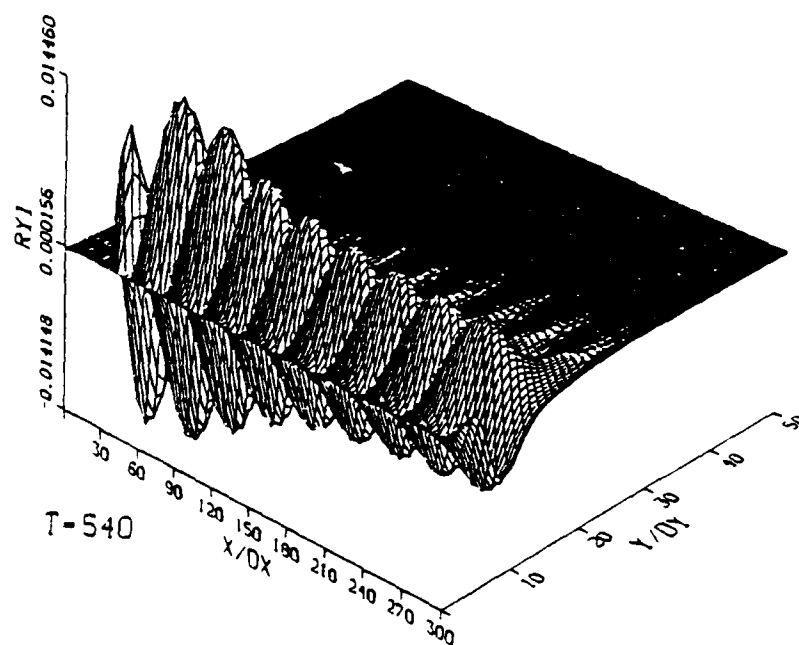
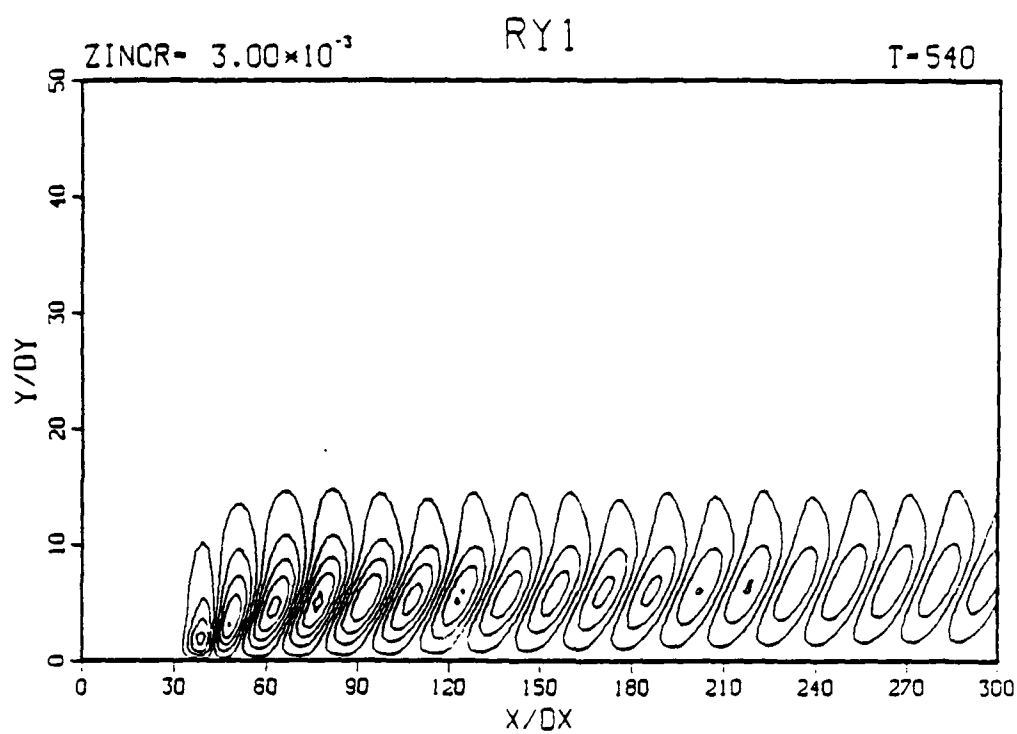
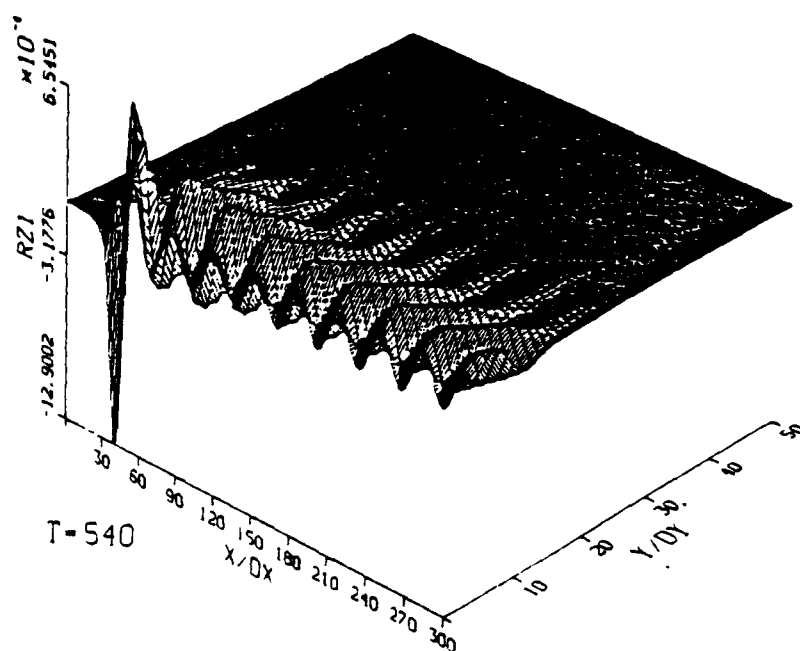
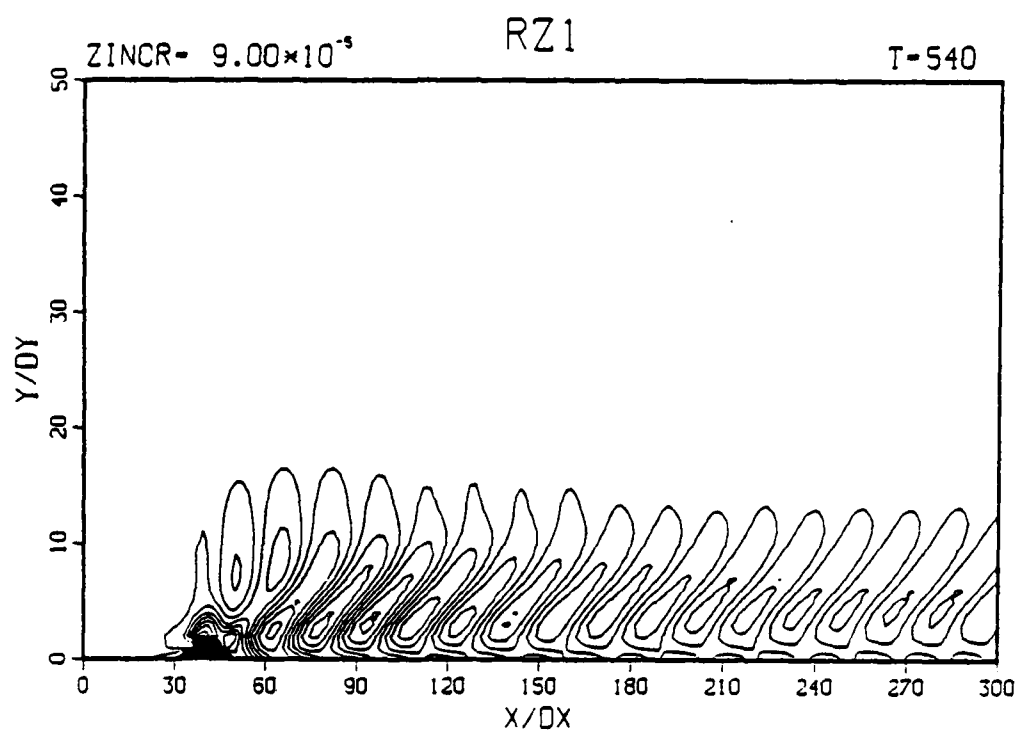
h) 3D streamwise vorticity,  $\Omega_{x1}$ 

Figure 6.18 continued



i) 3D normal vorticity,  $\Omega_{y1}$

Figure 6.18 continued



j) 3D spanwise vorticity,  $\Omega_z$ ,  
Figure 6.18 continued

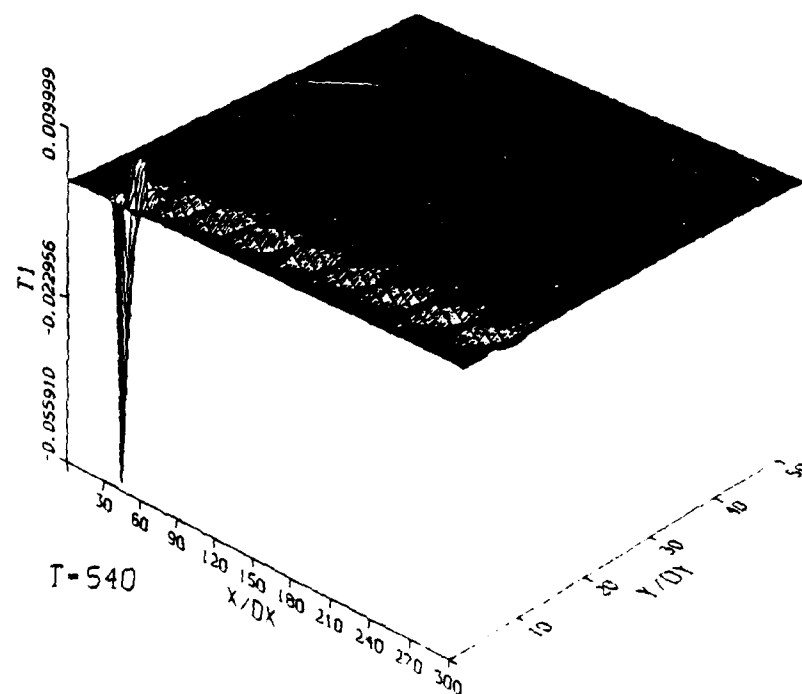
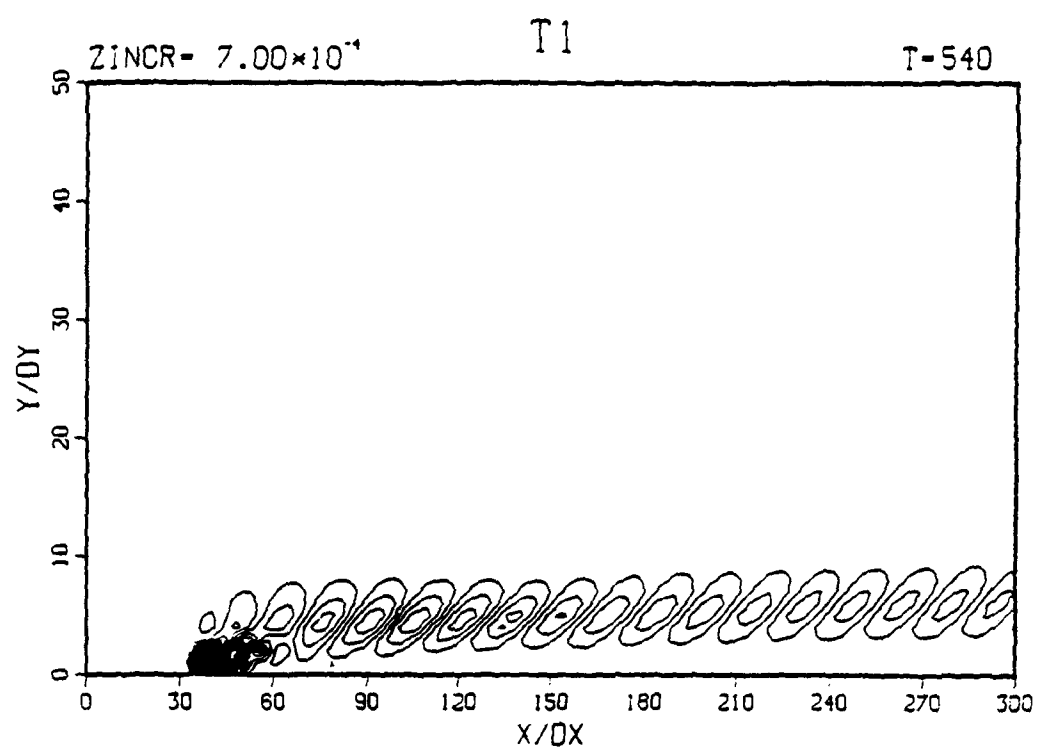
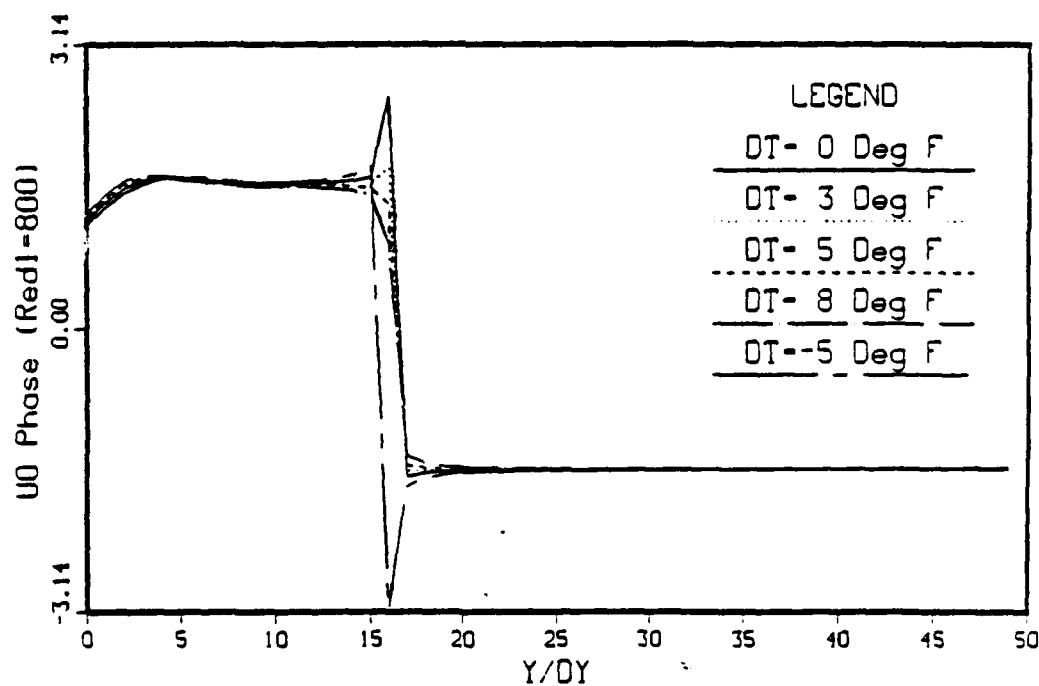
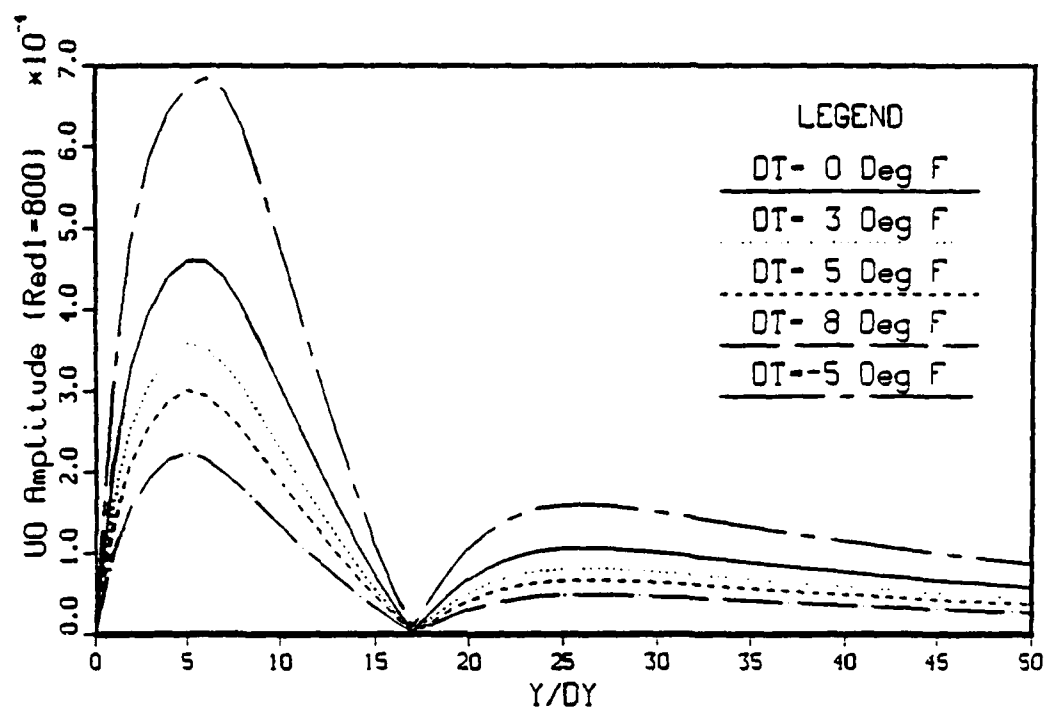
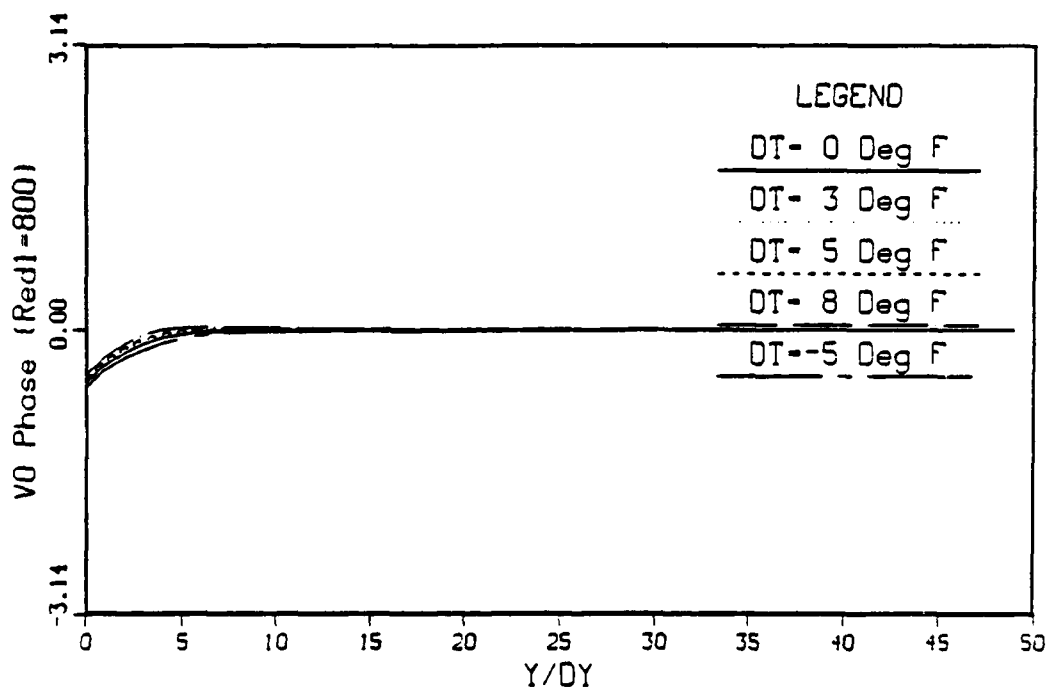
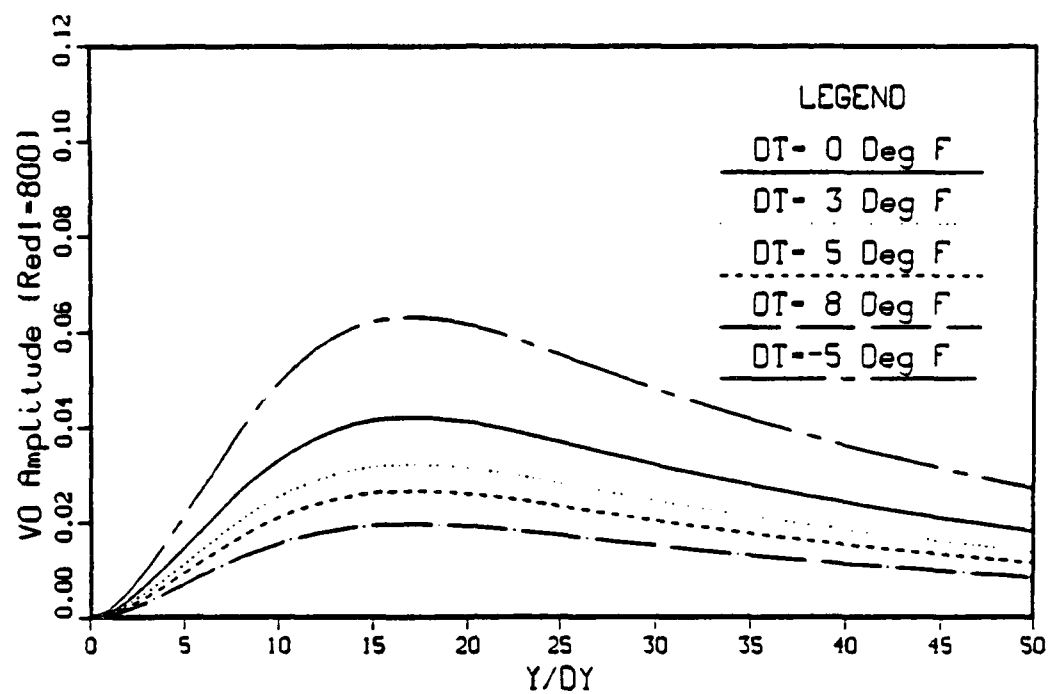
k) 3D temperature,  $\Theta_1$ 

Figure 6.18 continued



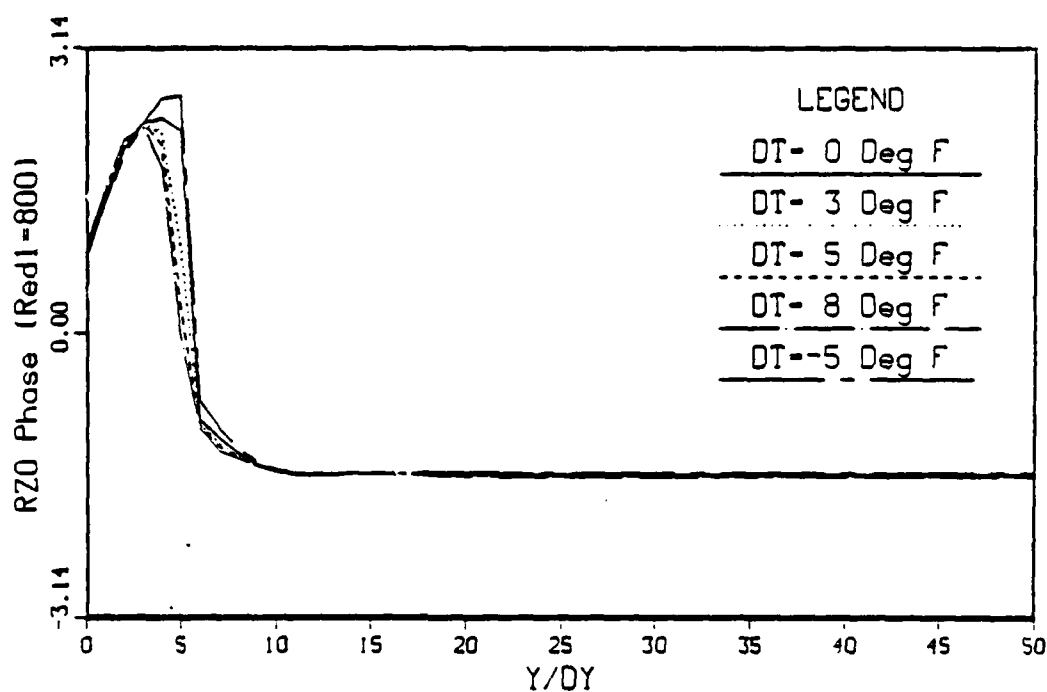
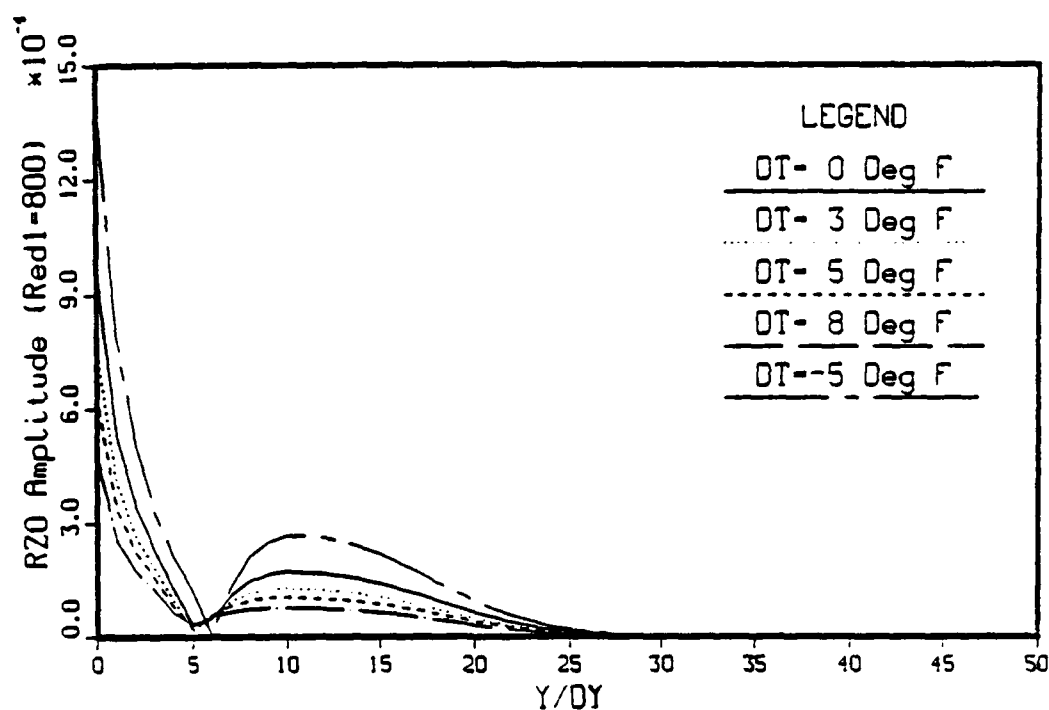
a) 2D streamwise velocity,  $U_0$

Figure 6.19 Amplitude and phase comparison at  $Re_{\delta_1} = 800$  with uniform passive control applied,  $F = 1$



b) 2D normal velocity,  $V_0$

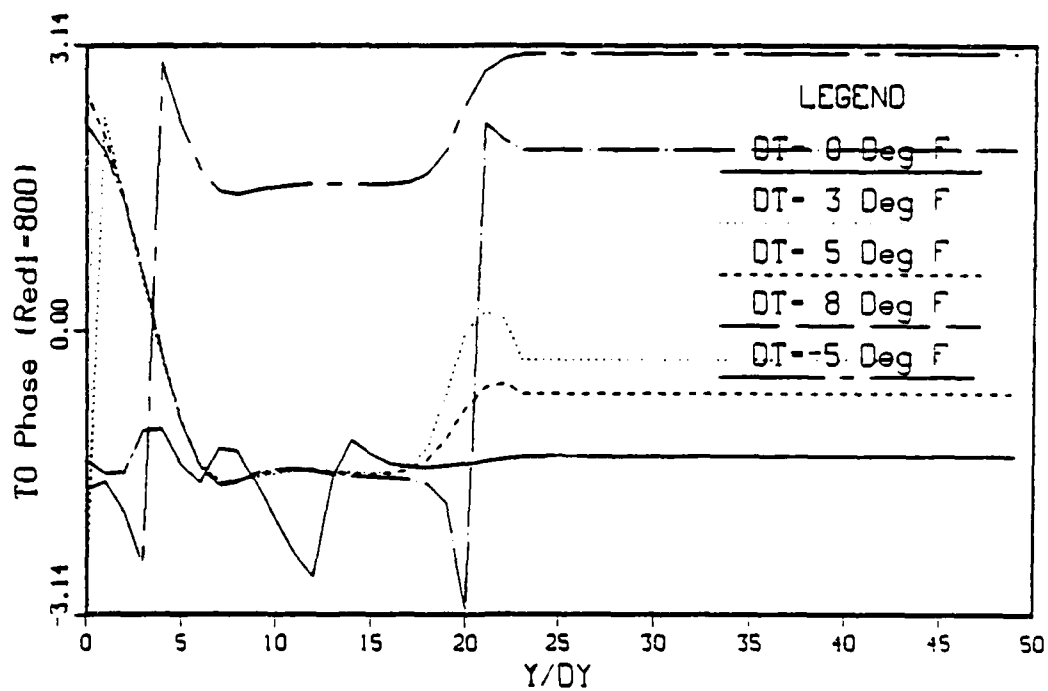
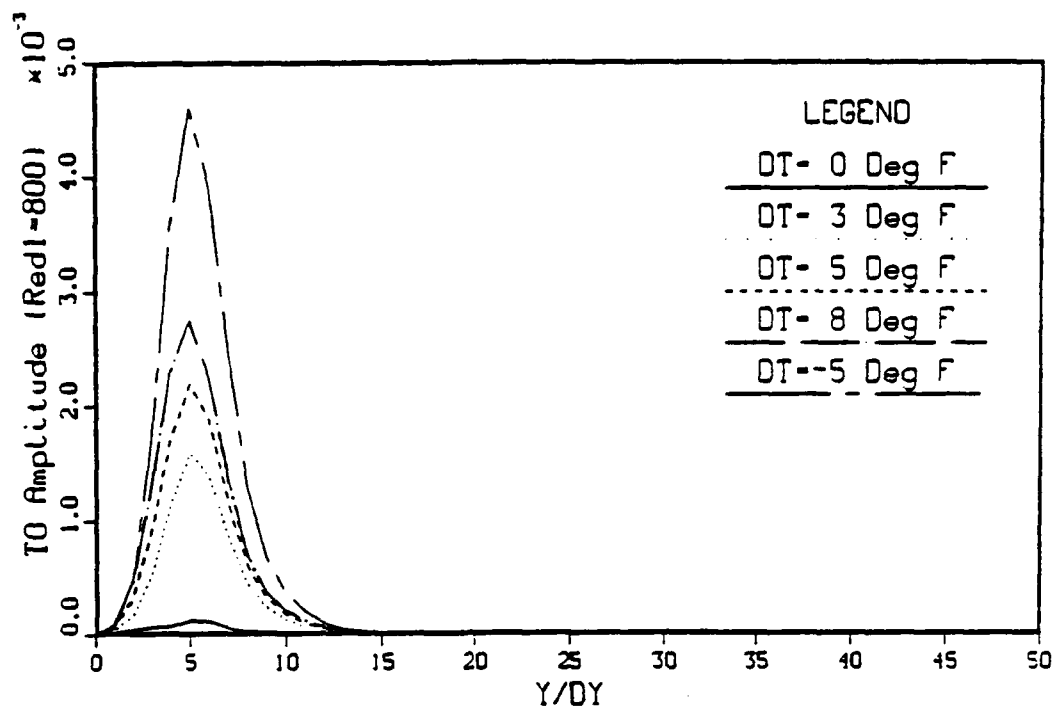
Figure 6.19 continued



c) 2D spanwise vorticity,  $\Omega_{zo}$

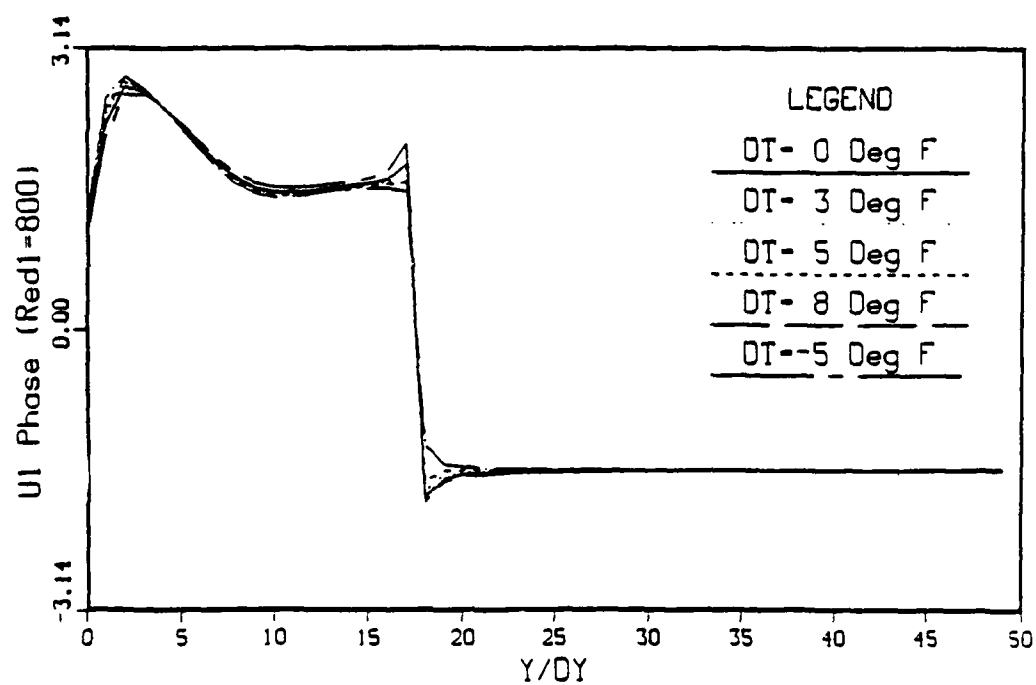
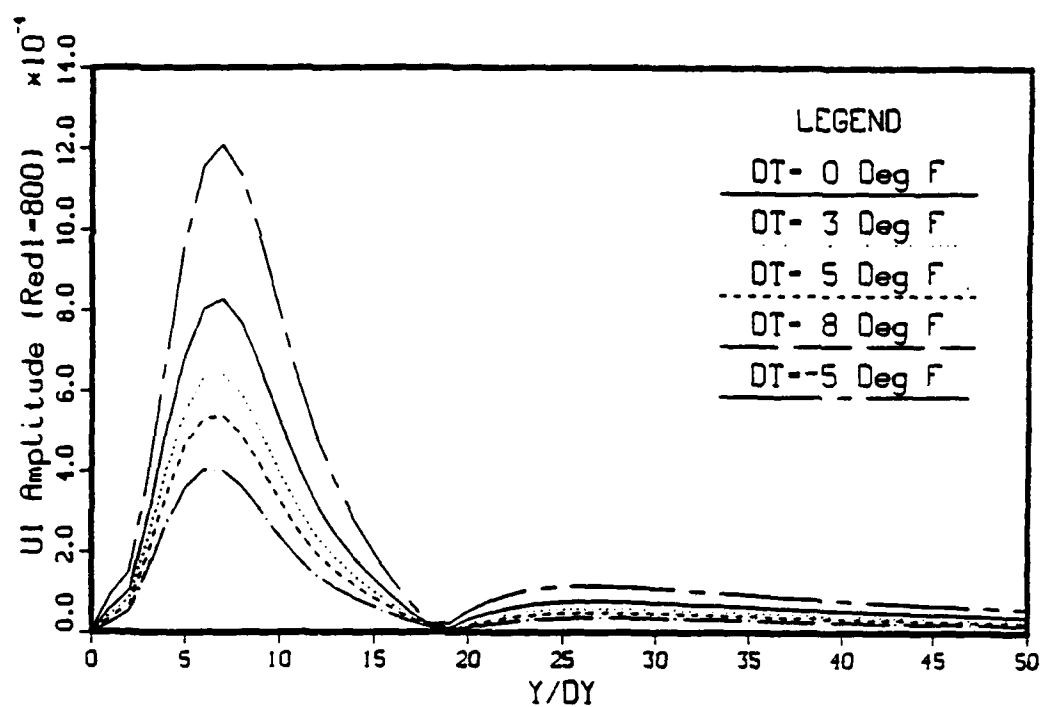
Figure 6.19 continued





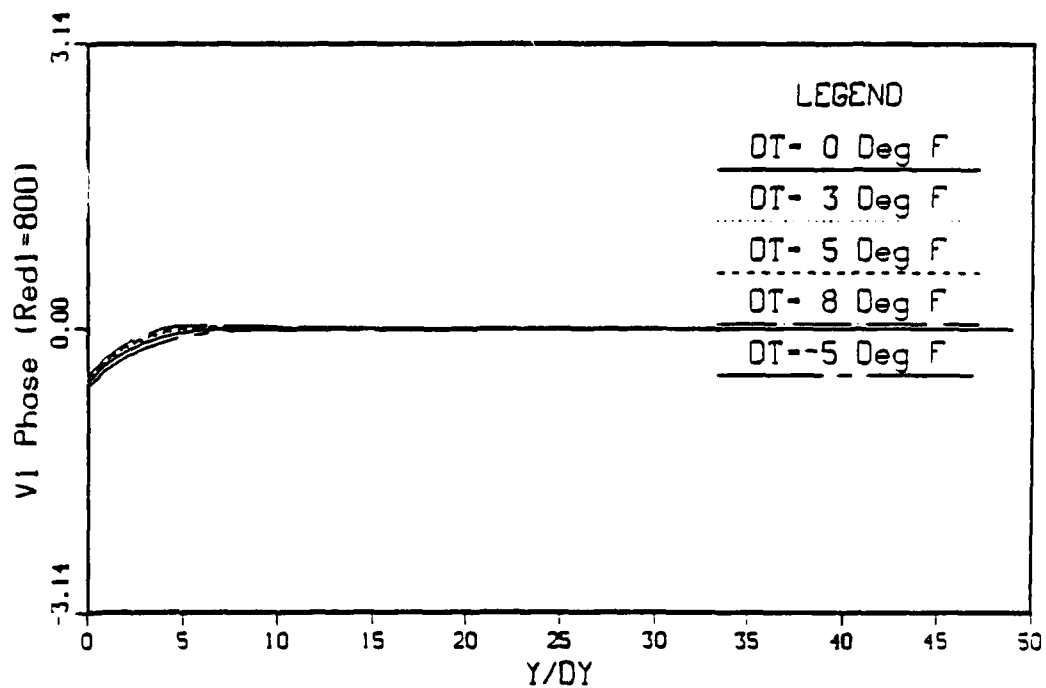
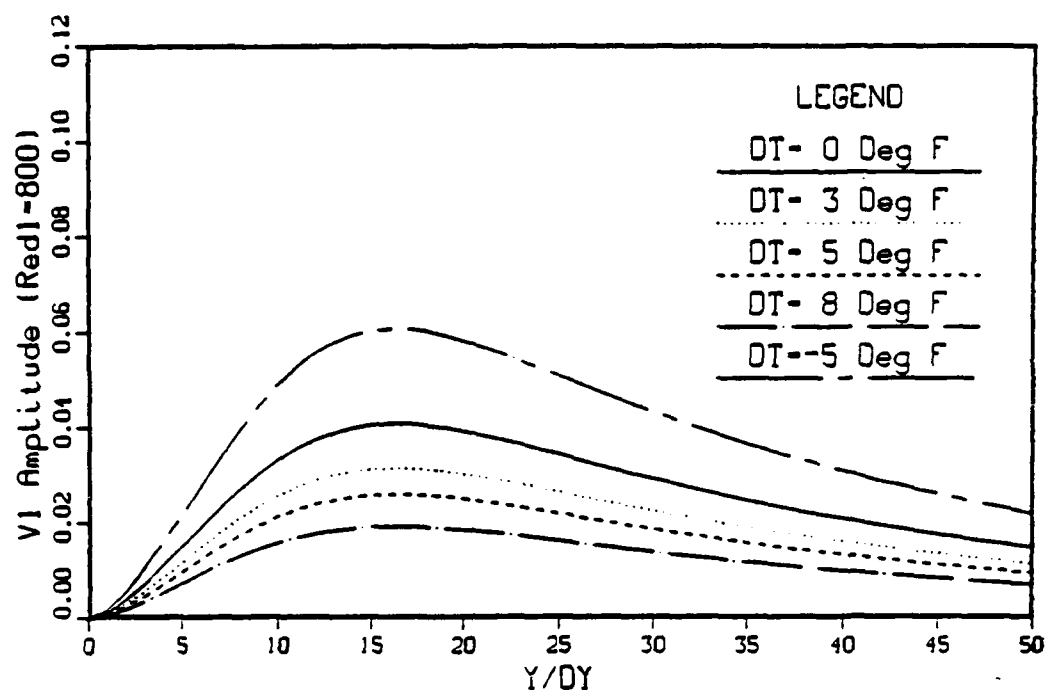
d) 2D temperature,  $\Theta_0$

Figure 6.19 continued



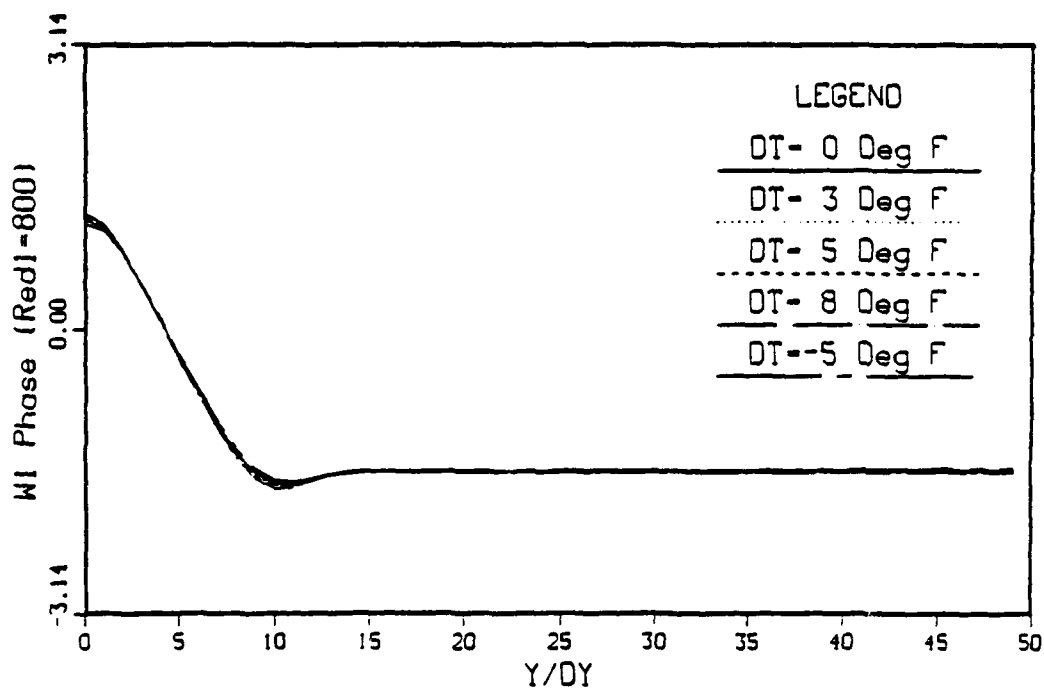
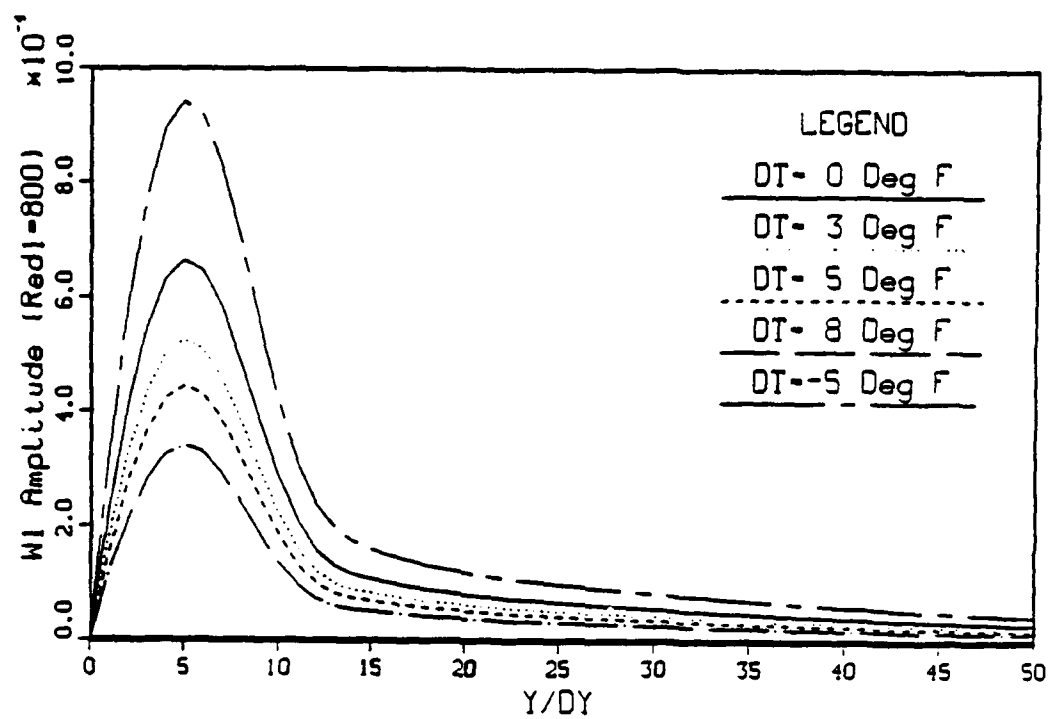
e) 3D streamwise velocity,  $U_1$

Figure 6.19 continued



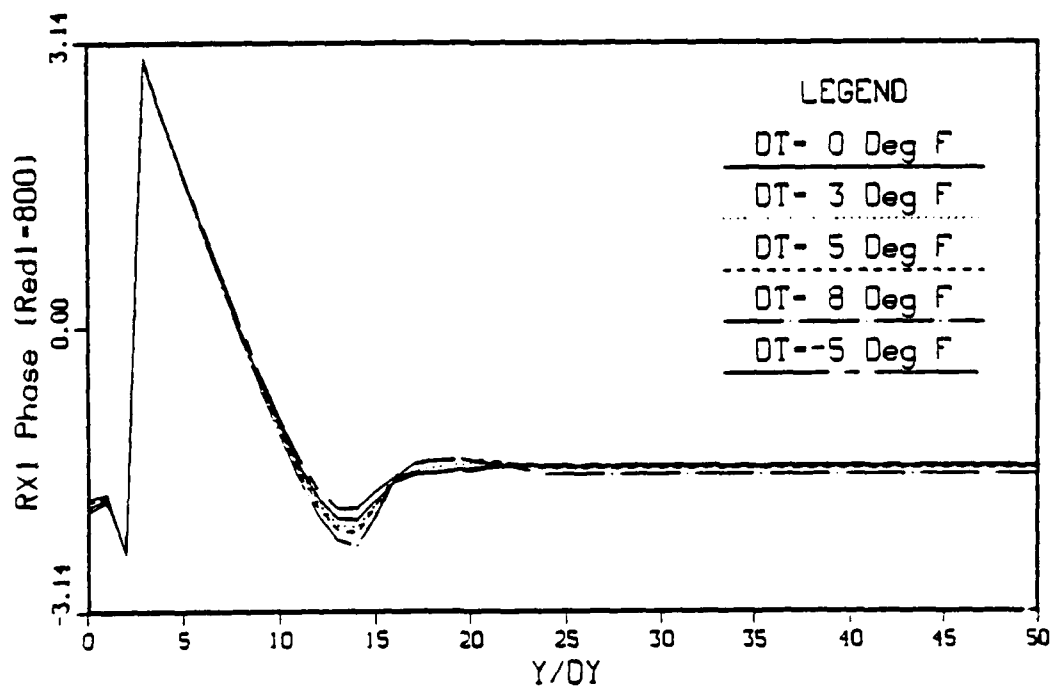
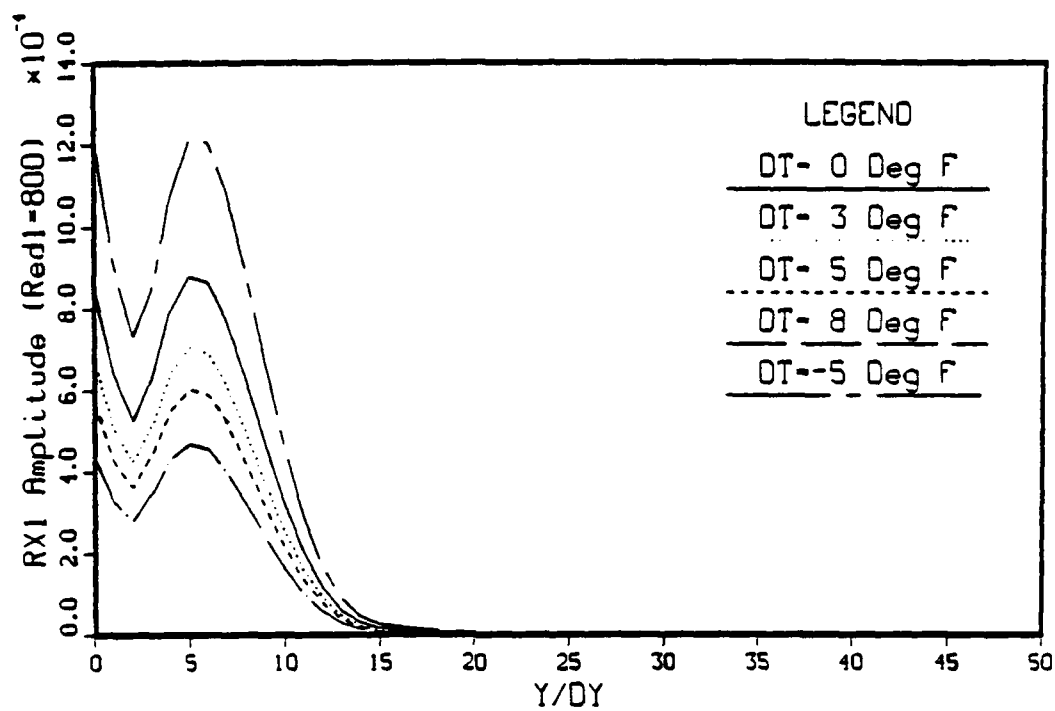
f) 3D normal velocity,  $V_1$

Figure 6.19 continued



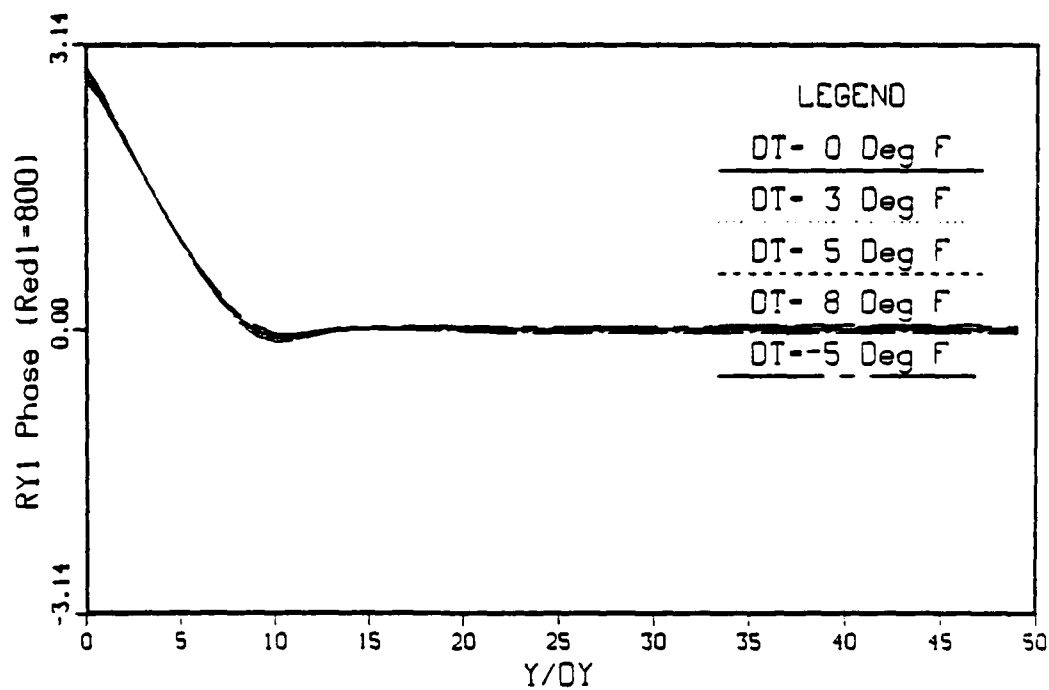
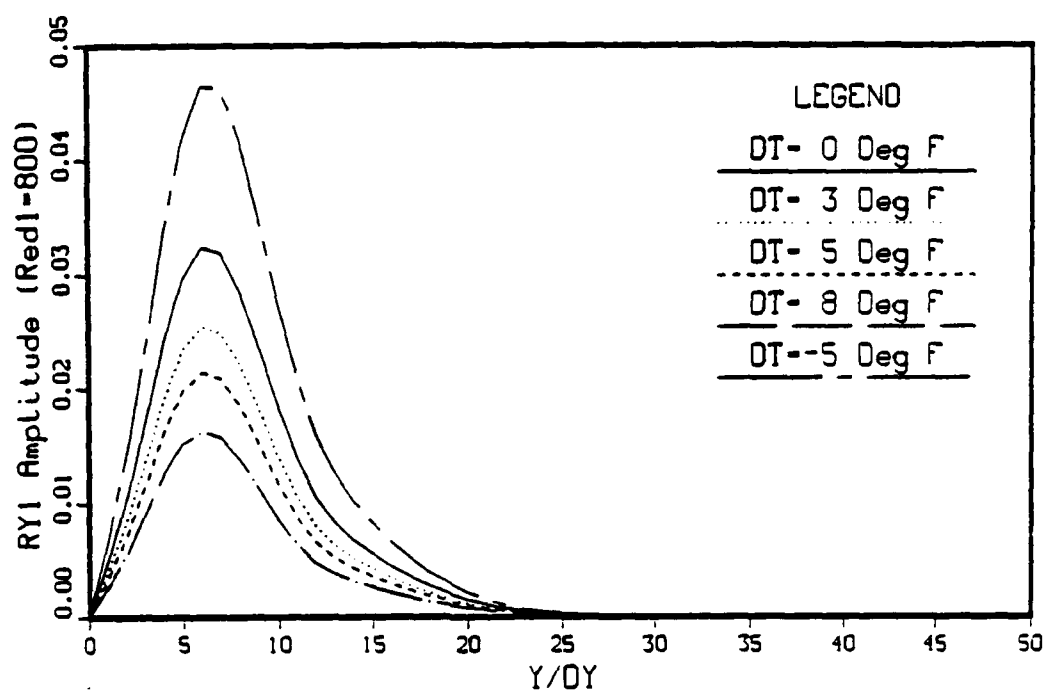
g) 3D spanwise velocity,  $W_1$

Figure 6.19 continued



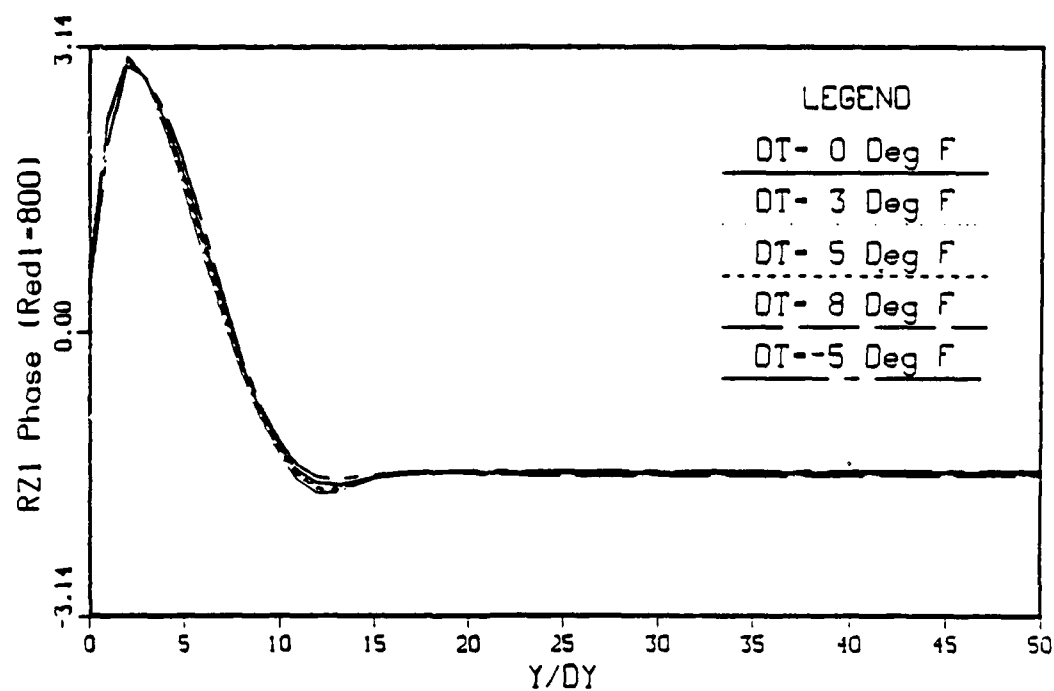
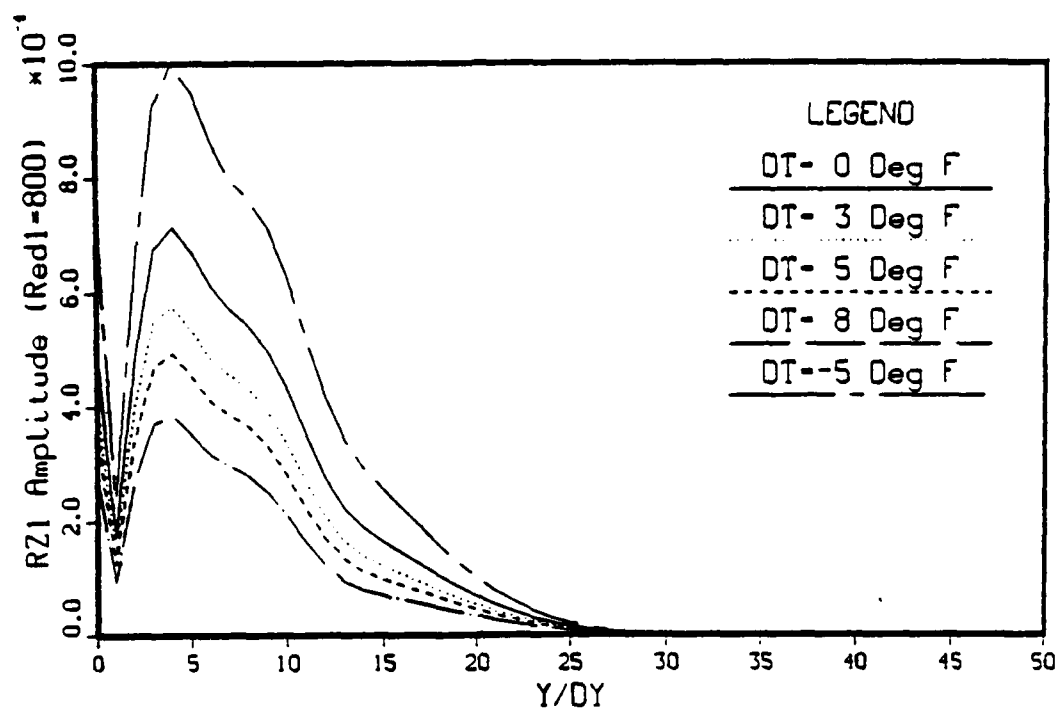
h) 3D streamwise vorticity,  $\Omega_{z1}$

Figure 6.19 continued



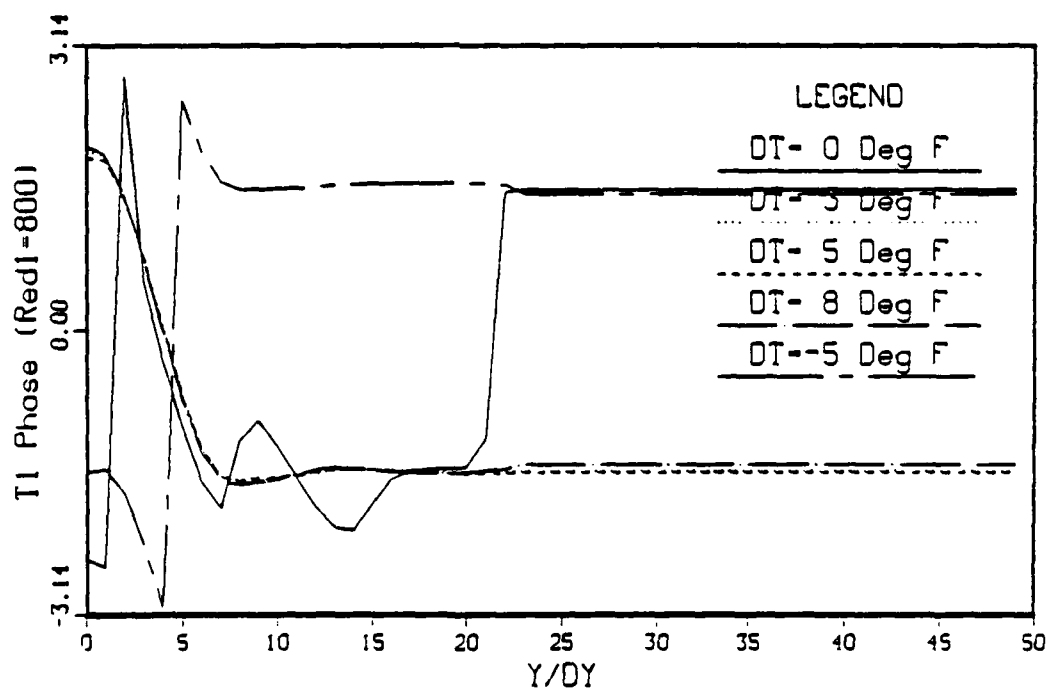
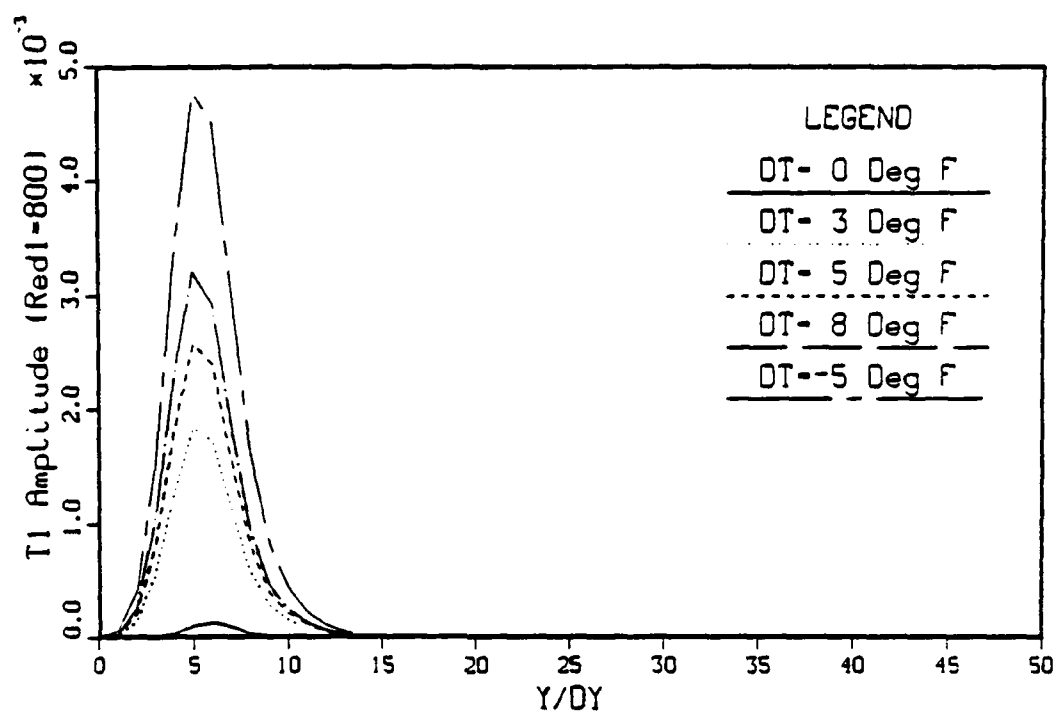
i) 3D normal vorticity,  $\Omega_{y_1}$

Figure 6.19 continued



j) 3D spanwise vorticity,  $\Omega_{z1}$

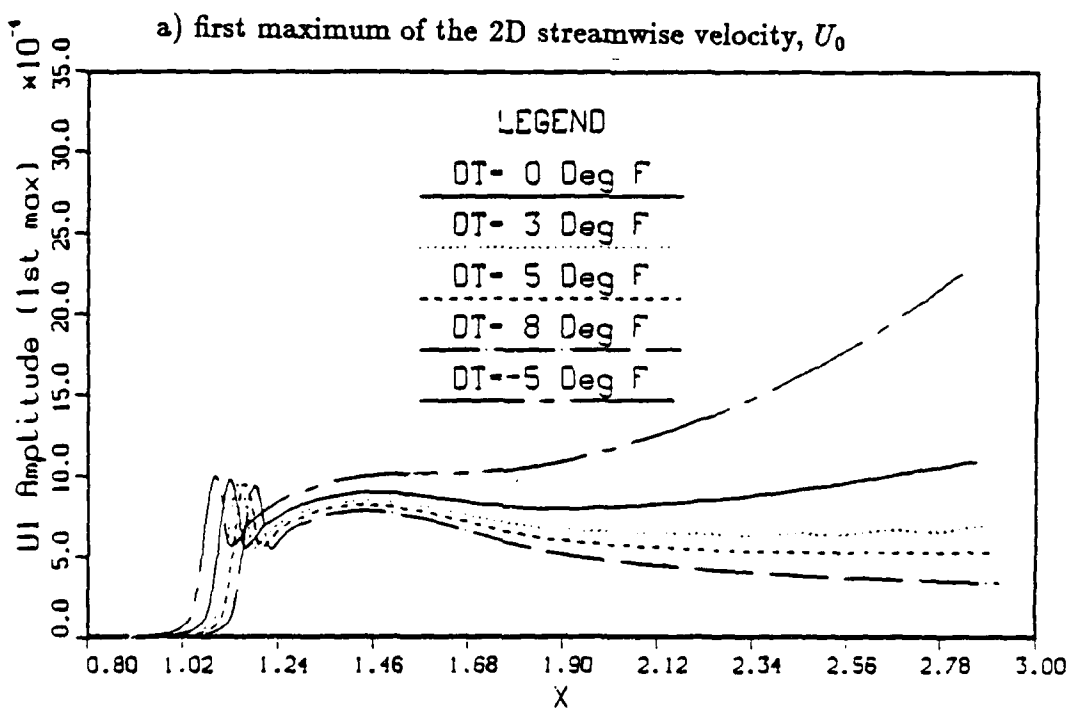
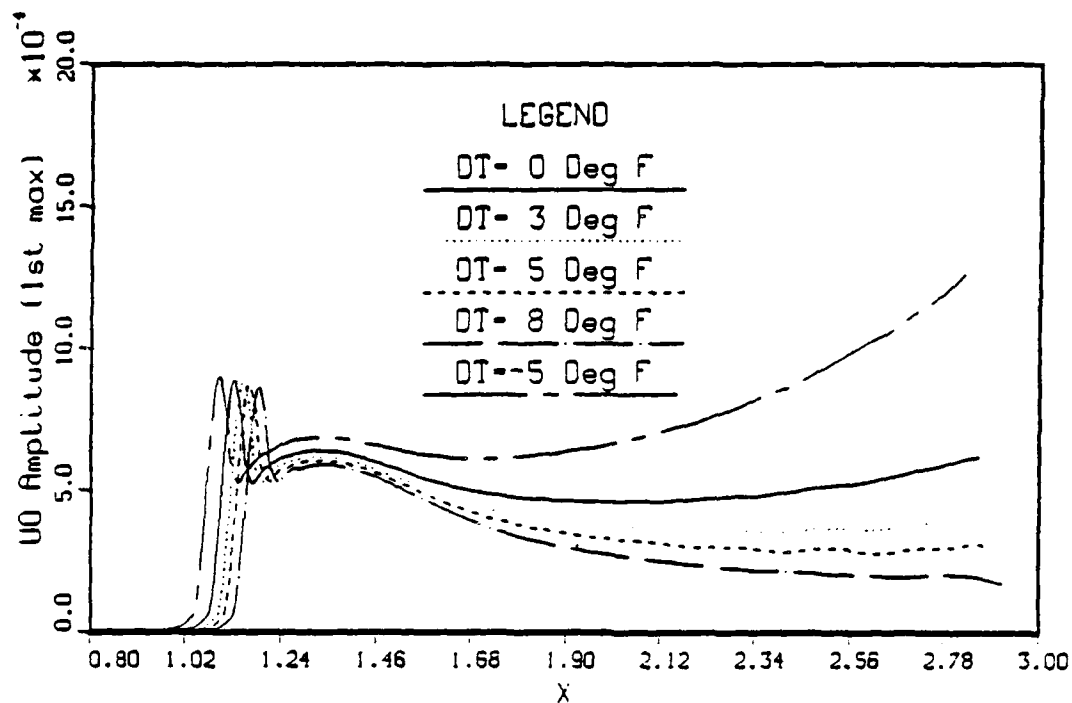
Figure 6.19 continued



k) 3D temperature,  $\Theta_1$

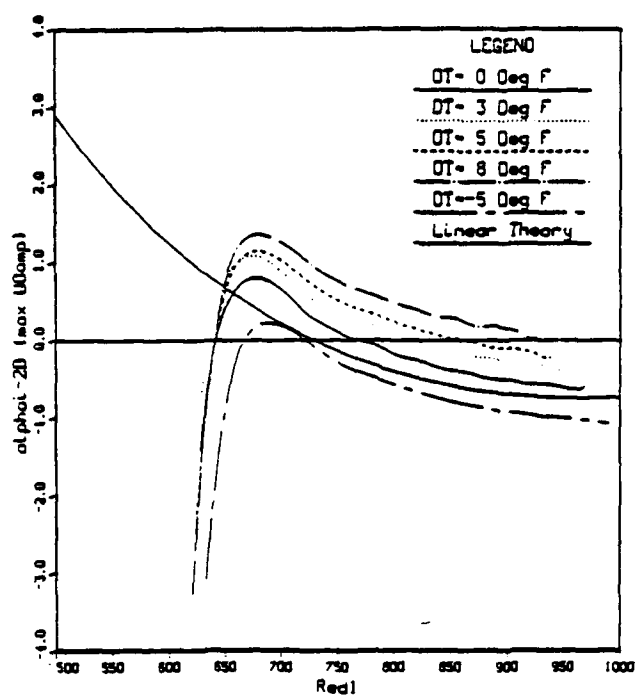
Figure 6.19 continued



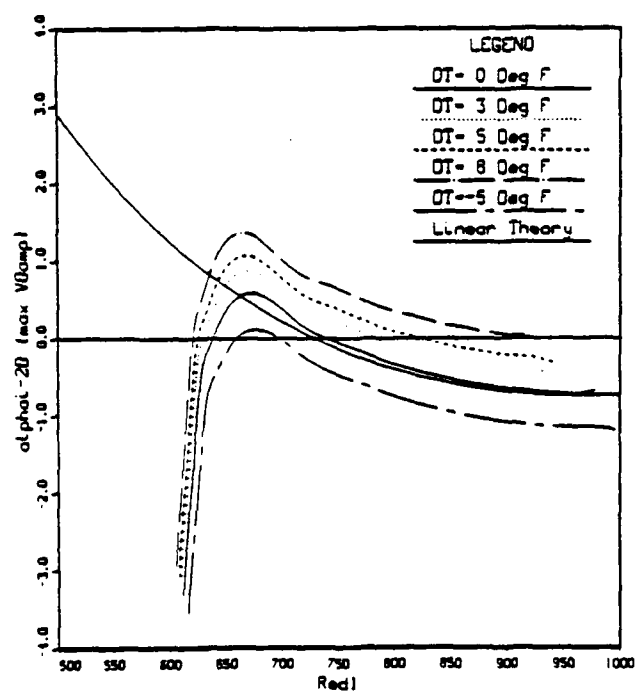


b) first maximum of the 3D streamwise velocity,  $U_1$

Figure 6.20 Influence of uniform passive control on the amplitude growth,  $F = 1$



a) first maximum of the 2D streamwise velocity,  $U_0$



b) maximum of the 2D normal velocity,  $V_0$

Figure 6.21 Influence of uniform passive control on the growth rates  $\alpha_i$ ,  $F = 1$

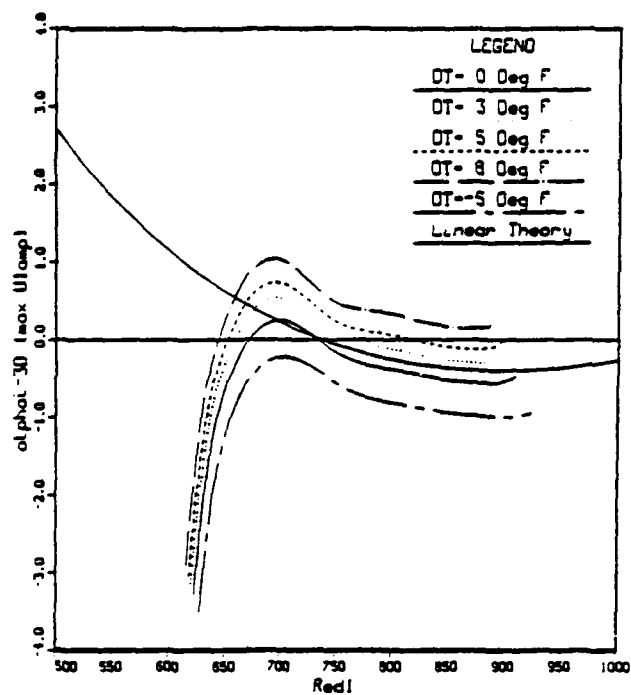
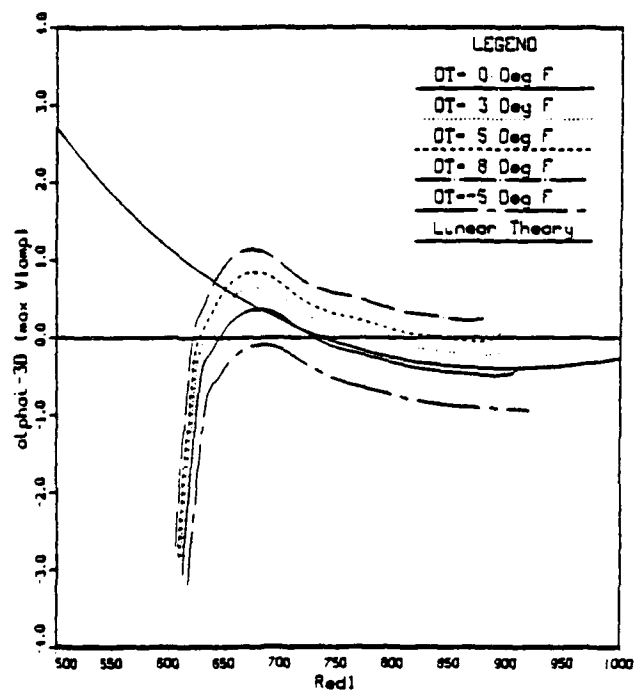
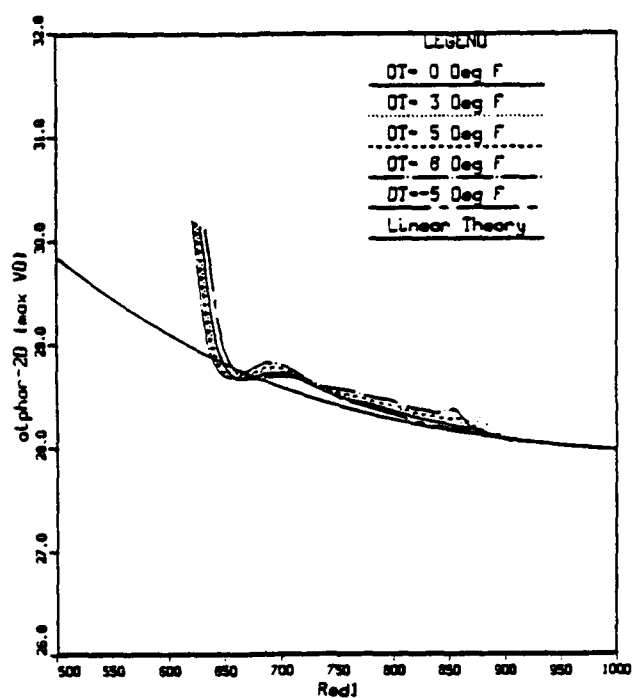
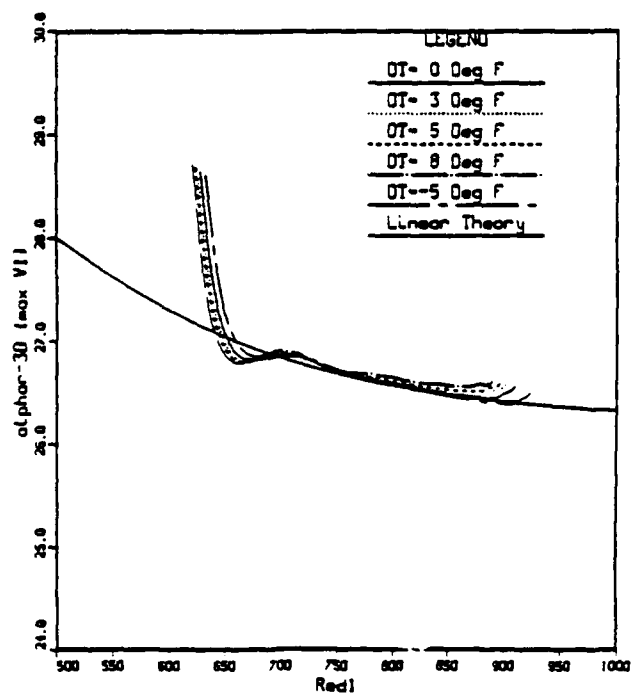
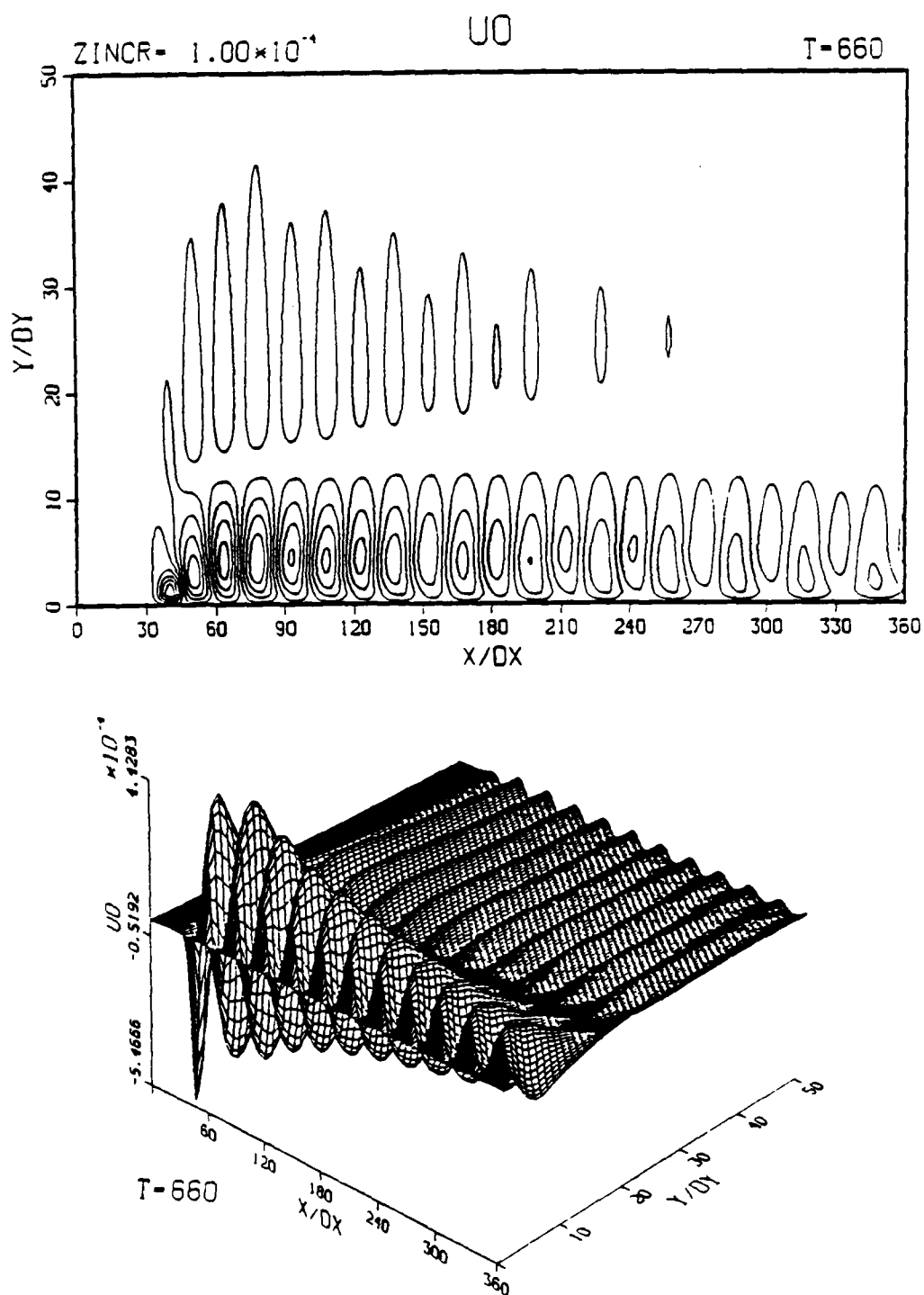
c) first maximum of the 3D streamwise velocity,  $U_1$ d) maximum of the 2D normal velocity,  $V_1$ 

Figure 6.21 continued

a) maximum of the 2D normal velocity,  $V_0$ b) maximum of the 3D normal velocity,  $V_1$ Figure 6.22 Influence of uniform passive control on the wavenumbers  $\alpha_r$ ,  $F = 1$



a) 2D streamwise velocity,  $U_0$

Figure 6.23 Disturbed flow after eleven periods of oscillation with  $\Delta \bar{T} = 8^\circ F$  passive control applied,  $F = 1.55$

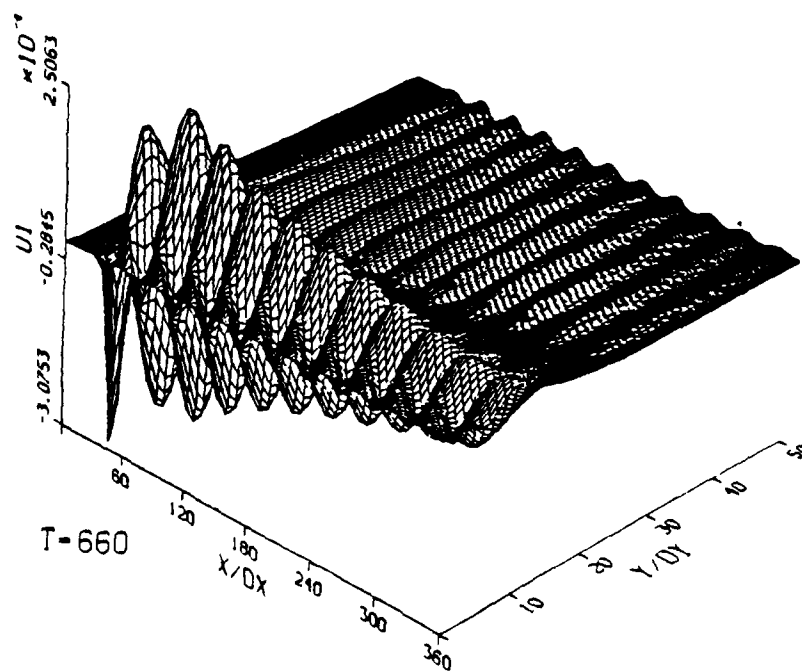
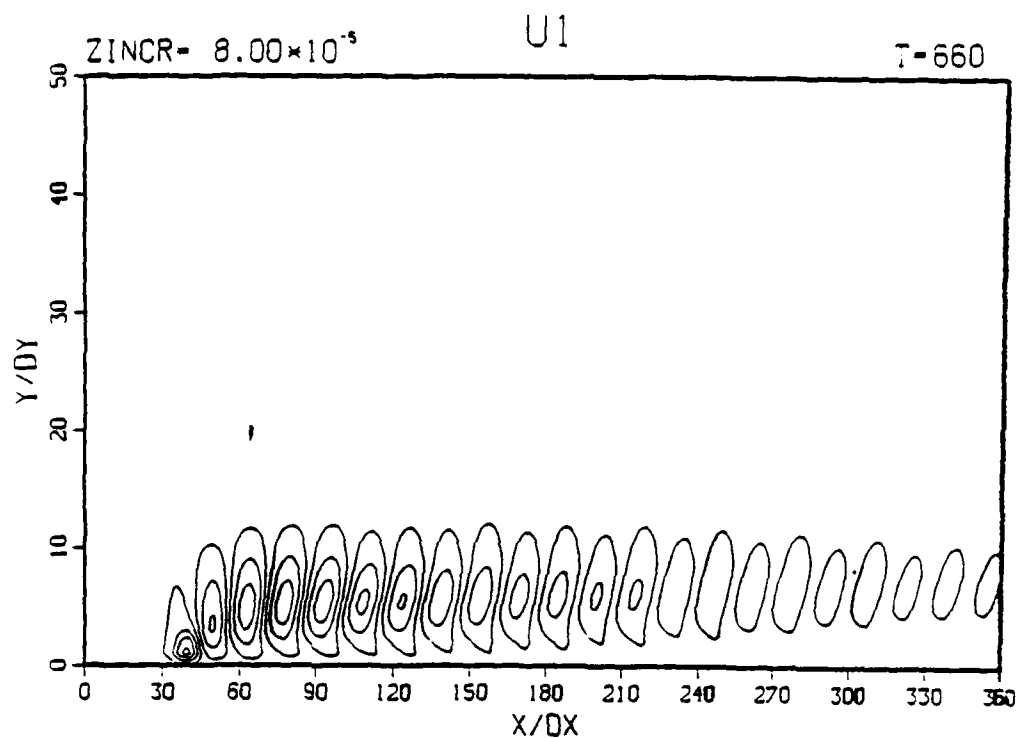
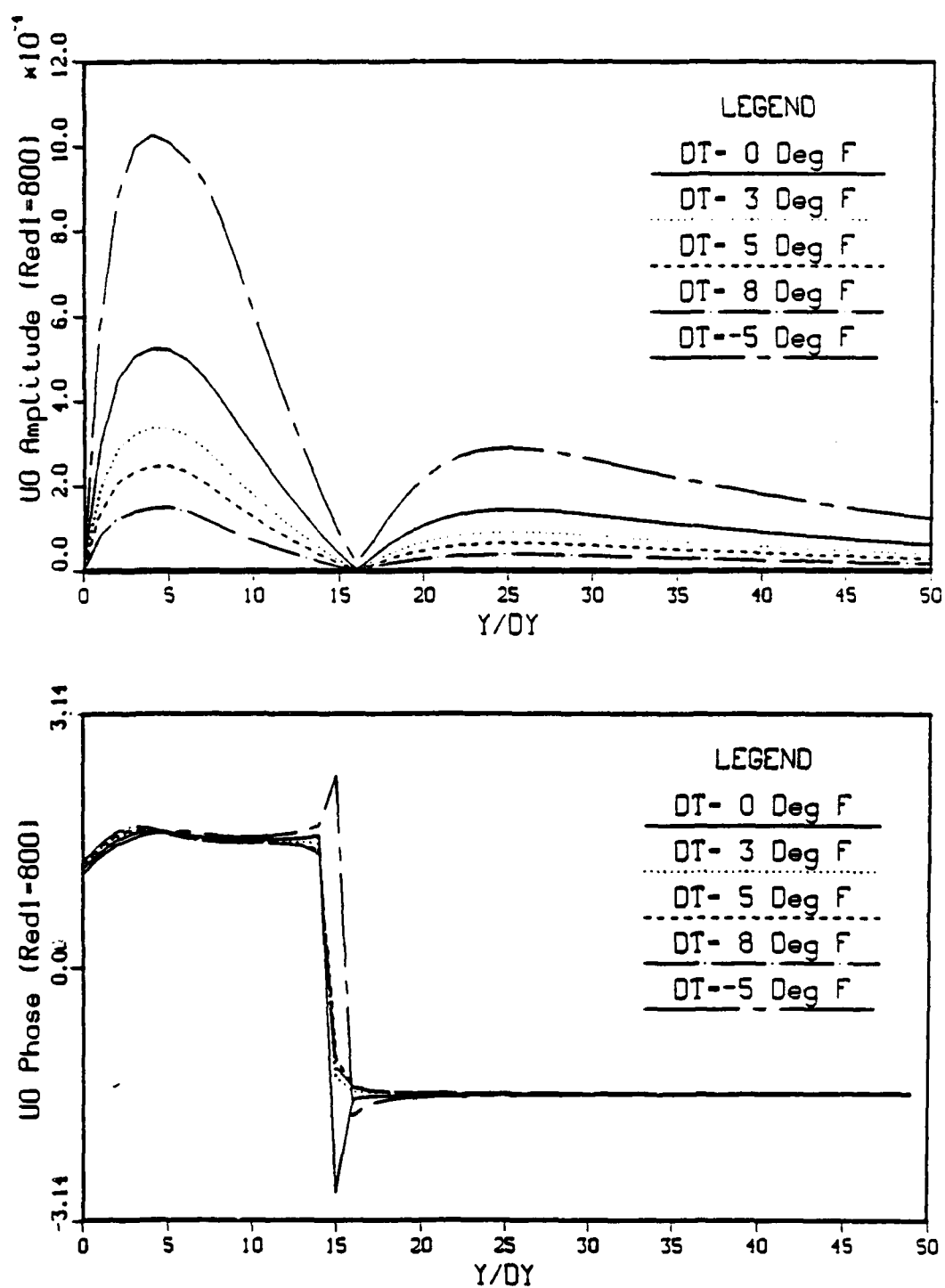
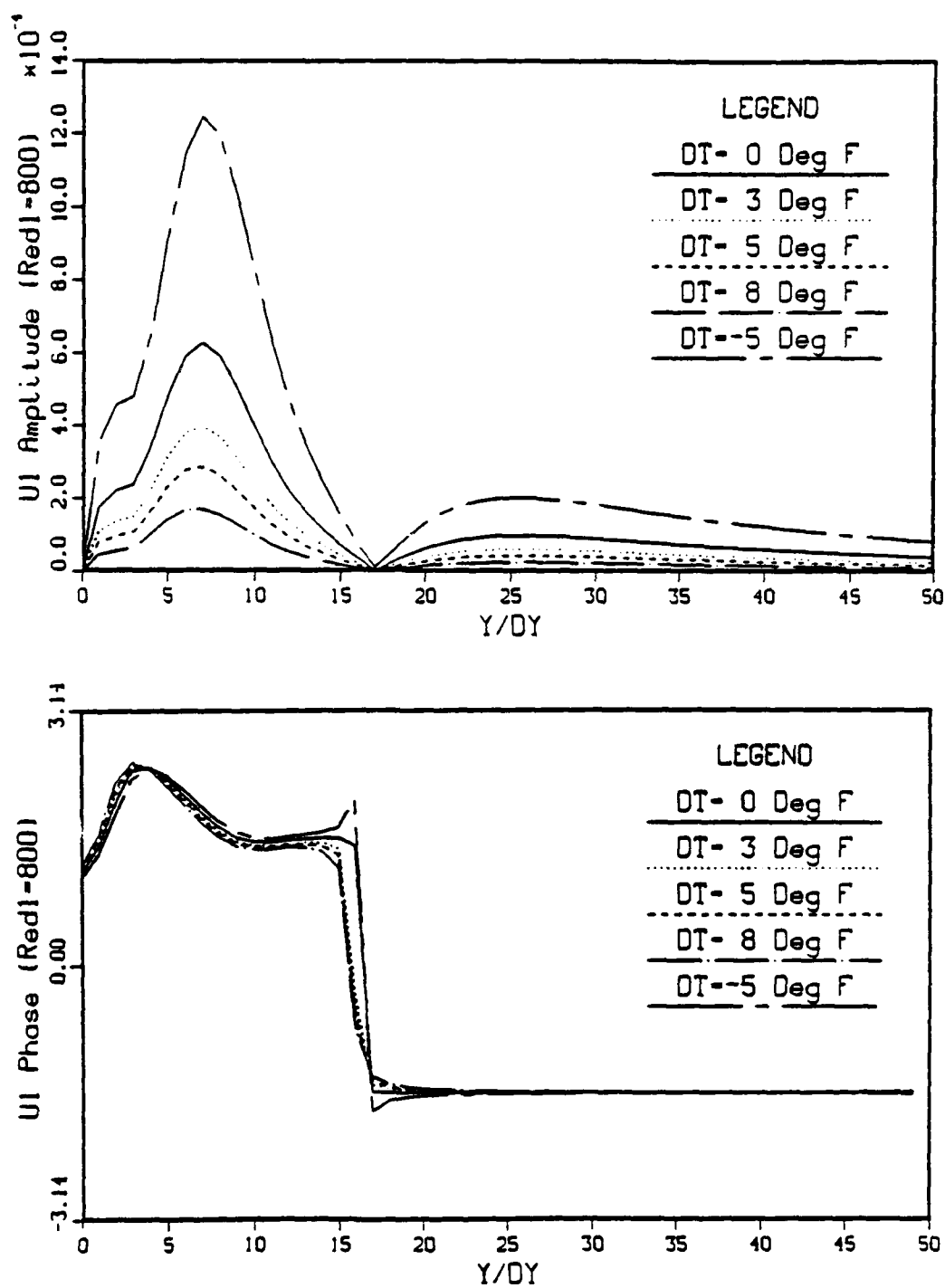
b) 3D streamwise velocity,  $U_1$ 

Figure 6.23 continued



a) 2D streamwise velocity,  $U_0$

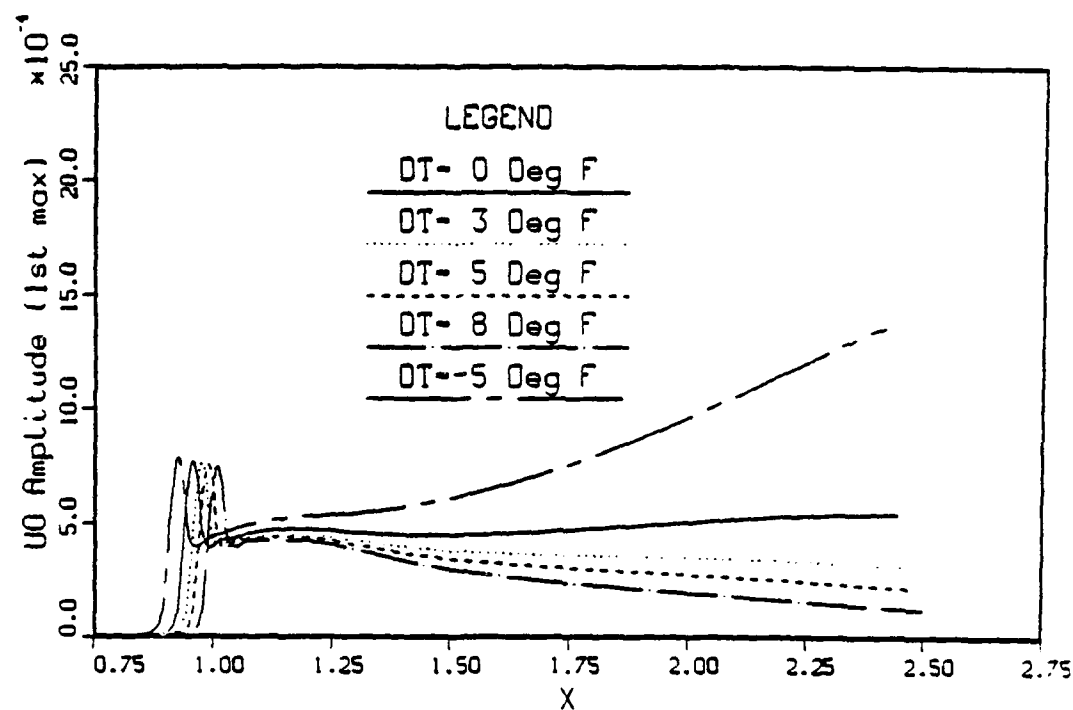
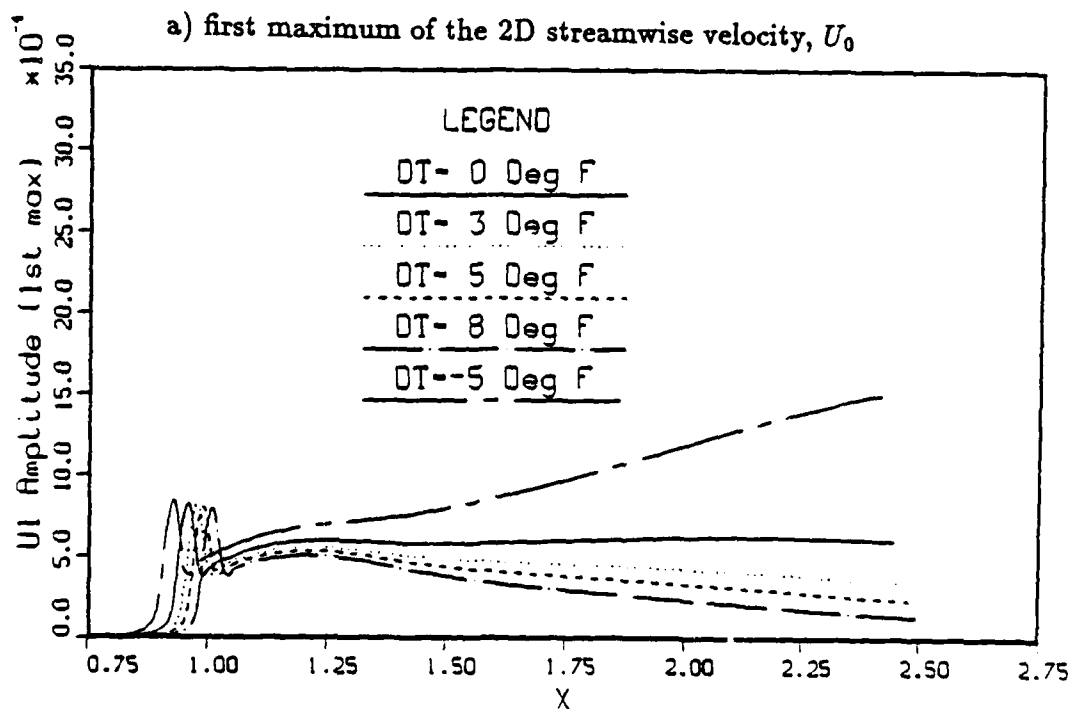
Figure 6.24 Amplitude and phase comparison at  $Re_{\delta_1} = 800$  with uniform passive control applied,  $F = 1.55$

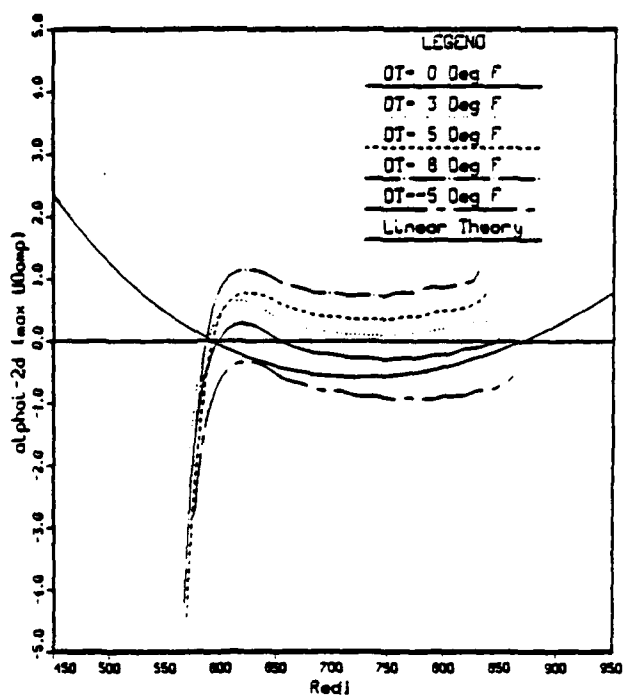


b) 3D streamwise velocity,  $U_1$

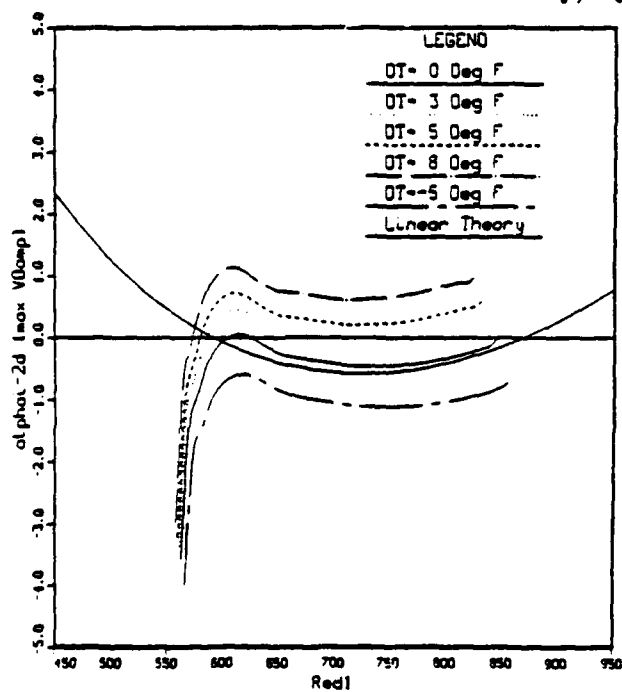
Figure 6.24 continued



a) first maximum of the 2D streamwise velocity,  $U_0$ b) first maximum of the 3D streamwise velocity,  $U_1$ Figure 6.25 Influence of uniform passive control on the amplitude growth,  $F = 1.55$



a) first maximum of the 2D streamwise velocity,  $U_0$



b) maximum of the 2D normal velocity,  $V_0$

Figure 6.26 Influence of uniform passive control on the growth rates  $\alpha_i$ ,  $F = 1.55$

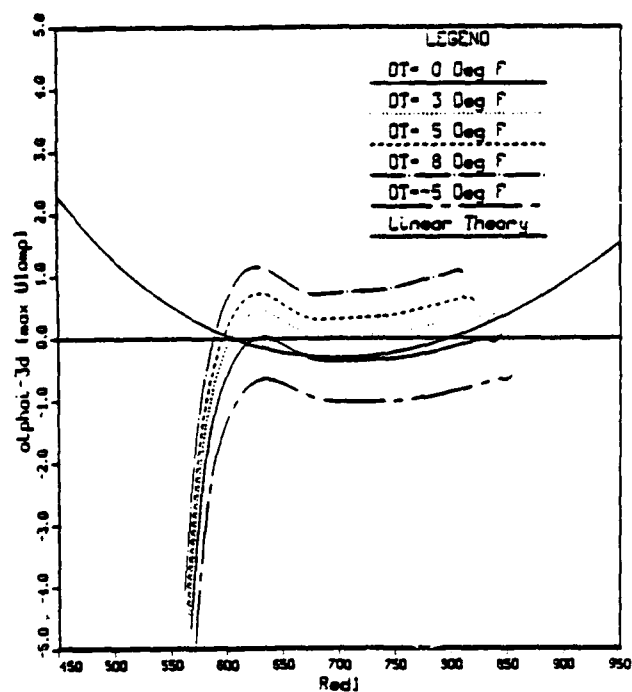
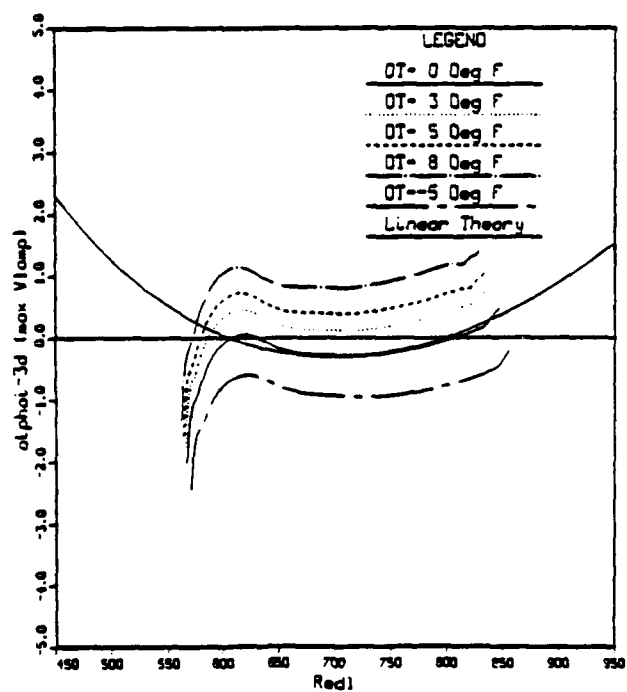
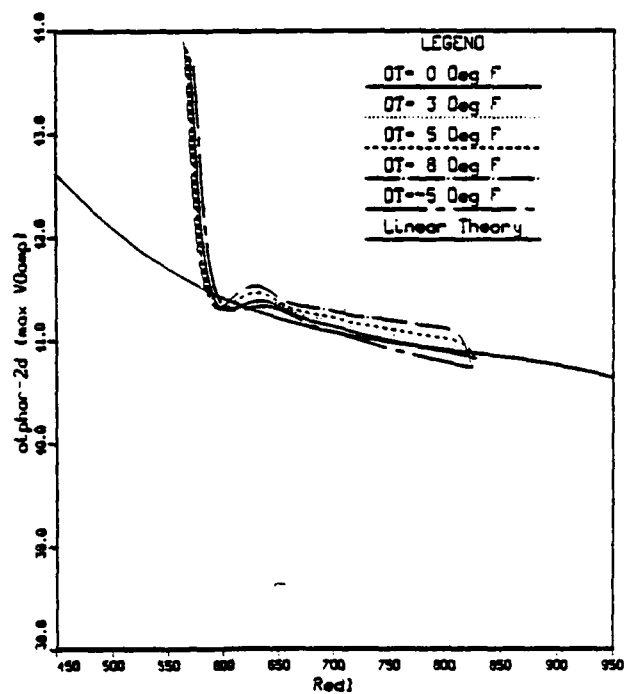
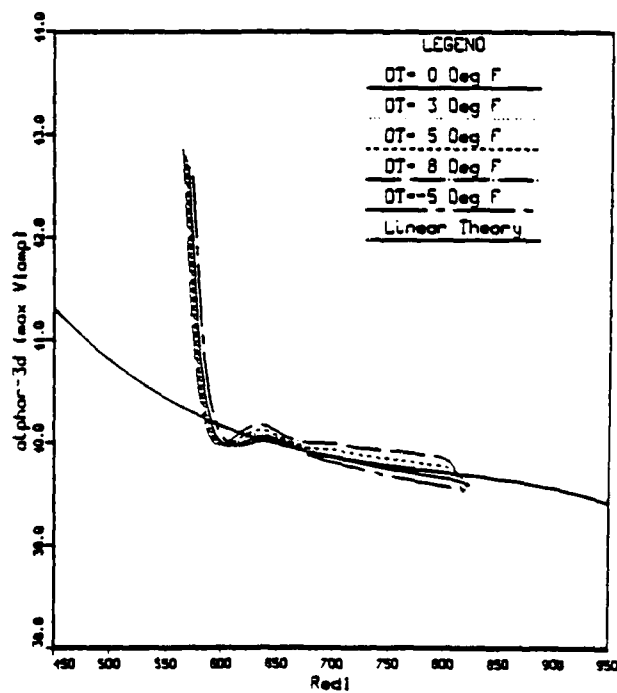
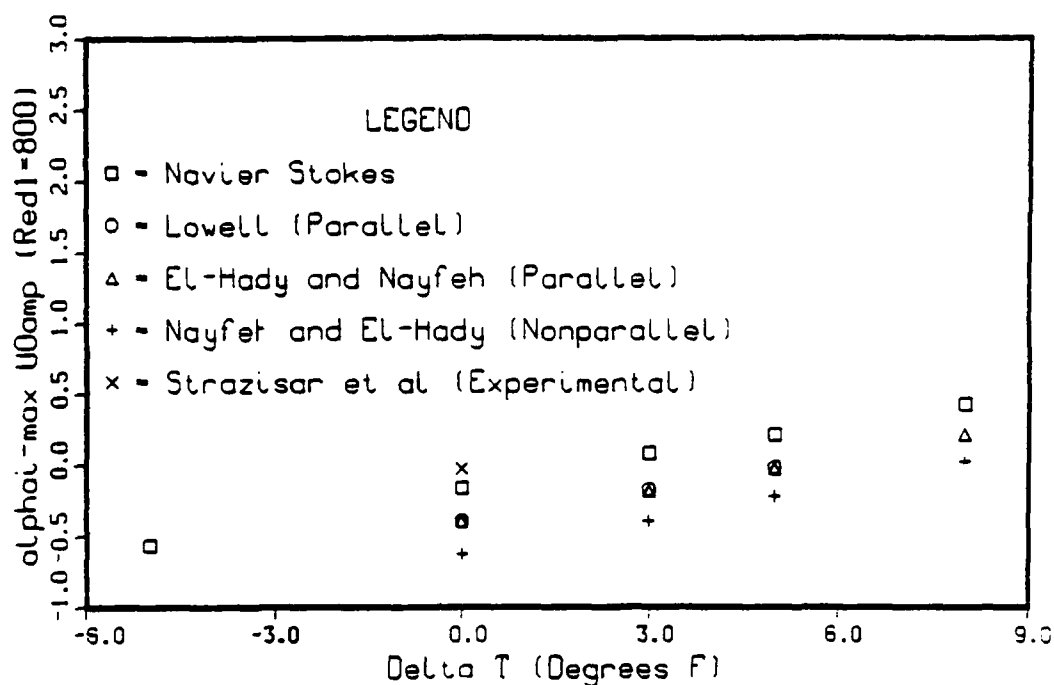
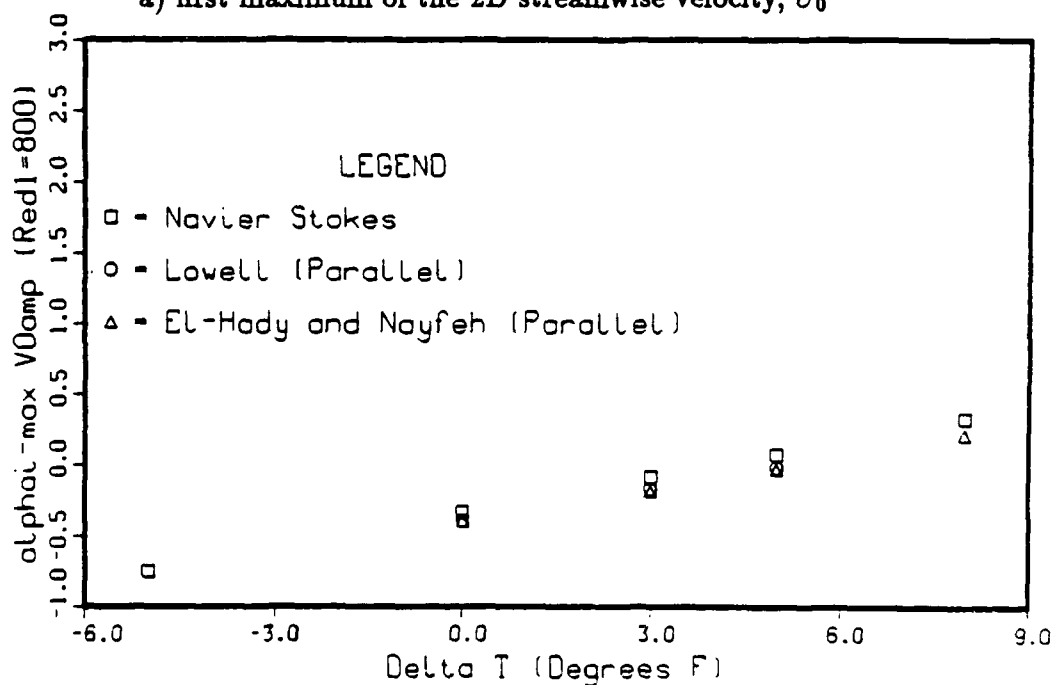
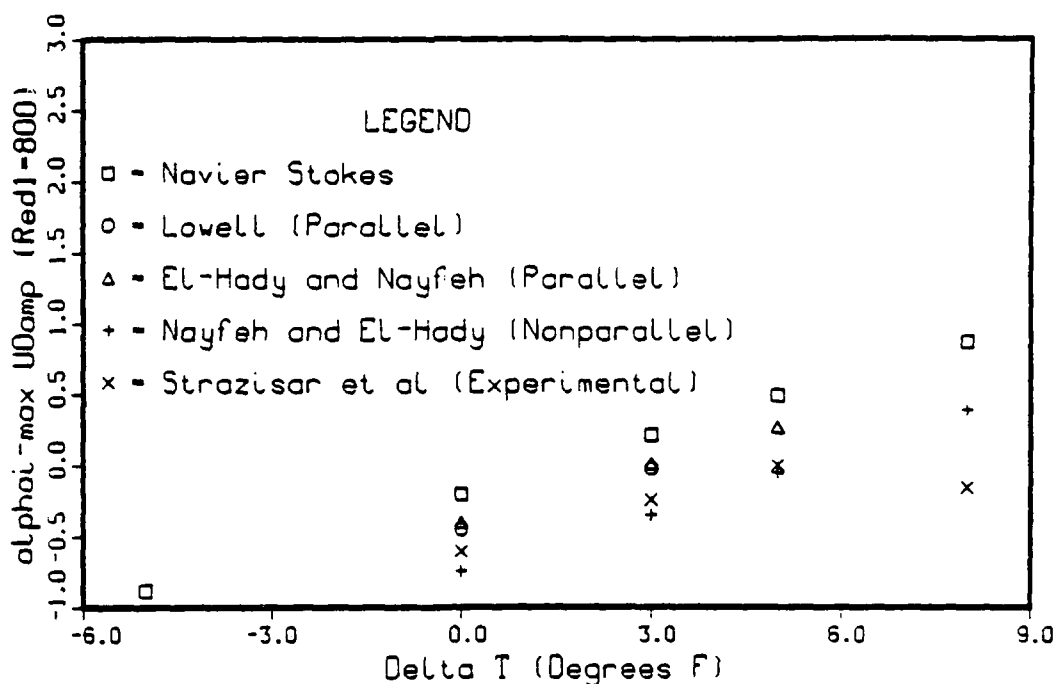
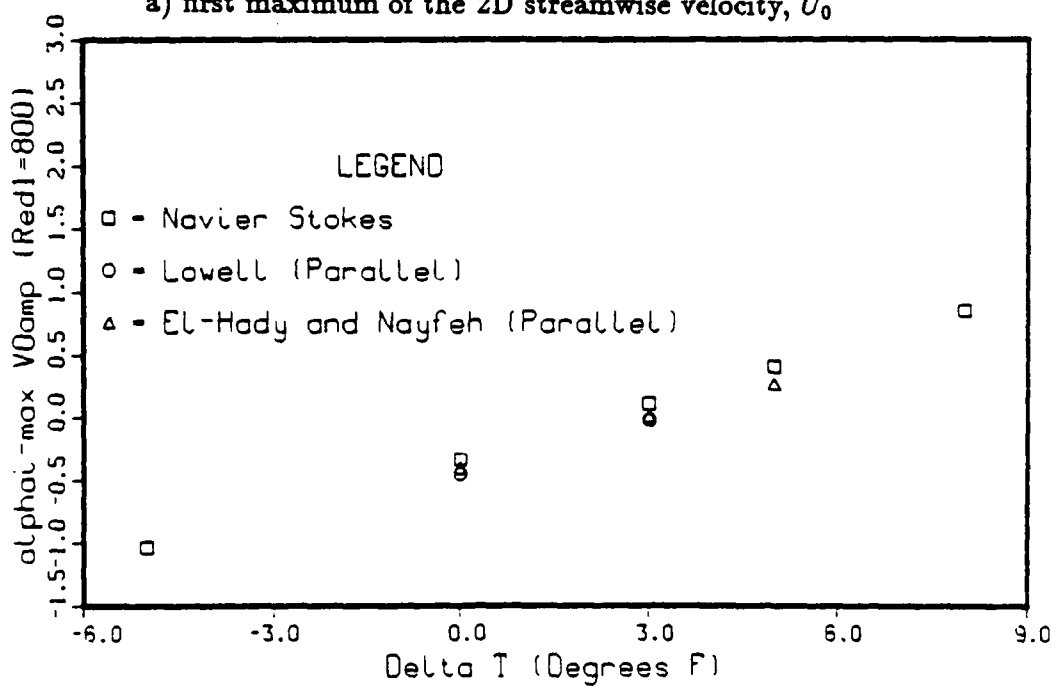
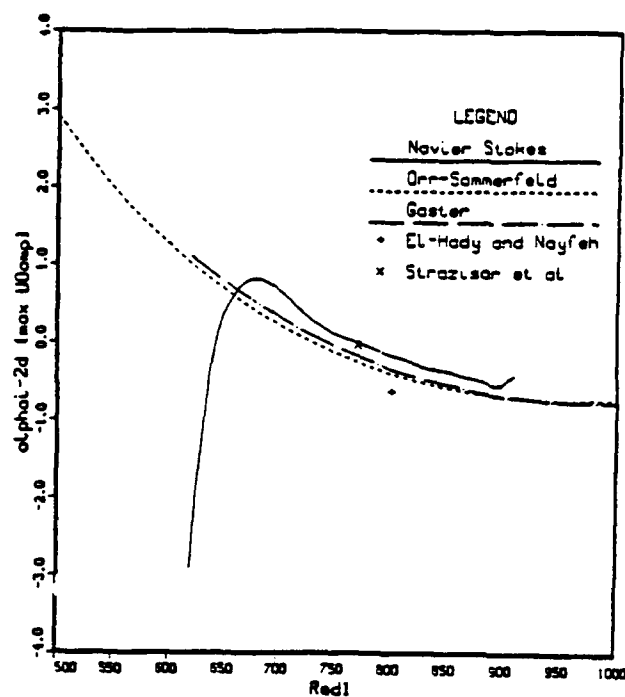
c) first maximum of the 3D streamwise velocity,  $U_1$ d) maximum of the 3D normal velocity,  $V_1$ 

Figure 6.26 continued

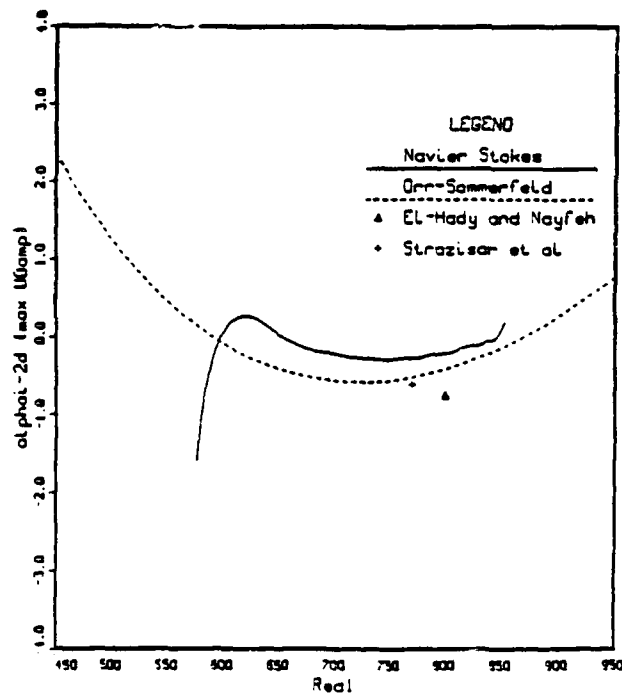
a) maximum of the 2D normal velocity,  $V_0$ b) maximum of the 3D normal velocity,  $V_1$ Figure 6.27 Influence of uniform passive control on the wavenumbers  $\alpha_r$ ,  $F = 1.55$

a) first maximum of the 2D streamwise velocity,  $U_0$ b) maximum of the 2D normal velocity,  $V_0$ Figure 6.28 Comparison of amplification rates for uniform passive control with theory and experiment,  $F = 1$

a) first maximum of the 2D streamwise velocity,  $U_0$ b) maximum of the 2D normal velocity,  $V_0$ Figure 6.29 Comparison of amplification rates for uniform passive control with theory and experiment,  $F = 1.55$

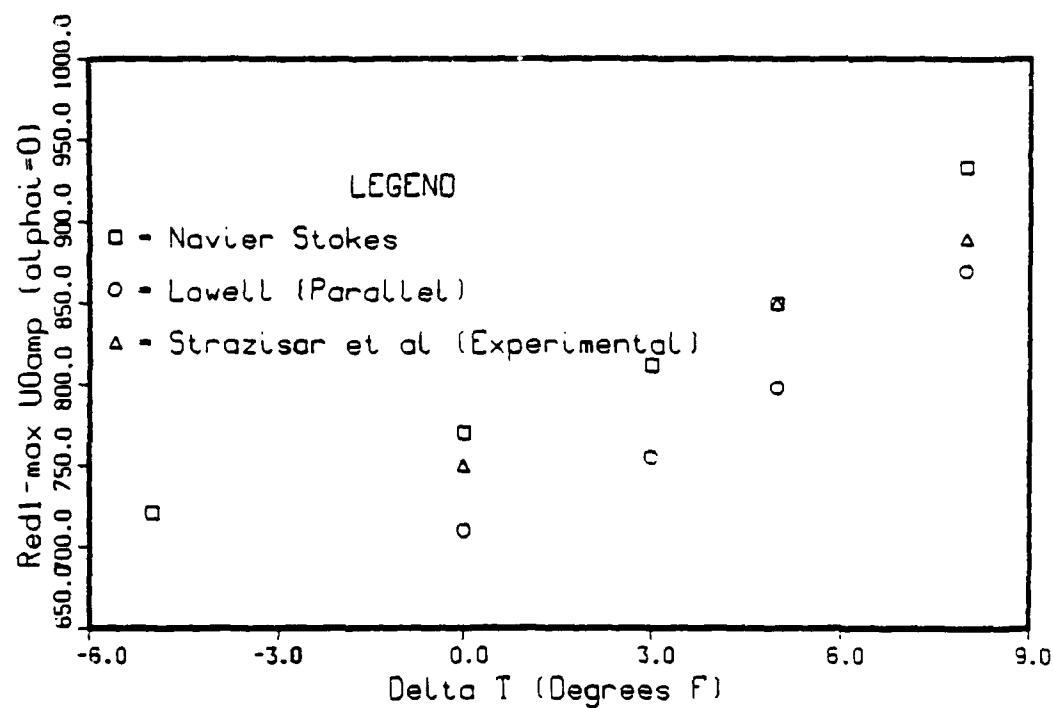
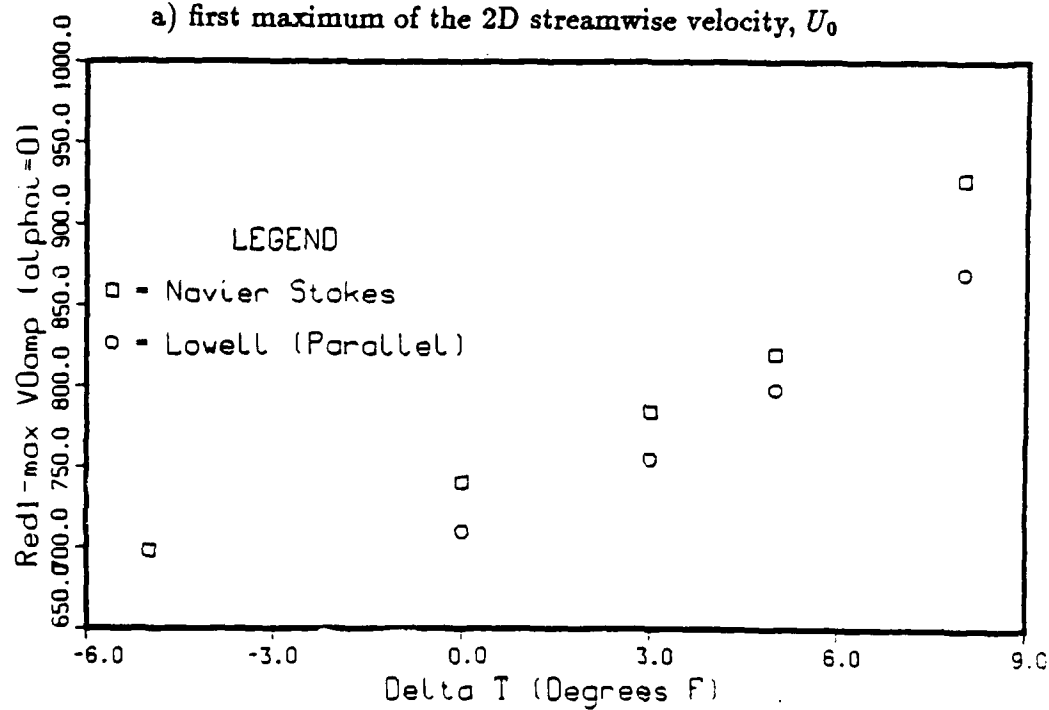


a) comparison of nonparallel theories and experiments,  $F = 1$



b) comparison of nonparallel theory and experiments,  $F = 1.55$

Figure 6.30 Comparison of amplification rates for the uncontrolled flow at the first maximum of the 2D streamwise velocity,  $U_0$

a) first maximum of the 2D streamwise velocity,  $U_0$ b) maximum of the 2D normal velocity,  $V_0$ Figure 6.31 Comparison of neutral points for uniform passive control with theory and experiment,  $F = 1$



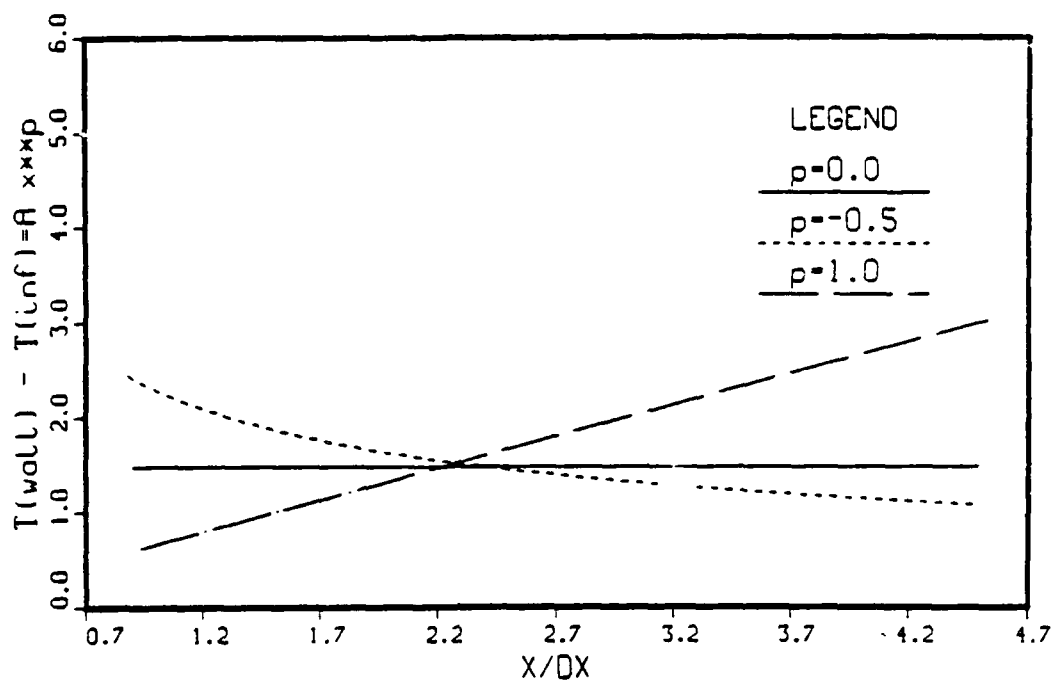
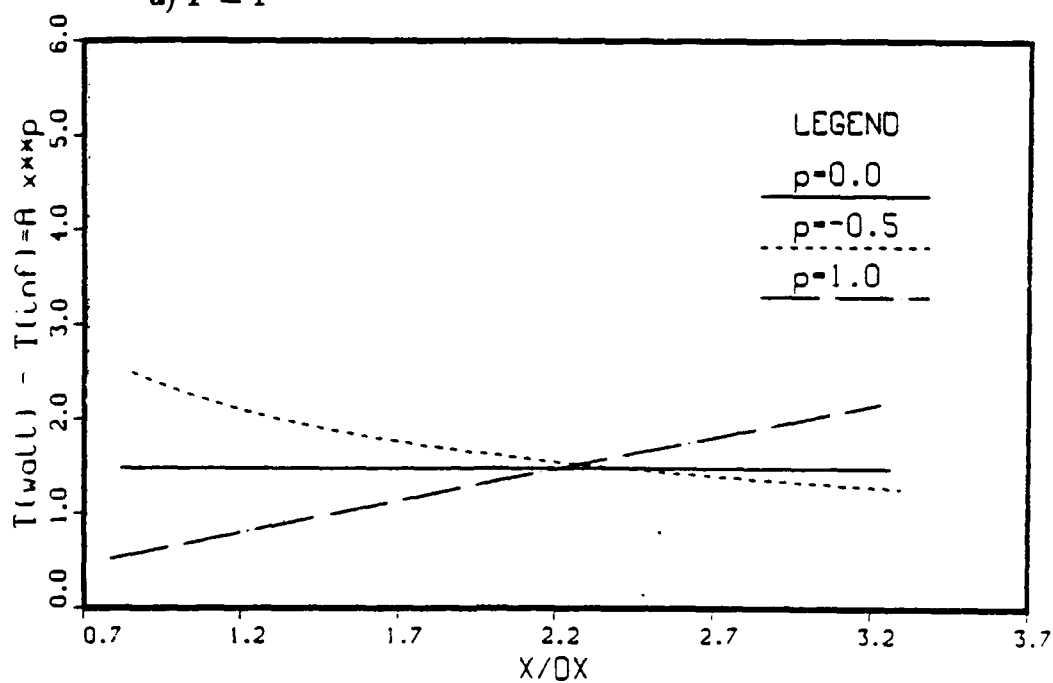
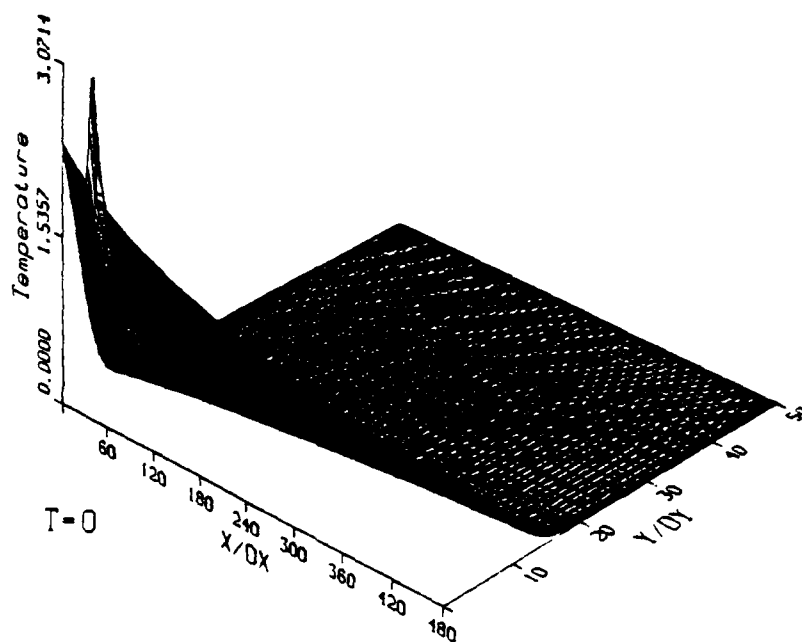
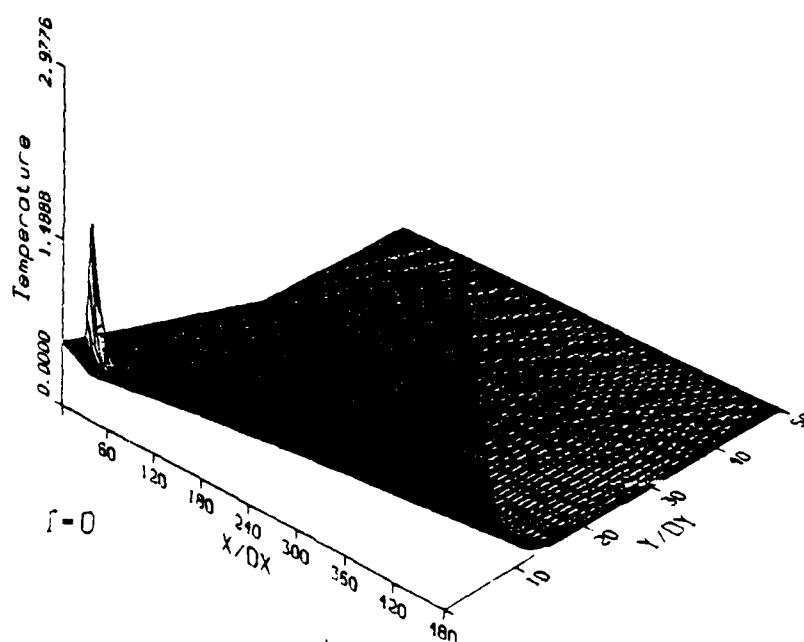
a)  $F = 1$ b)  $F = 1.55$ 

Figure 6.32 Power law temperature distributions for  $\Delta \bar{T} = A_0 x_n^p = 8^\circ F$  at  $Re_{\delta_1} = 800$



a)  $p = -0.5$



b)  $p = 1.0$

Figure 6.33 Undisturbed temperature distributions with nonuniform passive heating applied,  $\Delta \bar{T} = A_0 x_n^p = 8^\circ F$  at  $Re_{\delta_1} = 800$ ,  $F = 1$

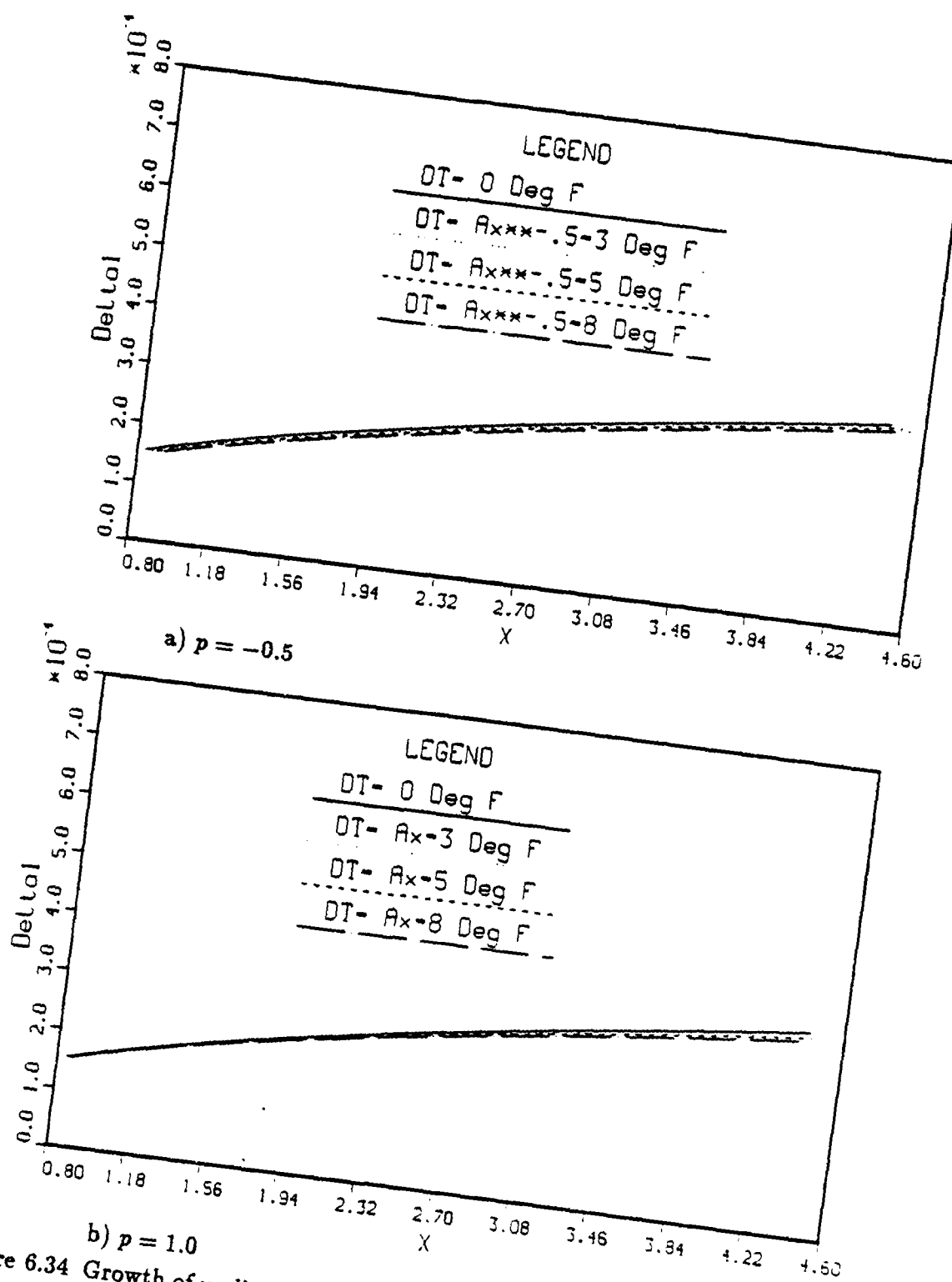
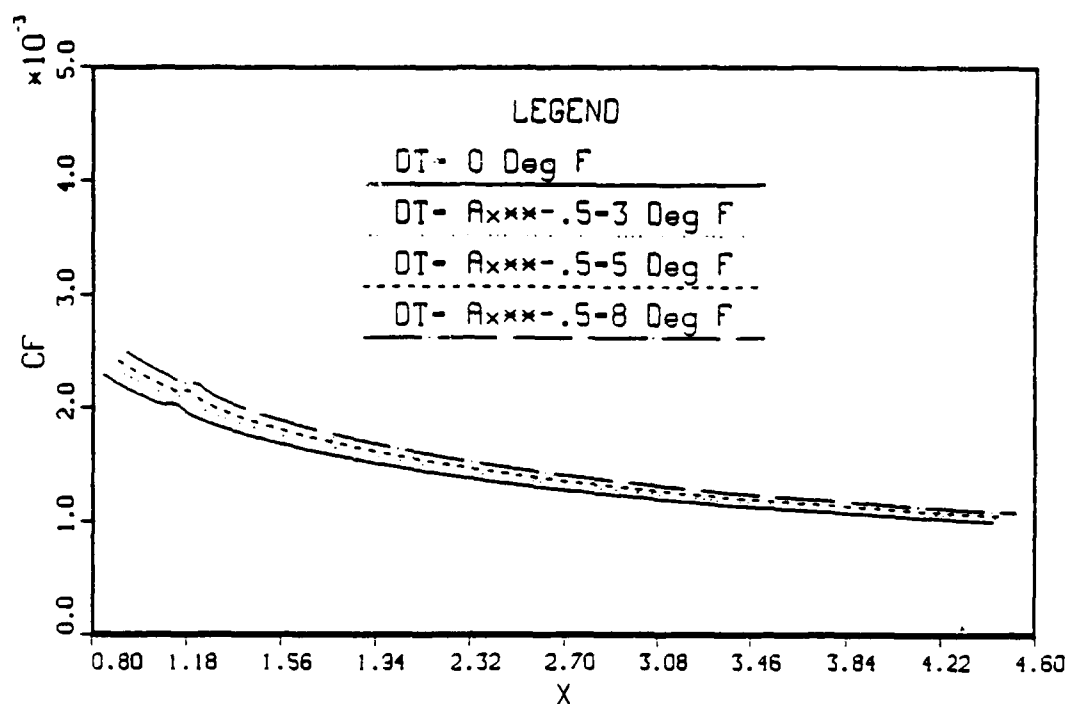
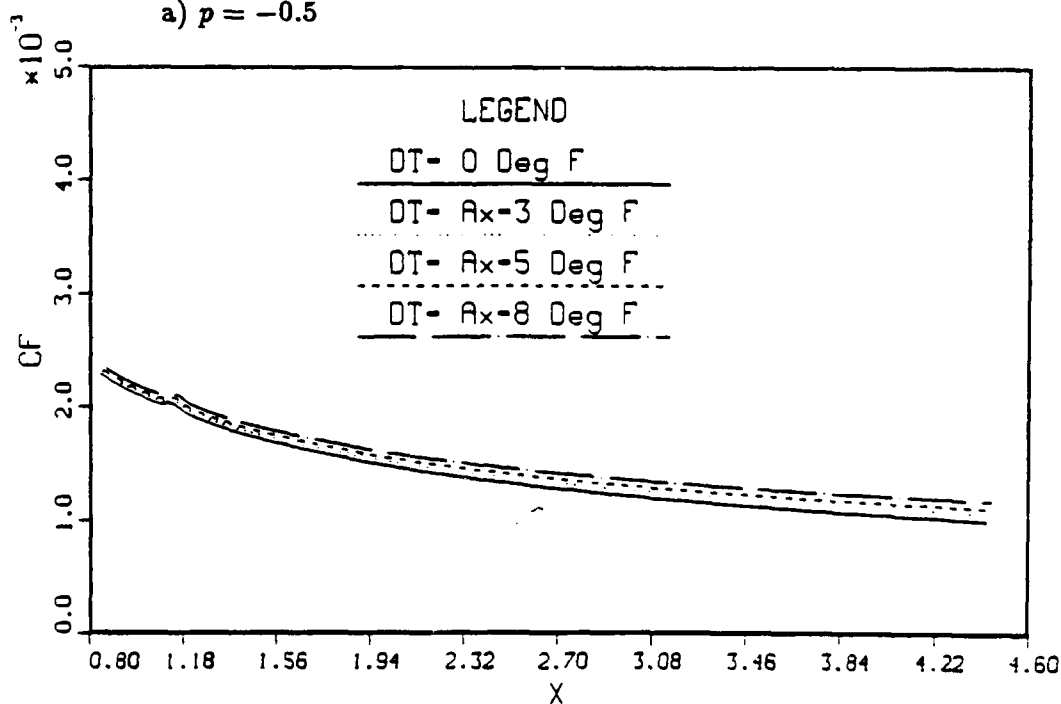


Figure 6.34 Growth of undisturbed boundary layer with nonuniform passive heating applied,  $\Delta \bar{T} = A_0 x_n^p$ ,  $F = 1$

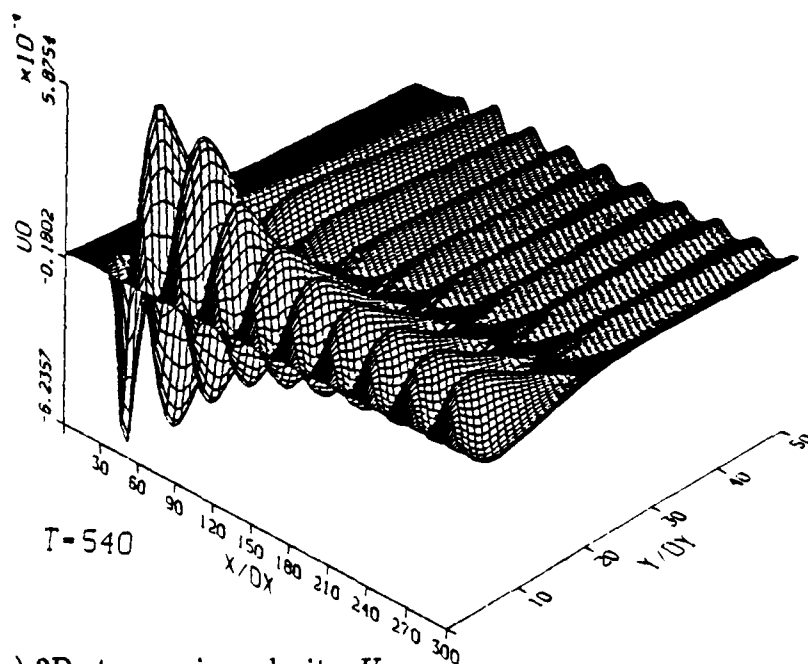
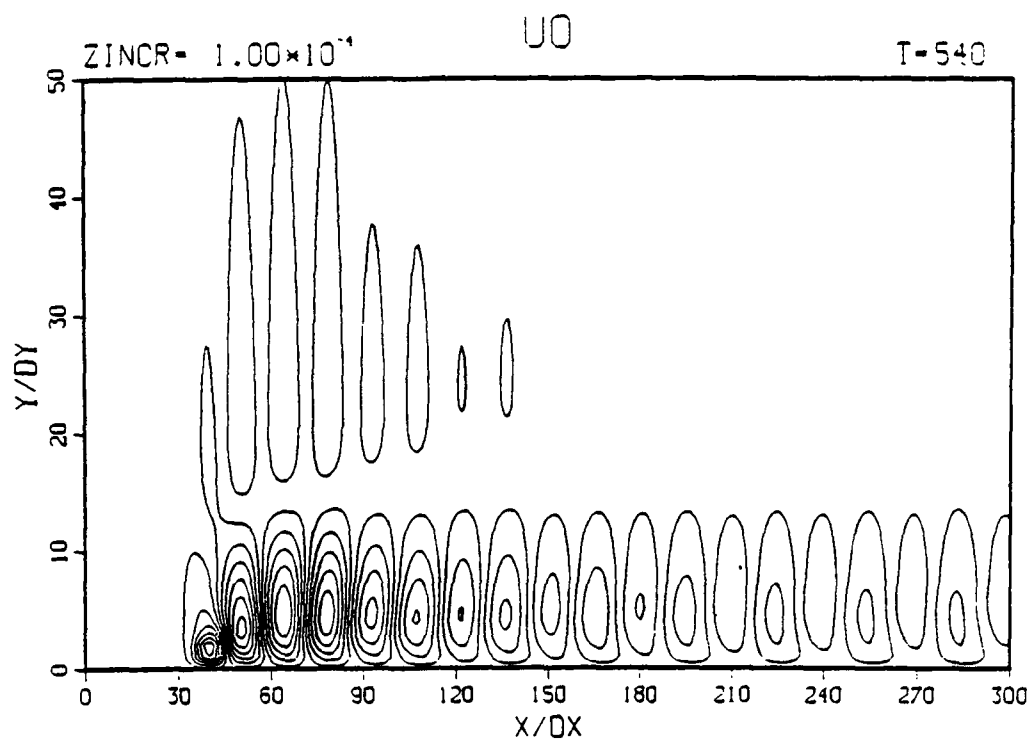


a)  $p = -0.5$



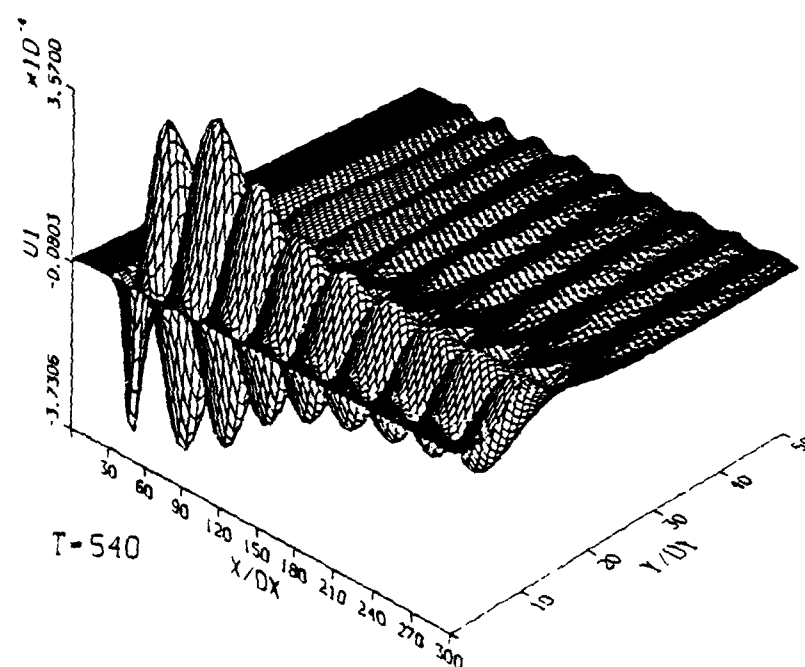
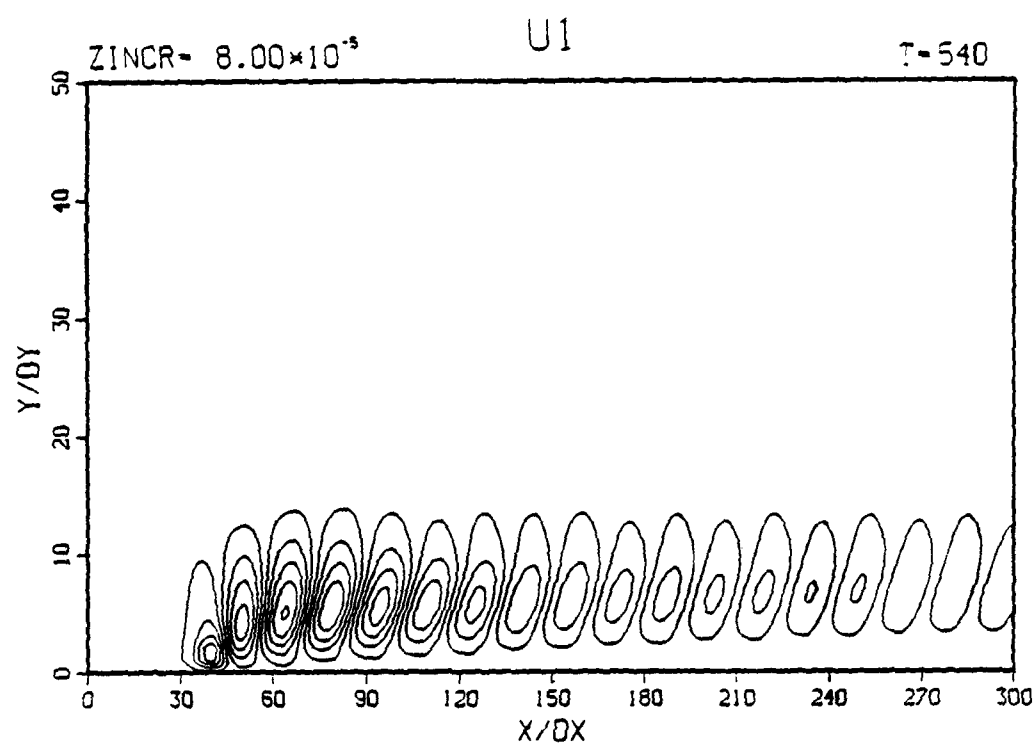
b)  $p = 1.0$

Figure 6.35 Comparison of skin friction with nonuniform passive heating applied,  $\Delta T = A_0 x_n^p$ ,  $F = 1$



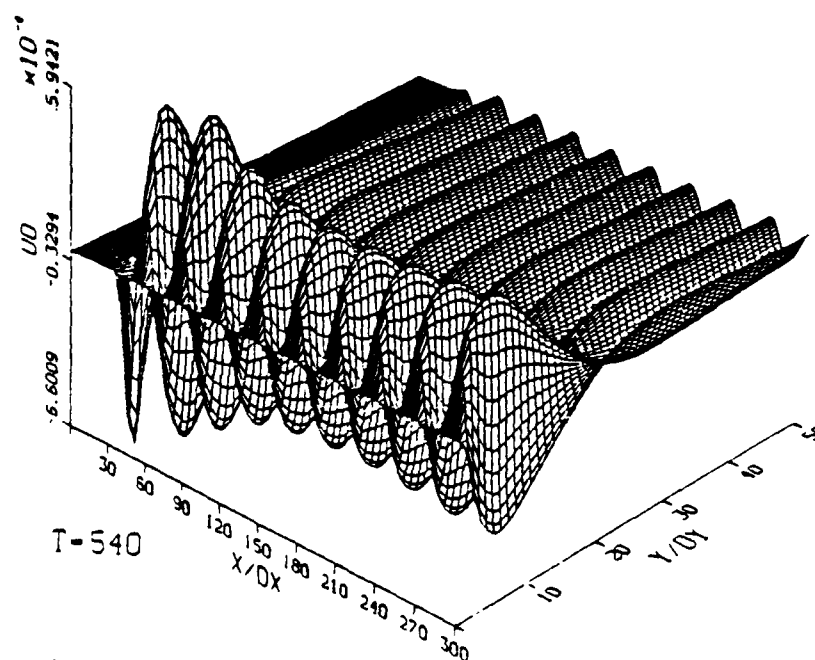
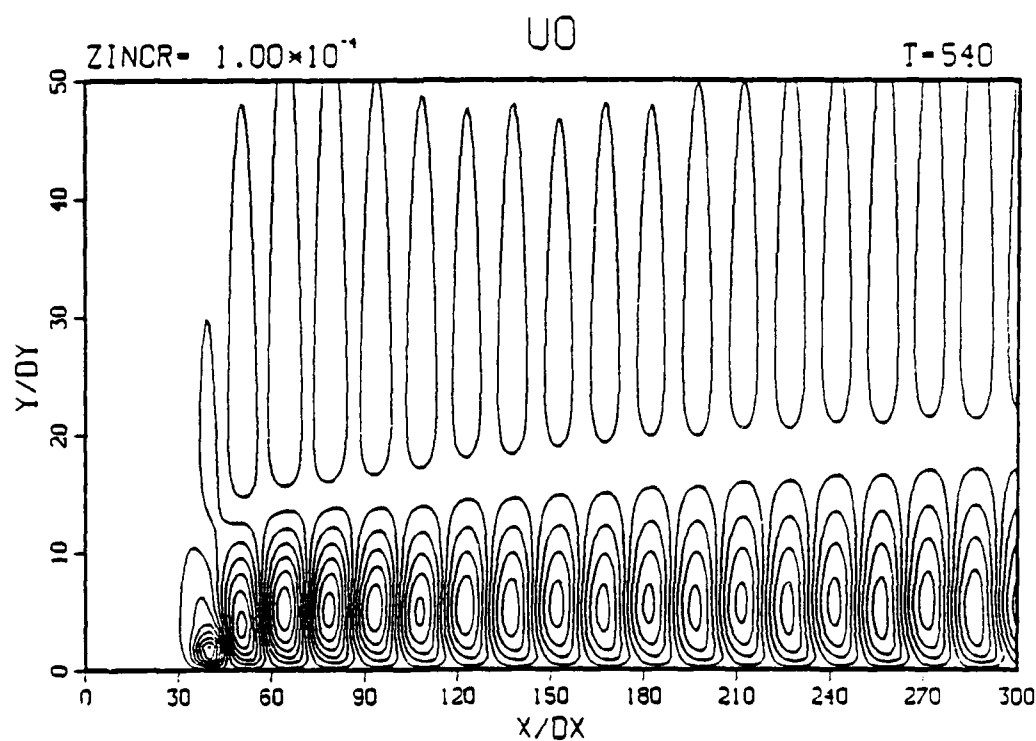
a) 2D streamwise velocity,  $U_0$

Figure 6.36 Disturbed flow after nine periods of oscillation with nonuniform surface temperature distribution  $\Delta \bar{T} = A_0 x_n^{-0.5} = 8^\circ F$  at  $Re_{\delta_1} = 800$  passive control applied,  $F = 1$



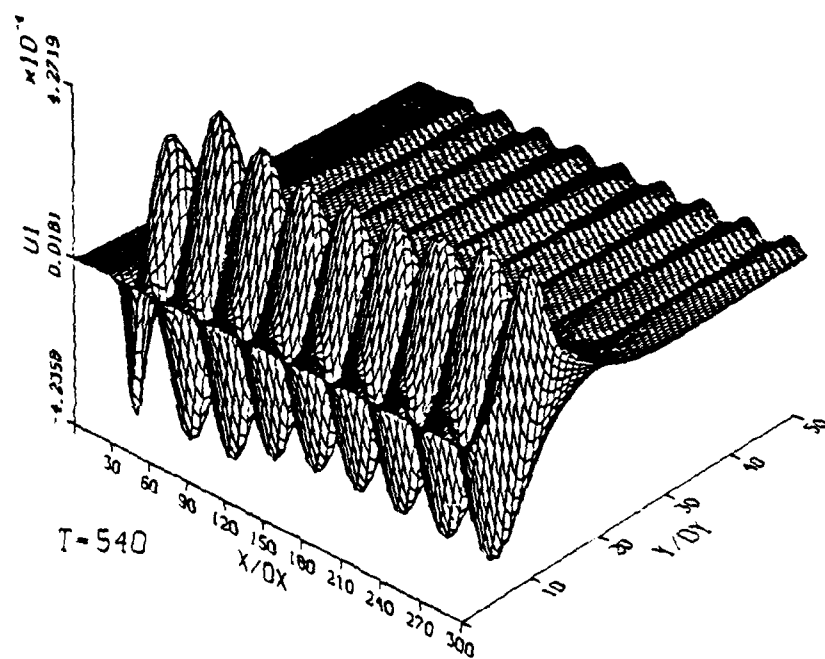
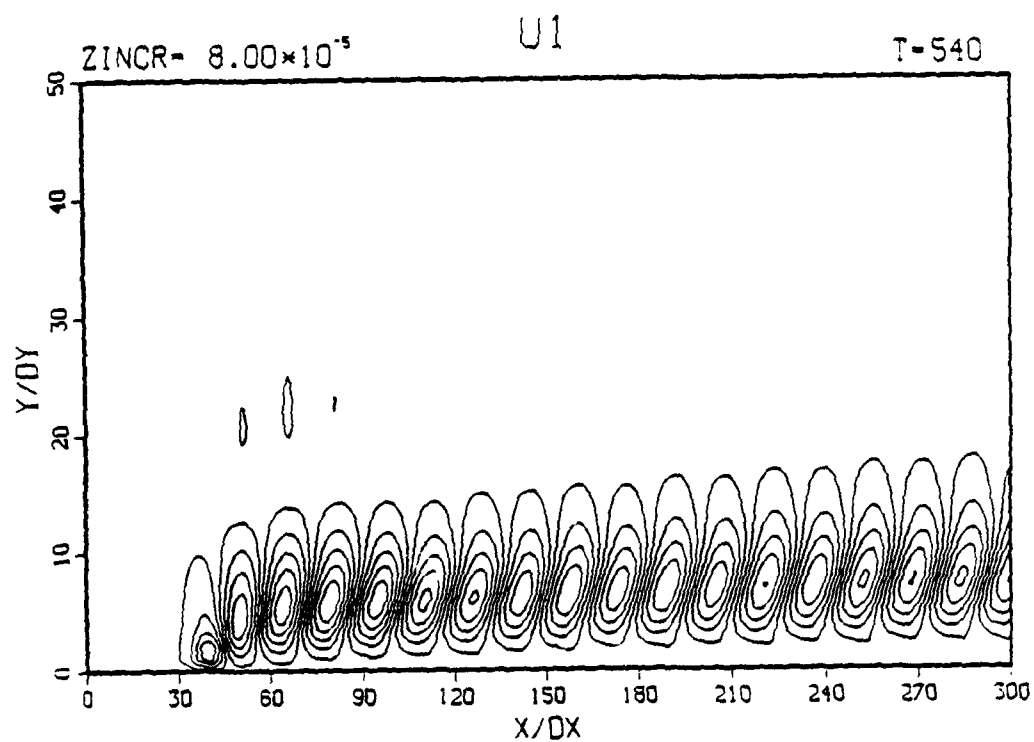
b) 3D streamwise velocity,  $U_1$

Figure 6.36 continued



a) 2D streamwise velocity,  $U_0$

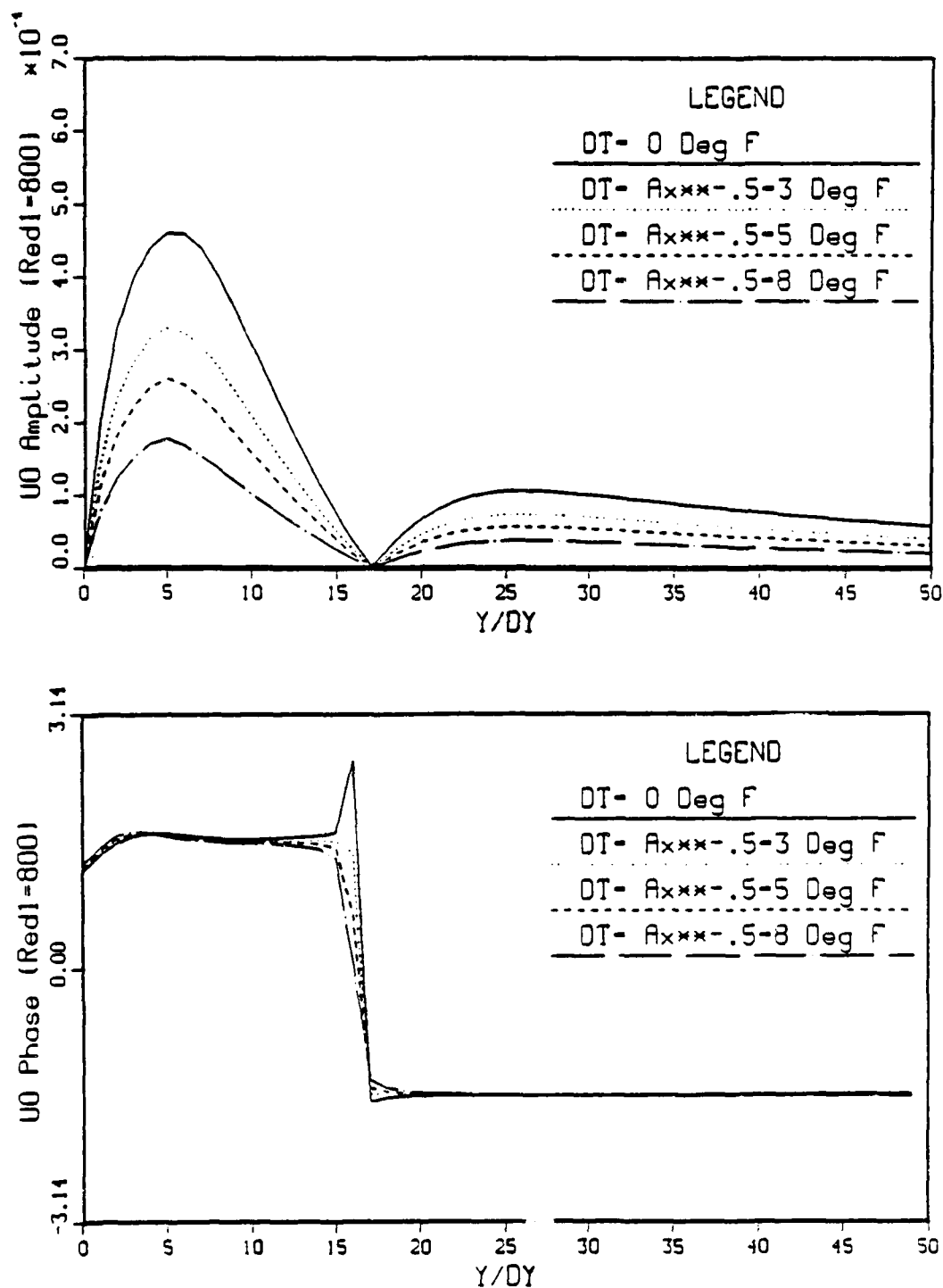
Figure 6.37 Disturbed flow after nine periods of oscillation with nonuniform surface temperature distribution  $\Delta \bar{T} = A_0 x_n^{1.0} = 8^\circ F$  at  $Re_{\delta_1} = 800$  passive control applied,  $F = 1$



b) 3D streamwise velocity,  $U_1$

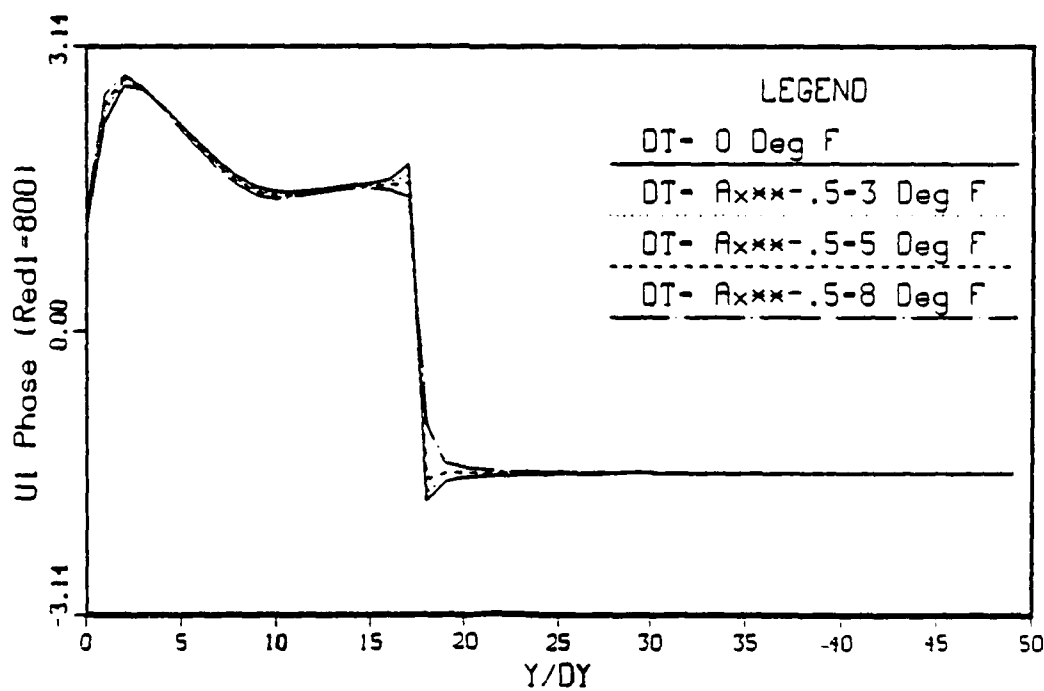
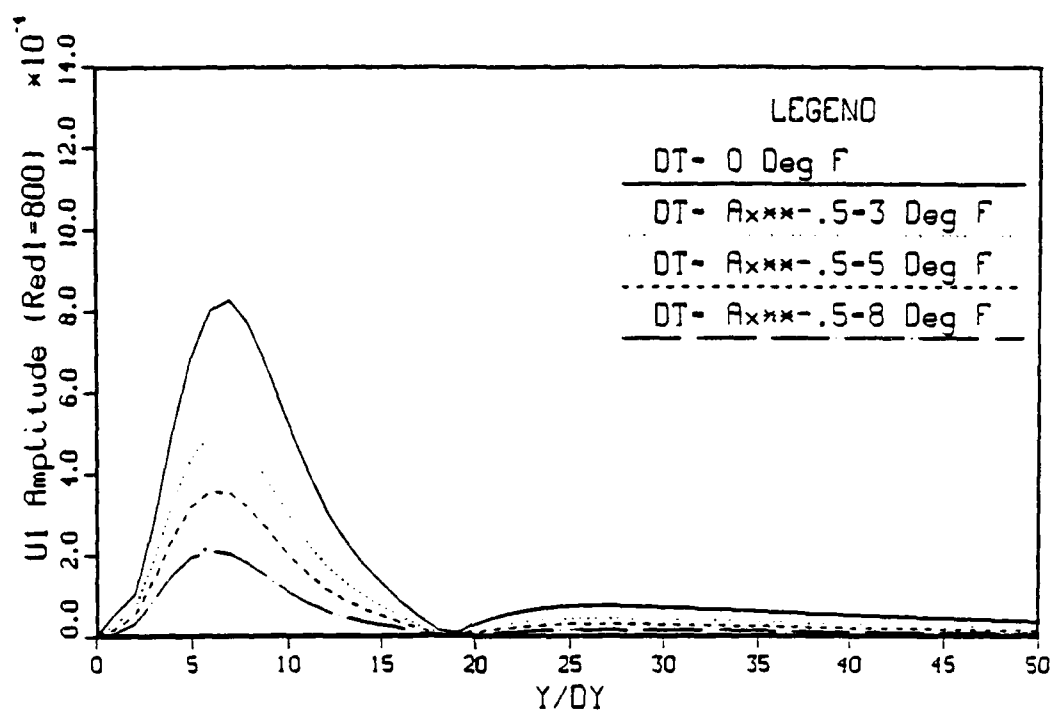
Figure 6.37 continued





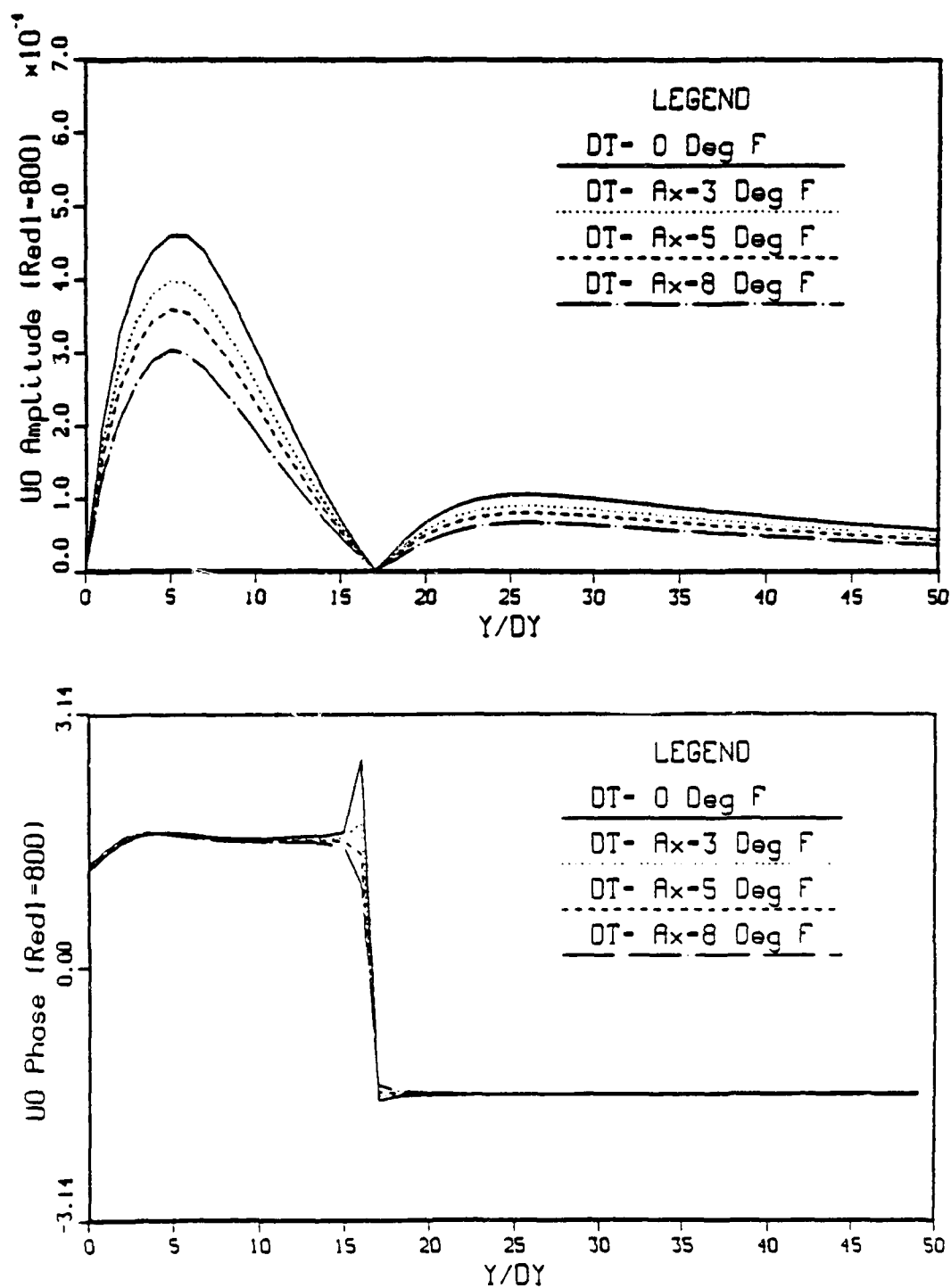
a) 2D streamwise velocity,  $U_0$

Figure 6.38 Amplitude and phase comparison at  $Re_{\delta_1} = 800$  with  $\Delta \bar{T} = A_0 x_n^{-0.5}$  nonuniform passive control applied,  $F = 1$



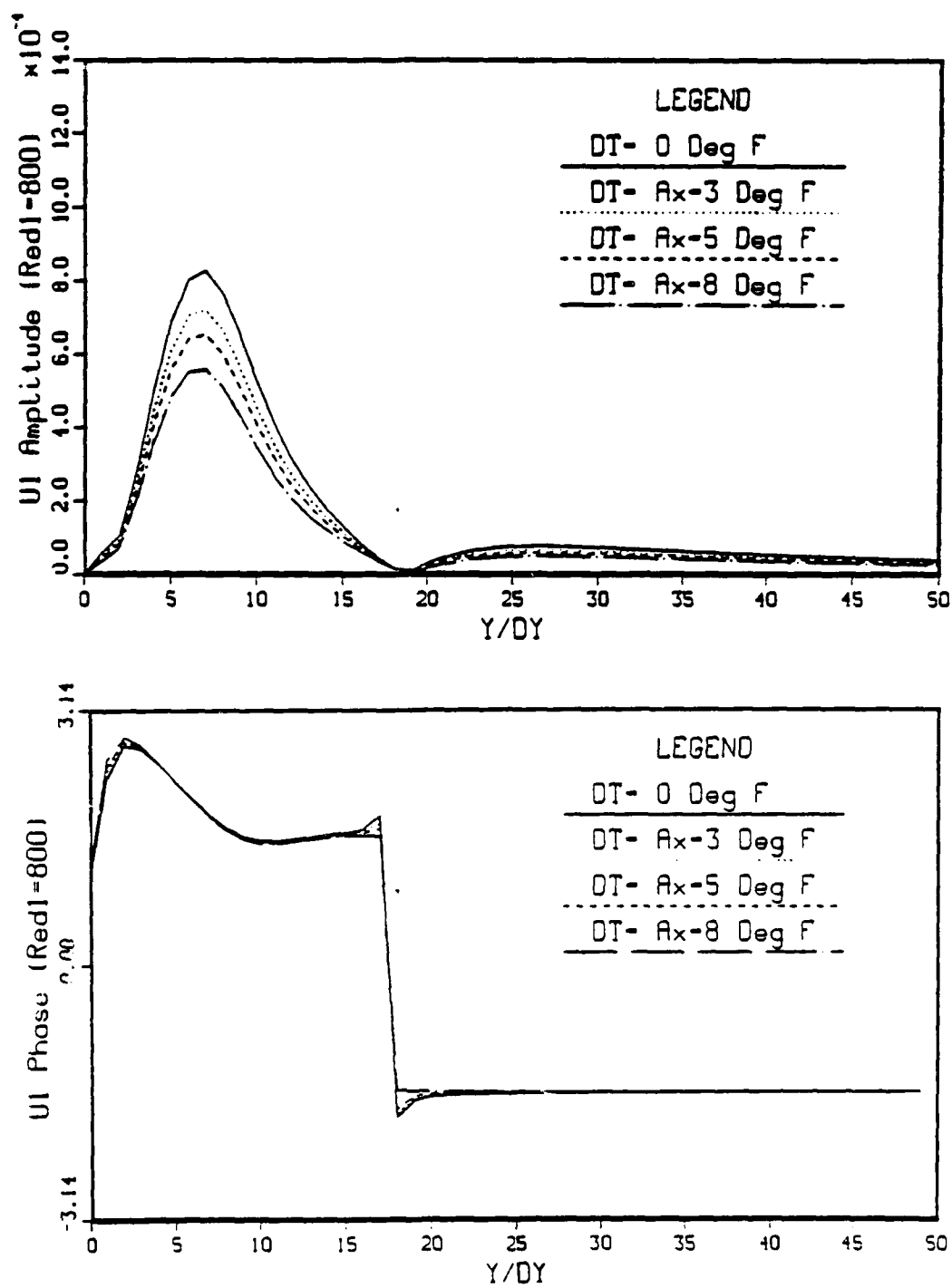
b) 3D streamwise velocity,  $U_1$

Figure 6.38 continued



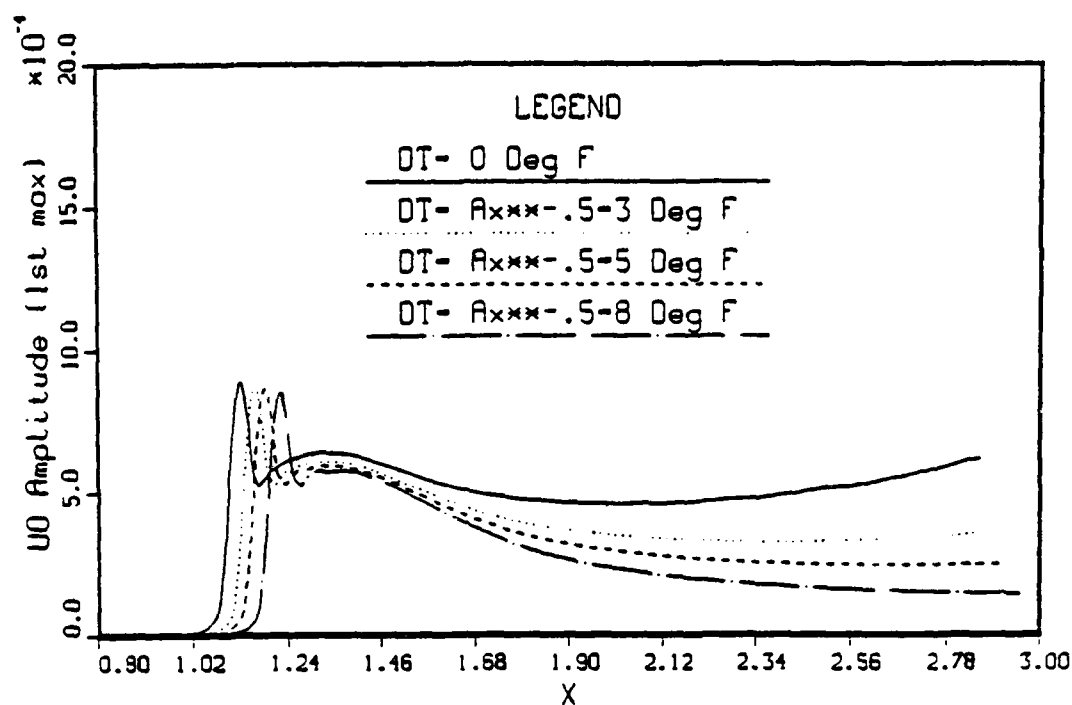
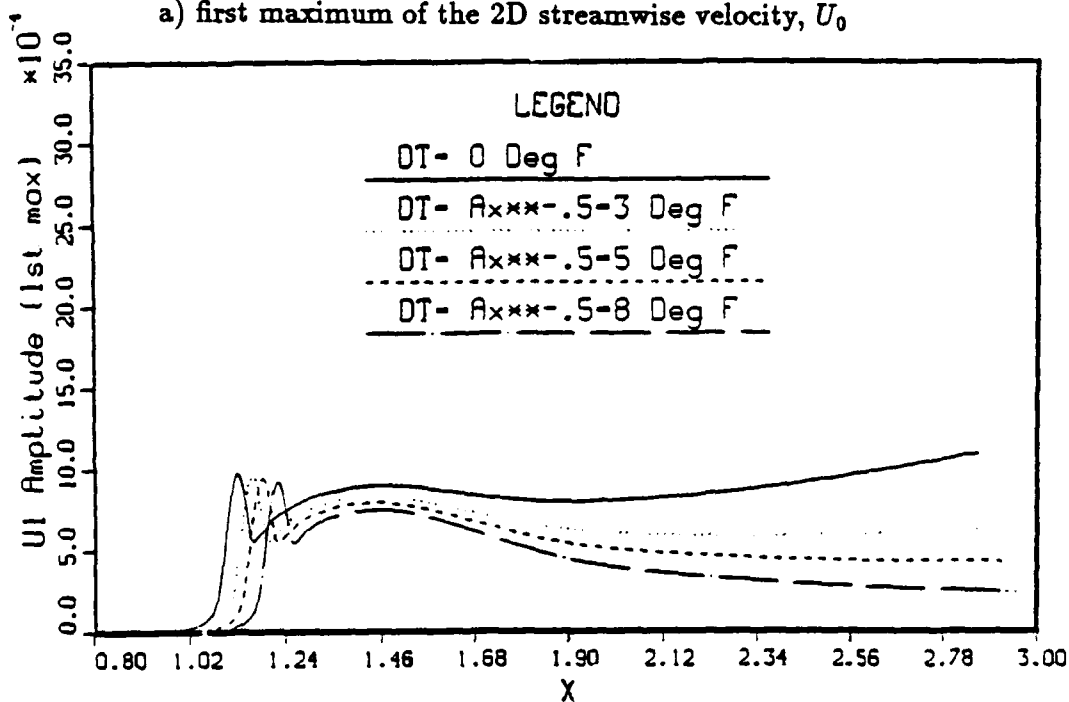
a) 2D streamwise velocity,  $U_0$

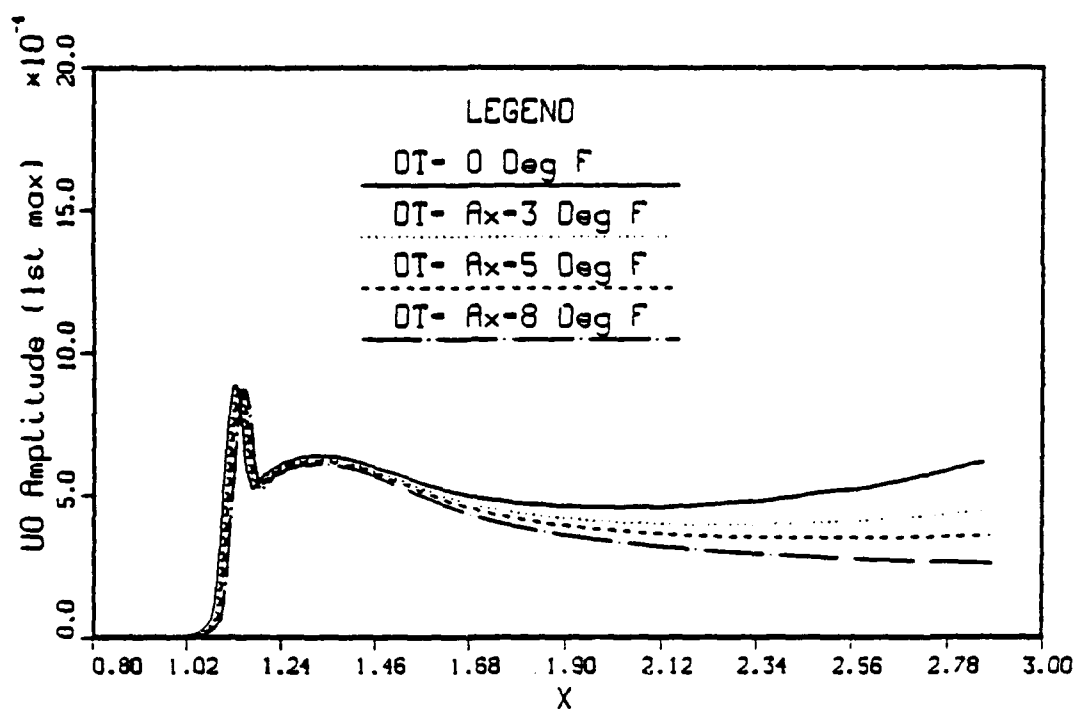
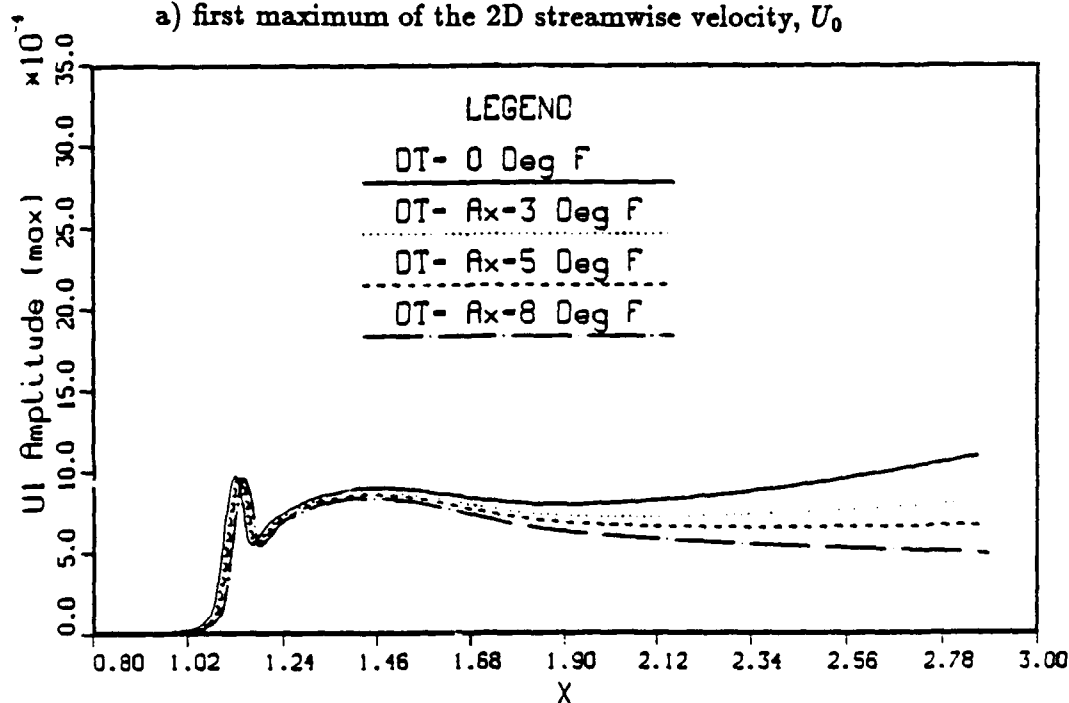
Figure 6.39 Amplitude and phase comparison at  $Re_{\delta_1} = 800$  with  $\Delta \bar{T} = A_0 x_n^{1.0}$  nonuniform passive control applied,  $F = 1$

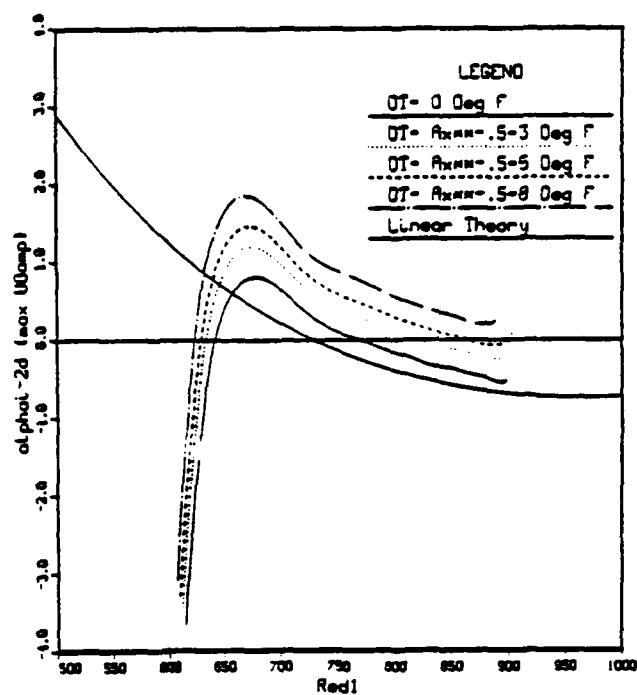


b) 3D streamwise velocity,  $U_1$

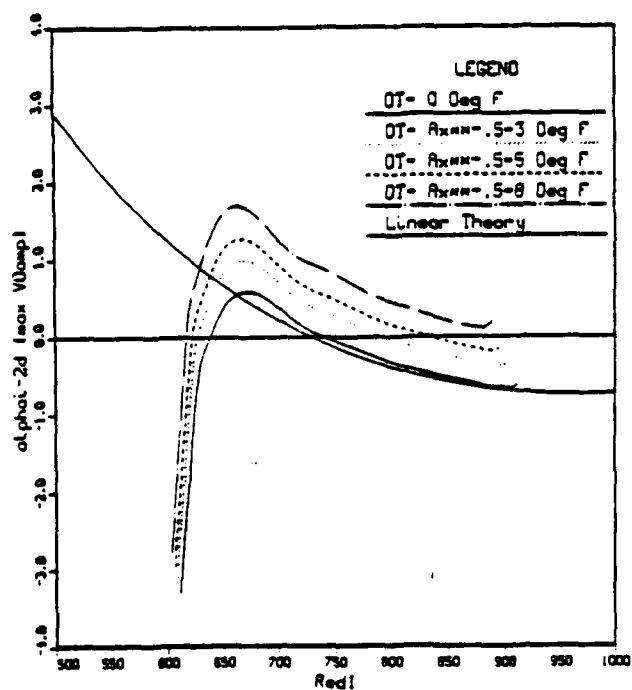
Figure 6.39 continued

a) first maximum of the 2D streamwise velocity,  $U_0$ b) first maximum of the 3D streamwise velocity,  $U_1$ Figure 6.40 Influence of nonuniform passive control on the amplitude growth for  $A_0 x_n^{-0.5}$ ,  $F = 1$

a) first maximum of the 2D streamwise velocity,  $U_0$ b) first maximum of the 3D streamwise velocity,  $U_1$ Figure 6.41 Influence of nonuniform passive control on the amplitude growth for  $A_0 x_n^{1.0}$ ,  $F = 1$

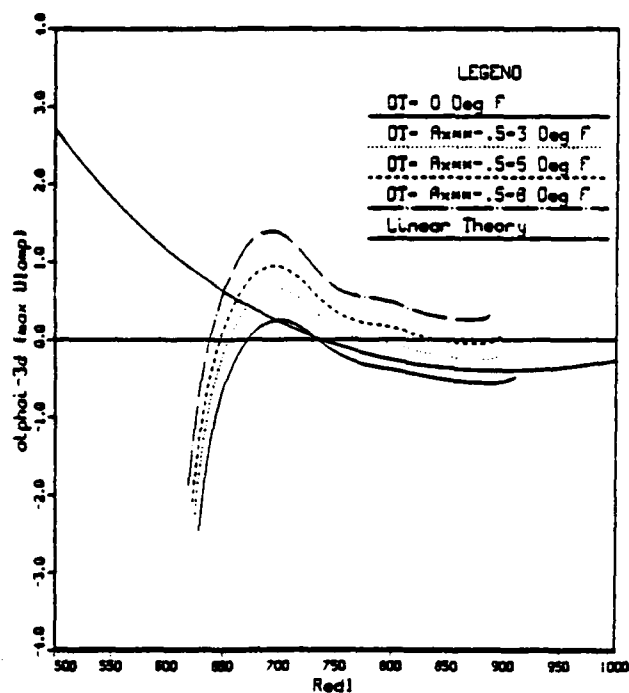


a) first maximum of the 2D streamwise velocity,  $U_0$  ( $p = -0.5$ )

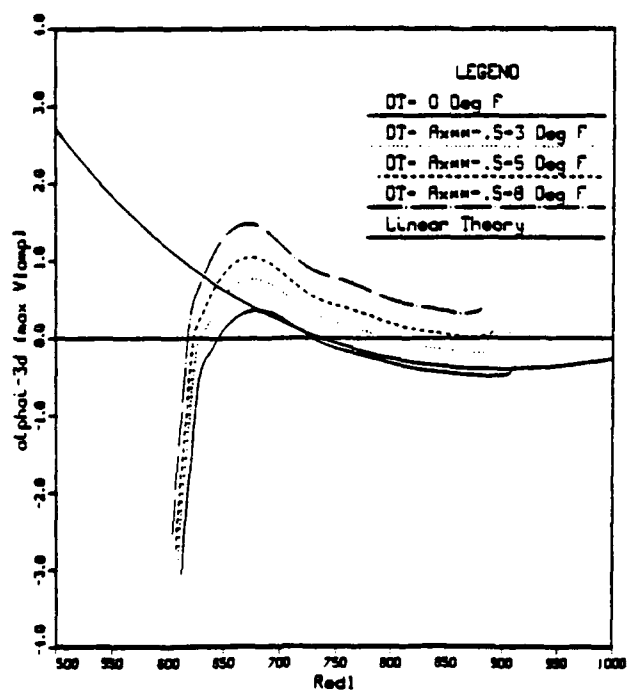


b) maximum of the 2D normal velocity,  $V_0$  ( $p = -0.5$ )

Figure 6.42 Influence of nonuniform heating on the growth rates  $\alpha_i$ ,  $F = 1$



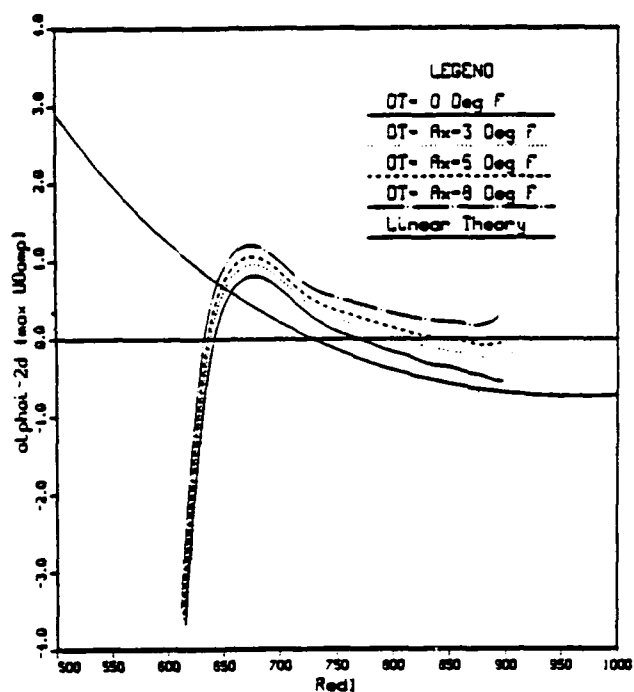
c) first maximum of the 3D streamwise velocity,  $U_1$  ( $p = -0.5$ )



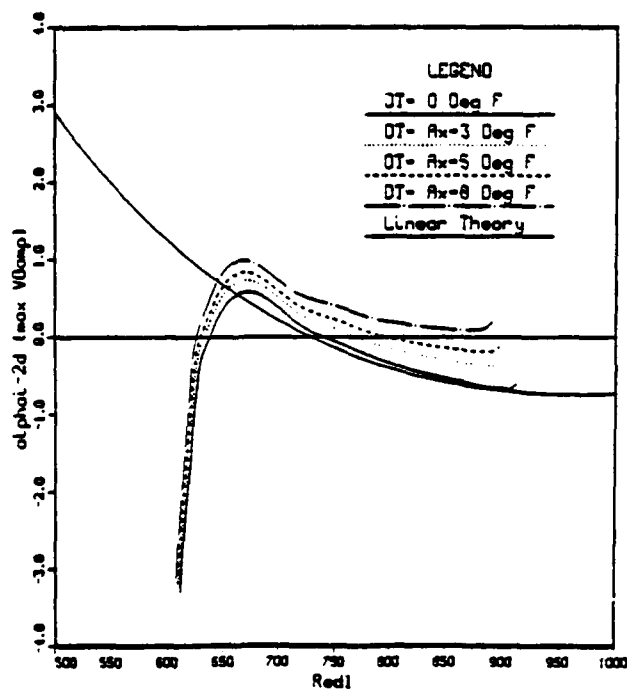
d) maximum of the 3D normal velocity,  $V_1$  ( $p = -0.5$ )

Figure 6.42 continued



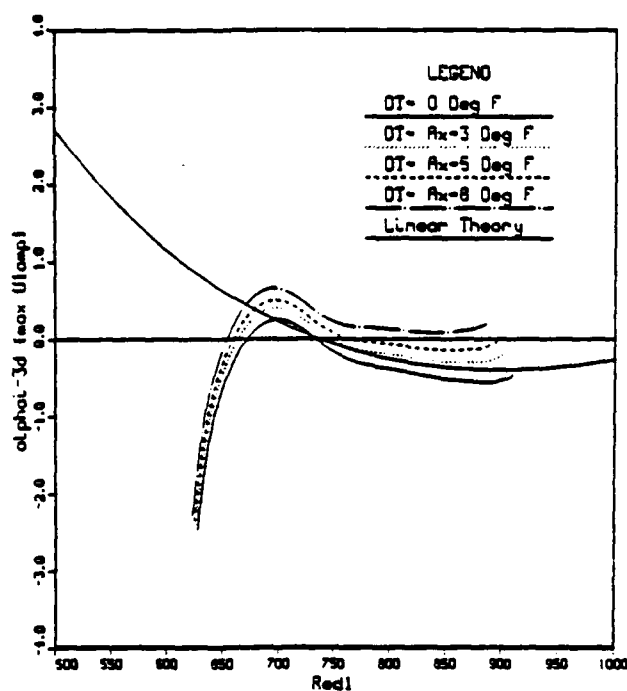


a) first maximum of the 2D streamwise velocity,  $U_0$  ( $p = 1.0$ )

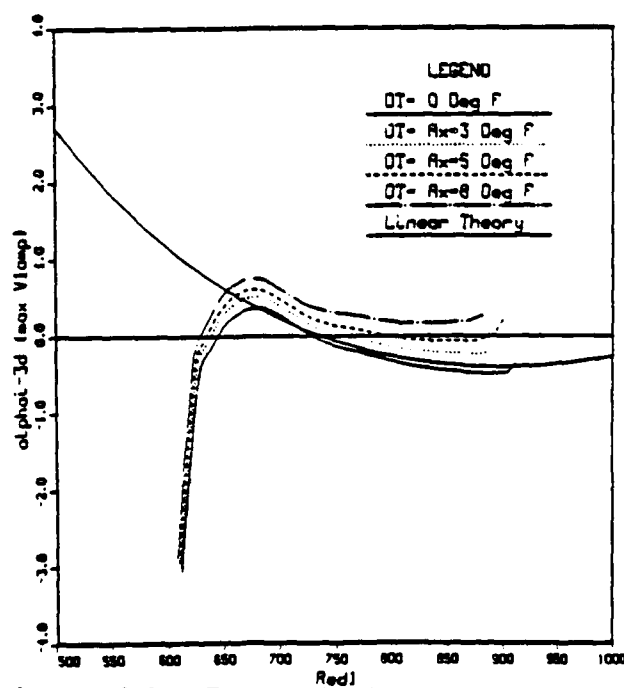


b) maximum of the 2D normal velocity,  $V_0$  ( $p = 1.0$ )

Figure 6.43 Influence of nonuniform heating on the growth rates  $\alpha_i$ ,  $F = 1$

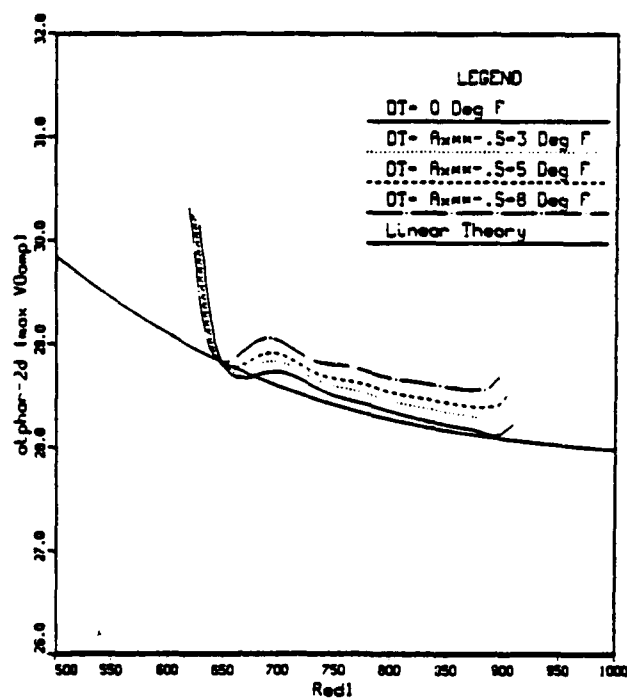


c) first maximum of the 3D streamwise velocity,  $U_1$  ( $p = 1.0$ )

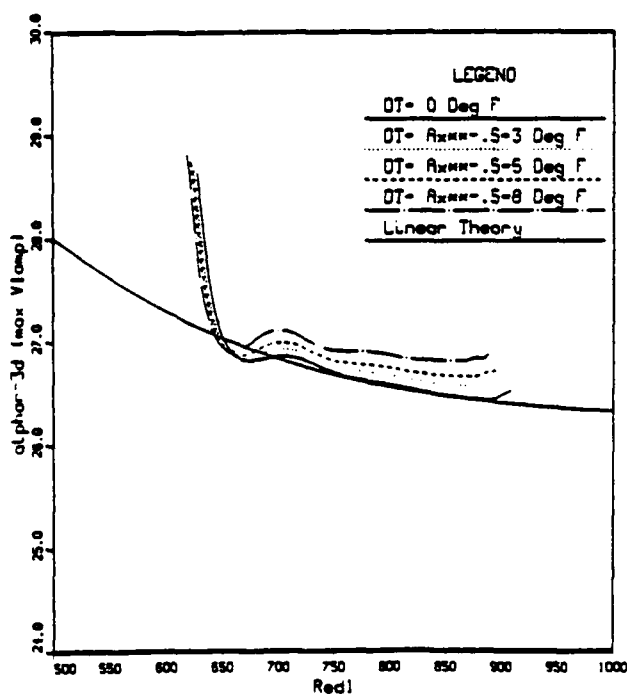


d) maximum of the 3D normal velocity,  $V_1$  ( $p = 1.0$ )

Figure 6.43 continued

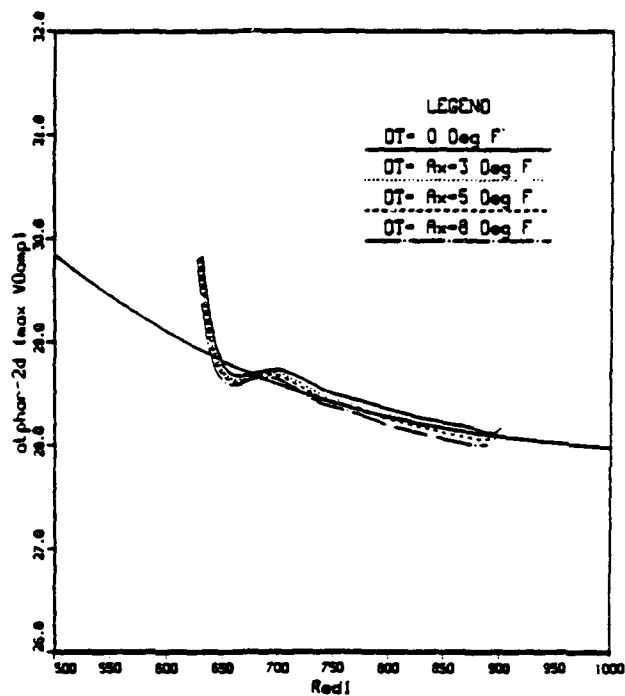
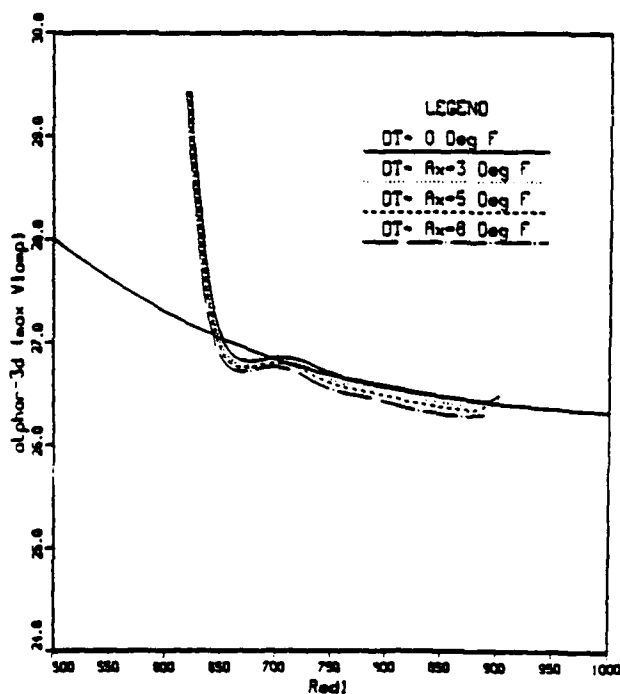


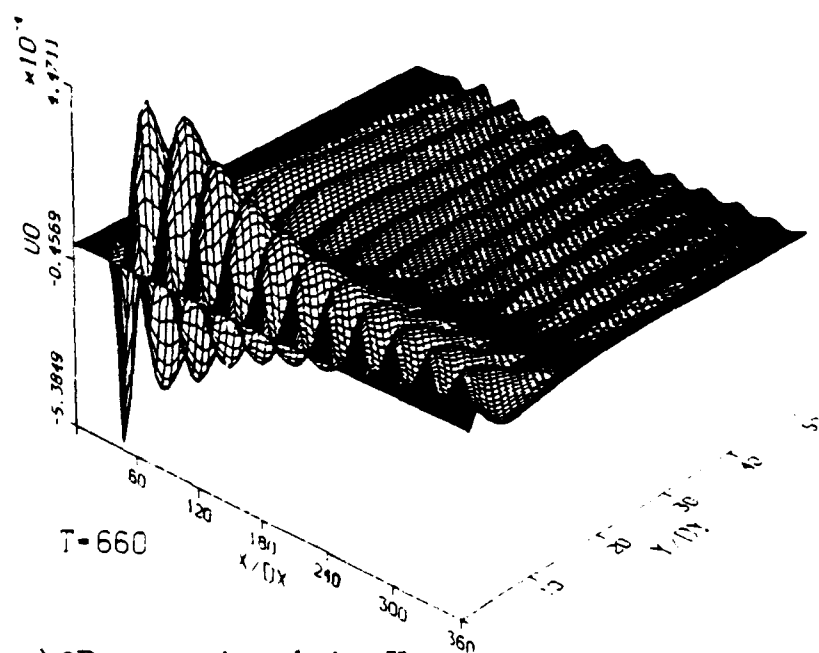
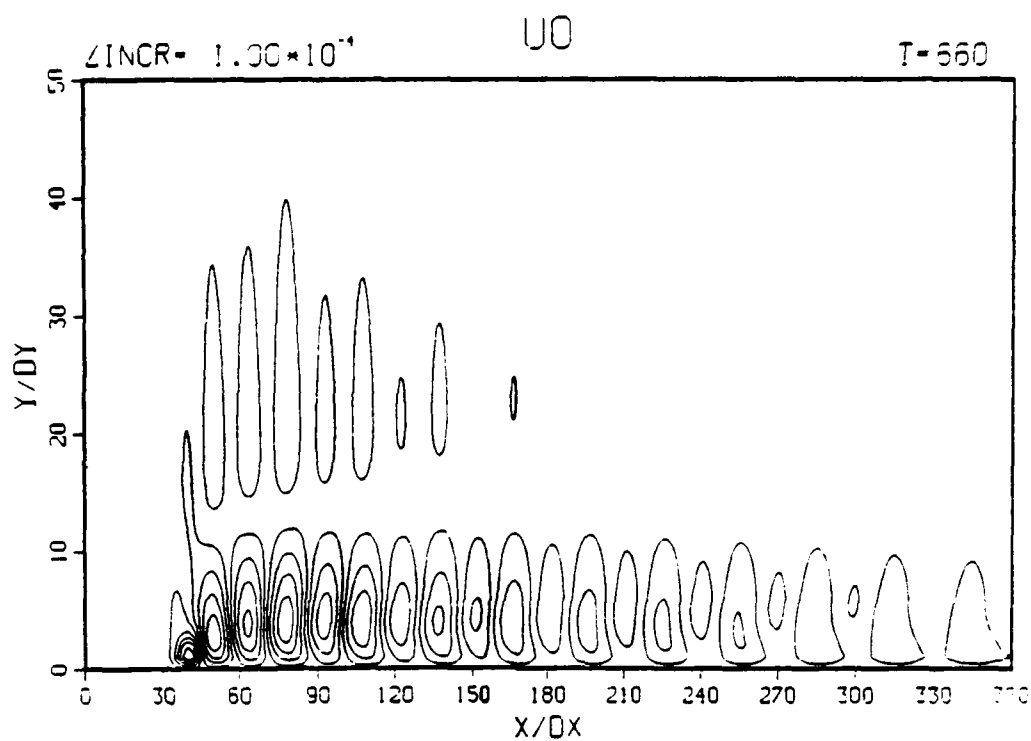
a) maximum of the 2D normal velocity,  $V_0$  ( $p = -0.5$ )



b) maximum of the 3D normal velocity,  $V_1$  ( $p = -0.5$ )

Figure 6.44 Influence of nonuniform heating on the wavenumbers  $\alpha_r$ ,  $F = 1$

a) maximum of the 2D normal velocity,  $V_0$  ( $p = 1.0$ )b) maximum of the 3D normal velocity,  $V_1$  ( $p = 1.0$ )Figure 6.45 Influence of nonuniform heating on the wavenumbers  $\alpha_r$ ,  $F = 1$



a) 2D streamwise velocity,  $U_0$

Figure 6.46 Disturbed flow after eleven periods of oscillation with nonuniform surface temperature distribution  $\Delta \bar{T} = A_0 x_n^{-0.5} = 8^\circ F$  at  $Re_{\delta_1} = 800$  passive control applied,  $F = 1.55$

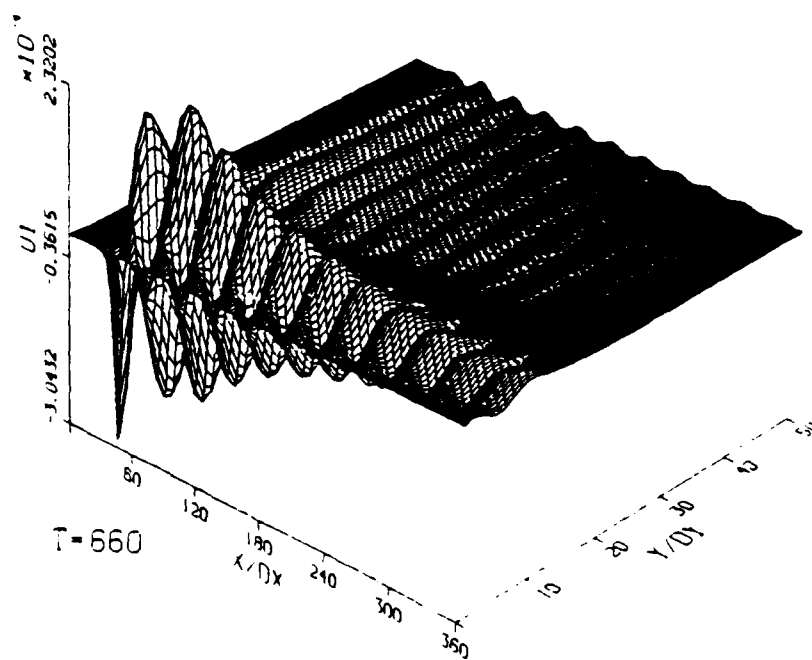
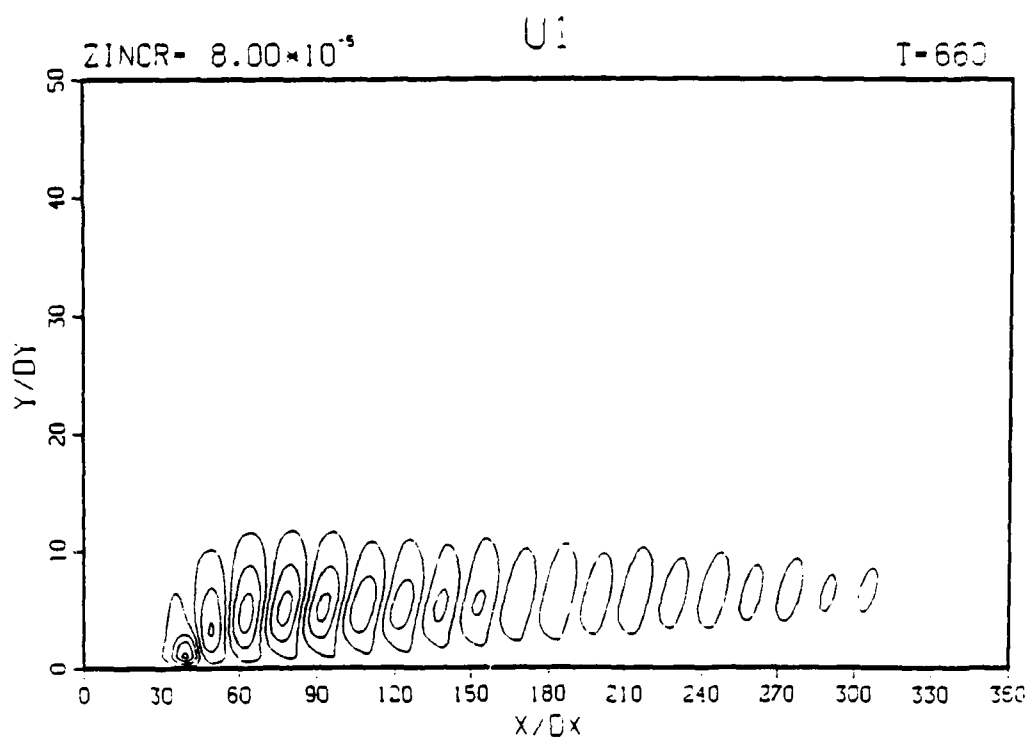
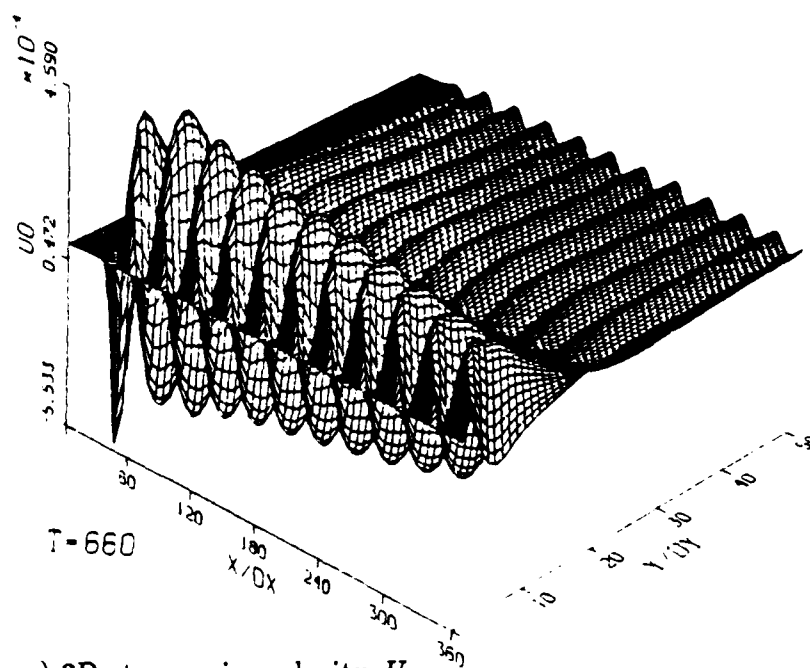
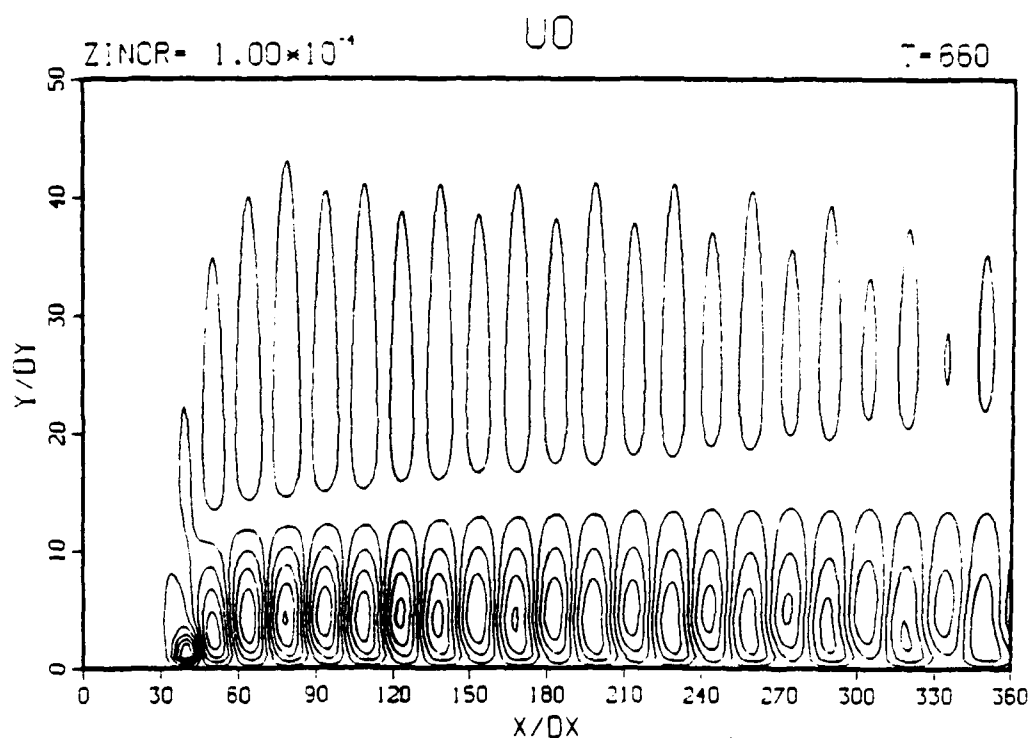
b) 3D streamwise velocity,  $U_1$ .

Figure 6.46 continued



a) 2D streamwise velocity,  $U_0$

Figure 6.47 Disturbed flow after eleven periods of oscillation with nonuniform surface temperature distribution  $\Delta \bar{T} = A_0 x_n^{1.0} = 8^\circ F$  at  $Re_{\delta_1} = 800$  passive control applied,  $F = 1.55$

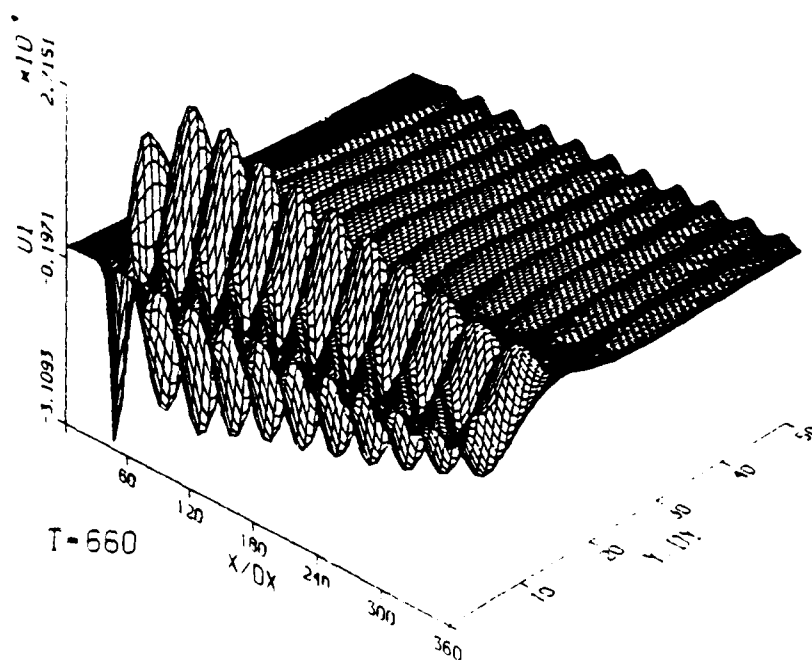
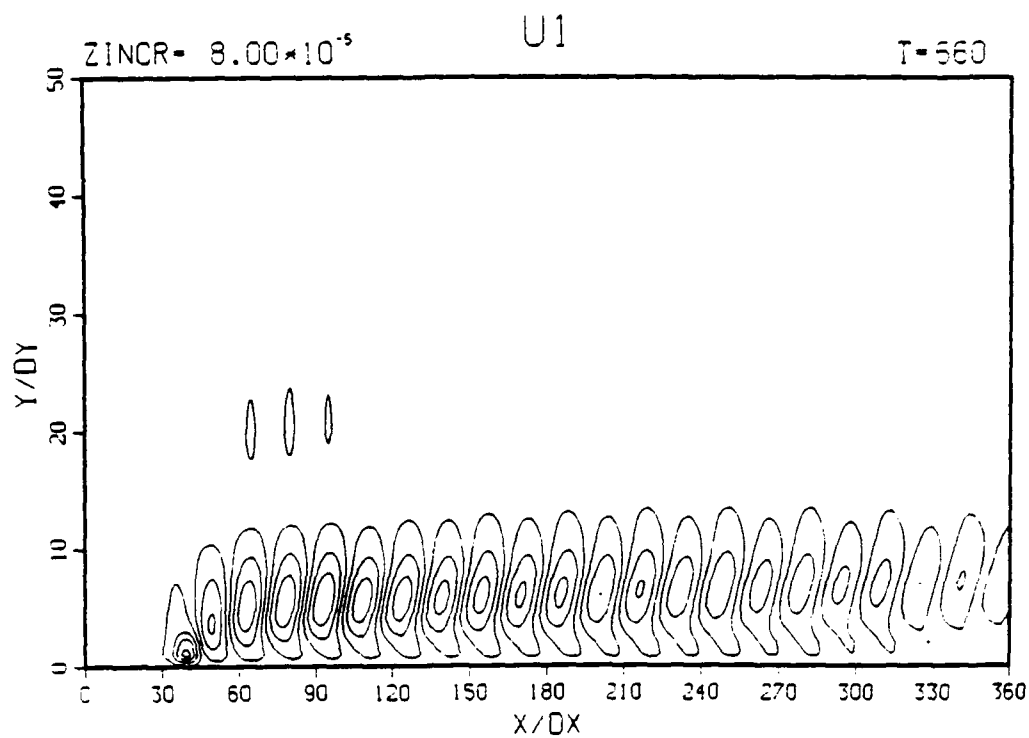
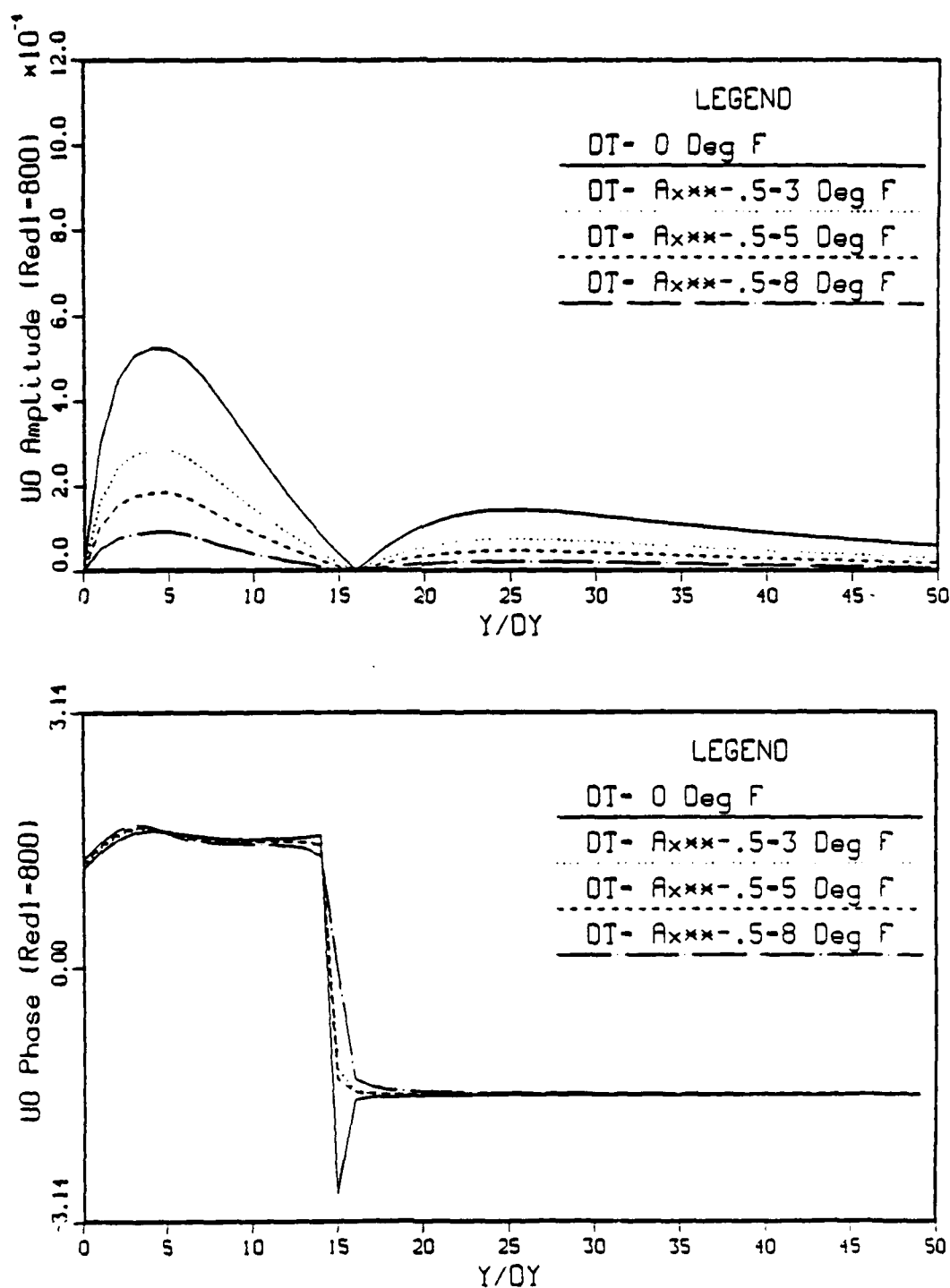
b) 3D streamwise velocity,  $U_1$ 

Figure 6.47 continued





a) 2D streamwise velocity,  $U_0$

Figure 6.48 Amplitude and phase comparison at  $Re_{\delta_1} = 800$  with  $\Delta \bar{T} = A_0 x_n^{-0.5}$  nonuniform passive control applied,  $F = 1.55$

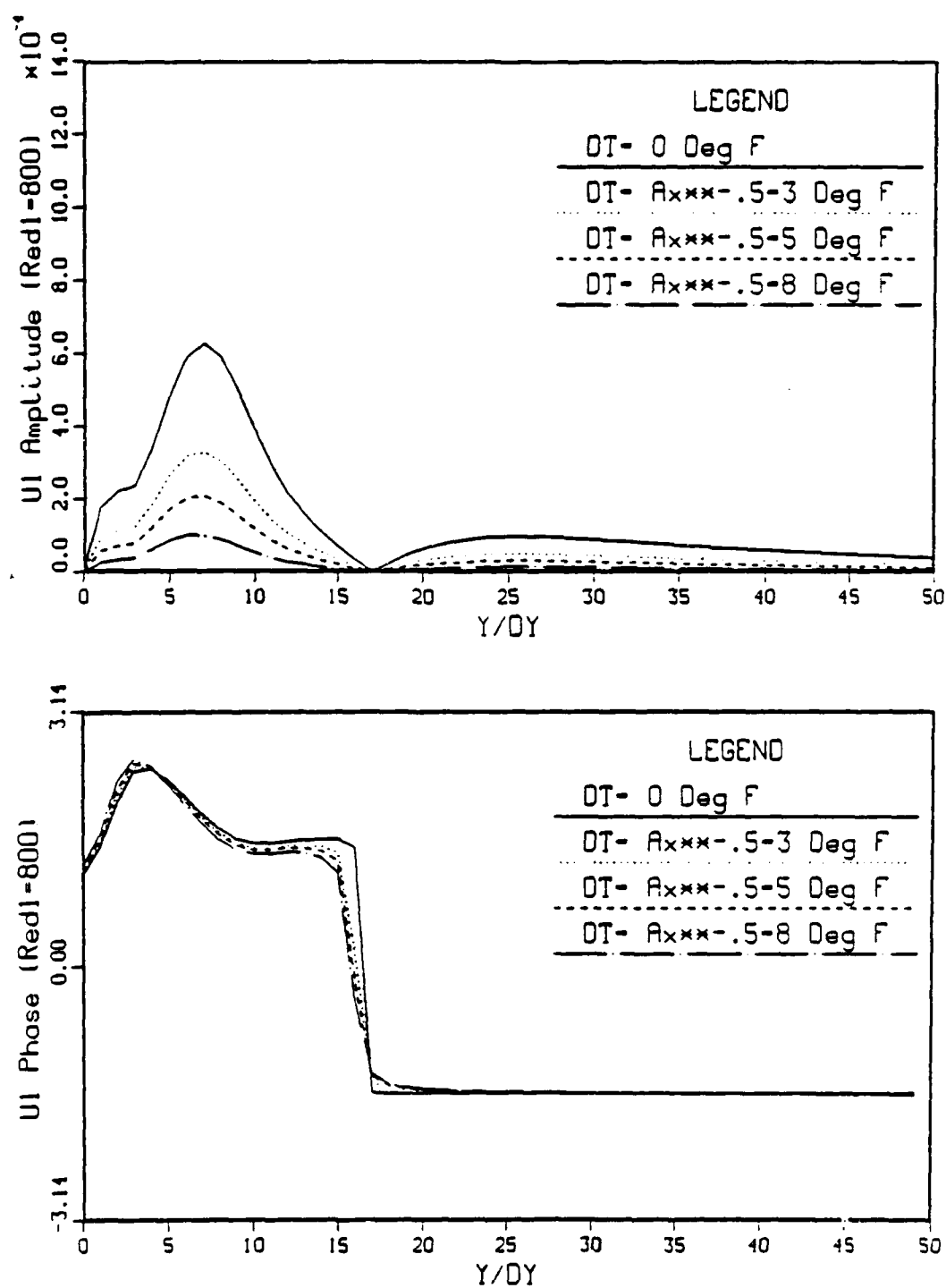
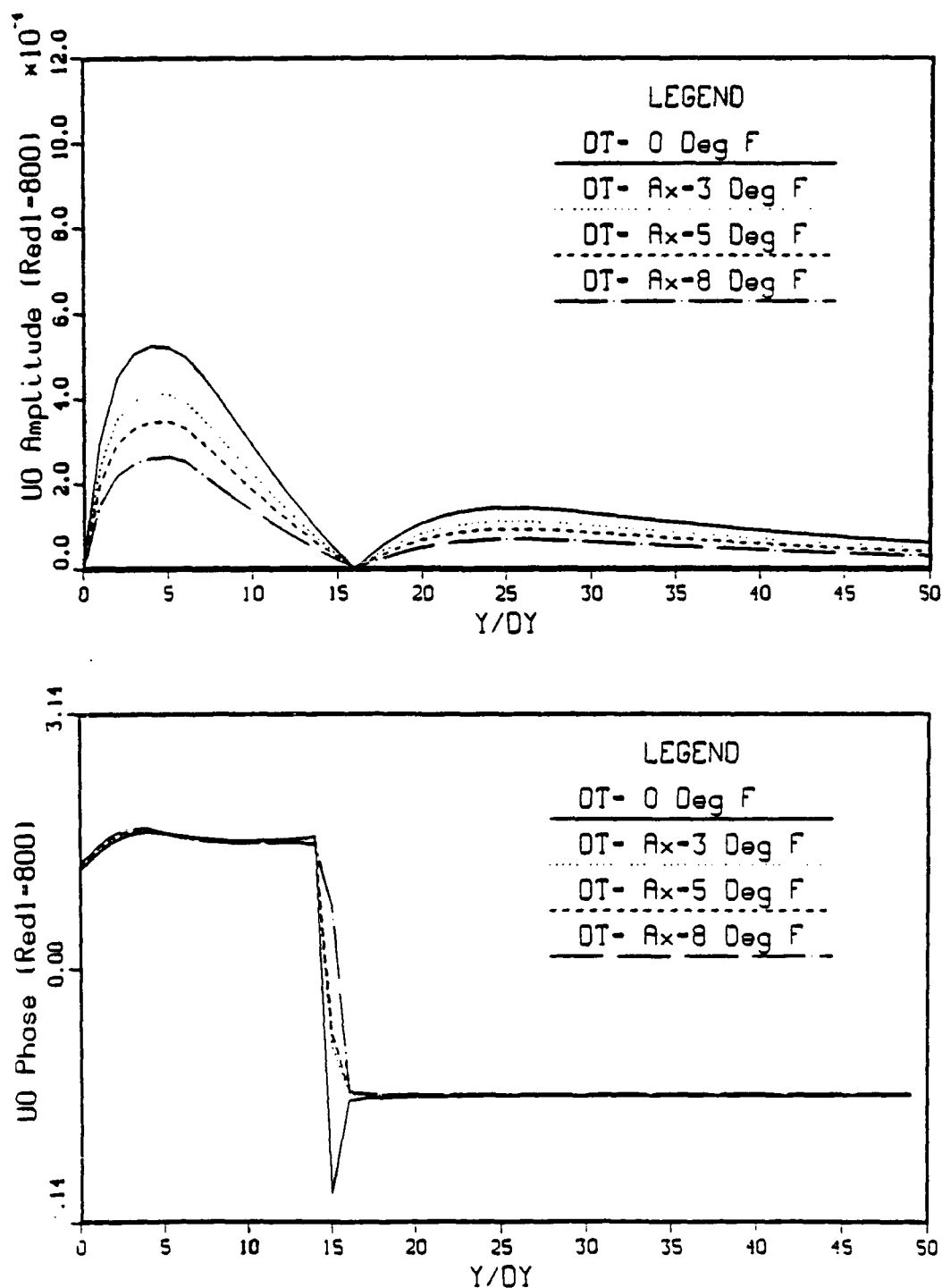
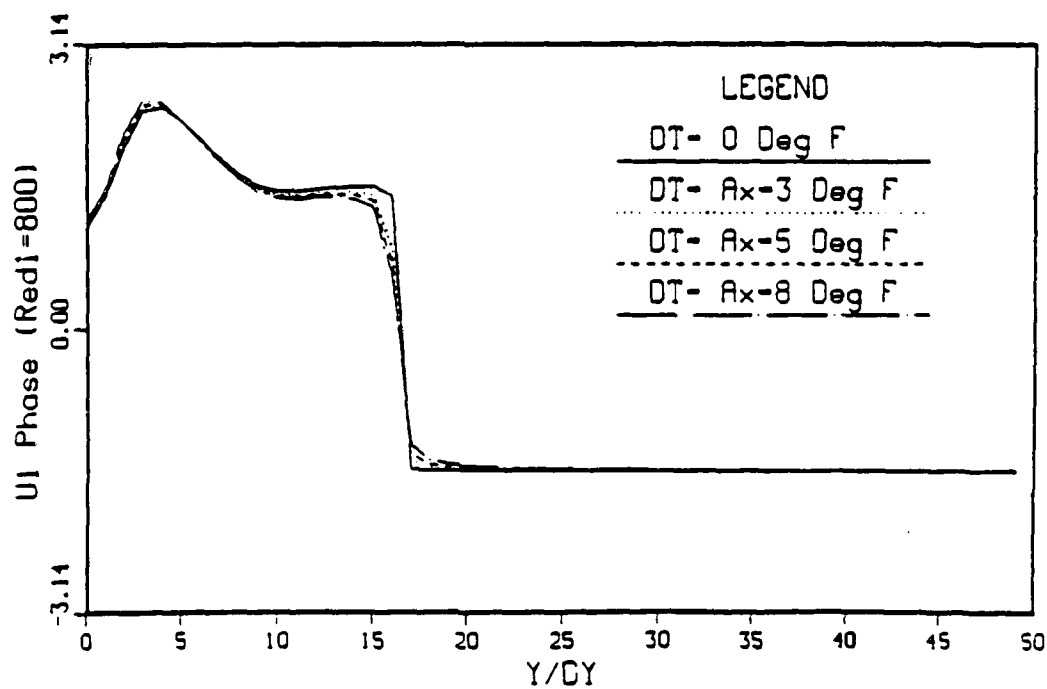
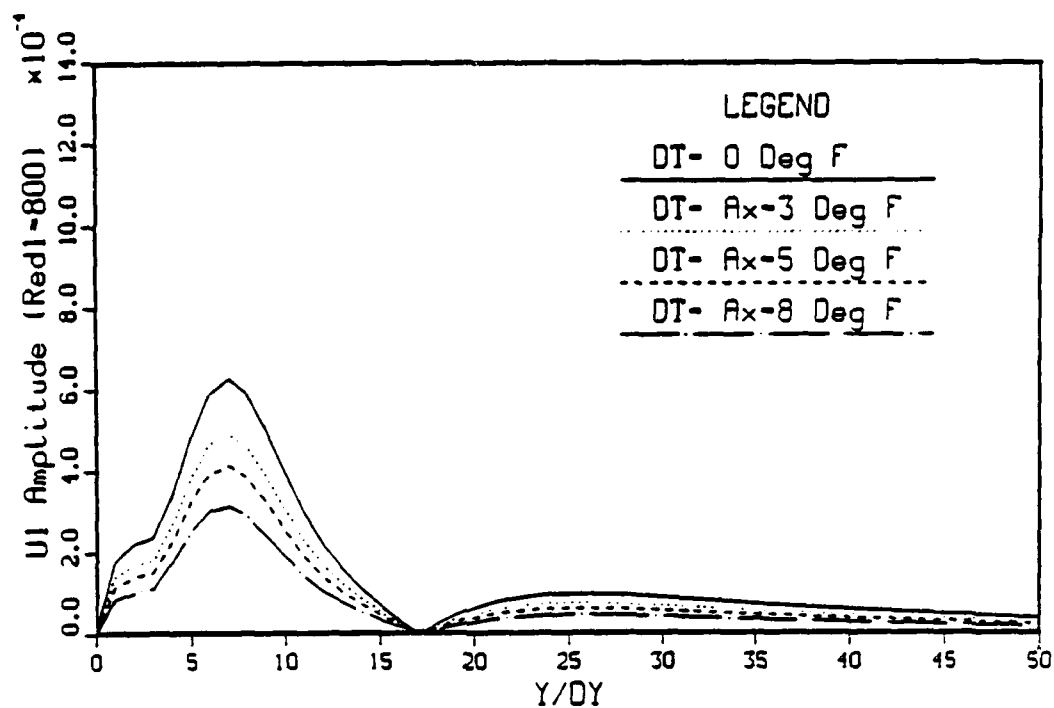
b) 3D streamwise velocity,  $U_1$ 

Figure 6.48 continued

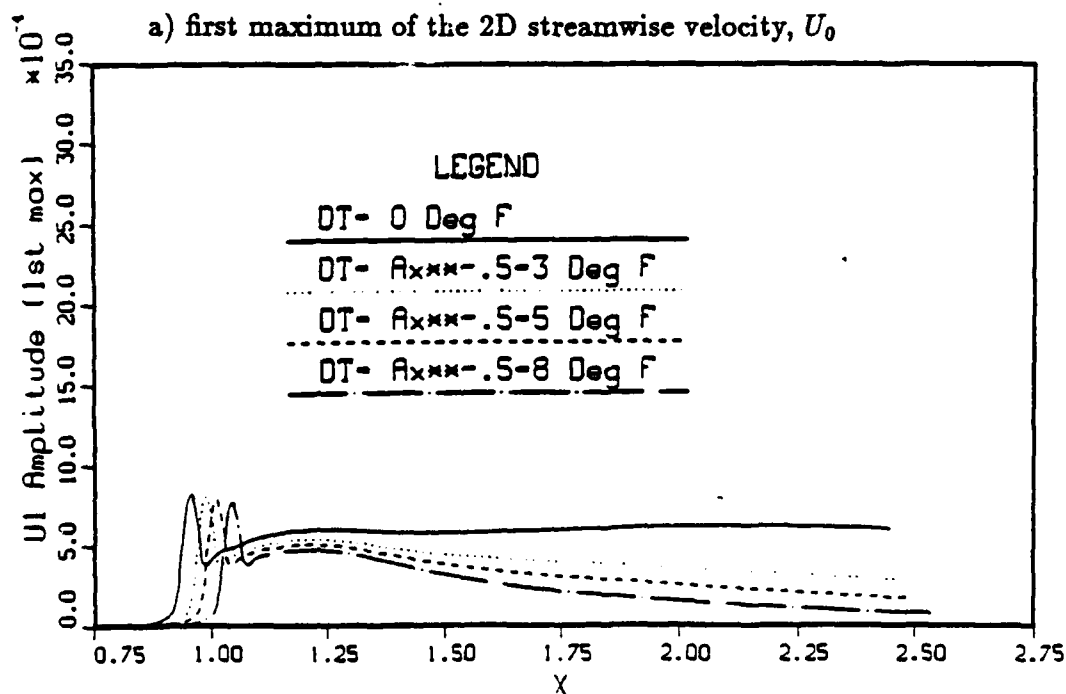
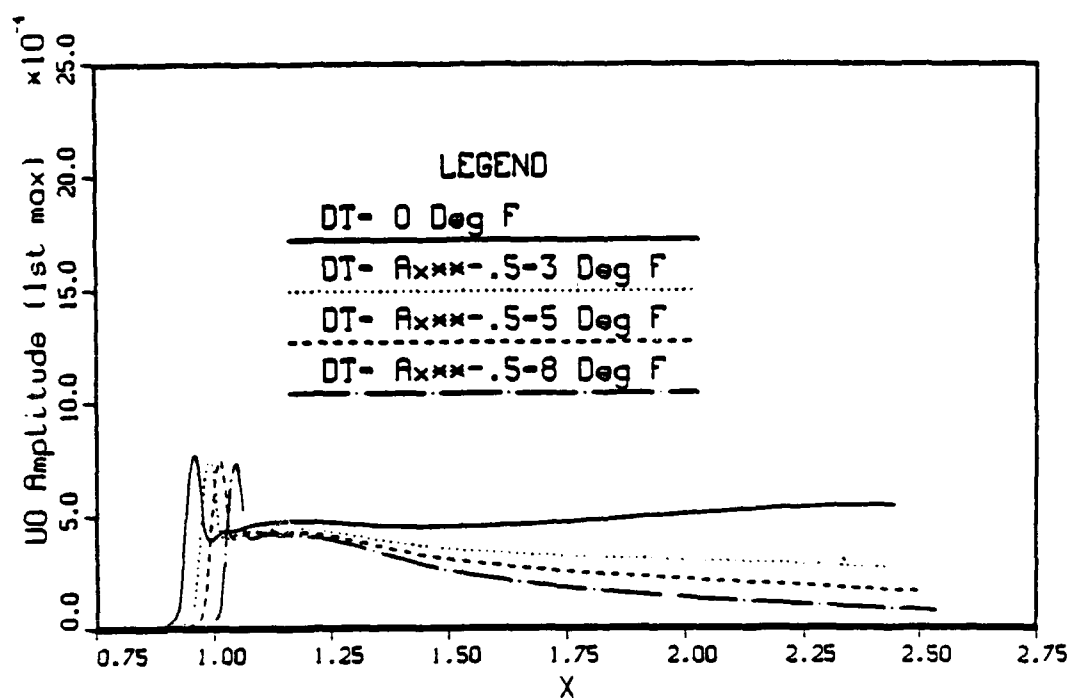


a) 2D streamwise velocity,  $U_0$

Figure 6.49 Amplitude and phase comparison at  $Re_{\delta_1} = 800$  with  $\Delta \bar{T} = A_0 x_n^{1.0}$  nonuniform passive control applied,  $F = 1.55$



b) 3D streamwise  
Figure 6.49 continued



b) first maximum of the 3D streamwise velocity,  $U_1$

Figure 6.50 Influence of nonuniform passive control on the amplitude growth for  $A_0 x_n^{-0.5}$ ,  $F = 1.55$

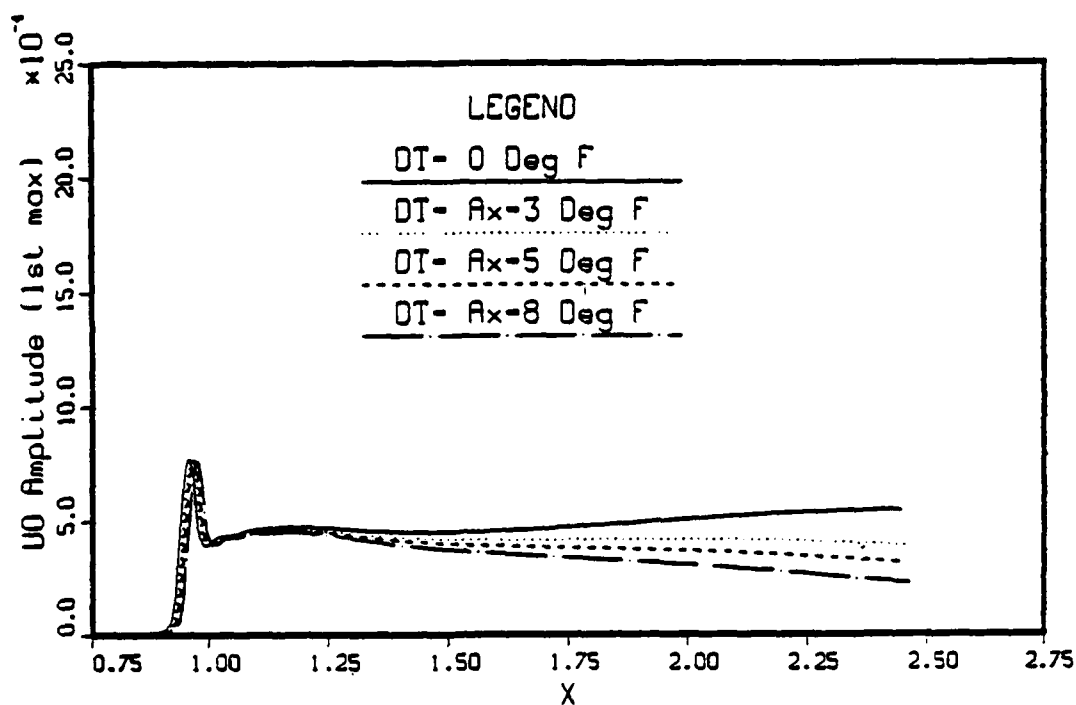
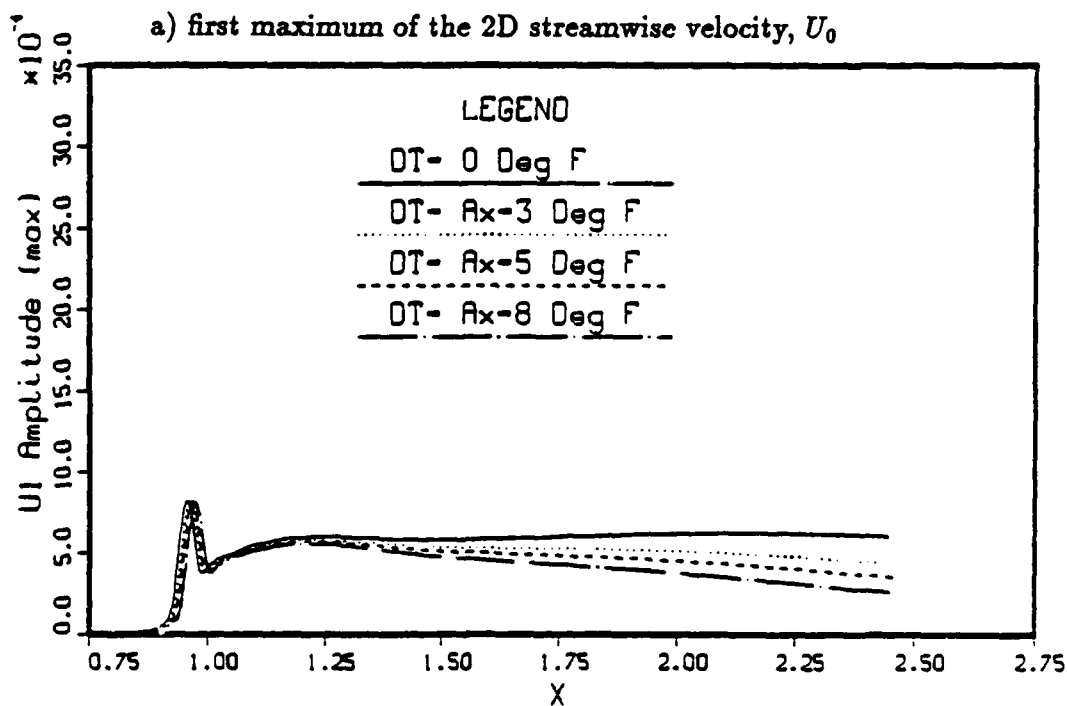
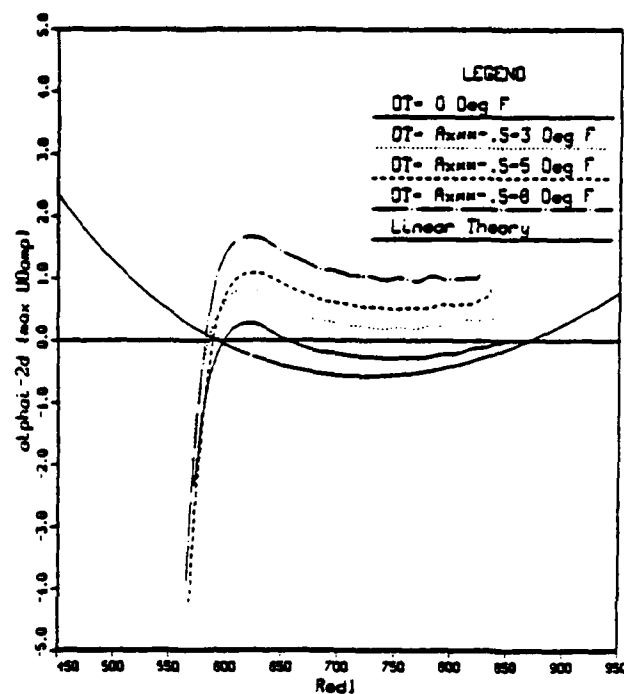
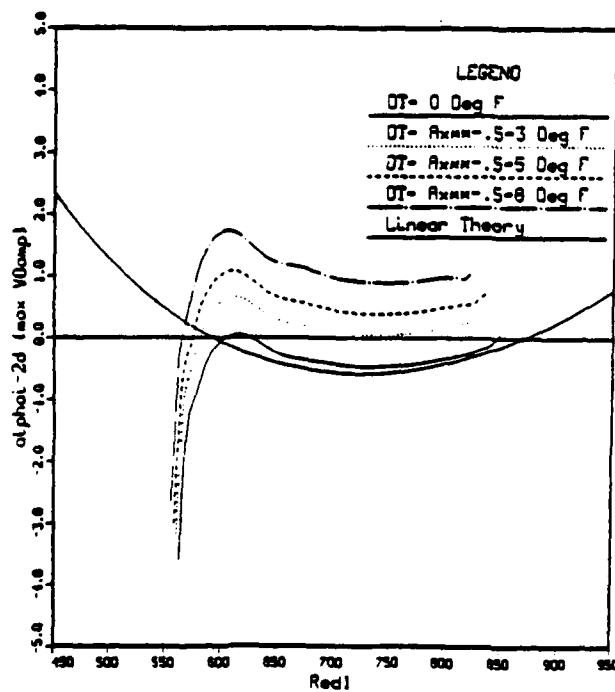
a) first maximum of the 2D streamwise velocity,  $U_0$ b) first maximum of the 3D streamwise velocity,  $U_1$ 

Figure 6.51 Influence of nonuniform passive control on the amplitude growth for  $A_0 x_n^{1.0}$ ,  $F = 1.55$

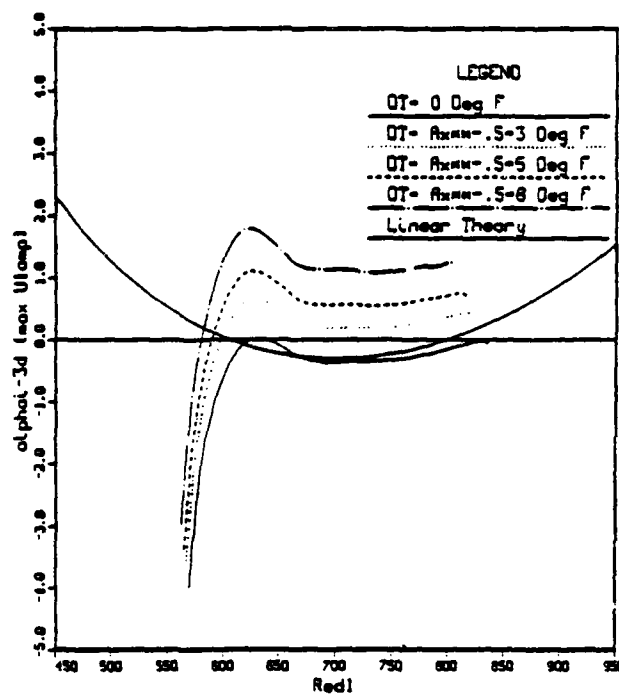


a) first maximum of the 2D streamwise velocity,  $U_0$  ( $p = -0.5$ )

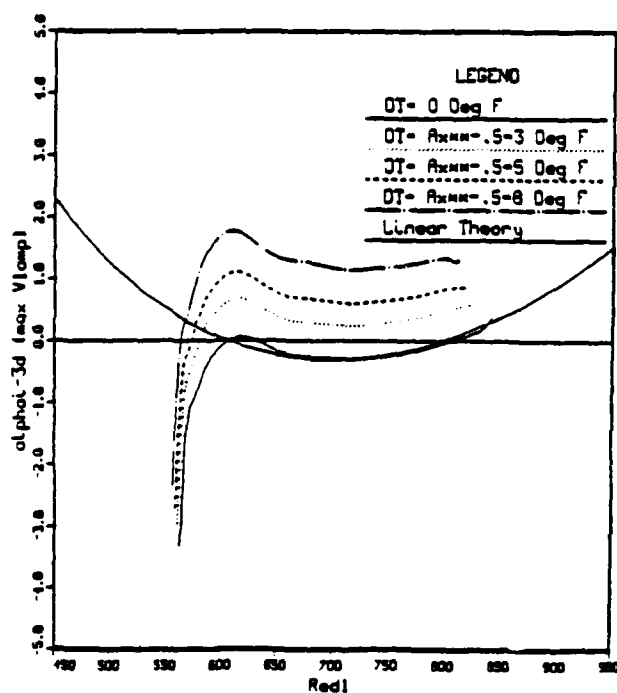


b) maximum of the 2D normal velocity,  $V_0$  ( $p = -0.5$ )

Figure 6.52 Influence of nonuniform heating on the growth rates  $\alpha_i$ ,  $F = 1.55$



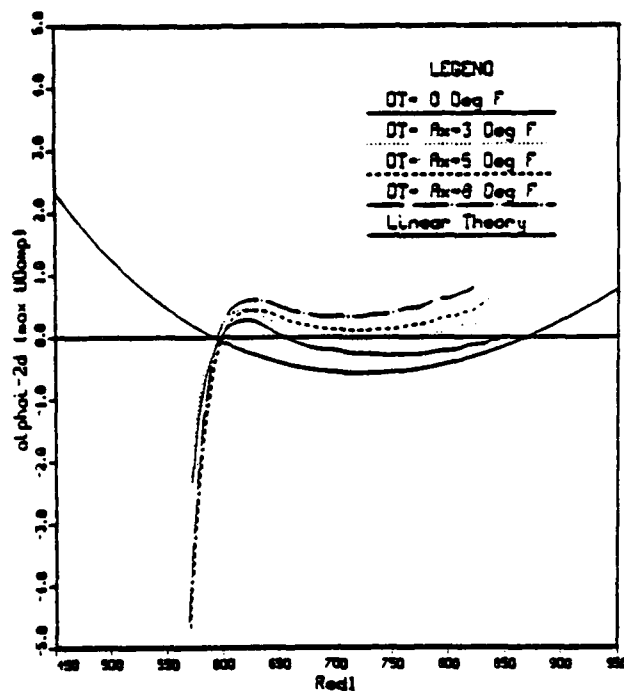
c) first maximum of the 3D streamwise velocity,  $U_1$  ( $p = -0.5$ )



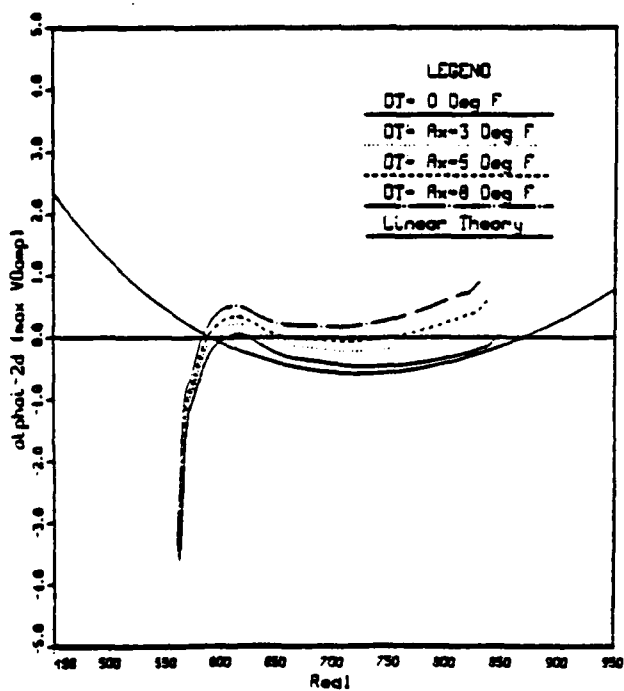
d) maximum of the 3D normal velocity,  $V_1$  ( $p = -0.5$ )

Figure 6.52 continued



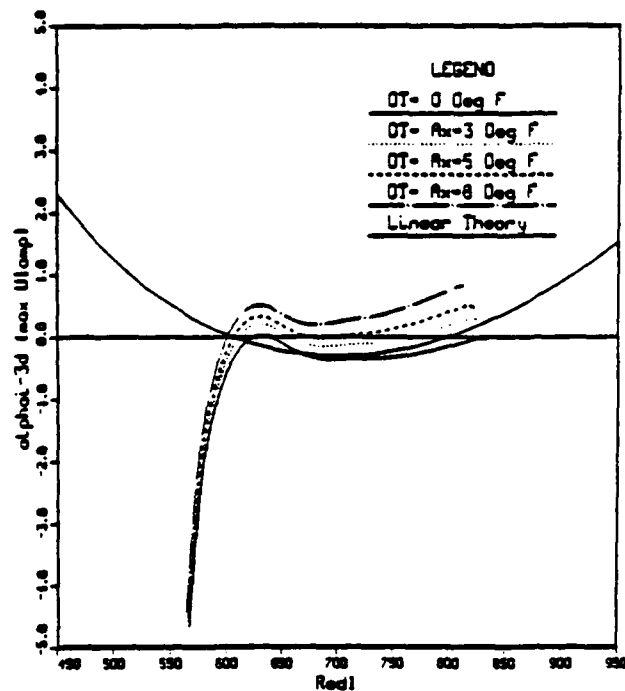


a) first maximum of the 2D streamwise velocity,  $U_0$  ( $p = 1.0$ )

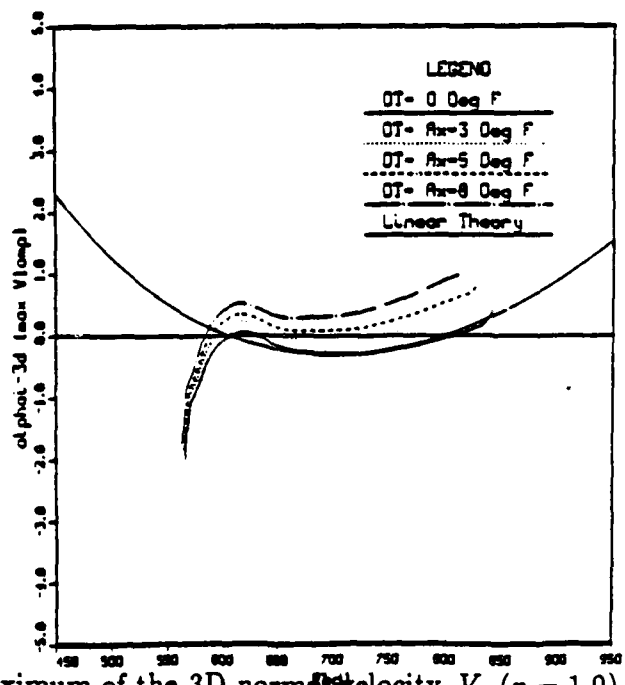


b) maximum of the 2D normal velocity,  $V_0$  ( $p = 1.0$ )

Figure 6.53 Influence of nonuniform heating on the growth rates  $\alpha_i$ ,  $F = 1.55$

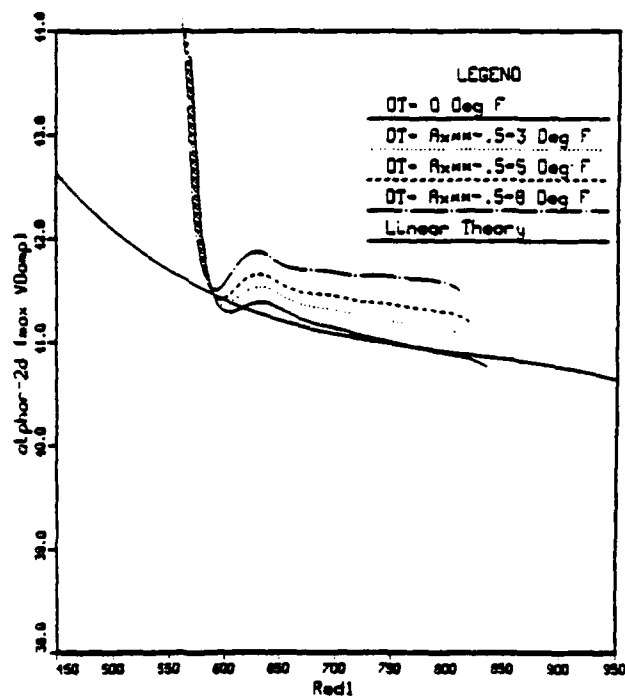


c) first maximum of the 3D streamwise velocity,  $U_1$  ( $p = 1.0$ )

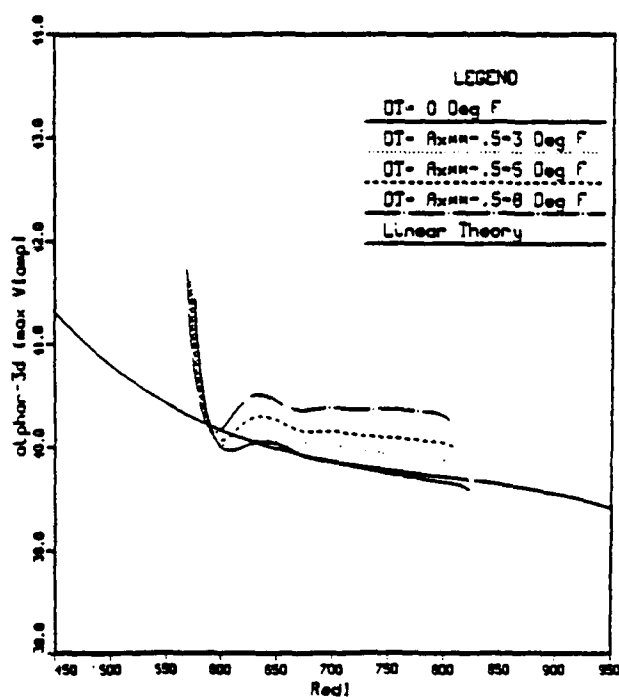


d) maximum of the 3D normal velocity,  $V_1$  ( $p = 1.0$ )

Figure 6.53 continued

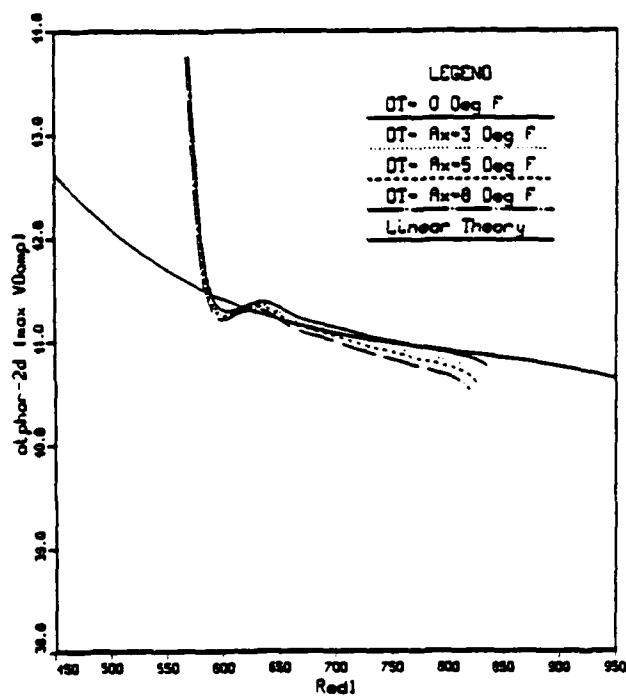


a) maximum of the 2D normal velocity,  $V_0$  ( $p = -0.5$ )

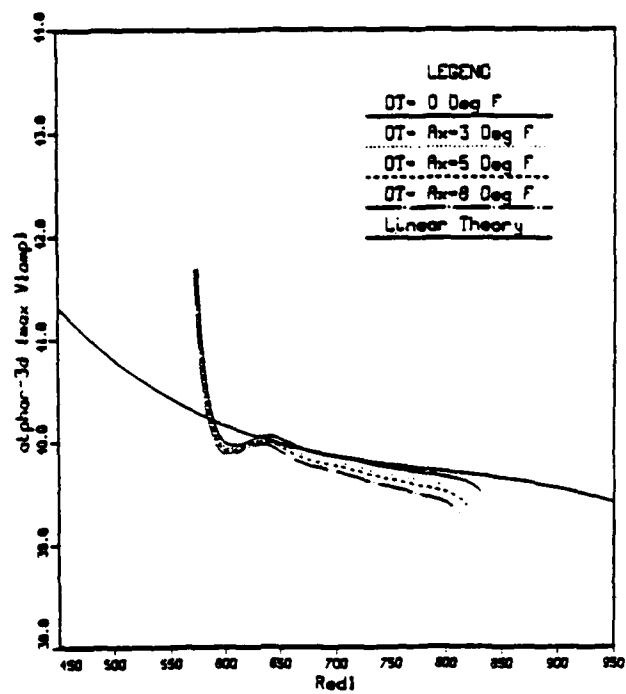


b) maximum of the 3D normal velocity,  $V_1$  ( $p = -0.5$ )

Figure 6.54 Influence of nonuniform heating on the wavenumbers  $\alpha_r$ ,  $F = 1.55$

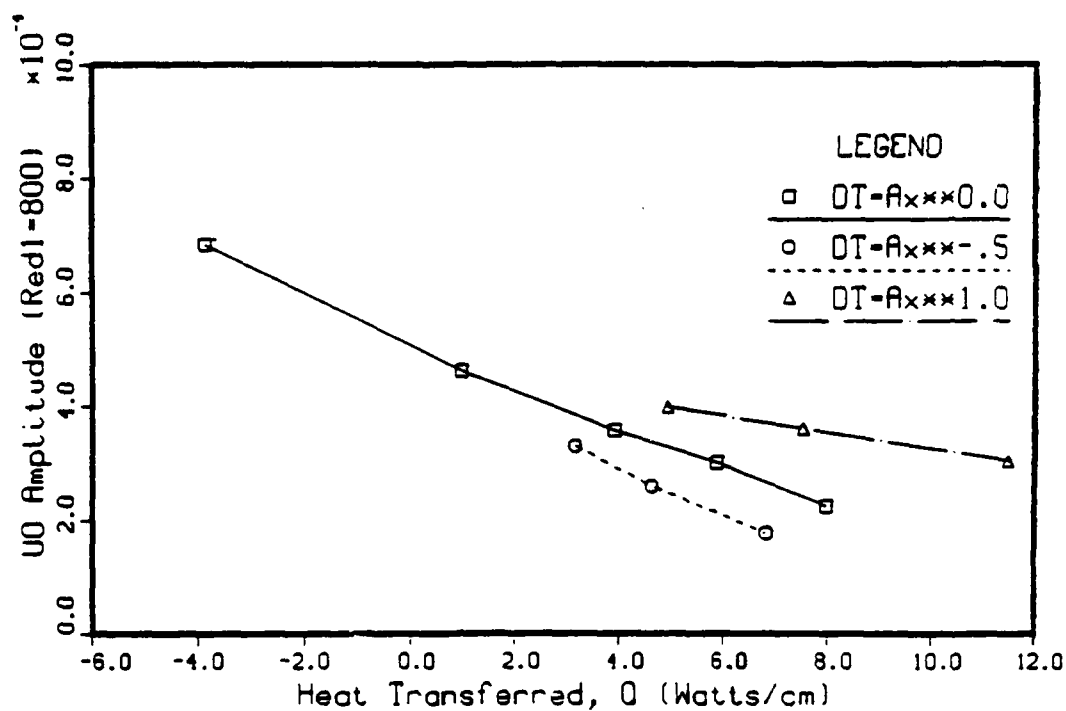
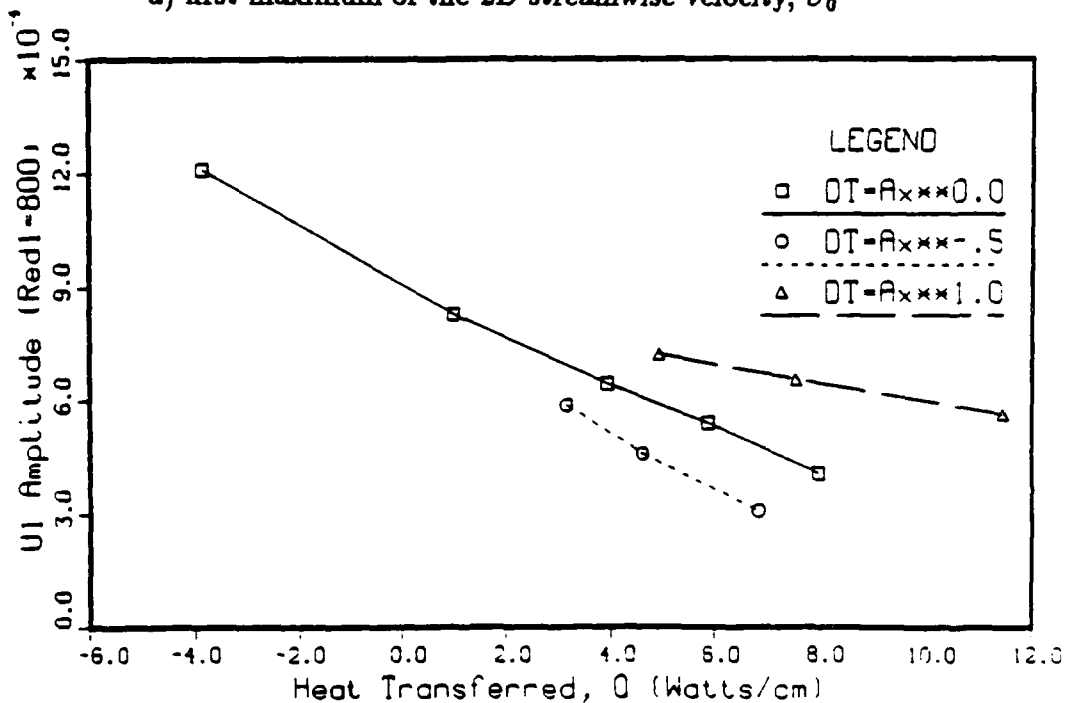


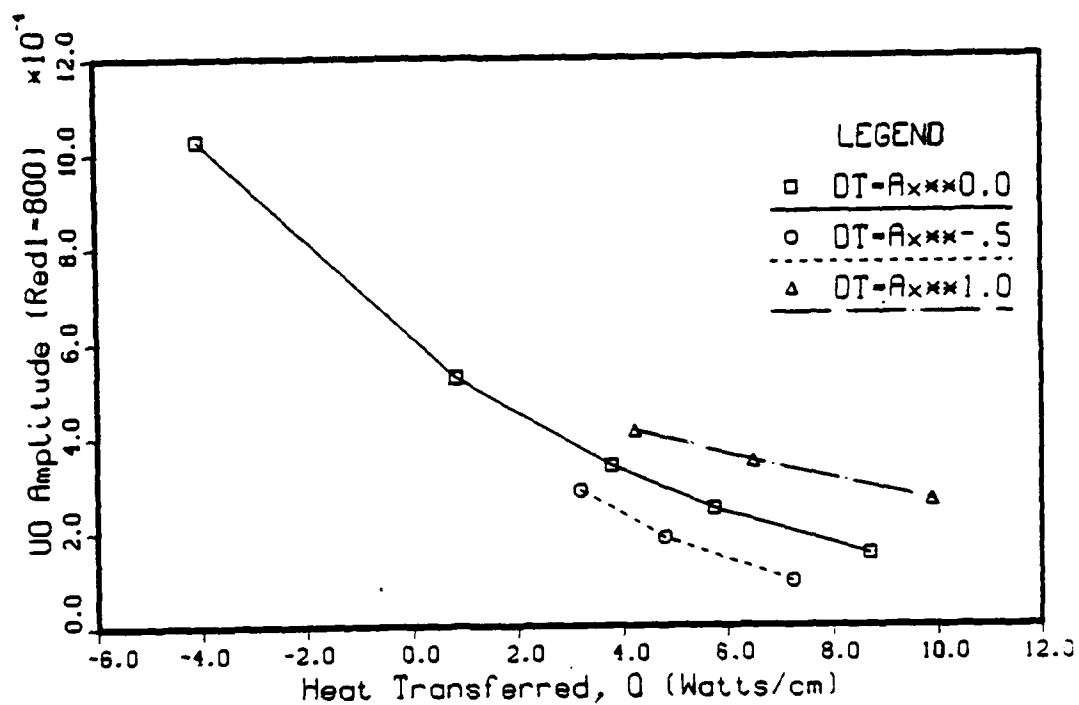
a) maximum of the 2D normal velocity,  $V_0$  ( $p = 1.0$ )



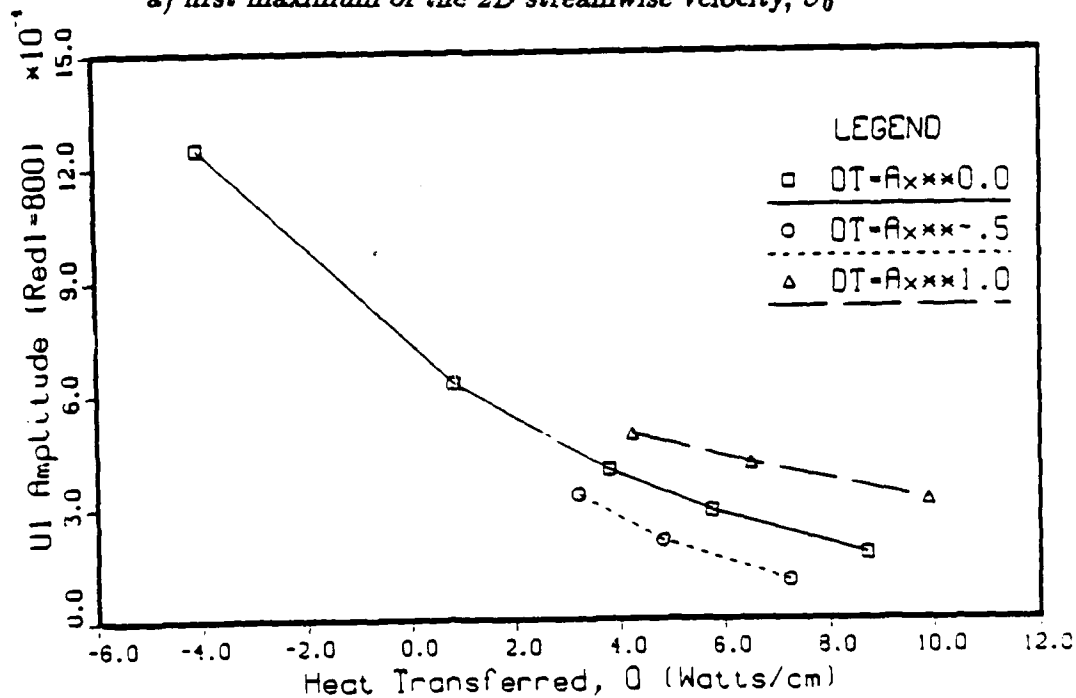
b) maximum of the 3D normal velocity,  $V_1$  ( $p = 1.0$ )

Figure 6.55 Influence of nonuniform heating on the wavenumbers  $\alpha_r$ ,  $F = 1.55$

a) first maximum of the 2D streamwise velocity,  $U_0$ b) first maximum of the 3D streamwise velocity,  $U_1$ Figure 6.56 Comparison of wall heat input and level of control achieved,  $F = 1$

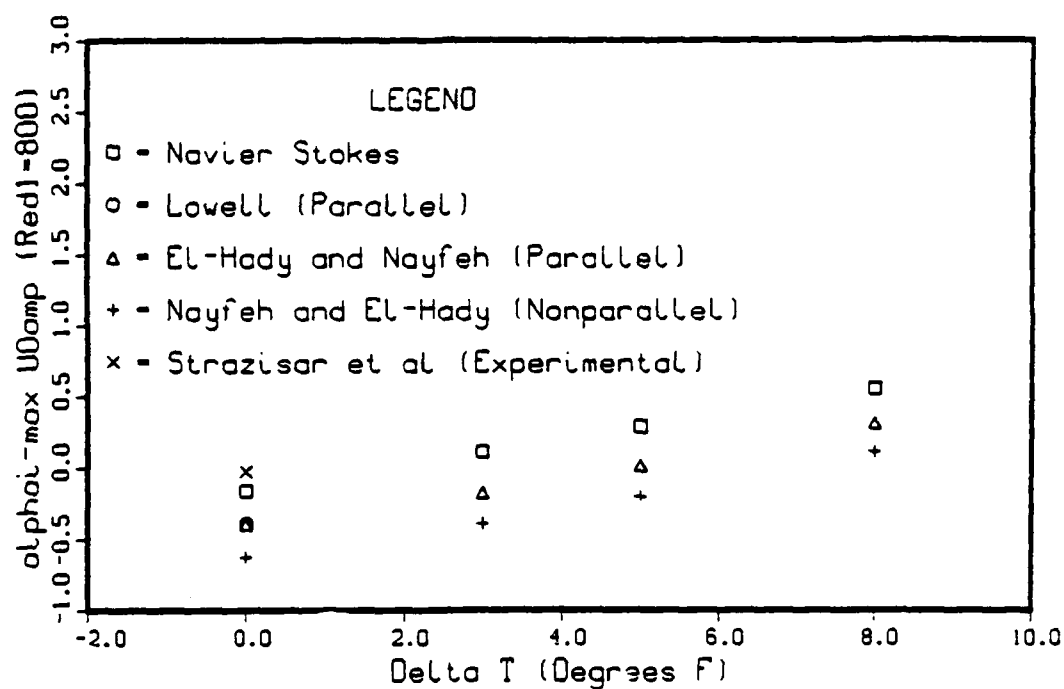


a) first maximum of the 2D streamwise velocity,  $U_0$

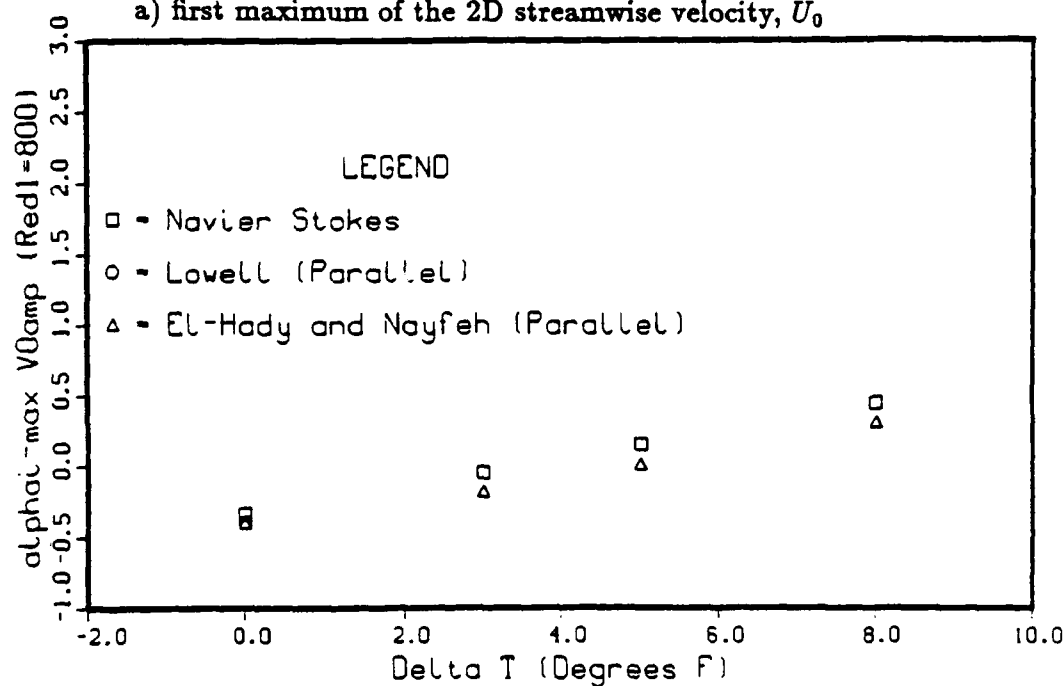


b) first maximum of the 3D streamwise velocity,  $U_1$

Figure 6.57 Comparison of wall heat input and level of control achieved,  $F = 1.55$

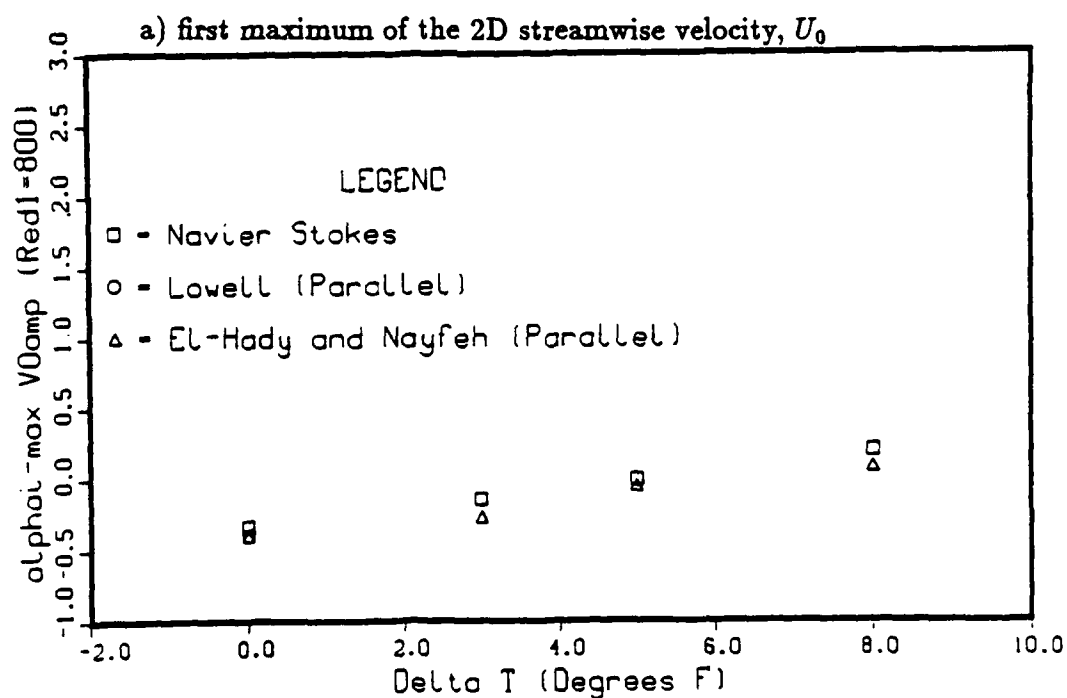
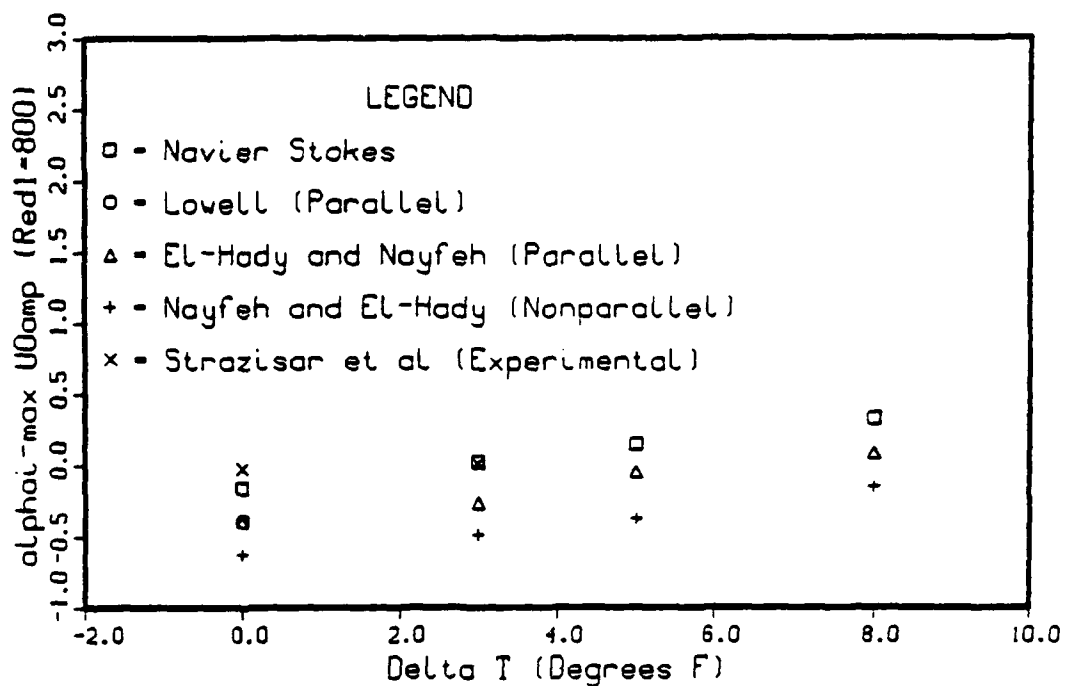


a) first maximum of the 2D streamwise velocity,  $U_0$



b) maximum of the 2D normal velocity,  $V_0$

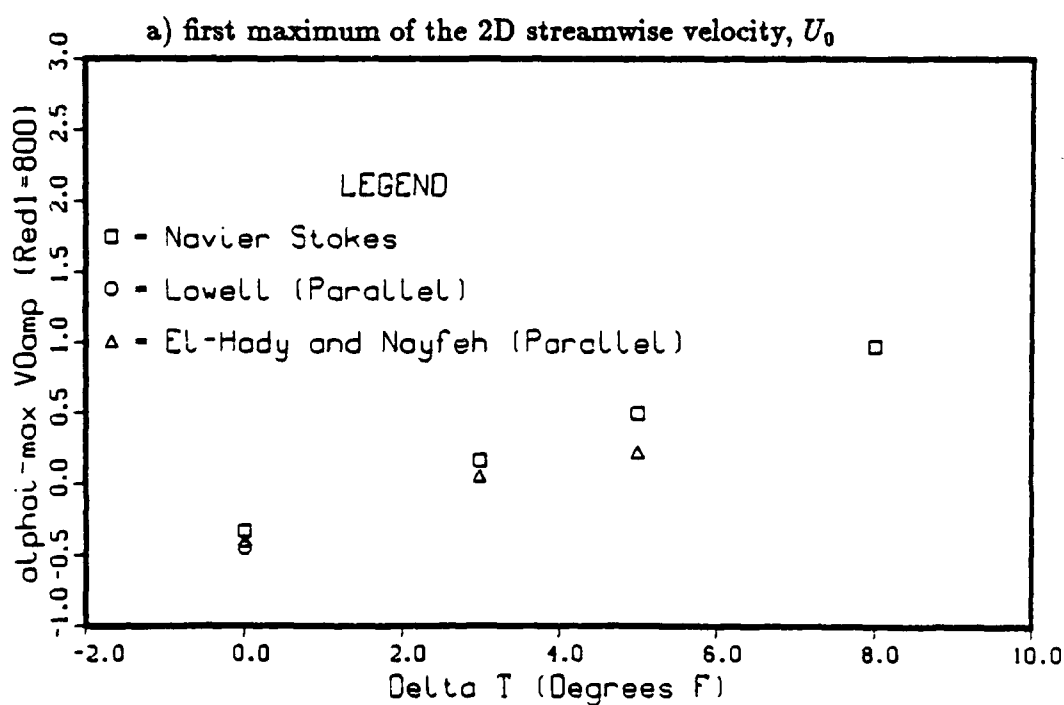
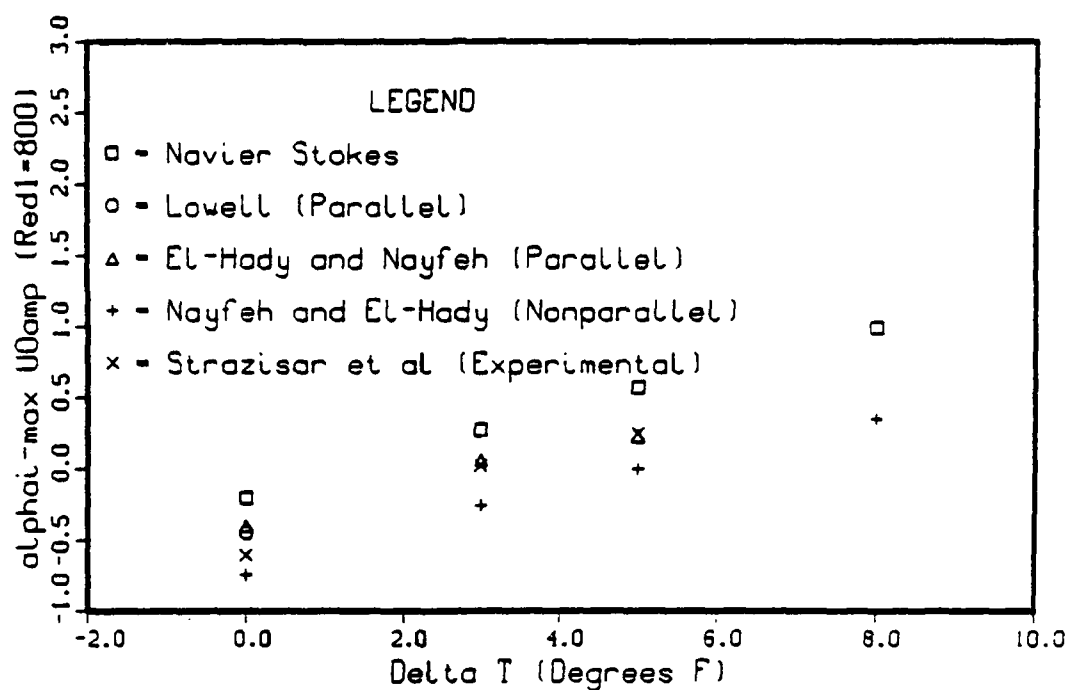
Figure 6.58 Comparison of amplification rates for nonuniform passive control ( $p = -0.5$ ) with theory and experiment,  $F = 1$



b) maximum of the 2D normal velocity,  $V_0$

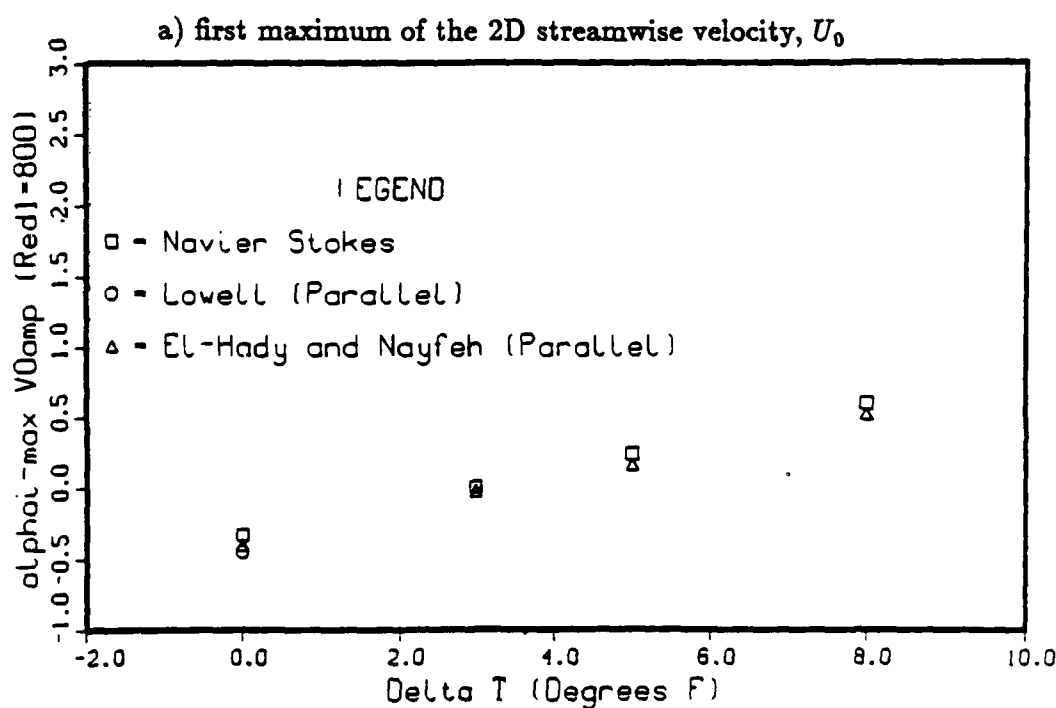
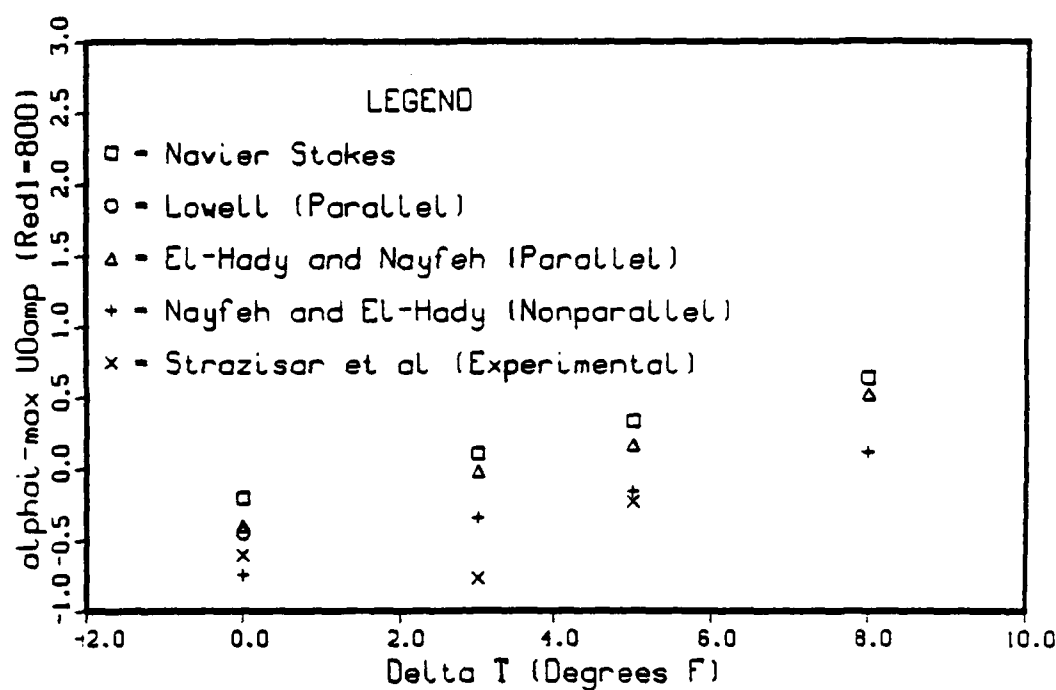
Figure 6.59 Comparison of amplification rates for nonuniform passive control ( $p = 1.0$ ) with theory and experiment,  $F = 1$





b) maximum of the 2D normal velocity,  $V_0$

Figure 6.60 Comparison of amplification rates for nonuniform passive control ( $p = -0.5$ ) with theory and experiment,  $F = 1.55$



b) maximum of the 2D normal velocity,  $V_0$

Figure 6.61 Comparison of amplification rates for nonuniform passive control ( $p = 1.0$ ) with theory and experiment,  $F = 1.55$

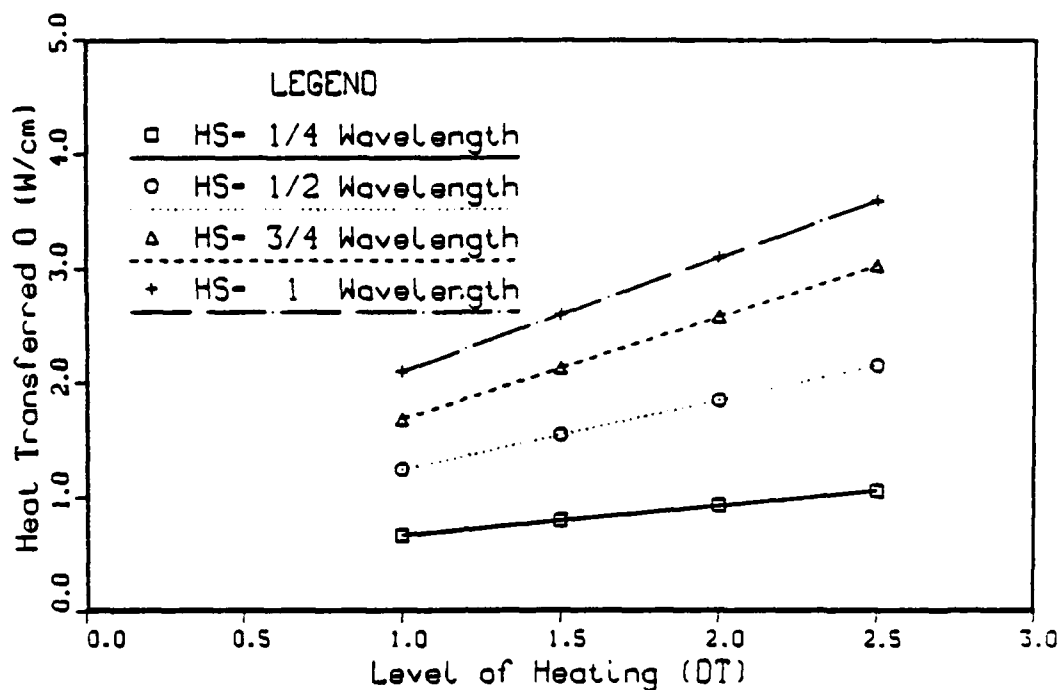


Figure 6.62 Comparison of heat transferred to heater strip for four different widths of heater strips

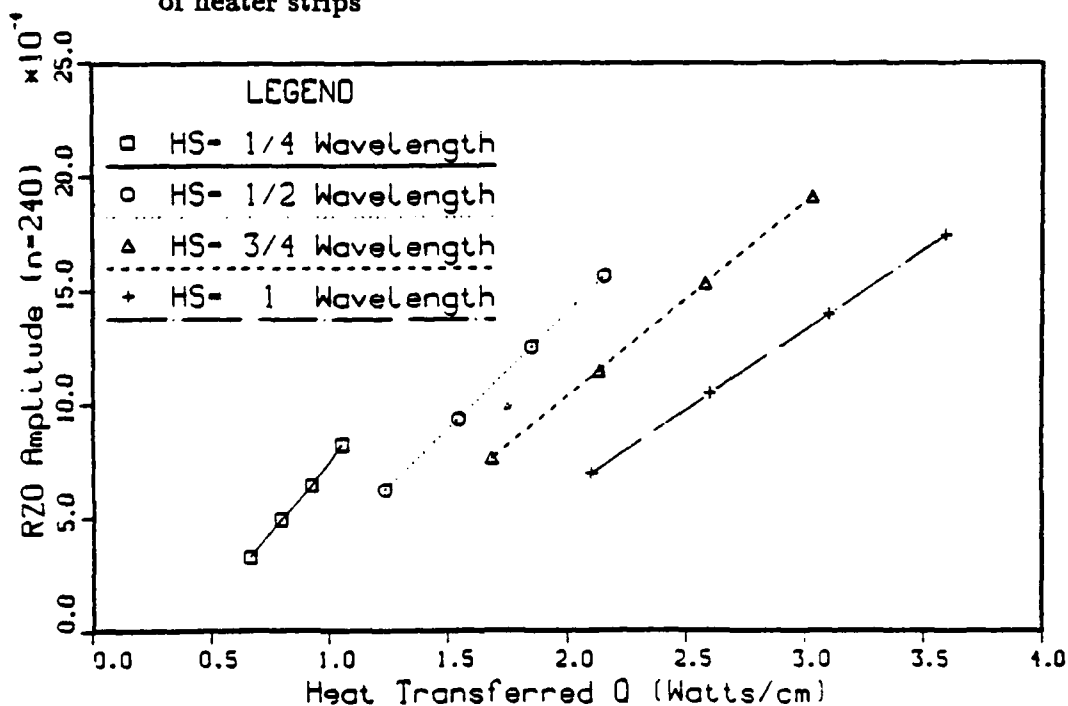


Figure 6.63 Comparison of spanwise wall vorticity amplitude  $\Omega_{z0}$  for different amounts of heat input and heater strip width

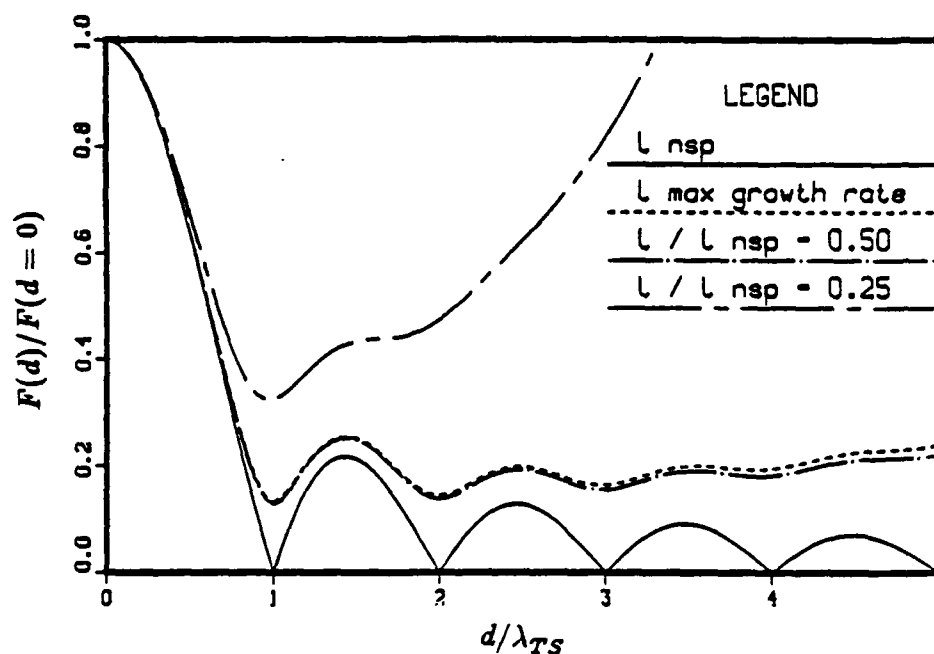
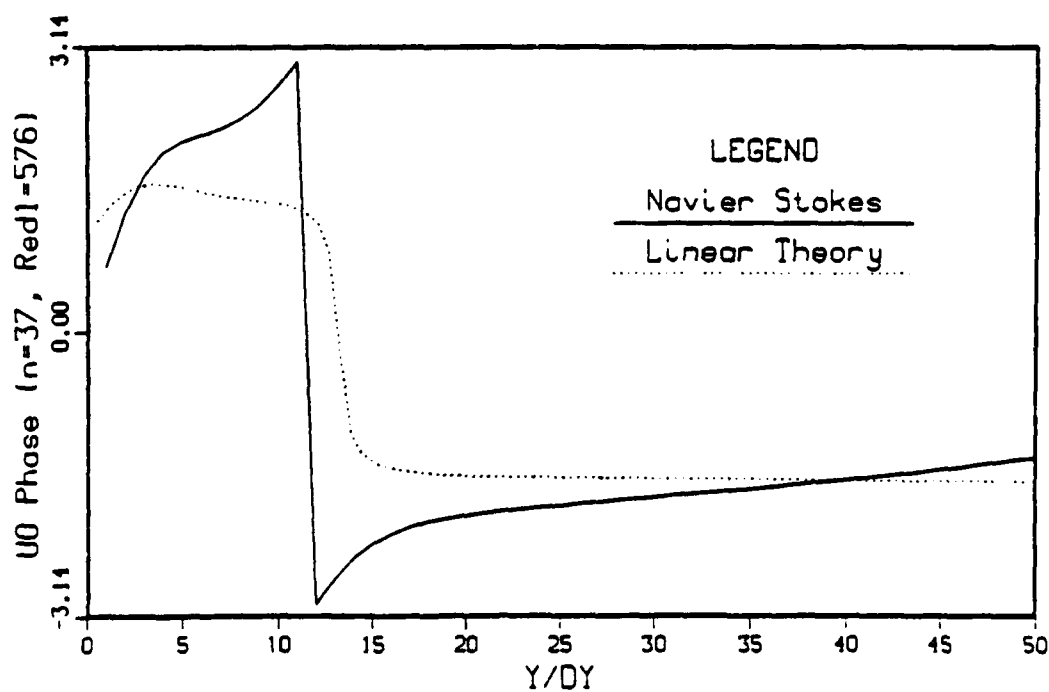
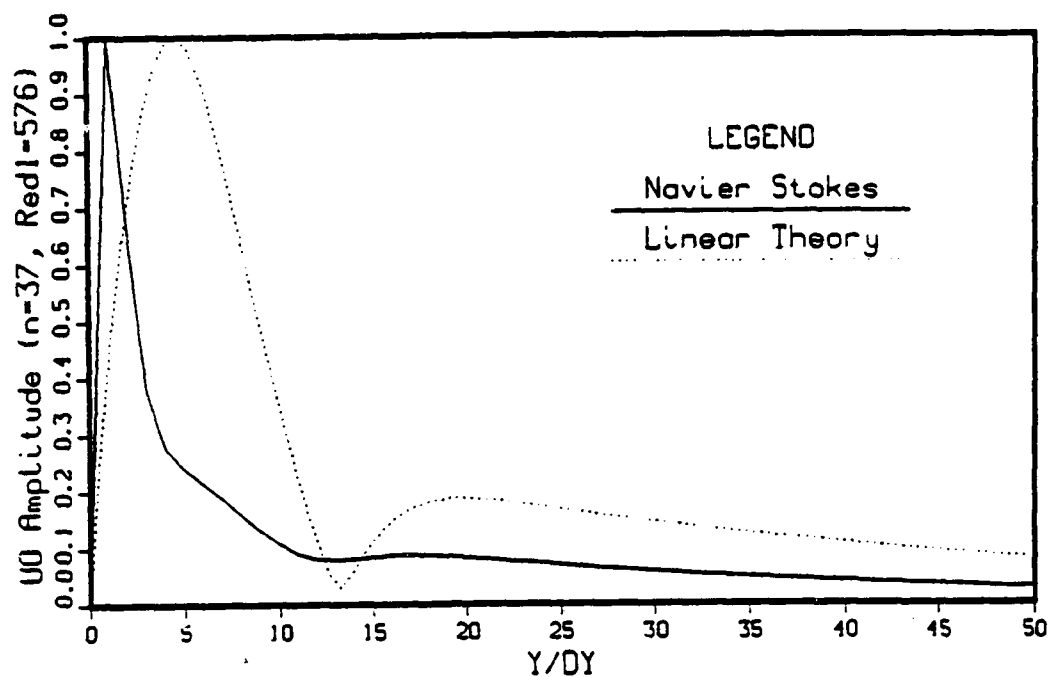
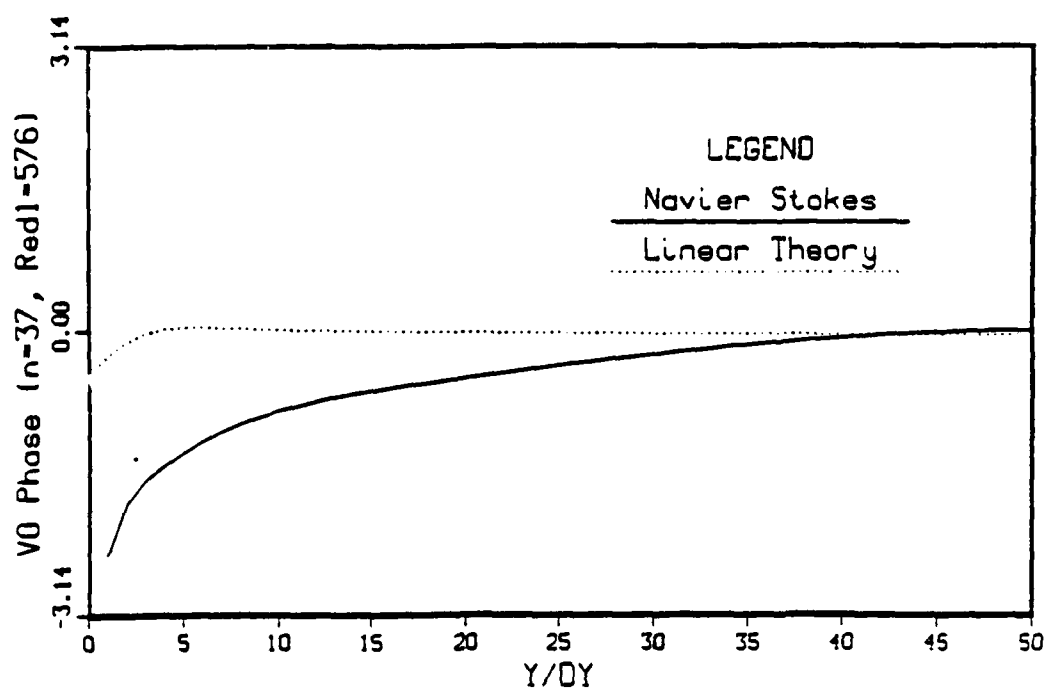
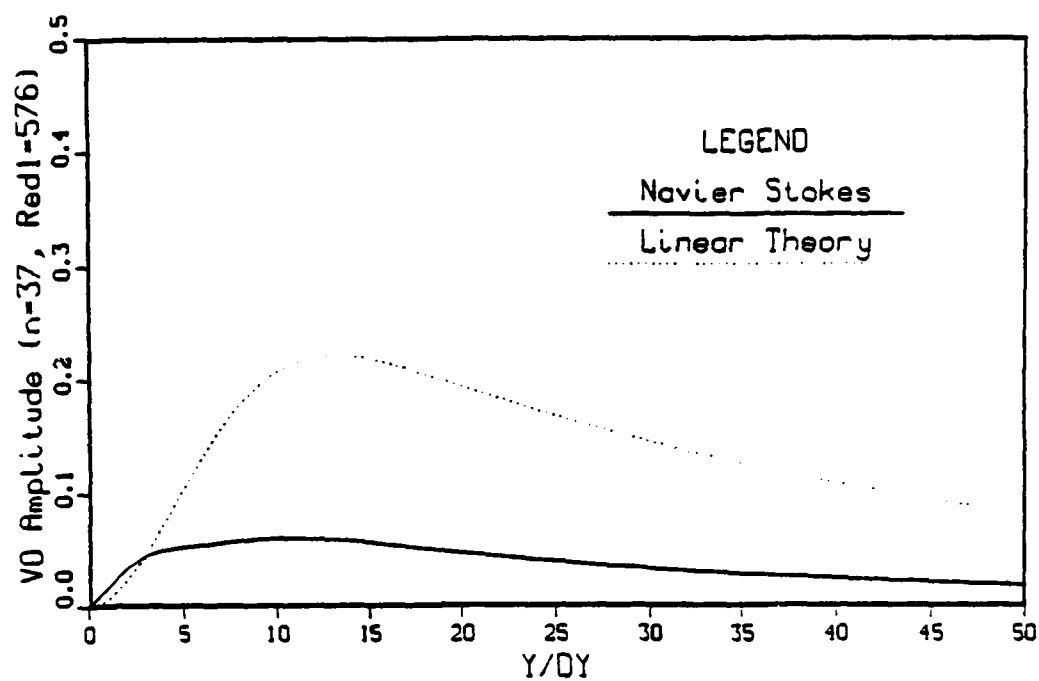


Figure 6.64 Comparison of receptivity at a suction surface hard wall junction from theoretical analysis of Heinrich, Choudari, and Kerschen (1988).  $F(d)$  is the receptivity coefficient defined as the ratio between the Tollmien-Schlichting amplitude and the input amplitude and  $d$  is the width of the suction blowing strip. The distance from the leading edge is defined by  $l$ , the location of the neutral stability point is defined by  $l_{nsp}$ , and the location of maximum growth is defined by  $l_{max \text{ growth rate}}$ .



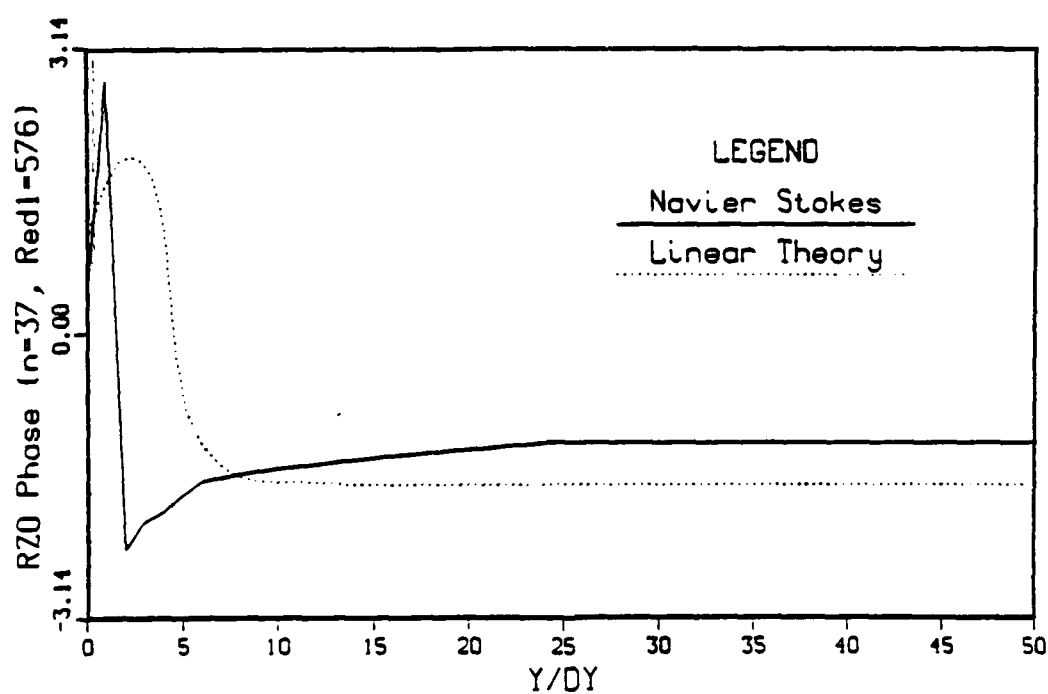
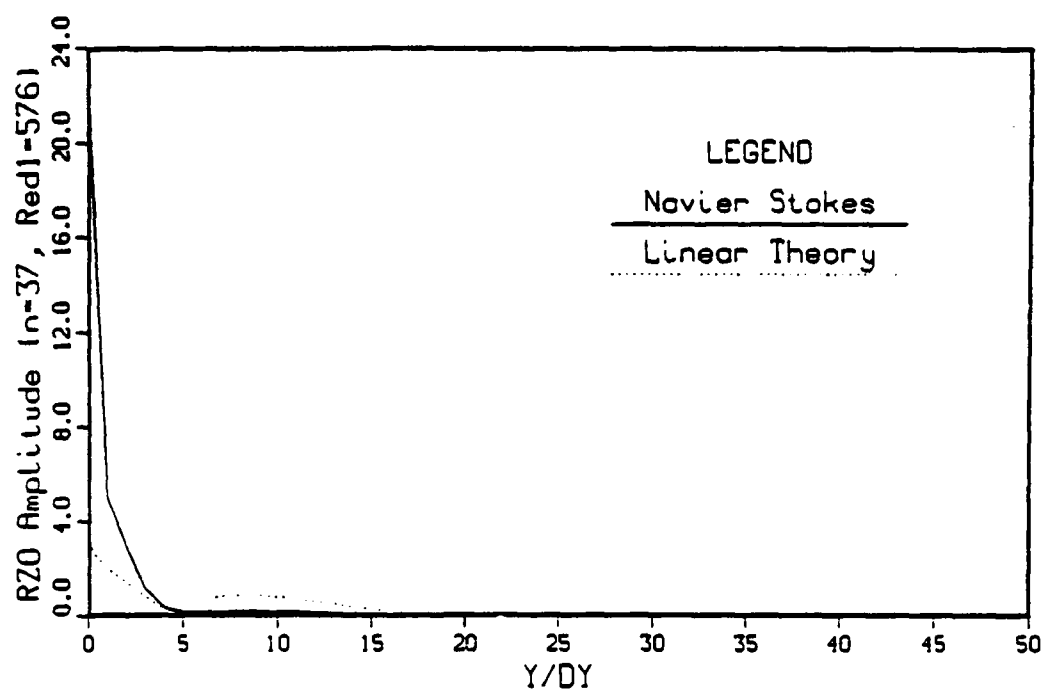
a) 2D streamwise velocity,  $U_0$

Figure 6.65 Amplitude and phase comparison with linear stability theory over heater strip,  $Re_{\delta_1} = 576$ ,  $F = 1$

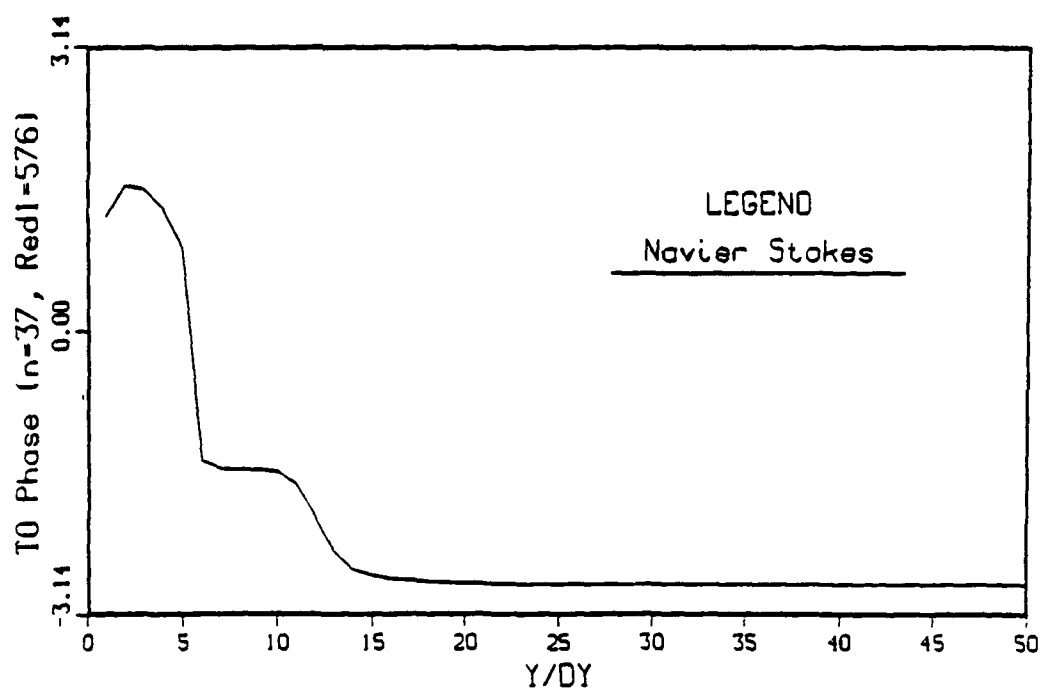
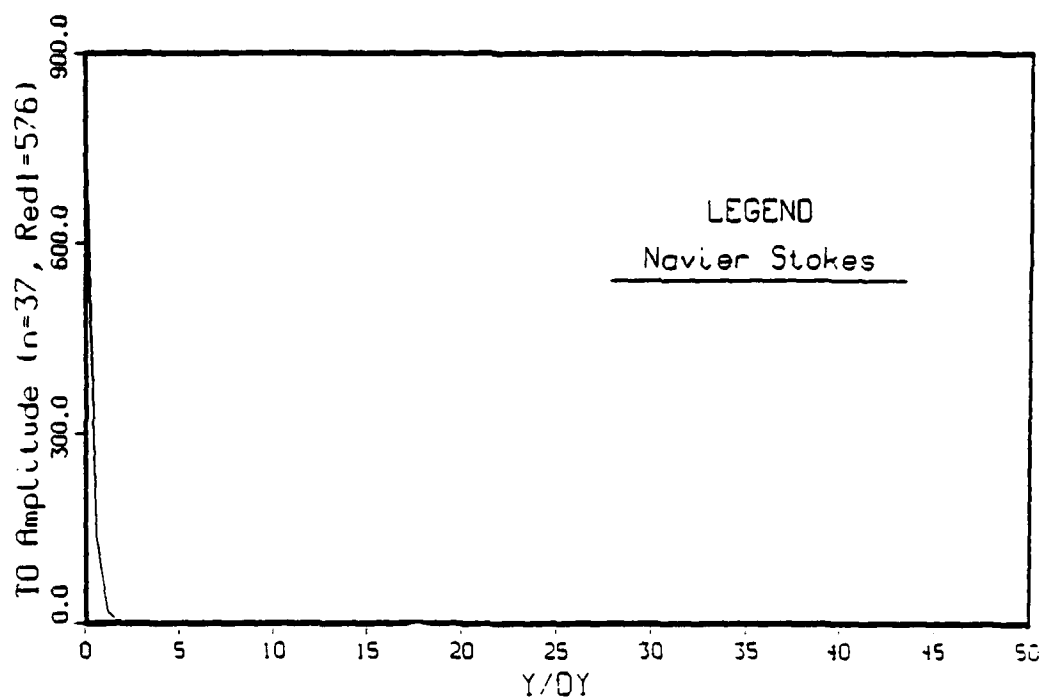


b) 2D normal velocity,  $V_0$

Figure 6.65 continued



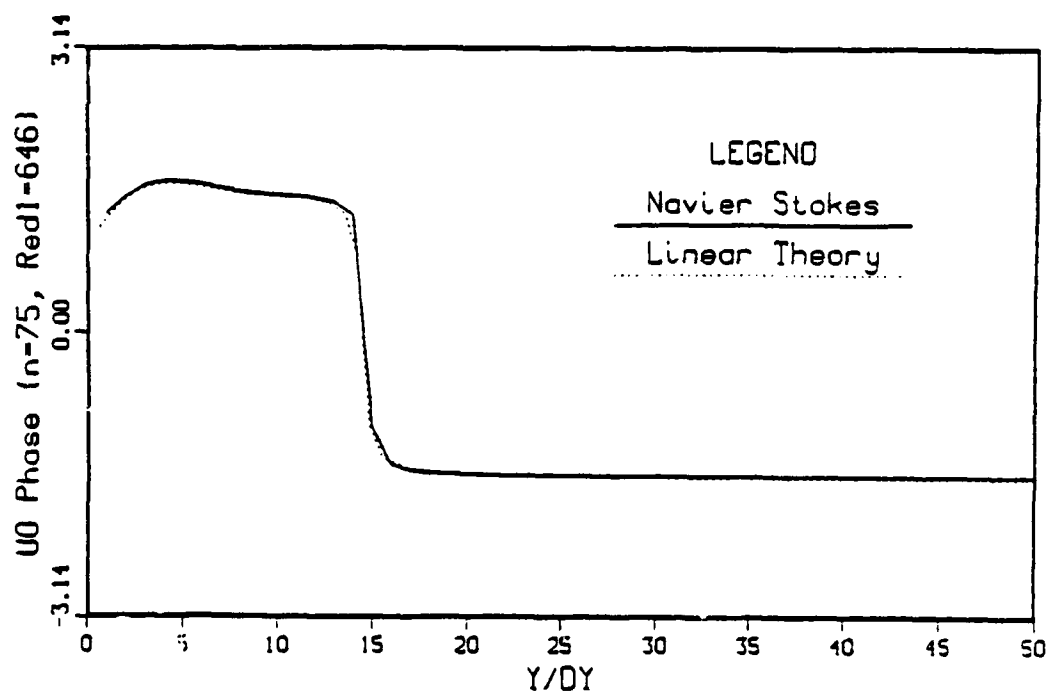
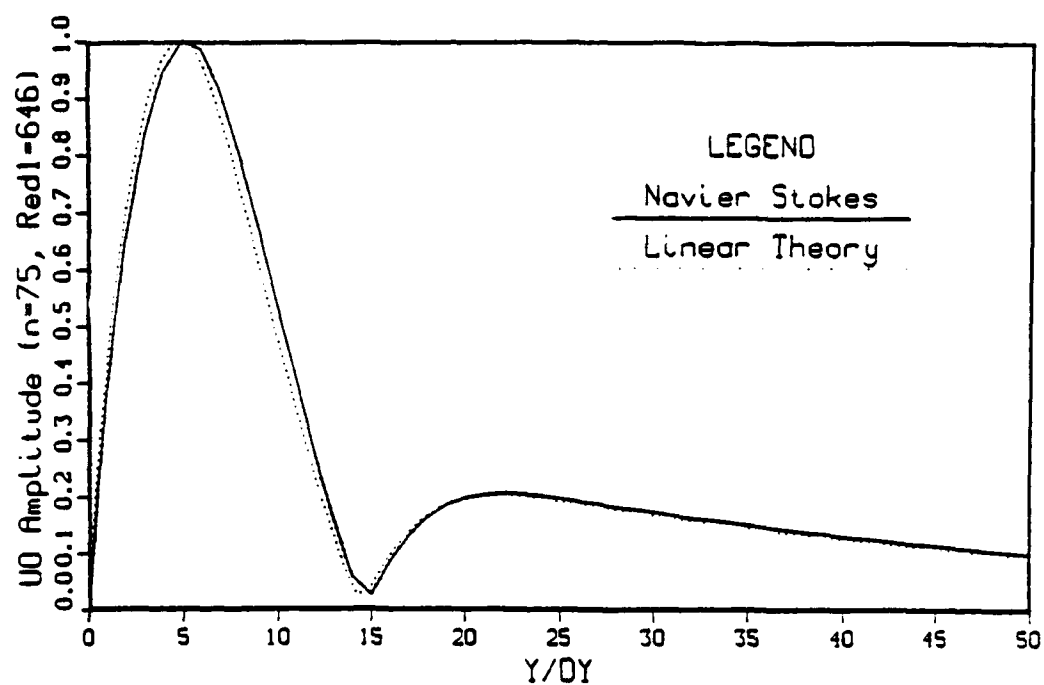
c) 2D spanwise vorticity,  $\Omega_{z0}$   
Figure 6.65 continued



d) 2D temperature,  $\Theta_0$

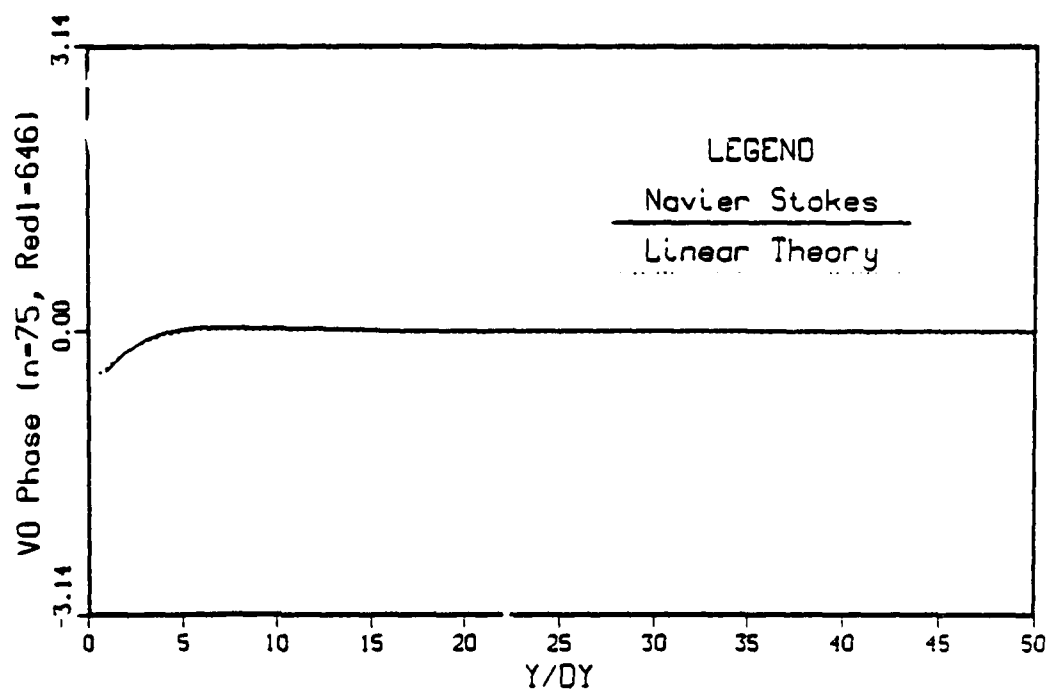
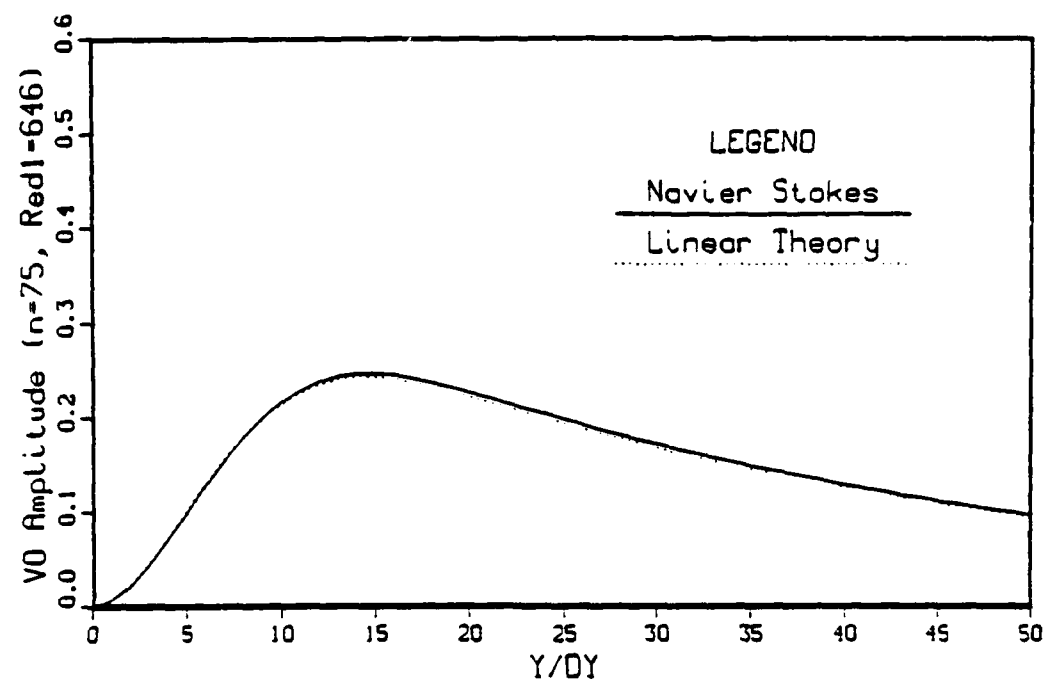
Figure 6.65 continued





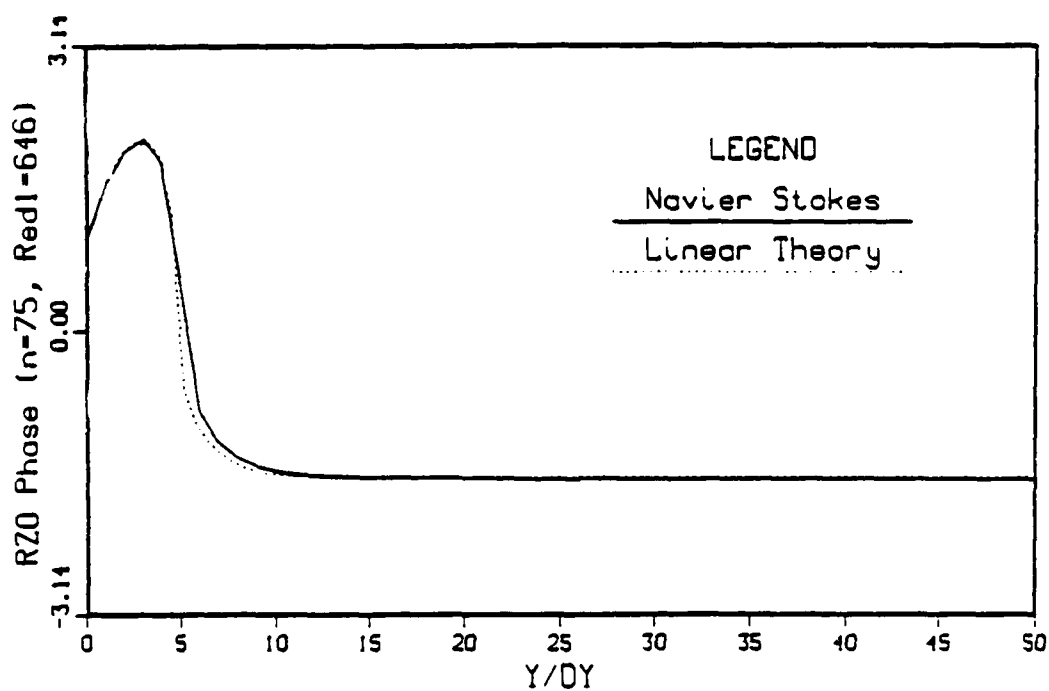
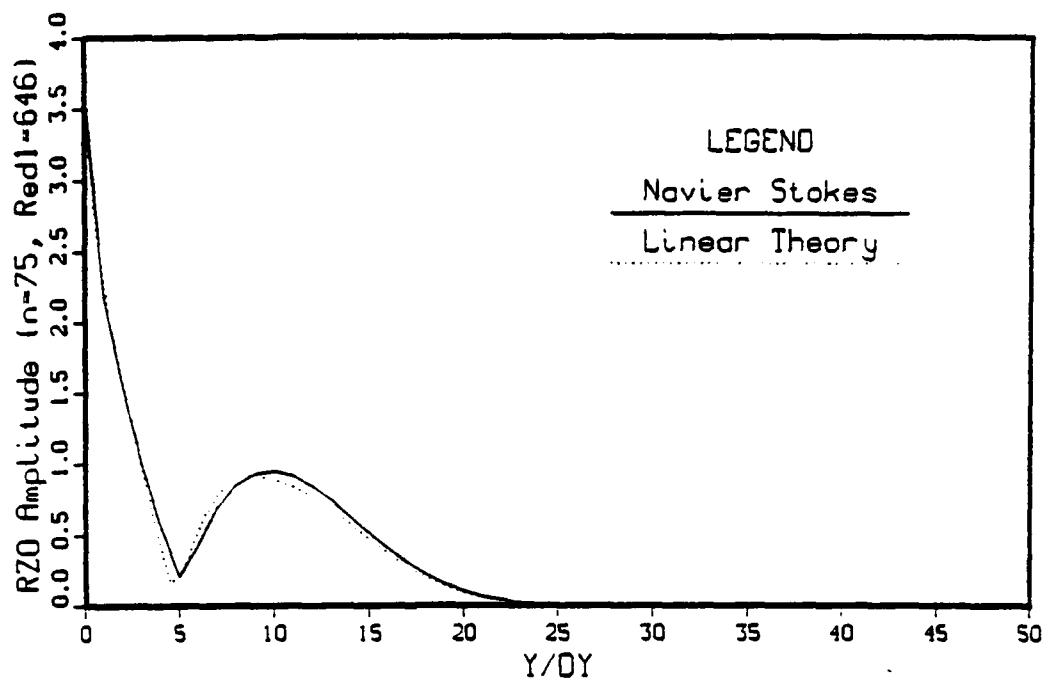
a) 2D streamwise velocity,  $U_0$

Figure 6.66 Amplitude and phase comparison with linear stability theory near heater strip,  $Re\delta_1 = 646$ ,  $F = 1$



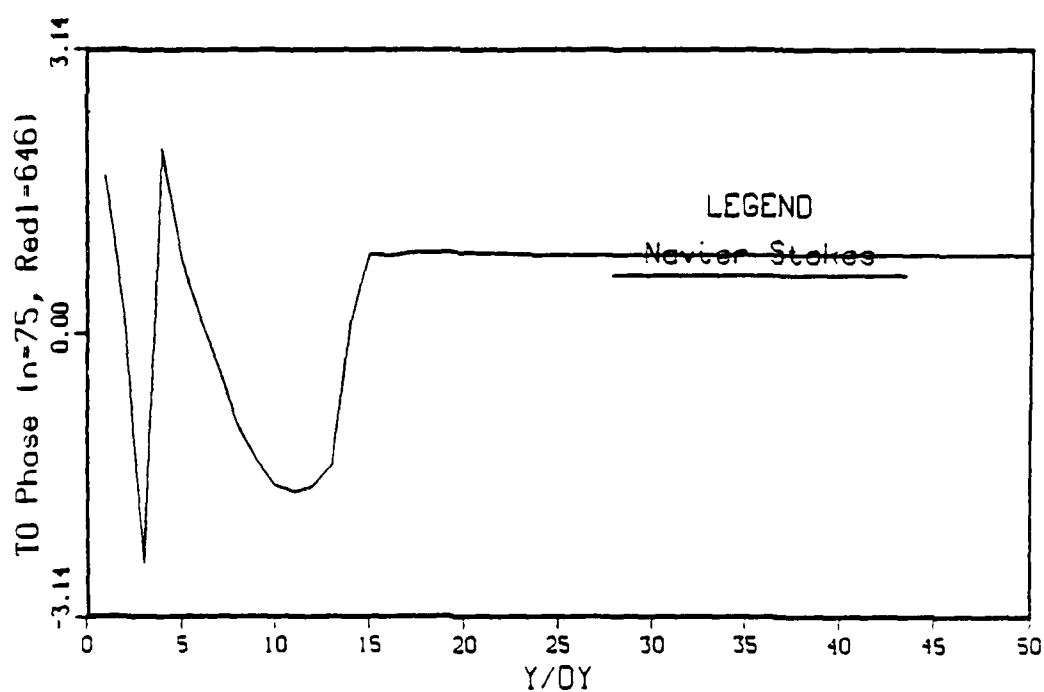
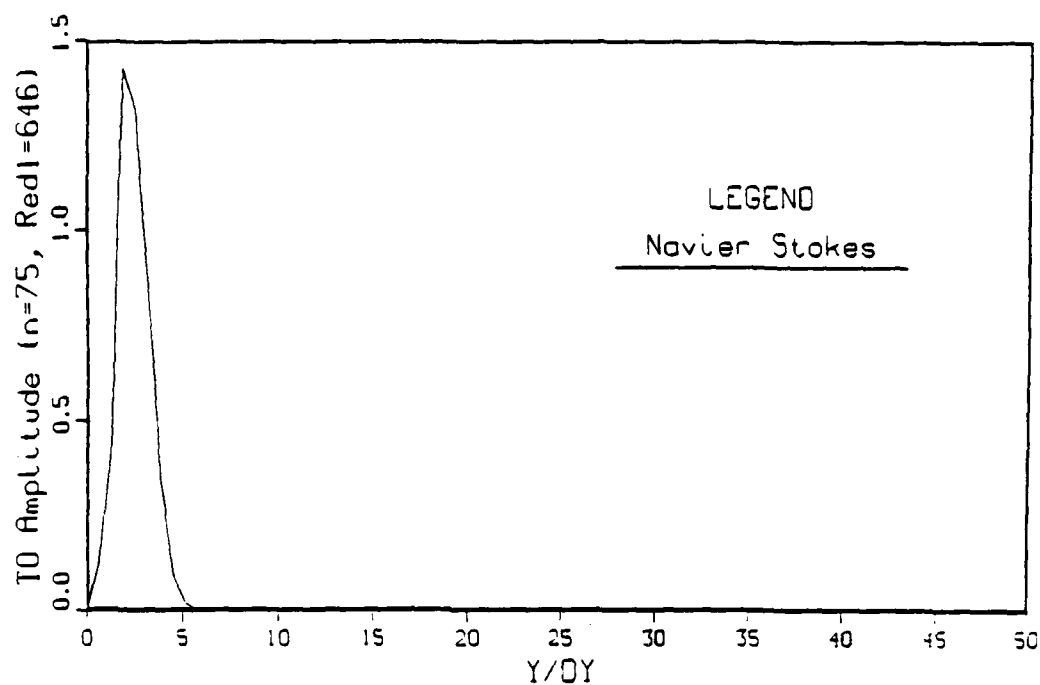
b) 2D normal velocity,  $V_0$

Figure 6.66 continued



c) 2D spanwise vorticity,  $\Omega_{z0}$

Figure 6.66 continued



d) 2D temperature,  $\Theta_0$

Figure 6.66 continued

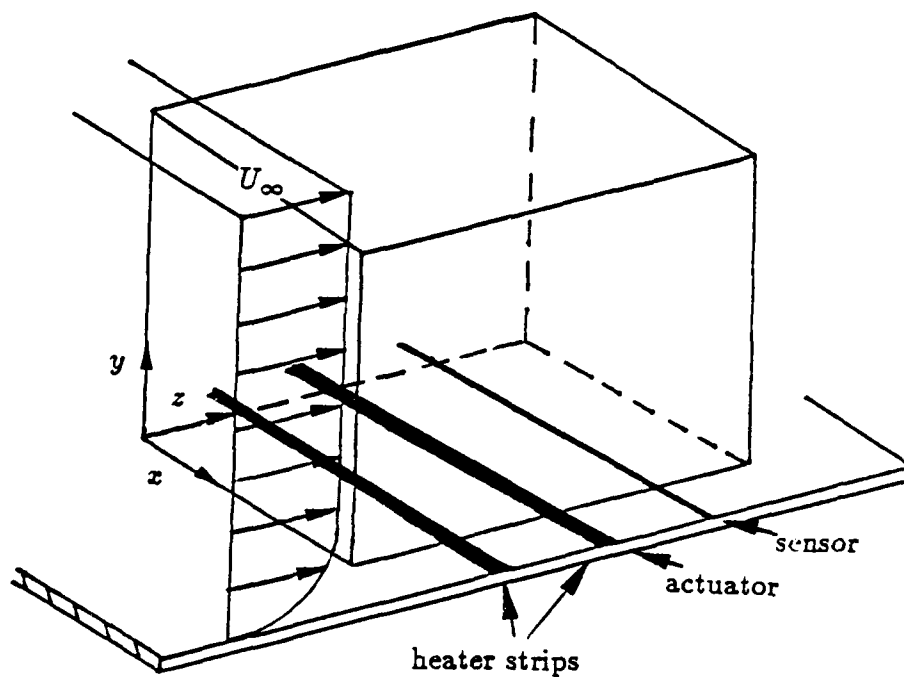


Figure 6.67 Schematic of surface heater strip arrangement for active control simulations

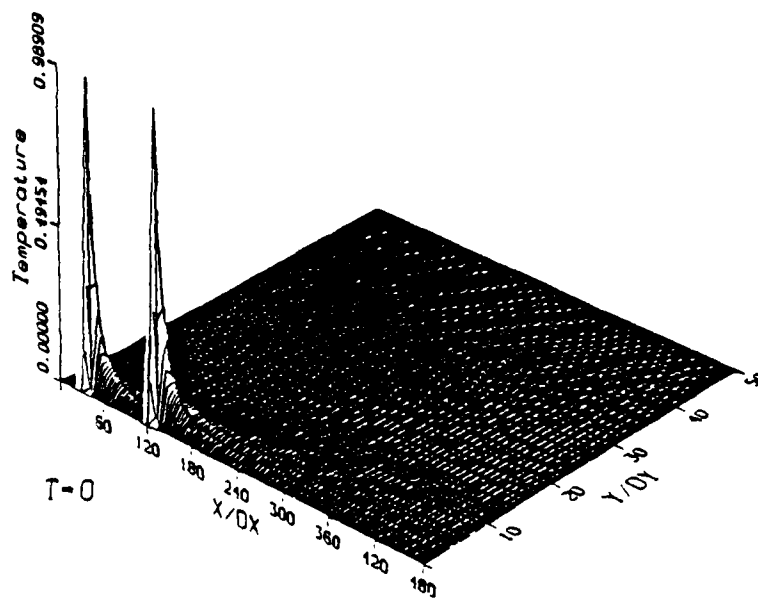
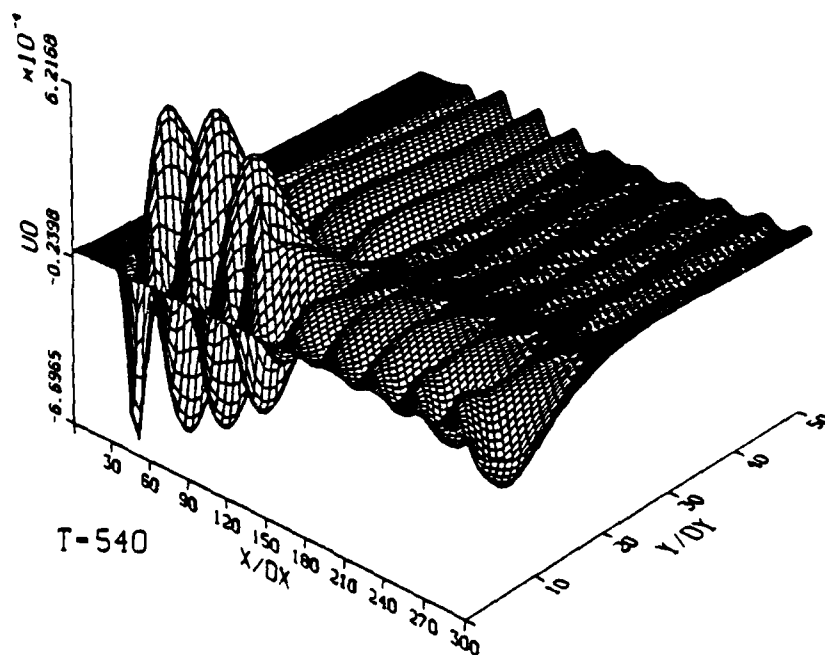
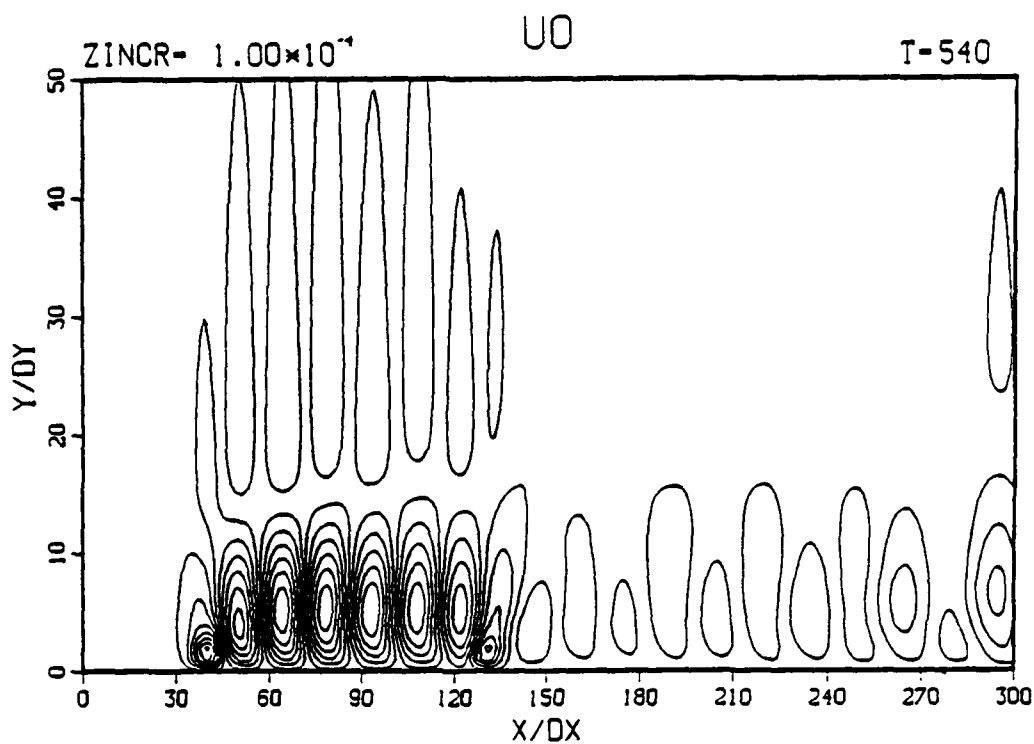
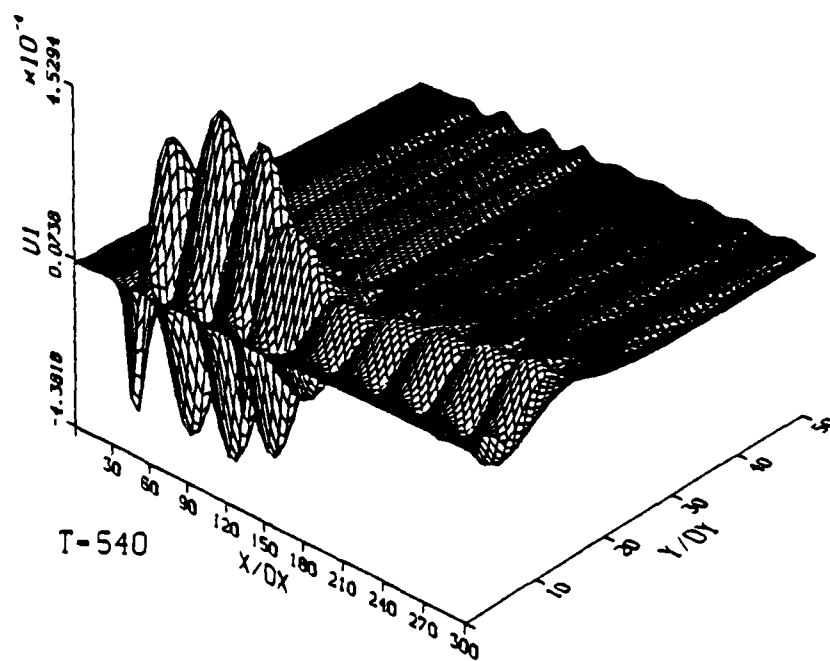
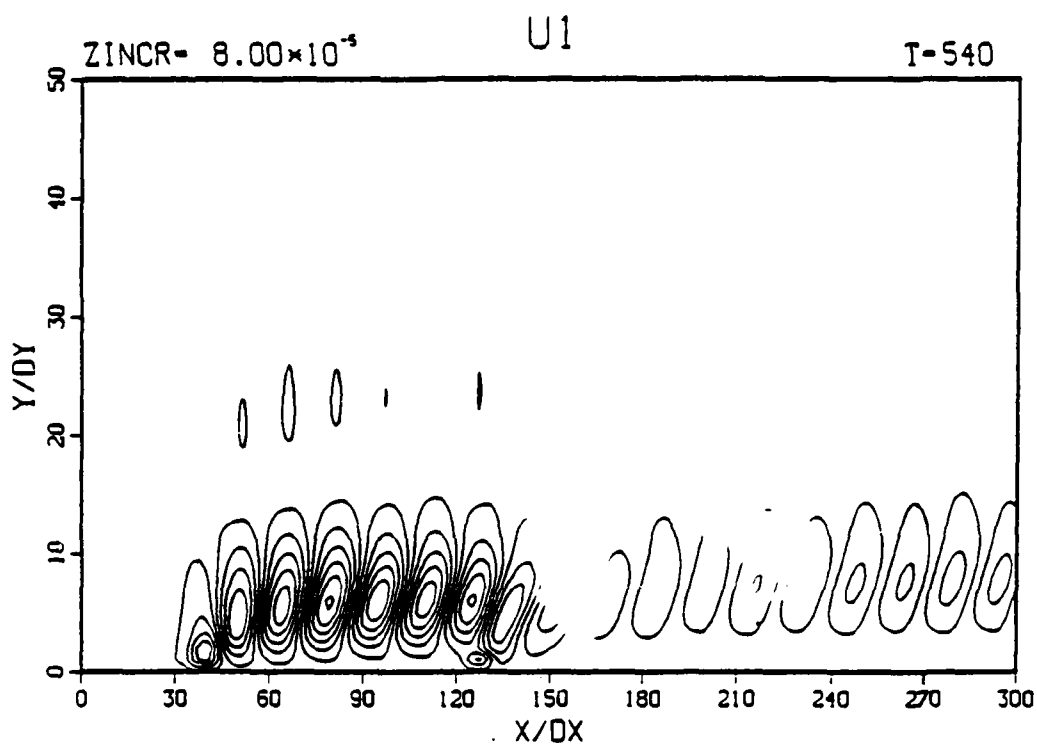


Figure 6.68 Undisturbed temperature distribution for active control simulations



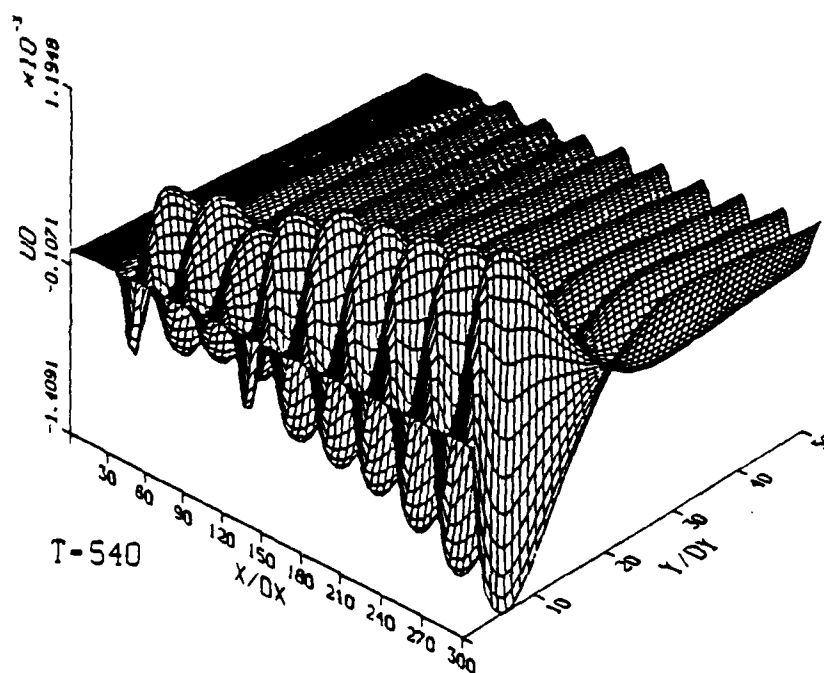
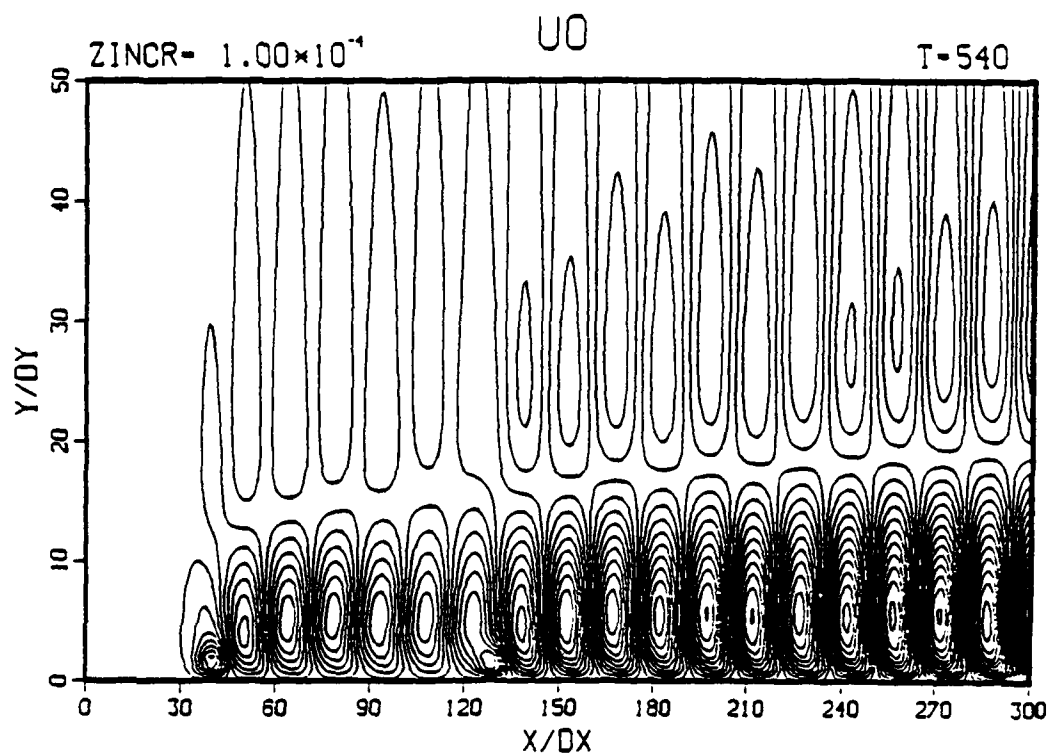
a) 2D streamwise velocity,  $U_0$

Figure 6.69 Disturbed flow with out of phase active control applied,  $F = 1$



b) 3D streamwise velocity,  $U_1$

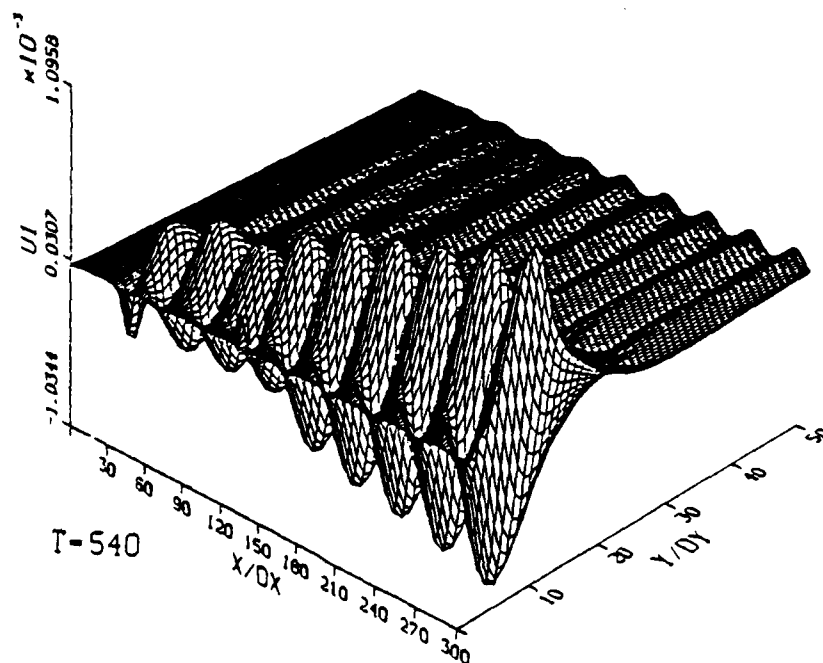
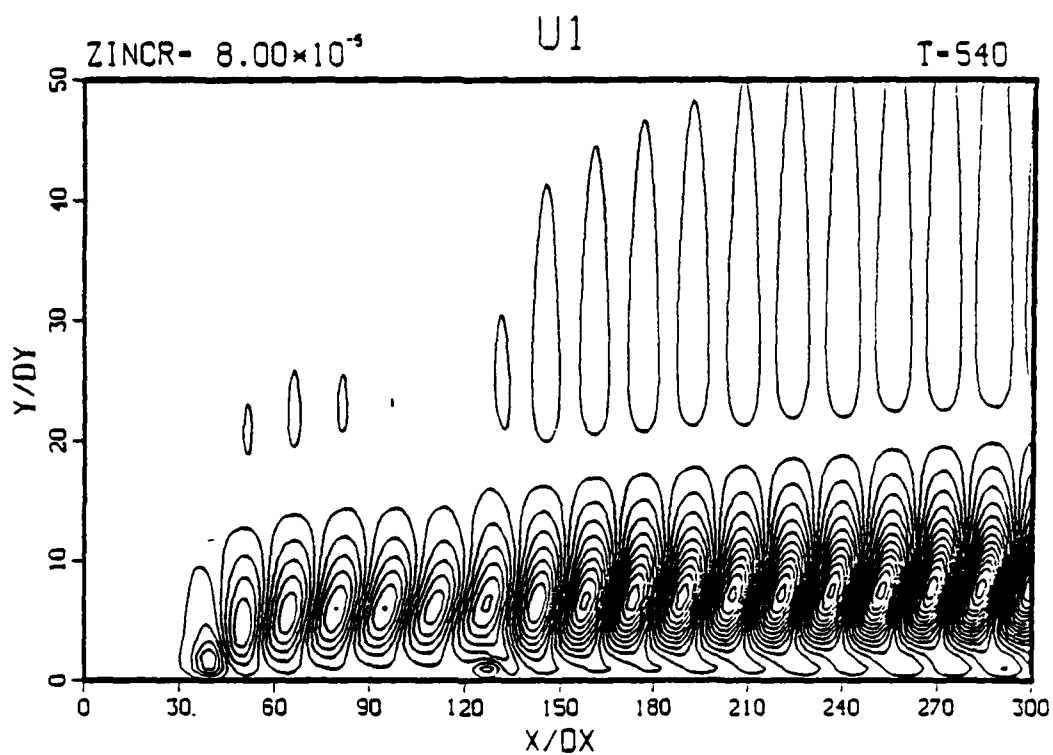
Figure 6.69 continued



a) 2D streamwise velocity,  $U_0$

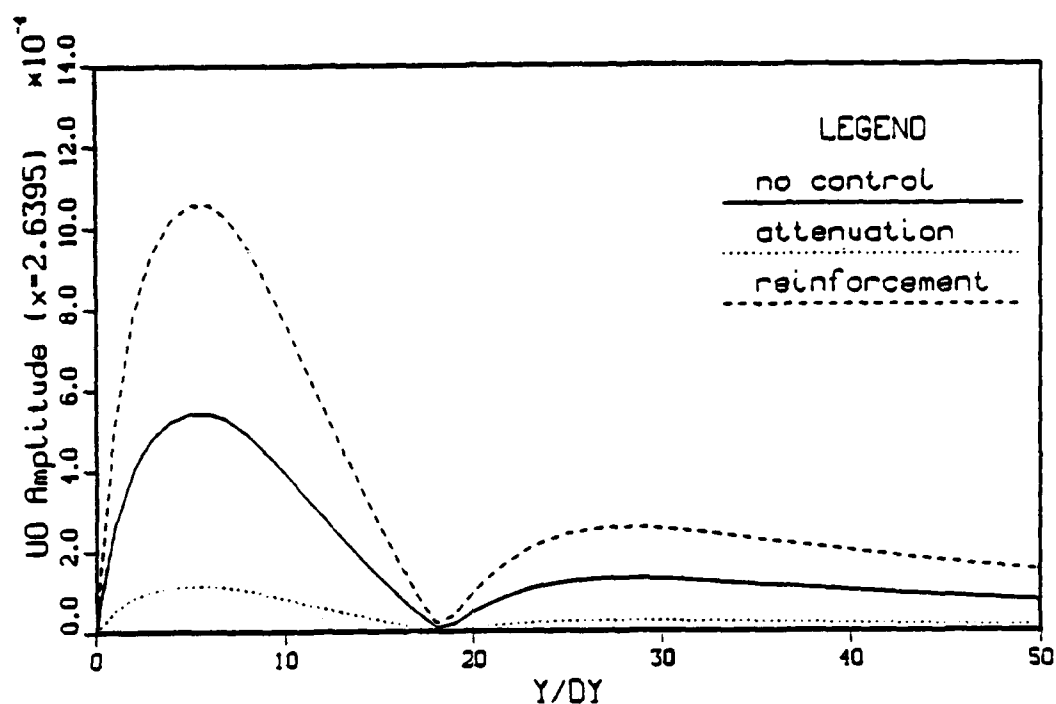
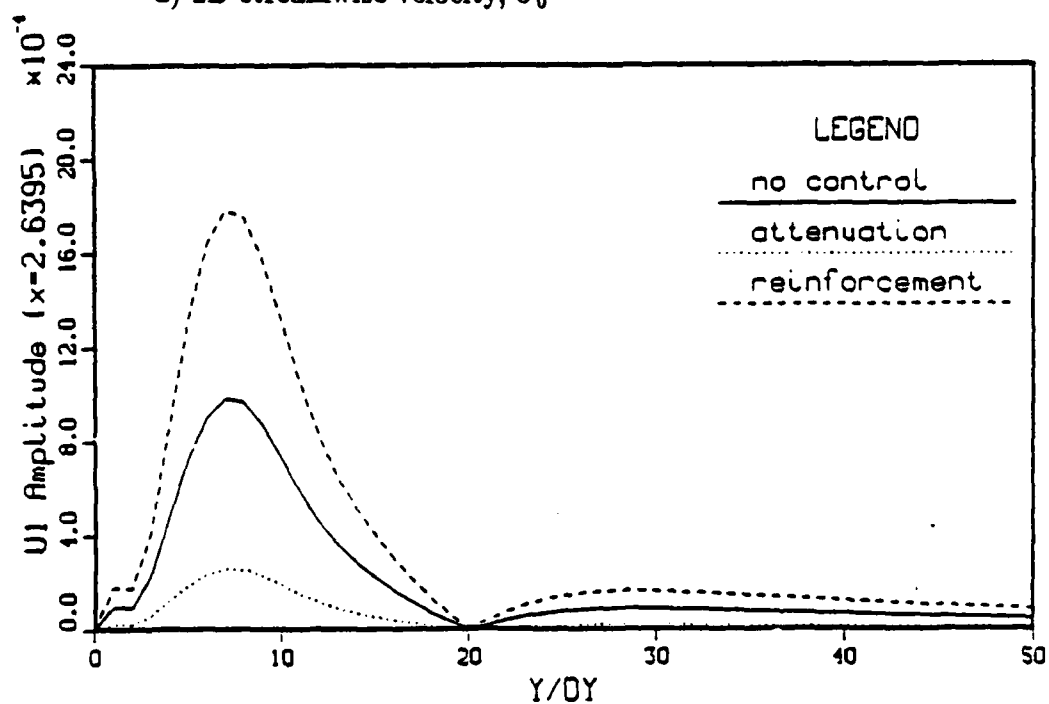
Figure 6.70 Disturbed flow with in phase active control applied,  $F = 1$

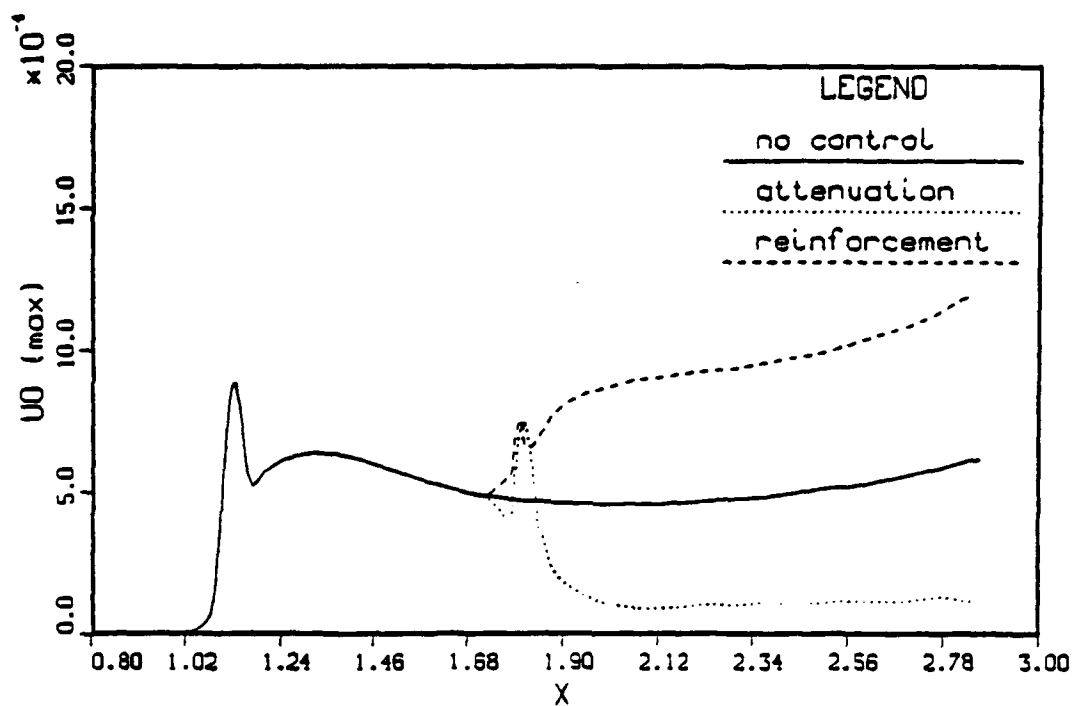
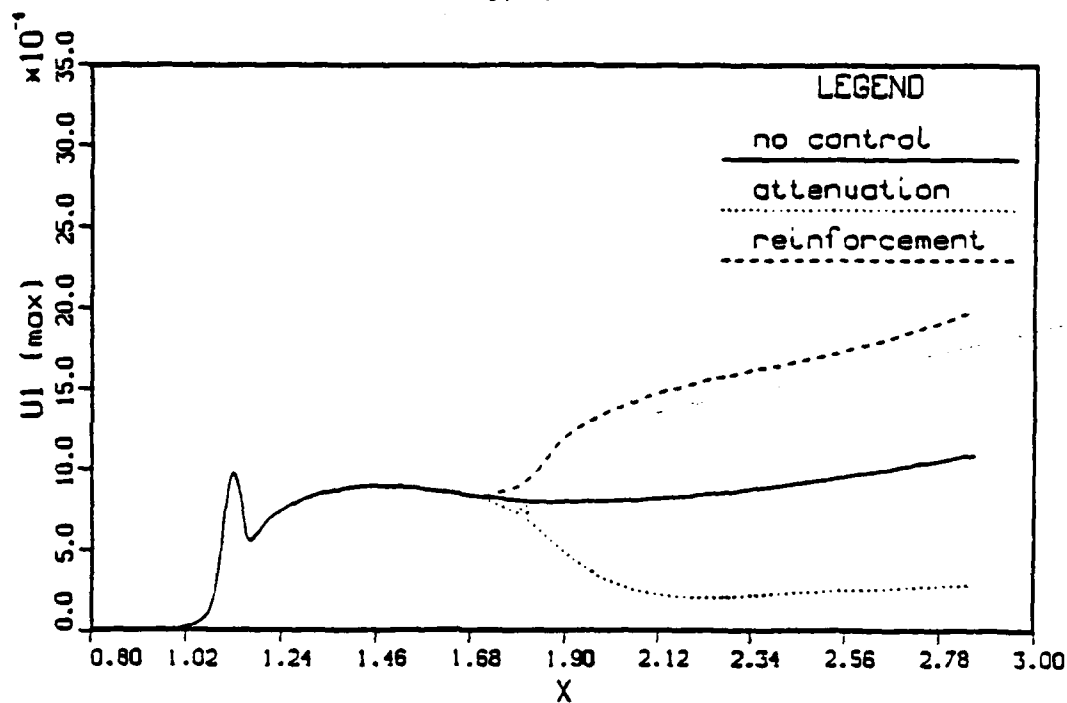


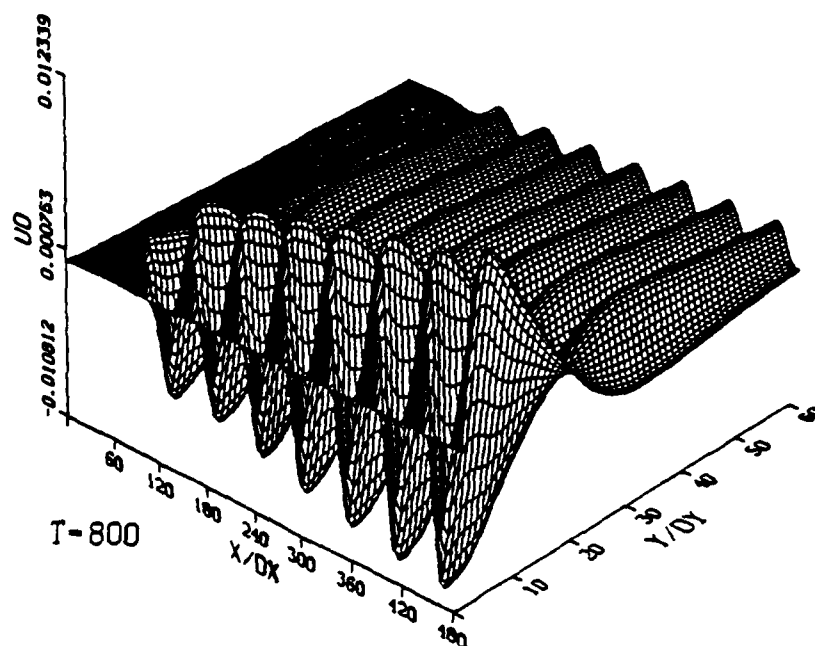


b) 3D streamwise velocity,  $U_1$

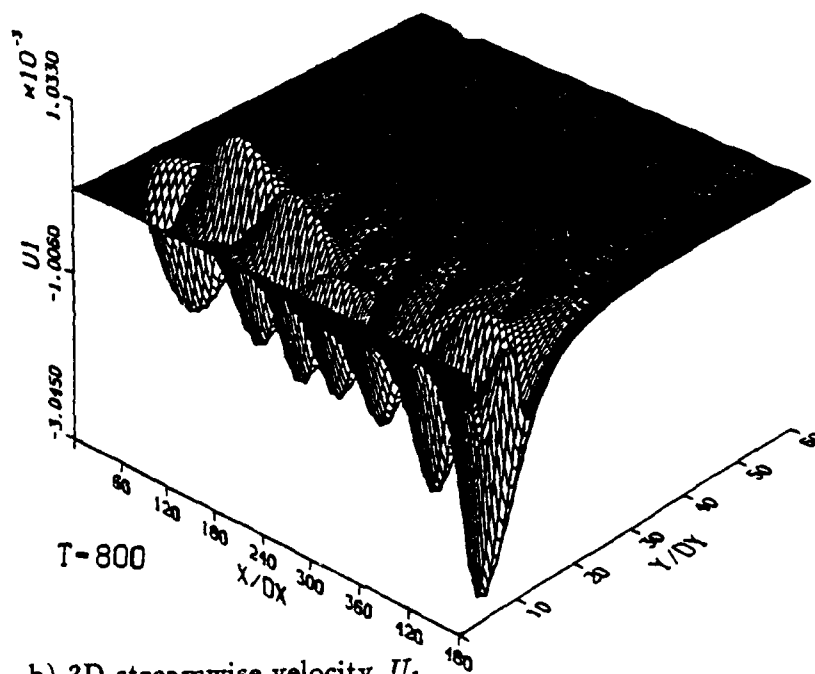
Figure 6.70 continued

a) 2D streamwise velocity,  $U_0$ b) 3D streamwise velocity,  $U_1$ Figure 6.71 Comparison of amplitude profiles with active control applied,  $F = 1$

a) 2D streamwise velocity,  $U_0$ b) 3D streamwise velocity,  $U_1$ Figure 6.72 Influence of active control on the amplitude growth,  $F = 1$

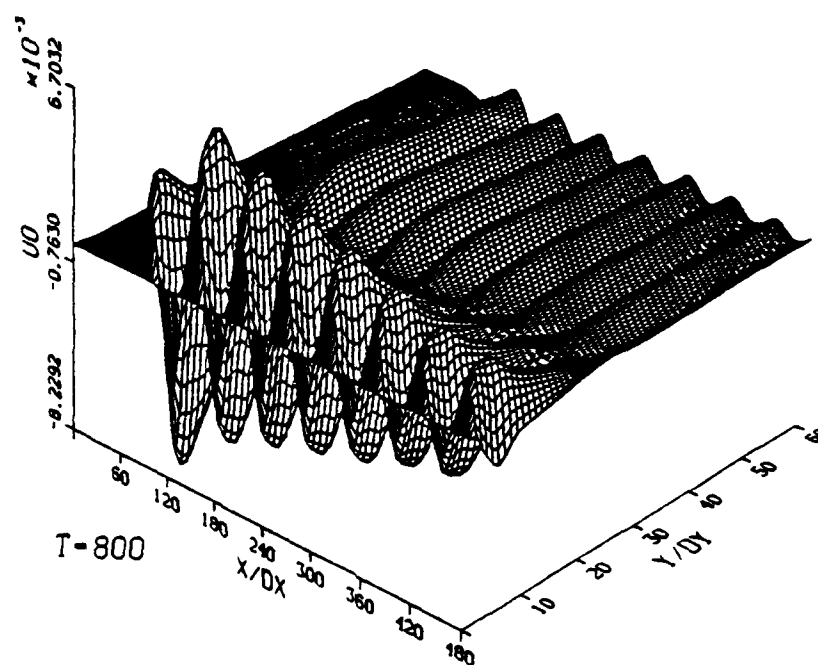


a) 2D streamwise velocity,  $U_0$

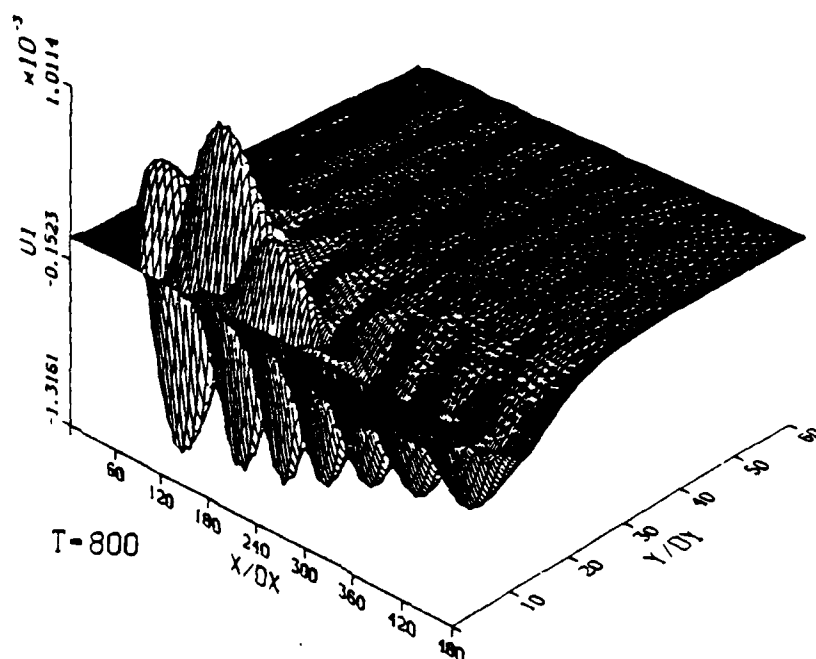


b) 3D streamwise velocity,  $U_1$

Figure 6.73 Uncontrolled disturbed flow for fundamental breakdown,  $F_{2D} = 0.588$ ,  $F_{3D} = 0.588$



a) 2D streamwise velocity,  $U_0$



b) 3D streamwise velocity,  $U_1$

Figure 6.74 Disturbed flow for fundamental breakdown with  $\Delta \bar{T} = 15^\circ F$  control applied,  $F_{2D} = 0.588$ ,  $F_{3D} = 0.588$

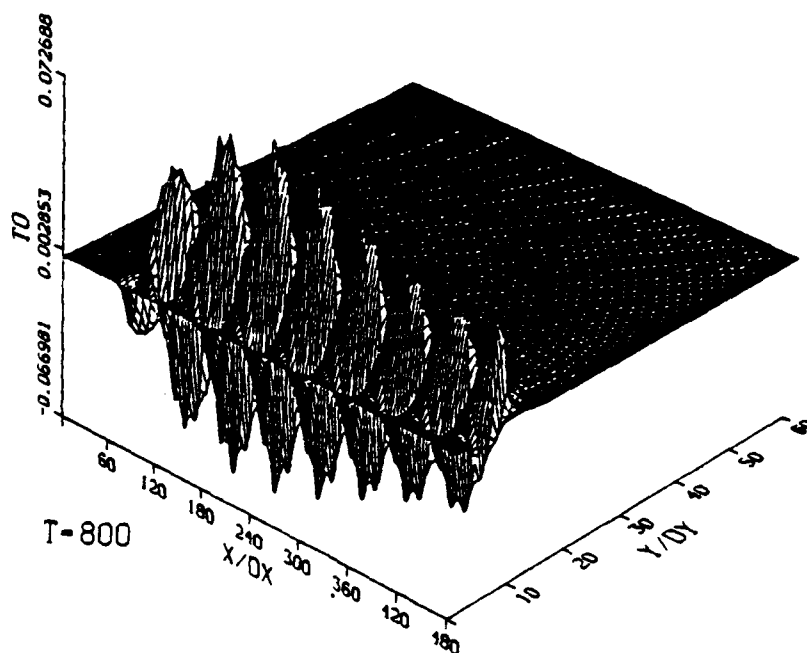
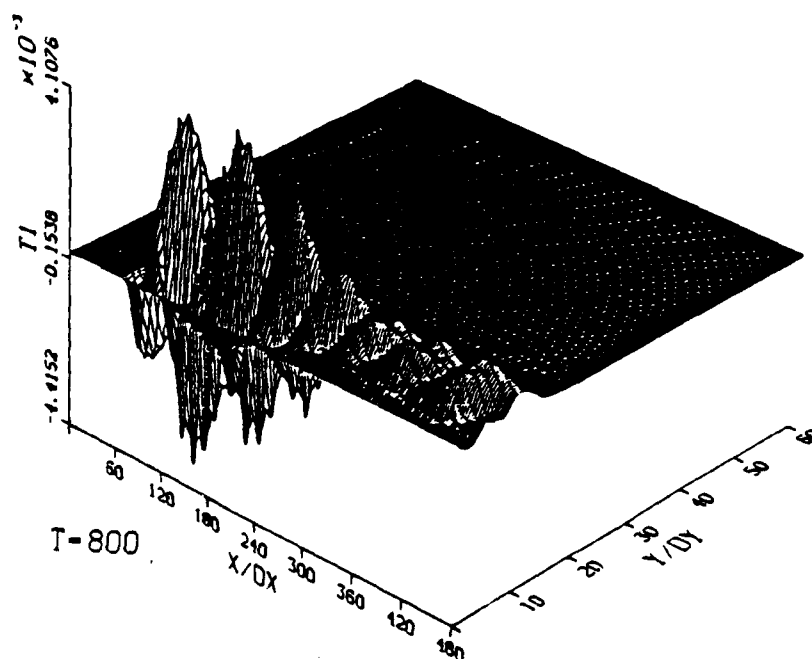
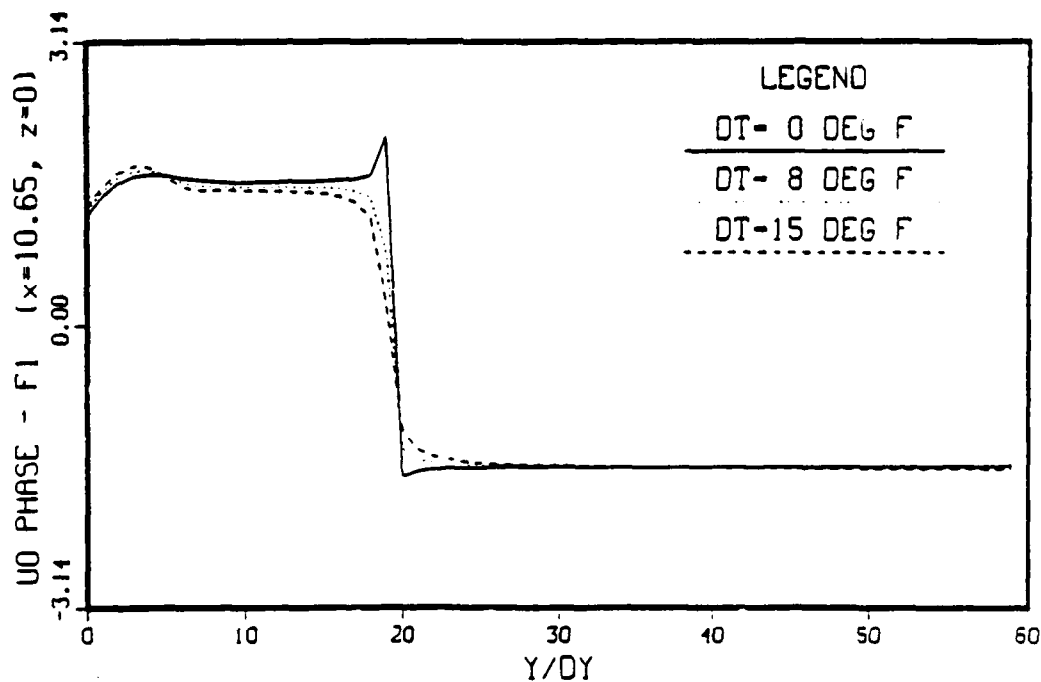
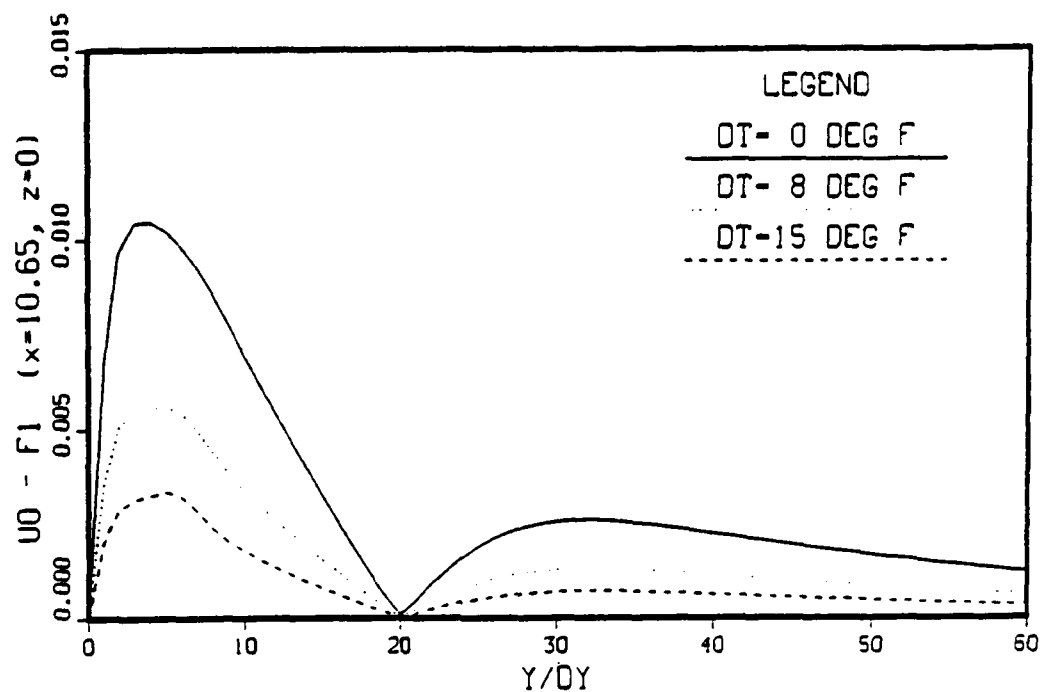
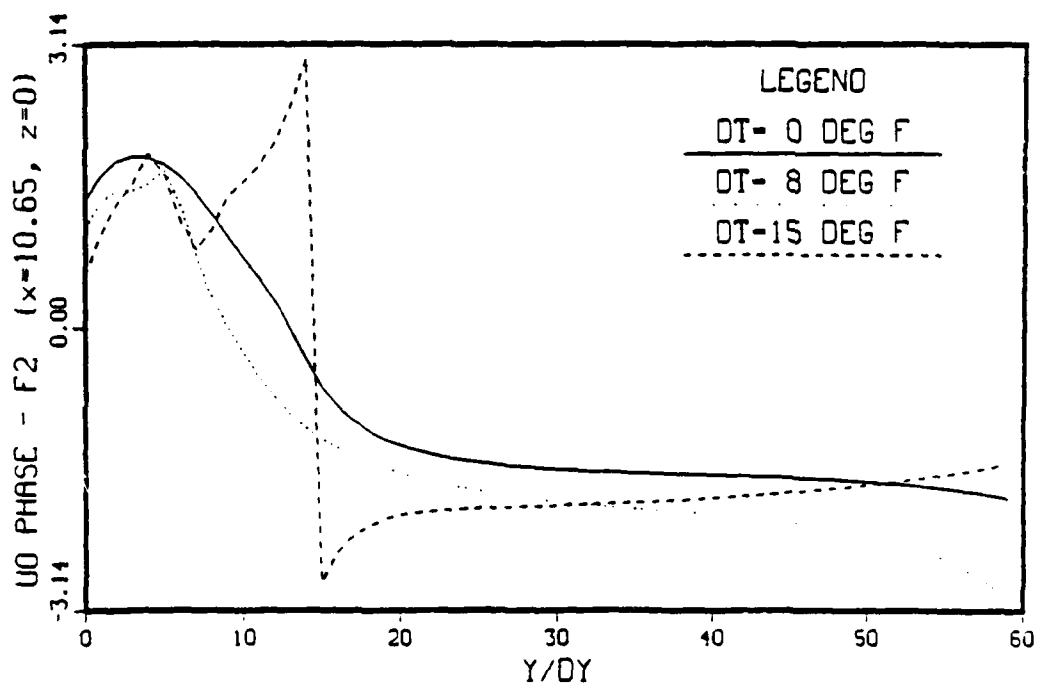
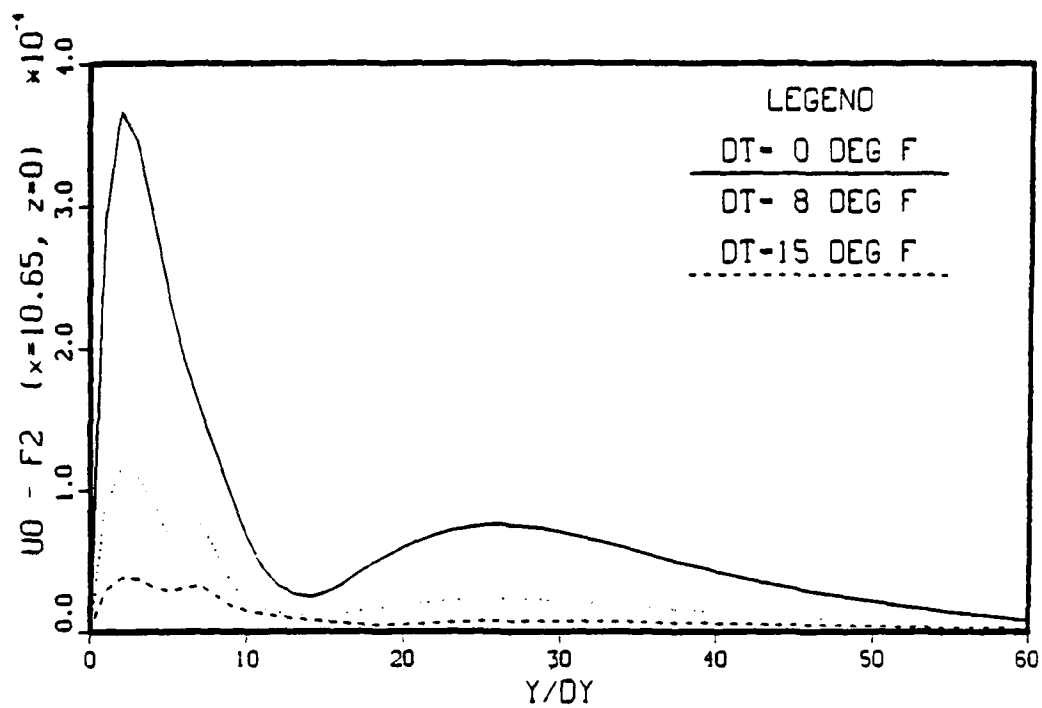
c) 2D temperature,  $\Theta_0$ d) 3D temperature,  $\Theta_1$ 

Figure 6.74 continued



a) 2D streamwise velocity,  $U_0, F_{2D}$

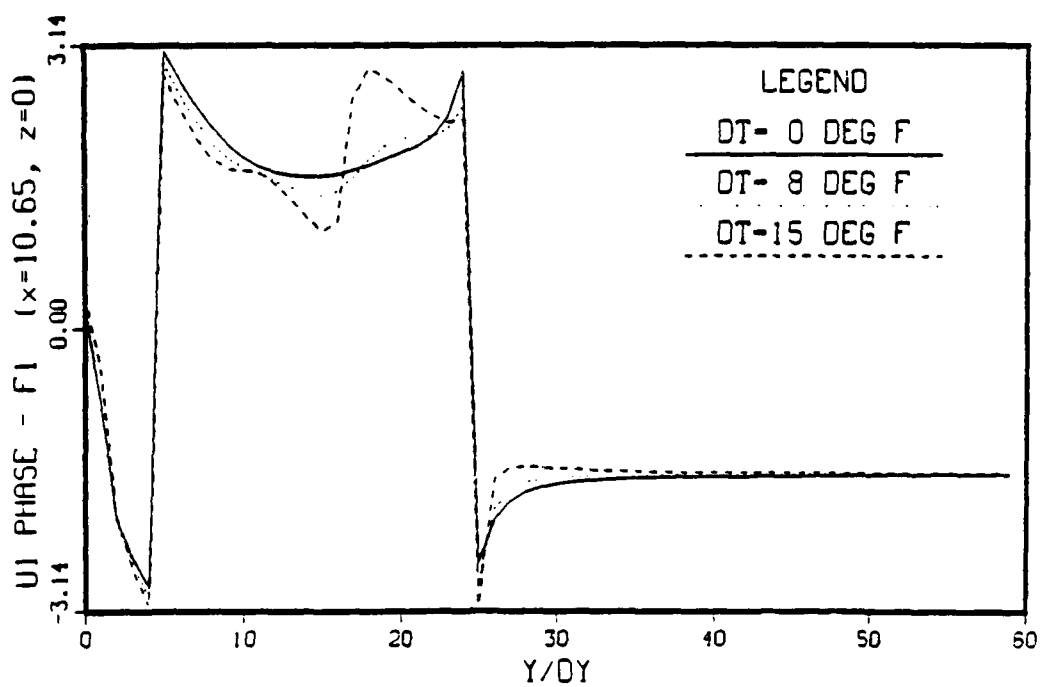
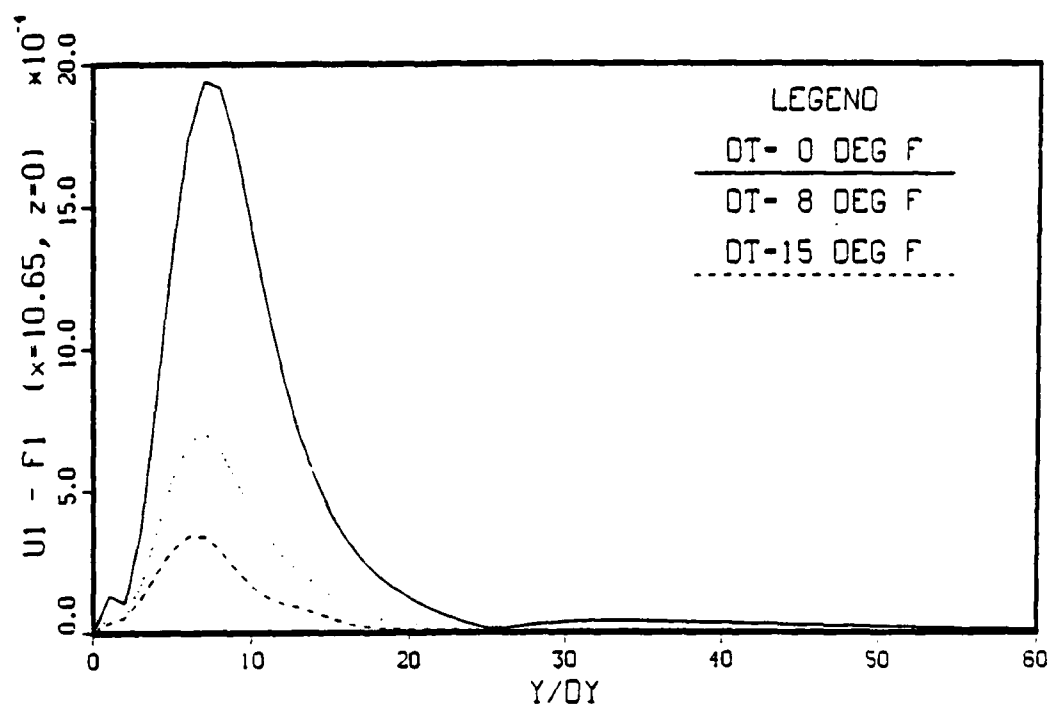
Figure 6.75 Amplitude and phase comparison at  $x = 10.65$  for fundamental breakdown with uniform passive control applied



b) 2D streamwise velocity,  $U_0$ ,  $2 F_{2D}$

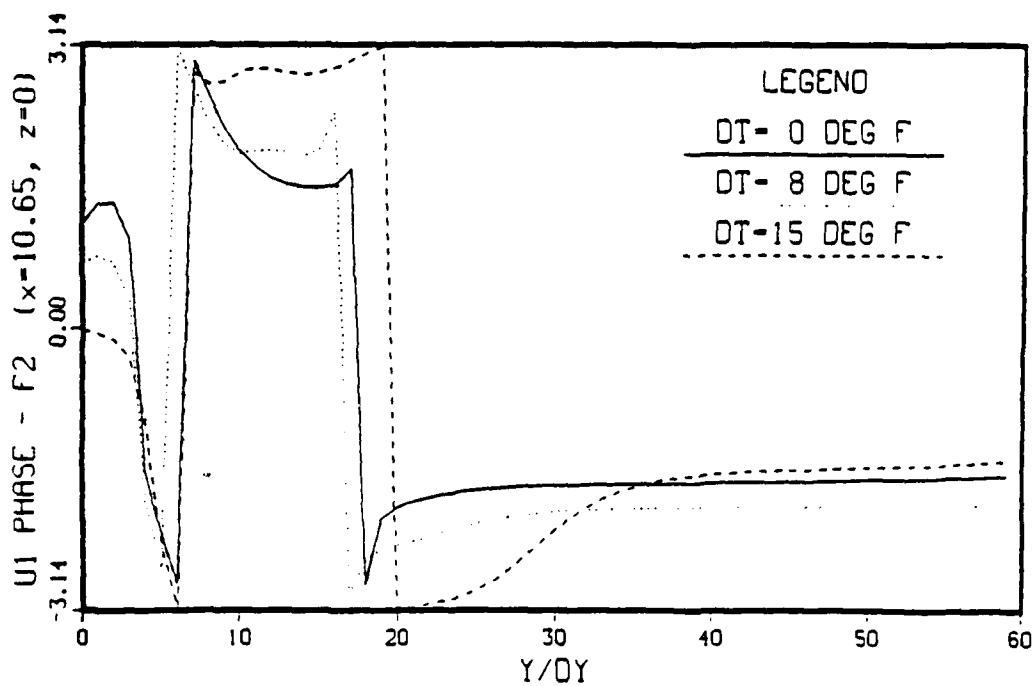
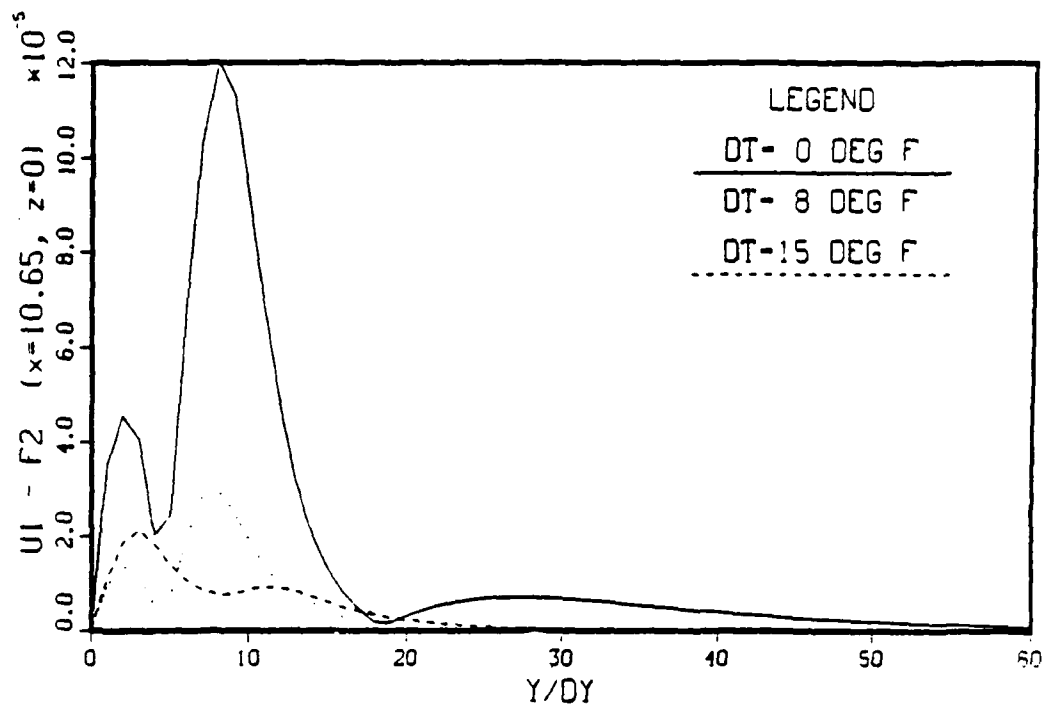
Figure 6.75 continued





c) 3D streamwise velocity,  $U_1$ ,  $F_{3D}$

Figure 6.75 continued



d) 3D streamwise velocity,  $U_1, 2 F_{3D}$

Figure 6.75 continued

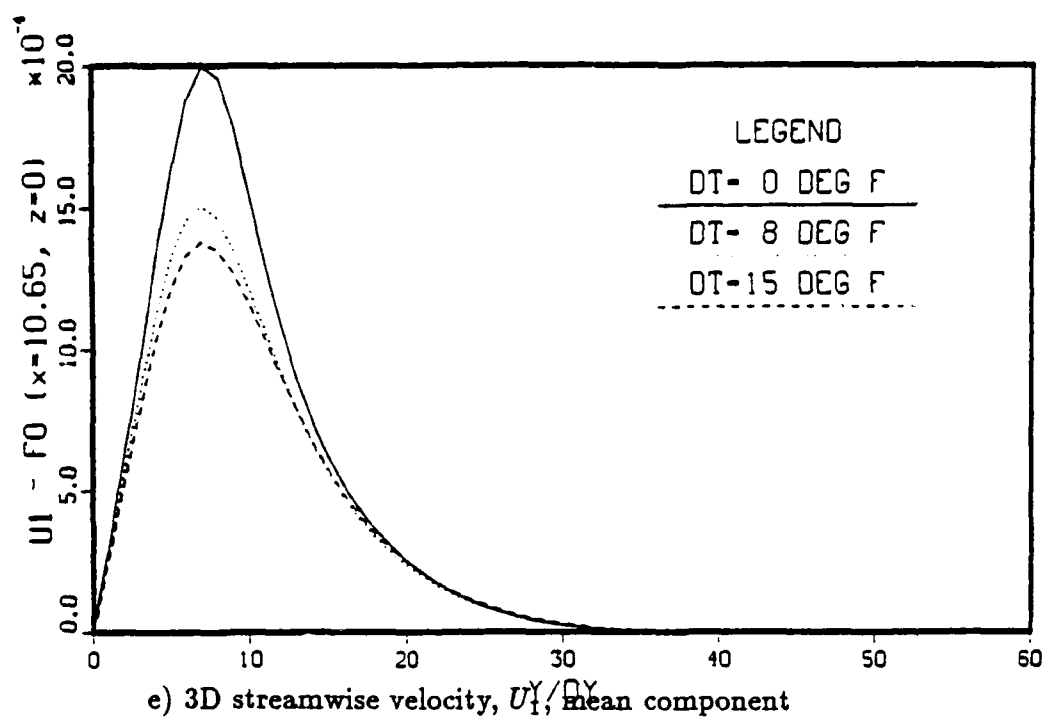


Figure 6.75 continued

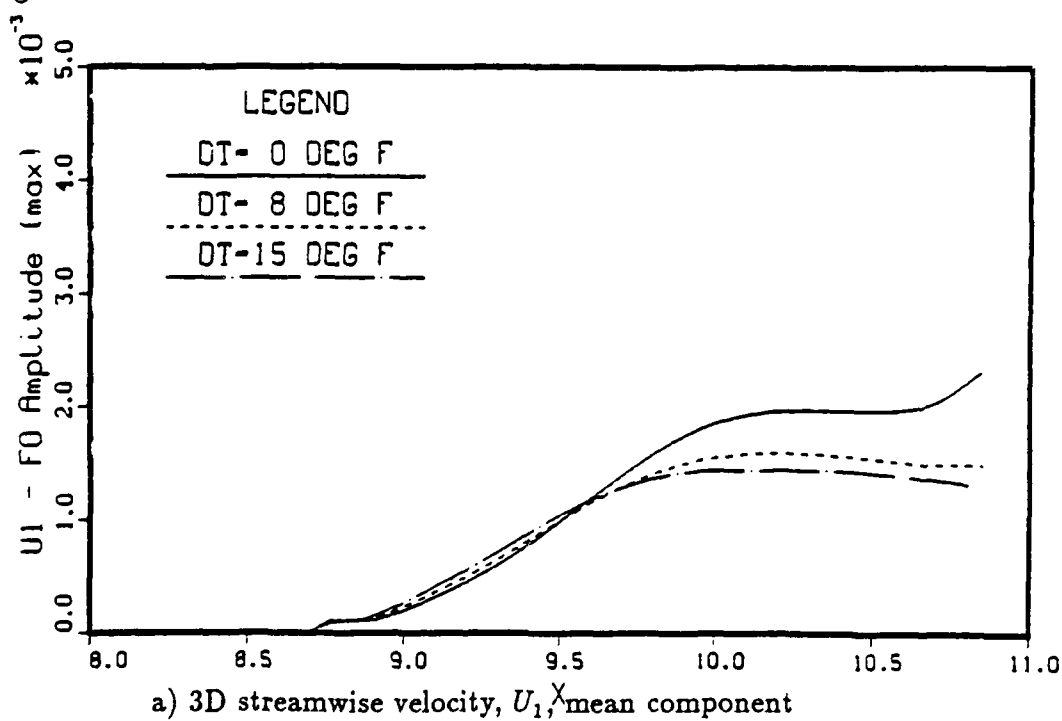


Figure 6.76 Influence of uniform passive control on the amplitude growth for fundamental breakdown

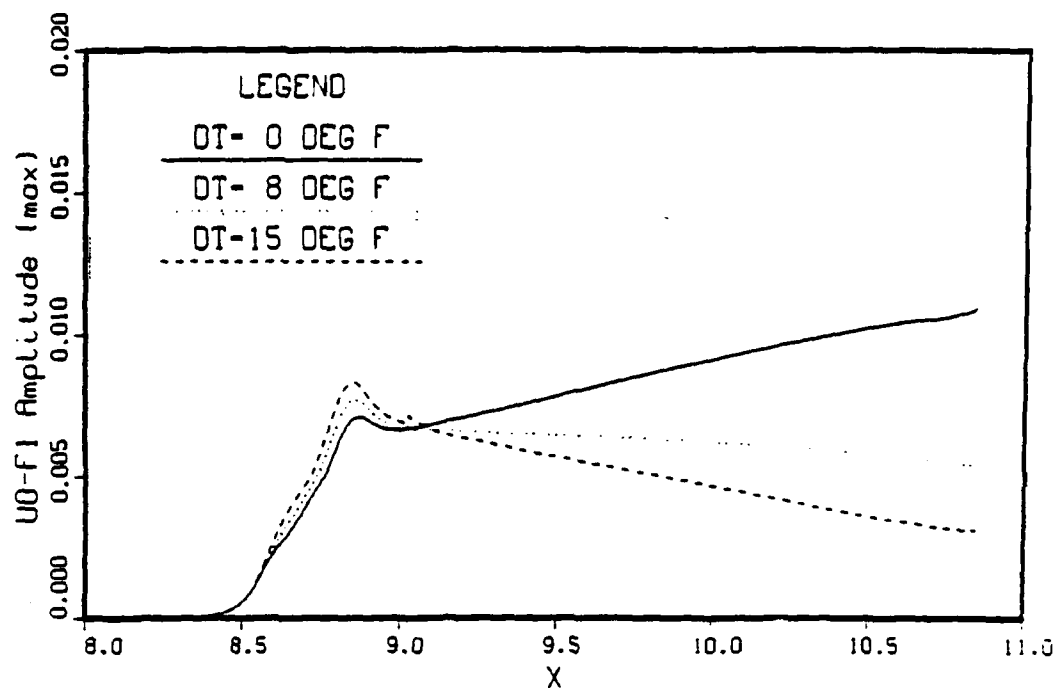
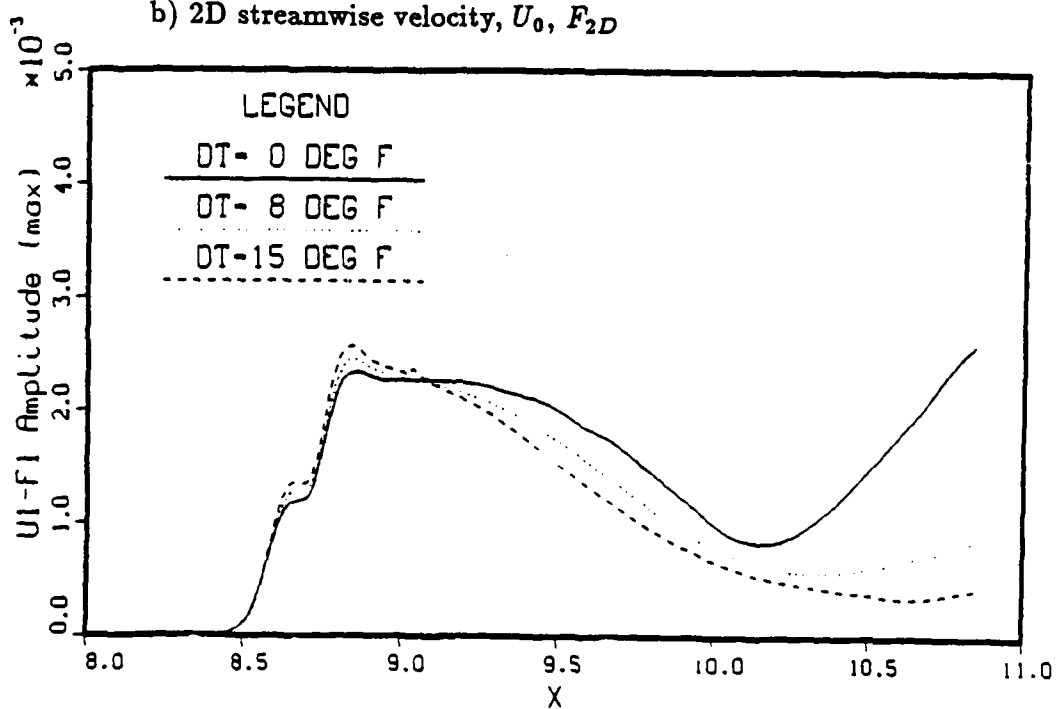
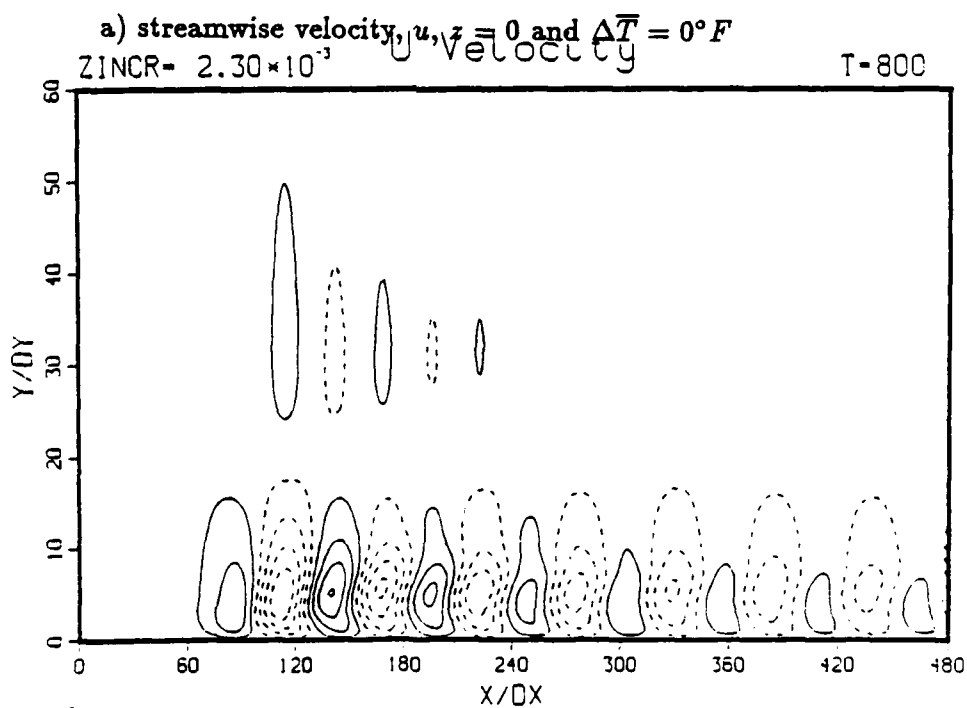
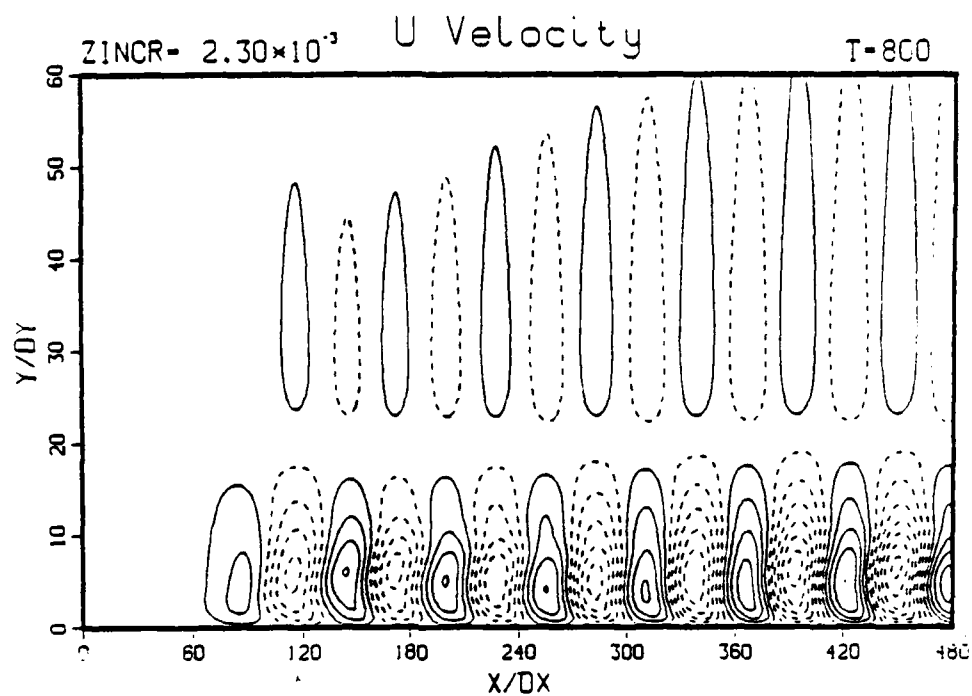
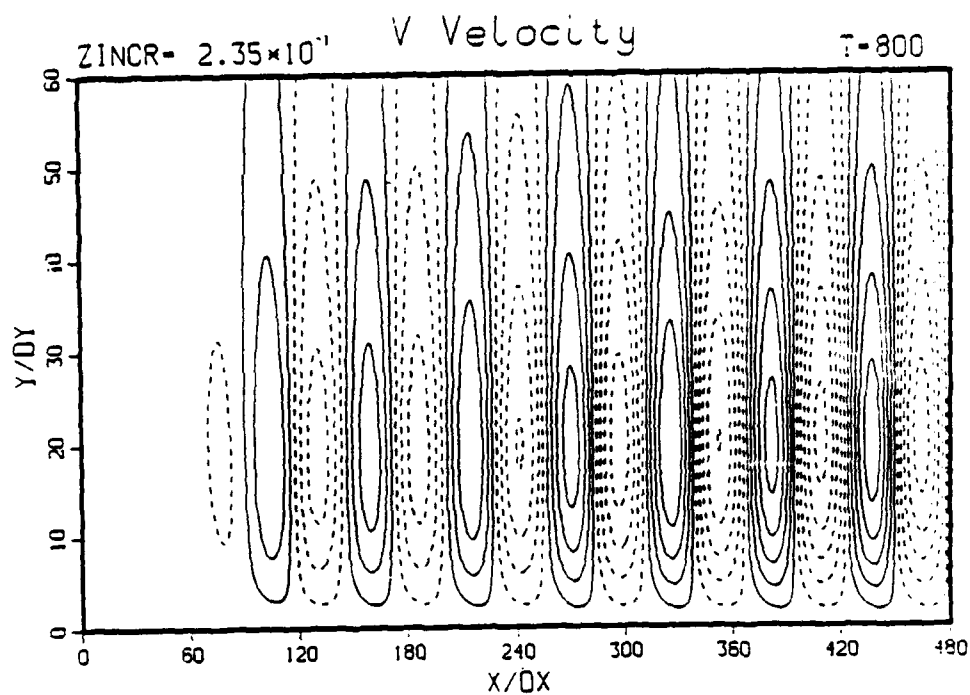
b) 2D streamwise velocity,  $U_0$ ,  $F_{2D}$ c) 3D streamwise velocity,  $U_1$ ,  $F_{3D}$ 

Figure 6.76 continued

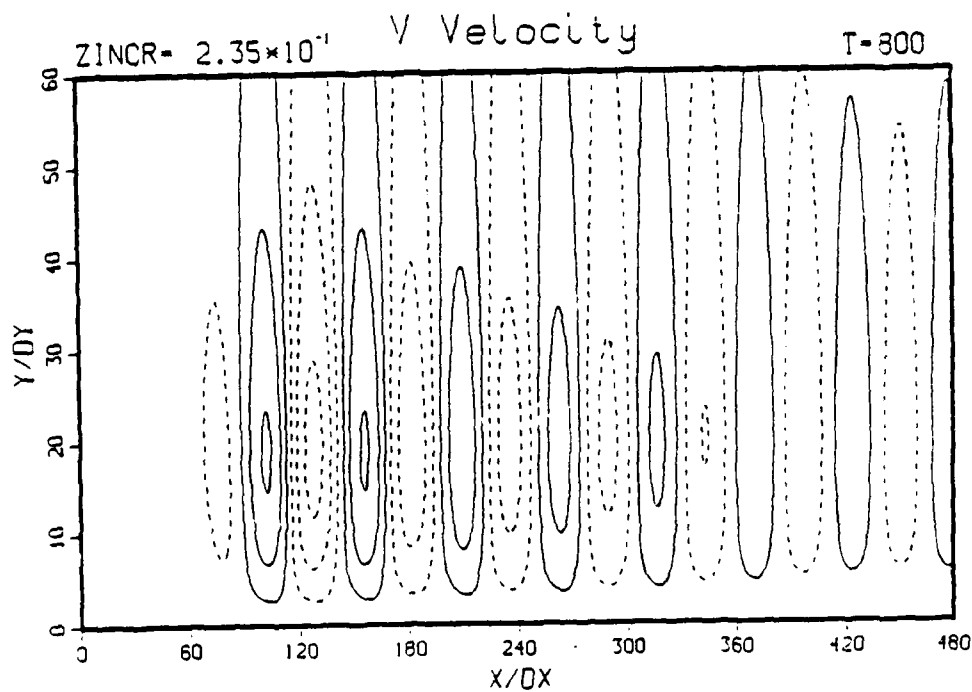


b) streamwise velocity,  $u, z = 0$  and  $\Delta \bar{T} = 15^\circ F$

Figure 6.77 Comparison of the disturbed flow for fundamental breakdown without control applied and with uniform passive heating applied at the peak plane in the spanwise direction

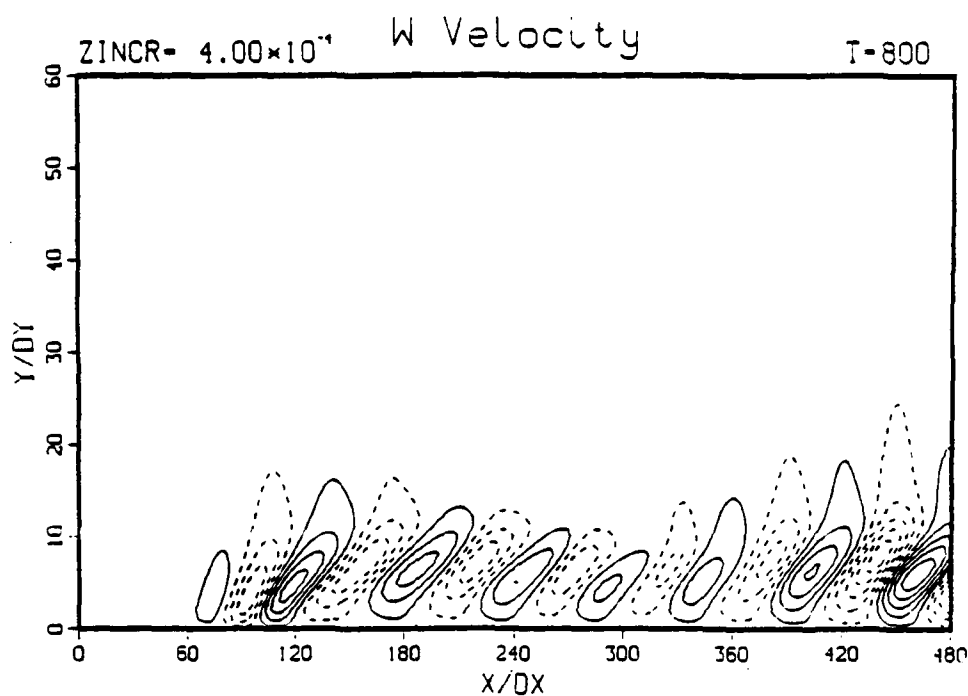


c) normal velocity,  $v$ ,  $z = 0$  and  $\Delta \bar{T} = 0^\circ F$

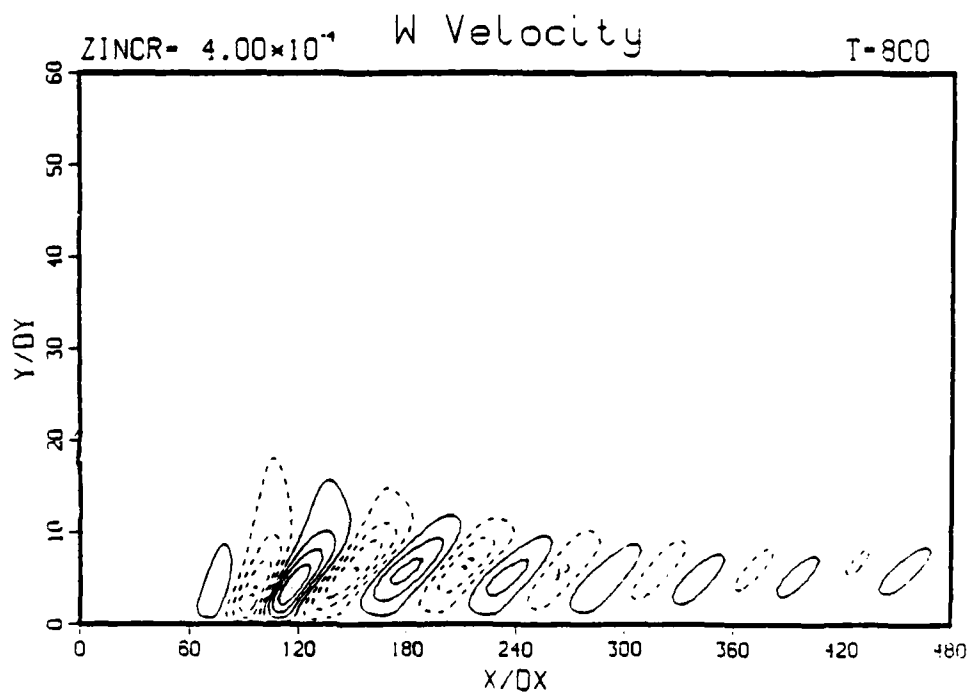


d) normal velocity,  $v$ ,  $z = 0$  and  $\Delta \bar{T} = 15^\circ F$

Figure 6.77 continued

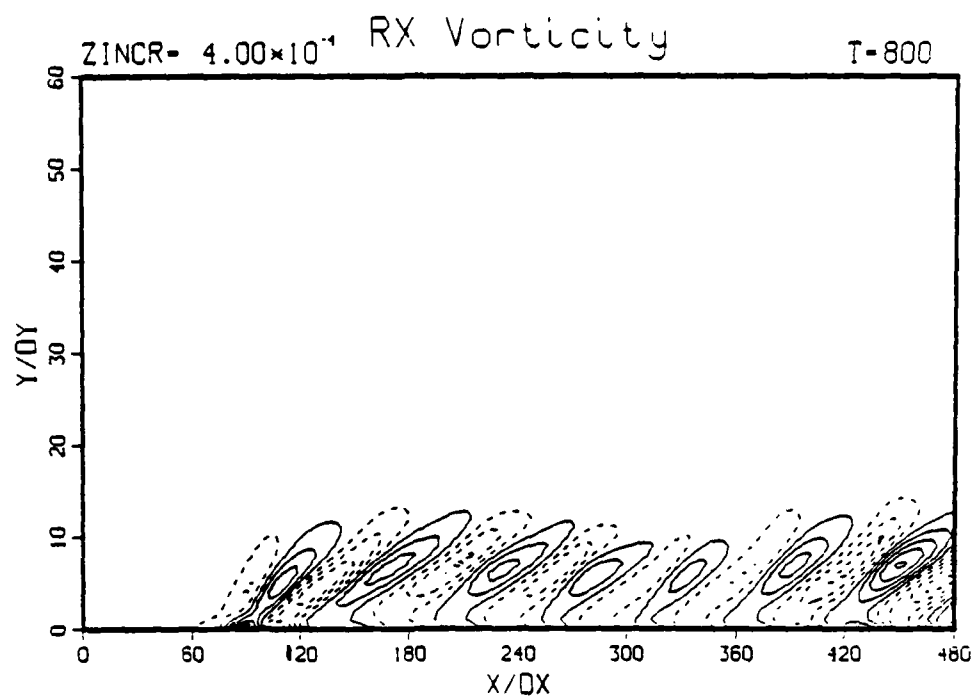


e) spanwise velocity,  $w$ ,  $z = \lambda_z/4$  and  $\Delta \bar{T} = 0^\circ F$

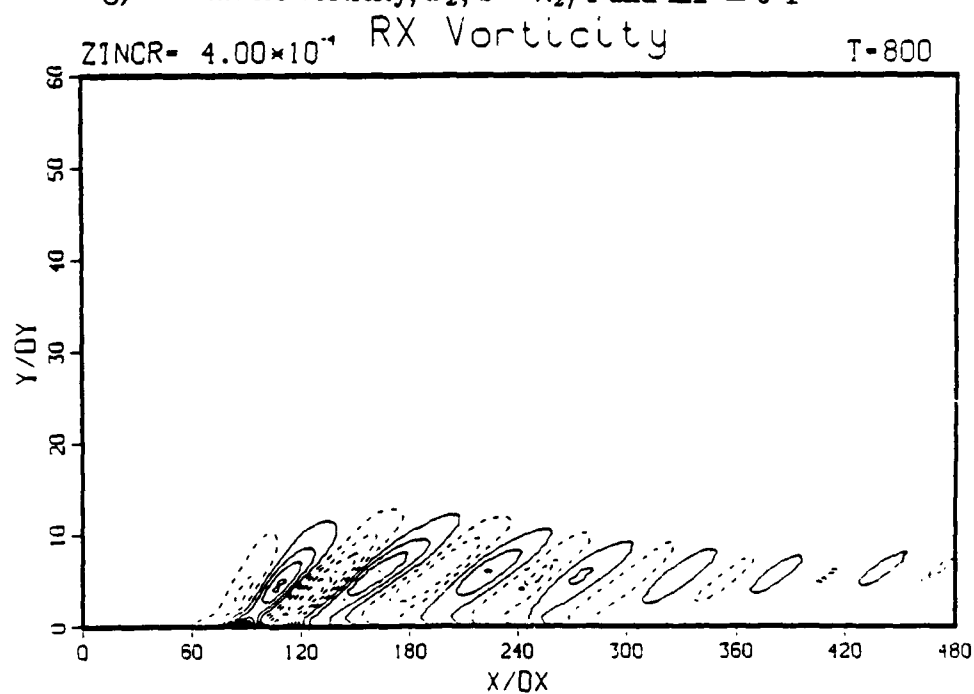


f) spanwise velocity,  $w$ ,  $z = \lambda_z/4$  and  $\Delta \bar{T} = 15^\circ F$

Figure 6.77 continued



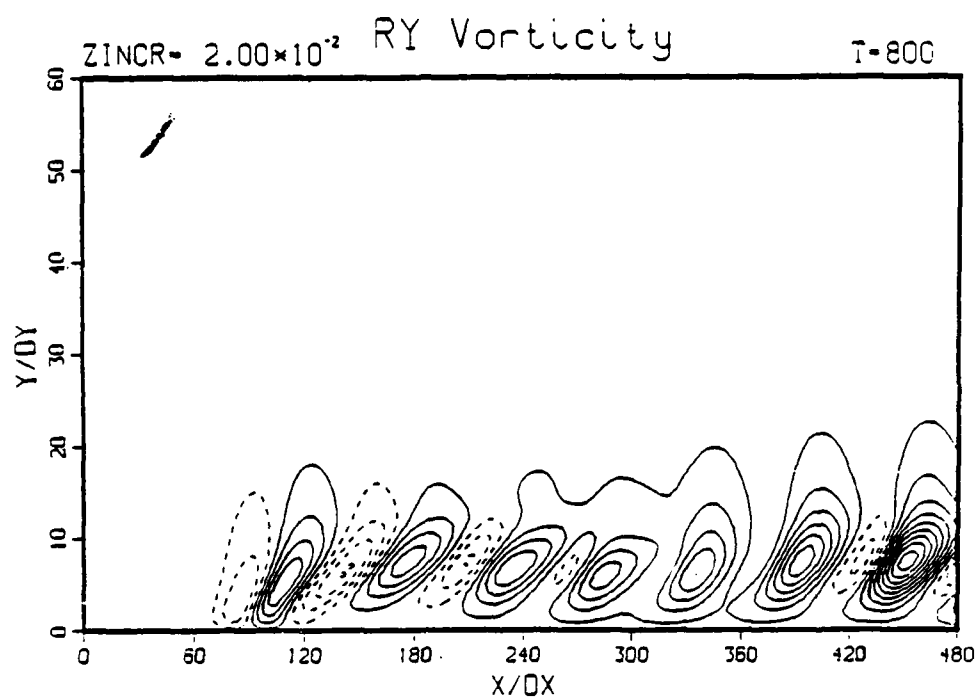
g) streamwise vorticity,  $\omega_z$ ,  $z = \lambda_z/4$  and  $\Delta T = 0^\circ F$



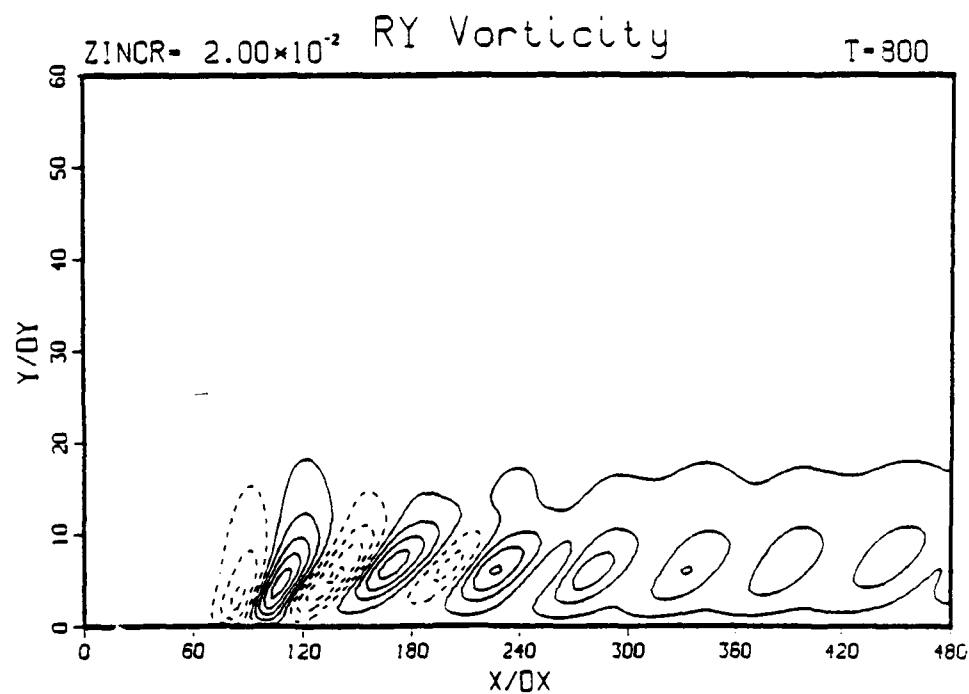
h) streamwise vorticity,  $\omega_z$ ,  $z = \lambda_z/4$  and  $\Delta T = 15^\circ F$

Figure 6.77 continued



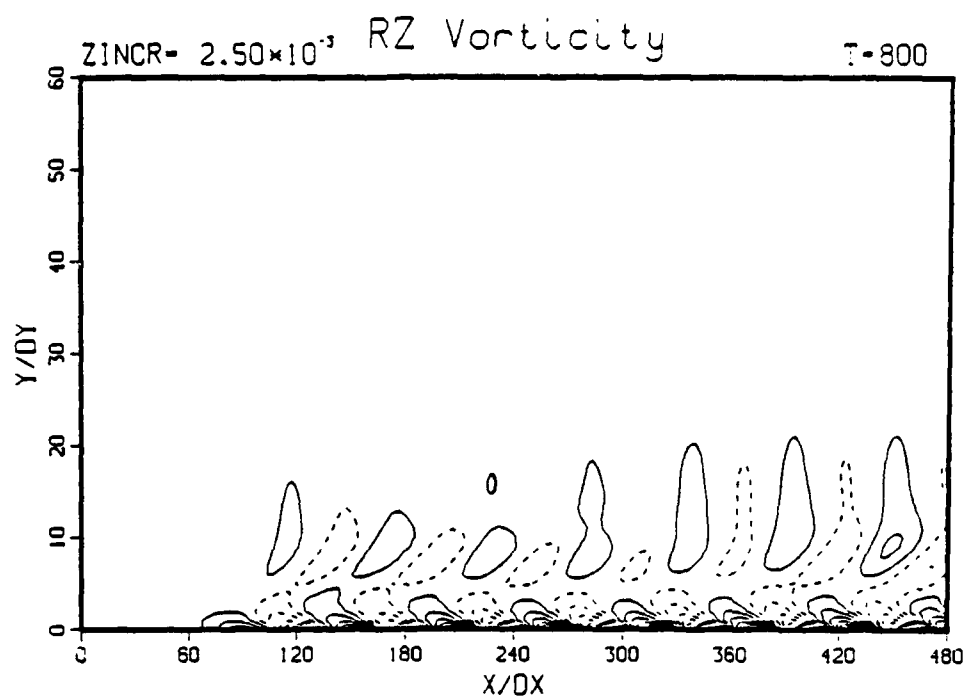


i) normal vorticity,  $\omega_y$ ,  $z = \lambda_z/4$  and  $\Delta \bar{T} = 0^\circ F$

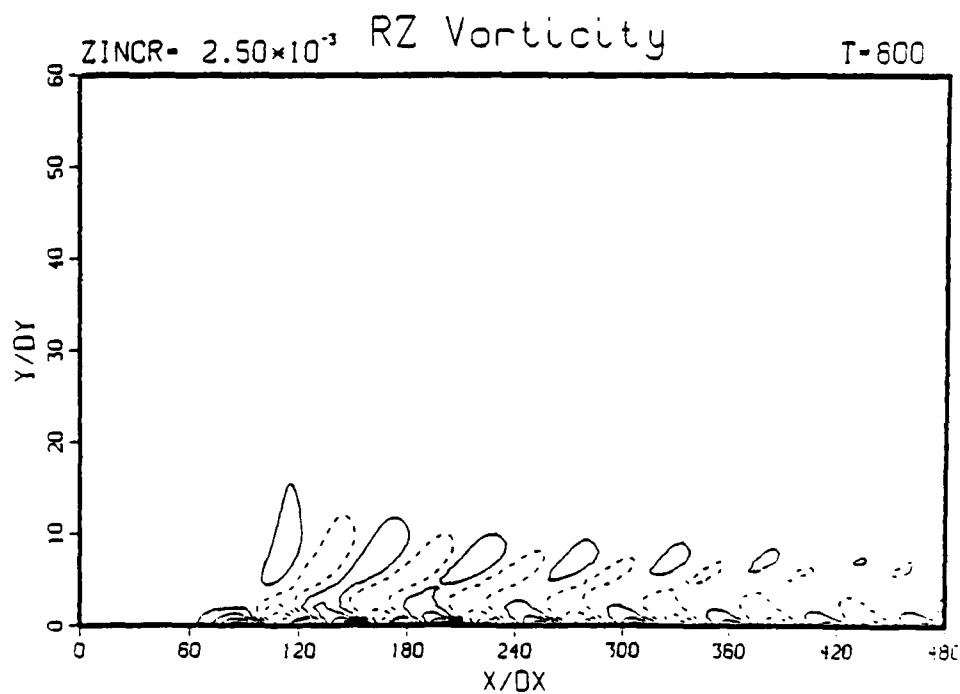


j) normal vorticity,  $\omega_y$ ,  $z = \lambda_z/4$  and  $\Delta \bar{T} = 15^\circ F$

Figure 6.77 continued

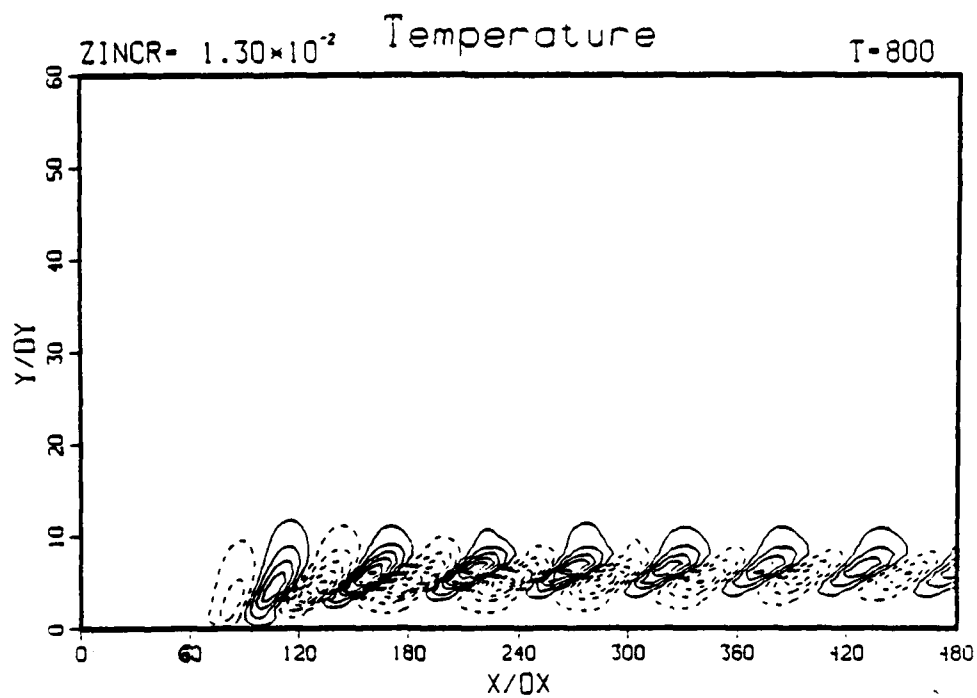


k) spanwise vorticity,  $\omega_z$ ,  $z = 0$  and  $\Delta T = 0^\circ F$



l) spanwise vorticity,  $\omega_z$ ,  $z = 0$  and  $\Delta T = 15^\circ F$

Figure 6.77 continued



m) temperature,  $T$ ,  $z = 0$  and  $\Delta \bar{T} = 15^\circ F$

Figure 6.77 continued

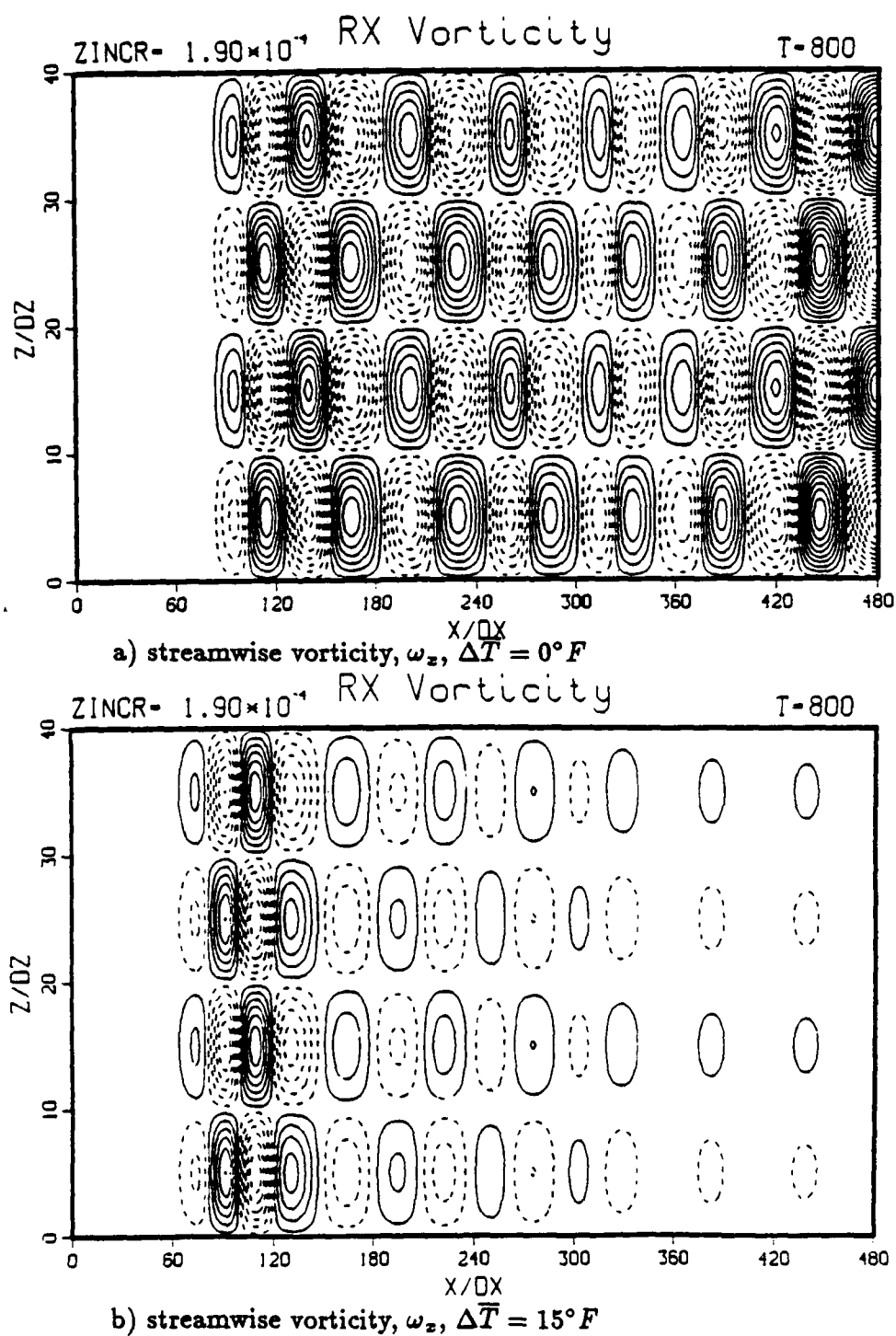
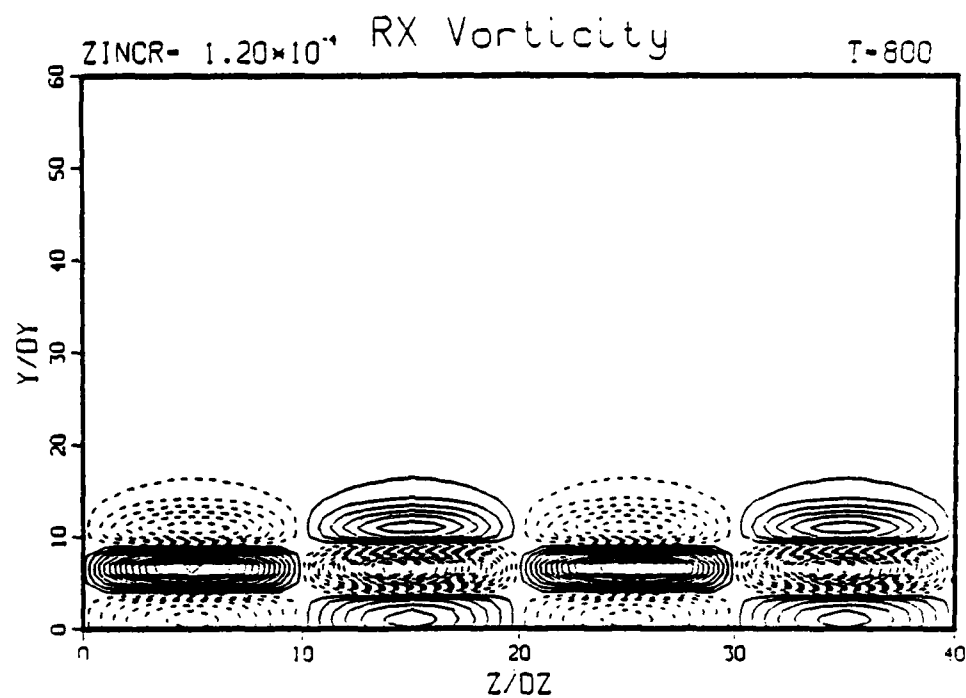
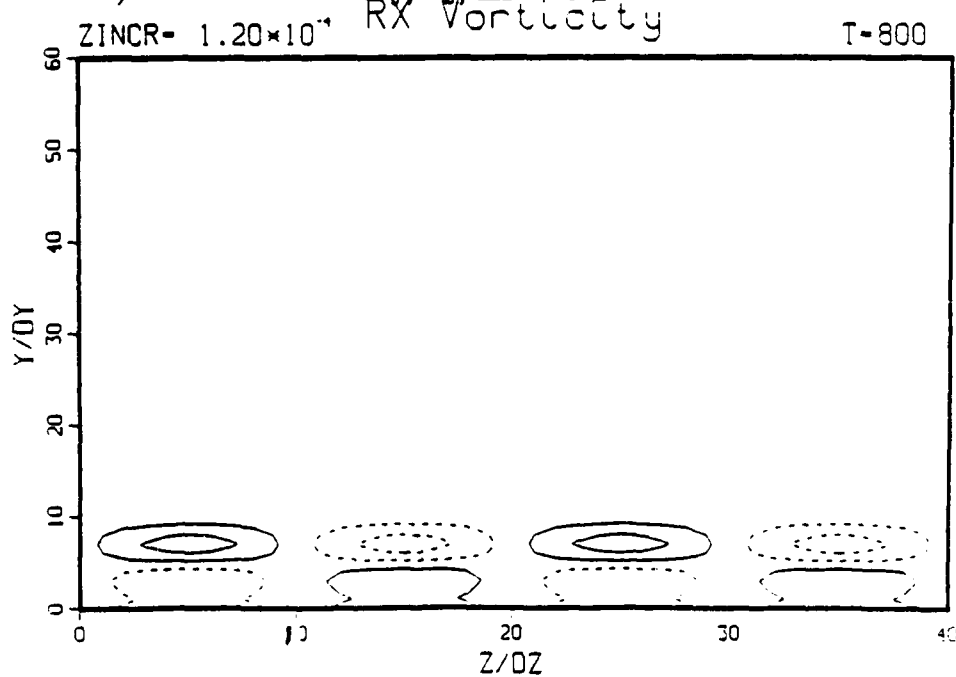


Figure 6.78 Comparison of the disturbed flow for fundamental breakdown without control applied and with uniform passive heating applied at  $y = 3.186$



a) streamwise vorticity,  $\omega_x$ ,  $\Delta \bar{T} = 0^\circ F$



b) streamwise vorticity,  $\omega_x$ ,  $\Delta \bar{T} = 15^\circ F$

Figure 6.79 Comparison of the disturbed flow for fundamental breakdown without control applied and with uniform passive heating applied at  $x = 11.0$

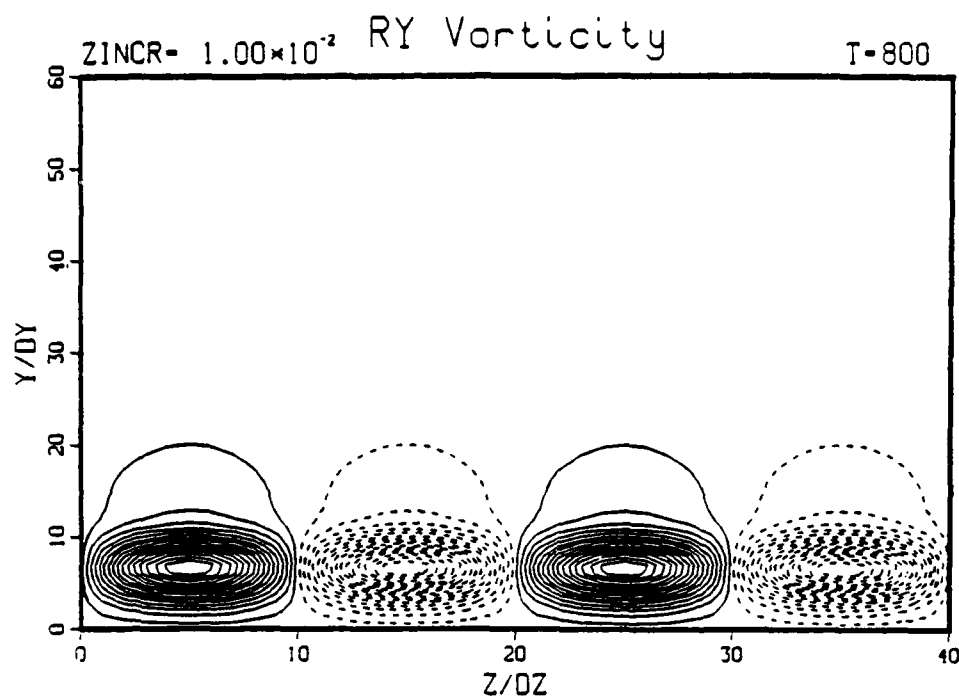
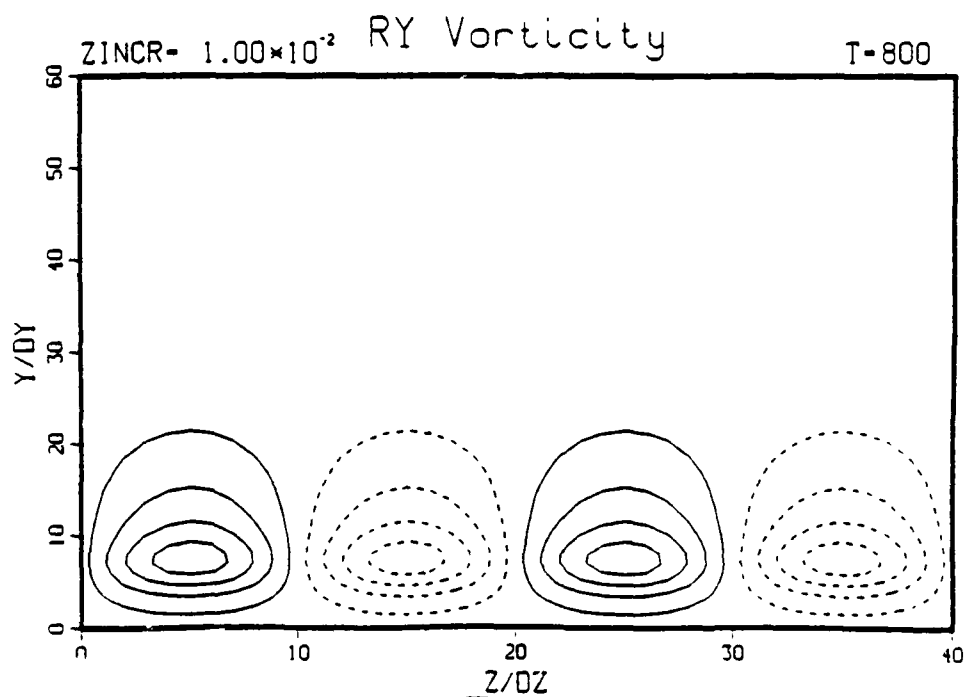
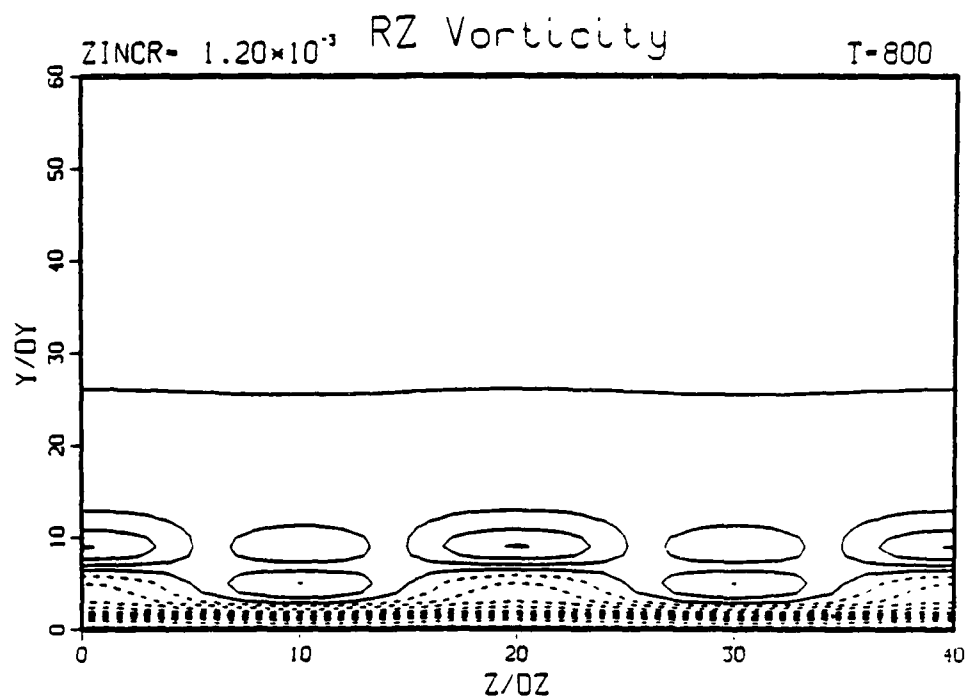
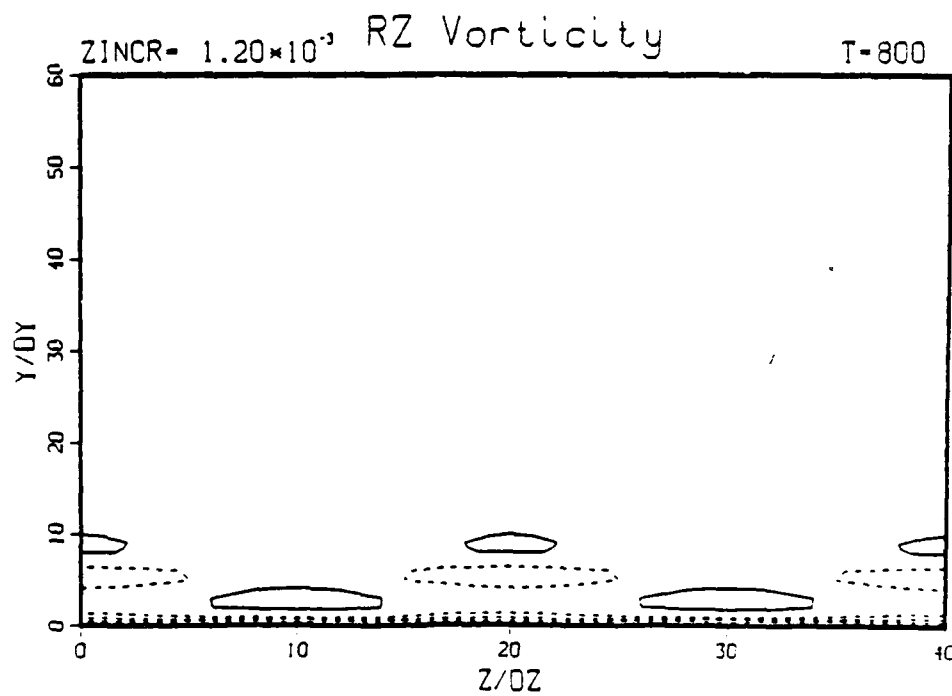
c) normal vorticity,  $\omega_y$ ,  $\Delta \bar{T} = 0^\circ F$ d) normal vorticity,  $\omega_y$ ,  $\Delta \bar{T} = 15^\circ F$ 

Figure 6.79 continued

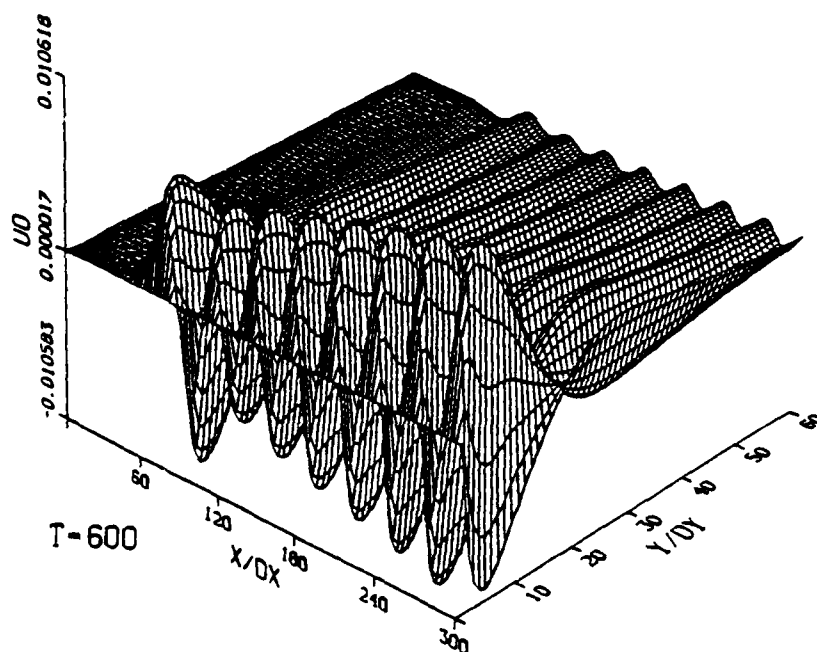


e) spanwise vorticity,  $\omega_z$ ,  $\Delta \bar{T} = 0^\circ F$

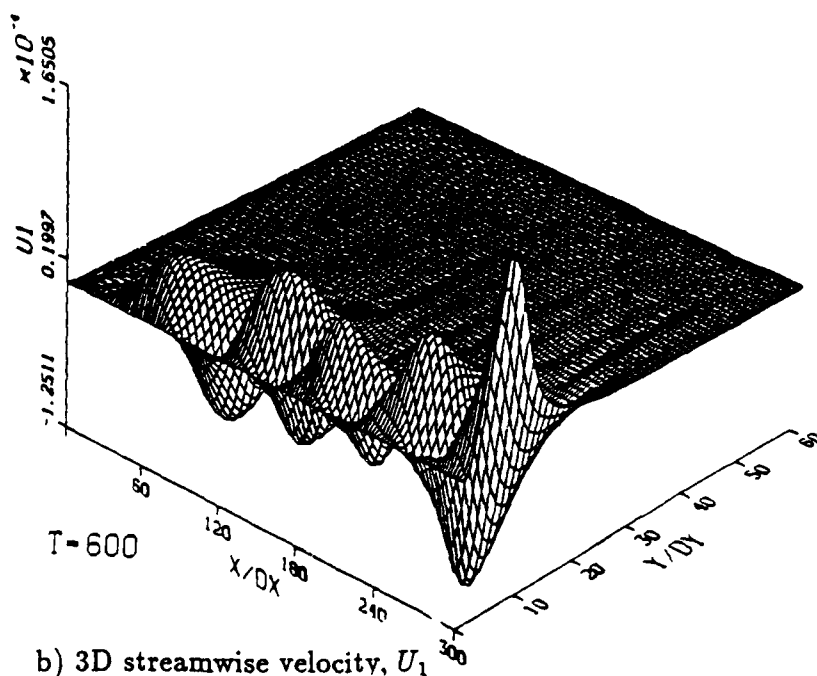


f) spanwise vorticity,  $\omega_z$ ,  $\Delta \bar{T} = 15^\circ F$

Figure 6.79 continued



a) 2D streamwise velocity,  $U_0$



b) 3D streamwise velocity,  $U_1$

Figure 6.80 Uncontrolled disturbed flow for subharmonic breakdown,  $F_{2D} = 1.24$ ,  $F_{3D} = 0.62$



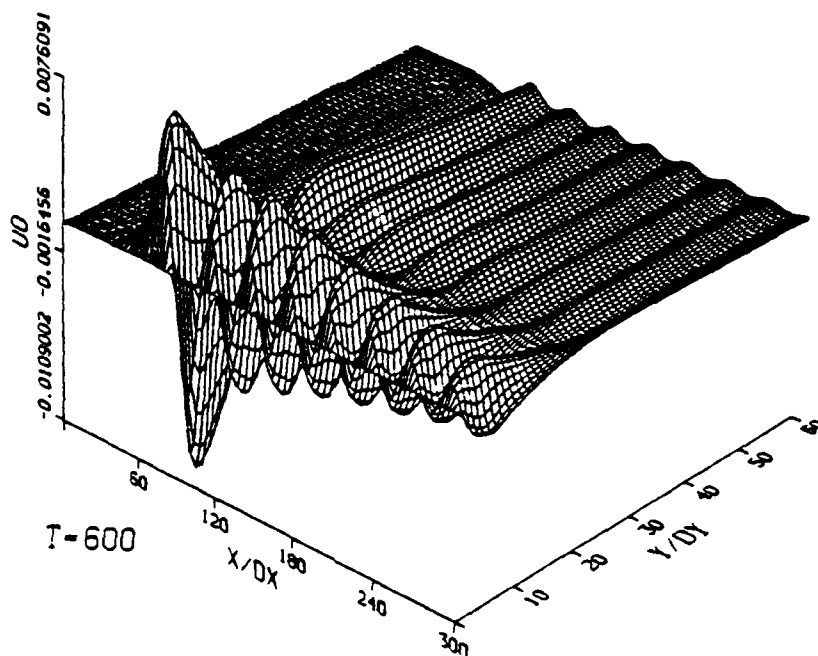
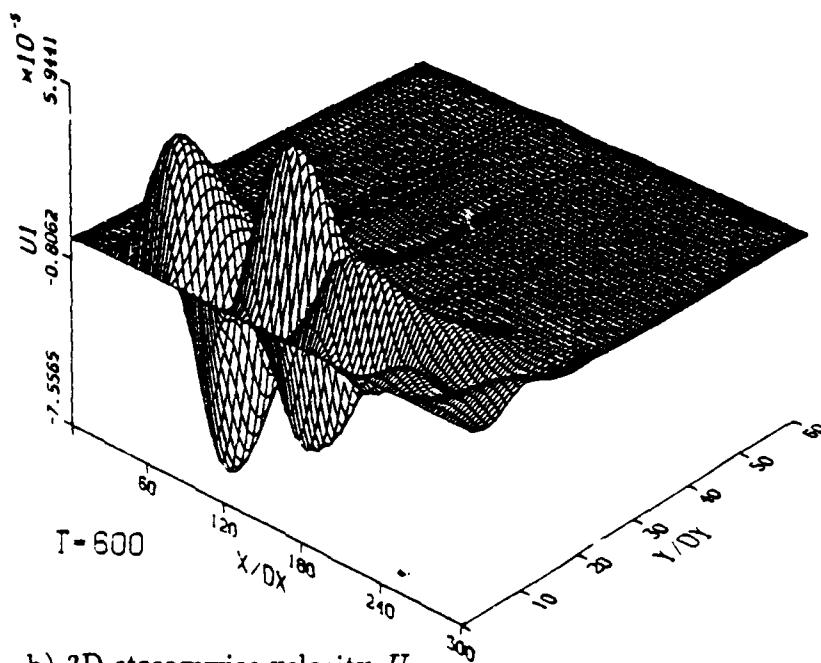
a) 2D streamwise velocity,  $U_0$ b) 3D streamwise velocity,  $U_1$ 

Figure 6.81 Disturbed flow for subharmonic breakdown with  $\Delta \bar{T} = 15^\circ F$  control applied,  $F_{2D} = 1.24$ ,  $F_{3D} = 0.62$

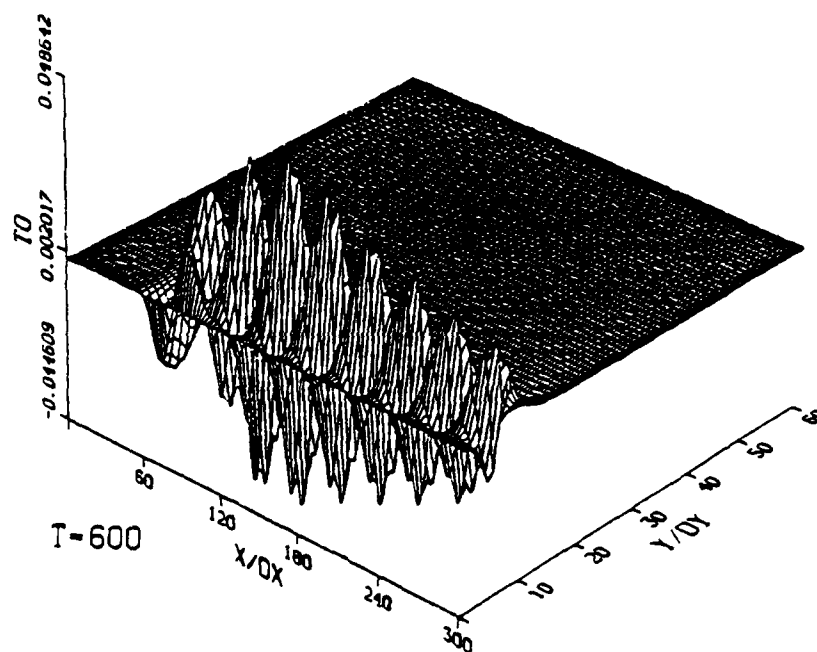
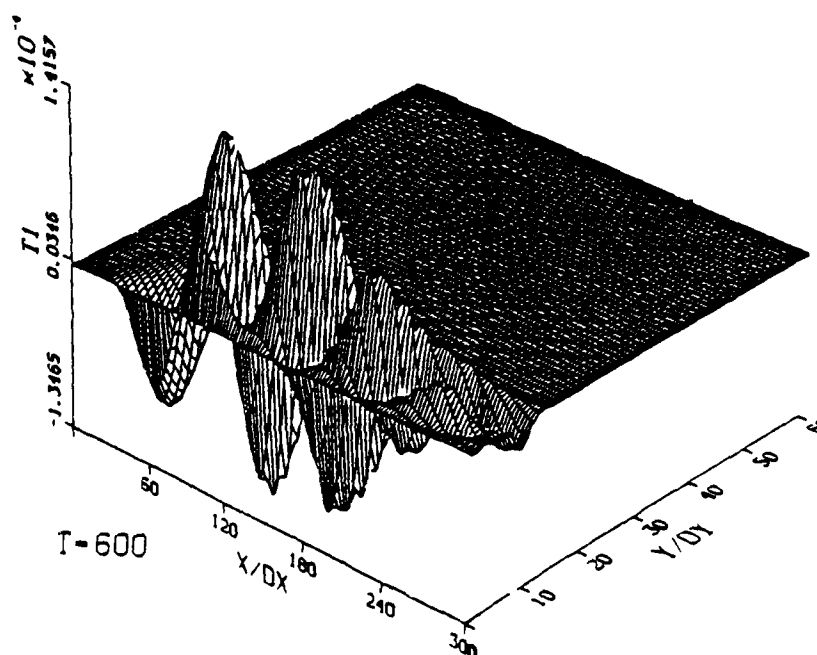
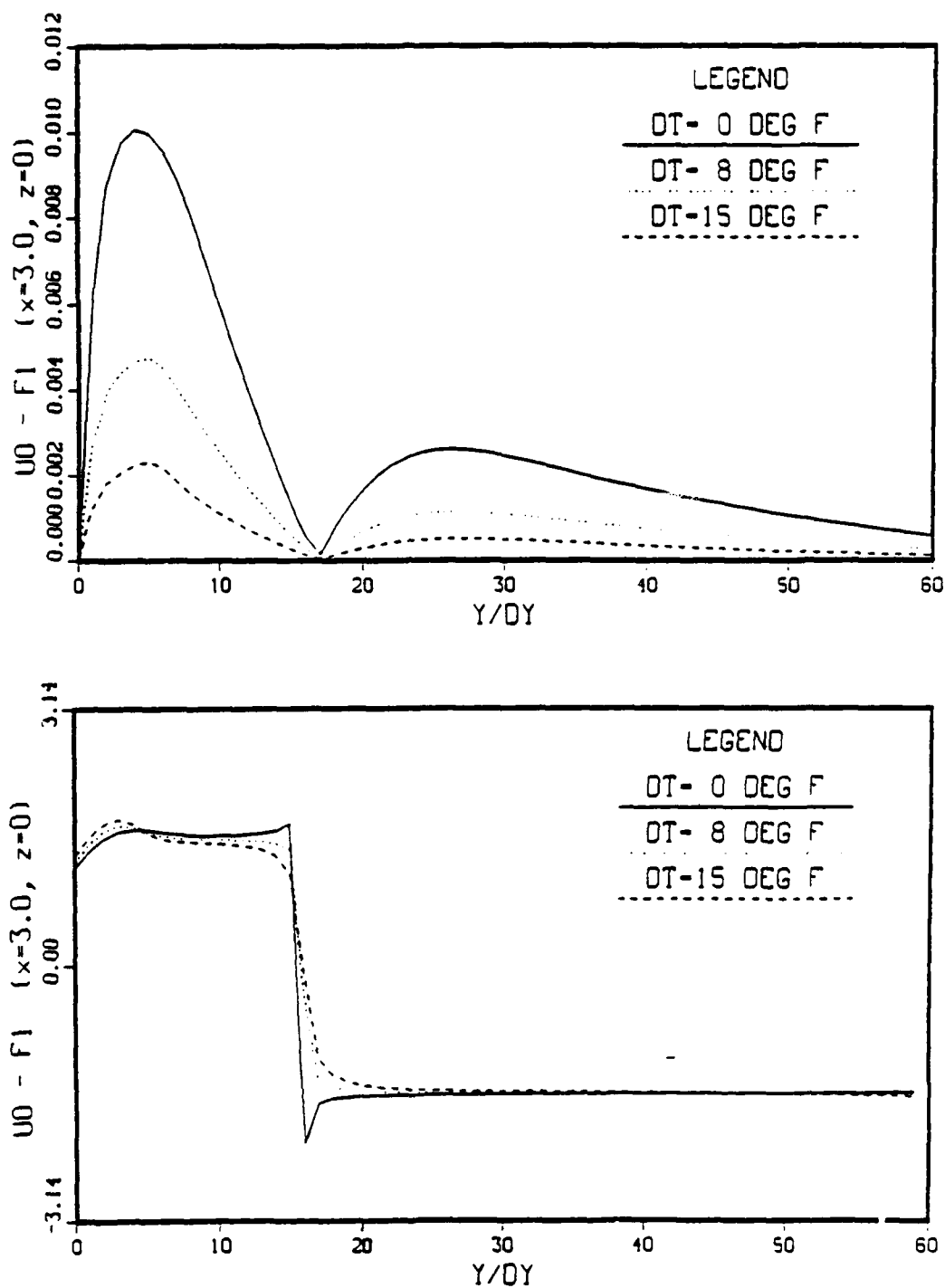
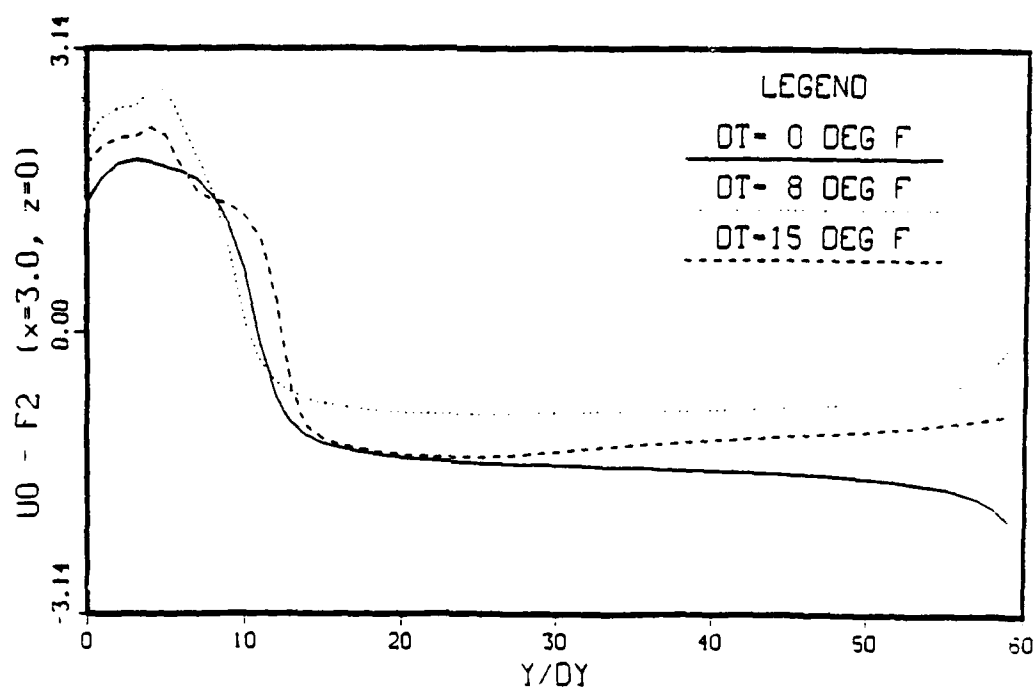
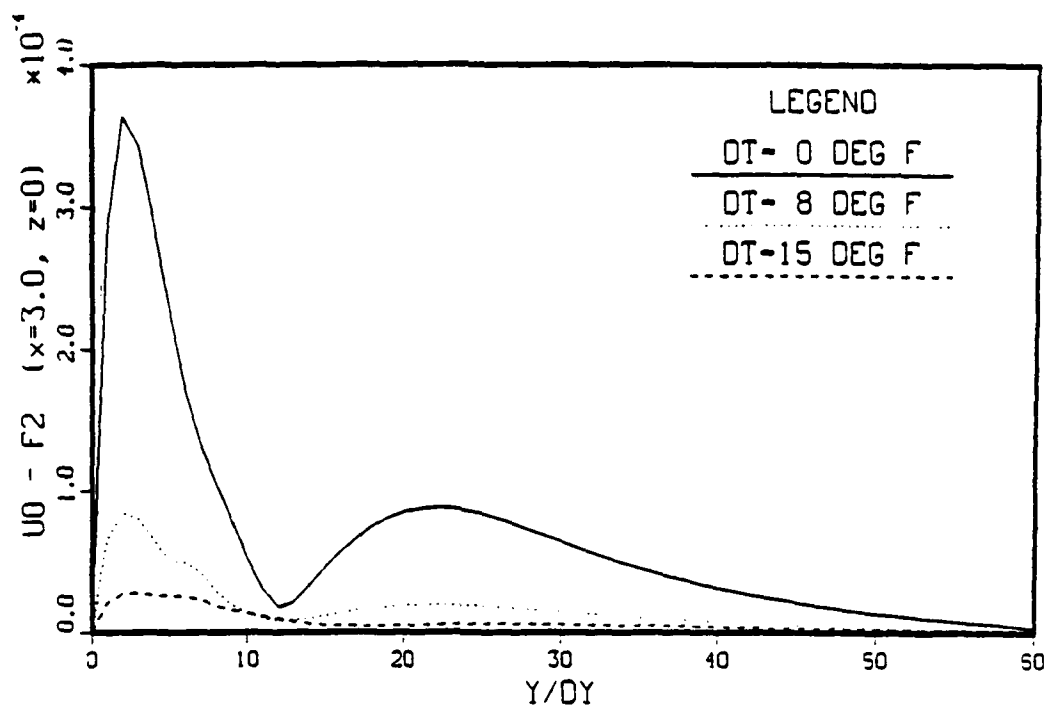
c) 2D temperature,  $\Theta_0$ d) 3D temperature,  $\Theta_1$ 

Figure 6.81 continued



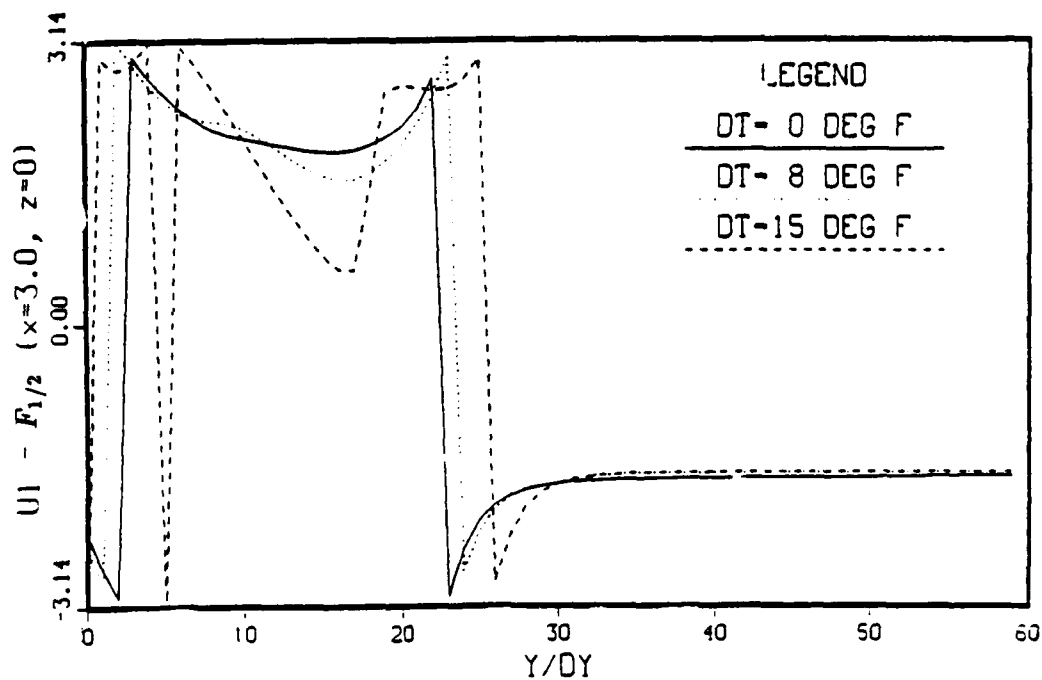
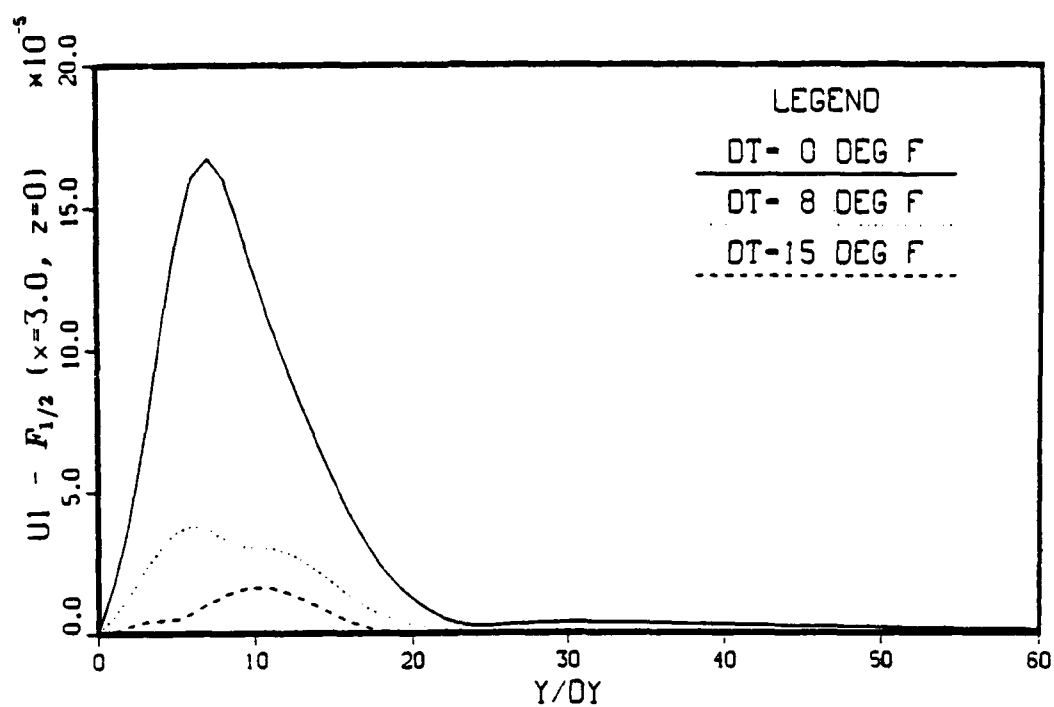
a) 2D streamwise velocity,  $U_0, F_{2D}$ ,

Figure 6.82 Amplitude and phase comparison at  $x = 3.0$  for subharmonic breakdown with uniform passive control applied



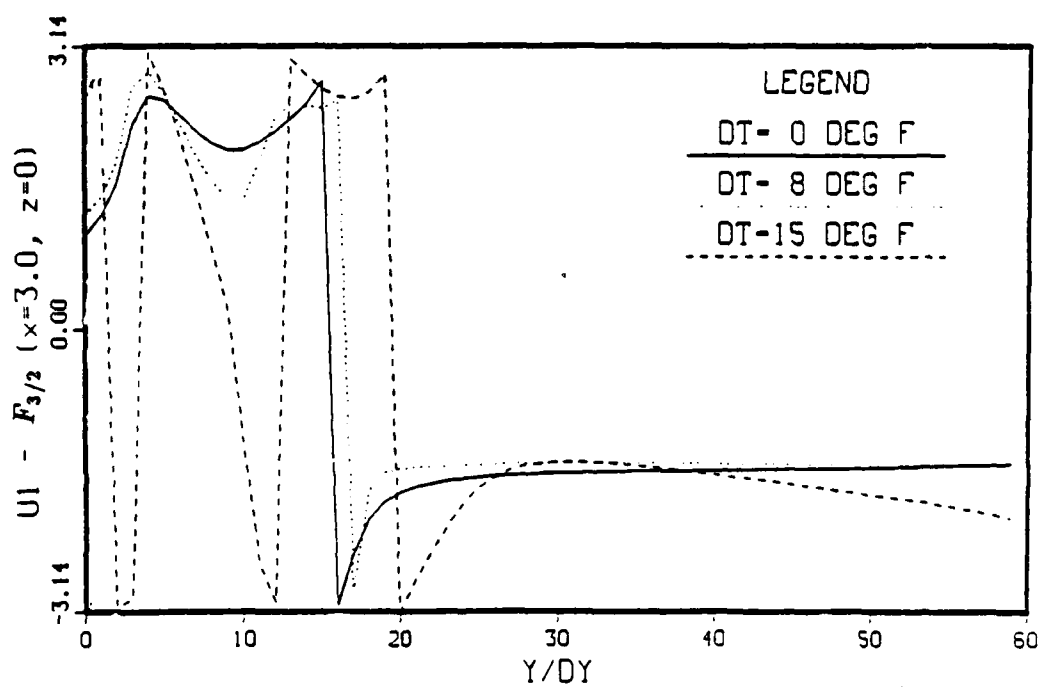
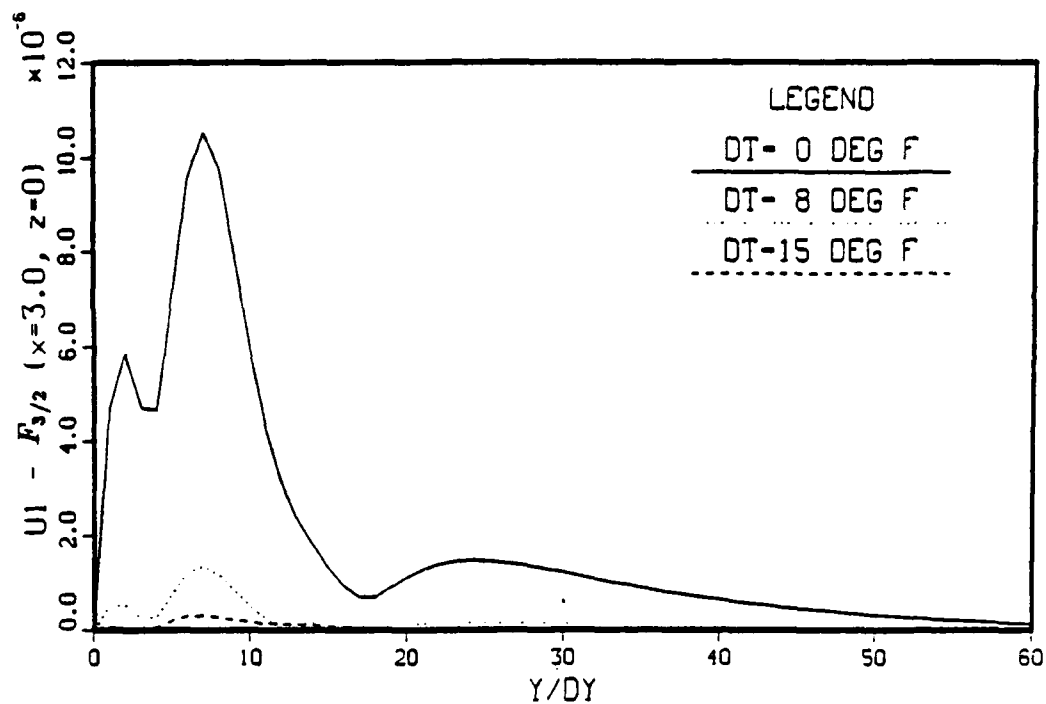
b) 2D streamwise velocity,  $U_0, 2 F_{2D}$

Figure 6.82 continued



c) 3D streamwise velocity,  $U_1, \frac{1}{2} F_{2D}$

Figure 6.82 continued



d) 3D streamwise velocity,  $U_1, \frac{3}{2} F_{2D}$

Figure 6.82 continued

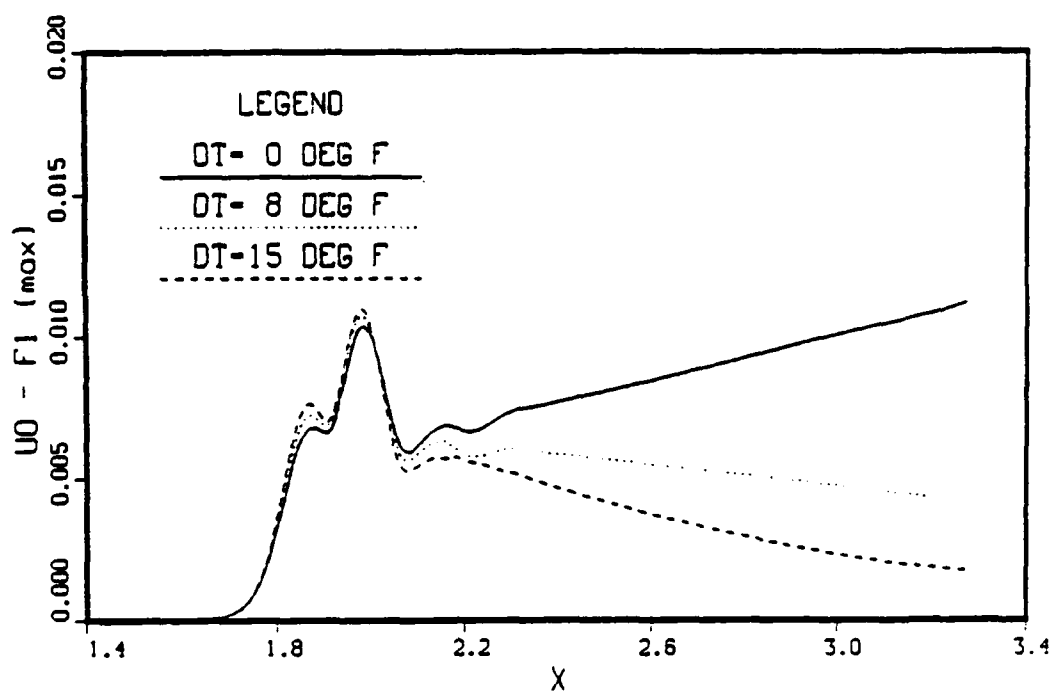
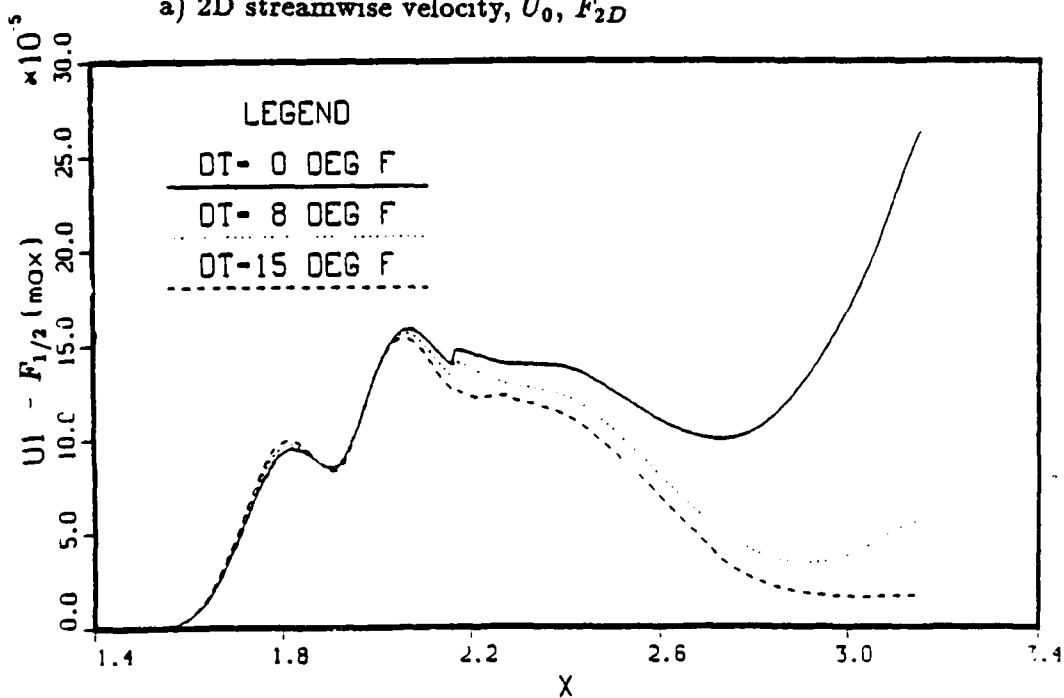
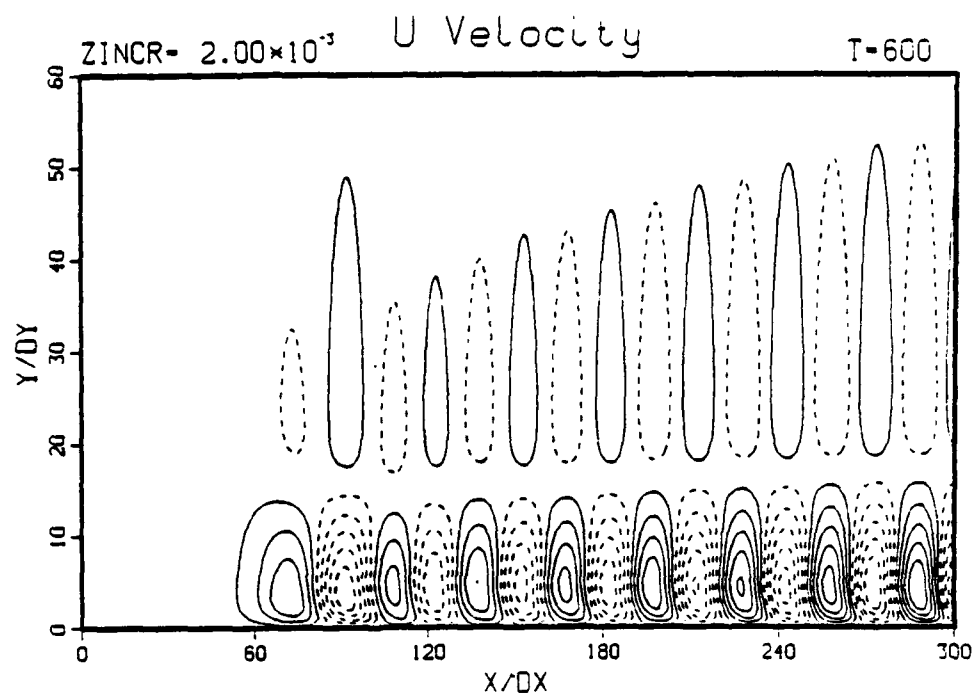
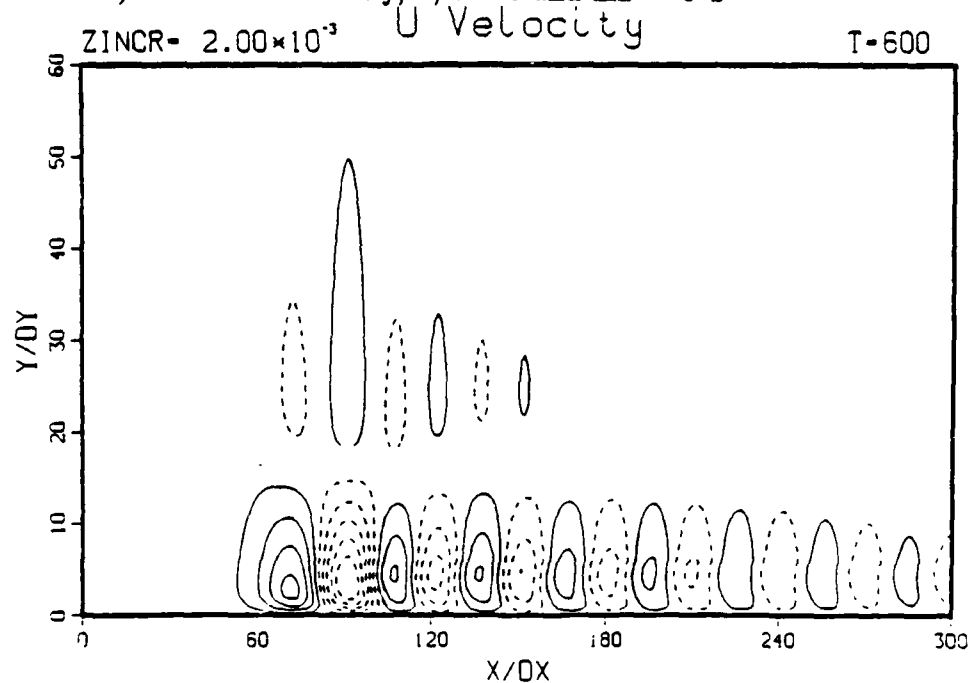
a) 2D streamwise velocity,  $U_0, F_{2D}$ b) 3D streamwise velocity,  $U_1, F_{3D}$ 

Figure 6.83 Influence of uniform passive control on the amplitude growth for sub-harmonic breakdown



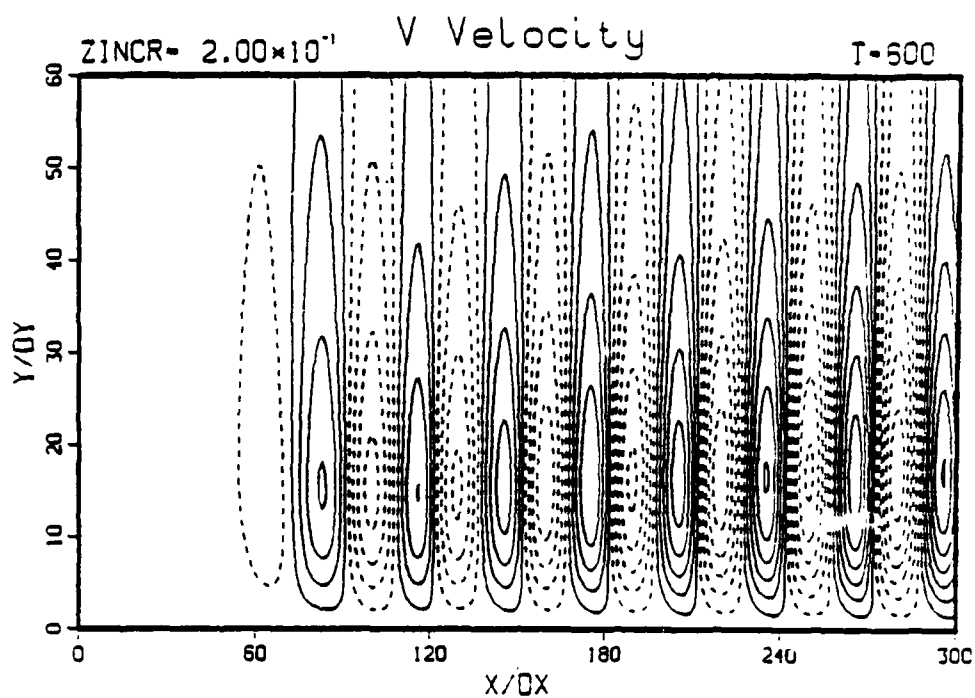
a) streamwise velocity,  $u$ ,  $z = 0$  and  $\Delta \bar{T} = 0^\circ F$



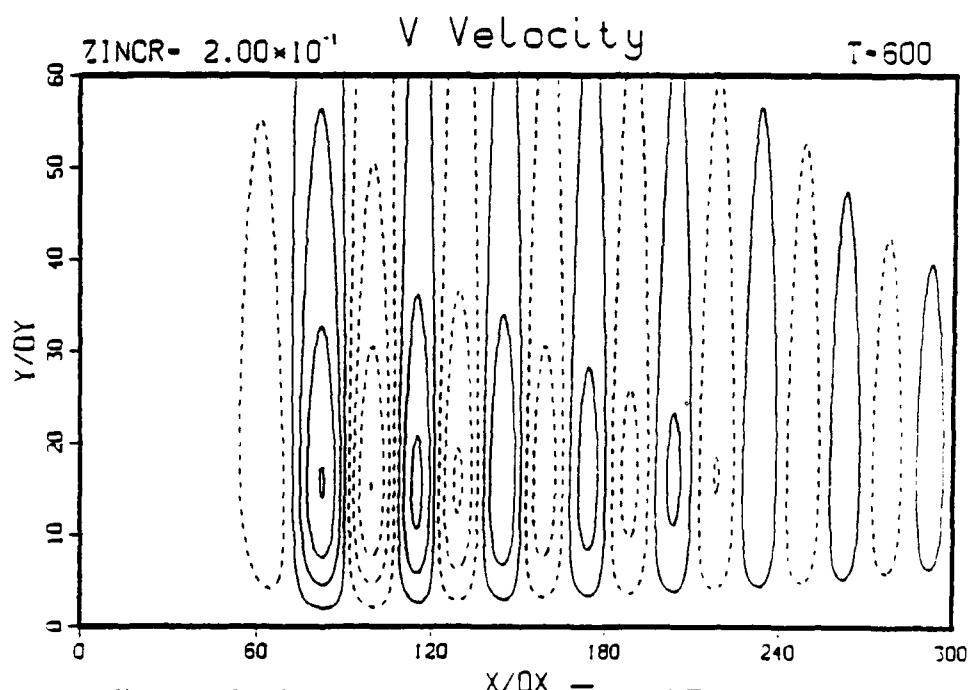
b) streamwise velocity,  $u$ ,  $z = 0$  and  $\Delta \bar{T} = 15^\circ F$

Figure 6.84 Comparison of the disturbed flow for subharmonic breakdown without control applied and with uniform passive heating applied at the peak plane in the spanwise direction



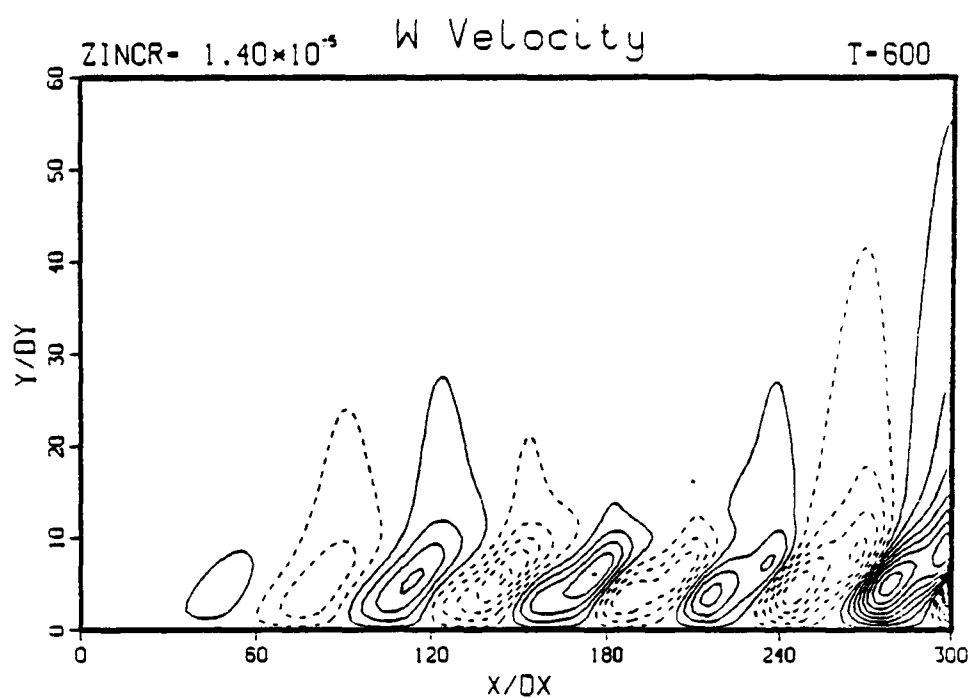


c) normal velocity,  $v$ ,  $z = 0$  and  $\Delta T = 0^\circ F$

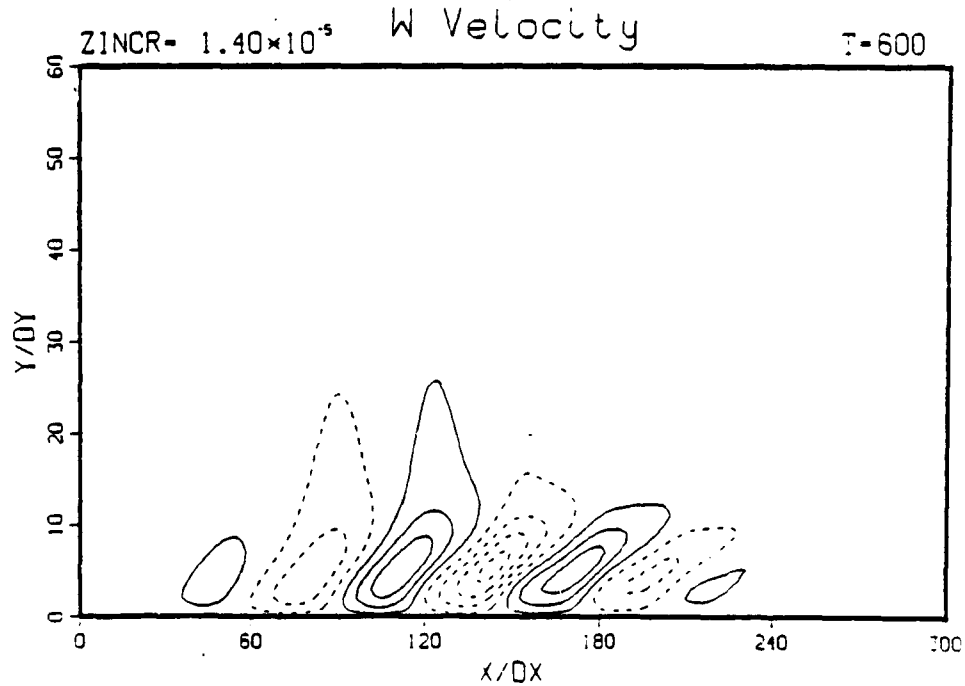


d) normal velocity,  $v$ ,  $z = 0$  and  $\Delta T = 15^\circ F$

Figure 6.84 continued

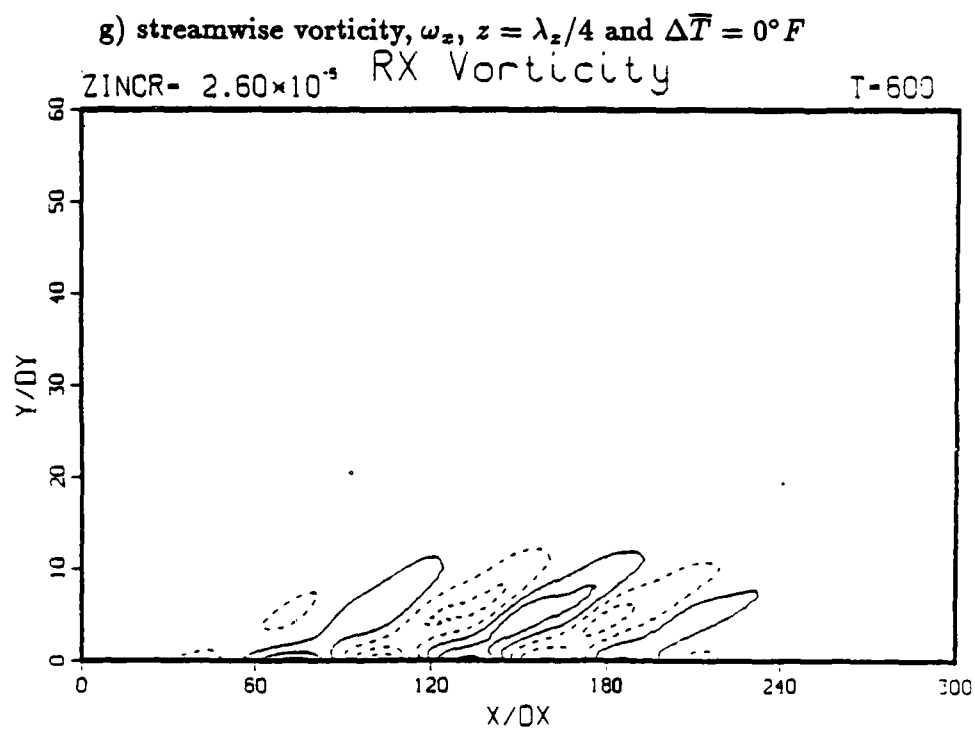
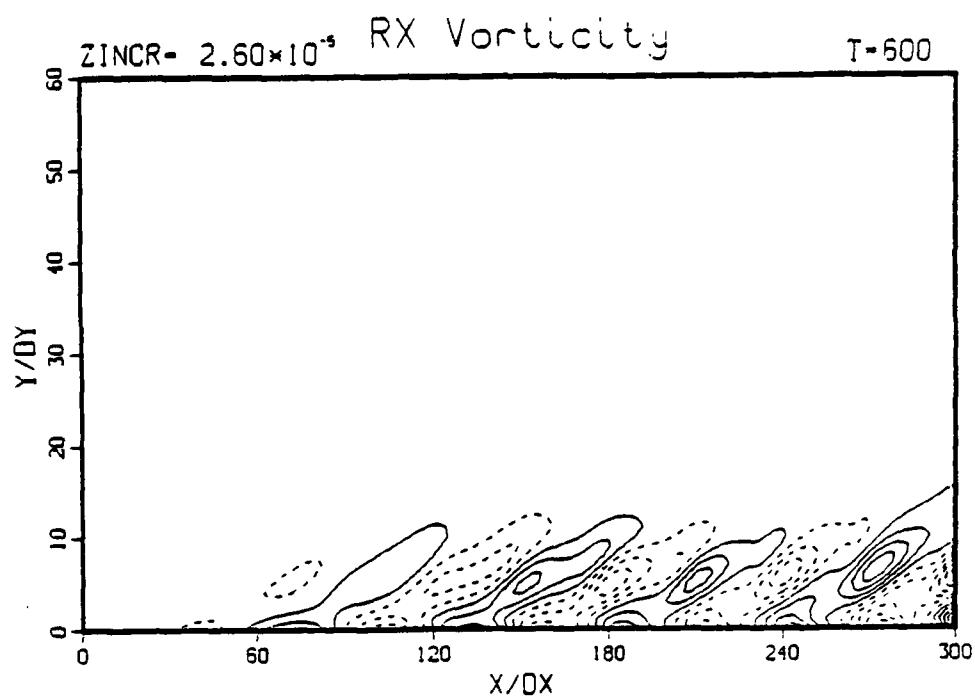


e) spanwise velocity,  $w$ ,  $z = \lambda_z/4$  and  $\Delta \bar{T} = 0^\circ F$



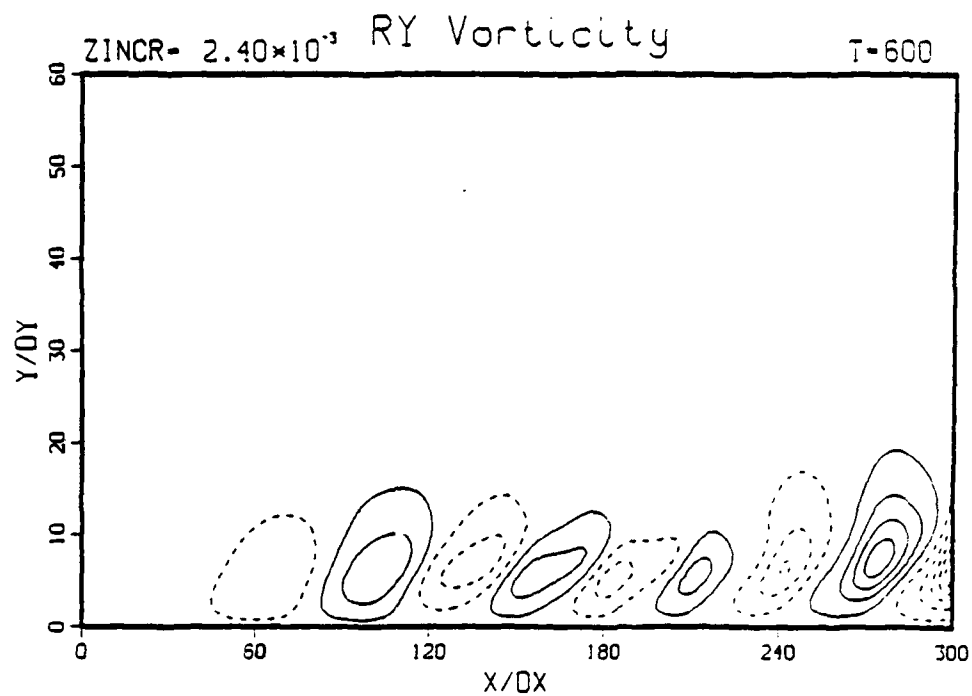
f) spanwise velocity,  $w$ ,  $z = \lambda_z/4$  and  $\Delta \bar{T} = 15^\circ F$

Figure 6.84 continued

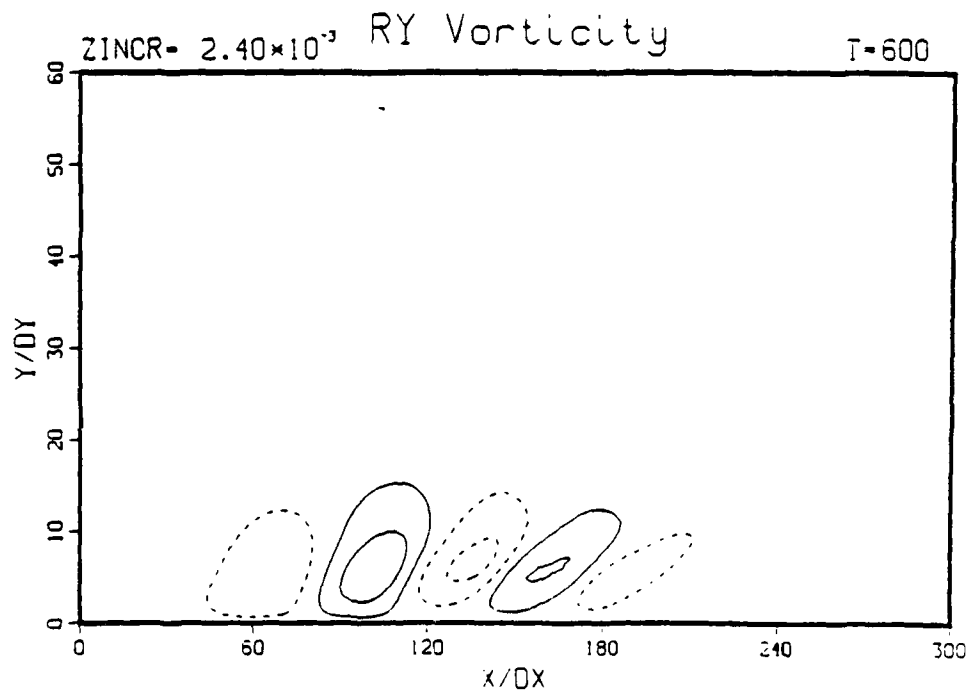


h) streamwise vorticity,  $\omega_z$ ,  $z = \lambda_z/4$  and  $\Delta \bar{T} = 15^\circ F$

Figure 6.84 continued

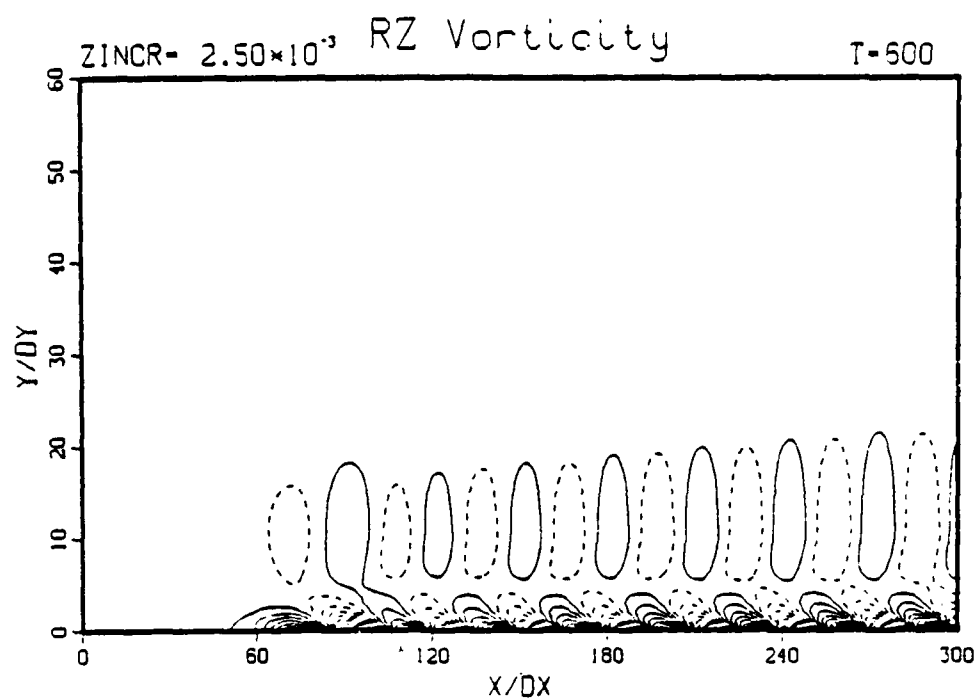


i) normal vorticity,  $\omega_y$ ,  $z = \lambda_z/4$  and  $\Delta \bar{T} = 0^\circ F$

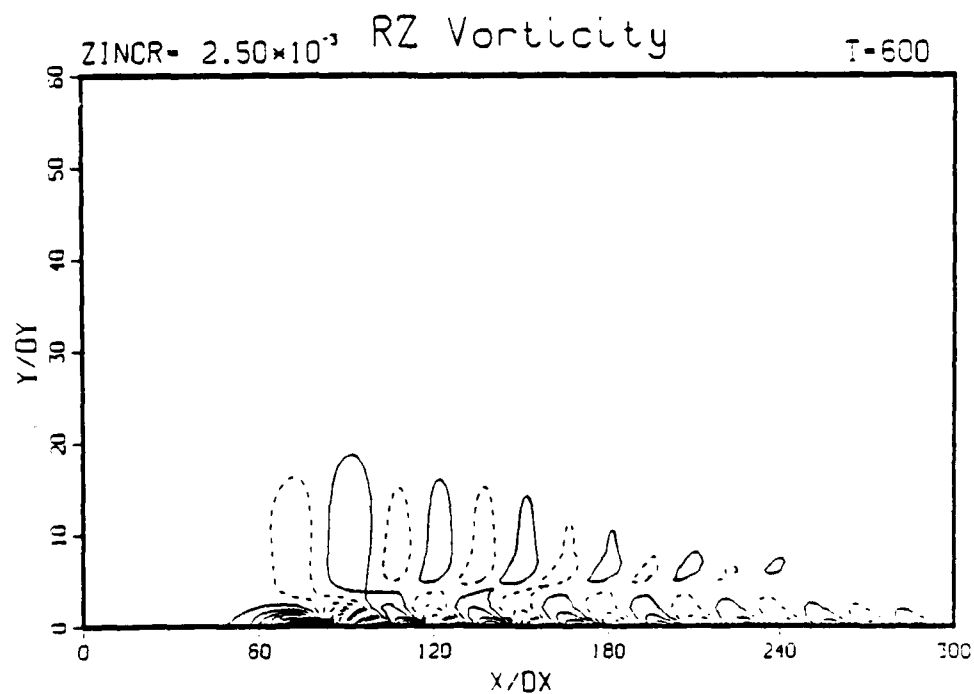


j) normal vorticity,  $\omega_y$ ,  $z = \lambda_z/4$  and  $\Delta \bar{T} = 15^\circ F$

Figure 6.84 continued

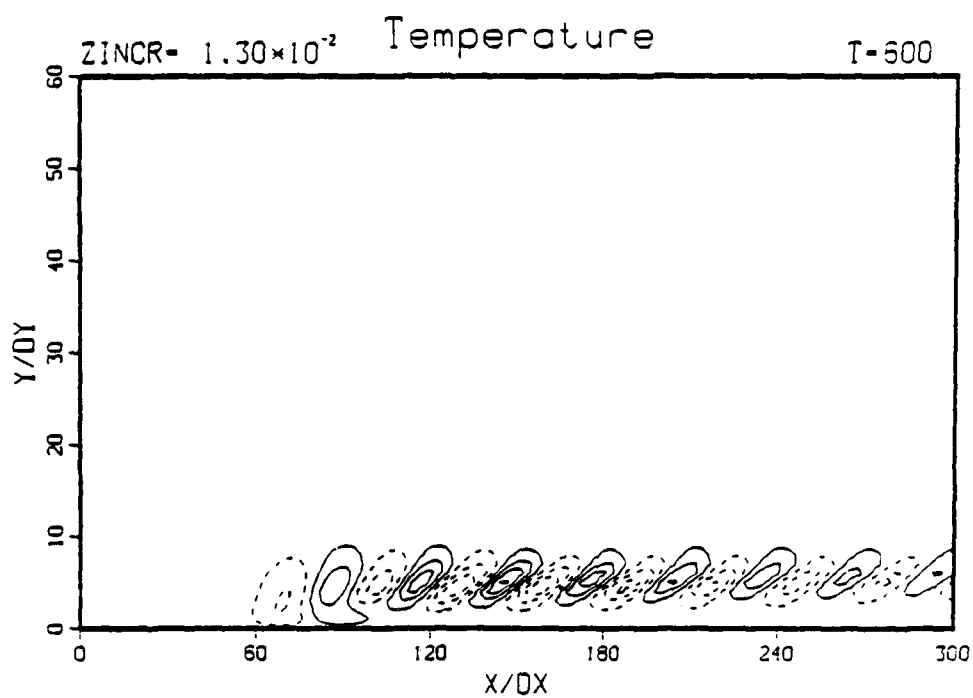


k) spanwise vorticity,  $\omega_z$ ,  $z = 0$  and  $\Delta \bar{T} = 0^\circ F$



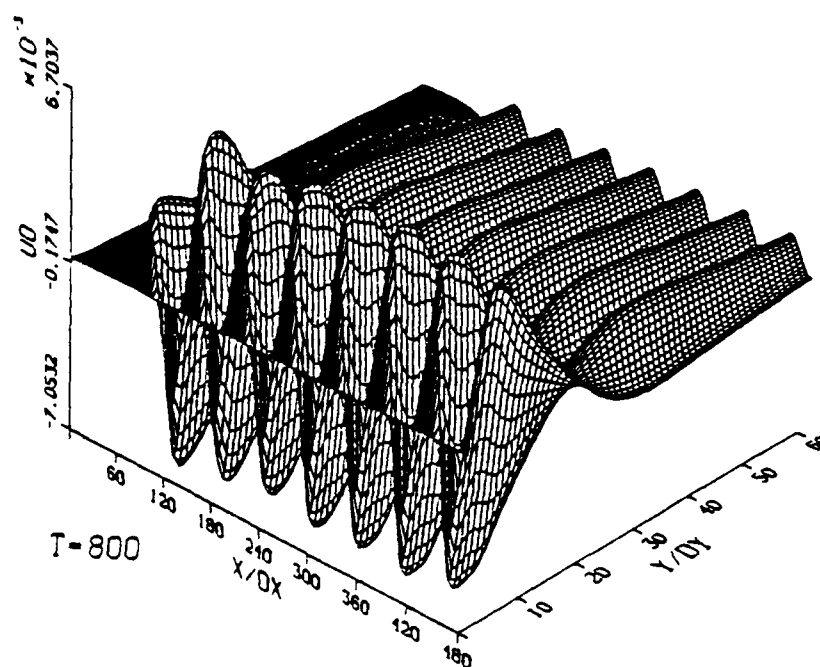
l) spanwise vorticity,  $\omega_z$ ,  $z = 0$  and  $\Delta \bar{T} = 15^\circ F$

Figure 6.84 continued

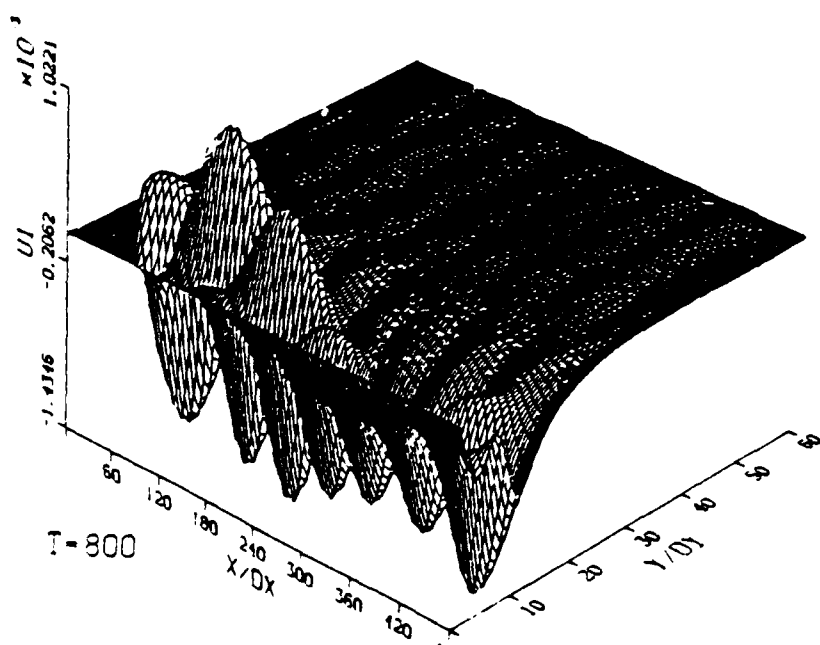


m) temperature,  $T$ ,  $z = 0$  and  $\Delta \bar{T} = 15^\circ F$

Figure 6.84 continued



a) 2D streamwise velocity,  $U_0$



b) 3D streamwise velocity,  $U_1^{180}$

Figure 6.85 Disturbed flow for fundamental breakdown with two-dimensional active control applied,  $F_{2D} = 0.588$ ,  $F_{3D} = 0.588$

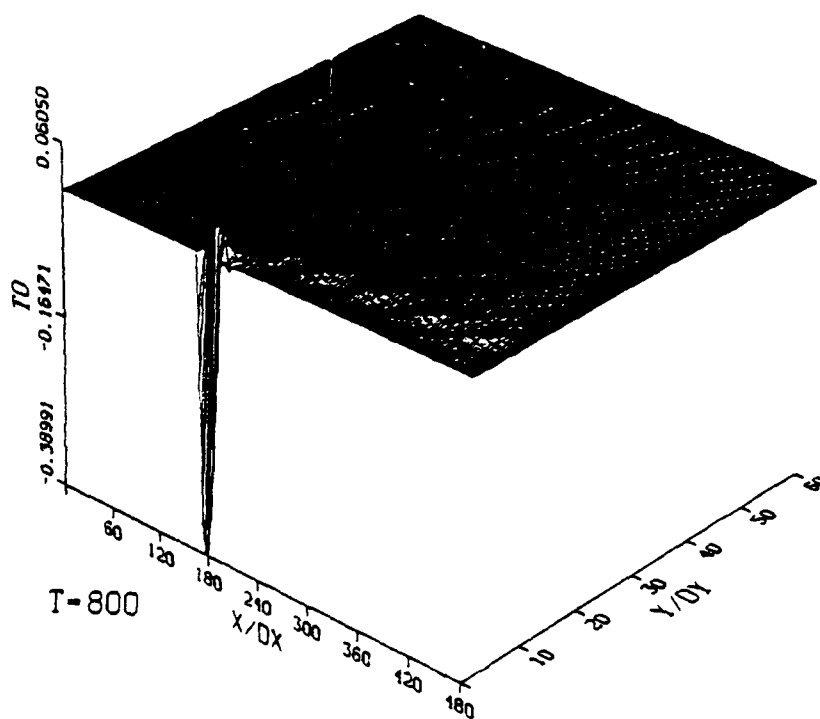
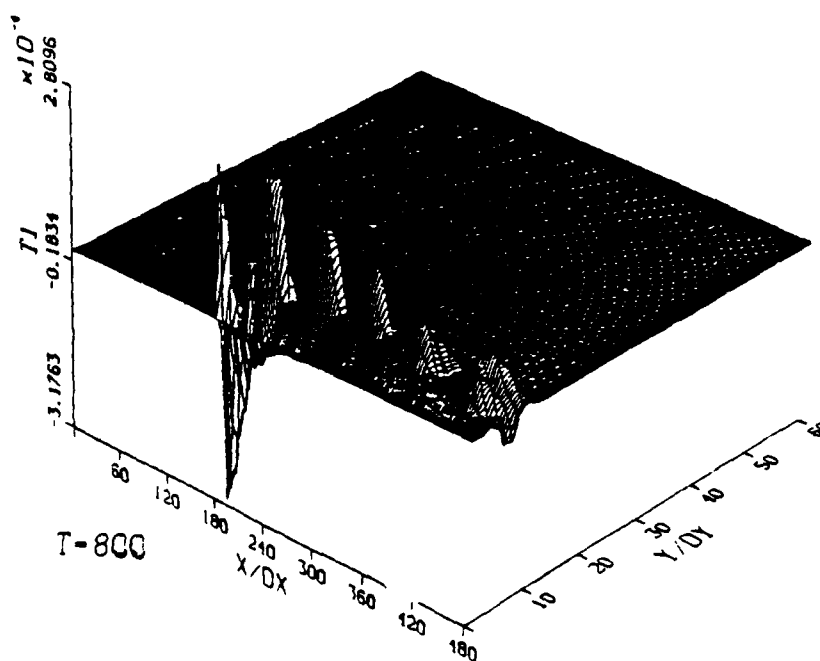
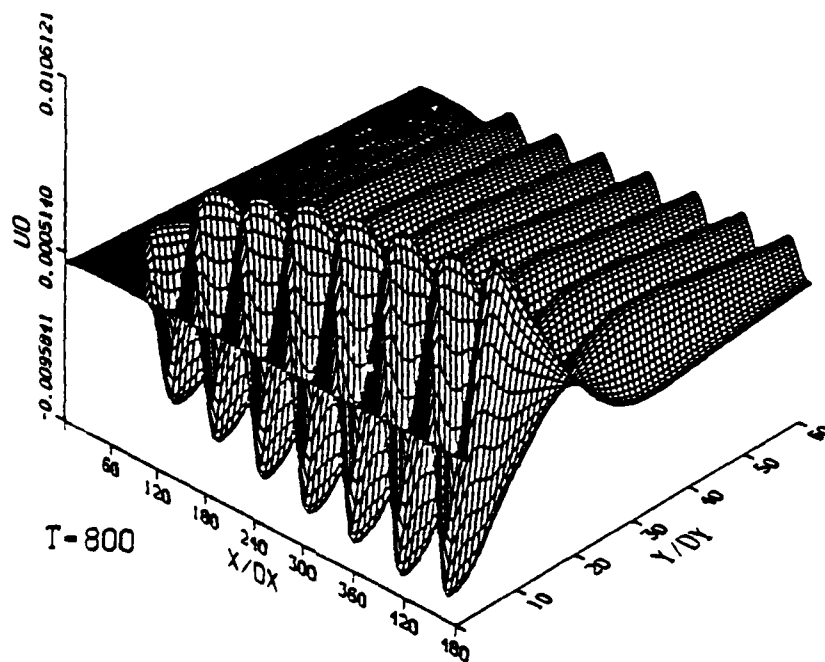
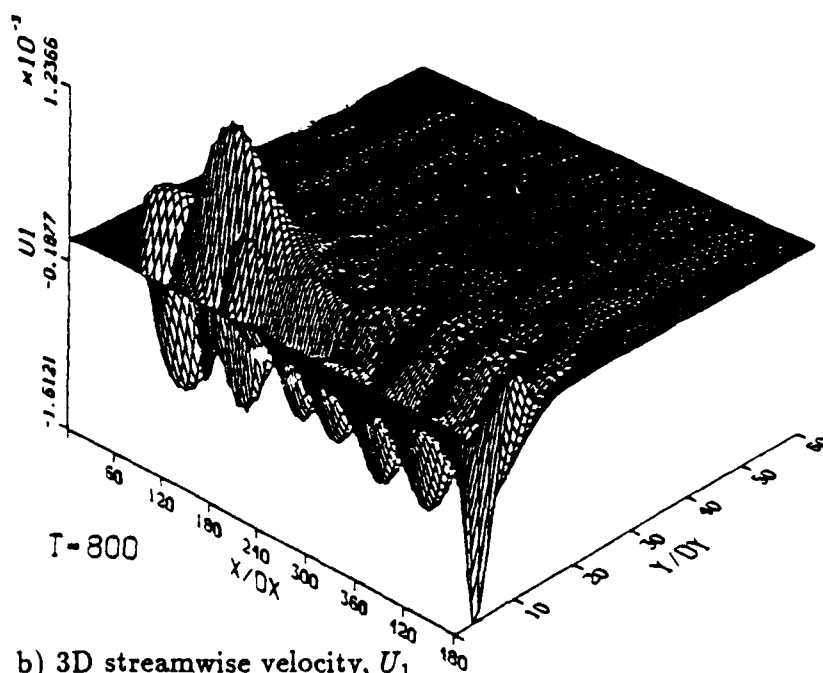
c) 2D temperature,  $\Theta_0$ d) 3D temperature,  $\Theta_1$ 

Figure 6.85 continued





a) 2D streamwise velocity,  $U_0$



b) 3D streamwise velocity,  $U_1$

Figure 6.86 Disturbed flow for fundamental breakdown with three-dimensional active control applied,  $F_{2D} = 0.588$ ,  $F_{3D} = 0.588$

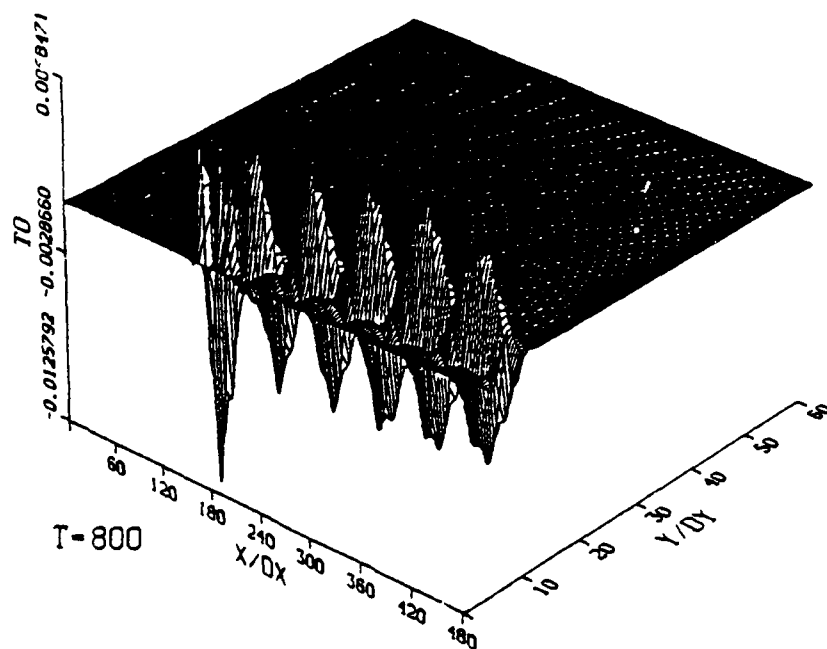
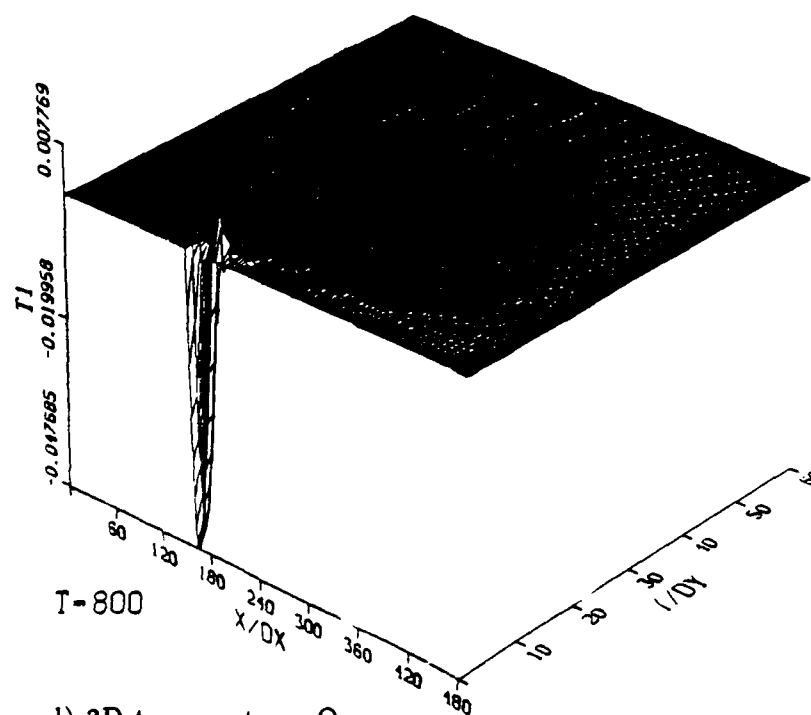
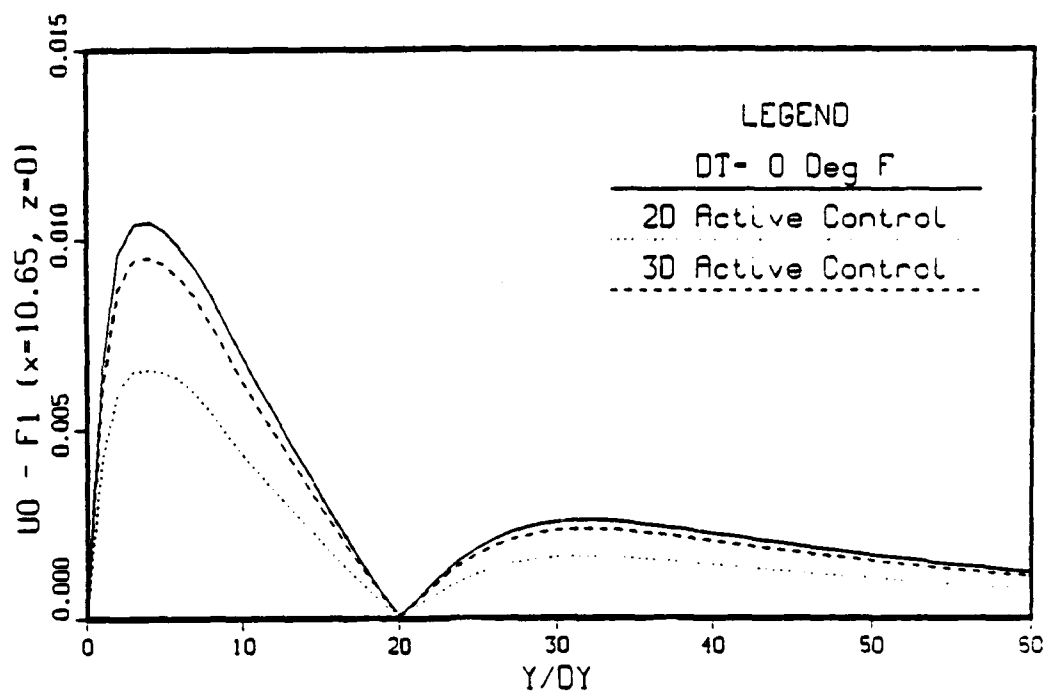
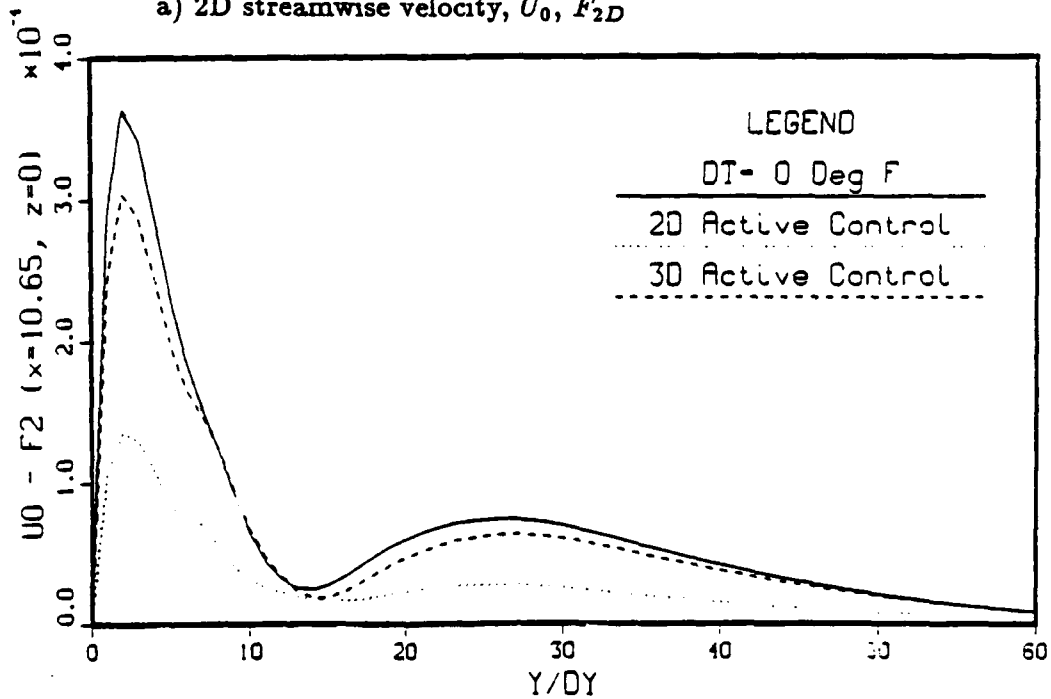
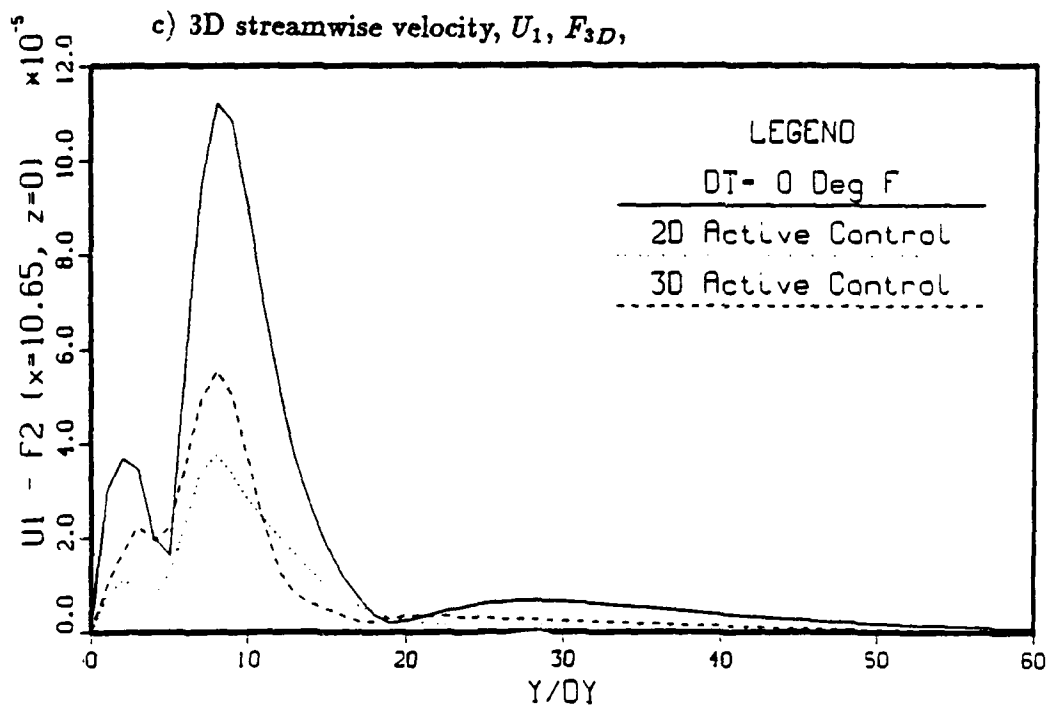
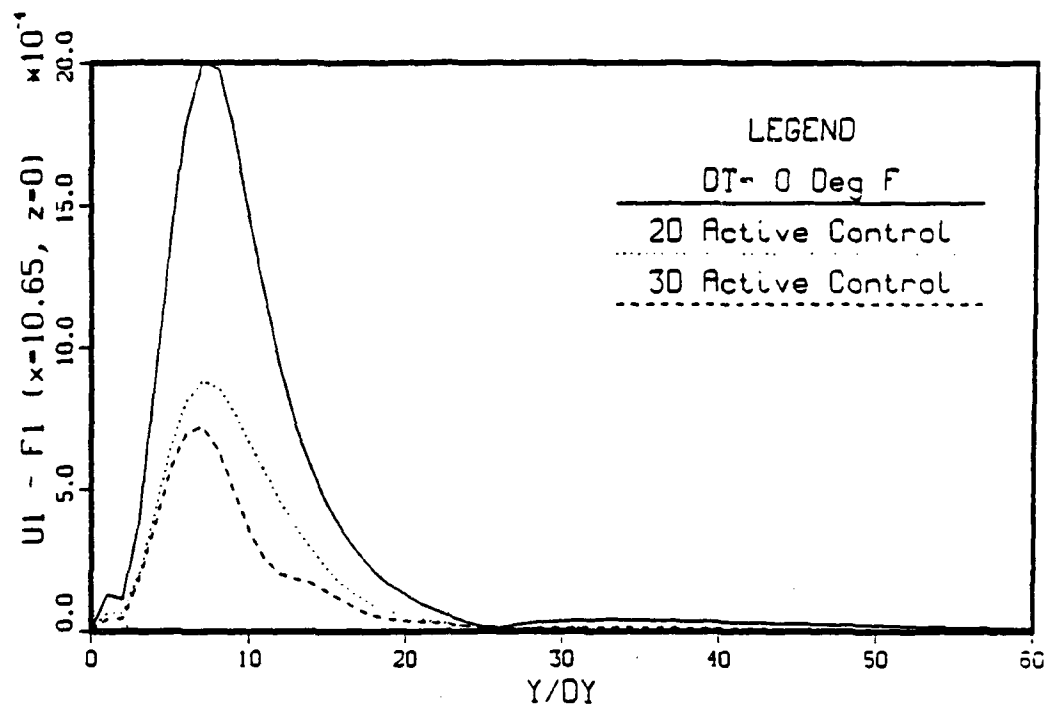
c) 2D temperature,  $\Theta_0$ d) 3D temperature,  $\Theta_1$ 

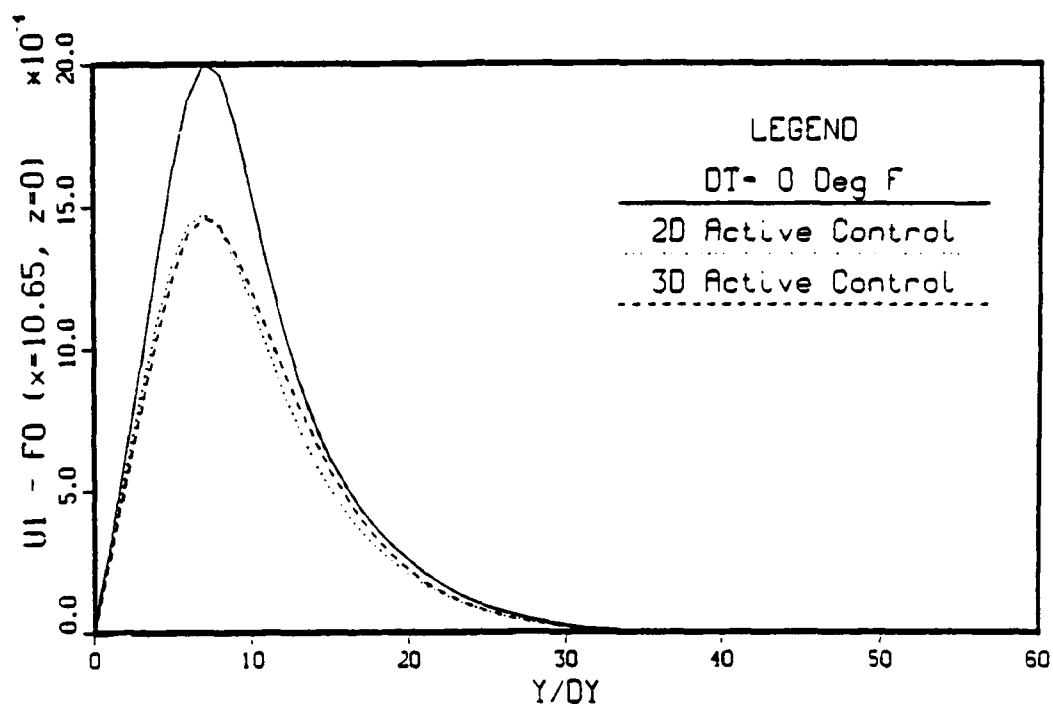
Figure 6.86 continued

a) 2D streamwise velocity,  $U_0, F_{2D}$ b) 2D streamwise velocity,  $U_0, 2 F_{2D}$ Figure 6.87 Amplitude comparison at  $x = 10.65$  for fundamental breakdown with active control applied



d) 3D streamwise velocity,  $U_1, 2 F_{3D}$ ,

Figure 6.87 continued



e) 3D streamwise velocity,  $U_1$ , mean component

Figure 6.87 continued

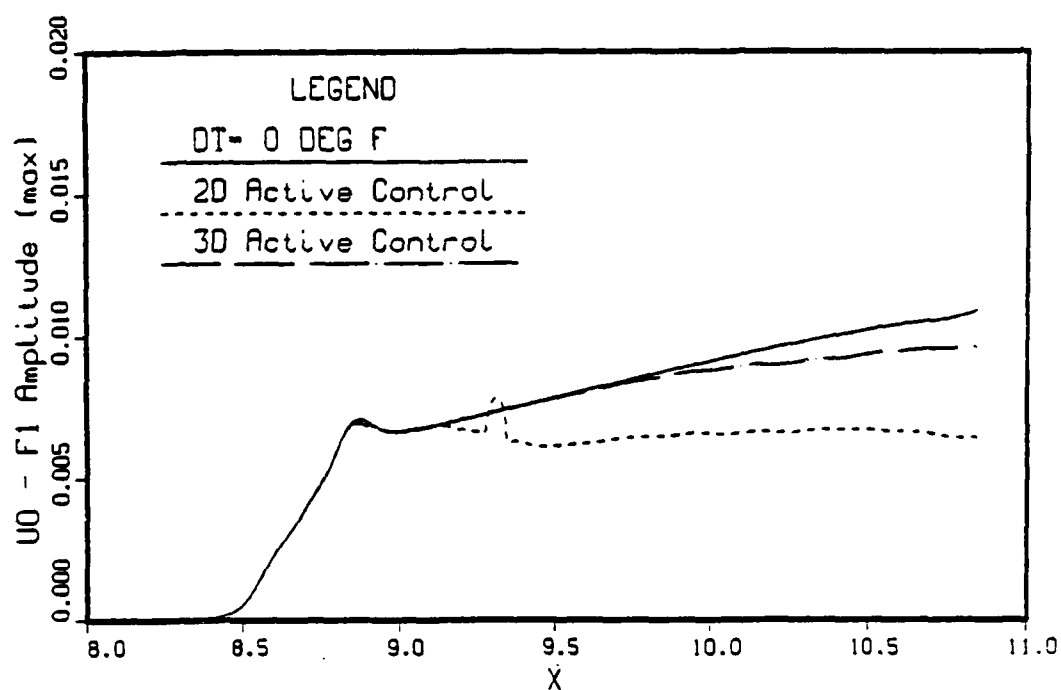
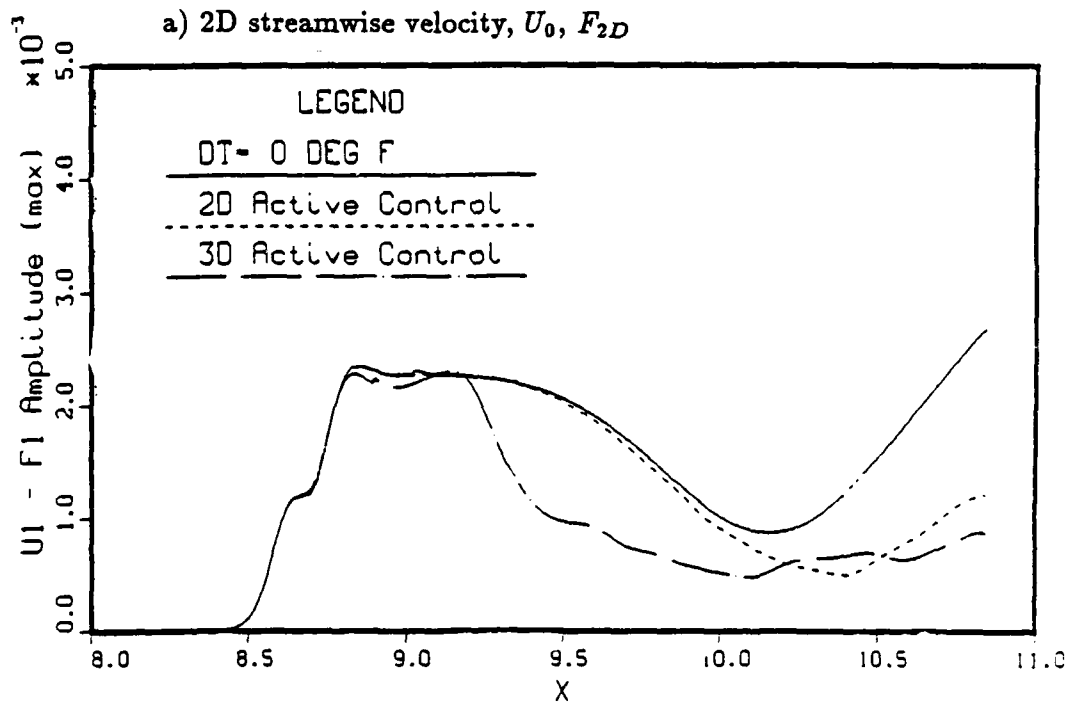
a) 2D streamwise velocity,  $U_0$ ,  $F_{2D}$ b) 3D streamwise velocity,  $U_1$ ,  $F_{3D}$ 

Figure 6.88 Influence of active control on the amplitude growth for fundamental breakdown

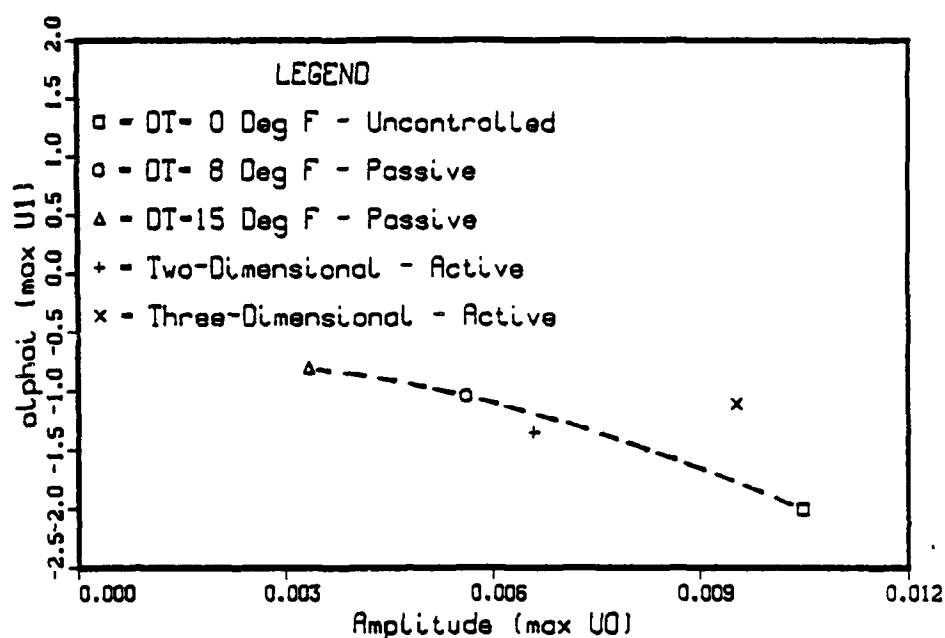


Figure 6.89 Influence of the two-dimensional amplitude level on the three-dimensional growth rate for both passive and active control of fundamental breakdown (quantities based on the maximum of the  $U_0$  and  $U_1$  velocities)

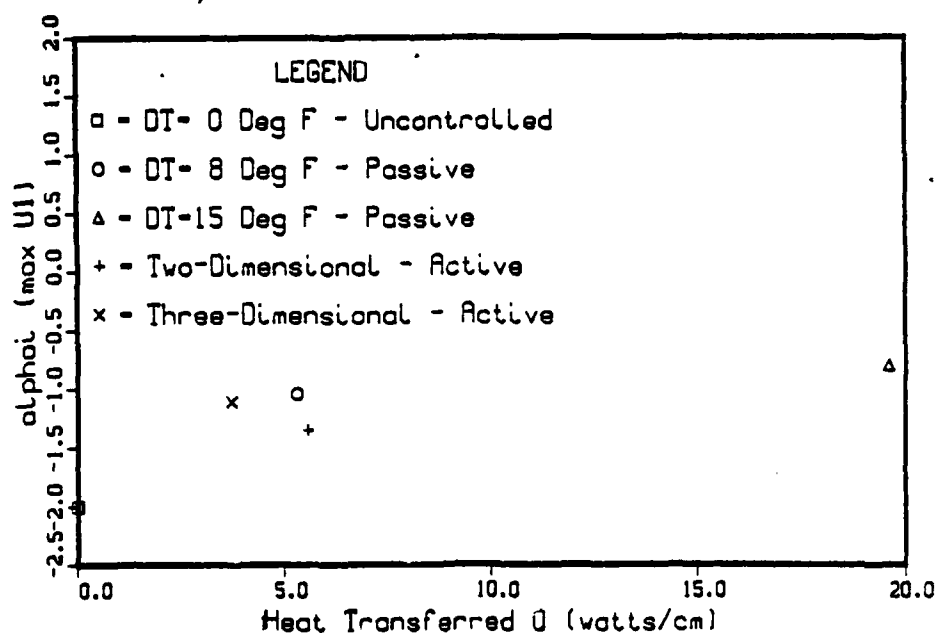
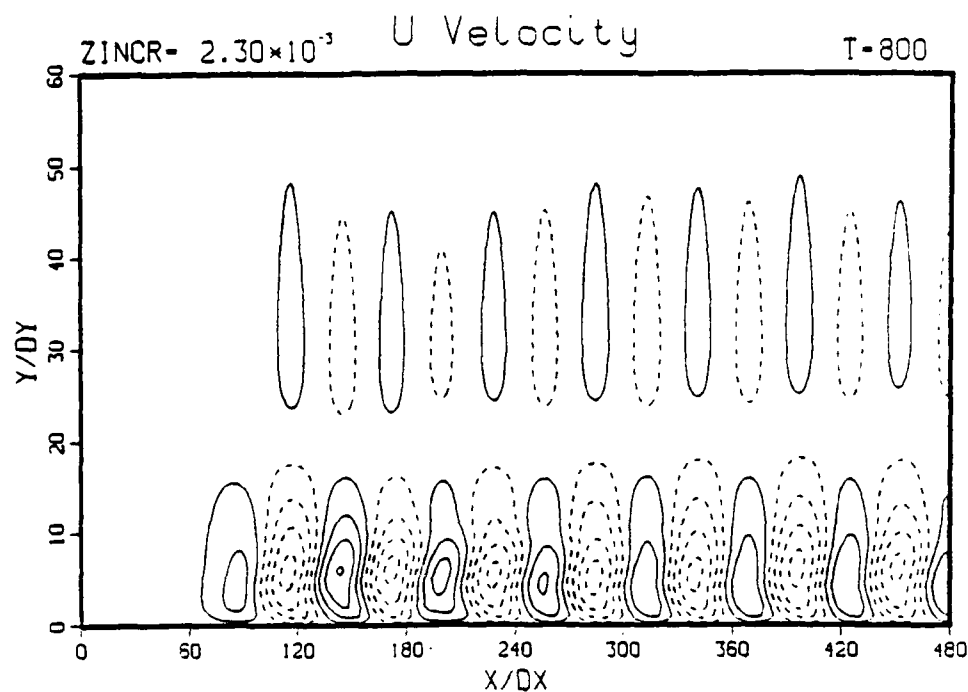
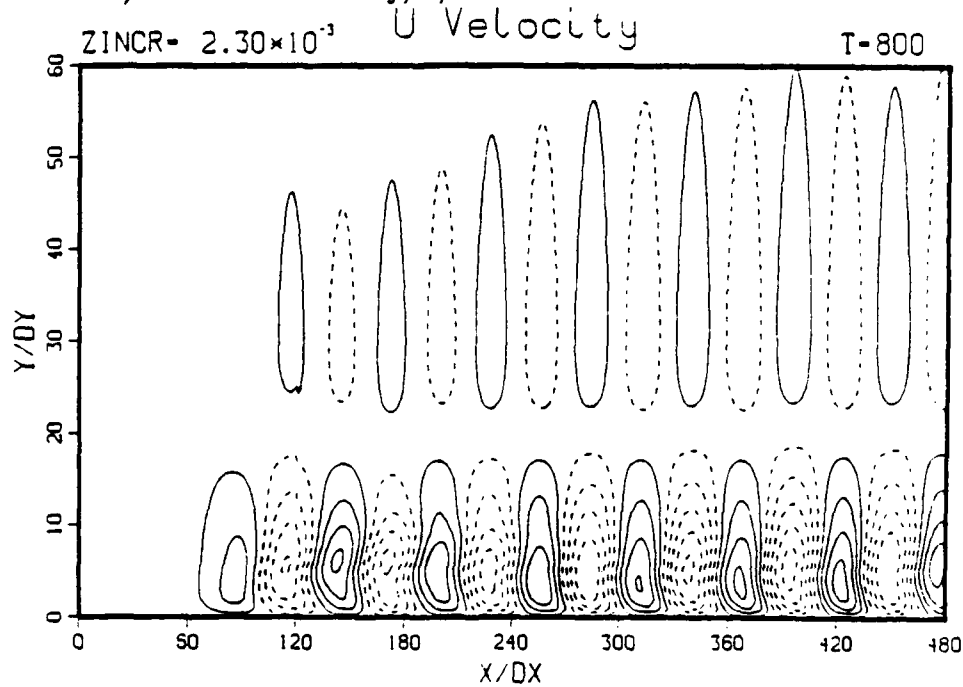


Figure 6.90 Comparison of heat transferred versus the three-dimensional growth rates for both passive and active control of fundamental breakdown



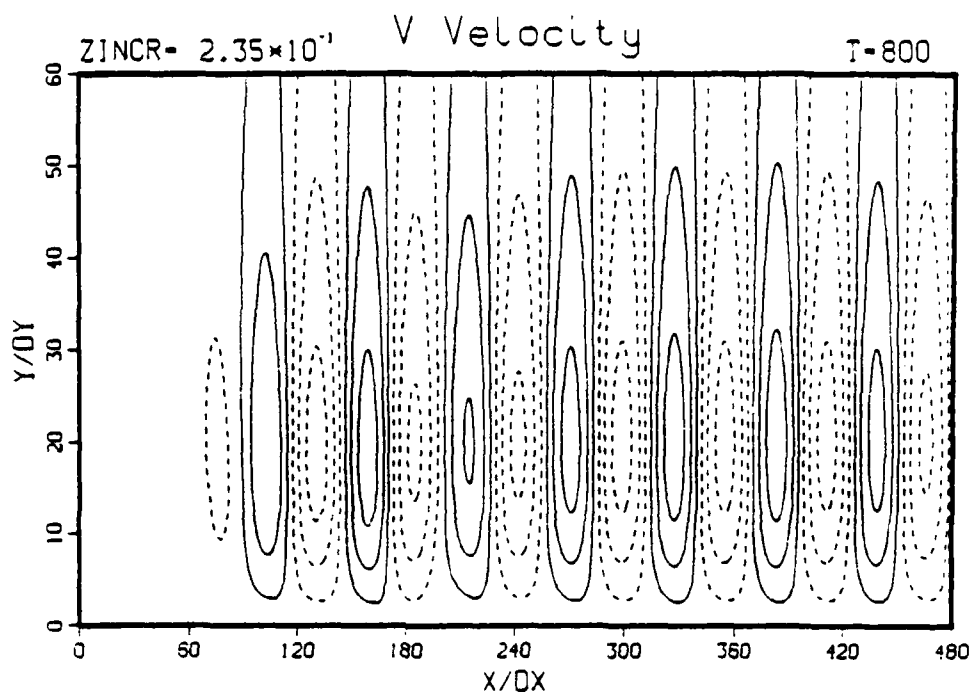
a) streamwise velocity,  $u$ ,  $z = 0$  and 2D active control



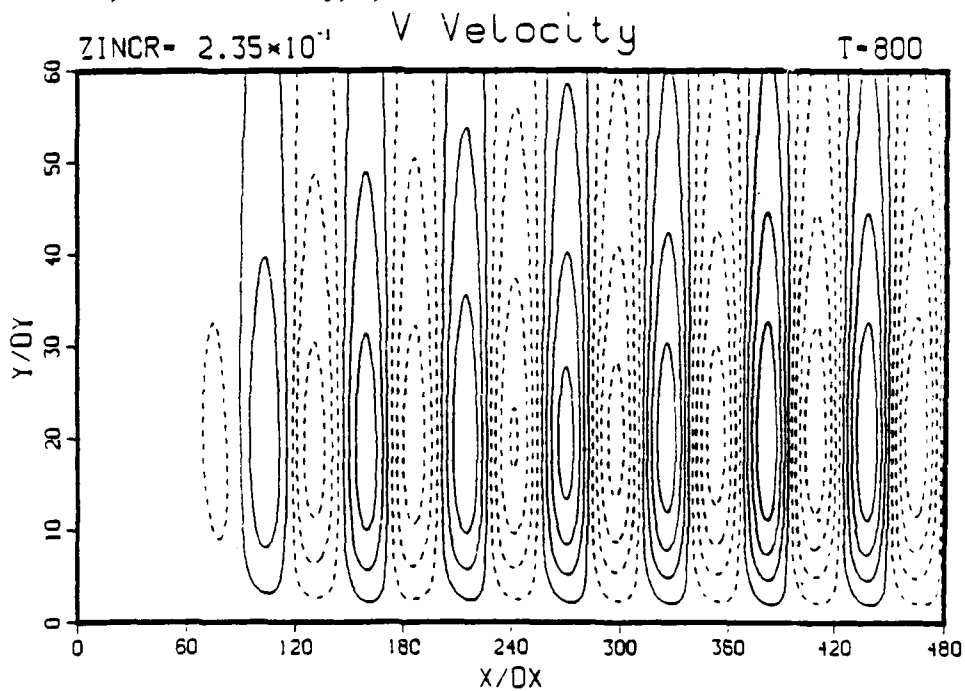
b) streamwise velocity,  $u$ ,  $z = 0$  and 3D active control

Figure 6.91 Comparison of the disturbed flow for fundamental breakdown with two-dimensional or three-dimensional active control applied at the peak plane in the spanwise direction



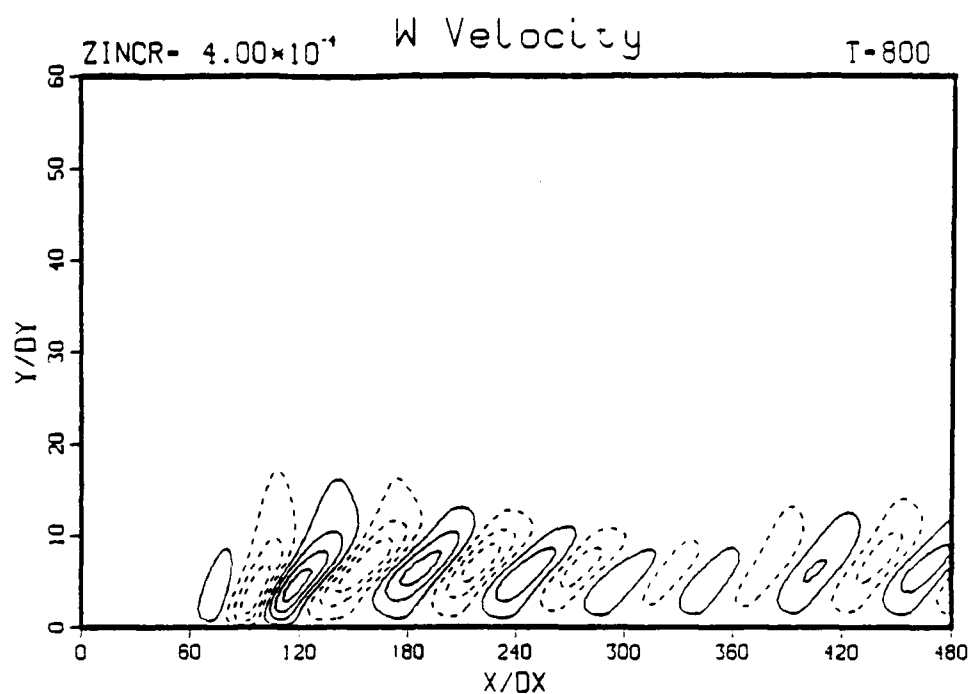


c) normal velocity,  $v$ ,  $z = 0$  and 2D active control

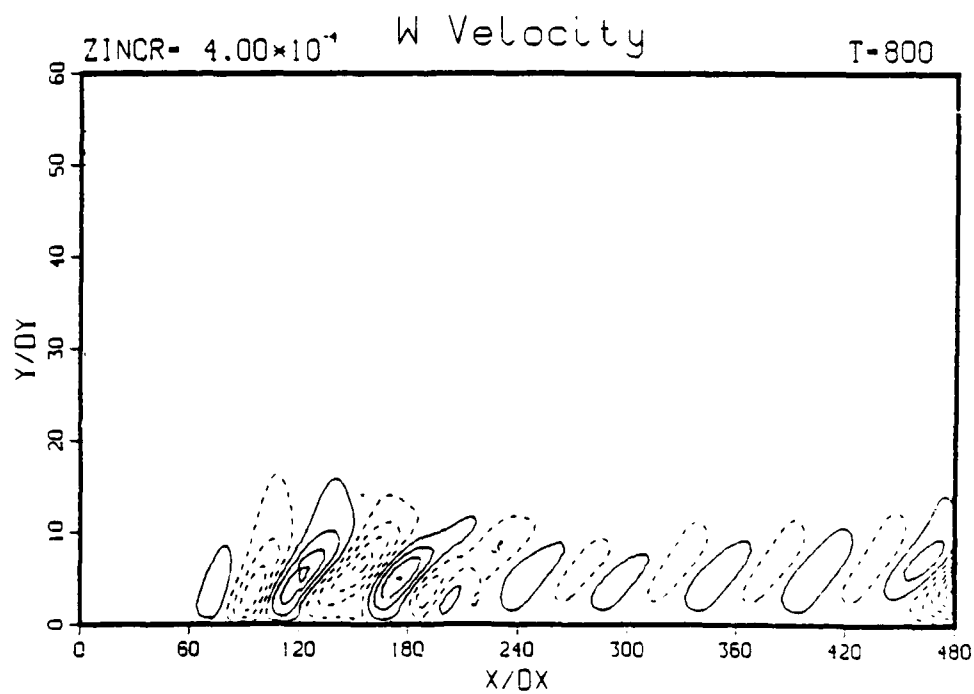


d) normal velocity,  $v$ ,  $z = 0$  and 3D active control

Figure 6.91 continued

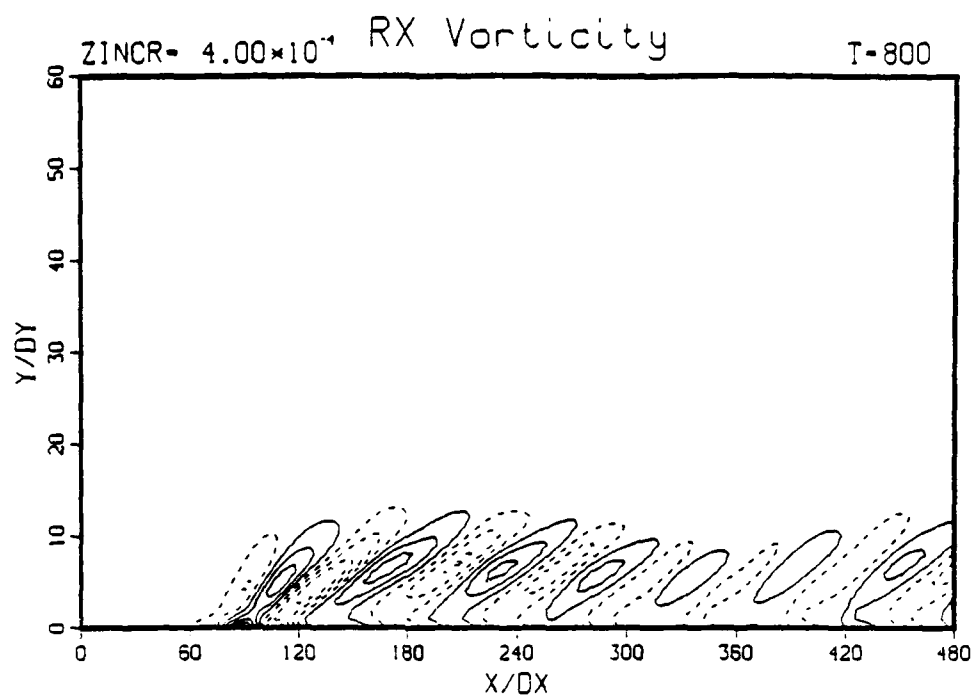


e) spanwise velocity,  $w$ ,  $z = \lambda_z/4$  and 2D active control

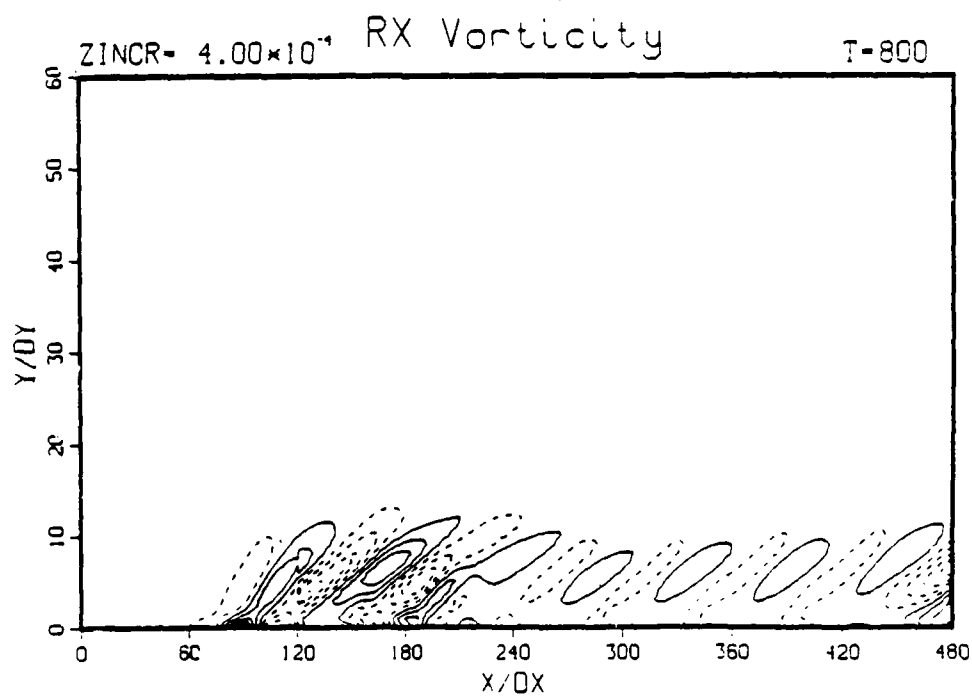


f) spanwise velocity,  $w$ ,  $z = \lambda_z/4$  and 3D active control

Figure 6.91 continued

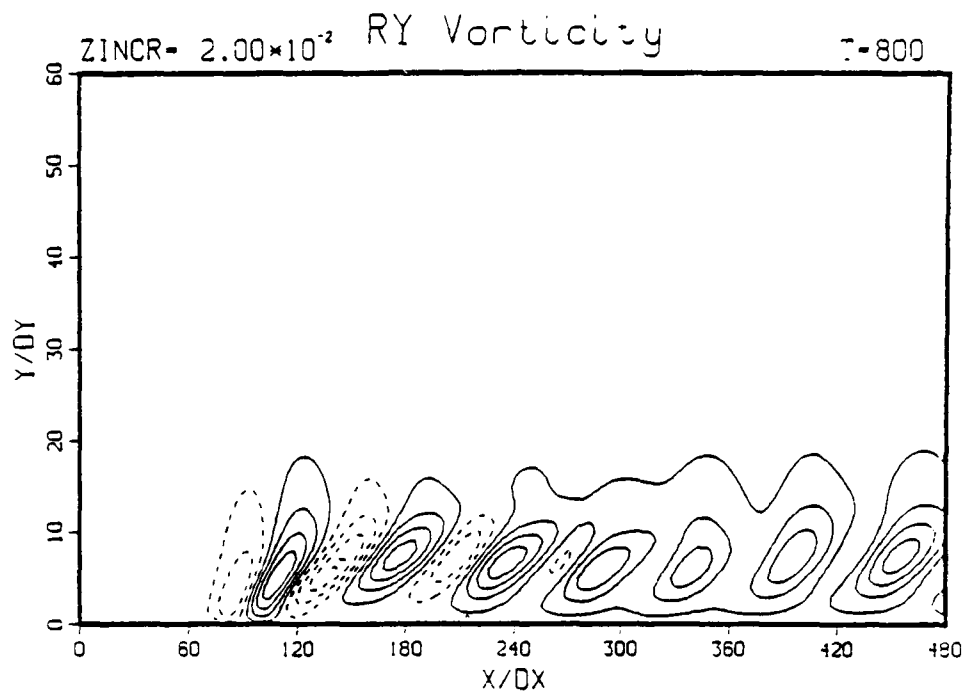


g) streamwise vorticity,  $\omega_x$ ,  $z = \lambda_z/4$  and 2D active control

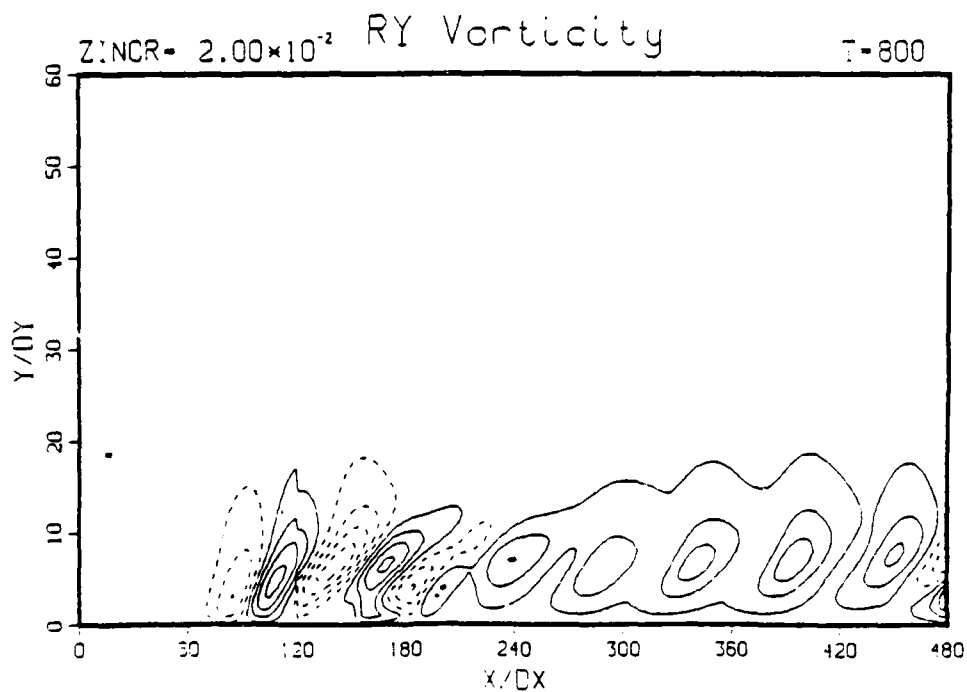


h) streamwise vorticity,  $\omega_x$ ,  $z = \lambda_z/4$  and 3D active control

Figure 6.91 continued



i) normal vorticity,  $\omega_y$ ,  $z = \lambda_z/4$  and 2D active control



j) normal vorticity,  $\omega_y$ ,  $z = \lambda_z/4$  and 3D active control

Figure 6.91 continued

AD-A204 329

NUMERICAL SIMULATION OF ACTIVE CONTROL OF BOUNDARY  
LAYER TRANSITION(U) ARIZONA UNIV TUCSON DEPT OF  
AEROSPACE AND MECHANICAL ENGINEERING L D KRAL ET AL.  
DEC 88 N00014-84-K-0515

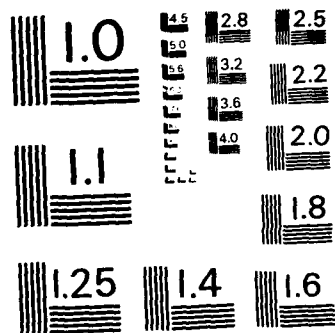
3/3

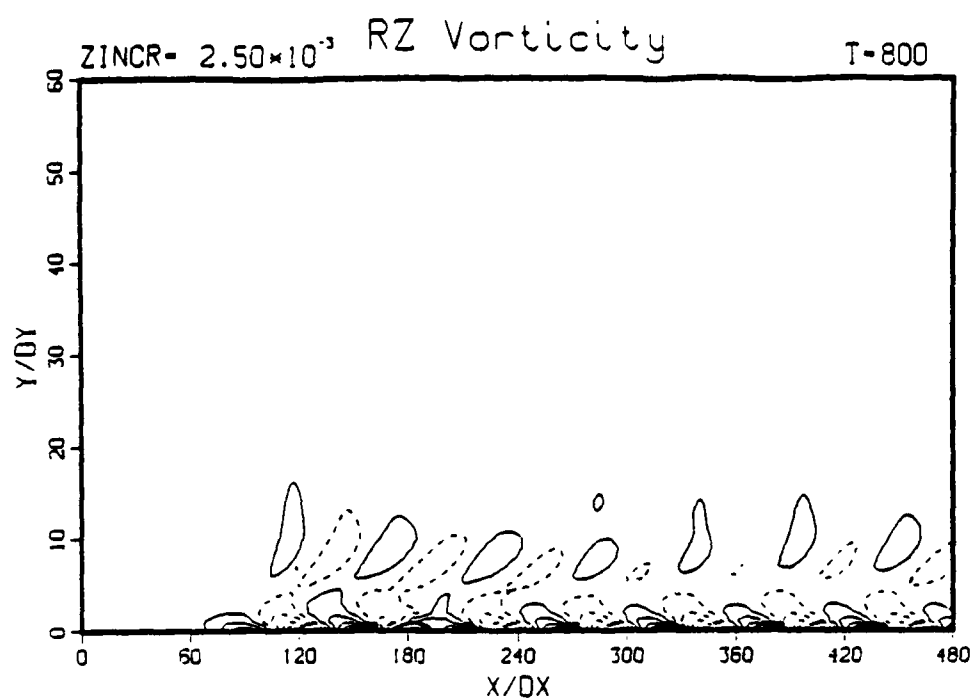
UNCLASSIFIED

F/G 20/4

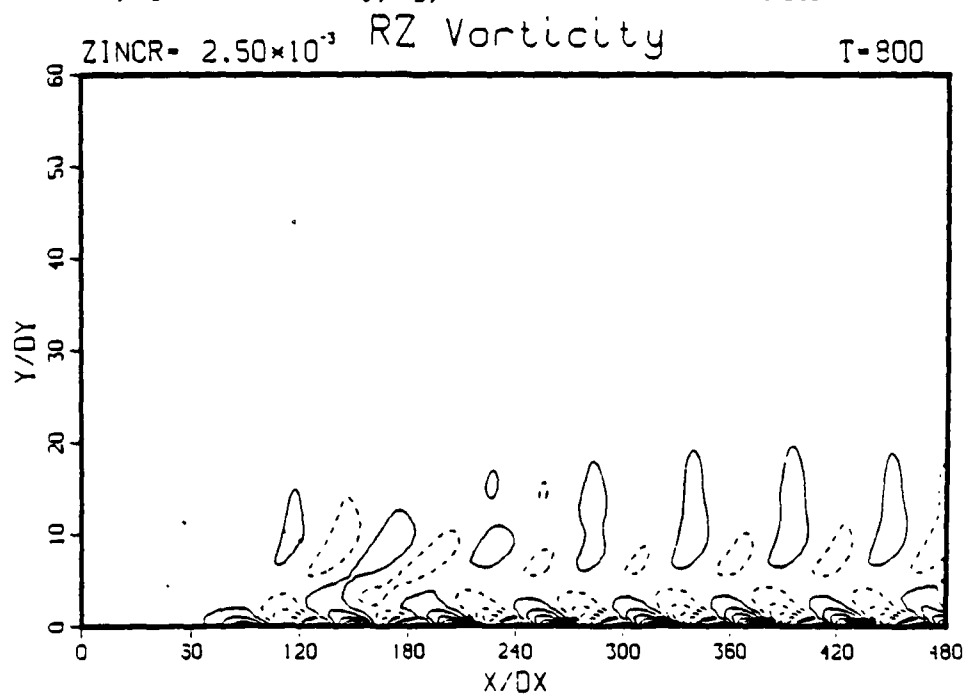
NL





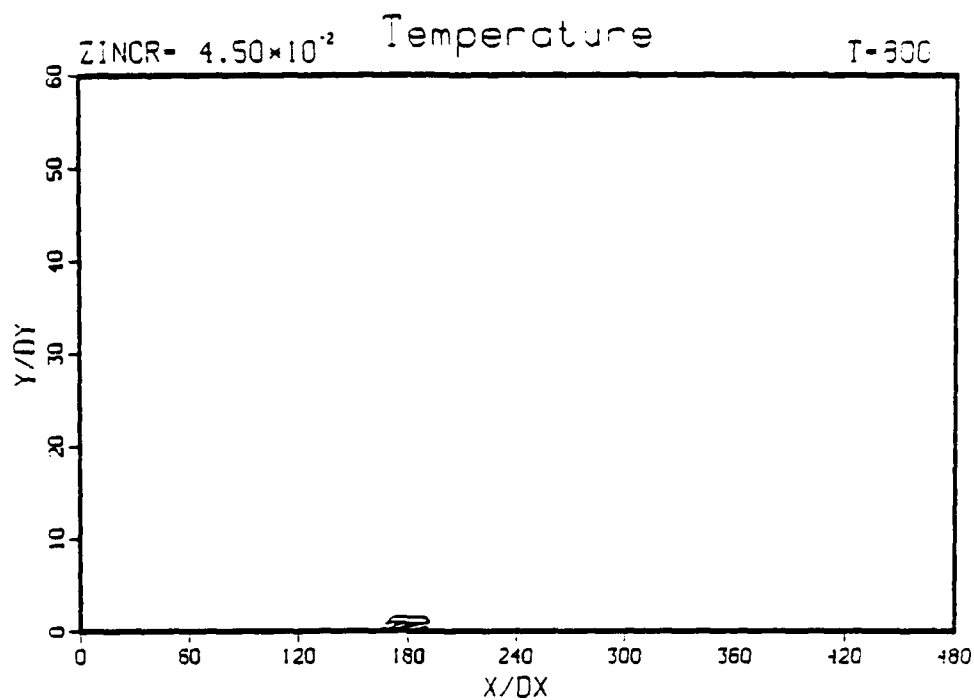


k) spanwise vorticity,  $\omega_z$ ,  $z = 0$  and 2D active control

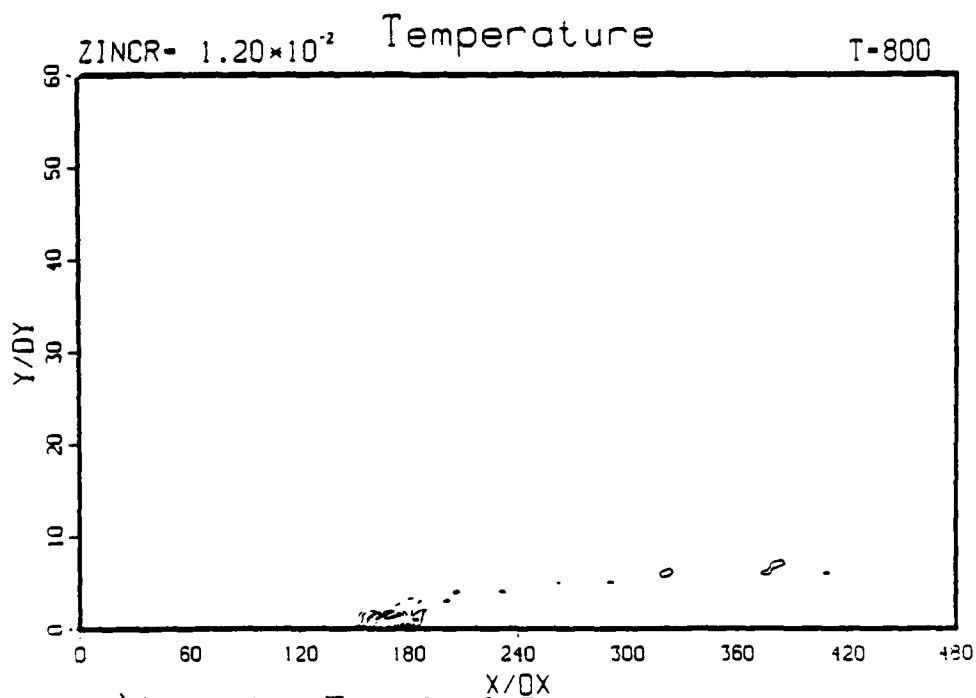


l) spanwise vorticity,  $\omega_z$ ,  $z = 0$  and 3D active control

Figure 6.91 continued



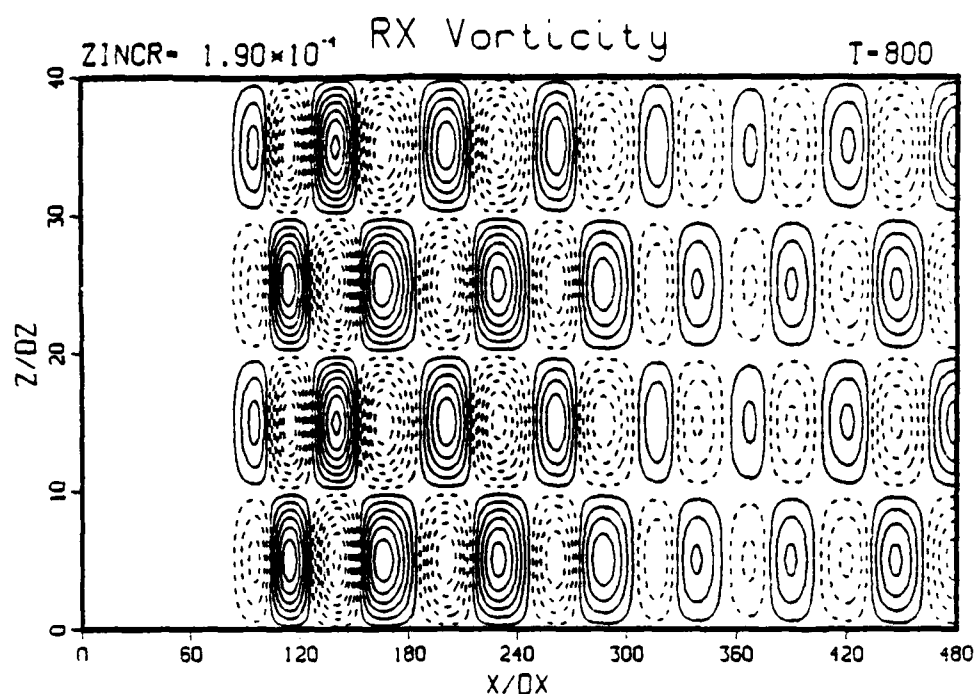
m) temperature,  $T$ ,  $z = 0$  and 2D active control



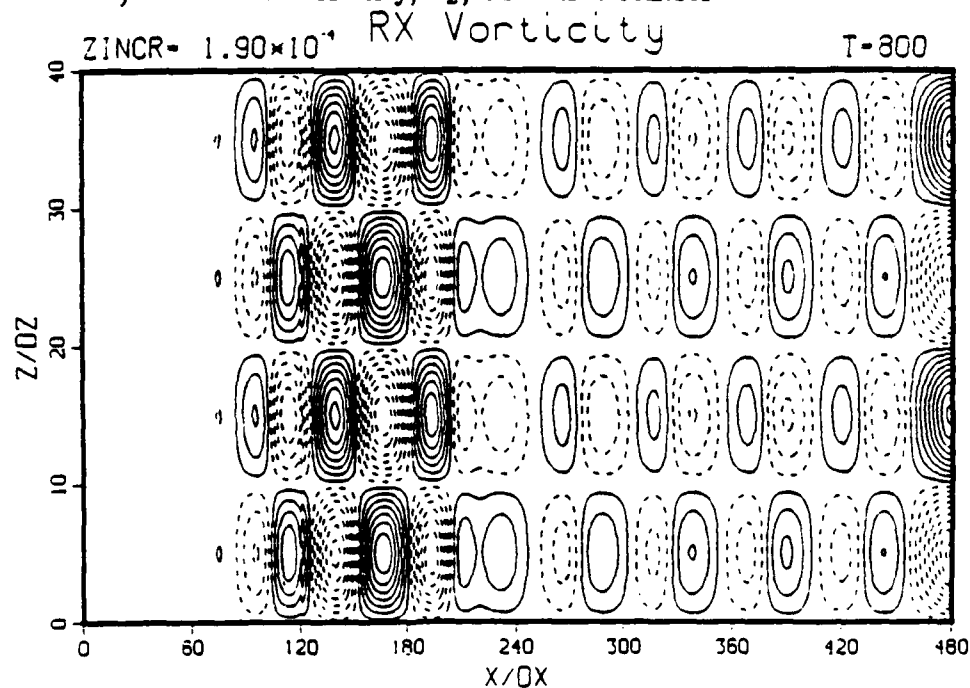
n) temperature,  $T$ ,  $z = 0$  and 3D active control

Figure 6.91 continued



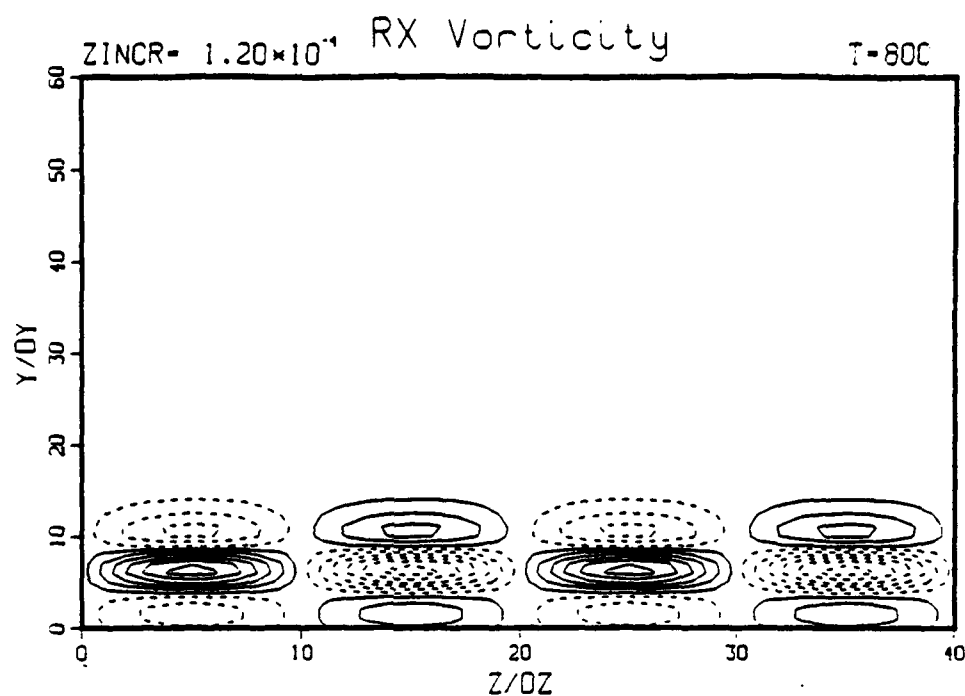


a) streamwise vorticity,  $\omega_z$ , 2D active control

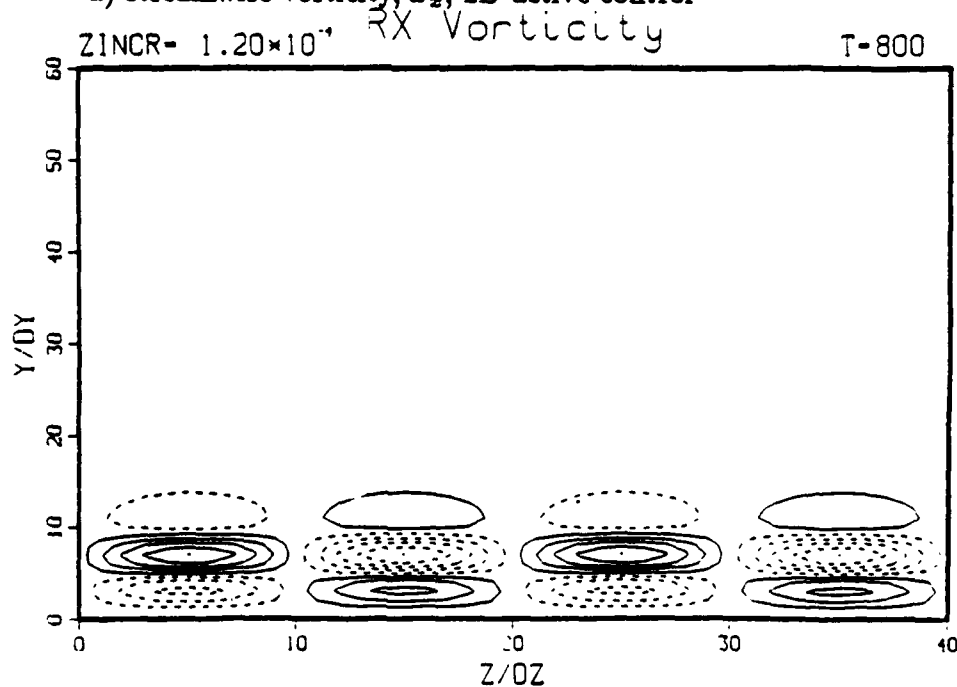


b) streamwise vorticity,  $\omega_z$ , 3D active control

Figure 6.92 Comparison of the disturbed flow for fundamental breakdown with two-dimensional or three-dimensional active control applied at  $y = 3.186$



a) streamwise vorticity,  $\omega_z$ , 2D active control



b) streamwise vorticity,  $\omega_z$ , 3D active control

Figure 6.93 Comparison of the disturbed flow for fundamental breakdown with two-dimensional or three-dimensional active control applied at  $x = 11.0$

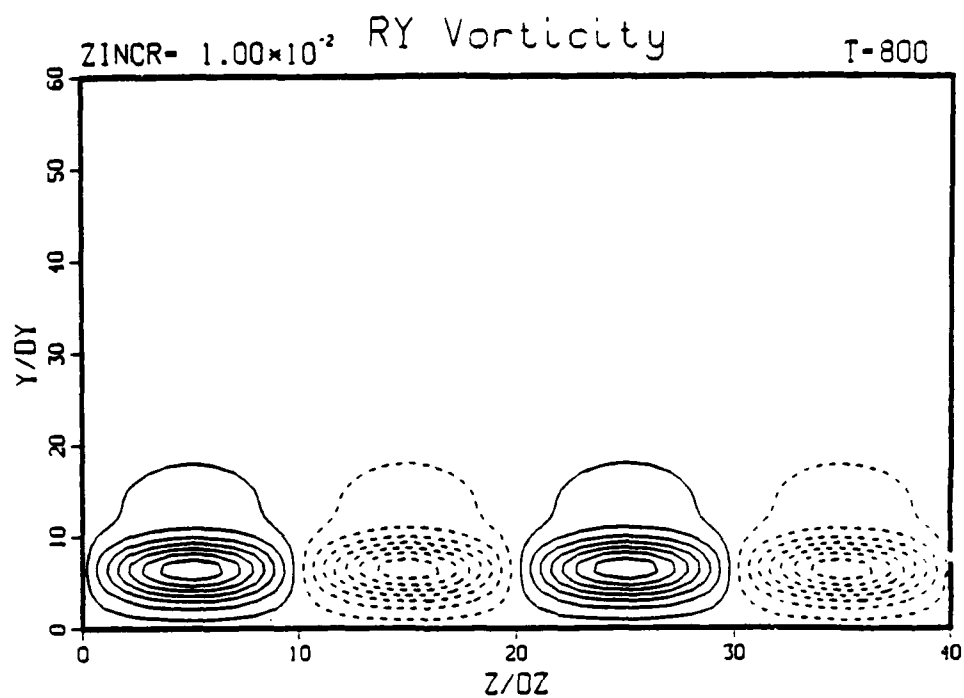
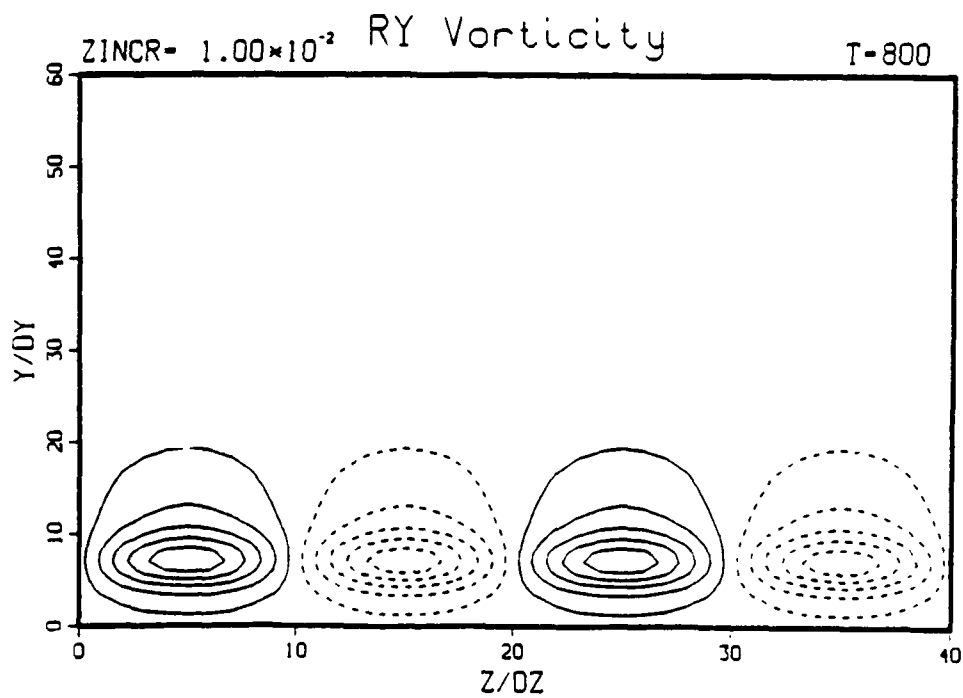
c) normal vorticity,  $\omega_y$ , 2D active controld) normal vorticity,  $\omega_y$ , 3D active control

Figure 6.93 continued

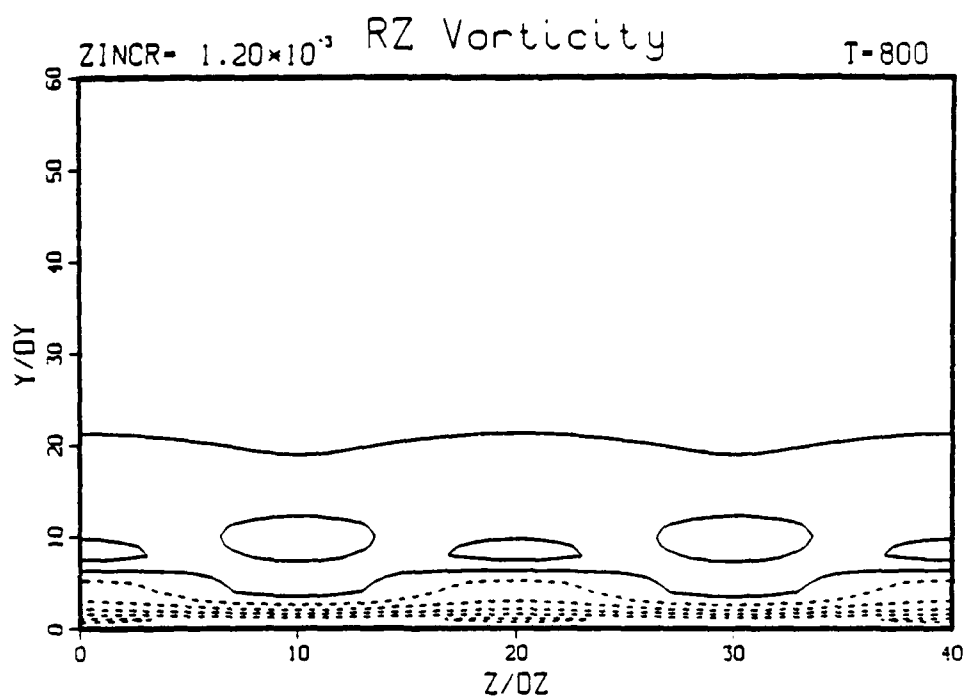
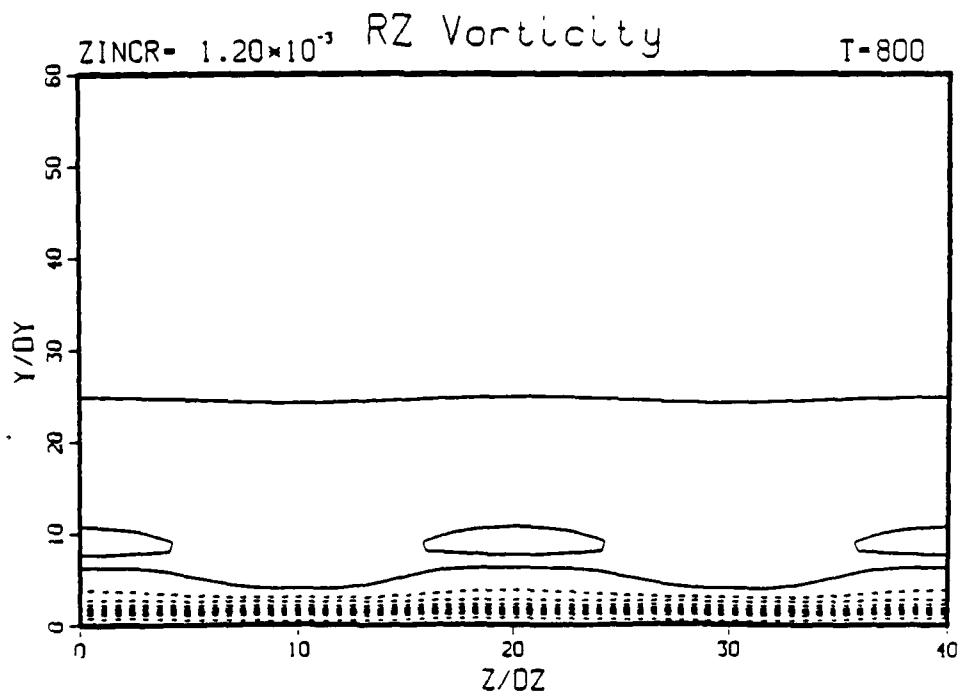
e) spanwise vorticity,  $\omega_z$ , 2D active controlf) spanwise vorticity,  $\omega_z$ , 3D active control

Figure 6.93 continued

## APPENDIX A

SIMILARITY SOLUTION OF THE FLAT PLATE BOUNDARY LAYER  
WITH UNIFORM WALL HEATING

A similarity solution is one in which the velocity profiles at all streamwise  $x$  locations are geometrically similar and differ only by a multiplying factor, i.e.,  $\bar{u}(\bar{x}, \bar{y}) = f[\bar{y} \cdot g(\bar{x})]$  where the normal coordinate is scaled by  $\eta = \bar{y} \cdot g(\bar{x})$ . Then  $\bar{u} = f(\eta)$ . The bars again denote dimensional quantities. The partial differential equation is reduced to an ordinary differential equation.

The similarity solution for a heated boundary layer with variable viscosity is used in this work. The method for obtaining this similarity solution is now presented. The two dimensional boundary layer equations, including the viscosity variation with temperature, are

$$\frac{\partial \bar{u}}{\partial \bar{x}} + \frac{\partial \bar{v}}{\partial \bar{y}} = 0 \quad (\text{A.1})$$

$$\bar{u} \frac{\partial \bar{u}}{\partial \bar{x}} + \bar{v} \frac{\partial \bar{u}}{\partial \bar{y}} = \bar{\nu} \frac{\partial^2 \bar{u}}{\partial \bar{y}^2} + \frac{\partial \bar{\nu}}{\partial \bar{y}} \frac{\partial \bar{u}}{\partial \bar{y}} \quad (\text{A.2})$$

$$\bar{u} \frac{\partial \bar{T}}{\partial \bar{x}} + \bar{v} \frac{\partial \bar{T}}{\partial \bar{y}} = \frac{1}{Pr} \frac{\partial^2 \bar{T}}{\partial \bar{y}^2} \quad (\text{A.3})$$

These equations are the steady state boundary layer equations for a flat plate. The same assumptions that were made in Chapter 3 are made here in regards to neglecting buoyancy, viscous dissipation, and all variable fluid properties except viscosity.

The similarity variable  $\eta$  and a stream function  $\bar{\psi}$  are defined as follows:

$$\eta = \bar{y} \sqrt{\frac{\bar{U}_\infty}{\bar{\nu}_\infty \bar{x}}} \quad (\text{A.4})$$

$$\bar{\psi}(\bar{x}, \bar{y}) = \sqrt{\bar{\nu}_\infty \bar{U}_\infty \bar{x}} f(\eta) \quad (\text{A.5})$$

where  $f$  is an unknown function of  $\eta$ . Expressions for the velocities can then be derived from the definition of the stream function:

$$\bar{u} = \frac{\partial \bar{\psi}}{\partial \bar{y}} = \bar{U}_\infty f'(\eta) \quad (\text{A.6})$$

$$\bar{v} = -\frac{\partial \bar{\psi}}{\partial \bar{x}} = \frac{1}{2} \sqrt{\frac{\bar{\nu}_\infty \bar{U}_\infty}{\bar{x}}} [\eta f'(\eta) - f(\eta)] . \quad (\text{A.7})$$

The vorticity  $\bar{\omega}_z$  is also derived from the stream function as follows:

$$\begin{aligned} \bar{\omega}_z &= \frac{\partial \bar{u}}{\partial \bar{y}} - \frac{\partial \bar{v}}{\partial \bar{x}} \\ &= \sqrt{\frac{\bar{U}_\infty}{\bar{\nu}_\infty \bar{x}}} \left\{ f''(\eta) + \frac{\bar{\nu}_\infty}{4\bar{x}} [\eta^2 f''(\eta) + \eta f'(\eta) - f(\eta)] \right\} . \end{aligned} \quad (\text{A.8})$$

The primes in the above equations denote differentiation with respect to  $\eta$ . Introducing definitions (A.4), (A.6), and (A.7) into equations (A.2) and (A.3) yields the following two nonlinear ordinary differential equations for  $f$  and  $T$ :

$$\frac{\bar{\nu}(\eta)}{\bar{\nu}_\infty} f'''(\eta) + \frac{1}{2} f(\eta) f''(\eta) + \frac{\bar{\nu}'(\eta)}{\bar{\nu}_\infty} f''(\eta) = 0 \quad (\text{A.9})$$

$$T'''(\eta) + \frac{Pr}{2} f(\eta) T'(\eta) = 0 . \quad (\text{A.10})$$

The temperature and viscosity in the flat plate also satisfy the similarity conditions and can be rewritten in nondimensional form as

$$H(\eta) = \frac{\bar{T}(\bar{x}, \bar{y}) - \bar{T}_\infty}{\bar{T}_w - \bar{T}_\infty} \quad (\text{A.11})$$

$$\nu(\eta) = \frac{\bar{\nu}(\bar{x}, \bar{y})}{\bar{\nu}_\infty} . \quad (\text{A.12})$$

Introducing the nondimensional temperature and viscosity into Equations (A.9) and (A.10) yields the following two nonlinearly coupled equations:

$$\nu(\eta) f'''(\eta) + \frac{1}{2} f(\eta) f''(\eta) + \nu'(\eta) f''(\eta) = 0 \quad (\text{A.13})$$

$$H''(\eta) + \frac{Pr}{2} f(\eta) H'(\eta) = 0 . \quad (\text{A.14})$$

The empirical relationship given in Chapter 3 for the viscosity is used in the calculation here. The viscosity derivative  $\nu'(\eta)$  is rewritten as

$$\nu'(\eta) = \frac{d\nu}{dH} H'. \quad (\text{A.15})$$

The boundary conditions for the momentum equations are

$$f(0) = 0 \quad (\text{A.16a})$$

$$f'(0) = 0 \quad (\text{A.16b})$$

$$f'(\infty) = 1 \quad (\text{A.16c})$$

and the boundary conditions for the energy equation are

$$H(0) = 1 \quad (\text{A.17a})$$

$$H(\infty) = 0. \quad (\text{A.17b})$$

These boundary conditions follow those given in Chapter 4 for uniform wall heating.

Equations (A.13) and (A.14) are numerically integrated using the fourth order Runge-Kutta shooting method. Since the two equations are nonlinearly coupled through the viscosity dependence on temperature, the iteration of the equations required for the initial value shooting approach is combined with the iteration required due to the coupling. Once  $f(\eta)$  and  $H(\eta)$  are obtained, the velocities  $\bar{u}(\bar{x}, \bar{y})$ ,  $\bar{v}(\bar{x}, \bar{y})$ , the vorticity  $\bar{\omega}_z(\bar{x}, \bar{y})$ , and the temperature  $\bar{T}(\bar{x}, \bar{y})$  are determined from Equations (A.6), (A.7), (A.8), and (A.11).

## APPENDIX B

SOLUTION OF THE THREE-DIMENSIONAL  
ORR-SOMMERFELD EQUATION

The Orr-Sommerfeld equation governs the linear stability of a viscous fluid with mean velocity  $\bar{U}(\bar{y})$ . The three-dimensional Orr-Sommerfeld equation was shown in Chapter 1 and is repeated here for convenience:

$$\left(\bar{U} - \frac{\bar{\beta}}{\bar{\alpha}}\right) \left[\bar{v}''(\bar{y}) - \bar{\alpha}^2 \bar{v}(\bar{y})\right] - \bar{U}'' \bar{v}(\bar{y}) = -\frac{i}{\bar{\alpha} Re_{\delta_1}} \left[\bar{v}''''(\bar{y}) - 2\bar{\alpha}^2 \bar{v}''(\bar{y}) + \bar{\alpha}^4 \bar{v}(\bar{y})\right] \quad (\text{B.1})$$

where

$$\bar{\alpha} = \sqrt{\alpha^2 + \gamma^2}.$$

The primes denote differentiation with respect to  $\bar{y}$ . This three-dimensional Orr-Sommerfeld equation relates the stability of three-dimensional disturbances in the form of oblique waves:

$$\bar{v}'(\bar{x}, \bar{y}, \bar{z}, \bar{t}) = \bar{v}(\bar{y}) e^{i(\bar{\alpha}\bar{x} + \bar{\gamma}\bar{z} - \bar{\beta}\bar{t})} \quad (\text{B.2})$$

where the prime here denotes a disturbance quantity. The three-dimensional Orr-Sommerfeld equation reduces to the two-dimensional Orr-Sommerfeld equation for  $\bar{\gamma} = 0$ . The dimensionless variables in (B.1) and (B.2) are denoted by the superscript “ $\bar{\cdot}$ ” so that confusion can be avoided in comparing with the scaling used in the previous chapters. The nondimensionalization is defined as follows:

$$\bar{x} = \frac{x}{\delta_1}, \quad \bar{y} = \frac{y}{\delta_1}, \quad \bar{z} = \frac{z}{\delta_1},$$



$$\begin{aligned}
\bar{t} &= \frac{\bar{t} \bar{U}_\infty}{\bar{\delta}_1}, & \bar{U} &= \frac{\bar{U}}{\bar{U}_\infty}, & \bar{v}' &= \frac{\bar{v}'}{\bar{U}_\infty}, \\
\bar{\alpha} &= \bar{\alpha} \bar{\delta}_1, & \bar{\gamma} &= \bar{\gamma} \bar{\delta}_1, & \bar{\beta} &= \frac{\bar{\beta} \bar{\delta}_1}{\bar{U}_\infty}, \\
Re_{\delta_1} &= \frac{\bar{U}_\infty \bar{\delta}_1}{\bar{\nu}_\infty}.
\end{aligned} \tag{B.3a}$$

The length scale  $\bar{\delta}_1$  is the boundary layer displacement thickness of the velocity profile  $\bar{U}(\bar{y})$ .

The Orr-Sommerfeld equation is an eigenvalue problem whose eigenvalue is either  $\bar{\alpha}$  or  $\bar{\beta}$ , depending on spatial or temporal stability theory. A discussion of linear theory was given in Chapter 1. Spatial stability theory is considered here, where  $\bar{\beta}$  is a purely real constant and the solution of Equation (B.1) yields the complex eigenvalue  $\bar{\alpha} = \bar{\alpha}_r + i \bar{\alpha}_i$  and the complex eigenfunction  $\bar{v}(\bar{y})$ . The real part  $\bar{\alpha}_r$  is the wave number and the imaginary part  $-\bar{\alpha}_i$  is the amplification rate.

Once the perturbation velocity  $\bar{v}'$  is known, the other perturbation components  $\bar{u}'$ ,  $\bar{w}'$ ,  $\bar{\omega}'_x$ ,  $\bar{\omega}'_y$ , and  $\bar{\omega}'_z$  can be found. These five components are nondimensionalized as follows:

$$\begin{aligned}
\bar{u}' &= \frac{\bar{u}'}{\bar{U}_\infty}, & \bar{w}' &= \frac{\bar{w}'}{\bar{U}_\infty}, \\
\bar{\omega}'_x &= \frac{\bar{\omega}'_x \bar{\delta}_1}{\bar{U}_\infty}, & \bar{\omega}'_y &= \frac{\bar{\omega}'_y \bar{\delta}_1}{\bar{U}_\infty}, & \bar{\omega}'_z &= \frac{\bar{\omega}'_z \bar{\delta}_1}{\bar{U}_\infty}.
\end{aligned} \tag{B.3b}$$

First the  $\omega_y$  vorticity transport equation (Equation 3.68) known as Squire's equation must be solved. Squire's equation is found by considering a procedure analogous to the Orr-Sommerfeld equation. The three-dimensional travelling wave ansatz is again used for all components and after linearizing the following equation results:

$$\left\{ \frac{1}{Re_{\delta_1}} \left[ \frac{\partial^2}{\partial \bar{y}^2} - \bar{\alpha}^2 \right] - i \bar{\alpha} \left[ \bar{U} - \frac{\bar{\beta}}{\bar{\alpha}} \right] \right\} \bar{\omega}_y(\bar{y}) = -i \bar{\gamma} \bar{U}' \bar{v}(\bar{y}). \tag{B.4}$$

This ordinary differential equation for  $\hat{\omega}_y(\tilde{y})$  contains a forcing term on the right hand side. Once Equation (B.4) is solved for  $\hat{\omega}_y(\tilde{y})$  the remaining flow components can be calculated. First the  $\tilde{u}'$  perturbation velocity is calculated using the  $u$  Poisson equation (3.71), or

$$\hat{u}(\tilde{y}) = \frac{1}{\tilde{\alpha}^2} \left[ i \tilde{\alpha} \frac{\partial \hat{v}(\tilde{y})}{\partial \tilde{y}} + i \tilde{\gamma} \hat{\omega}_y(\tilde{y}) \right]. \quad (\text{B.5})$$

The  $\tilde{w}'$  perturbation velocity is calculated next from the  $w$  Poisson equation (3.73):

$$\hat{w}(\tilde{y}) = \frac{1}{\tilde{\alpha}^2} \left[ i \tilde{\gamma} \frac{\partial \hat{v}(\tilde{y})}{\partial \tilde{y}} - i \tilde{\alpha} \hat{\omega}_y(\tilde{y}) \right]. \quad (\text{B.6})$$

Finally, the  $\tilde{\omega}'_x$  and  $\tilde{\omega}'_z$  vorticities are calculated using the  $v$  Poisson equation (3.72) and the zero vorticity divergence condition (3.70) so that

$$\hat{\omega}_x(\tilde{y}) = \frac{1}{\tilde{\alpha}^2} \left[ i \tilde{\alpha} \frac{\partial \hat{\omega}_y(\tilde{y})}{\partial \tilde{y}} - i \tilde{\gamma} \tilde{\nabla}^2 \hat{v}_y(\tilde{y}) \right] \quad (\text{B.7})$$

and

$$\hat{\omega}_z(\tilde{y}) = \frac{1}{\tilde{\alpha}^2} \left[ i \tilde{\gamma} \frac{\partial \hat{\omega}_y(\tilde{y})}{\partial \tilde{y}} + i \tilde{\alpha} \tilde{\nabla}^2 \hat{v}_y(\tilde{y}) \right] \quad (\text{B.8})$$

where

$$\tilde{\nabla}^2 = \frac{\partial^2 \hat{v}(\tilde{y})}{\partial \tilde{y}^2} - \tilde{\alpha}^2 \hat{v}(\tilde{y}).$$

Once the eigenfunctions are computed, the more convenient form of amplitude and phase distributions are calculated, e.g.,

$$\tilde{A}_\phi = \sqrt{(\Re[\hat{v}(\tilde{y})])^2 + (\Im[\hat{v}(\tilde{y})])^2} \quad (\text{B.9})$$

$$\tilde{\phi}_\phi = \tan^{-1} \left( \frac{\Im[\hat{v}(\tilde{y})]}{\Re[\hat{v}(\tilde{y})]} \right). \quad (\text{B.10})$$

Expressions analogous to (B.9) and (B.10) hold for all other flow components. Since (B.1) is an eigenvalue problem, any constant multiple of Equation (B.2) is also a solution. Therefore, the perturbations can be scaled by any arbitrary

amplitude. For comparison with the Navier-Stokes solution of this work (for the unheated boundary layer only), a scale factor  $c_{LST}$  was introduced in Chapter 6. The nondimensionalization of the Navier-Stokes equations is different than that used for the Orr-Sommerfeld equation. The proper conversions are shown below, including the scale factor:

$$\begin{aligned} x &= \frac{Re_{\delta_1}}{Re} \bar{x}, & y &= \frac{Re_{\delta_1}}{\sqrt{Re}} \bar{y}, & z &= \frac{Re_{\delta_1}}{Re} \bar{z}, \\ t &= \frac{Re_{\delta_1}}{Re} \bar{t}, & \alpha &= \frac{Re}{Re_{\delta_1}} \bar{\alpha}, & \gamma &= \frac{Re}{Re_{\delta_1}} \bar{\gamma}, & \beta &= \frac{Re}{Re_{\delta_1}} \bar{\beta}, \\ u' &= c_{LST} \bar{u}', & v' &= c_{LST} \sqrt{Re} \bar{v}', & w' &= c_{LST} \bar{w}', \\ \omega'_x &= c_{LST} \frac{\sqrt{Re}}{Re_{\delta_1}} \bar{\omega}'_x, & \omega'_y &= c_{LST} \frac{Re}{Re_{\delta_1}} \bar{\omega}'_y, & \omega'_z &= c_{LST} \frac{\sqrt{Re}}{Re_{\delta_1}} \bar{\omega}'_z. \end{aligned} \quad (B.11)$$

The solution technique applied to (B.1) is a direct fourth order finite difference method developed by Thomas (1953) and described in detail by Kurtz and Crandall (1962). A short description of the solution technique is given. The boundary conditions employed for Equation (B.1) are first shown. At the wall, the no slip condition and continuity equation are enforced:

$$\hat{v}(0) = 0 \quad (B.12a)$$

$$\hat{v}'(0) = 0. \quad (B.12b)$$

For the boundary layer profile,  $\bar{U}(\bar{y}) \rightarrow 1$  and  $\bar{U}''(\bar{y}) \rightarrow 0$  as  $\bar{y} \rightarrow \infty$ . The Orr-Sommerfeld equation (B.1) thus becomes

$$\begin{aligned} \hat{v}''''(\bar{y}) + \left[ i \left( \bar{\alpha} - \bar{\beta} \right) Re_{\delta_1} - 2 \bar{\alpha}^2 \right] \hat{v}''(\bar{y}) \\ + \left[ -i \left( \bar{\alpha} - \bar{\beta} \right) Re_{\delta_1} \bar{\alpha}^2 + \bar{\alpha}^4 \right] = 0. \end{aligned} \quad (B.13)$$

The general solution of this equation is

$$\hat{v}(\bar{y}) = A e^{-\bar{\alpha} \bar{y}} + B e^{+\bar{\alpha} \bar{y}} + C e^{-\bar{\kappa} \bar{y}} + D e^{+\bar{\kappa} \bar{y}}, \quad (B.14)$$

where

$$\bar{\kappa}^2 = \bar{\alpha}^2 + i Re_{\delta_1} (\bar{\alpha} - \bar{\beta})$$

but by physical considerations  $\hat{v} \rightarrow 0$  as  $\bar{y} \rightarrow \infty$  and generally  $|\bar{\kappa}| \gg |\bar{\alpha}|$ . These considerations yield the following gradient conditions:

$$\hat{v}'(\infty) = -\bar{\alpha}\hat{v}(\infty) \quad (B.15a)$$

$$\hat{v}''(\infty) = \bar{\alpha}^2 \hat{v}(\infty). \quad (B.15b)$$

The prime denotes differentiation with respect to  $\bar{y}$ .

The finite difference equation system is of the form  $A g(\hat{v}) = \bar{c} B g(\hat{v})$  where  $A$  and  $B$  are complex matrices. An IMSL library routine EIGZC is used to obtain the eigenvalues  $\bar{c}$  and eigenvectors  $\hat{v}$ . The most unstable eigenvalue is sought. Thus, given a  $\bar{\beta} = \bar{\beta}_r$ ,  $\bar{\gamma} = \bar{\gamma}_r$ ,  $Re_{\delta_1}$ , and an initial guess of  $\bar{\alpha} = \bar{\alpha}_r + i \bar{\alpha}_i$ , Equation (B.1) with boundary conditions (B.12) and (B.15) is solved using the direct method of Thomas (1953). The solution domain covers, e.g.,  $0 \leq \bar{y} \leq 10$ . Since the solution of the Orr-Sommerfeld equation gives the complex phase speed  $\bar{c} = \frac{\bar{\beta}}{\bar{\alpha}}$ , iteration is required to make  $\bar{F} \rightarrow 0$  where  $\bar{F} = \bar{\alpha}\bar{c} - \bar{\beta}$ . A complex secant method is used to refine the iterates of  $\bar{\alpha}$ :

$$\bar{\alpha}^{i+1} = \bar{\alpha}^i - \bar{F}^i \frac{\bar{\alpha}^i - \bar{\alpha}^{i-1}}{\bar{F}^i - \bar{F}^{i-1}} \quad (B.18)$$

where "i" denotes the iteration level.

The remaining equations for the other perturbation components are solved with the same fourth order finite difference molecule for consistency. Boundary conditions are needed for Equation (B.4) for the  $\omega'_y$  vorticity. The following boundary conditions are consistent with those presented in Chapter 4:

$$\hat{\omega}_y(0) = 0 \quad (B.19a)$$

$$\hat{\omega}_y(\infty) = 0. \quad (B.19b)$$

The remaining perturbation components are computed directly from the corresponding equations.

## REFERENCES

- Antonatos, P. P. (1966). "Laminar Flow Control - Concepts and Applications," *Astronautics and Aeronautics*, pp. 32-36, July.
- Asrar, W. and A. H. Nayfeh (1985). "Nonparallel Stability of Heated Two-Dimensional Boundary Layers," *Phys. Fluids*, 28, No. 5, pp. 1263-1272.
- Barker, S. J. and C. Jennings (1977). "The Effect of Wall Heating Upon Transition," *Proc. AGARD Symposium on Laminar-Turbulent Transition*, Copenhagen, Denmark.
- Barker, S. J. (1979). "Experiments on Heat-Stabilized Boundary Layers in a Tube," *Proc. of the Twelfth Symposium on Naval Hydrodynamics*, (National Academy of Sciences, Washington, D.C.), pp. 77-85.
- Bayliss, A., L. Maestrello, P. Parikh, and E. Turkel (1985). "Numerical Simulation of Boundary Layer Excitation by Surface Heating/Cooling," AIAA Paper 85-0565.
- Bestek, H., P. Dittrich, H. Fasel (1987). "Einfluß der Wandtemperatur auf die Entwicklung von Tollmien-Schlichting-Wellen in Grenzschichtströmungen," *ZAMM*, 67, No. 5, pp. 256-258.
- Biringen, S. (1984). "Active Control of Transition by Periodic Suction-Blowing," *Phys. Fluids*, 27, No. 6, pp. 1345-1347.
- Biringen, S., W. E. Nutt, and M. J. Caruso (1985). "Transition Control by Periodic Suction-Blowing," AIAA Paper 85-1700.
- Blasius, H. (1908). "Grenzschichten in Flüssigkeiten mit Kleiner Reibung," *Z. Math. Phys.*, 56, pp. 1-37 (Engl. trans. NACA TM 1256).
- Bower, W. W., J. T. Kegelmann, A. Pal, and G. H. Meyer (1987). "A Numerical Study of Two-Dimensional Instability-Wave Control Based on the Orr-Sommerfeld Equation," *Phys. Fluids*, 30, No. 4, pp. 998-1004.
- Bower, W. W., A. Pal, and G. H. Meyer (1987). "Computations of Two-Dimensional Instability-Wave Control Through Surface Heating," *Proc. of the Twentieth Midwestern Mechanics Conference*, Purdue University.
- Bower, W. W., A. Pal, A. B. Cain, and G. H. Meyer (1988). "Two-Dimensional Multifrequency Instability Suppression Via Surface Mass Transfer: Linear Theory and Its Application," *Proc. of the Sixth Int. Conf. on Mathematical Modelling*, St. Louis, MO, August.
- Bushnell, D. M. (1983). "Turbulent Drag Reduction for External Flows," AIAA Paper 83-0227.

- Bushnell, D. M., and M. R. Malik (1985). "Application of Stability Theory to Laminar Flow Control - Progress and Requirements," ICASE/NASA Workshop on Stability of Time Dependent and Spatially Varying Flows.
- Craik, A. D. D. (1971). "Non-Linear Resonant Instability in Boundary Layers," *J. Fluid Mech.*, 50, pp. 393-413.
- Dittrich, P. A. (1985). "Numerische Integration der Navier-Stokes- und der Energiegleichung zur Untersuchung der Stabilität der Grenzschichtströmung Entlang einer Beheizten oder Gekühlten Ebenen Platte," Diplomarbeit, Universität Stuttgart.
- Dittrich, P. A. (1988). *Private Communication*.
- El-Hady, N. M. and A. H. Nayfeh (1979). "Nonparallel Stability of Two-Dimensional Heated Boundary Layer Flows," *Proc. of the Twelfth Symposium on Naval Hydrodynamics*, (National Academy of Sciences, Washington, D.C.), pp. 53-62.
- Fasel, H. (1974). "Untersuchungen zum Problem des Grenzschichtumschlages durch Numerische Integration der Navier-Stokes Gleichungen," Dissertation, Universität Stuttgart.
- Fasel, H. (1976). "Investigation of the Stability of Boundary Layers by a Finite-Difference Model of the Navier-Stokes Equations," *J. Fluid Mech.*, 78, pp. 355-383.
- Fasel, H., H. Bestek, and R. Schefenacker (1977). "Numerical Simulation Studies of Transitional Phenomena in Incompressible, Two-Dimensional Flows," *Proc. AGARD Symposium on Laminar-Turbulent Transition*, Copenhagen, Denmark.
- Fasel, H. and H. Bestek (1980). "Investigation of Nonlinear, Spatial Disturbance Amplification in Plane Poiseuille Flow," *Proc. IUTAM Symposium on Laminar-Turbulent Transition*, Stuttgart, West Germany, pp. 173-185.
- Fasel, H., U. Rist, and U. Konzelmann (1987). "Numerical Investigation of the Three-Dimensional Development in Boundary Layer Transition," AIAA Paper 87-1203.
- Gaster, M. (1962). "A Note on the Relation Between Temporally-Increasing and Spatially-Increasing Disturbances in Hydrodynamic Stability," *J. Fluid Mech.*, 14, pp. 222-224.
- Gaster, M. (1974). "On the Effects of Boundary-Layer Growth on Flow Stability," *J. Fluid Mech.*, 66, pp. 465-480.
- Gaster, M. (1986). *Private Communication per Uwe Konzelmann*.
- Gazley, C. Jr. and A. R. Wazzan (1985). "Control of Water Boundary Layer Stability and Transition by Surface Temperature Distribution," *Proc. of the*

Second IUTAM Symposium on Laminar-Turbulent Transition, Novosibirsk, USSR.

- Gedney, C. J. (1983). "The Cancellation of a Sound-Excited Tollmien-Schlichting Wave with Plate Vibration," *Phys. Fluids*, **26**, No. 5, pp. 1158-1160.
- Gottlieb, D. and S. A. Orszag (1977). *Numerical Analysis of Spectral Methods: Theory and Applications*, SIAM, Philadelphia.
- Hardy, R. C. and R. C. Cottingham (1949). *J. Res. NBS*, **42**, p. 573.
- Hauptmann, E. G. (1968). "The Influence of Temperature Dependent Viscosity on Laminar Boundary-Layer Stability," *Int. J. Heat Mass Transfer*, **11**, pp. 1049-1052.
- Hefner, J. N. (1988). "Dragging Down Fuel Costs," *Aerospace America*, pp. 14-16, January.
- Heinrich, R. A., M. Choudari, and E. J. Kerschen (1988). "A Comparison of Boundary Layer Receptivity Mechanisms," *Proc. of the 1st National Fluid Dynamics Congress*, AIAA/ASME/SIAM/APS Paper 88-3758, Cincinnati, Ohio, July 25-28.
- Herbert, T. (1984). "Analysis of the Subharmonic Route to Transition in Boundary Layers," AIAA Paper 84-0009.
- Herbert, T. (1985). "Three-Dimensional Phenomena in the Transitional Flat-Plate Boundary Layer," AIAA Paper 85-0489.
- Jordinson, R. (1970). "The Flat Plate Boundary Layer. Part 1. Numerical Integration of the Orr-Sommerfeld Equation," *J. Fluid Mech.*, **43**, pp. 801-811.
- Kachanov, Yu. S., and V. Ya. Levchenko (1984). "The Resonant Interaction of Disturbances at Laminar-Turbulent Transition in a Boundary Layer," *J. Fluid Mech.*, **138**, pp. 209-247.
- Klebanoff, P. S., K. D. Tidstrom, and L. M. Sargent (1962). "The Three-Dimensional Nature of Boundary-Layer Instability," *J. Fluid Mech.*, **12**, pp. 1-41.
- Kleiser, L. and E. Laurien (1984). "Three-Dimensional Numerical Simulation of Laminar-Turbulent Transition and its Control by Periodic Disturbances," *Proc. of the Second IUTAM Symposium on Laminar-Turbulent Transition*, Novosibirsk, USSR.
- Kleiser, L. and E. Laurien (1985). "Numerical Investigation of Interactive Transition Control," AIAA Paper 85-0566.
- Kovaszny, L. S. G., H. Komoda, and B. R. Vasudeva (1962). "Detailed Flow Field in Transition," *Proc. Heat Transfer and Fluid Mech. Institute*, pp. 1-26.

- Kurtz, E. and S. Crandall (1962). "Computer-Aided Analysis of Hydrodynamic Stability," *J. Math. Phys.*, 41, pp. 264-279.
- Laurien, E. and L. Kleiser (1985). "Numerical Simulation of Transition Control in Boundary Layers," *Proc. of the Sixth GAMM Conference on Numerical Methods in Fluid Mechanics*, Göttingen, West Germany.
- Laurien, E. (1985). "Numerische Simulation zur Aktiven Beeinflussung des Laminar-Turbulenten Übergangs in der Plattengrenzschichtströmung," Dissertation, Universität Karlsruhe.
- Liepmann, H. W. and G. H. Fila (1946). "Investigations of Effects of Surface Temperature and Single Roughness Elements on Boundary-Layer Transition," NACA Report No. 890, pp. 587-598.
- Liepmann, H. W., G. L. Brown, and D. M. Nosenchuck (1982). "Control of Laminar-Instability Waves Using a New Technique," *J. Fluid Mech.*, 118, pp. 187-200.
- Liepmann, H. W. and D. M. Nosenchuck (1982). "Active Control of Laminar-Turbulent Transition," *J. Fluid Mech.*, 118, pp. 201-204.
- Liepmann, H. W. and D. M. Nosenchuck (1983). *Private Communication*.
- Lowell, R. L. (1974). "Numerical Study of the Stability of a Heated, Water Boundary Layer," Dissertation, Case Western Reserve University.
- Maestrello, L. (1984). "Analysis of Active Control by Surface Heating," AIAA Paper 84-0173.
- Maestrello, L. (1985). "Active Transition Fixing and Control of the Boundary Layer in Air," AIAA Paper 85-0564.
- McMurray, J. T., R. W. Metcalfe, and J. J. Riley (1983). "Direct Numerical Simulations of Active Stabilization of Boundary Layer Flows," *Proc. of the Eighth Biennial Symposium on Turbulence*, University of Missouri-Rolla.
- Metcalfe, R. W., C. Rutland, J. H. Duncan, and J. J. Riley (1985). "Numerical Simulations of Active Stabilization of Laminar Boundary Layers," AIAA Paper 85-0567.
- Milling, R. W. (1981). "Tollmien-Schlichting Wave Cancellation," *Phys. Fluids*, 24, No. 5, pp. 979-981.
- Morkovin, M. V. (1969). "Critical Evaluation of Transition from Laminar to Turbulent Shear Layers with Emphasis on Hypersonically Travelling Bodies," Air Force Flight Dynamics Laboratory Report AFFDL-TR-68-149.
- Nayfeh, A. H. and N. M. El-Hady (1980). "Nonparallel Stability of Two-Dimensional Nonuniformly Heated Boundary-Layer Flows," *Phys. Fluids*, 23, No. 1, pp. 10-18.



- Nenni, J. P. and G. L. Gluyas (1966). "Aerodynamic Design and Analysis of an LFC Surface," *Astronautics and Aeronautics*, pp. 32-36, July.
- Nosenchuck, D. M. (1982). "Passive and Active Control of Boundary Layer Transition," Dissertation, California Institute of Technology.
- Orr, W. M. F. (1907). "The Stability of the Steady Motions of a Perfect Liquid and of a Viscous Liquid. Part I: A Perfect Liquid; Part II: A Viscous Liquid," *Proc. of the Royal Irish Academy*, 27, pp. 9-138.
- Pal, A., W. W. Bower, A. B. Cain, and G. H. Meyer (1988). "Numerical Simulations of Instability-Wave Suppression in the Blasius Boundary Layer," *Proc. of the Eleventh Symposium on Turbulence*, University of Missouri-Rolla, October 17-19.
- Pfenninger, W. and V. D. Reed (1966). "Laminar-Flow Research and Experiments," *Astronautics and Aeronautics*, pp. 32-36, July.
- Rayleigh, Lord (1880). "On the Stability, or Instability, of Certain Fluid Motions," *Proc. London Math Soc.*, 11, pp. 57-70.
- Reshotko, E. (1976). "Boundary-Layer Stability and Transition," *Ann. Rev. Fluid Mech.*, 8, pp. 311-349.
- Reshotko, E. (1979). "Drag Reduction by Cooling in Hydrogen-Fueled Aircraft," *Jour. Aircraft*, 16, No. 9, pp. 584-590.
- Robey, H. F. III (1986). "On the Nature of Oblique Instability Waves in Boundary Layer Transition," Dissertation, California Institute of Technology.
- Ross, J. A., F. H. Barnes, J. G. Burns, and M. A. S. Ross (1970). "The Flat Plate Boundary Layer. Part 3. Comparison of Theory with Experiment," *J. Fluid Mech.*, 43, pp. 819-832.
- Saric, W. S. and H. L. Reed (1983). "Effect of Suction and Blowing on Boundary-Layer Transition," AIAA Paper 83-0043.
- Saric, W. S. and A. S. W. Thomas (1983). "Experiments on the Subharmonic Route to Turbulence in Boundary Layers," *Proc. IUTAM Symposium on Turbulence and Chaotic Phenomena in Fluids*, Kyoto, Japan.
- Saric, W. S., V. V. Kozlov, and V. Ya. Levchenko (1984). "Forced and Unforced Subharmonic Resonance in Boundary-Layer Transition," AIAA Paper 84-0007.
- Schilz, W. (1965/66). "Experimentelle Untersuchungen zur Akustischen Beeinflussung der Strömungsgrenzschicht in Luft," *Acustica*, 16, pp. 208-223.
- Schubauer, G. B. and H. K. Skramstad (1948). "Laminar Boundary-Layer Oscillations and Transition on a Flat Plate," NACA Report No. 909, pp. 327-357.

- Smith, G. D. (1978). *Numerical Solution of Partial Differential Equations: Finite Difference Methods*, 2nd Ed., Oxford University Press, Oxford.
- Sommerfeld, A. (1908). "Ein Beitrag zur Hydrodynamischen Erklärung der Turbulenten Flüssigkeitsbewegungen," *Atti. del Fourth Congr. Internat. dei Math.*, 3, pp. 116-124, Rome.
- Spalart, P. R. and K.-S. Yang (1986). "Numerical Simulation of Boundary Layers: Part 2. Ribbon-Induced Transition in Blasius Flow," NASA TM 88221.
- Squire, H. B. (1933). "On the Stability for Three-Dimensional Disturbances of Viscous Fluid Flow Between Parallel Walls," *Proc. Roy. Soc. A.*, 142, pp. 621-628.
- Strazisar, A. J., E. Reshotko, and J. M. Pahl (1977). "Experimental Study of the Stability of Heated Laminar Boundary Layers in Water," *J. Fluid Mech.*, 83, pp. 225-247.
- Strazisar, A. J. and E. Reshotko (1978). "Stability of Heated Laminar Boundary Layers in Water with Nonuniform Surface Temperature," *Phys. Fluids*, 21, No. 5, pp. 727-735.
- Strykowski, P. J. and K. R. Sreenivasan (1985). "The Control of Transitional Flows," AIAA Paper 85-0559.
- Swindells, J. F. (1982). NBS, unpublished results (From *CRC Handbook of Chemistry and Physics*, 63rd Ed., 1982-83, p. F-40, CRC Press).
- Thomas, A. S. W. (1983). "The Control of Boundary-Layer Transition Using a Wave-Superposition Principle," *J. Fluid Mech.*, 137, pp. 233-250.
- Thomas, L. H. (1949). "Elliptic Problems in Linear Difference Equations over a Network," Watson Scientific Computing Laboratory Report, Columbia University, New York.
- Thomas, L. H. (1953). "The Stability of Plane Poiseuille Flow," *Physical Review*, 91, No. 4, pp. 780-783.
- Wagner, R. D. and M. C. Fischer (1983). "Developments in the NASA Transport Aircraft Laminar Flow Program," AIAA Paper 83-0090.
- Wazzan, A. R., T. T. Okamura, and A. M. O. Smith (1968). "The Stability of Water Flow Over Heated and Cooled Flat Plates," *J. of Heat Transfer*, pp. 109-114, February.
- Wazzan, A. R., T. T. Okamura, and A. M. O. Smith (1970a). "The Stability of Incompressible Flat Plate Laminar Boundary Layer in Water with Temperature Dependent Viscosity," *Proc. Southeastern Seminar on Thermal Sciences*.

- Wazzan, A. R., T. T. Okamura, and A. M. O. Smith (1970b). "The Stability and Transition of Heated and Cooled Incompressible Laminar Boundary Layers," *Proc. of the Fourth International Heat Transfer Conference*.
- Wehrmann, O. H. (1965). "Tollmien-Schlichting Waves under the Influence of a Flexible Wall," *Phys. Fluids*, 8, pp. 1389-1390.
- Whites, R. C., R. W. Sudderth, and W. G. Wheldon (1966). "Laminar Flow Control on the X-21," *Astronautics and Aeronautics*, pp. 32-36, July.
- Williams, D. R., H. Fasel, and F. R. Hama (1984). "Experimental Determination of the Three-Dimensional Vorticity Field in the Boundary-Layer Transition Process," *J. Fluid Mech.*, 149, pp. 179-203.
- Wray, A. and M. Y. Hussaini (1984). "Numerical Experiments in Boundary-Layer Stability," *Proc. R. Soc. Lond. A*, 392, pp. 373-389.
- Zang, T. A., and M. Y. Hussaini (1985a). "Numerical Experiments on Subcritical Transition Mechanism," AIAA Paper 85-0296.
- Zang, T. A., and M. Y. Hussaini (1985b). "Numerical Experiments on the Stability of Controlled Shear Flows," AIAA Paper 85-1698.